Application of Micro Perforated and Impervious Membranes for Noise Barriers

Chenxi Li

School of Mechanical Engineering

The University of Adelaide

South Australia 5005

Australia

A thesis submitted for the degree of Doctor of Philosophy on the 5th of February 2016.

Contents

Abstract

Membrane materials have been commonly used for decades in buildings. When acoustic environments are concerned, the acoustic properties of these membrane structures are of special interest.

This thesis aims to investigate acoustic properties of micro perforated membranes (MPMs) and impervious membranes and enhance the sound insulation of double layer impervious membranes by combining these with MPMs, thereby increasing the internal loss mechanisms of what is essentially a reactive wall. This thesis firstly develops a new model of an impervious membrane, taking into consideration the tension and the internal damping due to the membrane curvature.

The sound absorption of MPMs inserted between the impervious layers has been studied by introducing a new boundary condition where the particle velocity at the hole wall boundary is assumed to be equal to the membrane vibration velocity. The comparison between the predicted and measured results demonstrates that MPM 1 to 3 can be considered impervious due to their sufficiently small perforation radii, and MPM 4 is sound absorbing due to its larger perforations.

Non-linear sound absorption of MPM 4 has been observed in the experiments. It was found that the non-linear sound absorption coefficient is strongly dependent on both the magnitude of the SPLs and the waveform of the excitation. Two analytical models were developed for the non-linear acoustic impedance of MPMs. In the first model, the non-linear impedance of MPMs is considered to be the sum of the linear impedance, and the non-linear acoustic impedance dependent on the particle velocity within the perforations. The second analytical model presented is inspired by the air motion equation and the mass continuity equation considering the density variation in the time and spatial domains, and provides the most accurate predicted results among the models considered in this study.

The analytical models have been developed to predict the STL of double layer impervious membranes separated by a finite-sized air cavity, taking into consideration the fluid-structure coupling on each membrane surface. Comparing the predicted results to the measured STLs,

it is found that considering the sound absorbing boundaries of the cavity can enhance the accuracy of the models.

STL measurements of double layer impervious membranes with four types of MPMs have been conducted in a diffuse field to quantify the effectiveness of the MPM insertion. The experimental results indicate that the MPM insertion can enhance the STL of the double layer impervious membranes significantly at frequencies above the first resonance frequency of the air cavity. MPMs 1 to 3 have similar main impacts on the STLs, however, MPM 4 has a different effect because of its larger perforations.

The normal incidence and diffuse field models for the double layer impervious membranes with inserted MPMs 1 to 3 were developed and the predicted results were compared with the experimental results. The models with MPM 4 were developed by taking into consideration the acoustic impedance of the MPM 4 due to its perforations. These developed models can be used as tools for design of membrane structures.

Statement of Originality

I certify that this work contains no material which has been accepted for the award of any other degree or diploma in any university or other tertiary institution and, to the best of my knowledge and belief, contains no material previously published or written by another person, except where due reference has been made in the text. In addition, I certify that no part of this work will, in the future, be used in a submission for any other degree or diploma in any university or other tertiary institution without the prior approval of the University of Adelaide and where applicable, any partner institution responsible for the joint-award of this degree.

I give consent to this copy of my thesis when deposited in the University Library, being made available for loan and photocopying, subject to the provisions of the Copyright Act 1968.

The author acknowledges that copyright of published works contained within this thesis resides with the copyright holder(s) of those works.

I also give permission for the digital version of my thesis to be made available on the web, via the University's digital research repository, the Library catalogue and also through web search engines, unless permission has been granted by the University to restrict access for a period of time.

Chenxi Li

Acknowledgements

I would like to acknowledge all the people who contributed to this thesis and supported me in the last four years. I would like to thank the China Scholar Council (CSC) and the University of Adelaide for the scholarships I received while doing my PhD project.

First and foremost, I would like to give acknowledgement to my supervisors Professor Ben Cazzolato and Associate Professor Anthony Zander. This thesis could not be accomplished without their help, guidance and support.

I also thank Associate Professor Carl Howard for his suggestions about ANSYS; Dr Will Robertson, Dr Tao Zhu and Dr Peter Lanspeary for their assistance with experiments; and Dr Boyin Ding for his advice on both academic and daily life. I would like to give acknowledgement to Dr Zhao Tian and Mr Xiao Chen for their patience answering my silly questions on fluid dynamics. I would like to thank Mr Md Ayub for proofreading sections of this thesis, Dr Akhilesh Mimani for the discussions about 3-D sound propagation in a cavity, and my colleagues who share the office with me for the enjoyable time we spent together.

I wish to acknowledge the assistance of Dr Erwin Gamboa and Associate Professor Reza Ghomashchi for measuring the radii of the MPM sample perforations. I'm also very grateful to the staff of the electronic and mechanical workshops in the School of Mechanical Engineering at the University of Adelaide for their assistance when manufacturing the samples and equipment used in this thesis. I would like to give special thanks to my lab neighbours, the staff of the electronic workshop, for their suffering of the loud noises I generated in the STL and non-linear sound absorption experiments.

I'm thankful to Dr Robyn Groves in the Writing Centre at the University of Adelaide and Ms Alison-Jane Hunter for assisting me with my academic writing for this thesis and the journal papers arising from this thesis. I wish to acknowledge the staff in the administration office and the finance team in the School of Mechanical Engineering, for their support over the last four years.

I wish to express my warm thanks to my friends for their friendship. Finally, I would like to thank my family for their encouragement and understanding.

List of Figures

List of Tables

List of Symbols

η	Damping ratio	11
ξ	Membrane vibration displacement	11
t	Time variable	11
T	Tension per unit length	11
T_0	Real static tension	11
x	Position coordinate in x-axis	13
y	Position coordinate in y-axis	13
ρ_s	Surface density of membrane	13
ω	Angular frequency	14
∇^2	Two dimensional Laplace operator	14
R	Radial position in the polar coordinate system	14
η	Internal damping ratio	16
ρ_{string}	Mass per unit length of the string	16
R_0	Radius of a circular membrane	20
p_i	Incident sound pressure	20
p_r	Reflected sound pressure	20
p_t	Transmitted sound pressure	20
Δp	Differential sound pressure applied across the membrane surface	20
J_0	Bessel function of the first kind and zero order	22
J_1	Bessel function of the first kind and first order	25
ρ_0	Density of air	26
c_0	Speed of sound	26
D	Depth of air cavity	26
Re	Real part of impedance, resistance	26
Im	Imaginary part of impedance, reactance	26
l_x	The width of the rectangular membrane	29
l_y	The height of the rectangular membrane	29

$X(x)$	Function of the membrane displacement only related to the x coordinate	29
$Y(y)$	Function of the membrane displacement only related to the y coordinate	29
n_x	x-axis modal index	31
N_x	Maximum mode number of n_x	31
n_y	y-axis modal index	31
N_y	Maximum mode number of n_y	31
θ	incidence angle of p_i	36
$\theta_{\max}$	Upper limit of θ	36
STL_{diffuse}	STL in a diffuse field	36
l_1	Distance from microphone 1 to the MPM surface	40
l_2	Distance from microphone 2 to the MPM surface	40
s	Distance between the microphones	40
$R^2_{\text{determination}}$	Coefficient of determination	41
n_{freq}	Index of the measured frequency	41
N_{freq}	Total number of measured frequencies	41
$\alpha_{\text{prediction}}$	Predicted sound absorption coefficient	41
$\alpha_{\text{experiment}}$	Measured sound absorption coefficient	41
r_0	Radius of a perforation	57
v	Air particle velocity in a perforation	57
r	Radial coordinate in a perforation	57
t	Time parameter	57
μ	Viscous ratio of air	57
Δp	Pressure difference between the front and back surfaces of the membrane/panel	57
h	Thickness of the membrane/panel	57
ω	Angular frequency	57
f	Frequency	57
J_0	Bessel function of the first kind and zero order	59
J_1	Bessel function of the first kind and first order	59

$Z_{\text{perforation}}$	Acoustic impedance of the perforation	59
δ	Perforation ratio of MPP/MPM	60
d	Hole diameter	60
σ	Dynamic viscosity in air	60
x	Perforation constant	60
v_{membrane}	Vibration velocity of membranes	61
$\bar{v}$	Average particle velocity in perforations	61
R	Distance from the centre of the circular membrane to the perforation location	62
η	Internal damping ratio of MPMs	64
n	nth hole on MPM surface	65
R_n	Radial coordinate of the nth hole	65
N	Total number of holes	65
x_{skip}	Centre to centre distance of holes on x axis	65
y_{skip}	Centre to centre distance of holes on y axis	65
x	Hole x coordinate	66
y	Hole y coordinate	66
D	Depth of air cavity between MPP/MPM and its rigid backing wall	68
$\text{Re}(z)$	Resistance of acoustic impedance	68
$\text{Im}(z)$	Reactance of acoustic impedance	68
$\text{Im}(z_{\text{overall}})$	Reactance of MPMs	69
$f\alpha_{\text{max}}$	Resonance frequency where the maximum sound absorption is achieved	73
$f\alpha_{\text{half}}$	Frequency where half of the maximum sound absorption coefficient is obtained	73
f_{min}	Lowest analysis frequency	73
f_{max}	Highest analysis frequency	73
R_s	Acoustic impedance of a perforation due to thermo-viscous friction	74
H_{s1}	Transfer function between microphone 1 and the sound source	94
H_{s2}	Transfer function between microphone 2 and the sound source	94

p_1	Measured sound pressure at microphone 1	94
p_2	Measured sound pressure at microphone 2	94
p_{source}	Voltage signal input into the power amplifier	94
H_{12}	Transfer function between microphones 1 and 2	94
Re	Reynolds number	116
p_1	Measured sound pressure on microphone 1	116
H	Measured transfer function between two microphones	116
k_0	Wavenumber in air	116
E	Young's modulus	122
ν	Poisson's ratio	122
$\text{Re}_{\text{nonlinear}}$	Resistance of the non-linear impedance	136
z_{linear}	Normalized acoustic impedance of the MPP or MPM in the linear regime	139
x_{length}	Position coordinate in the length direction	139
$k_{\text{Maa}} = \frac{d}{2}\sqrt{\frac{\omega\rho_0}{\mu}}$	MPP constant	140
a	Parameter determined by curve fitting	141
b	Parameter determined by curve fitting	141
p_{i2}	Incident sound on Membrane 2	165
p_{r2}	Reflected sound on Membrane 2	165
$\xi_1(x,y)$	Displacement of Membrane 1	166
$v_1(x,y)$	Velocity of Membrane 1	166
Δp_1	Sound pressure difference on Membrane 1	167
ρ_{s1}	Surface density of Membrane 1	167
$X_0(x)$	Sound pressure component in the x-direction within the cavity	170
$Y_0(x)$	Sound pressure component in the y-direction within the cavity	170
$Z_0(x)$	Sound pressure component in the z-direction within the cavity	170
k_{0x}	Component of k_0 in the x-direction within the cavity	170
k_{0y}	Component of k_0 in the y-direction within the cavity	170
k_{0z}	Component of k_0 in the z-direction within the cavity	170
v_x	Air particle velocity in the x direction within the air cavity	171
v_y	Air particle velocity in the y direction within the air cavity	171

SPL_{source}	Measured sound pressure level in the source chamber	236
p_{source}	Measured sound pressure in the source chamber	236

Chapter 1

Introduction

1.1 Introduction to multiple layer membrane structures

Membrane materials have commonly been used in buildings for decades. They are highly valued for their light weight, low carbon footprint as far as the environment is concerned, and their convenience for transportation and storage when not inflated.

These membrane materials can be used as permanent and temporary building materials. For permanent use, lightweight membrane structures have been used as components of roofs, walls or ceilings. Transparent membrane structures are particularly favoured for ceilings because of their effective light transmission. Figure 1.1a is a picture of the Beijing national aquatics centre, also known as the Water Cube, which is a permanent building with membrane roof and walls.

(a) The ”Water Cube”: an example of a permanent membrane structure.

(b) Champions League Dome in Madrid: an example of a temporary membrane structure.

Figure 1.1: Examples of permanent and temporary membrane structures constructed from membranes.

For temporary use, membrane structures usually consist of multiple membrane layers connected together and between them lies a cavity pressurised to maintain rigidity. These

inflatable structures have been used as temporary field hospitals, temporary theatres and conference halls (Tectoniks 2010), as shown in Figure 1.1b.

However, the acoustic properties of these membrane structures may lead to some problems. For example, it has been reported that the Water Cube suffered from high noise levels inside when it rained (Network 2015, WaterCube 2008), which was ascribed to the acoustic properties of the ETFE (Ethylene Tetrafluoroethylene) membranes used in the structure. This issue has been addressed by using triple and quadruple layers of membranes to reduce the noise (WaterCube 2008). For temporary membrane buildings, especially for these temporary theatres and conference halls, the high acoustic transmissibility of the walls may lead to significant community noise levels.

Together with their use as building materials, the sound insulation of membrane structures has also been investigated for decades. Impervious membranes can block sound transmission and be used as noise barriers, although their sound insulation is not as effective as conventional massive noise barriers (Mehra 2002). Hence, many efforts have been made to enhance the sound insulation of membrane structures. For example, adding small weights on the membrane surfaces (Hashimoto et al. 1996) and adding porous materials in the cavity between the double membrane layers (Bolton et al. 1996, Sgard et al. 2000) have been investigated to improve the sound transmission loss of membrane structures. However, these methods increase the overall mass and the overall thickness of the membrane structures.

It is known that membranes when coupled with backing air cavities can form effective absorbers. If membranes are perforated with holes in the order of one millimetre in diameter, they form micro-perforated membranes and are categorised as sound absorbing materials. Therefore, micro-perforated membrane (MPM) insertions are proposed in this thesis to enhance the sound transmission loss of multiple layer membrane structures. This combined theoretical and experimental investigation on the sound transmission of membrane structures and MPMs also broadens the knowledge of the acoustic properties of the membrane structures and MPMs. Potentially, these multiple layer membranes can be used as noise barriers, and the analytical models developed in this thesis can be used in their design.

1.2 Motivation and contributions of this thesis

This thesis aims to investigate acoustic properties of micro-perforated membranes, and impervious membranes, to ultimately enhance the sound insulation of double layer impervious membranes by combining these with micro-perforated membranes (MPMs), thereby increasing the internal loss mechanisms of what is essentially a reactive wall. The investigation on the acoustic properties of impervious membrane structures and MPMs is conducted both theoretically and experimentally.

As mentioned in Section 1.1, membrane materials may not only insulate sound but may also absorb sound.Impervious membranes can be used as noise barriers (Mehra 2002) due to their effective sound insulation. Multiple-layer membrane structures with an air cavity can be considered as membrane-type sound absorbers. The sound absorption of membranes can be enhanced by perforating small holes on their surface, forming MPMs. These MPMs are used as an alternative to porous sound absorbing material. Therefore, both the sound absorption and sound transmission of membrane materials are investigated in this thesis. To be specific, the sound absorption and transmission of single layer impervious membranes are studied. A new analytical model for the acoustic impedance of a single layer impervious membrane is developed by considering the internal damping due to the membrane curvature. This model is validated with the measured sound absorption coefficients at normal incidence in an impedance tube and the measured sound transmission loss in a diffuse sound field.

This thesis aims to capitalise on the sound absorption properties of MPMs and use this to enhance the sound transmission loss of double layer impervious membranes. A novel analytical model for the acoustic impedance of MPMs is developed, and its accuracy is verified with the measured sound absorption of MPMs in an impedance tube. This model is based on a new boundary condition where the particle velocity at the hole wall boundary, which is assumed to be zero in Maa's theory (Maa 1975), is assumed to be equal to the membrane vibration velocity. This model extends the understanding of the coupling between the acoustic impedance arising from membrane vibration and the acoustic impedance due to the perforations of MPMs. It offers an accurate model for predicting the performance of flexible finite-sized MPMs.

In this thesis, the non-linear sound absorption characteristics of MPMs has also been

investigated experimentally and theoretically. Non-linearities in the sound absorption of micro-perforated panels (MPPs) and orifices has been studied previously (Bodén 2007, Ingard & Ising 1967, Maa 1994, Tayong et al. 2010), however, there is very limited research on the non-linear sound absorption of MPMs. The previous analytical models for the non-linear sound absorption of micro-perforated panels and orifices do not capture all the physics and consequently do not adequately predict the behaviour under certain conditions. The research on the non-linear sound absorption of MPMs in this thesis fulfils this gap and further explores the physical mechanisms of the non-linearities observed in the MPM sound absorption. The effects of incident sound pressure levels for both broadband and monochromatic noise sources are investigated experimentally. Moreover, analytical models of the sound absorption of MPMs for different types of sound sources are developed. These models not only provide more accurate predicted results, but also better reflect the absorption physics than previous models.

As stated earlier, capitalising on the sound absorption offered by MPMs, the sound transmission of double layer impervious membranes without and with an internal MPM is investigated in this thesis. The sound transmission of double layer impervious membranes (without an internal MPM) is modelled for both a normally-incident plane wave and in a diffuse field. It is found that these models underestimate the sound transmission loss (STL) experimentally observed. This underestimation is ascribed to sound absorption of the boundaries of the air cavity, which is neglected in previous models. By taking into consideration the sound absorption of the boundaries, the newly developed model has good agreement with the experimental results.

The effectiveness of inserting an MPM between two impervious membranes is measured experimentally. Analytical models of double layer impervious membranes with an internal MPM are developed for a normally-incident plane wave and also in a diffuse field. The effects of the sound absorbing boundaries and the non-linear sound absorption are studied, based on the previous research. The analytical models are useful tools to design and predict the performance of membrane type noise barriers and improve the sound environment of membrane buildings.

1.3 Overview of this thesis

This thesis starts with an introduction to multiple layer membrane structures in Chapter 1, followed by an overview of the thesis and a list of the publications arising from this study. Rather than a single literature review chapter, due to the diverse aspects of this thesis, a detailed literature review is included in each chapter from Chapters 2 to 7, culminating in the particular research gaps pertinent to each chapter. This thesis consists of two major parts: the study of the sound absorption of micro-perforated membranes; and the study of the sound transmission of single and double layer impervious membranes without and with internal micro-perforated membranes. Figure 1.2 shows a graphical overview of this thesis.

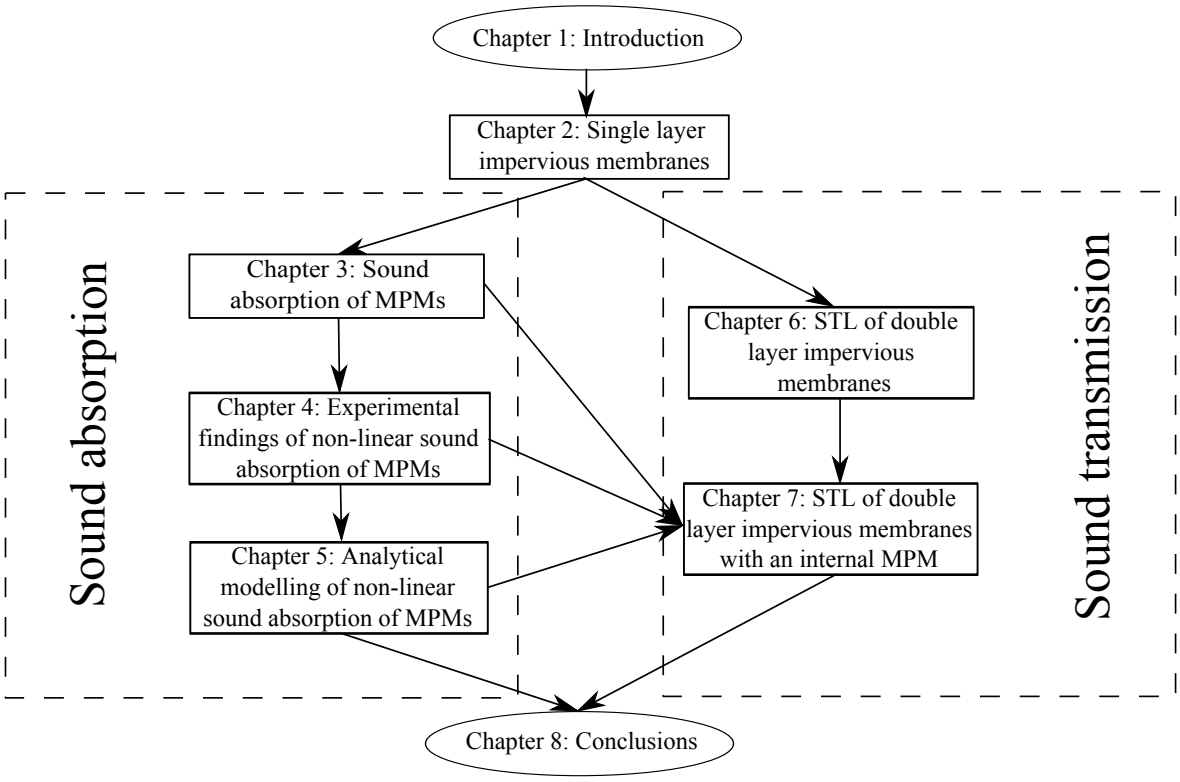

Figure 1.2: Overview of this thesis. The dashed blocks represent the two main parts of this thesis. The arrows show the relationship between the chapters.

Chapter 2 investigates the sound absorption and transmission of single layer impervious membranes. An analytical model which incorporates the internal damping due to the membrane curvature is proposed and is validated by experiments and forms the foundation of the research in this thesis on the sound absorption of MPMs and the design of combined membranes used as noise barriers.

Based on the developed models for the acoustic impedance of rectangular and circu-

lar impervious membranes in Chapter 2, the acoustic properties of MPMs and impervious membranes are investigated in the subsequent chapters. Chapter 3 introduces a velocity continuity condition at the perforation boundary of MPMs. An accurate prediction method for the acoustic impedance of MPMs is developed based on the velocity continuity condition and is validated by experimental results.

When conducting the sound absorption experiments, non-linear sound absorption properties of the MPMs are observed with both broadband and monochromatic excitation. These experimental findings are presented in Chapter 4. The effects of different types of sound sources and different amplitudes of the incident sound pressure on the MPMs are studied. The novel experimental findings are presented in Chapter 4.

To further investigate the non-linear sound absorption of MPMs excited by high SPLs, Chapter 5 re-derives Maa's non-linear MPP model and introduces a new non-linear model for the prediction of the acoustic impedance of MPMs. This model provides accurate predicted results and better reflects the physical system compared to previous models.

Chapter 6 investigates the sound transmission of double layer impervious membranes separated by an air cavity. The effects of the incident sound angle, the high-order cross modes of both the membranes and the air cavity, and the sound absorption at the boundary of the air cavity are considered. The developed model shows good agreement with the experimental results in a diffuse field.

To enhance the sound insulation of the double layer impervious membranes investigated in Chapter 6, MPMs are inserted into the air cavity and the resulting behaviour is investigated in Chapter 7. An analytical model for the combined membrane structure is developed and validated in this chapter. It is found that the MPM contributes little to the transmission loss below the fundamental cavity mode formed between the two impervious membranes. However, above the fundamental acoustic mode of the cavity, the transmission loss is increased significantly and remains enhanced over the frequency range tested. The analytical models are further developed by extending the models developed in Chapter 6. The effects of four MPMs are studied, as well as the non-linear sound absorption. However, it is found that the non-linear sound absorption of the MPM has negligible impact on the predicted STL.

This thesis investigates the sound absorption and sound transmission of MPMs and impervious membranes in detail both theoretically and experimentally. Several new models are

developed and validated by experimental results. These models extend the understanding of the linear and non-linear sound absorption of MPMs and the sound transmission of membrane structures, and hence can assist future research and design of MPMs and membrane noise barriers.

1.4 Publications arising from this thesis

The journal and conference publications arising from this thesis are as follows:
Journal publications:

- Li, C., Cazzolato, B., and Zander, A. (**2016**). "Acoustic impedance of micro perforated membranes: Velocity continuity condition at the perforation boundary," *Journal of the Acoustical Society of America* 139(1), 93-103.

- Li, C., Cazzolato, B., and Zander, A. (**2016**). "Non-linear effects of sound absorption of micro-perforated membranes", *Journal of Sound and Vibration*, under review.

- Li, C., Cazzolato, B., and Zander, A. (**2016**). "Analytical modelling for non-linear sound absorption of micro-perforated membranes", *Journal of the Acoustical Society of America*, in preparation.

Conference publications:

- Li, C., Cazzolato, B., and Zander, A. (**2014**). "Boundary condition for the acoustic impedance of lightweight micro-perforated panels and membranes", In: *Proceedings of the 21st International Congress on Sound and Vibration* (ICSV21), Beijing, China vol. 3: 2726-2733.

- Li, C., Cazzolato, B., and Zander, A. (**2013**). "Sound transmission loss of double layer impervious membranes with an internal micro-perforated membrane", In: *Annual Conference of the Australian Acoustical Society 2013, Acoustics 2013: Science, Technology and Amenity*, Victor Harbor, South Australia: 68-74.

Chapter 2

Acoustic properties of single layer impervious membranes under tension

2.1 Introduction

This thesis aims to study the acoustic characteristics of double and triple layer membranes used as noise barriers. Consequently, it is crucial to understand the acoustic properties of a single membrane layer. This chapter investigates the acoustic properties of a single layer impervious membrane under tension. A model which incorporates the internal damping due to the membrane curvature is proposed. The model consists of two parts; the modelling of a circular membrane excited by a normally incident plane wave, and the modelling of a rectangular membrane in a diffuse field. To validate these models, the sound absorption coefficients of impervious circular membranes are measured, as well as the sound transmission losses of impervious rectangular membranes.

In this chapter, Section 2.1.1 summarises the previous research on the acoustic properties of a single layer membrane, including pervious and impervious membranes. The gaps arising from these studies and the contributions of this chapter are presented in Section 2.1.2. The analytical modelling starts with the general motion equation of an impervious membrane in Section 2.2.1. The expressions for the damping effect which have been widely used in previous research and the proposed expression for the internal damping of an impervious membrane are discussed in Sections 2.2.2.1 and 2.2.2.2. The motion equation including the proposed internal damping is solved in the polar and Cartesian coordinate systems in Sections 2.2.3 and 2.2.4. Consequently, the sound absorption coefficients of circular impervious membranes were measured in an impedance tube to validate the model in the polar coordinate system and are presented in Section 2.3.1. The accuracy of the solution in the Cartesian

coordinate system is verified by sound transmission loss testing conducted in a diffuse field, and is presented in Section 2.3.2. The findings on the effect of the proposed damping expression on the sound absorption and transmission of an impervious membrane are discussed in Section 2.4. There is also a conclusion in Section 2.5.

2.1.1 Literature review

Membrane structures have been available for decades as building materials used in architecture and in construction. These membrane structures are usually lightweight and easily curved and are preferred for their acoustic properties.

Acoustic properties of single layer impervious membranes have been studied for decades. As early as 1954, Ingard (1954) investigated the sound transmission of an ideal membrane stretched in a rigid tube and indicated that a membrane under high tension provides high sound transmission loss over a broadband frequency range. Romilly (1964) extended Ingard's approximate results to series form and studied the resonance and antiresonance frequencies of an ideal circular membrane in detail. Croome (1985) investigated the sound absorption and transmission of flexible membranes, using a model which involved mass only. Frommhold et al. (1994) indicated that when investigating the sound absorption of a membrane absorber with a normally incident plane wave, the system could be considered as a combination of a Helmholtz resonator and a plate absorber. Sakagami et al. (1996) studied the effects of mass and tension on the sound absorption of a membrane backed by an air cavity with obliquely incident plane waves. However, they assumed that the membrane is infinite-sized and hence the finite size effects were neglected. Sakagami et al. (2002) extended this model to investigate the acoustic properties of double layer membranes with a pervious membrane facing the incident sound.

Conventionally, membranes used as sound absorbing materials are combined with an air cavity and a rigid wall. Sometimes, porous materials are inserted into the cavity to enhance the sound absorption. Bosmans et. al. (1999) investigated the sound absorption and transmission of an impervious membrane combined with mineral wool or plastic foams in the cavity. Their analytical model is in matrix form, which simplifies the calculation of multiple layer structures. However, in their model, all the damping effects, including those arising from air, energy dissipation on the membrane surface and membrane curvature, were neglected.

Sakagami et al. (2005) explored the possibilities of using single and double layer membranes as a space sound absorber. In their design, the air cavities and porous materials which usually fill the air cavity are eliminated. By assuming that the sound is incident from both sides of the membrane samples, the sound absorption of the membranes were studied in a diffuse field. However, the sound absorption of this novel membrane space absorber was still lower than that of the conventional porous materials, even when optimisations were applied. The tension effects of the membranes were neglected in their research.

With the development of material technology, membranes made by metamaterials have been investigated. Yang et al. (2008) analysed the sound transmission of a circular metamaterial membrane with a small mass attached in its centre using finite element analysis. The effect of negative dynamic mass was studied. It was found that the membrane reflects nearly all the sound at a frequency between two eigenmodes. However, their simulation was conducted in COMSOL Multiphysics and no analytical model was provided in their paper. Similar research has been done by Zhang et al. (2012) with a theoretical model. In Zhang et al.'s model, the spatial position of the additional mass varies and the effect of the position of the mass has been investigated. Tian et al. (2014) extended Zhang et al.'s model to a model where the additional mass was no longer a point mass but a ring mass.

Tension has been considered in these studies on sound transmission of metamaterial membranes, however the damping effect has been neglected. In addition to preventing the displacement being infinite at the resonance frequency, the damping effect of a membrane under tension is also important in practice. There are two expressions typically used for the damping of a membrane. Kinsler et al. (1999) indicated in their book that the effect of damping could be considered as "a damping force" which is given by

$$-\eta\frac{\partial\xi}{\partial t}, \tag{2.1}$$

where η is the damping factor, ξ is the membrane vibration displacement and t is the time variable. Obviously, this damping is related to the velocity of the membrane vibration.

Furthermore, Song & Bolton (2002, 2003) used a complex tension factor to represent the effect of damping. In their derivation, the constant tension is expressed by

$$T = T_0(1+j\eta), \tag{2.2}$$

where T is the tension per unit length on the membrane surface and T_0 is the real-valued

static tension. Equation (2.2) implies that the damping is not related to the velocity of the membrane vibration, but represents energy dissipated by the membrane flexural vibration.

While the damping expressions in Equation (2.1) used by Kinsler et al. (1999) arise from the velocity of the membrane vibration and the damping factor in Equation (2.2) used by Song & Bolton (2002, 2003) is related to energy dissipation due to the membrane flexural vibration, the damping due to the membrane curvature has been neglected in the previous research. However, if a two dimensional case such as the vibration of a flexible string is considered, the damping of the system is ascribed to the curvature of the string (Walstijn 2009). Similarly, in the three dimensional case of membrane vibration, the damping could also be related to the curvature of the membrane. This curvature-related damping has been barely discussed previously.

2.1.2 Gaps and contribution

This chapter aims to investigate the acoustic properties of a single layer impervious membrane under constant tension by considering the internal damping due to the internal friction effect arising from the membrane curvature. To include this damping, the motion equation for vibration of a membrane under tension is discussed in Section 2.2.1. The conventional expressions of damping and the presented expression are compared in Sections 2.2.2.1 and 2.2.2.2, respectively. The developed motion equation is solved in the polar and the Cartesian coordinate systems in Sections 2.2.3 and 2.2.4.

To validate the model developed in the polar coordinate system, the sound absorption coefficients of two types of impervious membranes are compared with the predicted results in Section 2.3.1. The accuracy of the model of a rectangular membrane in a diffuse field is verified with the measured sound transmission loss of two rectangular membranes in Section 2.3.2. Good agreements are achieved between these predicted results and the measured results. Discussions on the effects of the parameters on the sound absorption and transmission of impervious single layer membranes are presented in Section 2.4, followed by the conclusion of this chapter in Section 2.5.

This chapter contributes new knowledge as it explores the modelling of the acoustic properties of single layer impervious membranes using a new damping expression due to the membrane curvature. Analytical models for the predictions of sound absorption and

transmission of circular and rectangular membranes in plane wave and diffuse fields are presented. These models are validated by experiments. Furthermore, this chapter discusses the effects of tension and damping on circular and rectangular membranes in detail and provides increased understanding of the effect of tension and internal damping on the sound absorption and sound transmission of impervious membranes. These models are useful tools when designing membrane-type sound absorbers and noise barriers in practice.

2.2 Analytical modelling of the acoustic properties of single layer impervious membranes under tension

This section aims to develop a predictive model for the acoustic properties of a membrane under constant tension and with internal damping due to the membrane curvature. Conventional damping expressions and the newly developed expression are compared theoretically. The motion equation considering the damping due to the membrane curvature has been solved in a polar coordinate system for the sound absorption of a circular membrane with a normally-incident plane wave, and in a Cartesian coordinate system for the sound transmission of a rectangular membrane in a diffuse field. There are also discussions on the influence of the different damping expressions on the sound absorption and transmission of single layer impervious membranes.

2.2.1 Motion equation of the free vibration of a single layer tensioned impervious membrane

In this section, the vibratory motion of a thin membrane under constant tension is investigated. The membrane is assumed to be uniform with negligible bending stiffness and perfectly elastic. A constant tension T is applied on the membrane surface (with units of newton per unit length), as shown in Figure 2.1. If no additional force is involved, the motion equation of the membrane for free vibration is given by (Kinsler et al. 1999)

$$T\left(\frac{\partial^2 \xi(x,y,t)}{\partial x^2}+\frac{\partial^2 \xi(x,y,t)}{\partial y^2}\right)=\rho_s \frac{\partial^2 \xi(x,y,t)}{\partial t^2}, \tag{2.3}$$

where x and y are the position coordinates in the x- and y-axis, respectively, and ρ_s is the surface density of the membrane ($\mathrm{kg/m^2}$). The left-hand side of Equation (2.3) represents the force due to the membrane tension. The right-hand side of Equation (2.3) is the product

of the unit mass multiplied by the acceleration $\frac{\partial^2 \xi(x,y,t)}{\partial t^2}$. Therefore, Equation (2.3) is based on Newton's second law and represents the motion of the membrane for free vibration.

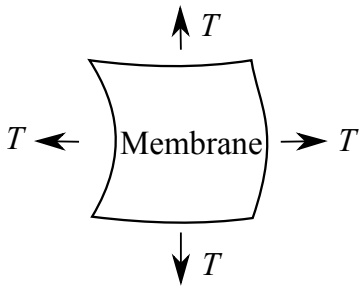

Figure 2.1: Constant tension applied on the membrane surface.

If the membrane displacement ξ is rewritten as

$$\xi(x,y,t) = \xi(x,y)\, e^{j\omega t}, \tag{2.4}$$

where ω denotes the angular frequency, Equation (2.3) becomes

$$T\left(\frac{\partial^2 \xi(x,y)}{\partial x^2} + \frac{\partial^2 \xi(x,y)}{\partial y^2}\right) + \omega^2 \rho_s \xi(x,y) = 0. \tag{2.5}$$

The time variable t is eliminated in Equation (2.5). Note that Equation (2.5) is also a motion equation of the membrane for free vibration.

Moreover, using the two dimensional Laplace operator ∇^2, Equation (2.5) is simplified as

$$T\nabla^2 \xi(x,y) + \omega^2 \rho_s \xi(x,y) = 0. \tag{2.6}$$

Letting $K_{\text{mem}}^2 = \frac{\omega^2 \rho_s}{T}$ yields

$$\nabla^2 \xi(x,y) + K_{\text{mem}}^2 \xi(x,y) = 0. \tag{2.7}$$

Note that the two dimensional Laplace operator ∇^2 in the Cartesian coordinate system is expressed as

$$\nabla^2 = \frac{\partial^2}{\partial x^2} + \frac{\partial^2}{\partial y^2}. \tag{2.8}$$

Conversely, the two dimensional Laplace operator in a polar coordinate system is given by

$$\nabla^2 = \frac{\partial^2}{\partial R^2} + \frac{1}{R}\frac{\partial}{\partial R}, \tag{2.9}$$

where R denotes the radial position coordinate in the polar coordinate system. In Equation (2.9), the angle coordinate θ is neglected due to the isotropic vibration of the membrane. The

substitution of Equations (2.8) and (2.9) into Equation (2.6) gives the forced motion equation of membrane vibration in the Cartesian coordinate system and the polar coordinate system, respectively.

2.2.2 Damping of a single layer tensioned impervious membrane

In Section 2.2.1, the effect of damping on the membrane vibration is neglected. However, damping is important theoretically and practically. In theoretical analysis, considering damping can prevent the displacement being infinite at the resonance frequency. In practice, damping always exists in the system and therefore utilisation of damping improves the accuracy of the prediction model.

The conventional damping expressions mentioned in Section 2.1.1 are investigated in this section. The damping due to the membrane curvature is presented and theoretically compared with the conventional damping forms.

2.2.2.1 Conventional constant damping

As mentioned in Section 2.1.1, there are two conventional expressions for the damping factor of a membrane under tension. Kinsler et al. (1999) used "damping force" to express the effect of viscous damping. The expression of this "damping force" is given by Equation (2.1). This damping is related to the local velocity of the membrane vibration and represents a viscous damping with a constant damping ratio η. Substituting Equation (2.1) into Equation (2.5) gives

$$T\nabla^2\xi(x,y) + \omega^2\rho_s\,\xi(x,y) - j\omega\,\eta\,\xi(x,y) = 0. \tag{2.10}$$

Equation (2.10) may be rewritten as

$$\nabla^2\xi(x,y) + \frac{\omega^2\rho_s - j\omega\,\eta}{T}\xi(x,y) = 0. \tag{2.11}$$

Let this $K_{\text{mem}}^2 = \frac{\omega^2\rho_s - j\omega\,\eta}{T}$ and Equation (2.11) is simplified as

$$\nabla^2\xi(x,y) + K_{\text{mem}}^2\xi(x,y) = 0. \tag{2.12}$$

Alternatively, the effect of damping can also be expressed as a complex tension (Song & Bolton 2002, 2003), as shown in Equation (2.2). The imaginary part of this complex tension represents the energy dissipation by the membrane, which is related to the local displacement of the membrane. The energy dissipation is represented by a constant η. By substituting the

complex tension into Equation (2.5), the motion equation of the membrane for free vibration is given by

$$T(1+j\eta)\nabla^2\xi(x,y)+\omega^2\rho_s\xi(x,y)=0. \tag{2.13}$$

Equation (2.13) is simplified as

$$\nabla^2\xi(x,y)+\frac{\omega^2\rho_s}{T(1+j\eta)}\xi(x,y)=0. \tag{2.14}$$

Letting $K_{\text{mem}}^2=\frac{\omega^2\rho_s}{T(1+j\eta)}$ and substituting it into Equation (2.14) yields

$$\nabla^2\xi(x,y)+K_{\text{mem}}^2\xi(x,y)=0. \tag{2.15}$$

Comparing Equation (2.12) with (2.15), it is found that they are identical except for the differing expressions for the parameter K_{mem} in each equation. This implies that the free vibration of an impervious membrane under tension can be described in the forms of Equations (2.12) and (2.15). The parameters such as surface density, tension and damping, only affect the factor K_{mem}. The expression for K_{mem} thus differs with the various representations of the damping mechanisms.

2.2.2.2 Internal damping due to curvature

As mentioned previously, the conventional damping expressions shown in Equations (2.1) and (2.2) neglect the internal damping due to the membrane curvature. In the two dimensional case of the free vibration of a flexible string, the damping due to the string curvature is expressed as (Walstijn 2009)

$$T\frac{\partial^2\xi(x,t)}{\partial x^2}+2\eta\frac{\partial^3\xi(x,t)}{\partial t\partial x^2}=\rho_{\text{string}}\frac{\partial^2\xi(x,t)}{\partial t^2}, \tag{2.16}$$

where η denotes the internal damping ratio and ρ_{string} denotes the mass per unit length of the string. In Equation (2.16), the damping part $2\eta\frac{\partial^3\xi(x)}{\partial t\partial x^2}$ is not only related to the vibration velocity of the string, but also related to the string curvature. This part denotes the internal friction effect due to the string curvature.

By extending the one dimensional flexible string analysis to a two dimensional flexible membrane, Equation (2.16) is changed to

$$T\nabla^2\xi(x,y,t)+2\eta\frac{\partial\nabla^2\xi(x,y,t)}{\partial t}=\rho_s\frac{\partial^2\xi(x,y,t)}{\partial t^2}. \tag{2.17}$$

Eliminating the time variable t gives

$$T\nabla^2\xi(x,y) + 2j\omega\eta\nabla^2\xi(x,y) + \omega^2\rho_s\xi(x,y) = 0. \tag{2.18}$$

Equation (2.18) may be simplified as

$$\nabla^2\xi(x,y) + \frac{\omega^2\rho_s}{T+2j\omega\eta}\xi(x,y) = 0. \tag{2.19}$$

Letting $K_{\text{mem}}^2 = \frac{\omega^2\rho_s}{T+2j\omega\eta}$ yields

$$\nabla^2\xi(x,y,t) + K_{\text{mem}}^2\xi(x,y) = 0. \tag{2.20}$$

This is the motion equation of the free vibration of a membrane under tension, considering the damping due to the membrane curvature.

Comparing Equation (2.20) with Equations (2.12) and (2.15), it is found that they are in the same form except for the different expressions for K_{mem}. Note that the different expressions for K_{mem} are ascribed to the different expressions of the damping effect arising from different physical mechanisms. The differences are discussed further in Section 2.2.2.3.

2.2.2.3 Comparison of the expressions of damping

It is concluded from the motion equations of an impervious membrane vibrating under constant tension that the motion equation follows the same form as shown in Equations (2.12), (2.15) and (2.20). The only difference among these equations are the different expressions of the factor K_{mem}^2. Table 2.1 shows a comparison of the expressions for K_{mem}^2.

Obviously, if the damping effect is neglected, the value of K_{mem}^2 is purely real, otherwise it is complex. Since the order of magnitude of the damping coefficient is usually around 0.01, while that of the tension is usually three orders of magnitude higher than the damping coefficient, it is presumed that the real parts of the conventional expressions of K_{mem}^2 (i.e. expressions No. 2 and 3) should be close to each other. It is difficult to verify the imaginary parts of the expressions by estimating the orders of magnitude of tension and damping. Therefore, an example is utilised here to present the theoretical comparison of the four expressions. Assume that an impervious membrane with a surface density $\rho_{\text{s}} = 0.485\,\text{kg/m}^2$, is stretched under a constant tension $T = 100\,\text{N/m}$ and its internal damping ratio is $\eta = 0.01$. The K_{mem}^2 values calculated using each of the four expressions are shown in Figure 2.2. In Figure 2.2a, the curves calculated using the first three expressions are identical, which veri-

Table 2.1: Comparison of different expressions of K^2_{mem} due to damping.

No.	Expression K^2_{mem}	Source	Physical meanings
1	$K^2_{\text{mem}} = \frac{\omega^2 \rho_s}{T}$	Equation (2.7)	No damping
2	$K^2_{\text{mem}} = \frac{\omega^2 \rho_s - j\omega\eta}{T}$	Equation (2.1) (Kinsler et al. 1999)	"Damping force" due to viscous damping
3	$K^2_{\text{mem}} = \frac{\omega^2 \rho_s}{T(1+j\eta)} = \frac{\omega^2 \rho_s (1-j\eta)}{T(1+\eta^2)}$	Equation (2.2) (Song & Bolton 2002, 2003)	Energy dissipated by the membrane
4	$K^2_{\text{mem}} = \frac{\omega^2 \rho_s}{T+2j\omega\eta} = \frac{\omega^2 \rho_s (T-2j\omega\eta)}{T^2+4\omega^2\eta^2}$	Equation (2.16) presented model	Friction effects due to the membrane curvature

fies the presumption that the conventional expressions should be close to each other. The real part predicted by the presented expression is close to those of the other expressions below 400 Hz and significantly lower than those of the other expressions in the middle and high frequency ranges. It is shown in Figure 2.2b that although the calculated values using the first expression is zero and is close to zero for expressions No. 2 and 3, the predicted values using the presented expression are significantly greater in magnitude. Therefore, it is concluded that the values of K^2_{mem} predicted by the conventional expressions, including those without damping, are very similar. Conversely, the values calculated using the presented expression differ significantly from those conventional values. The significant difference implies a significant effect of the membrane curvature on the acoustic properties of the membrane. The accuracy of these expressions are verified by experiments in Section 2.3.

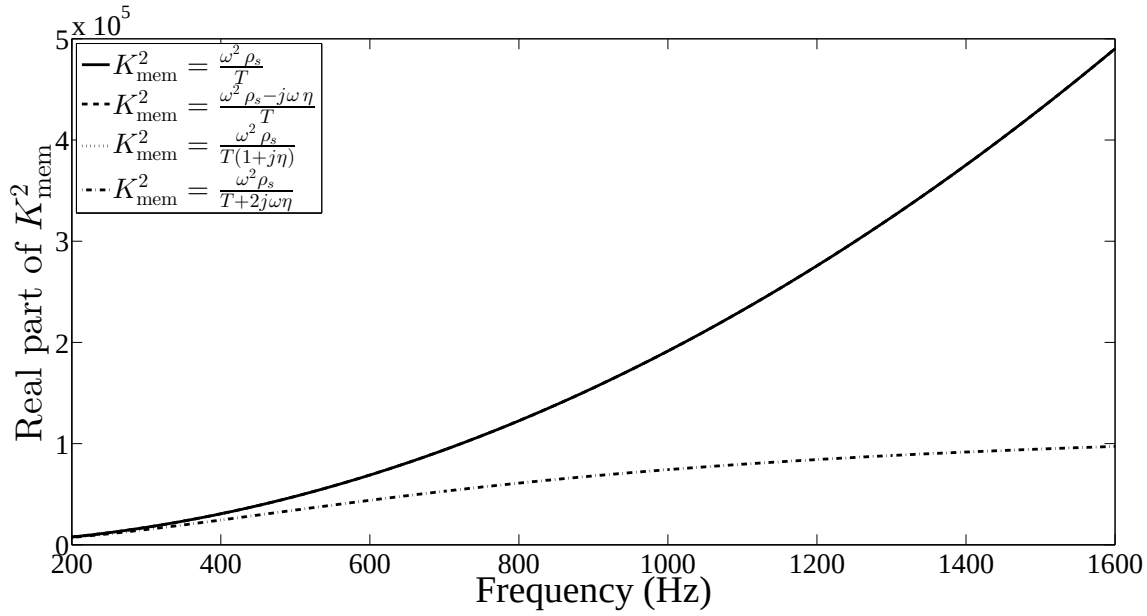

(a) Real part of K^2_{mem}.

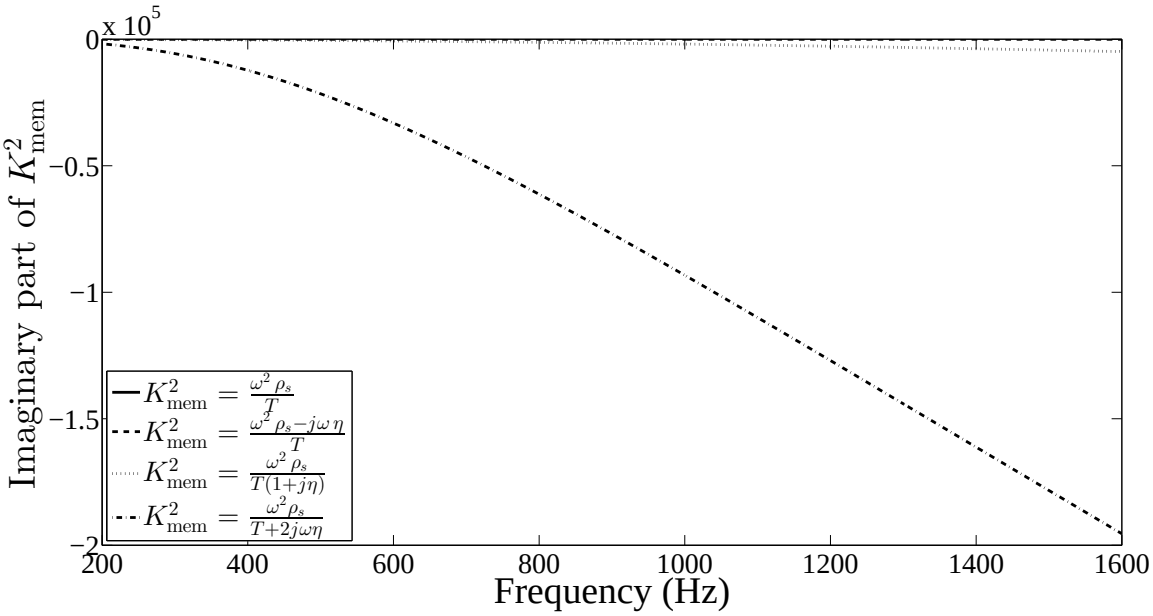

(b) Imaginary part of K^2_{mem}.

Figure 2.2: Comparison of K^2_{mem} expressed in different forms in Table 2.1. Surface density $\rho_s = 0.485\,\text{kg/m}^2$; tension $T = 100\,\text{N/m}$; internal damping ratio $\eta = 0.01$. Solid lines represent $K^2_{\text{mem}} = \frac{\omega^2\rho_s}{T}$ for no damping. Dashed lines and dotted lines represent two conventional expressions for $K^2_{\text{mem}} = \frac{\omega^2\rho_s - j\omega\eta}{T}$ (viscous damping) and $K^2_{\text{mem}} = \frac{\omega^2\rho_s}{T(1+j\eta)}$ (energy dissipation), respectively. Dashed dotted lines represent $K^2_{\text{mem}} = \frac{\omega^2\rho_s}{T+2j\omega\eta}$ calculated by the presented model for curvature damping.

2.2.3 Acoustic impedance and sound absorption of a cricular impervious membrane with a normally-incident plane wave

The general motion equation of a membrane under tension and damping has been investigated in Sections 2.3 and 2.2.2. It is known that Equation (2.7) is valid in both the Cartesian coordinate system and the polar coordinate system, except that in each coordinate system the Laplace operator ∇^2 is expressed differently.

This section aims to solve the motion equation in the polar coordinate system and the corresponding expressions for the acoustic impedance and sound absorption coefficient of a circular impervious membrane under tension and with internal damping for each of the damping representation of no damping, viscous damping, energy dissipation damping and curvature damping. As shown in Figure 2.3, the impervious membrane is stretched on a circular rim. The radius of the membrane and the internal radius of the rim are R_0. Note that the membrane is excited by a sound pressure p_i which is incident on the membrane surface normally. The membrane reflects back some of the sound energy with a reflected pressure component, denoted by p_r. Some of the sound is transmitted to the opposite side of the membrane and this sound pressure is named as p_t. Hence, the total sound pressure applied on the membrane surface can be expressed as

$$\Delta p = p_i + p_r - p_t. \tag{2.21}$$

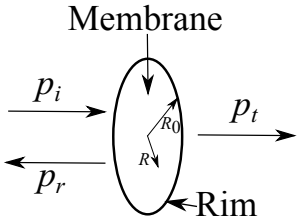

Figure 2.3: A circular membrane stretched on a circular rim, where R_0 is the radius of the circular membrane and R is the radial coordinate on the membrane surface.

If the sound pressure Δp is applied on the membrane surface, Equation (2.5) is given by

$$T\nabla^2\xi(x,y) + \omega^2\rho_s\xi(x,y) = -\Delta p. \tag{2.22}$$

In Equation (2.22), the sum of $T\nabla^2\xi(x,y)$ and Δp is the total force applied on the membrane surface, which equals the product of the unit mass ρ_s multiplied by the acceleration $-\omega^2\xi(x,y)$. Therefore, Equation (2.22) also follows Newton's second law and represents

the forced vibration motion of a membrane under external pressure Δp. Equation (2.22) can be rewritten as

$$\begin{aligned} \nabla^2\xi(x,y) + \frac{\omega^2\rho_s}{T}\,\xi(x,y) &= \frac{-\Delta p}{T}, \qquad \text{or} \\ \nabla^2\xi(x,y) + K_{\text{mem}}^2\xi(x,y) &= \frac{-\Delta p}{T}, \end{aligned} \tag{2.23}$$

where $K_{\text{mem}}^2 = \frac{\omega^2\rho_s}{T}$. Equation (2.23) is the motion equation of the forced vibration of a circular membrane without damping.

Adding the sound pressure $-\Delta p$ to the right-hand side of Equation (2.10) yields the forced motion equation of the membrane with damping force, which is given by

$$\begin{aligned} \nabla^2\xi(x,y) + \frac{\omega^2\rho_s - j\omega\eta}{T}\,\xi(x,y) &= \frac{-\Delta p}{T}, \qquad \text{or} \\ \nabla^2\xi(x,y) + K_{\text{mem}}^2\,\xi(x,y) &= \frac{-\Delta p}{T}, \end{aligned} \tag{2.24}$$

where $K_{\text{mem}}^2 = \frac{\omega^2\rho_s - j\omega\eta}{T}$. This equation represents the forced vibration of a circular membrane, considering the damping force.

If the damping is considered as the sound energy dissipated by the membrane vibration, it is necessary to use the complex tension $T(1+j\eta)$ (Song & Bolton 2002, 2003). In this way, the forced vibration motion is expressed as

$$\begin{aligned} \nabla^2\xi(x,y) + \frac{\omega^2\rho_s}{T(1+j\eta)}\,\xi(x,y) &= \frac{-\Delta p}{T(1+j\eta)}, \qquad \text{or} \\ \nabla^2\xi(x,y) + K_{\text{mem}}^2\,\xi(x,y) &= \frac{-\Delta p}{T(1+j\eta)}, \end{aligned} \tag{2.25}$$

where $K_{\text{mem}}^2 = \frac{\omega^2\rho_s}{T(1+j\eta)}$.

In the presented model, the damping is considered due to the rate of change of membrane curvature. Adding Δp to Equation (2.19) yields

$$\begin{aligned} \nabla^2\xi(x,y) + \frac{\omega^2\rho_s}{T+2j\omega\eta}\xi(x,y) &= \frac{-\Delta p}{T+2j\omega\eta}, \qquad \text{or} \\ \nabla^2\xi(x,y) + K_{\text{mem}}^2\xi(x,y) &= \frac{-\Delta p}{T+2j\omega\eta}, \end{aligned} \tag{2.26}$$

where $K_{\text{mem}}^2 = \frac{\omega^2\rho_s}{T+2j\omega\eta}$.

Equations (2.23), (2.24), (2.25) and (2.26) are inhomogeneous differential equations. Each of their solutions is the sum of the solution of the corresponding homogeneous differential equation and its particular solution. Comparing these equations, it is found that the

left-hand sides of these equations are identical, except that the expressions for K_{mem} differ each equation. The differing expressions for K_{mem} have been discussed previously in Section 2.2.2.3. Therefore, the homogeneous differential equations are identical, and are given by

$$\nabla^2 \xi(R) + K_{\text{mem}}^2 \xi(R) = 0. \tag{2.27}$$

Substituting the Laplace operator Equation (2.9) into Equation (2.27) yields the motion equation of the free vibration of a circular membrane in the polar coordinate system, which is expressed as

$$\frac{\partial^2 \xi(R)}{\partial R^2} + \frac{1}{R}\frac{\partial \xi(R)}{\partial R} + K_{\text{mem}}^2 \xi(R) = 0. \tag{2.28}$$

Letting $x = K_{\text{mem}}R$, the two differentials from Equation (2.28) become

$$\frac{\partial \xi(R)}{\partial R} = \frac{\partial \xi(x)}{\partial \frac{x}{K_{\text{mem}}}} = K_{\text{mem}}\frac{\partial \xi(x)}{\partial x}, \tag{2.29}$$

and

$$\frac{\partial^2 \xi(R)}{\partial R^2} = \frac{\partial \left[K_{\text{mem}}\frac{\partial \xi(x)}{\partial x}\right]}{\partial \frac{x}{K_{\text{mem}}}} = K_{\text{mem}}^2\frac{\partial^2 \xi(x)}{\partial x^2}. \tag{2.30}$$

Substituting Equations (2.29) and (2.30) into Equation (2.28) gives

$$K_{\text{mem}}^2\frac{\partial^2 \xi(x)}{\partial x^2} + \frac{K_{\text{mem}}}{R}\frac{\partial \xi(x)}{\partial x} + K_{\text{mem}}^2 \xi(x) = 0. \tag{2.31}$$

Multiplying Equation (2.31) by R^2 gives

$$K_{\text{mem}}^2 R^2\frac{\partial^2 \xi(x)}{\partial x^2} + K_{\text{mem}}R\frac{\partial \xi(x)}{\partial x} + K_{\text{mem}}^2 R^2 \xi(x) = 0. \tag{2.32}$$

Letting $x = K_{\text{mem}}R$, Equation (2.32) is simplified as

$$x^2\frac{\partial^2 \xi(x)}{\partial x^2} + x\frac{\partial \xi(x)}{\partial x} + x^2 \xi(x) = 0. \tag{2.33}$$

Equation (2.33) is Bessel's differential equation of the first kind and zero order, the solution of which is given by (Temme 2011)

$$\xi(R) = AJ_0(K_{\text{mem}}R), \tag{2.34}$$

where J_0 is the Bessel function of the first kind and zero order and A is a constant depending on the boundary condition of the membrane.

To calculate a particular solution of Equations (2.23), (2.24), (2.25) and (2.26), it is

assumed that the particular solution is a constant. Hence, these equations are rewritten as

$$\text{No damping} \qquad K_{\text{mem}}^2 \xi(R) = \frac{-\Delta p}{T}, \tag{2.35a}$$

$$\text{Viscous damping} \qquad K_{\text{mem}}^2 \xi(R) = \frac{-\Delta p}{T}, \tag{2.35b}$$

$$\text{Energy dissipation damping} \qquad K_{\text{mem}}^2 \xi(R) = \frac{-\Delta p}{T(1+j\eta)}, \tag{2.35c}$$

$$\text{Curvature damping} \qquad K_{\text{mem}}^2 \xi(R) = \frac{-\Delta p}{T+2j\omega\eta}. \tag{2.35d}$$

Note that Equation (2.35a) seems identical with Equation (2.35b), however, since the expressions of K_{mem} differ, so do these equations. Substituting the expressions of K_{mem} into Equation (2.35) yields

$$\text{No damping} \qquad \frac{\omega^2 \rho_s}{T} \xi(R) = \frac{-\Delta p}{T}, \tag{2.36a}$$

$$\text{Viscous damping} \qquad \frac{\omega^2 \rho_s - j\omega\eta}{T} \xi(R) = \frac{-\Delta p}{T}, \tag{2.36b}$$

$$\text{Energy dissipation damping} \qquad \frac{\omega^2 \rho_s}{T(1+j\eta)} \xi(R) = \frac{-\Delta p}{T(1+j\eta)}, \tag{2.36c}$$

$$\text{Curvature damping} \qquad \frac{\omega^2 \rho_s}{T+2j\omega\eta} \xi(R) = \frac{-\Delta p}{T+2j\omega\eta}. \tag{2.36d}$$

The solutions of Equation (2.36) are

$$\text{No damping} \qquad \xi(R) = \frac{-\Delta p}{\omega^2 \rho_s}, \tag{2.37a}$$

$$\text{Viscous damping} \qquad \xi(R) = \frac{-\Delta p}{\omega^2 \rho_s - j\omega\eta}, \tag{2.37b}$$

$$\text{Energy dissipation damping} \qquad \xi(R) = \frac{-\Delta p}{\omega^2 \rho_s}, \tag{2.37c}$$

$$\text{Curvature damping} \qquad \xi(R) = \frac{-\Delta p}{\omega^2 \rho_s}. \tag{2.37d}$$

Equations (2.37a), (2.37c) and (2.37d) are identical in form, because the factors related to the tension T and the damping η are eliminated. However, Equation (2.37b) involves the damping factor η.

The sum of Equations (2.34) and (2.37) forms the general solution of the inhomogeneous differential equation for each of the damping representations, given by Equations (2.23),

(2.24), (2.25) and (2.26). The solutions are obtained as

$$\text{No damping} \qquad \xi(R) = AJ_0(K_{\text{mem}}R) + \frac{-\Delta p}{\omega^2 \rho_s}, \tag{2.38a}$$

$$\text{Viscous damping} \qquad \xi(R) = AJ_0(K_{\text{mem}}R) + \frac{-\Delta p}{\omega^2 \rho_s - j\omega\eta}, \tag{2.38b}$$

$$\text{Energy dissipation damping} \qquad \xi(R) = AJ_0(K_{\text{mem}}R) + \frac{-\Delta p}{\omega^2 \rho_s}, \tag{2.38c}$$

$$\text{Curvature damping} \qquad \xi(R) = AJ_0(K_{\text{mem}}R) + \frac{-\Delta p}{\omega^2 \rho_s}. \tag{2.38d}$$

As mentioned previously, the variable A in each solution is dependent on the boundary condition. Since the membrane is assumed to be stretched on a circular rim, the boundary condition is given by

$$\xi(R = R_0) = 0. \tag{2.39}$$

Applying this boundary condition to Equation (2.38) yields

$$\text{No damping} \qquad \xi(R = R_0) = AJ_0(K_{\text{mem}}R_0) + \frac{-\Delta p}{\omega^2 \rho_s} = 0, \tag{2.40a}$$

$$\text{Viscous damping} \qquad \xi(R = R_0) = AJ_0(K_{\text{mem}}R_0) + \frac{-\Delta p}{\omega^2 \rho_s - j\omega\eta} = 0, \tag{2.40b}$$

$$\text{Energy dissipation damping} \qquad \xi(R = R_0) = AJ_0(K_{\text{mem}}R_0) + \frac{-\Delta p}{\omega^2 \rho_s} = 0, \tag{2.40c}$$

$$\text{Curvature damping} \qquad \xi(R = R_0) = AJ_0(K_{\text{mem}}R_0) + \frac{-\Delta p}{\omega^2 \rho_s} = 0. \tag{2.40d}$$

The solutions of Equation (2.40) are

$$\text{No damping} \qquad A = \frac{\Delta p}{\omega^2 \rho_s J_0(K_{\text{mem}}R_0)}, \tag{2.41a}$$

$$\text{Viscous damping} \qquad A = \frac{\Delta p}{(\omega^2 \rho_s - j\omega\eta) J_0(K_{\text{mem}}R)}, \tag{2.41b}$$

$$\text{Energy dissipation damping} \qquad A = \frac{\Delta p}{\omega^2 \rho_s J_0(K_{\text{mem}}R_0)}, \tag{2.41c}$$

$$\text{Curvature damping} \qquad A = \frac{\Delta p}{\omega^2 \rho_s J_0(K_{\text{mem}}R)}. \tag{2.41d}$$

Substituting Equation (2.41) into Equation (2.38) yields

No damping

$$\xi(R) = \frac{\Delta p J_0(K_{\text{mem}}R)}{\omega^2 \rho_s J_0(K_{\text{mem}}R_0)} + \frac{-\Delta p}{\omega^2 \rho_s} = \frac{\Delta p}{\omega^2 \rho_s}\left[\frac{J_0(K_{\text{mem}}R)}{J_0(K_{\text{mem}}R_0)} - 1\right], \tag{2.42a}$$

Viscous damping

$$\xi(R) = \frac{\Delta p J_0(K_{\text{mem}}R)}{(\omega^2 \rho_s - j\omega\eta) J_0(K_{\text{mem}}R)} + \frac{-\Delta p}{\omega^2 \rho_s - j\omega\eta} = \frac{\Delta p}{\omega^2 \rho_s - j\omega\eta}\left[\frac{J_0(K_{\text{mem}}R)}{J_0(K_{\text{mem}}R_0)} - 1\right], \tag{2.42b}$$

Energy dissipation damping

$$\xi(R) = \frac{\Delta p J_0(K_{\text{mem}}R)}{\omega^2 \rho_s J_0(K_{\text{mem}}R_0)} + \frac{-\Delta p}{\omega^2 \rho_s} = \frac{\Delta p}{\omega^2 \rho_s}\left[\frac{J_0(K_{\text{mem}}R)}{J_0(K_{\text{mem}}R_0)} - 1\right], \tag{2.42c}$$

Curvature damping

$$\xi(R) = \frac{\Delta p J_0(K_{\text{mem}}R)}{\omega^2 \rho_s J_0(K_{\text{mem}}R)} + \frac{-\Delta p}{\omega^2 \rho_s} = \frac{\Delta p}{\omega^2 \rho_s}\left[\frac{J_0(K_{\text{mem}}R)}{J_0(K_{\text{mem}}R_0)} - 1\right]. \tag{2.42d}$$

Similar to Equation (2.37), Equations (2.42a), (2.42c) and (2.42d) are identical, because the factors related to the tension T and the damping η are eliminated and these factors affect these equations by affecting the variable K_{mem}. However, Equation (2.42b) involves the damping factor η.

Integrating the displacement over the membrane area and dividing by the area, the average displacement is expressed as

$$\begin{aligned}\bar{\xi} &= \frac{\int_0^{R_0} \xi(R) 2\pi R \mathrm{d}R}{{R_0}^2 \pi} \\ &= \begin{cases} \frac{\Delta p}{\omega^2 \rho_s}\left[\frac{2}{K_{\text{mem}}R_0}\frac{J_1(K_{\text{mem}}R_0)}{J_0(K_{\text{mem}}R_0)} - 1\right] & \text{for no damping, energy dissipation} \\ & \text{and curvature damping;} \\ \frac{\Delta p}{\omega^2 \rho_s - j\omega\eta}\left[\frac{2}{K_{\text{mem}}R_0}\frac{J_1(K_{\text{mem}}R_0)}{J_0(K_{\text{mem}}R_0)} - 1\right] & \text{for viscous damping,} \end{cases}\end{aligned} \tag{2.43}$$

where J_1 denotes the Bessel function of the first kind and first order.

Note that Equation (2.42) represents the displacement of the membrane vibration under

sound excitation. The corresponding velocity is given by

$$v(R) = \frac{\partial \xi(R)\, e^{j\omega t}}{\partial t} = \begin{cases} \frac{j\,\omega \Delta p}{\omega^2 \rho_s} \left[\frac{J_0(K_{\text{mem}} R)}{J_0(K_{\text{mem}} R_0)} - 1\right] & \text{for no damping, energy dissipation} \\ & \text{and curvature damping;} \\ \frac{j\,\omega \Delta p}{\omega^2 \rho_s - j\omega\,\eta} \left[\frac{J_0(K_{\text{mem}} R)}{J_0(K_{\text{mem}} R_0)} - 1\right] & \text{for viscous damping.} \end{cases} \tag{2.44}$$

Taking the integration over the membrane area and dividing by the area, the average velocity is expressed as

$$\bar{v} = \frac{\int_0^{R_0} v(R) 2\pi R \mathrm{d}R}{{R_0}^2 \pi} = \begin{cases} \frac{j\,\omega \Delta p}{\omega^2 \rho_s} \left[\frac{2}{K_{\text{mem}} R_0} \frac{J_1(K_{\text{mem}} R_0)}{J_0(K_{\text{mem}} R_0)} - 1\right] & \text{for no damping, energy dissipation} \\ & \text{and curvature damping;} \\ \frac{j\,\omega \Delta p}{\omega^2 \rho_s - j\omega\,\eta} \left[\frac{2}{K_{\text{mem}} R_0} \frac{J_1(K_{\text{mem}} R_0)}{J_0(K_{\text{mem}} R_0)} - 1\right] & \text{for viscous damping.} \end{cases} \tag{2.45}$$

Hence, the normalised acoustic impedance of the membrane is obtained by

$$z_{\text{mem}} = \frac{\Delta p}{\bar{v} \rho_0\, c_0} = \begin{cases} \frac{\omega \rho_s}{j\,\rho_0\, c_0} \left[\frac{2}{K_{\text{mem}} R_0} \frac{J_1(K_{\text{mem}} R_0)}{J_0(K_{\text{mem}} R_0)} - 1\right]^{-1} & \text{for no damping, energy dissipation} \\ & \text{and curvature damping;} \\ \frac{\omega \rho_s - j\eta}{j\,\rho_0\, c_0} \left[\frac{2}{K_{\text{mem}} R_0} \frac{J_1(K_{\text{mem}} R_0)}{J_0(K_{\text{mem}} R_0)} - 1\right]^{-1} & \text{for viscous damping,} \end{cases} \tag{2.46}$$

where ρ_0 is the density of air, c_0 is the speed of sound in air and $\rho_0\, c_0$ denotes the characteristic impedance of air.

If the membrane is adjacent to an air cavity with a depth of D backed by a rigid wall, the combination of the membrane, the cavity and the rigid wall is defined as an membrane absorber. The total impedance of this absorber is given by

$$z_{\text{all}} = z_{\text{mem}} - j \cot \frac{\omega D}{c_0}. \tag{2.47}$$

Therefore, the sound absorption coefficient of the membrane absorber is expressed as (Maa 1975)

$$\alpha = \frac{4\text{Re}(z_{\text{all}})}{(1 + \text{Re}(z_{\text{all}}))^2 + \text{Im}(z_{\text{all}})^2}, \tag{2.48}$$

where Re denotes the real part of the impedance which is also known as resistance and Im denotes the imaginary part of the impedance which is also known as reactance.

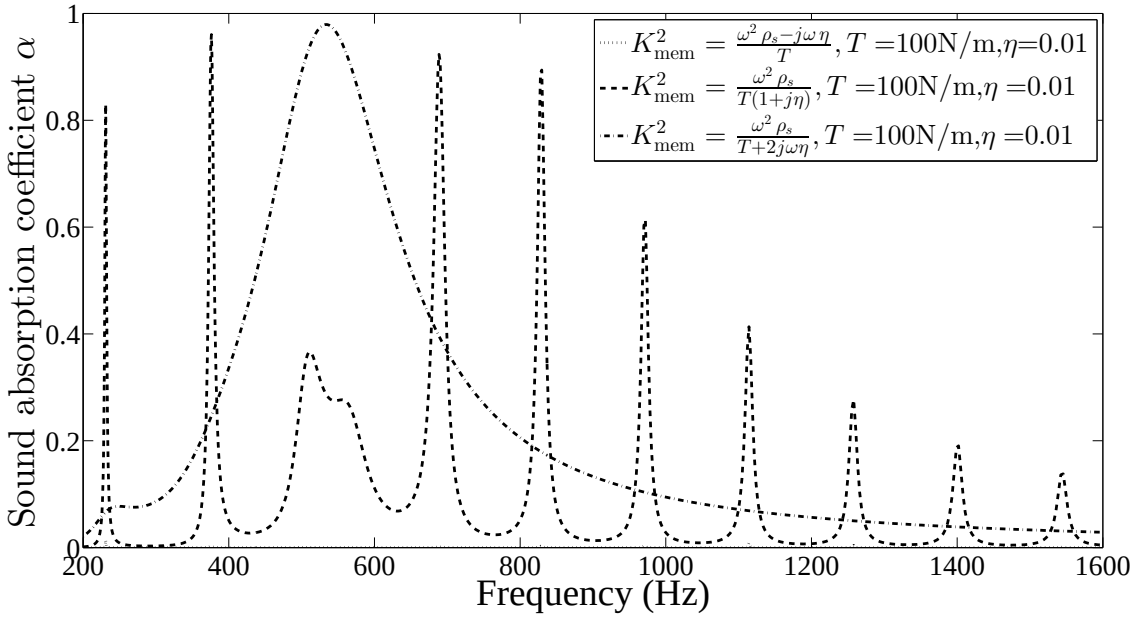

Figure 2.4: Effects of the different expression of K_{mem} on the sound absorption coefficients of a circular membrane. (Surface density $\rho_s = 0.485\,\text{kg/m}^2$; tension $T = 100\,\text{N/m}$; internal damping ratio $\eta = 0.01$.) Dashed lines and dotted lines represent two conventional expressions for $K^2_{\text{mem}} = \frac{\omega^2\rho_s - j\omega\eta}{T}$ (viscous damping) and $K^2_{\text{mem}} = \frac{\omega^2\rho_s}{T(1+j\eta)}$ (energy dissipation), respectively. Dashed dotted lines represent $K^2_{\text{mem}} = \frac{\omega^2\rho_s}{T+2j\omega\eta}$ calculated by the presented model for curvature damping.

An example is used here to investigate the effect of the different damping expressions on the sound absorption of the combined membrane-type absorber. Assuming that a circular membrane with a radius of $R_0 = 50\,\text{mm}$ and surface density $\rho_s = 0.485\,\text{kg/m}^2$ is stretched under a constant tension of $T = 100\,\text{N/m}$ and the internal damping is $\eta = 0.01$, the sound absorption coefficients of this membrane with cavity depth of $D = 25\,\text{mm}$ are shown in Figure 2.4. Obviously, the predicted results using Equation (2.46) are significantly different for the two differing expressions in Equation (2.46), which implies that the various representations of the damping effect have had a significant impact on the calculated values of the sound absorption of the membrane. The accuracy of these expressions is investigated in Section 2.3.1.

Note that in Figure 2.4, the values of the damping η were identical, although the damping expressions represent different physical mechanisms, namely, the viscous damping, the energy dissipation and the membrane curvature. When the viscous damping is considered, the real part of the acoustic impedance is close to zero, leading to a sound absorption coefficient

close to zero. When energy dissipation damping is considered, multiple sound absorbing peaks are observed due to the small damping ratio. Similar multiple sound absorbing peaks have been observed in theoretical sound absorption coefficients of MPPs provided by Song & Bolton (2002). The presented model for curvature damping demonstrates a smooth curve which is similar to the sound absorption curves typically obtained for micro-perforated panels and MPMs, implying that the presented damping expression based on curvature damping is realistic.

2.2.4 Acoustic impedance and sound transmission of a rectangular impervious membrane in a diffuse field

The sound absorption of a circular membrane has been investigated in Section 2.2.3. This section aims to investigate the acoustic impedance and sound transmission of a rectangular impervious membrane in a diffuse field. The modelling is firstly focussed on normally-incident sound waves in Section 2.2.4.1, and the corresponding sound transmission loss (STL) expression is developed in Section 2.2.4.2. By considering the oblique incidence angle, θ, the model with normally-incident sound waves is extended to a diffuse field in Section 2.2.4.3.

2.2.4.1 Motion equation of rectangular membrane vibration in the Cartesian coordinate system

In Section 2.2.3, the motion equation of the free vibration of a single layer circular impervious membrane under constant tension and damping was solved in the polar coordinate system. The prediction method for the normalised acoustic impedance and sound absorption is developed for a plane wave normally incident on the membrane surface.

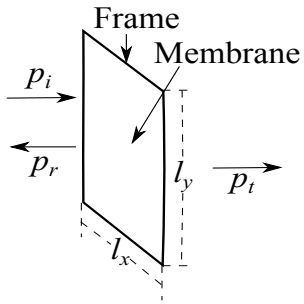

Figure 2.5: A rectangular membrane of dimension $l_x\, l_y$ stretched on a frame and excited by incident sound pressure p_i, with reflected pressure p_r and transmitted pressure p_t.

This section focusses on the sound transmission of a rectangular impervious membrane

in a diffuse field. The motion equation is solved in a Cartesian coordinate system. Assuming that plane waves are normally incident on the membrane surface, the membrane is stretched on a rectangular frame with a cross section area of $l_x l_y$, where l_x is the width of the rectangular membrane and l_y is the height of the rectangular membrane. As shown in Figure 2.5, the membrane is excited by the normally incident sound p_i. Some of the sound is reflected back with pressure p_r, and some is transmitted to the other side of the membrane, with pressure p_t. The vibration motion of the membrane is expressed by Equation (2.7). Substituting the Laplace operator in the Cartesian coordinate system yields

$$\begin{aligned} \nabla^2 \xi(x,y) + K_{\text{mem}}^2 \xi(x,y) &= 0, \\ \frac{\partial^2 \xi(x,y)}{\partial x^2} + \frac{\partial^2 \xi(x,y)}{\partial y^2} + K_{\text{mem}}^2 \xi(x,y) &= 0. \end{aligned} \tag{2.49}$$

The displacement function $\xi(x,y)$ is related to the x and y dimensions. Assuming that each dimension is independent of the other, the function $\xi(x,y)$ may be rewritten as

$$\xi(x,y) = X(x)Y(y), \tag{2.50}$$

where $X(x)$ denotes the function of the membrane displacement only related to the x coordinate and $Y(y)$ denotes that only related to the y coordinate. Substituting Equation (2.50) into Equation (2.49) yields

$$Y(y)\frac{\partial^2 X(x)}{\partial x^2} + X(x)\frac{\partial^2 Y(y)}{\partial y^2} + K_{\text{mem}}^2 X(x)Y(y) = 0. \tag{2.51}$$

Letting

$$K_{\text{mem,x}}^2 + K_{\text{mem,y}}^2 = K_{\text{mem}}^2, \tag{2.52}$$

where $K_{\text{mem,x}}$ denotes the x-component of K_{mem} and $K_{\text{mem,y}}$ denotes the y-component of K_{mem}, then Equation (2.51) becomes

$$\begin{aligned} Y(y)\frac{\partial^2 X(x)}{\partial x^2} + X(x)\frac{\partial^2 Y(y)}{\partial y^2} + \left(K_{\text{mem,x}}^2 + K_{\text{mem,y}}^2\right) X(x)Y(y) &= 0, \\ Y(y)\left[\frac{\partial^2 X(x)}{\partial x^2} + K_{\text{mem,x}}^2 X(x)\right] + X(x)\left[\frac{\partial^2 Y(y)}{\partial y^2} + K_{\text{mem,y}}^2 Y(y)\right] &= 0. \end{aligned} \tag{2.53}$$

To satisfy Equation (2.53), the two terms on the left-hand side must be equal to zero. Hence,

it is known that

$$\frac{\partial^2 X(x)}{\partial x^2} + K_{\text{mem,x}}^2 X(x) = 0, \tag{2.54a}$$

$$\frac{\partial^2 Y(y)}{\partial y^2} + K_{\text{mem,y}}^2 Y(y) = 0. \tag{2.54b}$$

The solutions of Equation (2.54) are given by

$$X(x) = A_x \sin(K_{\text{mem,x}} x) + B_x \cos(K_{\text{mem,x}} x), \tag{2.55a}$$

$$Y(y) = A_y \sin(K_{\text{mem,y}} y) + B_y \cos(K_{\text{mem,y}} y). \tag{2.55b}$$

Applying the boundary condition

$$X(x = 0) = 0, \tag{2.56a}$$

$$X(x = l_x) = 0, \tag{2.56b}$$

$$Y(y = 0) = 0, \tag{2.56c}$$

$$Y(y = l_y) = 0, \tag{2.56d}$$

the values of the constants in Equation (2.55) are obtained as

$$B_x = 0, \tag{2.57a}$$

$$B_y = 0, \tag{2.57b}$$

and

$$\sin(K_{\text{mem,x}} l_x) = 0, \tag{2.58a}$$

$$\sin(K_{\text{mem,y}} l_y) = 0, \tag{2.58b}$$

where

$$K_{\text{mem,x}} = \frac{n_x \pi}{l_x}, \qquad n_x = 1, 2, 3, \cdots \tag{2.59a}$$

$$K_{\text{mem,y}} = \frac{n_y \pi}{l_y}, \qquad n_y = 1, 2, 3, \cdots \tag{2.59b}$$

Equation (2.55) is simplified by the sum of the response of each mode is given by

$$X(x) = A_x \sin(\frac{n_x \pi}{l_x} x), \tag{2.60a}$$

$$Y(y) = A_y \sin(\frac{n_y \pi}{l_y} y). \tag{2.60b}$$

Based on the modal analysis method, the solution of Equation (2.49) is expressed as

$$\xi(x,y) = \sum_{n_x=1}^{N_x} \sum_{n_y=1}^{N_y} A_{n_x} A_{n_y} \sin(\frac{n_x \pi}{l_x} x) \sin(\frac{n_y \pi}{l_y} y), \tag{2.61}$$

where n_x is the x-axis modal index, N_x is the maximum mode number of n_x, n_y is the y-axis modal index and N_y is the maximum mode number of n_y. Equation (2.61) can be rewritten as

$$\xi(x,y) = \sum_{n=1}^{N} A_n \, \xi_n(x,y), \tag{2.62}$$

where

$$\xi_n(x,y) = \sin(\frac{n_x \pi}{l_x} x) \sin(\frac{n_y \pi}{l_y} y), \qquad n = N_y(n_x - 1) + n_y. \tag{2.63}$$

and $N = N_x \times N_y$. Note that in Equation (2.62), the variable A_n is unknown. The determination of the A_n values depends on the coupling between the acoustic pressure and the membrane vibration motion, which is examined in Section 2.2.4.2.

2.2.4.2 Coupling between acoustic pressure and membrane vibration and sound transmission loss with normally incident sound

With the displacement of the membrane vibration expressed by Equation (2.62), the vibration velocity of the membrane is obtained as

$$v(x,y) = \sum_{n=1}^{N} j\omega A_n \, \xi_n(x,y). \tag{2.64}$$

Due to the continuity of the normal particle velocity on the two sides of the membrane, the boundary conditions on each side are given by

$$\frac{p_i - p_r}{\rho_0 c_0} = v(x,y), \tag{2.65a}$$

$$\frac{p_t}{\rho_0 c_0} = v(x,y). \tag{2.65b}$$

Equation (2.65) may be rewritten as

$$p_r = p_i - \rho_0 c_0 \, v(x,y), \tag{2.66a}$$

$$p_t = \rho_0 c_0 \, v(x,y). \tag{2.66b}$$

Therefore, the sound pressure difference applied on the membrane surface is expressed as

$$\Delta p = p_i + p_r - p_t = 2p_i - 2\rho_0 c_0 \, v(x,y) = 2p_i - 2\rho_0 c_0 \, j\omega\xi(x,y). \tag{2.67}$$

When the membrane is excited by the incident sound pressure, the motion of the membrane vibration and the sound field are coupled. Hence, the membrane motion equation when forced by Δp is expressed as

$$(T+2j\omega\eta)\nabla^2\xi(x,y)+\omega^2\rho_s\xi(x,y)=-\Delta p=-2p_i+2\rho_0 c_0\, j\omega\xi(x,y). \tag{2.68}$$

Equation (2.68) is simplified as

$$(T+2j\omega\eta)\nabla^2\xi(x,y)+\left(\omega^2\rho_s-2\rho_0 c_0\, j\omega\right)\xi(x,y)=-2p_i. \tag{2.69}$$

Substituting Equation (2.62) into Equation (2.69) yields

$$(T+2j\omega\eta)\nabla^2\sum_{n=1}^{N}A_n\,\xi_n(x,y)+\left(\omega^2\rho_s-2\rho_0 c_0\, j\omega\right)\sum_{n=1}^{N}A_n\,\xi_n(x,y)=-2p_i. \tag{2.70}$$

Letting

$$\xi_m(x,y)=\sin(\frac{n_x\pi}{l_x}x)\sin(\frac{n_y\pi}{l_y}y),\qquad m=N_y(n_x-1)+n_y, \tag{2.71}$$

multiplying each side of Equation (2.70) by $\xi_m(x,y)$ and integrating over the membrane surface area gives

$$\begin{aligned}(T+2j\omega\eta)\int_0^{l_x}\int_0^{l_y}\xi_m(x,y)\nabla^2\sum_{n=1}^{N}A_n\,\xi_n(x,y)\mathrm{d}x\mathrm{d}y+\\ \left(\omega^2\rho_s-2\rho_0 c_0\, j\omega\right)\int_0^{l_x}\int_0^{l_y}\xi_m(x,y)\sum_{n=1}^{N}A_n\,\xi_n(x,y)\mathrm{d}x\mathrm{d}y\\ =-2p_i\int_0^{l_x}\int_0^{l_y}\xi_m(x,y)\mathrm{d}x\mathrm{d}y.\end{aligned} \tag{2.72}$$

Equation (2.70) is thus changed from one equation to a group of N equations given by Equation (2.72) which can be considered as a system of equations with respect to A_n and hence can be solved using matrices. By solving these equations, the variable A_n is obtained with respect to p_i. Although the value of p_i is unknown, the sound transmission loss (STL) is defined as

$$STL=20\times\log_{10}\left(\frac{1}{\tau}\right), \tag{2.73}$$

where

$$\tau=\left|\frac{p_t}{p_i}\right|. \tag{2.74}$$

Equation (2.72) can be considered in matrix form as an $N \times 1$ vector

$$\mathbf{A} = \begin{pmatrix} A_1 \\ A_2 \\ A_3 \\ \vdots \\ A_N \end{pmatrix}. \tag{2.75}$$

The factor $\int_0^{l_x}\int_0^{l_y} \xi_m(x,y)\nabla^2 \sum_{n=1}^{N} A_n \xi_n(x,y)\mathrm{d}x\mathrm{d}y$ in the left-hand side of Equation (2.72) is rewritten as

$$\begin{aligned} &\int_0^{l_x}\int_0^{l_y} \xi_m(x,y)\nabla^2 \sum_{n=1}^{N} A_n \xi_n(x,y)\mathrm{d}x\mathrm{d}y \\ &= \int_0^{l_x}\int_0^{l_y} \xi_m(x,y) \sum_{n=1}^{N} A_n \left[-\left(\frac{n_x \pi}{l_x}\right)^2 - \left(\frac{n_y \pi}{l_y}\right)^2 \right] \xi_n(x,y)\mathrm{d}x\mathrm{d}y. \end{aligned} \tag{2.76}$$

Letting

$$C_n = -\left(\frac{n_x \pi}{l_x}\right)^2 - \left(\frac{n_y \pi}{l_y}\right)^2, \qquad n = N_y(n_x - 1) + n_y, \tag{2.77}$$

yields an $N \times 1$ vector

$$\mathbf{C} = \begin{pmatrix} C_1 \\ C_2 \\ \vdots \\ C_n \end{pmatrix}. \tag{2.78}$$

Assuming that

$$\boldsymbol{\psi_1} = \begin{pmatrix} C_1 \int_0^{l_x}\int_0^{l_y} \xi_1(x,y)\xi_1(x,y)\mathrm{d}x\mathrm{d}y & C_2 \int_0^{l_x}\int_0^{l_y} \xi_1(x,y)\xi_2(x,y)\mathrm{d}x\mathrm{d}y & \dots & C_n \int_0^{l_x}\int_0^{l_y} \xi_1(x,y)\xi_n(x,y)\mathrm{d}x\mathrm{d}y \\ C_1 \int_0^{l_x}\int_0^{l_y} \xi_2(x,y)\xi_1(x,y)\mathrm{d}x\mathrm{d}y & C_2 \int_0^{l_x}\int_0^{l_y} \xi_2(x,y)\xi_2(x,y)\mathrm{d}x\mathrm{d}y & \dots & C_n \int_0^{l_x}\int_0^{l_y} \xi_2(x,y)\xi_n(x,y)\mathrm{d}x\mathrm{d}y \\ \vdots & \vdots & \ddots & \vdots \\ C_1 \int_0^{l_x}\int_0^{l_y} \xi_m(x,y)\xi_1(x,y)\mathrm{d}x\mathrm{d}y & C_2 \int_0^{l_x}\int_0^{l_y} \xi_m(x,y)\xi_2(x,y)\mathrm{d}x\mathrm{d}y & \dots & C_n \int_0^{l_x}\int_0^{l_y} \xi_m(x,y)\xi_n(x,y)\mathrm{d}x\mathrm{d}y \end{pmatrix}, \tag{2.79}$$

then Equation (2.80) is simplified to

$$\int_0^{l_x}\int_0^{l_y}\xi_m(x,y)\nabla^2\sum_{n=1}^{N}A_n\,\xi_n(x,y)\mathrm{d}x\mathrm{d}y=\int_0^{l_x}\int_0^{l_y}\xi_m(x,y)\sum_{n=1}^{N}A_n\left[-\left(\frac{n_x\pi}{l_x}\right)^2-\left(\frac{n_y\pi}{l_y}\right)^2\right]\xi_n(x,y)\mathrm{d}x\mathrm{d}y$$
$$=\boldsymbol{\psi_1}\times\mathbf{A}. \tag{2.80}$$

Similarly, the factor $\int_0^{l_x}\int_0^{l_y}\xi_m(x,y)\sum_{n=1}^{N}A_n\,\xi_n(x,y)\mathrm{d}x\mathrm{d}y$ is rewritten as

$$\int_0^{l_x}\int_0^{l_y}\xi_m(x,y)\sum_{n=1}^{N}A_n\,\xi_n(x,y)\mathrm{d}x\mathrm{d}y=\boldsymbol{\psi_2}\times\mathbf{A}, \tag{2.81}$$

where

$$\boldsymbol{\psi_2}=\begin{pmatrix}\int_0^{l_x}\int_0^{l_y}\xi_1(x,y)\xi_1(x,y)\mathrm{d}x\mathrm{d}y & \int_0^{l_x}\int_0^{l_y}\xi_1(x,y)\xi_2(x,y)\mathrm{d}x\mathrm{d}y & \dots & \int_0^{l_x}\int_0^{l_y}\xi_1(x,y)\xi_n(x,y)\mathrm{d}x\mathrm{d}y\\ \int_0^{l_x}\int_0^{l_y}\xi_2(x,y)\xi_1(x,y)\mathrm{d}x\mathrm{d}y & \int_0^{l_x}\int_0^{l_y}\xi_2(x,y)\xi_2(x,y)\mathrm{d}x\mathrm{d}y & \dots & \int_0^{l_x}\int_0^{l_y}\xi_2(x,y)\xi_n(x,y)\mathrm{d}x\mathrm{d}y\\ \vdots & \vdots & \ddots & \vdots\\ \int_0^{l_x}\int_0^{l_y}\xi_m(x,y)\xi_1(x,y)\mathrm{d}x\mathrm{d}y & \int_0^{l_x}\int_0^{l_y}\xi_m(x,y)\xi_2(x,y)\mathrm{d}x\mathrm{d}y & \dots & \int_0^{l_x}\int_0^{l_y}\xi_m(x,y)\xi_n(x,y)\mathrm{d}x\mathrm{d}y\end{pmatrix}. \tag{2.82}$$

The factor $\int_0^{l_x}\int_0^{l_y}\xi_m(x,y)\mathrm{d}x\mathrm{d}y$ in the right-hand side of Equation (2.72) is rewritten as

$$\mathbf{D}=\int_0^{l_x}\int_0^{l_y}\xi_m(x,y)\mathrm{d}x\mathrm{d}y=\begin{pmatrix}\int_0^{l_x}\int_0^{l_y}\xi_1(x,y)\mathrm{d}x\mathrm{d}y\\ \int_0^{l_x}\int_0^{l_y}\xi_2(x,y)\mathrm{d}x\mathrm{d}y\\ \vdots\\ \int_0^{l_x}\int_0^{l_y}\xi_m(x,y)\mathrm{d}x\mathrm{d}y\end{pmatrix}. \tag{2.83}$$

Substituting Equations (2.80), (2.81) and (2.83) into Equation (2.72) yields the motion equation of the forced vibration of the membrane in matrix form, which is given by

$$\left[(T+2j\omega\eta)\boldsymbol{\psi_1}+\left(\omega^2\rho_s-2\rho_0 c_0\, j\omega\right)\boldsymbol{\psi_2}\right]\mathbf{A}=-2p_i\mathbf{D}. \tag{2.84}$$

Therefore, the vector $\mathbf{A}$ is obtained as

$$\mathbf{A}=\frac{-2p_i\mathbf{D}}{(T+2j\omega\eta)\boldsymbol{\psi_1}+(\omega^2\rho_s-2\rho_0 c_0\, j\omega)\boldsymbol{\psi_2}}. \tag{2.85}$$

By substituting the vector $\mathbf{A}$ into Equation (2.62), integrating over the membrane area and dividing by the membrane area, the average displacement of the membrane is given by

$$\bar{\xi}=\frac{\sum_{n=1}^{N}A_n\int_0^{l_x}\int_0^{l_y}\xi_n(x,y)\mathrm{d}x\mathrm{d}y}{l_x l_y}=\frac{\boldsymbol{D}^{\mathrm{T}}\boldsymbol{A}}{l_x l_y}. \tag{2.86}$$

Hence, the average velocity $\bar{v}$ is expressed as

$$\bar{v} = \frac{\sum_{n=1}^{N} j\omega A_n \int_0^{l_x}\int_0^{l_y} \xi_n(x,y)\mathrm{d}x\mathrm{d}y}{l_x l_y} = \frac{j\omega}{l_x l_y}\boldsymbol{D}^{\mathrm{T}}\boldsymbol{A}, \tag{2.87}$$

where $\boldsymbol{D}^{\mathrm{T}}$ is the transpose of vector $\boldsymbol{D}$.

Based on the continuity of the normal particle velocity, the transmitted sound pressure p_t is obtained by substituting Equation (2.87) into Equation (2.66b), which is given by

$$p_t = \rho_0 c_0 \bar{v} = \frac{j\omega\rho_0 c_0}{l_x l_y}\boldsymbol{D}^{\mathrm{T}}\boldsymbol{A}. \tag{2.88}$$

Substituting Equations (2.85) and (2.88) into Equation (2.74) gives the expression of the normal sound transmission coefficient

$$\begin{aligned}\tau &= \left|\frac{p_t}{p_i}\right| = \left|\frac{\frac{j\omega\rho_0 c_0}{l_x l_y}\boldsymbol{D}^{\mathrm{T}}\boldsymbol{A}}{p_i}\right| \\ &= \left|\frac{j\omega\rho_0 c_0}{l_x l_y}\boldsymbol{D}^{\mathrm{T}}\frac{-2}{(T+2j\omega\eta)\boldsymbol{\psi_1}+(\omega^2\rho_s-2\rho_0 c_0 j\omega)\boldsymbol{\psi_2}}\boldsymbol{D}\right|.\end{aligned} \tag{2.89}$$

Note that the parameter p_i is eliminated in Equation (2.89). Therefore, the normal incidence STL is obtained by substituting Equation (2.89) into Equation (2.92). Equation (2.89) is in the same form as the expression derived by Zhang et al. (2012) for the sound transmission of meta-material membranes, except that no additional mass is attached on the membrane surface in the analysis presented here.

Since Equation (2.72) is based on the proposed curvature damping model, Equation (2.89) is the expression for the normal sound transmission coefficient based on curvature damping. If the conventional damping models are considered, Equation (2.89) becomes

$$\tau = \left|\frac{j\omega\rho_0 c_0}{l_x l_y}\boldsymbol{D}^{\mathrm{T}}\frac{-2}{T\boldsymbol{\psi_1}+(\omega^2\rho_s-j\omega\eta-2\rho_0 c_0 j\omega)\boldsymbol{\psi_2}}\boldsymbol{D}\right| \tag{2.90}$$

for the viscous damping model, and

$$\tau = \left|\frac{j\omega\rho_0 c_0}{l_x l_y}\boldsymbol{D}^{\mathrm{T}}\frac{-2}{(T+j\eta)\boldsymbol{\psi_1}+(\omega^2\rho_s-2\rho_0 c_0 j\omega)\boldsymbol{\psi_2}}\boldsymbol{D}\right| \tag{2.91}$$

for the the complex tension model. Furthermore, the expression for the STL is given by (Bies & Hansen 2009)

$$STL = 20\log_{10}\left(\frac{1}{\tau}\right). \tag{2.92}$$

2.2.4.3 Sound transmission loss in a diffuse field

In Section 2.2.4.2, the expressions for the transmission coefficient and STL with a normally-incident sound field were derived. This section aims to investigate the sound transmission of a rectangular impervious membrane in a diffuse field. The transmission coefficient in a diffuse field is defined as (Fahy & Gardonio 2007)

$$\tau_{\text{diffuse}} = \frac{\int_0^{\theta_{\max}} \tau(\theta)\sin(\theta)\cos(\theta)\mathrm{d}\theta}{\int_0^{\theta_{\max}} \sin(\theta)\cos(\theta)\mathrm{d}\theta}, \tag{2.93}$$

where θ is the incidence angle of p_i and $\theta_{\max}$ is the upper limit of θ. The value of $\theta_{\max}$ is 90° theoretically, however, it is dependent on the experimental results in practice. It is commonly accepted that $\theta_{\max} = 78°$. The corresponding STL of Equation (2.93) is the STL in a diffuse field denoted by STL_{diffuse}. Moreover, Bies & Hansen (2009) provided an approximate equation described as "the field incidence transmission loss", which is given by

$$STL_{\text{field}} = STL - 5.5, \tag{2.94}$$

where the subtrahend may vary. Bies & Hansen (2009) mentioned that a value of 5.5 is acceptable for predictions in 1/3 octave bands, and 4 should be used for octave band predictions. However, Fahy & Gardonio (2007) instead used 5 for 1/3 octave. Hence, the subtrahend is an estimated value and depends on the experimental configuration.

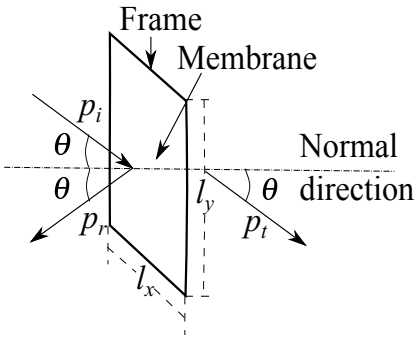

Figure 2.6: A rectangular membrane stretched on a frame and excited by a sound pressure with an obliquely incidence angle of θ.

To calculate the STL in a diffuse field, it is necessary to derive the expression for the transmission coefficient with oblique sound incidence. When a rectangular impervious membrane is excited by incident sound with an angle of θ, as shown in Figure 2.6, the boundary conditions due to the continuity of the particle velocity in the normal direction are expressed

as

$$\frac{(p_i - p_r)\cos(\theta)}{\rho_0 c_0} = v(x,y), \tag{2.95a}$$

$$\frac{p_t \cos(\theta)}{\rho_0 c_0} = v(x,y). \tag{2.95b}$$

Note that $v(x,y)$ is the vibration velocity of the membrane, hence it is also equal to the particle velocity in the normal direction. Therefore, by rearranging Equation (2.95), the following is obtained

$$p_r = p_i - \frac{\rho_0 c_0 v(x,y)}{\cos(\theta)}, \tag{2.96}$$

and

$$p_t = \frac{\rho_0 c_0 v(x,y)}{\cos(\theta)}. \tag{2.97}$$

Consequently, Equation (2.67) becomes

$$\Delta p = p_i + p_r - p_t = 2p_i - \frac{2\rho_0 c_0 j\omega}{\cos(\theta)}\xi(x,y), \tag{2.98}$$

and the motion equation is expressed by

$$(T + 2j\omega\eta)\nabla^2\xi(x,y) + \left[\omega^2\rho_s - \frac{2\rho_0 c_0 j\omega}{\cos(\theta)}\right]\xi(x,y) = -2p_i. \tag{2.99}$$

Note that Equation (2.99) is similar to Equation (2.69). Moreover, if $\theta = 0^\circ$ then $\cos(\theta) = 1$, and Equation (2.99) is identical to Equation (2.69). The similarity between Equations (2.99) and (2.69) implies that the former can be solved following the same strategy used when solving the latter. Therefore, the sound transmission coefficient with oblique incidence angle θ is obtained as

$$\tau = \left| \frac{j\omega\rho_0 c_0}{l_x l_y \cos(\theta)} \boldsymbol{D}^{\mathrm{T}} \frac{-2}{(T + 2j\omega\eta)\boldsymbol{\psi_1} + \left[\omega^2\rho_s - \frac{2\rho_0 c_0 j\omega}{\cos(\theta)}\right]\boldsymbol{\psi_2}} \boldsymbol{D} \right|. \tag{2.100}$$

Similarly, if $\theta = 0^\circ$ and $\cos(\theta) = 1$, Equation (2.100) is identical to Equation (2.74), which implies the consistency of the derivation. By substituting Equation (2.100) into Equations (2.93) and (2.92), the STL in a diffuse field, STL_{diffuse}, is obtained.

Note that this derivation is based on the proposed damping expression due to membrane

curvature. If the conventional damping models are considered, Equation (2.100) becomes

$$\tau = \left| \frac{j\omega\rho_0 c_0}{l_x l_y \cos(\theta)} \boldsymbol{D}^{\mathrm{T}} \frac{-2}{T\boldsymbol{\psi_1} + \left[\omega^2\rho_s - j\omega\eta - \frac{2\rho_0 c_0 j\omega}{\cos(\theta)}\right]\boldsymbol{\psi_2}} \boldsymbol{D} \right| \tag{2.101}$$

for the viscous damping model, and

$$\tau = \left| \frac{j\omega\rho_0 c_0}{l_x l_y \cos(\theta)} \boldsymbol{D}^{\mathrm{T}} \frac{-2}{(T + j\eta)\boldsymbol{\psi_1} + \left[\omega^2\rho_s - \frac{2\rho_0 c_0 j\omega}{\cos(\theta)}\right]\boldsymbol{\psi_2}} \boldsymbol{D} \right| \tag{2.102}$$

for the the energy dissipation damping model.

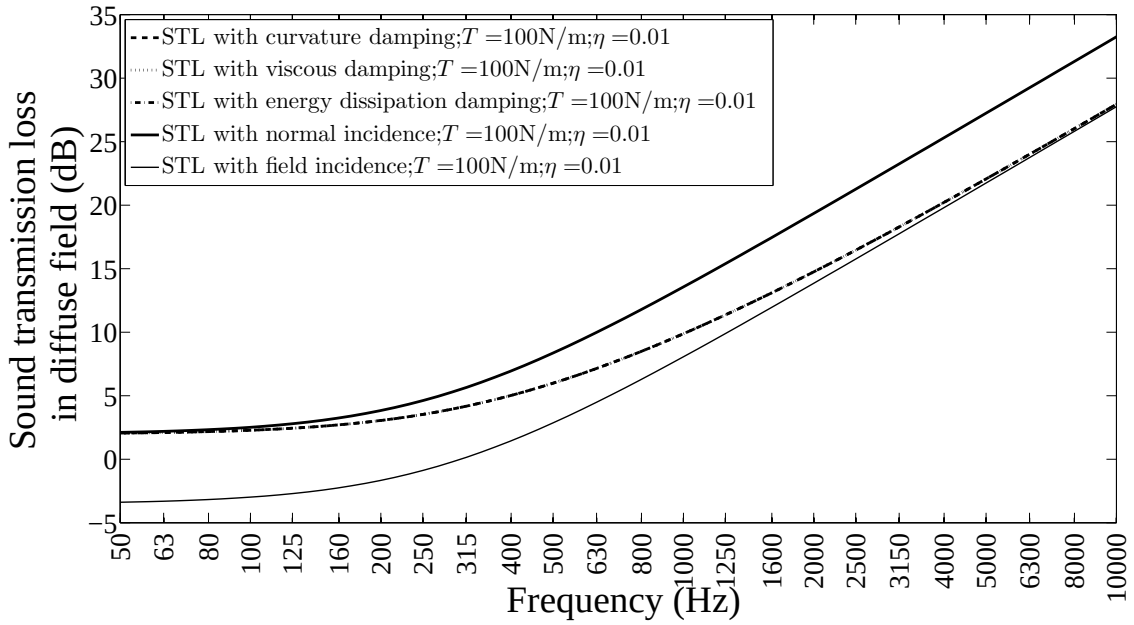

Figure 2.7: Effects of the different damping expressions η on the one-third octave STL of a rectangular membrane. (Surface density $\rho_s = 0.485\,\mathrm{kg/m^2}$; tension $T = 100\,\mathrm{N/m}$; internal damping ratio $\eta = 0.01$; $l_x = 1\mathrm{m}$; $l_y = 1.5\mathrm{m}$; $N = M = 150$, $\theta_{\max} = 85°$). The dashed line represents the STL in a diffuse field calculated using Equation (2.100). The dotted line and dashed-dotted lines represent the predictions for viscous damping and energy dissipation damping given by Equations (2.101) and (2.102), respectively. The thick solid line is the prediction result for curvature damping with a normally incident plane wave. The thin solid line is that for the field incidence for curvature damping using Equation (2.94).

Figure 2.7 shows a comparison of the predictions for the STL of a single layer membrane in a diffuse field using Equations (2.100), (2.101) and (2.102). The parameters used for the sample membrane are identical with that used in Section 2.2.4.2. The results predicted by the curvature damping model, viscous damping model and energy dissipation model are very similar because Equations (2.100), (2.101) and (2.102) are very similar except for the different expressions for damping. The influence of the damping ratio is relatively small

compared to the membrane tension and mass, and hence has a small impact on the predicted STLs.

In Figure 2.7, the thick solid line shows the STL with a normally incident plane wave predicted by Equation (2.89). The predicted STL in a diffuse field is close to that of the normal incidence model in the low frequency range from 50 Hz to 125 Hz. However, the former is lower than the latter from 125 Hz to 10 kHz. This indicates that the oblique incidence of sound waves affects the STL in the high frequency range more significantly than it does in the low frequency range. The thin solid line is the STL with field incidence which is expressed by Equation (2.94). It agrees with the predicted STLs in a diffuse field very well at the frequencies above 3150 Hz, however, in the low frequency range below 315 Hz, its values were negative. This is because Equation (2.94) is only valid at the frequencies where $f > \frac{\rho_0 c_0}{\rho_s}$ (Bies & Hansen 2009). In the case shown in Figure 2.7, $f > \frac{\rho_0 c_0}{\rho_s} = 858$ Hz, implying that the field incidence transmission loss is expected to be below 858 Hz.

2.3 Experimental validation

The analytical models for the sound absorption of a circular impervious membrane with a normally incident plane wave and the sound transmission of a rectangular impervious membrane in a diffuse field were presented in Section 2.2. This section presents the experimental validation for these developed models. The details of the experiments are presented in Sections 2.3.1 and 2.3.2.

2.3.1 Sound absorption coefficient of single layer impervious membranes

To validate the analytical model for the sound absorption of a circular impervious membrane, sound absorption experiments were conducted in an impedance tube with a normally-incident plane wave. The radius of the impedance tube is $R_0 = 50$mm. Two circular membrane samples with their parameters shown in Table 2.2 were tested. Figure 2.8 shows photographs of the samples. The sound absorption coefficient of each sample was measured with two cavity depths of $D = 25$mm and $D = 50$mm. The measurement frequency range was from 200 Hz to 1600 Hz. The two microphone transfer function method (as shown in Figure 2.9) was used to obtain the sound absorption coefficient (Chung & Blaser 1980*a*). Based on

this method, the sound absorption coefficient can be estimated by

$$\alpha = 1 - \left| \frac{H_{12} - e^{-jk_0 s}}{e^{jk_0 s} - H_{12}} e^{j2k_0 l_1} \right|^2 \tag{2.103}$$

where H_{12} is the transfer function between the measured sound pressure at microphone 1 and 2, l_1 and l_2 are the distances from each microphone to the MPM surface, and $s = l_1 - l_2$ is the distance between the microphones.

Table 2.2: Parameters of the impervious membranes.

Membrane number	Material	Surface density $(\mathrm{kg/m^2})$	Thickness (mm)
1	PVC	0.4850	0.42
2	PVC	0.9315	0.71

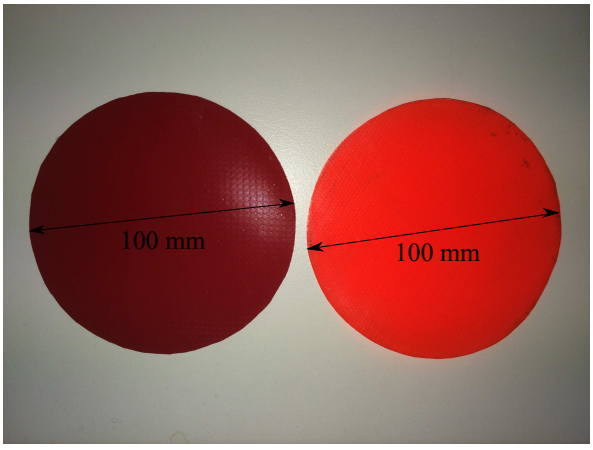

Figure 2.8: Photographs of two membrane samples used for sound absorption experiments.

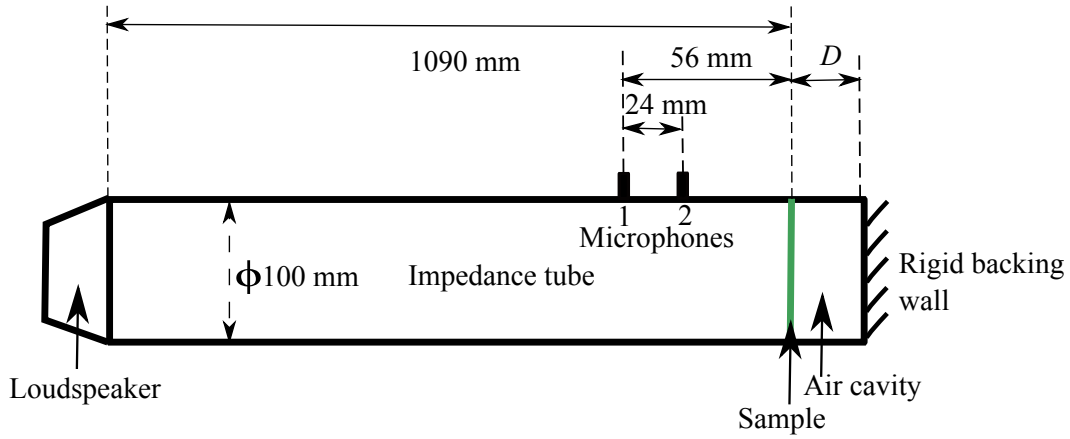

Figure 2.9: Measurement of the sound absorption coefficient using the two microphone transfer function method in an impedance tube.

Note that the values of the tension T and the internal damping factor η are unable to be measured directly. Hence the equivalent values of T and η used in the analytical model

have been obtained by fitting the measured data to the prediction using the Matlab optimisation toolbox with the constraints (Waltz et al. 2006) of positive tension and damping ratio. Moreover, the damping ratio is usually less than 0.05 in practice. The constraint of η for the optimisation is extended from zero to one to find the global optimised η. Comparison of the measured data to the predicted data using the conventional and the proposed expressions for the internal damping factor is shown in Figures 2.10 to 2.13.

To assess the accuracy of the three prediction models for membrane damping, the coefficient of determination, $R^2_{\text{determination}}$, for each model is defined as

$$R^2_{\text{determination}} = 1 - \frac{\sum_{n_{\text{freq}}=1}^{N_{\text{freq}}} \left(\alpha_{\text{experiment}} - \alpha_{\text{prediction}}\right)^2}{\sum_{n_{\text{freq}}=1}^{N_{\text{freq}}} \left(\alpha_{\text{experiment}} - \overline{\alpha_{\text{experiment}}}\right)^2}, \tag{2.104}$$

where n_{freq} denotes the index of the measured frequency, N_{freq} denotes the total number of measured frequencies, $\alpha_{\text{prediction}}$ denotes the predicted sound absorption coefficient and $\alpha_{\text{experiment}}$ denotes the measured sound absorption coefficient. As $R^2_{\text{determination}}$ approaches unity, the fidelity of the model increases.

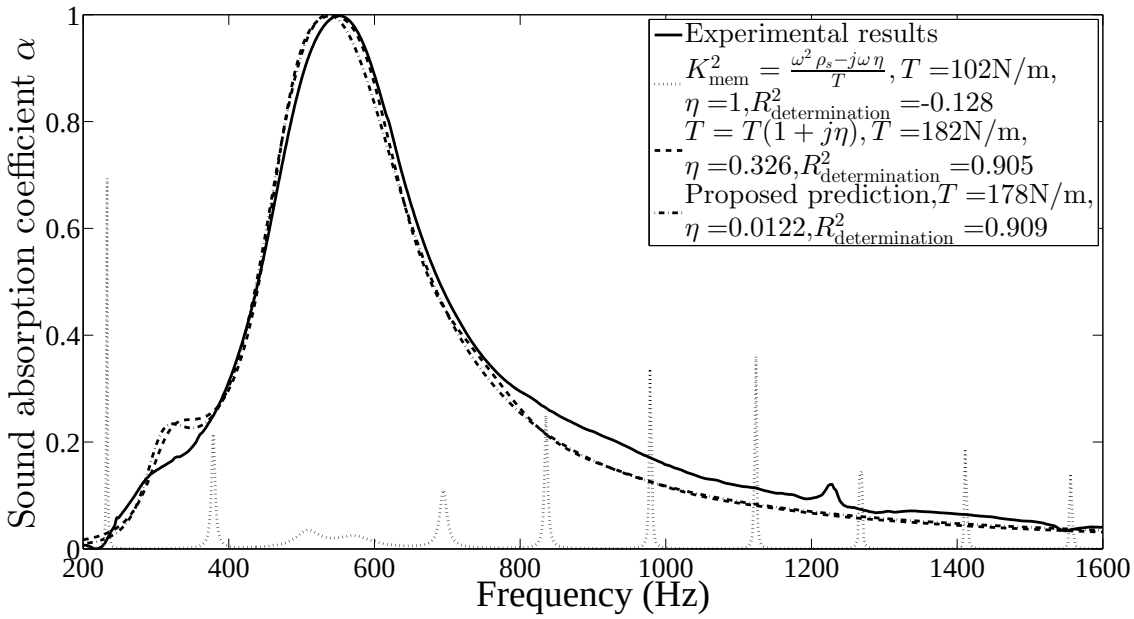

Figure 2.10: Normal incidence sound absorption coefficients of Membrane 1 for $D = 25$mm.

For all the membrane samples, the $R^2_{\text{determination}}$ of the presented model is the closest to unity amongst the three prediction methods. Hence, the presented model provides the

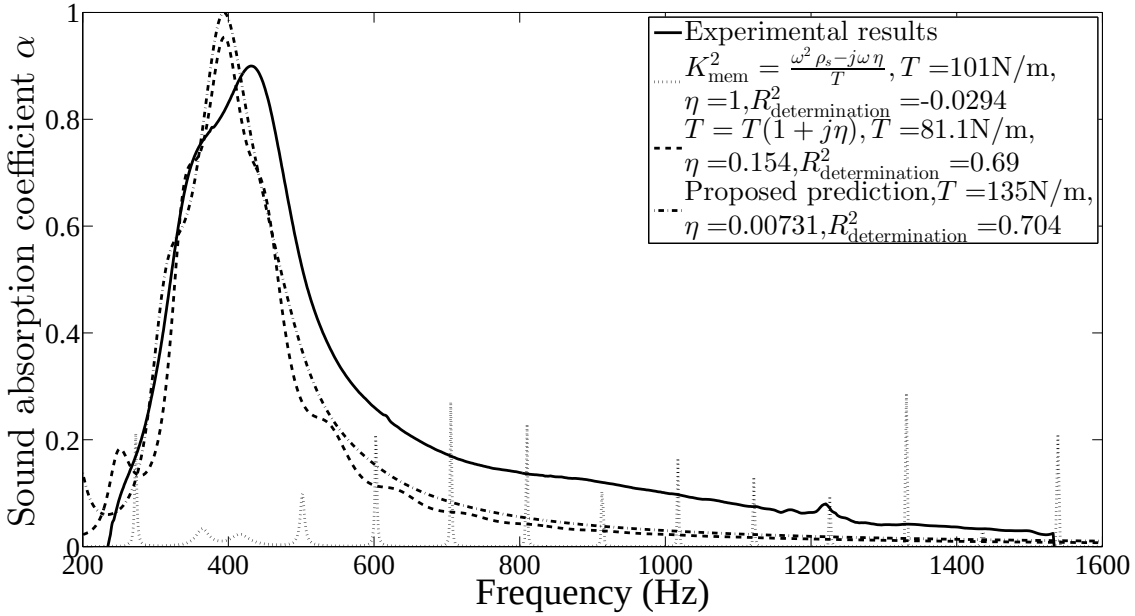

Figure 2.11: Normal incidence sound absorption coefficients of Membrane 2 for $D = 25$mm.

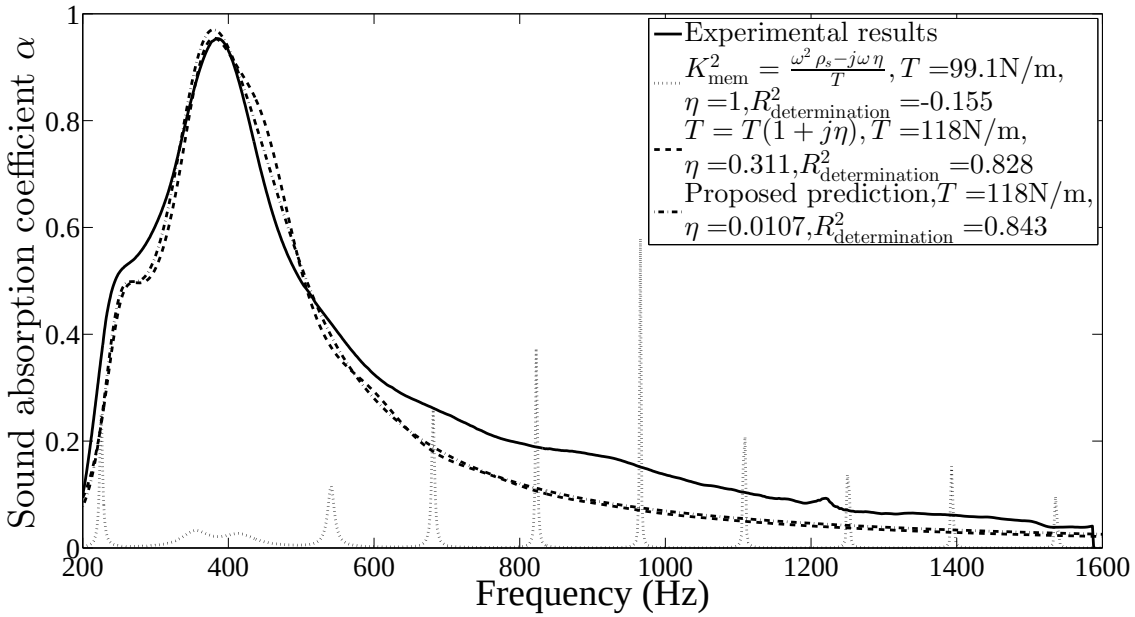

Figure 2.12: Normal incidence sound absorption coefficients of Membrane 1 for $D = 50$mm.

best agreement with the experimental results and is suitable for the prediction of the sound absorption of impervious membranes.

The values of $R^2_{\text{determination}}$ using the viscous damping model were negative, implying the inaccuracy of this model. The dashed curves represent the predicted sound absorption coefficients using the viscous damping method. Oscillatory sound absorption peaks are shown

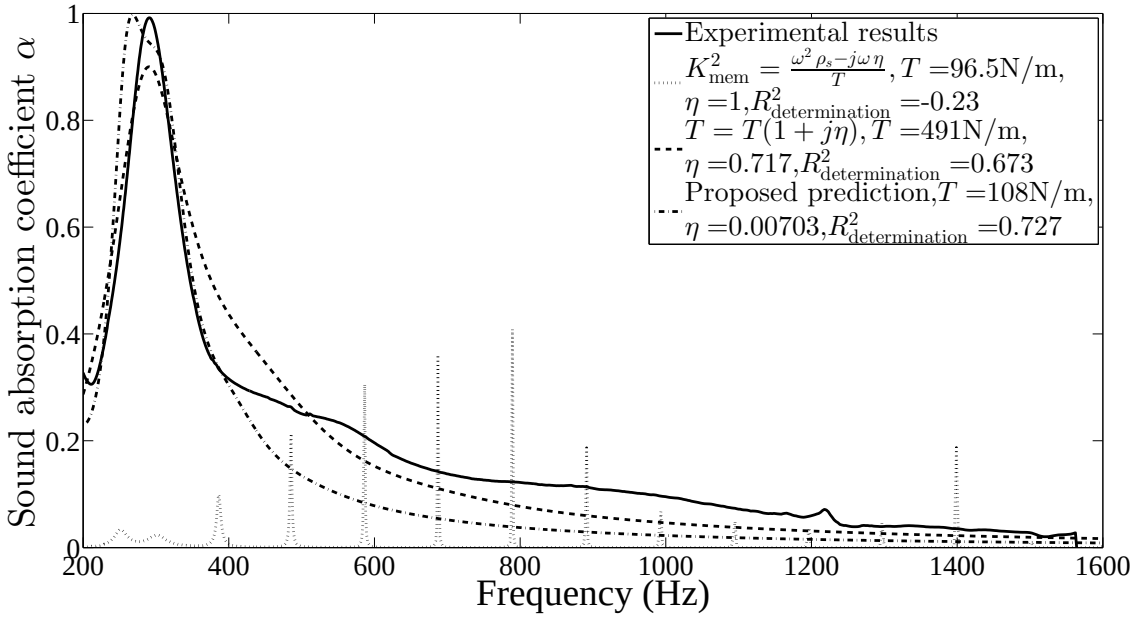

Figure 2.13: Normal incidence sound absorption coefficients of Membrane 2 for $D = 50$mm.

on the curves due to the oscillation of its corresponding K^2_{mem}. Similar oscillatory sound absorption peaks were observed in Figure 2.4 and have been presented by Song & Bolton (2002).

Although the predictions using the complex tension $T(1+j\eta)$ representing energy dissipation damping show reasonable agreement with the measured results, it is noticed that its $R^2_{\text{determination}}$ is lower than that of the proposed model. Moreover, the damping ratio is usually less than 0.05 in practice. However, the optimal damping ratios obtained from the optimisation using the complex tension $T(1+j\eta)$ model are 0.326 and 0.311 for Membrane 1 with cavity depths of 25 mm and 50 mm, and 0.154 and 0.717 for Membrane 2 with cavity depths of 25 mm and 50 mm. These values for damping appear to be unrealistic. This may also imply that the energy dissipation model is not realistic for the membranes used in this thesis.

In this section, the proposed model for the sound absorption prediction of a circular impervious membrane is validated by experiments. The conventional expressions for the damping factor are compared with the proposed model and the experimental results. The comparison indicates that the proposed model provides the best agreement with the measured sound absorption coefficients among the models investigated. The optimised tension and damping ratio using the proposed model appear to be reasonable. Therefore, the pro-

posed model can be used as a tool to predict the sound absorption properties of single layer impervious membranes. The internal damping of the membrane structure under constant tension is most likely ascribed to the membrane curvature.

Furthermore, the first natural frequency of a circular impervious membrane is given by Kinsler et al. (1999)

$$f_{\text{natural}} = \frac{2.405\sqrt{\frac{T}{\rho_s}}}{2\pi R_0}, \tag{2.105}$$

where 2.405 is the first positive root of $J_0 = 0$. The first natural frequencies of the circular membrane samples used in Figures 2.10, 2.11, 2.12, and 2.13 are shown in Table 2.3. It is

Table 2.3: Natural frequencies of the circular membrane samples used in Figures 2.10, 2.11, 2.12, and 2.13.

Figure number	T (N/m)	ρ_s (kg/m^2)	D (mm)	First natural frequency
Figure 2.10	178	0.485	25	f_{natural} =146 Hz
Figure 2.11	135	0.9315	25	f_{natural} =92 Hz
Figure 2.12	118	0.485	50	f_{natural} =119 Hz
Figure 2.13	108	0.9315	50	f_{natural} =82 Hz

demonstrated that all the first natural frequencies of the membrane samples are lower than the lowest measured frequency (200 Hz), and hence the membrane samples are in the mass controlled region of the fundamental mode. However, Equations (2.46) and (2.48) imply that the sound absorption of the circular membranes is dependent on the real and imaginary parts of the acoustic impedance, and hence is related to the tension and internal damping, as well as the mass.

2.3.2 Diffuse field sound trasmission loss of single layer impervious membranes

Sound transmission losses of two types of impervious membrane were measured to validate the model proposed in Section 2.2.4.3. The measurement was conducted in the two reverberation chambers at the University of Adelaide of dimensions listed in Table 2.4. The parameters of the membrane samples are shown in Table 2.5. The sound pressure levels (SPLs) of the source room and the receiver room were spatially and temporally averaged over three minutes at the centre frequencies of the one-third octave bands between 50 Hz and 10 kHz.

The tension constant T and the damping ratio η are unable to be measured directly. The values of T and η used in the analytical model were obtained by fitting the measured data to

Table 2.4: Dimensions of the reverberation chambers used to measure the diffuse field STL.

Chambers	Source chamber	Receiver chamber	Test window
Length (m)	6.085	6.840	N/A
Width (m)	5.175	5.565	1.005
Height (m)	3.355	4.720	1.510
Surface area (m^2)	135.5	193.2	1.52
Volume (m^3)	105.6	179.7	N/A

Table 2.5: Parameters of the impervious membranes.

Membrane number	Material	Surface density (kg/m^2)	Thickness (mm)
1 (same as that used in Section 2.3.1)	PVC	0.4850	0.42
3	Rubber	0.9848	0.81

the prediction using the Matlab optimisation toolbox (Waltz et al. 2006).

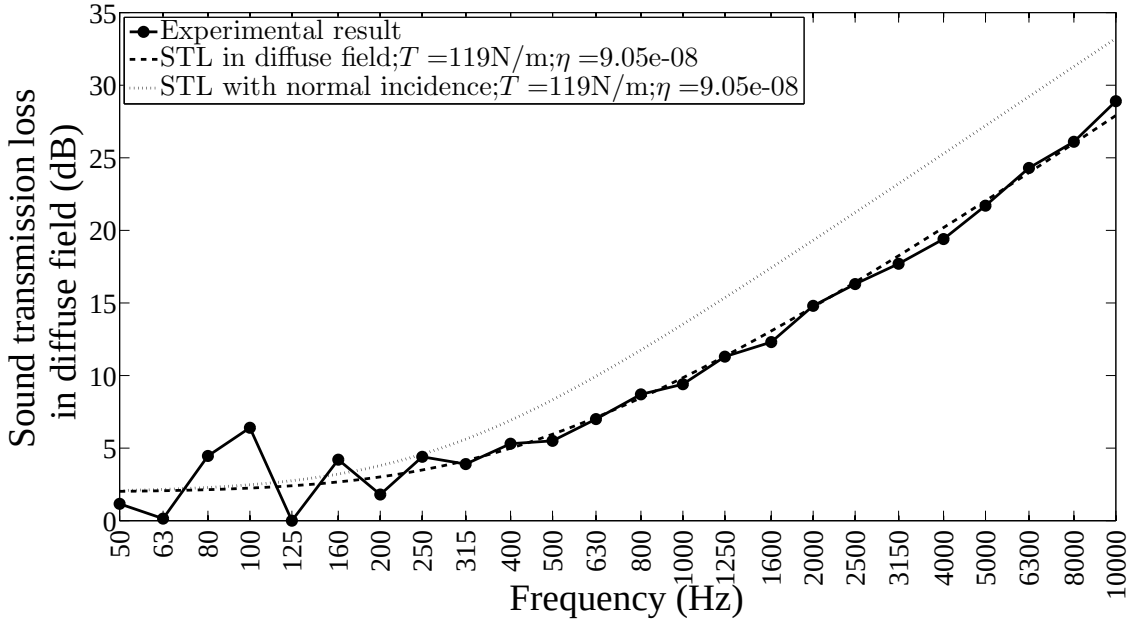

Figure 2.14: STL of Membrane 1 in a diffuse field calculated by the presented model using Equation (2.100).

In the prediction, the maximum membrane model indices of eight for the width and twelve for the length were used. The upper limit for the incidence angle $\theta_{\max}$ is 85°. The predicted results are compared with the measured results in Figures 2.14 and 2.15.

In Figure 2.14, the predicted diffuse field STL of Membrane 1 agrees well with the measured STL above 315Hz, which implies the accuracy of the proposed model. However, in the low frequency range below 315Hz, the measured data differs from the predicted data. Similar disagreement between the predicted and measured data is seen in Figure 2.15 for Membrane 3. The reason for the disagreement is due to the chamber properties. The sound fields in

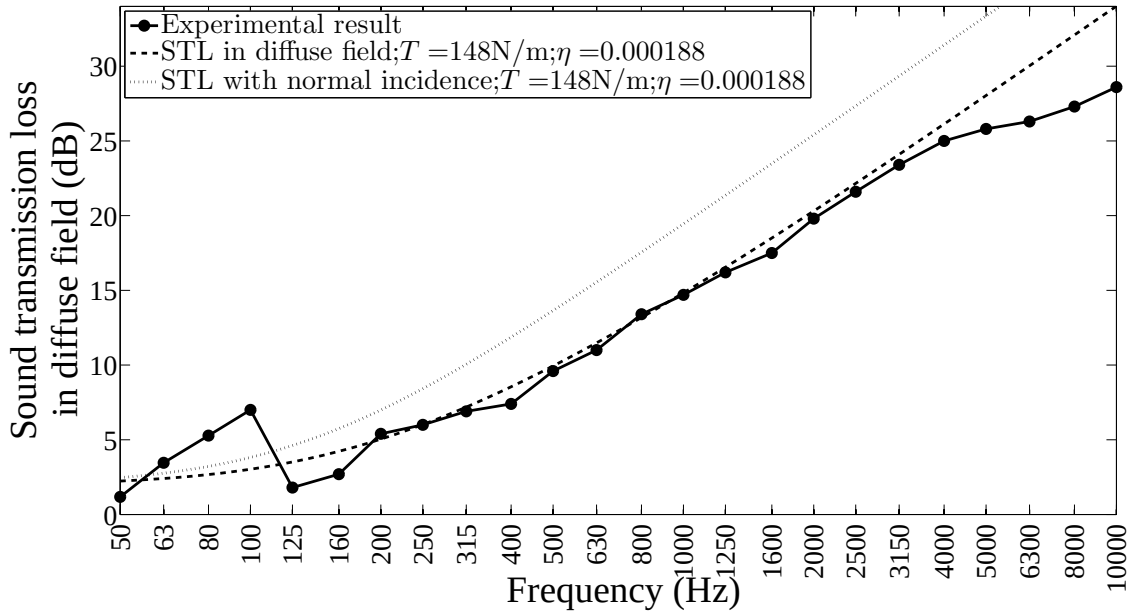

Figure 2.15: STL of Membrane 3 in a diffuse field calculated using Equation (2.100).

both the source chamber and the receiver chamber are assumed to be uniform. However, according to ISO 140.4 (ISO140.4 2006), the sound field is non-uniform in the frequency range below 400 Hz, because fewer modes are excited in the chambers and the wave length is significantly longer in this frequency range than in the middle and high frequency range. These non-uniform sound fields lead to inaccuracy of the measured STL in the low frequency range.

In Figure 2.15, the predicted STL of Membrane 3 shows good agreement with the measured STL from 200 Hz to 4 kHz. Hence, the accuracy of the proposed model has been verified. However, the measured STL is lower than the predicted STL from 4 kHz to 10 kHz. This overestimation in the high frequency range has also been observed by Sewell (1970). Although his research examined the STL of an infinite-sized limp lead panel and the upper limit of the measured frequency range was 3200 Hz, he investigated the effect of different boundary conditions on the predicted STL theoretically and found experimentally that the diffuse field STL of massive panels in the middle and high frequency range was related to the edge condition. The predicted STL could hence differ from the experimental results depending on edge condition, such as simply-supported edges or clamped edges. Hence, it is possible that the overestimation of the presented model is due to the neglected edge effects. With regard to Membrane 1, the edge effect may have an unobservable impact on the pre-

dicted STL due to its light weight. The further consideration of edge effects is beyond the scope of this thesis.

Note that the magnitude of the optimised damping ratio η is 10^{-8} for Membrane 1 and 10^{-5} for Membrane 3, both of which are close to zero. This implies that they would be expected to have similar responses as they are both lightly damped. The natural frequency of a rectangular impervious membrane is given by (Kinsler et al. 1999)

$$f(n,m) = \frac{\sqrt{\frac{T}{\rho_s}}}{2}\sqrt{\left(\frac{n}{l_x}\right)^2 + \left(\frac{m}{l_y}\right)^2}. \tag{2.106}$$

The first natural frequencies of the membrane samples listed in Table 2.6 are lower than the lower limit of the measured frequency range (50 Hz). Hence, the membrane samples behave in the mass controlled region of the fundamental mode in the measured frequency range where the mass is the governing factor and the tension and damping are of less importance than the mass. This also explains the similarity between the predicted results using the three models in Figure 2.7.

Table 2.6: Natural frequencies of the circular membrane samples used in Figures 2.14 and 2.15.

Figure number	T (N/m)	ρ_s (kg/m^2)	First natural frequency
Figure 2.14	119	0.485	$f(1,1)$ =9 Hz
Figure 2.15	148	0.9848	$f(1,1)$ =7 Hz

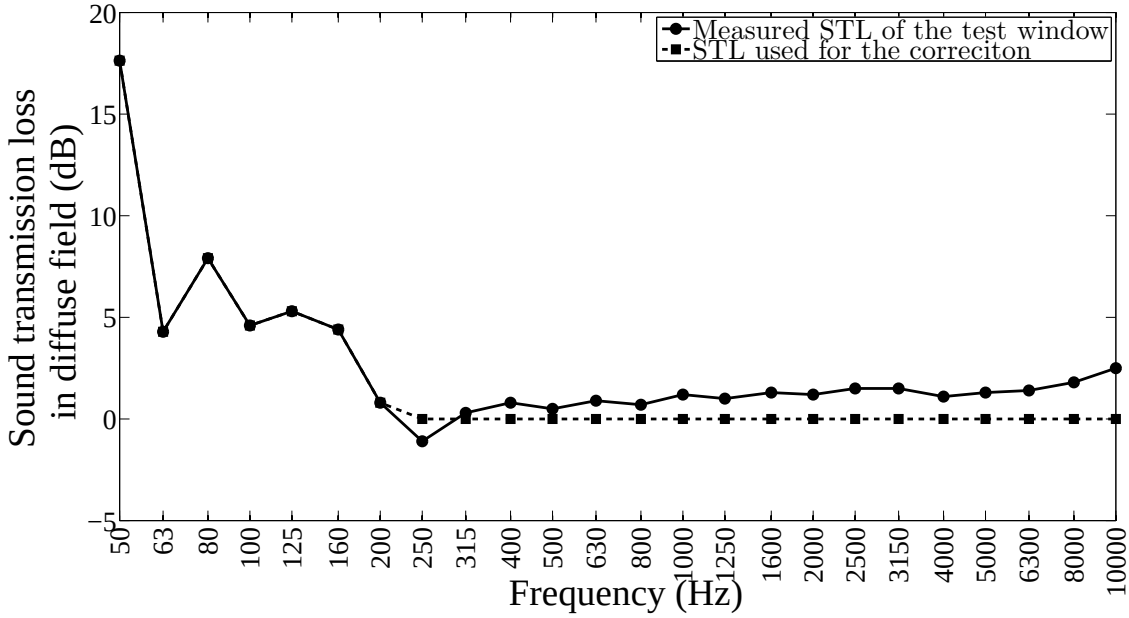

Figure 2.16: Diffuse field STL of the test window without a sample present.

It should be noted that all the measured STLs presented have been subtracted by a correction based on the STL of the test window. This is because, theoretically, the STL of an open window is equal to zero, however in practice, for small apertures the STL is a small finite value varying with frequency (Martin 2008). The effect could be significant at low frequencies below 200 Hz, as shown in Figure 2.16 where the solid line with circular markers shows the measured STL of the test window used in this study. The measured STL of the test window is extremely high at 50 Hz and around 5 dB from 63 Hz to 160 Hz. The measured STL of the membrane samples can be considered to be the total STL due to the acoustic properties of both the open window and the membrane samples. Assuming that the membrane motion and the air motion of the open window are completely decoupled, the total STL can be expressed as

$$STL_{\text{total}} = 20 \times \log_{10}\left(\frac{p_{\text{air},1}}{p_i}\frac{p_i}{p_t}\frac{p_t}{p_{\text{air},2}}\right) = STL_{\text{window}} + STL_{\text{sample}}, \tag{2.107}$$

where $p_{\text{air},1}$ and $p_{\text{air},2}$ denote the sound pressure on two surfaces of the test window. Hence, the STL of the sample is given by

$$STL_{\text{sample}} = STL_{\text{total}} - STL_{\text{window}}. \tag{2.108}$$

In an attempt to eliminate the effect of the window on the measured STLs of the samples, the measured STLs of the membranes were subtracted by the STL of the test window using Equation (2.108). However, it was found that subtracting the STL of the test window leads to an overestimation of the predicted results in the middle and high frequency range. In the frequency range above 200 Hz, the predicted results agree with the STL of the membranes better if the latter is not subtracted by the STL of the test window. Therefore, a modified correction has been used for the STLs of the membranes which is equal to the STL of the test window at low frequencies (below 200 Hz) and is zero at frequencies above 200 Hz, as illustrated in Figure 2.16.

2.4 Discussion on the effect of tension and damping on the sound absorption and sound transmission of single layer impervious membranes

In Section 2.2, the effects of the tension and damping ratio on the sound absorption and transmission of single layer impervious membranes have been studied theoretically. Based on the theoretical investigation, it is presumed that the damping ratio affects the sound absorption of the membranes significantly. However, for the STL results, the two membrane samples were in the mass controlled region and their damping ratios were found to be close to zero based on the optimisation approach used here. The mass has a more important impact on the STLs than the tension and damping ratio.

There are several reasons which may contribute to the different significance of the damping ratio on the sound absorption and sound transmission of a single layer membrane. Firstly, the sound absorption coefficients and the STLs in a diffuse field were measured in different frequency ranges. It is known that the damping and tension mainly affect the acoustic properties of membranes in the low frequency range (Fahy & Gardonio 2007). The measurement range of the sound absorption coefficients is from 200 Hz to 1600 Hz, which is in a relatively low frequency range compared to the measurement range of the STL experiments which were measured at the centre frequencies of the one-third octave bands from 50 Hz to 10 kHz. Hence, the STL experiments show more characteristics in the middle and high frequency ranges and due to inaccuracies with the STL measurement it is difficult for the STL tests to reveal the damping effect in the low frequency range.

Additionally, the frequency resolution may also affect the observation of the damping effects. The sound absorption coefficients were measured at each frequency from 200 Hz to 1600 Hz. However, the STLs were measured at the centre frequencies of the one-third octave bands from 50 Hz to 10 kHz, which means 24 sets of data were obtained to represent the STLs over a large frequency range. Consequently, more details of the frequency response can be observed in the sound absorption data than in the STL data.

Moreover, the scale of the samples for the sound absorption experiments and for the STL experiments differ significantly, as well as the sound field in each experiment. As

mentioned in Section 2.3.1, the circular membranes are 0.0079 m^2 in area, whereas the rectangular samples for the STL experiments were 1.52 m^2 in area, such that the boundary conditions would be expected to have differing influences on the results. The sound field in the sound absorption experiments was a plane wave travelling in a direction normal to the samples. By contrast, the rectangular membranes were measured in reverberation chambers where sound waves are randomly obliquely incident on the membrane surface. Hence, in the sound absorption experiments, a small membrane was measured in a simple sound field. In the STL experiments, a large membrane was measured in a complicated sound field. It is reasonable to presume that the rectangular membrane had significantly more modes excited than the circular membrane. Hence, its vibration motion was more complicated than that of the circular membrane, as well as the sound fields related to its motion. The complexity of the sound fields may make the STL measurements less accurate than the sound absorption coefficient measurements.

2.5 Conclusions

In this chapter, the acoustic properties of single layer impervious membranes were investigated. A new analytical model was proposed for the prediction of the sound absorption and transmission of single layer impervious membranes under tension. Conventional models usually consider the damping arising from viscus damping or energy dissipation on the membrane surface. However, the proposed model includes the damping due to the membrane curvature. This model is developed by extending the two-dimensional string vibration model to the three-dimensional membrane vibration model. Consequently, the motion equation for the membrane vibration, considering the damping due to membrane curvature, is derived. The proposed motion equation has been solved in the polar coordinate system for a circular membrane and in the Cartesian coordinate system for a rectangular membrane.

In the polar coordinate system, the expressions for the sound absorption coefficient and acoustic impedance of the circular membrane with a normally-incident plane wave have been derived. The predicted results of the developed model have been compared with those from the conventional models. It has been found that the different damping expressions affect the predicted results significantly. Sound absorption experiments of two impervious membranes have been conducted to validate the proposed model. The experimental results verify that

the prediction using the proposed model based on membrane curvature damping shows the best agreement with the experimental results among the investigated models.

In the Cartesian coordinate system, the rectangular membrane is assumed to be excited by normally and obliquely incident sound waves. Based on the proposed motion equation and the modal superposition method, the expressions for the sound transmission coefficient and transmission loss are derived for normal incidence and in a diffuse field. The similarity between the theoretical prediction of the proposed damping expression and the conventional damping expressions implies that the damping effect on the sound transmission can be neglected. This presumption and the proposed model for the sound transmission prediction have been validated by the measured STLs of two impervious membranes in a diffuse field.

Comparing the solutions for the polar and Cartesian coordinate systems, it is found that the damping due to the membrane curvature affects the sound absorption significantly, however, it is close to zero for the sound transmission prediction. It is known that the proposed damping expression results from the membrane curvature, which mainly affects the acoustic properties in the low frequency range. Hence, the significance of the damping on sound absorption and the damping being close to zero on sound transmission may be due to the measurement frequency range, the sampling ratio, the scale of the samples and the complexity of the sound field for the STL experiments. Furthermore, the approach of estimating the sample tension and damping ratio from the measured results appears to be more accurate using narrowband results in the low frequency range obtained in the impedance tube, compared with using one-third octave band results obtained from STL measurements using two adjacent reverberation chambers.

This chapter introduced a new damping expression due to membrane curvature for the modelling of the acoustic properties of single layer impervious membranes. The proposed model was validated by experiments. The findings presented in this chapter increase the understanding of the tension and damping effects on the sound absorption and transmission of impervious membranes. The proposed models are useful tools to design membrane-type sound absorbers and noise barriers in practice. They are the foundation of the design of combined membranes used as sound barriers, which will be investigated further in Chapters 6 and 7.

Chapter 3

Sound absorption of micro-perforated membranes

3.1 Introduction

As mentioned in Chapter 1, although pressurised double layer impervious membranes can be used as noise barriers, their sound reduction is less effective than that of traditional massive noise barriers. It is believed that inserting sound absorbing materials into the cavity of double walled impervious membranes can enhance their sound transmission loss. Sound absorbing materials typically consist of porous materials and micro perforated materials. In this thesis, micro perforated membranes (MPMs) are utilised for their flexibility and light weight, as well as their ability to fit between the impervious membranes when the structure is collapsed. Therefore it is necessary to investigate the sound absorption of MPMs.

In this chapter, a literature review of the sound absorption of micro perforated materials is presented in Section 3.1.1, followed by gaps resulting from the literature review and the contribution of this thesis in Section 3.1.2. A new model for the prediction of the acoustic impedance of MPMs is introduced in Section 3.2. To validate this model, sound absorption experiments on MPMs are conducted and the experimental results are shown in Section 3.3. This chapter is concluded in Section 3.4.

3.1.1 Literature review

Sound absorbing materials typically consist of two broad categories: porous materials and micro perforated materials. Porous materials, such as mineral wool, foams, wood wool and glass wool, can provide effective broadband sound absorption with low cost and hence have been widely used in noise control projects. Numerous researchers have used such materials to enhance the sound transmission loss through membrane structures. Vries (2011) inserted

porous materials into the cavities of triple layer membrane structures. Experimental results show that filling the cavities between the membranes with porous materials enhances the sound insulation of the triple membrane structure. However, the porous materials need to be sufficiently thick to maintain effective sound absorption. For example, the glass wool used in Vries's work (2011) was 200 mm thick. Hence, the thickness and mass of these porous materials prevent their use in applications where limited thickness and light weight are required, as is the case in this thesis.

Micro perforated panels (MPPs) have been used in noise control projects for decades as an alternative to conventional porous materials. Micro perforated panels (MPPs) are thin panels perforated with sub-millimetre sized holes. When backed with an air cavity and a rigid wall, the MPP exhibits effective sound absorption, and this combined structure is called a micro perforated absorber (MPA). Although its sound absorbing bandwidth is relatively narrow compared with porous materials of similar thickness, the MPA is favoured for its unique properties. Unlike porous materials, MPPs are able to be used in hospitals and electronic industries where particles must be avoided (Pfretzschner et al. 2006). If MPPs are made of metal panels, they are capable of reducing noise inside the engines of cars and aircraft due to their resistance to high temperature. In addition, the analytical model for the prediction of the sound absorption ability of MPPs is well developed, which offers the opportunity to design MPPs to control specific sources of noise (Maa 1998). However, MPPs are usually made of thin metal or plastic panels which make them relatively massive. Traditional MPPs are rigid and hence unsuitable to be inserted into membrane structures, which are of interest in this thesis.

Similar to MPPs, micro perforated membranes (MPMs) are thin membranes which are perforated, often with millions of holes of sub millimetre diameter. MPMs have significant advantages over MPPs due to the flexibility of membranes and have been widely used in architecture and noise control projects. The sound absorption of MPMs has been investigated for many years. Kang & Fuchs (1999) found that MPMs can absorb sound effectively.

To predict the sound absorption properties of MPPs and MPMs, it is crucial to model their acoustic impedance. The classical analytical model for the prediction of the sound absorption and acoustic impedance of MPPs was developed by Maa (1975) and has been widely used since that time. In recent years, Wang et al. (2010) investigated the sound absorption of an

MPP backed by an irregular-shaped cavity based on Maa's theory. Using the classical theory, Liu & Herrin (2010) investigated partitioning the backing cavity of the MPA to enhance the absorption of normally incident plane waves. When Ruiz et al. (2011) investigated the sound absorption of multiple-layer MPPs, the acoustic impedance of each layer was obtained using the classic theory. Based on Maa's model, Park (2013) also analysed the combination of a micro perforated panel and a Helmholtz resonator. Herdtle et al. (2013) extended Maa's theory for micro perforated materials with tapered holes. However, these studies are all based on Maa's classic model and neglect the effect of the panel vibration.

Maa's classic model assumes the panel to be rigid and as a consequence the effect of the panel vibration is neglected. However, additional sound absorbing peaks, which are not observed in Maa's model, are observed in the low frequency range of experimental results (Toyoda et al. 2010). These unexpected peaks are evidence of the effect of panel vibration on the acoustic impedance of the MPA. This effect could be very significant when the panel is very light and thin, or if membranes are used in the form of a micro-perforated membrane (MPM).

The effect of the panel/membrane vibration on the acoustic impedance of an MPP/MPM can be investigated analytically by using the electric-acoustic analogy to combine the acoustic impedance due to the structural vibration with the acoustic impedance of the perforations, as predicted by Maa's model. Lee et al. (2005) investigated the acoustic impedance of a flexible rectangular MPP, where the finite size of the panel was considered based on a modal approach. Bravo et al. (2012) extended the method of Lee et al. (2005) to a circular MPP. Note that all three of these methods used Maa's model to calculate the acoustic impedance due to the perforation.

In Maa's (1975) classic model, the particle velocity at the hole wall boundary is assumed to be zero. This assumption is valid only if the panel/membrane vibration is negligible. The particles at the hole wall boundary adhere to the hole wall and their velocity can be assumed to be equal to the panel/membrane vibration velocity. If the panel/membrane vibration is significant, then assuming the particle velocity to be zero at the wall will lead to errors. The acoustic impedance due to the perforation is not constant, as in Maa's model, but varies depending on the position of the hole on the panel/membrane surface. This boundary condition and the spatially varying acoustic impedance of the MPM are previously unexplored.

3.1.2 Gaps and contribution

Since the flexible boundary condition and the spatially varying acoustic impedance of MPMs have not been investigated previously, this study aims to investigate the acoustic impedance and sound absorption of a finite-sized circular MPM under tension both theoretically and experimentally. A new boundary condition is introduced which assumes that the velocity of the air particles at the hole wall boundary is equal to the vibration velocity of the membrane. Based on this boundary condition, a new model for the accurate prediction of the acoustic impedance of flexible MPMs is developed and validated by experimental results. The good agreement between the predicted and measured results demonstrates the accuracy of the presented model.

This model is proposed as a tool to design lightweight flexible MPMs. The presented model is also helpful for the prediction and design of the acoustic properties of the combination of impervious membranes and MPMs used as noise barriers in this thesis. This study extends the classic micro perforated theory and offers an accurate model for predicting the performance of flexible finite-sized MPMs. This study provides increased understanding of the coupling between the membrane vibration impedance and the impedance due to the perforations of micro perforated membranes.

3.2 Analytical modelling of the sound absorption of micro perforated membranes

In this section, an analytical model using the proposed boundary condition is derived. The derivation starts in Section 3.2.1 with the motion equation of air particles in a small hole. The solutions of this equation using the conventional and the proposed boundary condition are compared theoretically in Sections 3.2.2 and 3.2.3. The expressions for the acoustic impedance due to each of the perforations and for the combined MPM are also presented in Sections 3.2.4 and 3.2.5. The sound absorption and total impedance of an MPM absorber, i.e, an MPM backed with a rigid wall and an air cavity between them, are presented in Section 3.2.6.

3.2.1 Motion equation of air particles in the perforations of MPMs

When a sound wave travels through the small perforations of a micro perforated material, the small hole could be considered as a small tube, and hence this problem becomes the classic acoustic propagation problem in a tube with circular cross section. When dealing with tubes of relatively large diameters, viscous effects are usually neglected. However, when the tube diameter is small, such as in the case of a micro perforated material, the viscous loss plays an important part and is necessary in the analytical modelling.

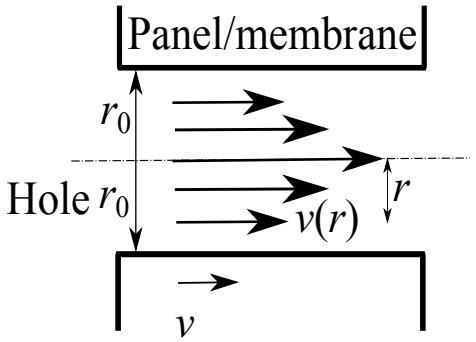

Figure 3.1: Particle velocity $v(r)$ in a hole of the micro perforated membrane or panel as a function of the distance, r, from the centre line.

Assuming that a sound wave travels through the small hole of a micro perforated membrane or panel with a hole of radius r_0, the particle velocity, v, is a function of the distance r from the centre of the hole to the position of the specific air particle due to viscous effects, as shown in Figure 3.1. This relationship between the particle velocity in the hole and the sound pressure applied on the membrane or panel surface is governed by the motion equation of the air particle (Maa 1975) in the polar coordinate system

$$\rho_0 \frac{\partial v(r,t)}{\partial t} - \frac{\mu}{r}\frac{\partial}{\partial r}\left(r\frac{\partial v(r,t)}{\partial r}\right) = \frac{\Delta p}{h}, \tag{3.1}$$

where $v(r,t)$ is the velocity of the air particle in the tube, t is the time parameter, μ denotes the viscous ratio of air, ρ_0 denotes the density of air, Δp denotes the pressure difference applied between the front and back surfaces of the membrane/panel and h denotes the thickness of the membrane/panel, which is also the length of the hole. The velocity can be expressed as

$$v(r,t) = v(r)\,e^{j\omega t}, \tag{3.2}$$

where ω denotes the angular frequency and is equal to $2\pi f$, where f is the frequency. The

partial derivative of the particle velocity with respect to the time variable t is obtained as

$$\frac{\partial v(r,t)}{\partial t} = j\,\omega\, v(r)\, e^{j\omega t} = j\,\omega\, v(r,t). \tag{3.3}$$

Substituting Equation (3.3) into Equation (3.1) and eliminating $e^{j\omega t}$ gives

$$\rho_0\, j\,\omega\, v(r) - \frac{\mu}{r}\left[\frac{\partial v(r)}{\partial r} + r\frac{\partial^2 v(r)}{\partial r^2}\right] = \frac{\Delta p}{h}. \tag{3.4}$$

Equation (3.4) may be simplified as

$$\frac{\partial^2 v(r)}{\partial r^2} + \frac{1}{r}\frac{\partial v(r)}{\partial r} - \frac{\rho_0\, j\,\omega}{\mu} v(r) = -\frac{\Delta p}{\mu h}. \tag{3.5}$$

Letting $K_{\text{air}}^2 = -\frac{\rho_0\, j\,\omega}{\mu}$, Equation (3.5) can be written as

$$\left(\frac{\partial^2}{\partial r^2} + \frac{1}{r}\frac{\partial}{\partial r} + K_{\text{air}}^2\right) v(r) = -\frac{\Delta p}{\mu h}. \tag{3.6}$$

Equation (3.6) is an inhomogeneous differential equation. Its solution is the sum of the solution of its homogeneous differential equation and a particular solution.

The homogeneous differential equation of Equation (3.6) is given by

$$\left(\frac{\partial^2}{\partial r^2} + \frac{1}{r}\frac{\partial}{\partial r} + K_{\text{air}}^2\right) v(r) = 0. \tag{3.7}$$

Letting $x = K_{\text{air}}\, r$, the differentials in Equation (3.7) are

$$\frac{\partial v(r)}{\partial r} = \frac{\partial v(x)}{\partial\left(\frac{x}{K_{\text{air}}}\right)} = K_{\text{air}}\frac{\partial v(x)}{\partial x}, \tag{3.8}$$

and

$$\frac{\partial^2 v(r)}{\partial r^2} = \frac{\partial\left(K_{\text{air}}\frac{\partial v(x)}{\partial x}\right)}{\partial\left(\frac{x}{K_{\text{air}}}\right)} = K_{\text{air}}^2\frac{\partial^2 v(x)}{\partial x^2}. \tag{3.9}$$

Substituting Equations (3.8) and (3.9) into Equation (3.7) gives

$$K_{\text{air}}^2\frac{\partial^2 v(x)}{\partial x^2} + \frac{K_{\text{air}}}{r}\frac{\partial v(x)}{\partial x} + K_{\text{air}}^2\, v(x) = 0. \tag{3.10}$$

Multiplying by r^2, Equation (3.10) becomes

$$x^2\frac{\partial^2 v(x)}{\partial x^2} + x\frac{\partial v(x)}{\partial x} + x^2\, v(x) = 0. \tag{3.11}$$

Equation (3.11) is the Bessel differential equation of the first kind and zero order and its solution is the Bessel function of the first kind and zero order, which is given by

$$v(x) = A\, J_0(x) = A\, J_0(K_{\text{air}}\, r), \tag{3.12}$$

where J_0 is the Bessel function of the first kind and zero order and the constant A can be obtained by applying the appropriate boundary condition.

To calculate a particular solution of Equation (3.6), it is assumed that the particular solution is a constant. This particular solution is expressed as

$$v_{\text{particular}}(r) = -\frac{\Delta p}{h\,\mu\,K_{\text{air}}^2}. \tag{3.13}$$

Therefore, the solution of Equation (3.6) is the sum of Equations (3.12) and (3.13), which is given by

$$v(r) = A\,J_0(K_{\text{air}} r) - \frac{\Delta p}{\mu\,h\,K_{\text{air}}^2}. \tag{3.14}$$

To obtain the value of the unknown constant A, boundary conditions need to be applied. The conventional rigid boundary condition and the proposed flexible boundary condition are discussed in Sections 3.2.2 and 3.2.3, respectively.

3.2.2 Solution under rigid boundary condition

To solve Equation (3.14), it is necessary to define the boundary condition. Due to the viscosity effects, the air particles at the hole wall boundary adhere to the hole wall and their velocities are equal to the vibration velocity of the material. Maa (1975, 1997) assumed that the panel vibration due to the incident sound pressure is negligible and the panel can therefore be considered to be rigid, i.e,

$$v(r = r_0) = 0. \tag{3.15}$$

Based on Maa's assumption, the particle velocity as a function of radius is obtained as

$$v(r) = \frac{-\Delta p}{h\,\mu\,K_{\text{air}}^2}\left[1 - \frac{J_0(K_{\text{air}} r)}{J_0(K_{\text{air}} r_0)}\right]. \tag{3.16}$$

Integrating over the area of the hole and dividing by the hole area yields the average particle velocity

$$\begin{aligned} \bar{v} &= \frac{\int_0^{r_0} v(r)\,2\,\pi\,r\,\mathrm{d}r}{\pi\,r_0^2} \\ &= \frac{\Delta p}{j\,\omega\,\rho_0\,h}\left[1 - \frac{2}{K_{\text{air}}\,r_0}\frac{J_1(K_{\text{air}}\,r_0)}{J_0(K_{\text{air}}\,r_0)}\right], \end{aligned} \tag{3.17}$$

where J_1 is the Bessel function of the first kind and first order.

Based on the definition of acoustic impedance, the acoustic impedance of the hole $Z_{\text{perforation}}$

is given by

$$Z_{\text{perforation}} = \frac{\Delta p}{\bar{v}} = j\,\omega\,\rho_0\,h\left[1 - \frac{2}{K_{\text{air}}\,r_0}\frac{J_1(K_{\text{air}}\,r_0)}{J_0(K_{\text{air}}\,r_0)}\right]^{-1}. \tag{3.18}$$

Therefore, the normalised impedance due to the perforation is expressed as

$$z_{\text{perforation}} = \frac{Z_{\text{perforation}}}{\rho_0\,c_0\,\delta} = \frac{j\,\omega\,\rho_0\,h}{\rho_0\,c_0\,\delta}\left[1 - \frac{2}{K_{\text{air}}r_0}\frac{J_1(K_{\text{air}}r_0)}{J_0(K_{\text{air}}r_0)}\right]^{-1}, \tag{3.19}$$

where c_0 is the sound speed in air and δ is the perforation ratio of the micro perforated material.

When the thickness of the material h is not much larger than the hole diameter d, Maa (1975) indicated that an end correction for the hole needs to be considered. The acoustic resistance is increased by $\frac{1}{2}\sqrt{2\,\rho_0\,\omega\,\sigma}$, where σ denotes the dynamic viscosity in air and is equal to $\sigma = \frac{\mu}{\rho_0}$. To consider the sound radiation at the ends of the holes, Maa (1975) used an equivalent thickness of the material $h + 0.85\,d$ for the reactance term. Considering the end correction and eliminating the constants and the Bessel functions, Equation (3.19) is simplified as (Maa 1997)

$$z_{\text{Maa}} = \frac{0.147}{d^2}\frac{h}{\delta}\left(\sqrt{1+\frac{x^2}{32}} + \frac{\sqrt{2}}{8}\frac{x\,d}{h}\right) + 0.294\times10^{-3}\frac{j\,\omega\,h}{\delta}\left(1 + \frac{1}{\sqrt{9+\frac{x^2}{2}}} + 0.85\frac{d}{h}\right), \tag{3.20}$$

where x is called the perforation constant and is expressed as $d\sqrt{\frac{f}{10}}$.

Equation (3.20) is widely used to calculate the acoustic impedance of micro perforated panels and is reported to show accurate agreement with experimental results. It should be noted that Equations (3.19) and (3.20) are both based on the assumption that the panel vibration velocity is equal to zero, and hence are valid only when the material vibration is negligible and the material can be assumed to be rigid.

3.2.3 Solution under flexible boundary condition

Equation (3.20) is accurate in the cases where the material vibration is neglected. However, for thin micro perforated panels and lightweight micro perforated membranes, the vibration of the structure is significant and needs to be considered. Therefore, the proposed boundary condition between a moving membrane, to be considered henceforth, and the air in the hole

can be expressed as

$$v(r = r_0) = v_{\text{membrane}}, \tag{3.21}$$

where v_{membrane} denotes the vibration velocity of the membrane and is given in Chapter 2. Substituting Equation (3.21) into Equation (3.14) gives

$$A = \frac{v_{\text{membrane}} + \frac{\Delta p}{\mu h K_{\text{air}}^2}}{J_0(K_{\text{air}} r_0)}. \tag{3.22}$$

Substituting Equation (3.22) into Equation (3.14), the particle velocity is obtained as

$$v(r) = v_{\text{membrane}} \frac{J_0(K_{\text{air}} r)}{J_0(K_{\text{air}} r_0)} - \frac{\Delta p}{h \mu K_{\text{air}}^2} \left[1 - \frac{J_0(K_{\text{air}} r)}{J_0(K_{\text{air}} r_0)} \right]. \tag{3.23}$$

Integrating over the area of the hole and dividing by the hole area yields the average particle velocity $\bar{v}$ in the hole

$$\begin{aligned} \bar{v} &= \frac{\int_0^{r_0} v(r)\, 2\pi r \, \mathrm{d}r}{\pi r_0^2} \\ &= v_{\text{membrane}} \frac{2}{K_{\text{air}} r_0} \frac{J_1(K_{\text{air}} r_0)}{J_0(K_{\text{air}} r_0)} + \frac{\Delta p}{j \omega \rho_0 h} \left[1 - \frac{2}{K_{\text{air}} r_0} \frac{J_1(K_{\text{air}} r_0)}{J_0(K_{\text{air}} r_0)} \right]. \end{aligned} \tag{3.24}$$

Therefore, the normalised acoustic impedance of a single hole is expressed as

$$\begin{aligned} z_{\text{perforation}} &= \frac{\Delta p}{\bar{v} \rho_0 c_0} \\ &= \frac{1}{\rho_0 c_0 \frac{v_{\text{membrane}}}{\Delta p} \frac{2}{K_{\text{air}} r_0} \frac{J_1(K_{\text{air}} r_0)}{J_0(K_{\text{air}} r_0)} + \frac{\rho_0 c_0}{j \omega \rho_0 h} \left[1 - \frac{2}{K_{\text{air}} r_0} \frac{J_1(K_{\text{air}} r_0)}{J_0(K_{\text{air}} r_0)} \right]}. \end{aligned} \tag{3.25}$$

Comparing Equation (3.25) with Equation (3.19), it could be observed that the factor

$$\frac{1}{j \omega \rho_0 h} \left[1 - \frac{2}{K_{\text{air}} r_0} \frac{J_1(K_{\text{air}} r_0)}{J_0(K_{\text{air}} r_0)} \right]$$

in Equation (3.25) is similar to Equation (3.19). This similarity implies that this factor represents the average particle velocity of a hole under Maa's rigid wall assumption. Therefore, Equation (3.25) can be rewritten as

$$\begin{aligned} z_{\text{perforation}} &= \frac{1}{\rho_0 c_0 \frac{v_{\text{membrane}}}{\Delta p} \frac{2}{K_{\text{air}} r_0} \frac{J_1(K_{\text{air}} r_0)}{J_0(K_{\text{air}} r_0)} + \frac{1}{z_{\text{Maa}} \delta}} \\ &= \frac{1}{\frac{2}{K_{\text{air}} r_0} \frac{J_1(K_{\text{air}} r_0)}{J_0(K_{\text{air}} r_0)} \frac{1}{z_{\text{membrane}}} + \frac{1}{z_{\text{rigid}} \delta}}, \end{aligned} \tag{3.26}$$

where z_{rigid} denotes the acoustic impedance of a single hole under the rigid wall assumption mentioned in Section 3.2.2 and can be obtained using Equation (3.19). Note that Equation (3.19) neglects the end correction. If Equation (3.20) is used to calculate this impedance

under the rigid panel condition instead, the end correction for the hole is included. Moreover, letting $v_{\text{membrane}} = 0$ and eliminating the corresponding factors yields the expression for the acoustic impedance of a perforation under the rigid wall assumption, which is consistent with the expressions in Section 3.2.2.

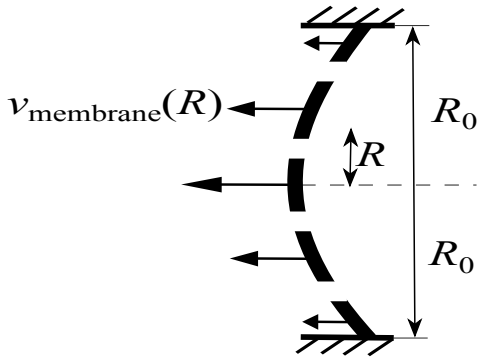

Figure 3.2: Distribution of the membrane vibration velocity (vibrating in the fundamental mode).

Equation (3.26) implies that the acoustic impedance of an MPM hole is a function of the acoustic impedance of the hole under the rigid wall assumption and the acoustic impedance of the membrane vibration in the vicinity of the hole. If it is a limp membrane, the membrane vibration velocity is a constant over the membrane surface when excited by a plane wave and the overall normal acoustic impedance of the MPM is obtained by combining the constant impedance due to the membrane vibration and the impedance due to the perforations. However, in acoustic engineering projects, membrane materials are commonly fixed on a rigid frame. Hence, the finite boundary condition of the fixed edge and the tension due to the stretching of the membrane affect the acoustic impedance of the membrane. This acoustic impedance of the finite sized membrane under tension will be a function of the position, as shown in Figure 3.2, where the variable R denotes the distance from the centre of the circular membrane to the perforation location. The effect of the holes on the membrane motion is neglected. This figure illustrates that the membrane vibration velocity varies with spatial position. Consequently, the acoustic impedance due to the membrane vibration also varies depending on location. Therefore, the acoustic impedance obtained from Equation (3.2) also varies depending on the position coordinates.

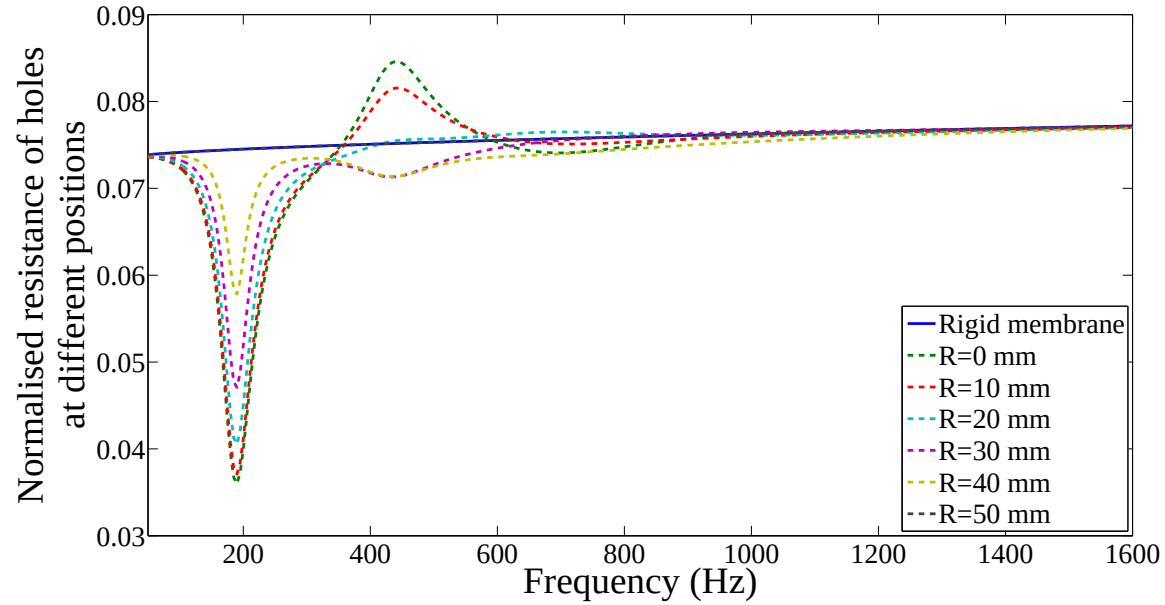

(a) Normalised resistance.

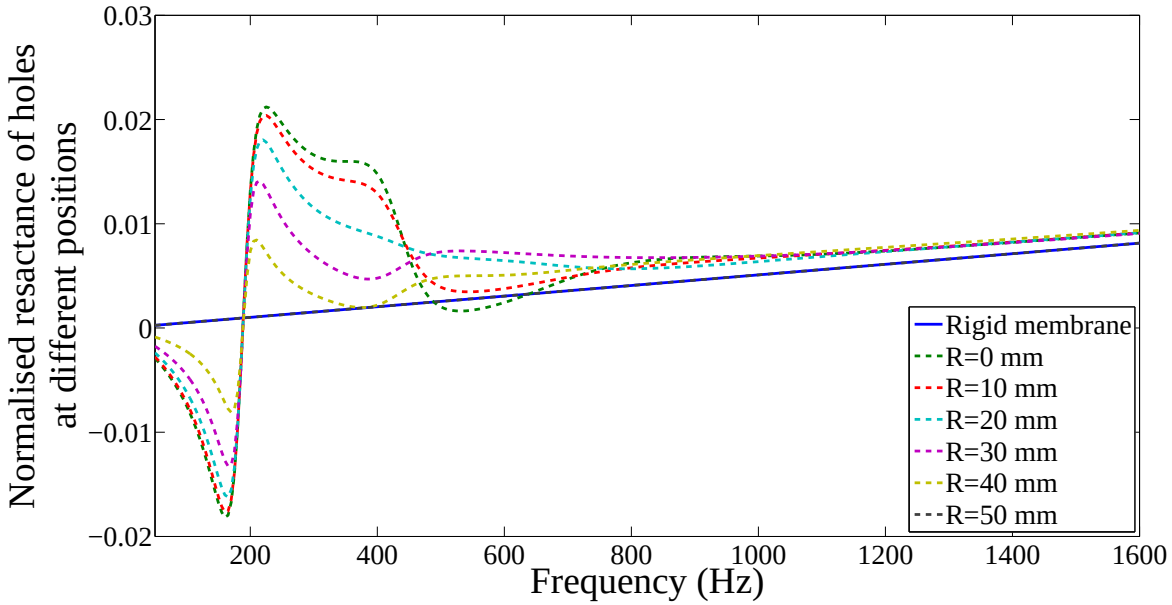

(b) Normalised reactance.

Figure 3.3: Normalised resistance and reactance of a hole for five radial coordinates varying from $R = 0\,\text{mm}$ to $R = 50\,\text{mm}$. (Surface density $\rho_p = 0.25\,\text{kg/m}^2$; tension $T = 125\,\text{N/m}$; internal damping ratio $\eta = 0.02$; membrane radius $R_0 = 50\,\text{mm}$; hole radius $r_0 = 0.0292\,\text{mm}$; membrane thickness $h = 0.17\,\text{mm}$; backing cavity depth $D = 25\,\text{mm}$; perforation ratio $\delta = 0.15\%$. Note that the normalised reactance of each hole based on Maa's theory for a rigid membrane is also shown and it is consistent with that of $R = 50\,\text{mm} = R_0$.) Note that the tension T and the damping ratio η are necessary for the prediction of the acoustic impedance of a membrane without perforations.

3.2.4 Acoustic impedance of each perforation of a circular micro perforated membrane

The acoustic impedance of a hole in a circular MPM as a function of its radius is expressed by Equation (3.26). This equation requires not only the structural parameters of the perforations but also the vibration velocity of the membrane. The latter is expressed in Section 2.2.3, Equation (2.44). Substituting Equation (2.44) into Equation (3.26) gives the acoustic impedance of a perforation as

$$z_{\text{perforation}}(R) = \frac{1}{\frac{2}{K_{\text{air}} r_0} \frac{J_1(K_{\text{air}} r_0)}{J_0(K_{\text{air}} r_0)} \frac{\rho_0 c_0 j}{\omega \rho_{\text{p}}} \left[\frac{J_0(K_{\text{mem}} R)}{J_0(K_{\text{mem}} R_0)} - 1 \right] + \frac{1}{z_{\text{Maa}}\, \delta}}, \tag{3.27}$$

where $K_{\text{mem}}^2 = \frac{\omega^2 \rho_s}{T + 2j\omega\eta}$. Equation (3.27) is a function of the radial coordinate R, which is related to the membrane geometry (not the radial coordinate r of the air particle in the hole). The effect of the hole position on the hole impedance can be predicted using Equation (3.27), although it is non-linear and hence is difficult to investigate analytically. Therefore, an example is utilised here, where a circular micro perforated membrane with surface density $\rho_{\text{p}} = 0.25\,\text{kg/m}^2$, is stretched under a tension $T = 125\,\text{N/m}$ and its internal damping ratio η is 0.02. It is fixed on a rigid ring with a radius of $R_0 = 50\,\text{mm}$. The perforation parameters are: hole radius $r_0 = 0.0292\,\text{mm}$; membrane thickness $h = 0.17\,\text{mm}$; backing cavity depth $D = 25\,\text{mm}$; perforation ratio $\delta = 0.15\%$. The resistances and reactances of five holes at different radii calculated using Equation (3.27), normalised by $\rho_0 c_0$, are shown in Figure 3.3. The radial coordinate R of these holes varies from $R = 0\,\text{mm}$ to $R = 50\,\text{mm}$ and has been chosen to show the variability of the perforation impedance. The normalised resistances and reactances of a hole calculated by Maa's classic model (Equation (3.20)) are also shown. Note that when $R = 50\,\text{mm}$, $\frac{J_0(K_{\text{mem}} R_0)}{J_0(K_{\text{mem}} R_0)} = 1$ and the prediction of Equation (3.27) is consistent with that of Equation (3.20) and thus Maa's theory.

It can be concluded from Figure 3.3 that the acoustic impedance of a hole near the centre of the membrane is more significantly affected by the membrane motion than that of a hole near the edge of the membrane. This is because the membrane elements near the centre vibrate more significantly than those near the membrane edge.

In addition, the effects of the membrane vibration on the perforation impedance occur mainly in the low frequency range where the tension and the internal damping affect the

membrane impedance significantly. In contrast, the surface density governs the membrane impedance in the high frequency range (mass controlled) and no significant effect of the membrane vibration on the perforation impedance is observed for a constant surface density.

3.2.5 Total acoustic impedances due to the perforations of MPMs

In Section 3.2.4, the acoustic impedance of each hole as a function of location is investigated. Neglecting the interaction between the adjacent holes, these holes are connected in parallel. Based on the electric-acoustic analogy, the overall acoustic impedance due to the perforations is expressed as

$$z_{\text{total perforation}} = \frac{1}{\sum_{n=1}^{N} \frac{\frac{r_0^2\pi}{R_0^2\pi}}{z_{\text{perforation}}(R_n)}}, \tag{3.28}$$

where n denotes the nth hole on the membrane surface, R_n denotes the radial coordinate of the nth hole and N is the total number of holes. Figure 3.4 shows the position and number of the perforations on the MPM surface. If $z_{\text{perforation}}$ is uniform, as it is in Maa's rigid wall model, Equation (3.28) can be rewritten as

$$z_{\text{total perforation}} = \frac{1}{N\frac{\frac{r_0^2\pi}{R_0^2\pi}}{z_{\text{perforation}}}} = \frac{z_{\text{perforation}}}{\delta}, \tag{3.29}$$

which is consistent with Equation (3.20).

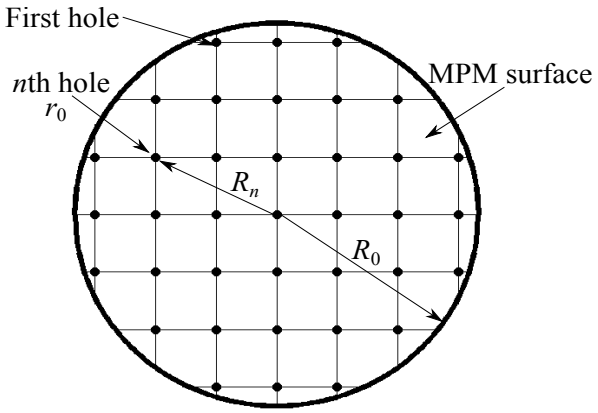

Figure 3.4: nth hole on the surface of an MPM, where R_0 is the radius of the MPM, R_n is the radial coordinate of the nth hole and r_0 is the radius of the hole.

Although the expressions were derived in the polar coordinate system, the calculation was conducted in Cartesian coordinate system. If the distance from the centre of one hole to that of its adjacent hole is given as x_{skip} and y_{skip}, a mesh which represents the spatial

coordinates of the holes (x,y) on the MPM surface can easily be generated, as shown in Figure 3.5. Assuming that the centre of the MPM is at (0,0) in the Cartesian coordinate system, the distance from the centre of the MPM to the nth hole is given by

$$R_n = \sqrt{x^2 + y^2}. \tag{3.30}$$

Substituting Equation (3.30) into Equation (3.27) gives the acoustic impedance of each perforation corresponding to its spatial coordinate in the Cartesian coordinate system. When conducting the analysis, only the holes within the boundary of the MPM ($R_n + r_0 < R_0$) were used.

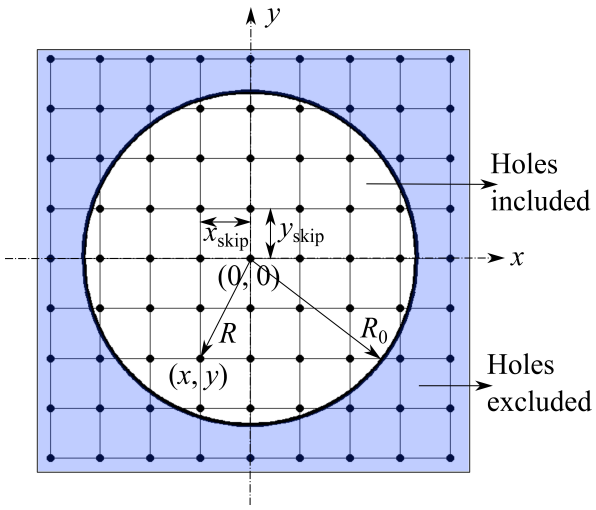

Figure 3.5: Cartesian grid of holes superimposed on an MPM, showing the holes included in and excluded from Equation (3.28).

The same example used in Section 3.2.4 is investigated here to demonstrate the effect of the membrane vibration on the overall impedance of the MPM. The overall acoustic impedance predicted by the presented model is compared with that predicted by Maa's model.

The normalised resistances and reactances predicted by the rigid-walled model and the finite circular membrane of radius $R_0 = 50$mm are shown in Figure 3.6. The resistance predicted by Equation (3.28) is lower than that predicted by Maa's rigid-wall model, while the reactance of this flexible membrane model is higher than that of the rigid wall model above 182 Hz. The most significant difference in the resistance and reactance is observed in the low frequency range near 200 Hz. It could be concluded that the flexible wall assumption leads to a significant change in the acoustic impedance caused by the perforation, especially in the low frequency range.

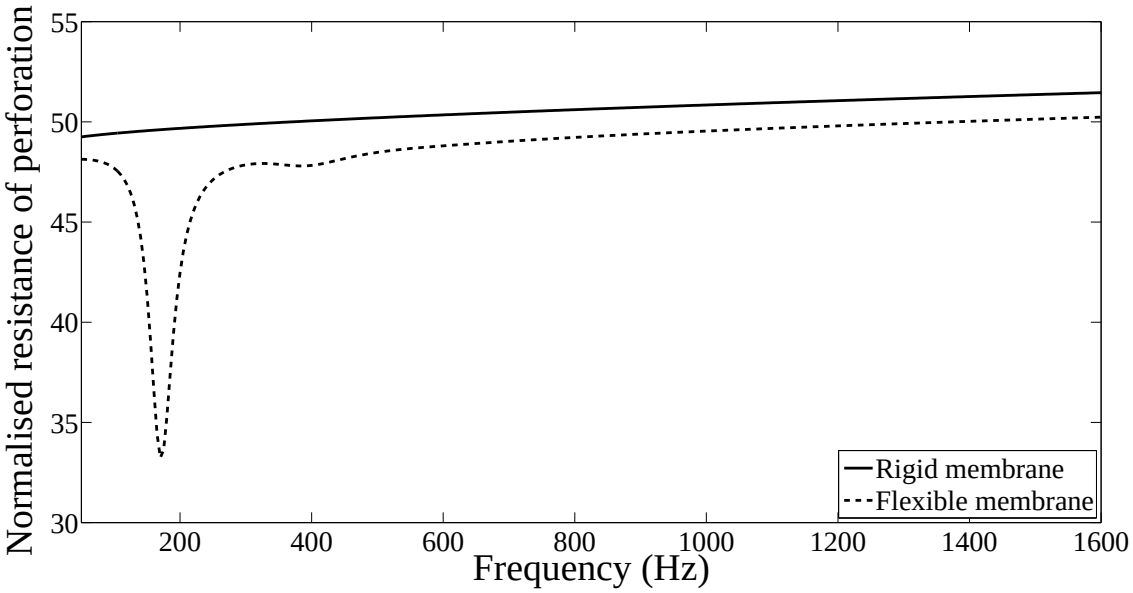

(a) Normalised resistance due to all of the holes.

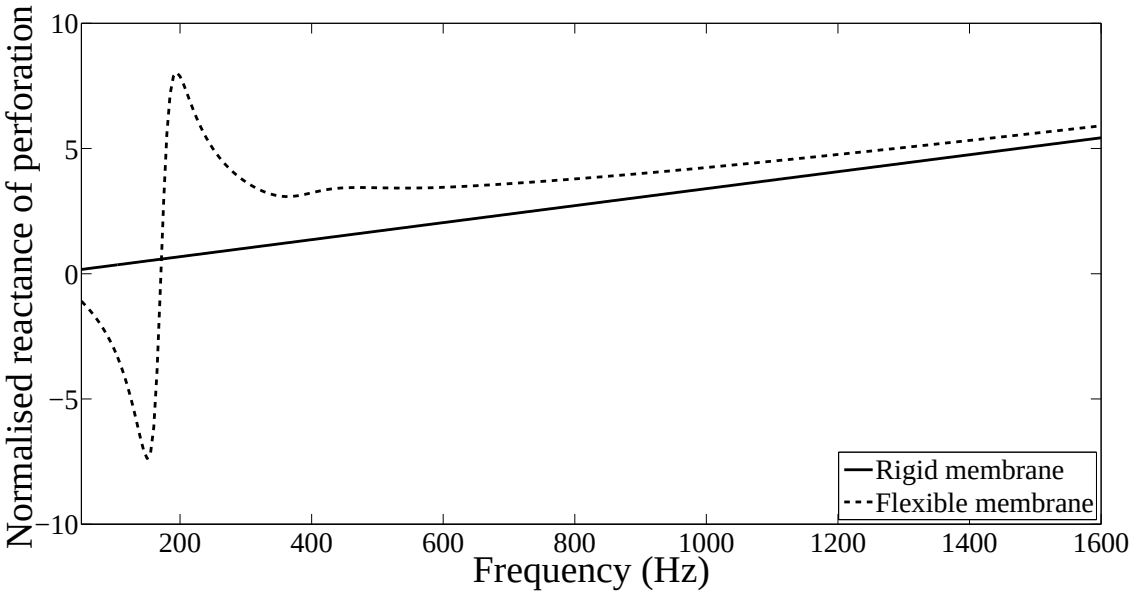

(b) Normalised reactance due to all of the holes.

Figure 3.6: Normalised resistance and reactance due to all of the holes on the MPM surface. (Surface density $\rho_p = 0.25\,\mathrm{kg/m^2}$; tension $T = 125\,\mathrm{N/m}$; internal damping ratio $\eta = 0.02$; membrane radius $R_0 = 50\,\mathrm{mm}$; hole radius $r_0 = 0.0292\,\mathrm{mm}$; membrane thickness $h = 0.17\,\mathrm{mm}$; backing cavity depth $D = 25\,\mathrm{mm}$; perforation ratio $\delta = 0.15\%$.)

3.2.6 Combined acoustic impedance of MPMs and the sound absorption coefficient of MPM absorbers

Note that Equation (3.28) considers only the acoustic impedance due to the perforations. However, the acoustic impedance of an MPM is not only due to the perforations but also due

to the membrane vibration (Kang & Fuchs 1999). To investigate the overall impedance of the MPM system, it is thus necessary to consider the acoustic impedance of the membrane vibration. If the impedance of the perforation and that of the membrane vibration are known, then the overall impedance may be calculated using the electric-acoustic analogy, giving

$$z_{\text{overall}} = \frac{1}{\frac{1}{z_{\text{total perforation}}} + \frac{1}{z_{\text{vibration}}}}, \tag{3.31}$$

where $z_{\text{total perforation}}$ denotes the impedance due to the perforations obtained by Equation (3.28) and $z_{\text{vibration}}$ denotes the membrane vibration impedance given by Equation (2.46).

Like MPPs, an MPM itself is an inefficient sound absorber (Maa 1997). However, an MPM/MPP with a rigid backing wall and an air cavity between can be very effective in absorbing sound. This MPM/MPP with a rigid backing wall and an air cavity is called an MPM/MPP absorber. When a sound wave is incident normally, the normalised acoustic impedance of the air cavity is given by

$$z_D = -j\cot\left(\frac{\omega D}{c_0}\right), \tag{3.32}$$

where D is the depth of the air cavity. This expression is more complicated when accounting for the cross modes, which is beyond the scope of this chapter.

Once the overall impedance of the MPM and the impedance of the air cavity are obtained, the impedance of the MPM absorber is expressed as

$$z = z_{\text{overall}} + z_D. \tag{3.33}$$

This is based on the electro-acoustic analogy which considers the MPM and the cavity as series connected. Therefore, the sound absorption coefficient of an MPM absorber is given by

$$\alpha = \frac{4\,\text{Re}(z)}{(1+\text{Re}(z))^2 + \text{Im}(z)^2}, \tag{3.34}$$

where $\text{Re}(z)$ and $\text{Im}(z)$ are the real and imaginary parts of z, respectively. They are also known as the resistance and reactance of the acoustic impedance.

Moreover, the acoustic impedance of an air cavity is purely imaginary, as indicated in Equation (3.32). Hence, the imaginary part of the MPM/MPP absorber is expressed as

$$\text{Im}(z) = \text{Im}(z_{\text{overall}}) + z_D, \tag{3.35}$$

where $\mathrm{Im}(z_{\mathrm{overall}})$ is the reactance of the MPMs/MPPs. If Equation (3.35) is equal to zero, Equation (3.34) reaches its maximum. The corresponding frequency is the peak absorption frequency of the MPM/MPP absorber. Obviously, this peak absorption frequency is only affected by the cavity depth and the reactance of the MPMs/MPPs.

3.3 Experimental validation of the sound absorption of micro perforated membranes

The following sections explore the experimental validation of the model derived in Section 3.2. The experimental results are compared with the predicted results. Good agreements are achieved and imply the accuracy of the presented model.

3.3.1 Experimental condition and parameter of MPM samples

To validate the model developed in this study, sound absorption experiments were carried out in an impedance tube with normally incident plane waves. The radius of the impedance tube is $R_0 = 50\,\mathrm{mm}$. The sound absorption coefficients of four commercially available MPMs were measured using the two-microphone transfer function method (Chung & Blaser 1980*a*), as shown in Figure 3.7. The four MPMs were tested for two cavity depths D, of 25 mm and 50 mm.

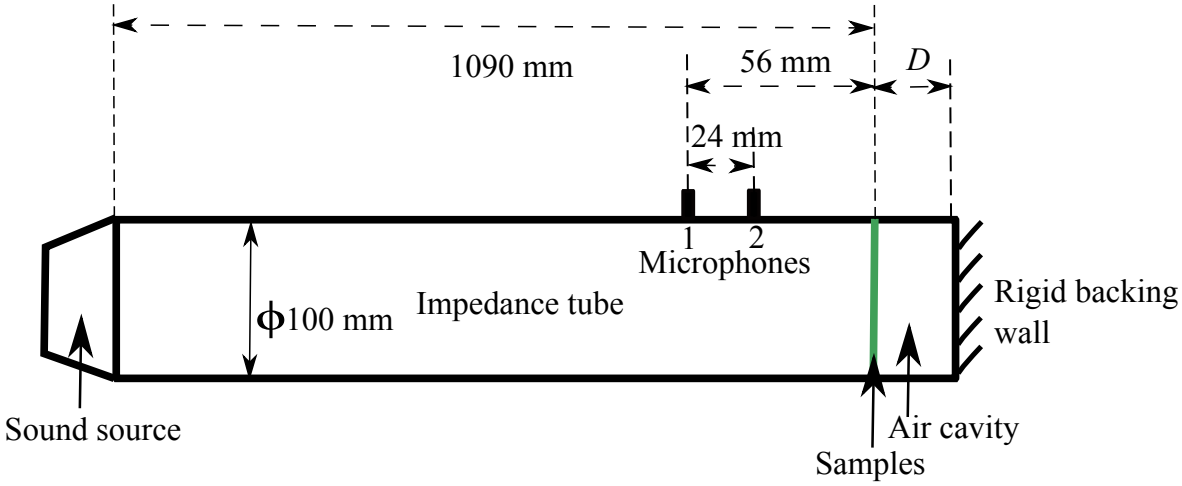

Figure 3.7: Schematic illustrating experimental configuration of sound absorption coefficient measurements conducted in an impedance tube.

To predict the sound absorption of MPMs, it is crucial to measure the structural parameters of the MPMs, including the radius of the perforations r_0. Four different MPMs were tested, denoted MPM 1 to 4. The perforations of MPMs 1 to 3 were punched and the perfor-

ations were irregular polygons, unlike the circular perforations of MPM 4. The photomicrographs of the perforations of MPM 1 and MPM 4 are shown in Figure 3.8 as examples. Because of the irregular geometry of the holes in MPMs 1 to 3, the equivalent hole radius r_0 needs to be estimated by calculating the average area of 10 randomly selected holes and determining the equivalent radius of the average area. The minimum, maximum and average hole radius of MPMs 1 to 3 are shown in Table 3.1 for 10 randomly selected holes. The standard deviation of the measured hole radius of each MPM is given as a measurement error.

Table 3.1: Measured hole radius of MPMs. The equivalent hole radius was determined from data fitting described in Section 3.3.2.

MPM	Minimum hole radius $r_{0\min}$ (mm)	Maximum hole radius $r_{0\max}$ (mm)	Average hole radius $\overline{r_0}$ (mm) of ten holes	Equivalent hole radius r_0 (mm)
1	0.016	0.030	0.026 ± 0.004	0.0226
2	0.011	0.040	0.022 ± 0.008	0.0211
3	0.009	0.042	0.029 ± 0.010	0.0248

Table 3.2: Measured MPM parameters

MPM	Surface density ρ_p (kg/m^2)	Hole radius r_0 (mm)	Membrane thickness h (mm)	Equivalent distance between hole centres b (mm)	Perforation ratio δ (%)
1	0.2501	0.0226 ± 0.004	0.17	1.32	0.092
2	0.2503	0.0211 ± 0.008	0.17	1.58	0.056
3	0.2448	0.0248 ± 0.010	0.17	1.63	0.073
4	0.2506	0.255 ± 0.031	0.17	5.29	0.730

Note that the perforations of MPM 4 were quite circular (as shown in Figure 3.8b), however in some cases the membrane material covered part of the hole area, as shown in Figure 3.8c. These areas need to be excluded during the calculation of the equivalent radius of MPM 4. Therefore, 20 holes on MPM 4 were randomly chosen and the equivalent radius measured from each photomicrograph was used to obtain an average equivalent radius for input to the analytical model. The physical parameters of the MPMs were measured and are shown in Table 3.2. The experimental results are compared with the predictions of the model presented in Section 3.2. Note that there are two unknown variables; the membrane tension T and the internal damping ratio η. These parameters can not be measured directly by experiments

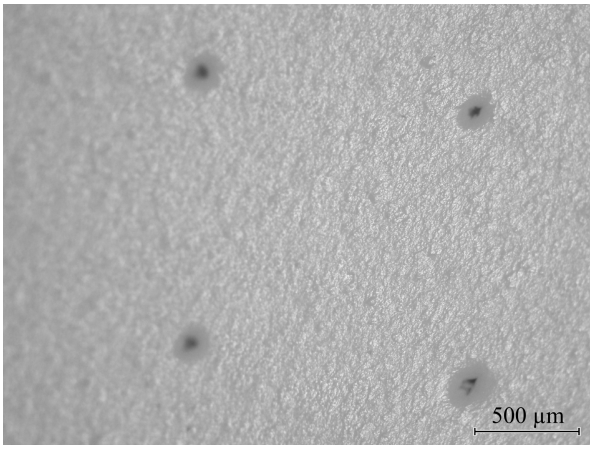

(a) MPM 1.

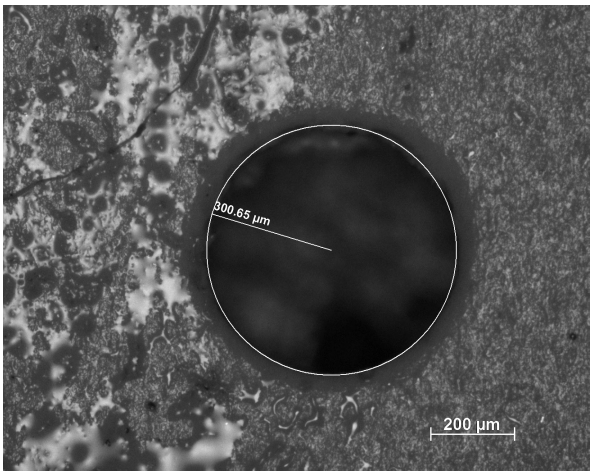

(b) MPM 4, example circular hole.

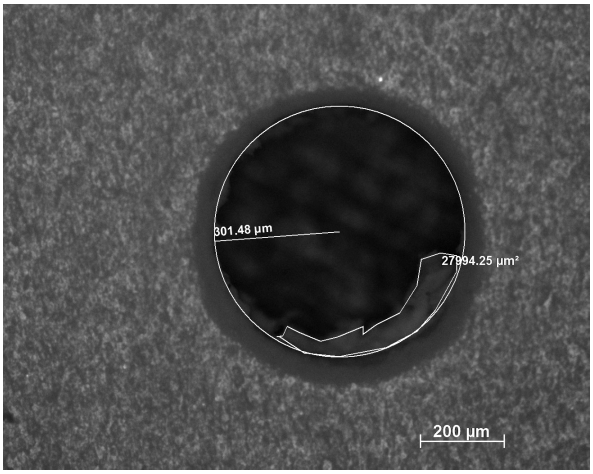

(c) MPM 4, example non-circular hole.

Figure 3.8: Photomicrographs of perforations of MPM 1 and MPM 4.

as they are dependent on the mounting arrangements. The determination of these parameters is described in Section 3.3.2.

3.3.2 Determination of tension and internal damping

It was not possible to measure the tension T and the damping ratio η directly by experiments. Hence, the equivalent value set T, η and r_0 used in the analytical model have been obtained from the experimental measurements by fitting the measured data to the model using the optimisation toolbox in Matlab under a number of constraints (Waltz et al. 2006): positive tension; damping ratio less than 0.05; and hole radius varying from the minimum measured value $r_{0\min}$ to the maximum measured value $r_{0\max}$ (listed in Table 3.1). The constrained non-linear optimisation was based on the subspace trust region method. The obtained values for T, η and r_0 are predicted in Figures 3.14 to 3.21.

As shown in Table 3.2, the radii of the holes are small, as well as the centre to centre distance of holes. Consequently, there are thousands of holes on each MPM. The significant number of holes makes the optimisation extremely time consuming. In order to reduce computational time whilst still obtaining accurate results, data at only nine frequencies were chosen to represent the characteristics of the sound absorption coefficient α.

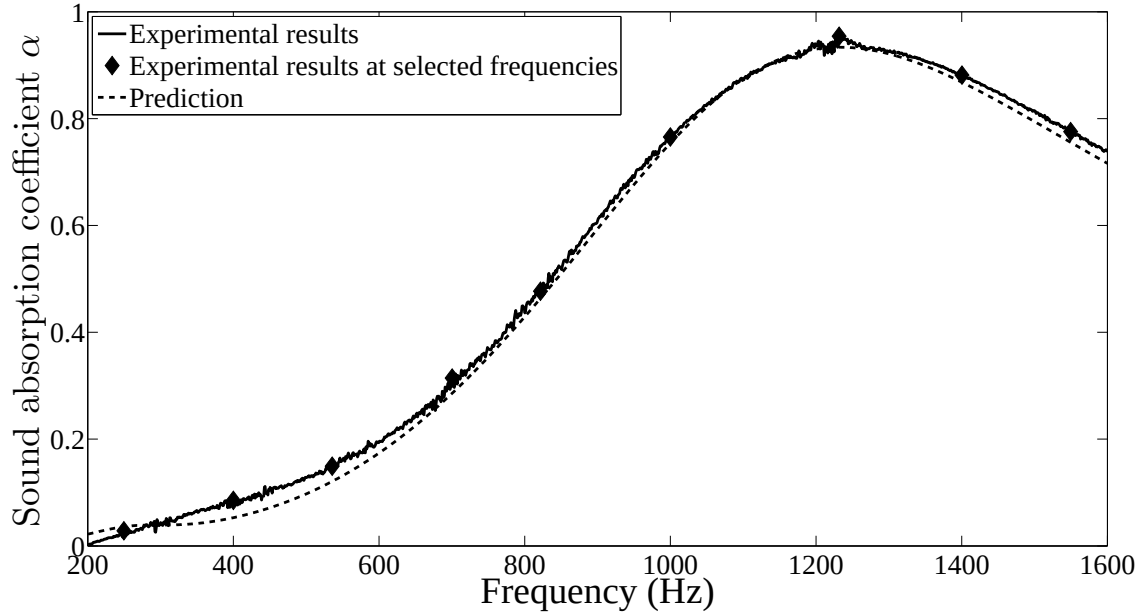

Figure 3.9: Experimental results of MPM 4 at nine frequencies chosen for the calculation of the tension and the damping ratio.

Figure 3.9 uses MPM 4 as an example to illustrate the frequency selection. It is widely

accepted that the indicators of the characteristics of the sound absorption of MPP/MPM are the peak absorption frequency with the highest sound absorption coefficient and the frequencies where half of the maximum sound absorption coefficient occur (Maa 1975). The peak absorption frequency $f_{\alpha_{\max}}$ where the maximum sound absorption is achieved, is of most significant importance and selected here. The frequency where half of the maximum sound absorption coefficient is obtained $f_{\alpha_{\text{half}}}$, is selected to indicate the sound absorbing bandwidth. Although the reliable measurement range is from 200 Hz to 1600 Hz, measurement errors may occur with this frequency range for many reasons, including the boundary condition of the samples and the poor coherence between the microphones. Consequently, the frequencies $f_{\min}$= 250Hz and $f_{\max}$= 1550Hz were chosen to indicate the properties of the MPM absorption at low and high frequencies, whilst minimising the occurrence of the measurement errors over the frequency range of interest. To increase the accuracy of the optimisation, the middle frequency between $f_{\alpha_{\max}}$ and $f_{\alpha_{\text{half}}}$ is selected, as well as the middle frequency between $f_{\alpha_{\max}}$ and $f_{\max}$. Since the frequency bandwidth from $f_{\min}$ to $f_{\alpha_{\text{half}}}$ is relatively large, three frequencies are selected evenly between them. Therefore, data at these nine frequencies have been chosen to represent the characteristics of the sound absorption of MPM 4 and to reduce the time required for the optimisation. It is shown in Figure 3.9 that the predicted sound absorption coefficient using the optimisation at these selected frequencies is in very good agreement with the experimental results, which implies the applicability of this frequency selection method.

3.3.3 Effects of thermo-viscous friction and viscous layer on acoustic impedance of MPMs

When predicting the acoustic impedance due to the perforations of MPM 4 using Equation (3.20), it was found that this equation underestimated the impedance. Similar underestimation has been observed by Tayong et al. (2010). They indicated that in practice, Equation (3.20) tends to underestimate the impedance due to the thermo-viscous friction. In Equation (3.20), the thermo-viscous effect is included as a part of the end correction. However, the impedance calculated is usually lower than the value measured in experiments. To correct for this effect, Tayong et al. (2010) suggested the use of

$$R_s = \frac{1}{2}\sqrt{2\,\omega\,\rho_0\,\sigma} \tag{3.36}$$

to estimate the resistance due to the thermo-viscous friction, where σ is the dynamic viscosity of air. They increased the normalised impedance due to the perforations by $4\frac{R_s}{\rho_0 c_0 \delta}$, resulting in a good agreement between the experimental and predicted results..

The constants used in Equation (3.36) are purely real. Hence, only the real part of the acoustic impedance obtained by Equation (3.20), i.e. the resistance, is affected by this additional thermo-viscous friction. However, tracing back to Rayleigh's (1896) original derivation, R_s was expressed as

$$R_s = \frac{1}{2}\sqrt{2\,\omega\,\rho_0\,\sigma}(1+j). \tag{3.37}$$

However, the imaginary part of Equation (3.37) was omitted by Rayleigh (1896) later, possibly to simplify the derivation, and consequently Equation (3.37) was reduced to Equation (3.36). Equation (3.36) has been widely cited thereafter (Ingard 1953, Maa 1975, Tayong et al. 2010).

It is found that the resonance peak of the predicted result using Equation (3.36) is slightly offset from that of the measured result, as shown in Figure 3.10. It is known from Equation (3.35) that the resonance frequency of the MPM absorber is dependent on the reactance of the absorber system. Therefore, it is reasonable to presume that the thermo-viscous friction affects not only the resistance but also the reactance and use of Equation (3.36) hence leads to the mismatch of the peak absorption frequency.

A comparison of the predicted results using the real and complex values of R_s is shown in Figure 3.10. The frequency mismatch due to use of a real value for R_s is eliminated by using the complex value given by Equation (3.37) and provides better agreement with the experimental results. Thus, in the presented model for MPM 4, Equation (3.37) was utilised instead of Equation (3.36) and $4\frac{R_s}{\rho_0 c_0 \delta}$ was added to Equation (3.20). The prediction results agree with the measured results, as shown in Figures 3.17 and 3.21.

The additional impedance arising from the thermo-viscous friction is only of importance for the acoustic impedance of MPM 4. This is because of the significant difference between the hole radii of MPMs 1 to 3 and the hole radius of MPM 4. Table 3.2 shows that the hole radius of MPM 4 is ten times larger than the hole radii of MPMs 1 to 3. The thickness of the viscous layer is given by Maa (1975) as

$$h_{\text{viscous}} = \sqrt{\frac{2\times\sigma}{\omega}}. \tag{3.38}$$

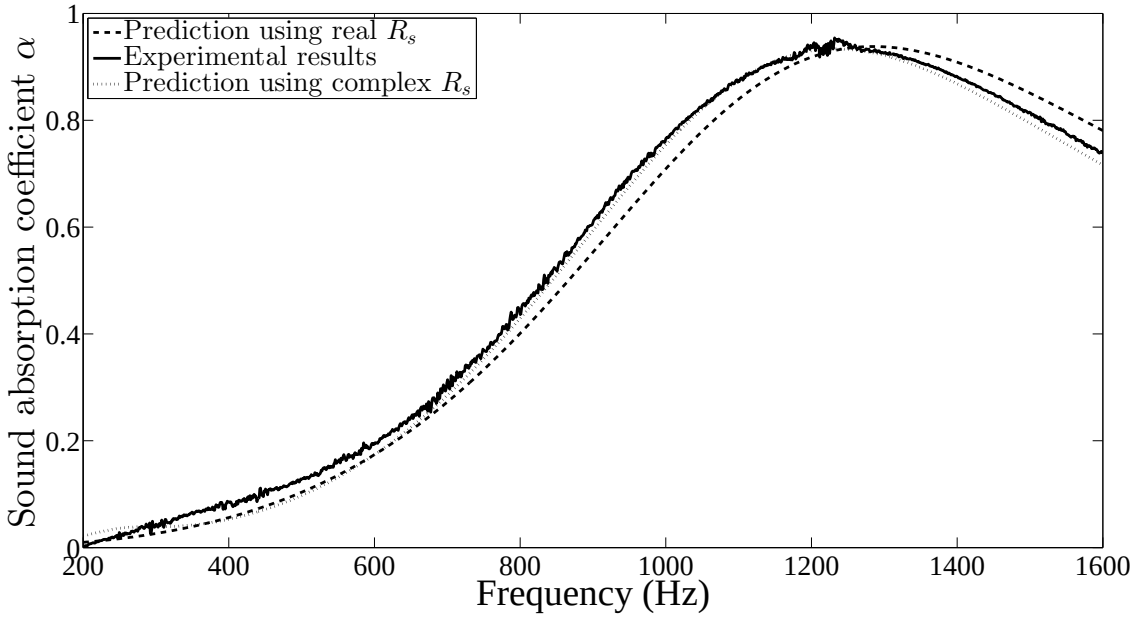

Figure 3.10: Comparison of results for use of real and complex values of R_s for the sound absorption prediction of MPM 4 with $D = 25$mm.

Figure 3.11 shows the comparison of the hole radii of MPMs and the thickness of the viscous layer calculated using Equation (3.38). Examination of Equation (3.38) reveals that the thickness of the viscous layer is independent of the parameters of the MPMs and is a function with respect to the frequency. The thickness of the viscous layer decreases with an increase in frequency.

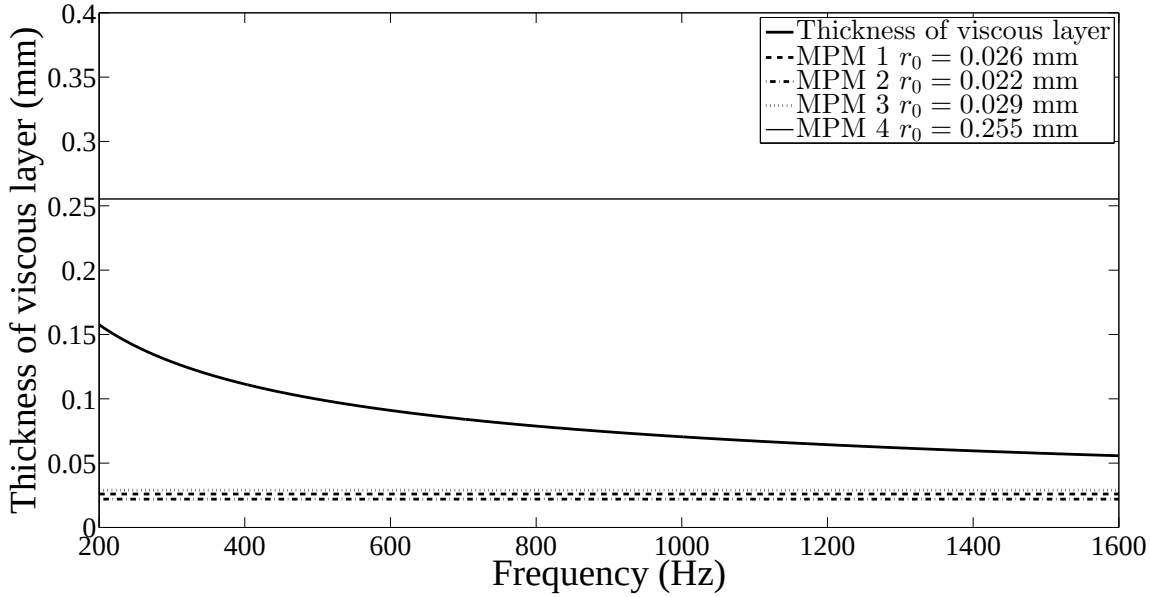

Figure 3.11: Thickness of viscous layer h_{viscous}, MPM hole diameters shown for illustration purposes.

For comparison, within the frequency range of interest the hole radii of MPMs 1 to 3 ($r_0 = 0.022$mm to 0.029 mm) are smaller than the thickness of the viscous layer and the hole radius of MPM 4 ($r_0 = 0.255$mm) is larger than the thickness of the viscous layer. For MPMs 1 to 3, the hole radii are sufficiently small that the entire area of the holes is covered by the viscous layer, which makes the particle velocity relatively small in these holes, as illustrated in Figure 3.12a. This results in high acoustic impedance of MPMs 1 to 3 and limited air flow through these holes. Hence, the thermo-viscous friction is negligible for MPMs 1 to 3.

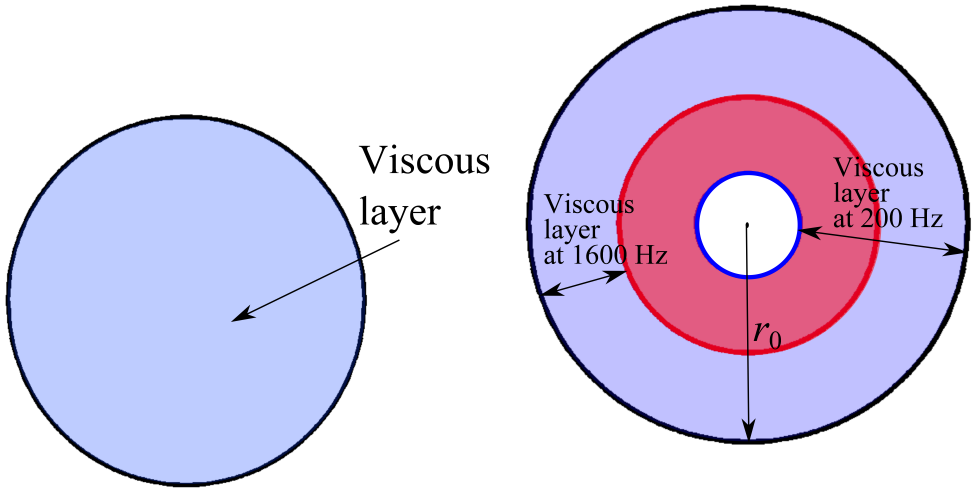

(a) Viscous layer of MPM 3.

(b) Viscous layers of MPM 4 at 200 Hz and 1600 Hz.

Figure 3.12: Viscous layers of MPMs 3 and 4. Note that schematic is not to scale.

As illustrated in Figure 3.12b, the hole radius of MPM 4 is larger than the thickness of the viscous layer, which allows the air to flow through the holes easily. A rotational jet is formed by the air flow through the holes, which increases the impedance of the perforations (Ingard & Ising 1967). Therefore, the thermo-viscous friction affects MPM 4 only and may be neglected for the other three MPMs.

Note that effective sound absorption of an MPM/MPP is usually related to high acoustic impedance, especially high resistance. However, Maa (2006) used Figure 3.13 to illustrate that extremely high resistance leads to ineffective sound absorption. Figure 3.13 shows the sound absorption coefficients calculated with the normalised resistance varying from 1 to 5. With an increase of the normalised resistance from 1 to 5, the sound absorption bandwidth increases but the maximum sound absorption coefficient decreases proportionally. This is consistent with the phenomenon observed on MPMs 1 to 3. As mentioned before, the hole radii of the MPMs 1 to 3 are very small and the viscous layer covers the entire area of

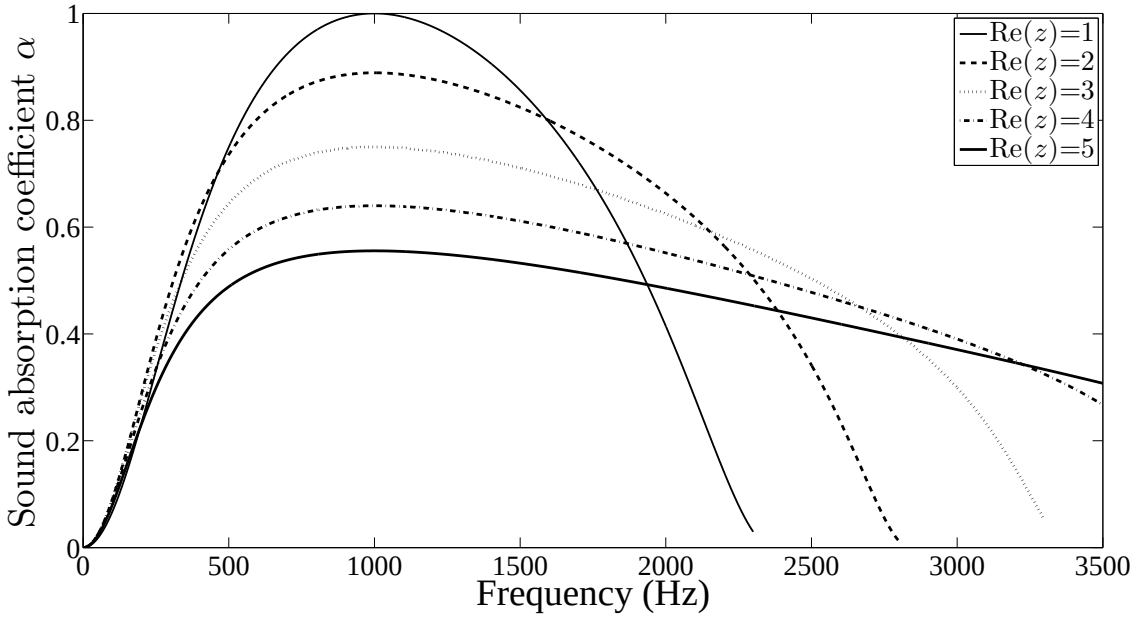

Figure 3.13: Low sound absorption due to high acoustic resistance of MPP ranging from 1 to 5 (Maa 2006).

the holes, resulting in the extremely high resistances of these MPMs. Hence, the sound absorption arising from the perforations of MPMs 1 to 3 are low, as shown in the sound absorption curves for these MPMs (Figures 3.14 to 3.16 and 3.18 to 3.20).

3.3.4 Comparison of the experimental and predicted sound absorption coefficients of MPMs

In this section, the measured results of MPMs 1 to 4 with an air cavity depth of $D = 25\,\text{mm}$ and $D = 50\,\text{mm}$ are shown in Figures 3.14 to 3.18. The experimental condition is as described in Section 3.3.1. These experimental results are compared with the prediction results of three models: Maa's classic rigid wall model (Equation (3.20)); the model of a membrane absorber without perforation (Equation (2.46)) and the presented model (Equation (3.31)). If the measured sound absorption curve is close to the prediction using Maa's model (represented by the dashed-dotted curves), this indicates that the perforations are the governing effect on the sound absorption of the MPM absorber because this model dose not consider membrane motion. The dotted curves in Figures 3.14 to 3.18 represent the results predicted considering the MPMs as impervious membranes of equivalent surface density but without perforations.

In some figures, the predicted results of the different models are close, which makes it difficult to identify the relative accuracy of these models. To quantify the accuracy of the

three models, the coefficient of determination $R^2_{\text{determination}}$ for each model is provided in Figures 3.14 to 3.18. As $R^2_{\text{determination}}$ approaches unity, the fidelity of the model increases.

For MPMs 1 to 4, the $R^2_{\text{determination}}$ of the presented model is close to unity. Hence, the presented model provides a good agreement with the experimental results and is suitable for the prediction of the sound absorption of these MPMs. These results confirm that the new boundary condition theory and the derived equations are valid for these MPM samples. The negative $R^2_{\text{determination}}$ seen in the alternative models is because the error between the measured data and the predicted result is larger than the difference between the measured data and its mean. The negative $R^2_{\text{determination}}$ indicates the inaccuracy of the corresponding model.

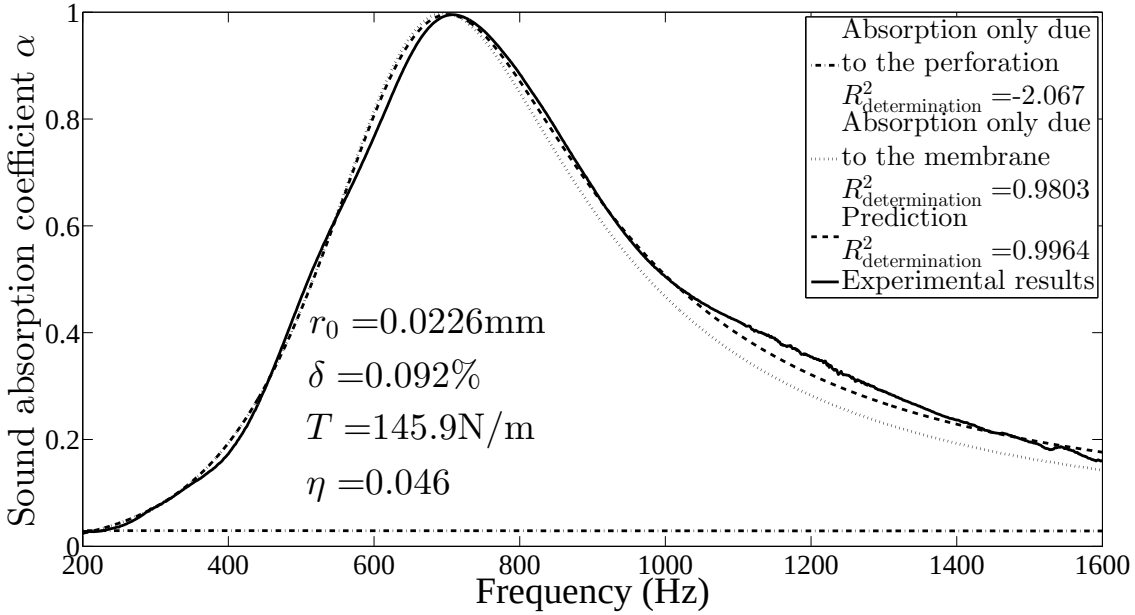

Figure 3.14: Normal incidence sound absorption coefficients of MPM 1 for $D = 25\,\text{mm}$.

Comparing the experimental results of the MPMs, we can conclude that the predominant absorption peaks of MPMs 1 to 3 are near the predominant absorption peaks of the membranes without perforation. For MPM 4, Figures 3.17 and 3.21 indicate that the predominant absorption peak is in the high frequency range and to the three models considered, corresponds most closely with the absorption peak for the predicted result using the flexible membrane model. This may imply that when the perforations are small, as is the case for MPMs 1 to 3, the MPM absorption is mainly due to the membrane itself. In these cases, the perforations marginally broaden the sound absorption bandwidth but do not move the

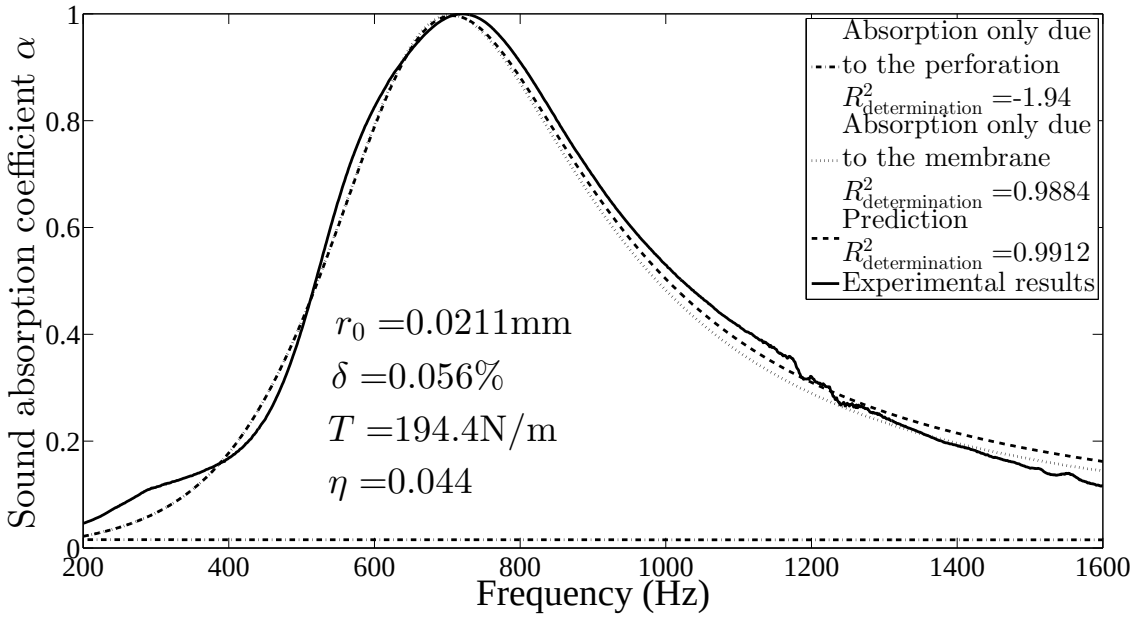

Figure 3.15: Normal incidence sound absorption coefficients of MPM 2 for $D = 25\,\text{mm}$.

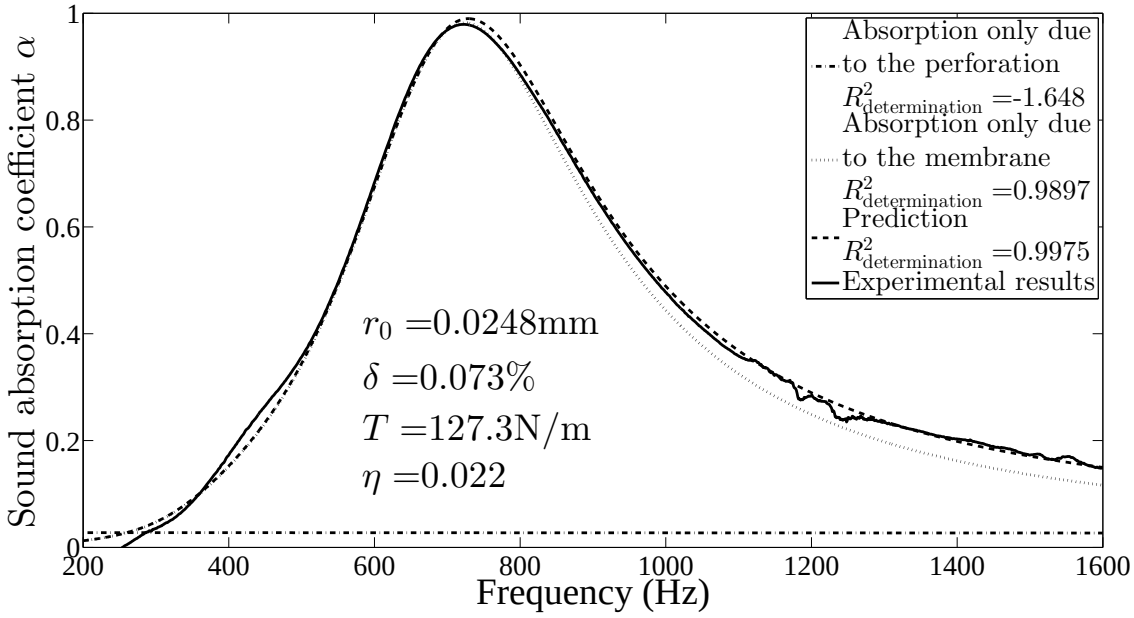

Figure 3.16: Normal incidence sound absorption coefficients of MPM 3 for $D = 25\,\text{mm}$.

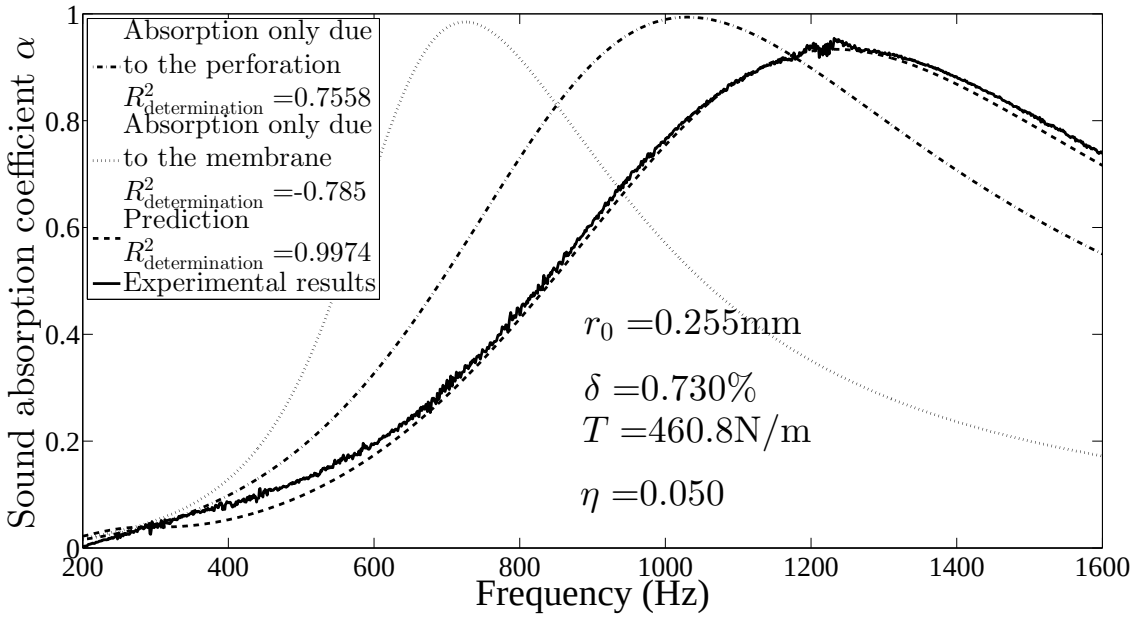

Figure 3.17: Normal incidence sound absorption coefficients of MPM 4 for $D = 25$ mm.

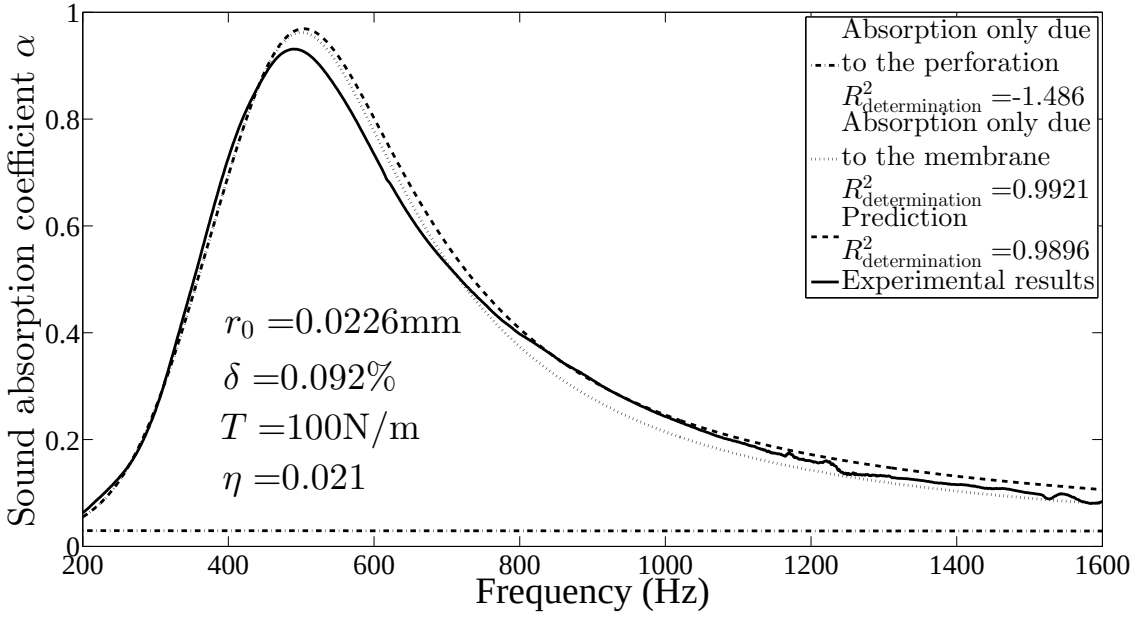

Figure 3.18: Normal incidence sound absorption coefficients of MPM 1 for $D = 50$ mm.

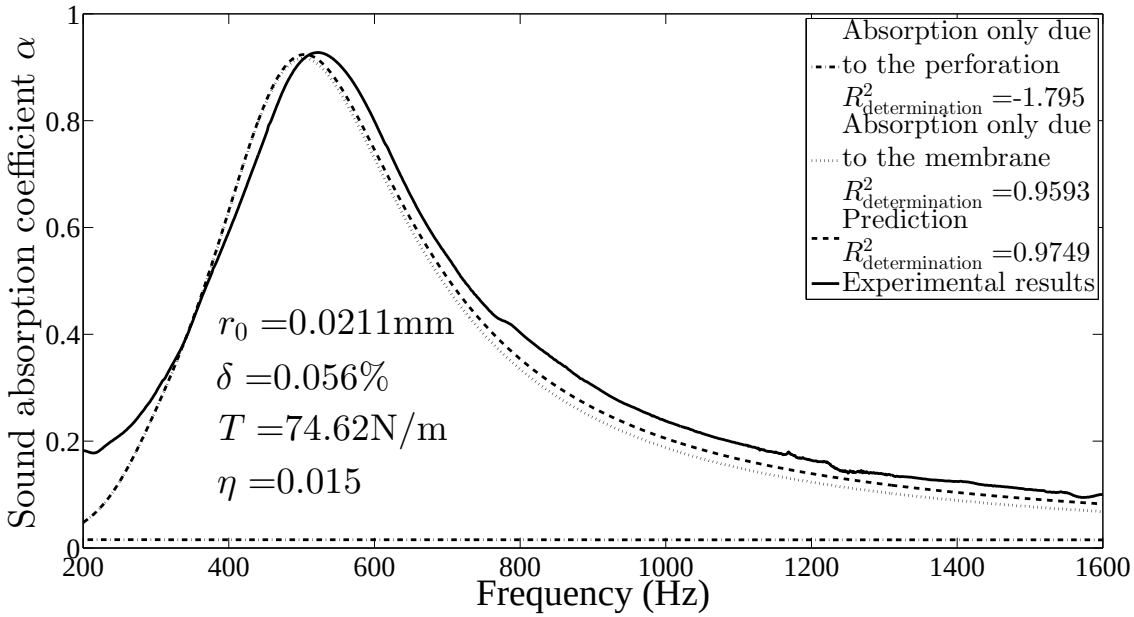

Figure 3.19: Normal incidence sound absorption coefficients of MPM 2 for $D = 50\,\text{mm}$.

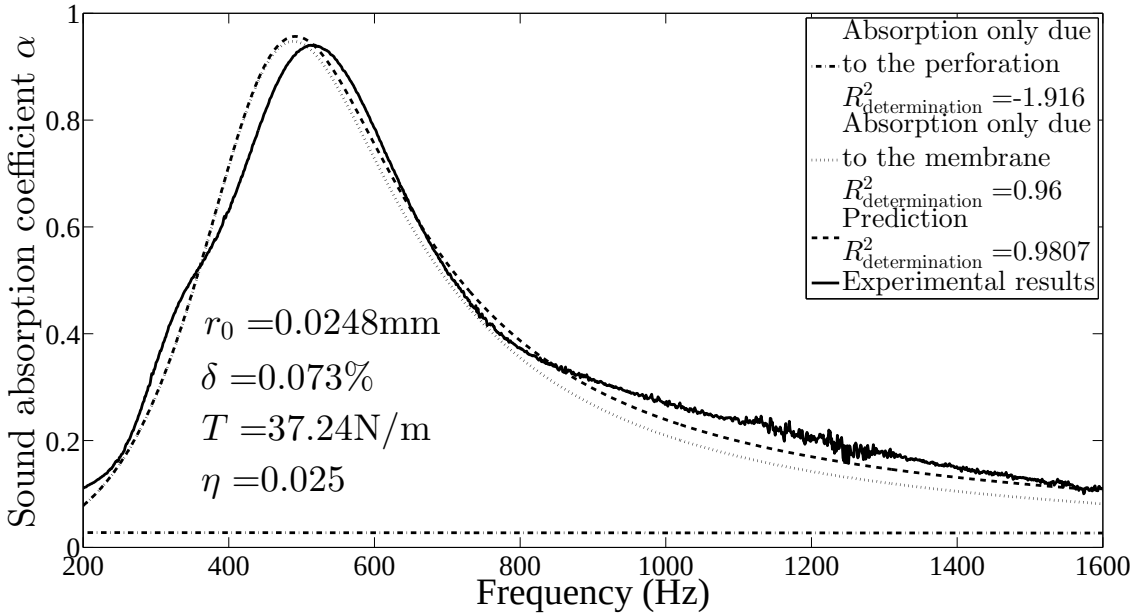

Figure 3.20: Normal incidence sound absorption coefficients of MPM 3 for $D = 50\,\text{mm}$.

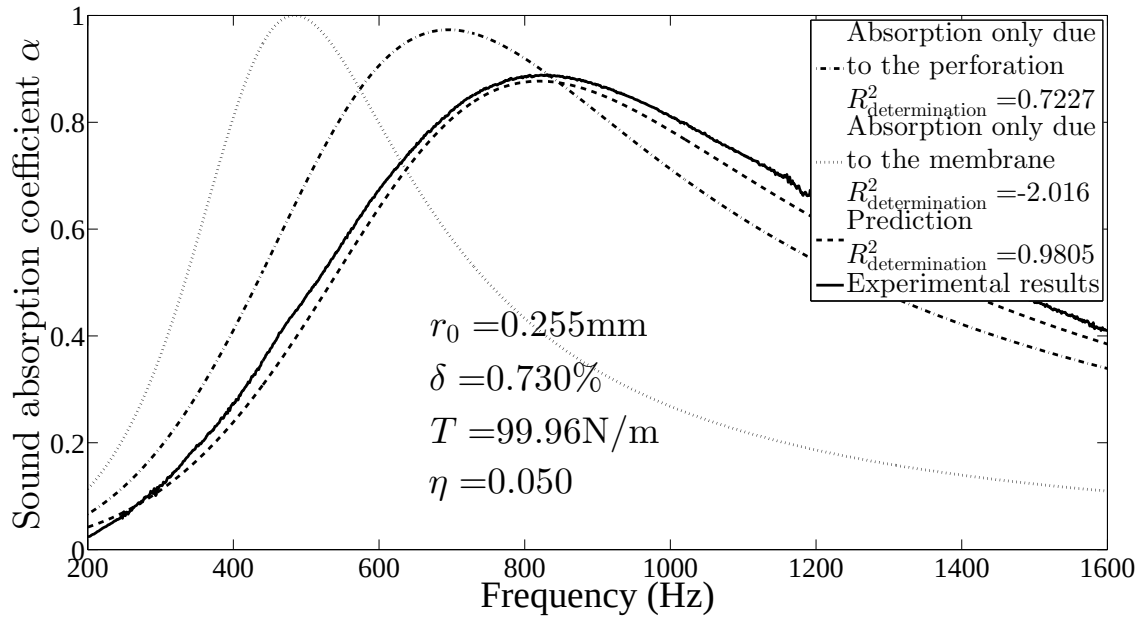

Figure 3.21: Normal incidence sound absorption coefficients of MPM 4 for $D = 50$ mm.

absorption peaks significantly. When MPM 4 is considered, the perforations are the main contributor to the sound absorption and the main absorption peak of the MPM is near the theoretical absorption peak due to a combination of the perforations and the membrane motion.

As mentioned in Section 3.3.3, the structural parameters of MPMs 1 to 4 are all in a similar range of values, except that MPM 4 has a hole diameter ten times larger than the other three MPMs. The hole diameter and perforation ratio of MPM 4 are close to the structural parameters of a classic MPP, which is typically around $r_0 = 1$ mm and $\delta = 1\%$. The impedance of the holes in MPM 4 is efficiently combined with the acoustic impedance due to the membrane vibration to offer effective sound absorption. On the contrary, the perforations in MPMs 1 to 3 are too small comparing to those in MPM 4, and the acoustic impedance due to the perforations is thus too high to contribute to the sound absorption effectively. Extremely high acoustic impedance leads to a poor sound absorption from MPP/MPM absorbers (Maa 2006).

Therefore, it is concluded that although the sound absorption bandwidths of MPM 1 to 3 have been marginally broadened due to the presence of the perforations, the sound absorption properties of these MPMs are mainly governed by the membrane itself. Considering the expense of manufacturing the perforations, incorporating perforations of this size in com-

mercial sound absorbing materials is likely to be ineffective. However, the sound absorption values obtained for MPM 4 indicate the effectiveness of such micro perforated membranes incorporating holes of a suitable size. To achieve their optimum sound absorption, MPMs need to be carefully designed to couple the membrane vibration impedance and the impedance due to the perforations effectively.

3.3.5 Structural resonance of the impedance tube

It is observed that there are small dips and peaks from 1200 Hz to 1260 Hz in the sound absorption coefficient measurements shown in Figures 3.14 to 3.21. They occur in the experimental results of all the MPMs and are independent of the cavity depth D. Hence, these are considered to be due to a structural resonance of the impedance tube itself.

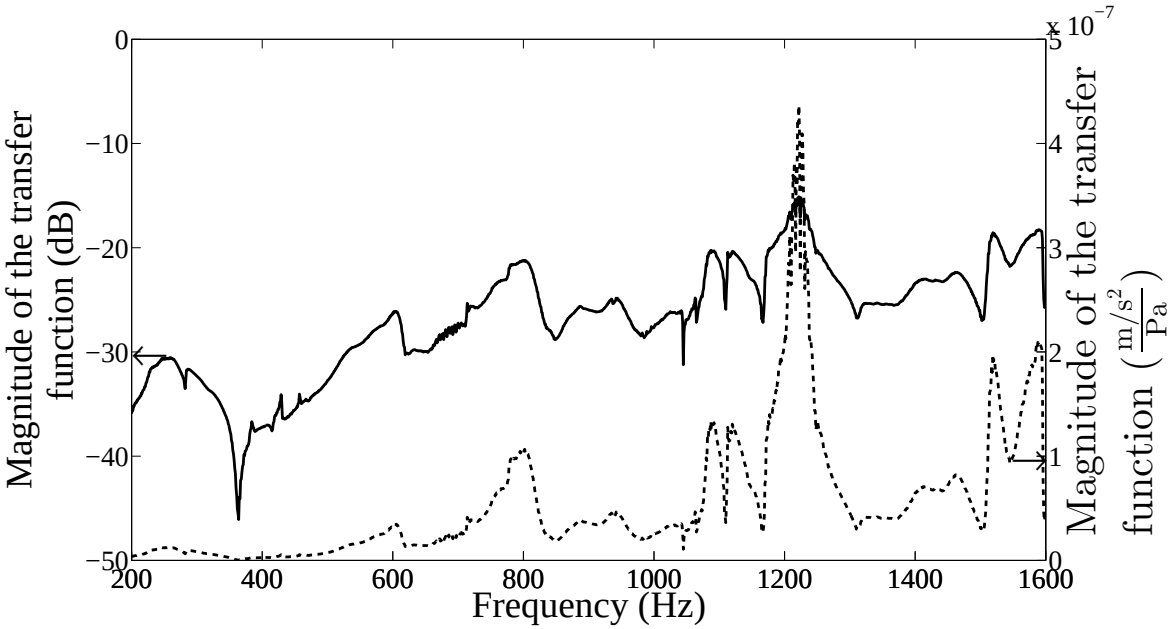

Figure 3.22: Magnitude of the transfer function between the acceleration of the impedance tube vibration and the sound pressure inside the impedance tube.

To validate the assumption of the structural resonance of the impedance tube, the transfer function between the acceleration of the impedance tube vibration and the sound pressure inside the impedance tube was measured using the same arrangement described in Section 3.3.1, except that an accelerometer was attached on the tube to measure the acceleration of the tube vibration. The magnitude of the transfer function is shown in Figure 3.22. It can be observed from the figure that the tube vibrates significantly at 1245 Hz, which corresponds to the small dips and peaks observed around 1250 Hz in Figures 3.14 to 3.21. Therefore, it is

concluded that the vibration of the impedance tube affects the sound absorption coefficient measured in the impedance tube at around 1250 Hz.

3.3.6 Effect of perforation positions on the sound absorption of MPMs

Based on the theory presented in Section 3.2, it is logical to assume that since the membrane vibration affects the acoustic impedance of the perforations, the overall impedance and sound absorption properties of an MPM could be affected by the perforation positions since the vibration is not uniform over the membrane. This presumption is in contrast to the conventional theories which assume that the overall impedance of a flexible micro perforate (thin plate or membrane) is given by the coupled impedances of the material vibration and the perforations based on electric-acoustic analogy or the average flow velocity. Hence, in the conventional theories, the overall impedance is independent of the position of the perforations.

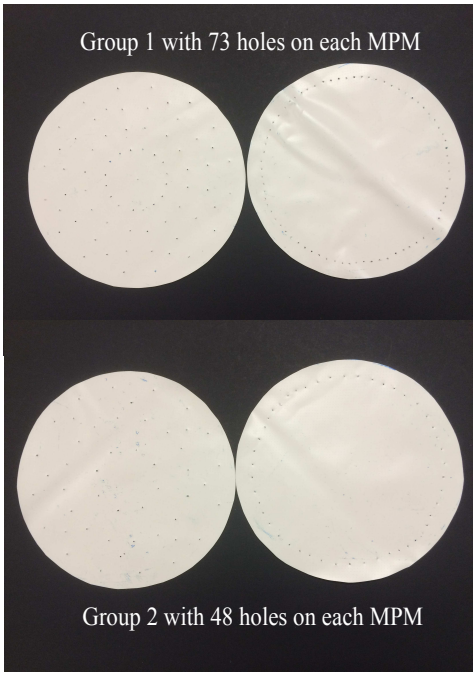

Figure 3.23: Photograph of the additional MPMs made using the MPM 1 material. There are 73 and 48 holes of 0.31 mm radius drilled in each of the membranes respectively.

To validate the assumption of the position dependence of the hole impedance, four additional MPMs were made using the same material as MPM 1 and are shown in Figure 3.23. In Section 3.3.4, it was shown that MPM 1 can essentially be considered unperforated due to its low perforation ratio and small hole diameter.

The four additional MPMs may be categorised into two groups. In Group 1, each MPM

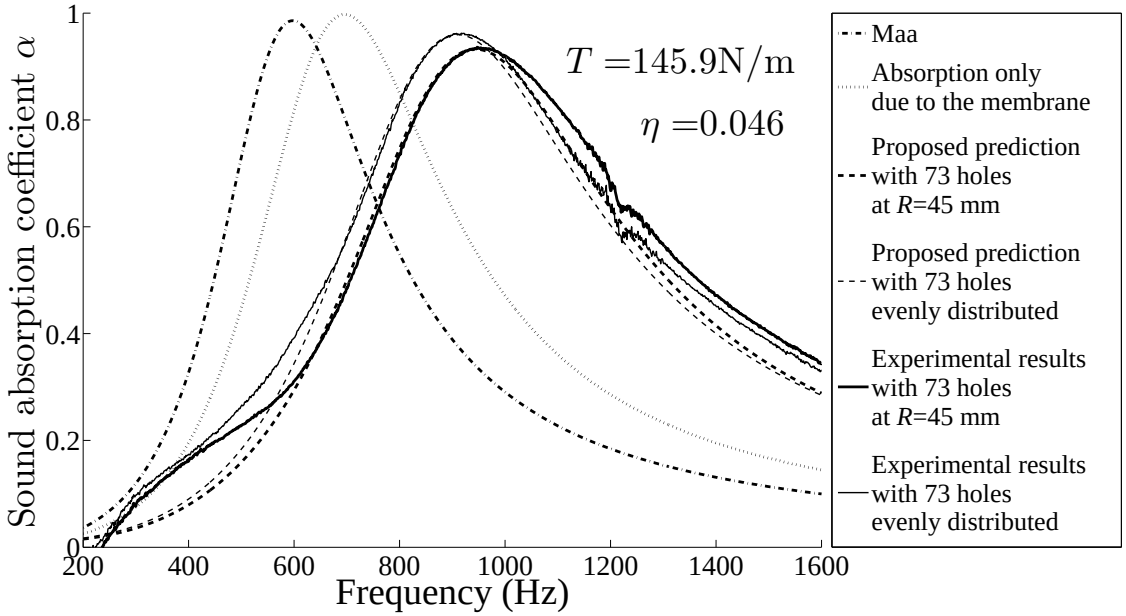

Figure 3.24: Normal incidence sound absorption coefficients of the manufactured MPMs with 73 holes, $D = 25$ mm. The thick solid curve represents the measured sound absorption coefficient of an MPM with 73 holes at a radius of $R = 45$ mm. The thin solid curve represents the measured sound absorption coefficient of the manufactured MPM with 73 holes evenly distributed on the membrane surface. The thick and thin dashed curves are the prediction results for each using the proposed method, respectively.

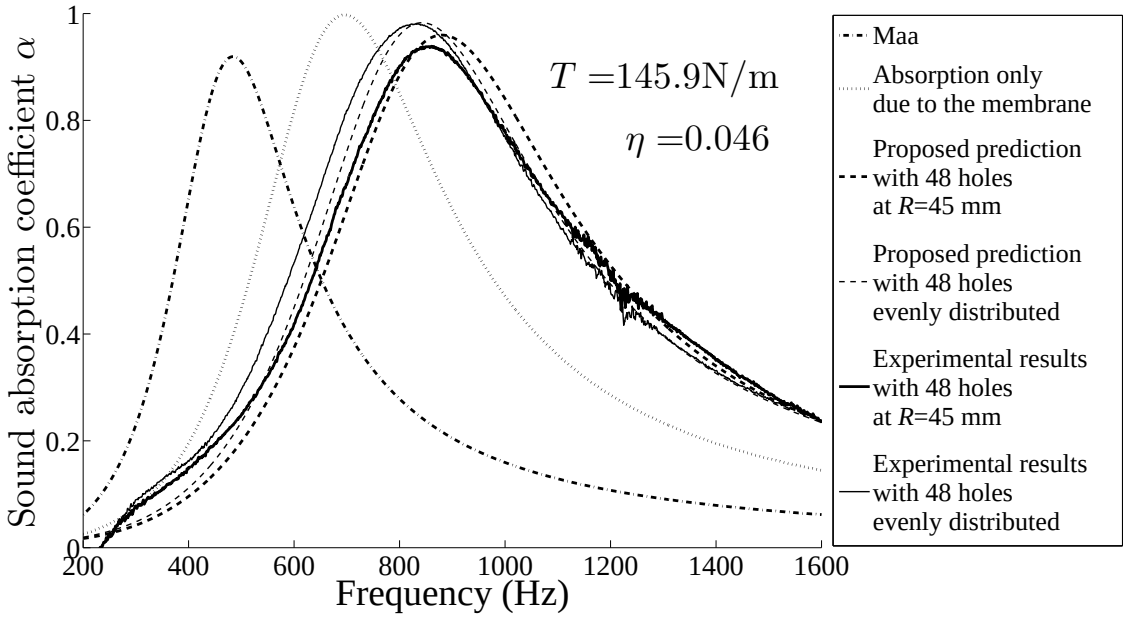

Figure 3.25: Normal incidence sound absorption coefficients of the manufactured MPMs with 48 holes, $D = 25$ mm. The thick solid curve represents the measured sound absorption coefficient of an MPM with 48 holes at a radius of $R = 45$ mm. The thin solid curve represents the measured sound absorption coefficient of the manufactured MPM with 48 holes evenly distributed on the membrane surface. The thick and thin dashed curves are the prediction results for each using the proposed method, respectively.

was drilled with 73 holes, with hole radius $r_0 = 0.31$ mm. The holes were arranged at $R =$ 45 mm for one of the manufactured MPMs and were evenly distributed over the membrane surface for the other. Therefore, in Group 1, the perforation ratios of two manufactured MPMs are identical and equal to 0.29%. Similarly, for Group 2, each MPM was drilled with 48 holes. The hole radius r_0 is also 0.31 mm. Therefore, the perforation ratio for each manufactured MPM in Group 2 is 0.19%. The holes were at $R = 45$ mm for one of the MPMs and were evenly distributed for the other. In each group, the parameters of the MPMs are identical. Based on the conventional theories, their sound absorption coefficients should be identical, however, based on the proposed theory, their sound absorption coefficients might differ due to the hole positions, i.e. the effect of the membrane vibration on the acoustic impedance of the perforations.

The different perforation positions are shown in Figure 3.23. The sound absorption measurements were conducted under the same experimental arrangement as described in Section 3.3.1. The measured sound absorption coefficients and the predicted results based on the proposed method are compared for each MPM group in Figures 3.24 and 3.25.

Note that the values of the tension and damping are identical to those in Figure 3.14 because it is assumed that the perforations have no effect on the mechanical properties of the membrane. The thick solid curves in Figures 3.24 and 3.25 are the measured sound absorption coefficient curves for the manufactured MPMs with holes at $R = 45$ mm and the thin solid curves are those for the manufactured MPMs with holes evenly distributed. There are obvious differences between these curves which demonstrates the effect of the hole positions on the acoustic impedance of the MPMs, and hence supports the proposed theory. Moreover, the predicted curves are close to the experimental results for the corresponding manufactured MPMs, which suggests that the proposed theory is accurate.

3.4 Conclusions

This chapter aimed to investigate the sound absorption of micro perforated membranes which will be used later in this thesis in Chapter 7 as an insert between two inflated membranes. A new method is introduced to predict the acoustic impedance and the sound absorption coefficient of a micro perforated membrane (MPM). This method is based on a new boundary condition where the particle velocity at the hole wall boundary, which is assumed to be zero

in Maa's theory, is assumed to be equal to the membrane vibration velocity. By applying this new boundary condition to a circular membrane, it is shown that the acoustic impedance due to the perforation is affected by the membrane vibration and becomes a function of the membrane radial coordinates.

Using this new boundary condition, analytical models for the acoustic impedances of both the impedances associated with the perforations and the membrane vibration impedance are derived. The variability of the perforation impedance with the hole location is investigated theoretically. The impedances due to the perforation and the membrane vibration are combined following the electro-acoustic analogy to present the overall impedance of the MPM. This new model is validated by experimental results for MPMs.

Moreover, the effect of the viscous layer on the sound absorption of the MPMs are discussed. Comparing the thickness of viscous layers and the hole radii, it is found that MPMs 1 to 3 have small hole radii (approximately 25μm) so that the viscous layer covers the entire hole area, resulting in extremely high acoustic impedance and ineffective sound absorption. Furthermore, their sound absorption curves are close to the theoretical results of impervious membranes with identical surface density, tension and damping ratio, which implies that the effects of the micro perforations on MPMs 1 to 3 are negligible and they can be assumed to be impervious membranes. However, MPM 4 which has larger holes (with a perforation radius of 255μm) not completely covered by the viscous layer, shows effective sound absorption due to the perforations and the membrane vibration. Additionally, based on the proposed theory, it is validated experimentally that the hole position affects the acoustic impedance and sound absorption of MPMs, even if the MPM parameters, such as the hole radii, the thickness and the perforation ratio, are identical.

This study extends the classic micro perforated theory and offers an accurate model for predicting the performance of flexible finite-sized MPMs. It also provides increased understanding of the coupling between the membrane vibration impedance and the impedance due to the perforations of micro perforated membranes.

Chapter 4

Nonlinearity of the sound absorption of micro perforated membranes under high SPL excitation

4.1 Introduction

When measuring the sound absorption coefficients of the MPM samples, non-linear behaviour was observed when measuring the sound absorption of MPM 4 (surface density $\rho_p = 0.2506\,\mathrm{kg/m^2}$, hole radius $r_0 = 0.255\,\mathrm{mm}$, membrane thickness $h = 0.17\,\mathrm{mm}$, hole spacing 5.29 mm and perforation ratio $\delta = 0.730\%$) with high SPL excitation. This chapter presents the experimental findings on the non-linearity of the sound absorption of MPM 4 excited by broadband and monochromatic sound signals. These results are essential for analytical modelling of the non-linear acoustic impedance of the MPM which is presented in Chapter 5, and are crucial for investigating the sound transmission in double impervious membranes with an internal MPM investigated in Chapter 7.

In this chapter, previous research on the non-linear acoustic properties of an orifice and MPPs is reviewed in Section 4.1.1. The resulting gaps and contributions of this chapter are described in Section 4.1.2. To investigate the non-linear sound properties of the MPM, it is crucial to validate the measurement method. This is presented in Section 4.2. Section 4.3 presents the experimental findings of the non-linear sound absorption of the MPM and further explores the physical explanations for these findings. This is followed by the conclusion in Section 4.4.

4.1.1 Literature review

Micro perforated materials have been widely used for sound absorption, and have been investigated in both linear and non-linear regimes. Conventionally, micro perforated panels (MPPs) are assumed to behave linearly under acoustic excitation (Bravo et al. 2012, Kang & Fuchs 1999, Maa 1994) and the type of sound source is assumed to have no impact on the measured sound absorption coefficient. By contrast, when samples are subjected to high sound pressure levels (SPLs), non-linear effects have been observed. Ingard & Ising (1967) indicated that the air flow travelling through an orifice under strong excitation forms a high velocity jet. Maa (1994) derived an expression which represents the non-linear effect on the resistance of MPPs under high excitation. Bodén (2007) investigated the non-linear impedance of perforates under high SPL excitation and indicated that pure tone excitation leads to a non-linear impedance dependent on the acoustic particle velocity at the frequency of the pure tone; however, broadband excitation leads to a non-linear impedance at a certain frequency dependent on the acoustic particle velocities at all excited frequencies. Tayong et al. (2010) investigated the non-linear effects of sound sources at the peak absorption frequency of MPP absorbers, both experimentally and theoretically, when subjected to very high SPLs (145 dB re 20 μPa).

However, questions remain about the non-linear properties of micro perforated materials. The previous research indicates that the non-linear properties of MPPs are closely related to the SPL magnitude; for example Maa (1994) indicated that theoretically non-linear behaviour exists when the SPL is 129 dB re 20 μPa and above, and Tayong et al. (2010) observed non-linear sound absorption of an MPP with an SPL of 145 dB re 20 μPa. There is limited discussion on the threshold SPL at which the non-linear impedance starts to occur, which affects the sound absorption non-linearly. While the previous studies focussed on MPPs, research on the non-linear performance of micro perforated membranes (MPMs) is very limited. Previous studies also indicated that the resistance is the dominating factor of the non-linearity of MPPs and the non-linear reactance impact is negligible (Ingard & Ising 1967, Tayong et al. 2010). However, it is unclear whether the SPL has a non-linear impact on the reactance of MPMs in the non-linear regime.

The measurement methods used in previous research for the sound absorption coefficient of an orifice, MPP or MPM in a non-linear regime can be categorised into three groups:

the hot wire method to measure the air particle velocity, the two-microphone standing-wave method and the two-microphone transfer-function method. The hot wire method is commonly used to measure the air particle velocity. Ingard & Ising (1967) used hot wires to measure the air particle velocity behind an orifice in a rigid baffle when the incident sound pressure was sufficiently high that the system was in a non-linear regime. This is one of the early pieces of research which experimentally demonstrates the proportional relationship between the sound pressure and the acoustic impedance of the orifice. Although the hot wire method is valid for an orifice, it is not an ideal measurement method for MPPs and MPMs. Comparing the size of hot wires to that of the perforations on conventional MPPs and MPMs, it is found that the hot wires are so large that when measuring the particle velocity, it is difficult to eliminate the interaction between the perforations, which leads to measurement errors and inaccurate results.

Before the transfer function method was introduced by Chung & Blaser (1980*a*), the conventional way to measure the sound absorption coefficient of a sample was the standing wave method. However, Zorumski & Parrott (1971) indicated that the standing wave method is only valid for the measurement using a pure harmonic wave and is invalid when the sound wave is distorted in a non-linear regime. They further developed a new method to measure the spectral impedance of a sample in a non-linear regime, using an additional microphone which is placed at the backing wall. Since then, this two-microphone method had been used by Melling (1973*a*,*b*) and Cummings (1984, 1986).

Chung & Blaser (1980*a*) developed the two-microphone transfer-function method, which is favoured by researchers for its convenient experimental process and accuracy. This method is commonly used for sound absorption measurements in both linear and non-linear regimes. Bodén (2007) and Tayong et al. (2010) investigated the non-linear acoustic properties of samples using this method. Tayong et al. (2010) further indicated that this method is valid when the sound propagation between the two microphones is linear.

4.1.2 Gaps and contributions

It is known from the literature review in Section 4.1.1 that there is very limited research about the non-linear sound absorption of MPMs under high SPL excitation. The threshold SPL where the non-linear properties start is unclear. It is also unknown whether the high

SPL has no impact on the reactance of MPMs, as in the case of MPPs.

This chapter presents the experimental findings on the non-linear effects of sound sources on the normal-incidence sound absorption of MPMs over a broadband frequency range. The frequency-dependent value of the incident sound pressure level at the surface of the MPM was varied from 15 dB re 20 μPa to 143 dB re 20 μPa. Significant non-linear behaviours of MPMs are observed, even at SPLs considered low for non-linear effects to occur. The details of the experiments are presented in Section 4.3 and the non-linear effects of sound sources are discussed in the subsequent sections.

However, before presenting the experimental findings, the two-microphone transfer-function method has been validated in Section 4.2. The transfer function between each microphone and the sound source was measured and the transfer function between the microphones was estimated, based on the former two measured transfer functions described in Section 4.2.2. The sound absorption coefficients obtained from the estimated and measured transfer functions are compared in Section 4.2.3. The agreement between these results indicates the validation of the two-microphone transfer-function method.

4.2 Validation of experimental method

This section aims to validate the two-microphone transfer-function method. This method is described in Section 4.2.1, as well as the validation method in Section 4.2.2. In the former, the transfer function between two microphones was measured. Instead, in the latter, the transfer function between each microphone and the sound source was measured to estimate the transfer function between the two microphones. The sound absorption coefficients obtained from the estimated and measured transfer functions are compared in Section 4.2.3 where a good agreement was achieved.

4.2.1 Two-microphone transfer-function method

This section describes the experimental set-up of the two-microphone transfer-function method according to ISO10534 (1998) and ASTM E1050 (2012). The sound absorption experiments were conducted in a steel impedance tube with a normally-incident plane wave. The internal radius of the impedance tube is $R_0 = 50$mm with a cut-off frequency of 1.7 kHz (Kinsler et al. 1999). The measurement range is from 200 Hz to 1600 Hz. The two micro-

phone transfer function method was used to obtain the sound absorption coefficient (Chung & Blaser 1980*a*), as shown in Figure 4.1. The sound pressures were measured using two microphones, from which the SPL on the surface of the MPM and the sound absorption coefficient were determined. The microphones used in this measurement were 1/4 inch pre-polarised microphones (Brüel & Kjær, type 4958). The loudspeaker was from the Brüel & Kjær standing wave apparatus type 4002. In this section, the measurement followed the standards ISO10534 (1998) and ASTM E1050 (2012), which implies that the transfer function between the two microphones was measured. The sound absorption coefficient can be obtained by Equation (2.103).

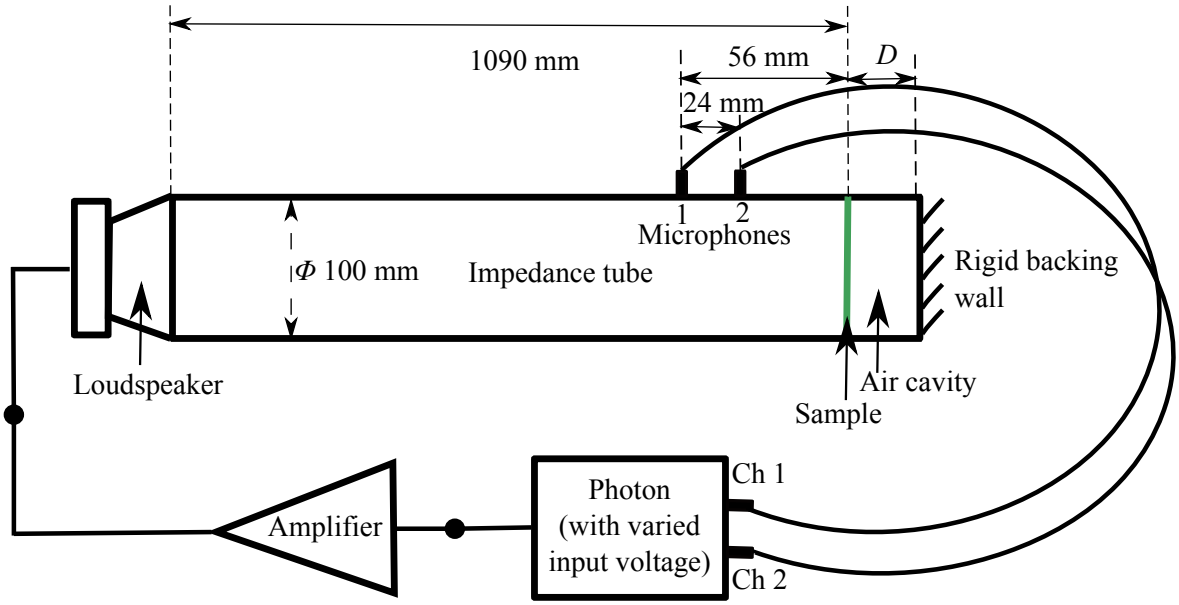

Figure 4.1: Measurement of sound absorption coefficient using two microphone transfer function method in an impedance tube.

Moreover, it is observed in the experiments that the measured sound absorption coefficient is sensitive to the mounting condition of the MPM sample. To prevent a measurement error due to the mounting condition, the MPM 4 sample used throughout was put into the tube before the measurements started and was not taken out until all the measurements were done.

4.2.2 Measurement of the transfer function between each microphone and the sound source

Tayong et al. (2010) indicated that the two-microphone transfer-function method is valid provided the sound wave propagates linearly in the impedance tube. In this section, the

transfer functions between the microphones and the sound source, named as H_{s1} and H_{s2}, were measured, and are given by

$$H_{s1} = \frac{p_1}{p_{source}}, \tag{4.1}$$

and

$$H_{s2} = \frac{p_2}{p_{source}}, \tag{4.2}$$

where p_1 denotes the measured sound pressure at microphone 1, p_2 denotes that at microphone 2 and p_{source} denotes the voltage signal input into the power amplifier which drives the sound source. Therefore, the transfer function between two microphones H_{12} is estimated by

$$H_{12} = \frac{H_{s2}}{H_{s1}} = \frac{p_2}{p_1}. \tag{4.3}$$

Note that the term H_{12} may also be measured directly using the two-microphone transfer-function method, as mentioned in Section 4.2.1.

4.2.3 Comparison of the measured sound absorption coefficients

This section compares the measured and estimated sound absorption coefficients obtained with the two methods mentioned in Sections 4.2.1 and 4.2.2. Both white noise and a stepped sine sweep were used as signals to generate the sound. The input voltage varied from 100 mV to 200 mV which was sufficiently high that the impedance of the sample was in a non-linear regime. The comparison is shown in Figures 4.2 to 4.5.

In Figures 4.2 to 4.5, the solid curves are the estimated sound absorption coefficients obtained using the two measured transfer functions between each microphone and the sound source, i.e. Equation (4.3). The dashed curves are the sound absorption coefficients obtained using the measured transfer functions between two microphones following the standards ISO10534 (1998) and ASTM E1050 (2012). In each figure, the solid curve agrees significantly with the dashed curve over the measured frequency range, except around the tube resonance frequency of 1250 Hz. This implies that the measured sound absorption coefficient usint the ISO/ASTM standards is identical to the estimated sound absorption coefficient via two intermediate transfer functions.

Additionally, Figures 4.6 to 4.9 illustrate the coherence functions measured using the methods in Sections 4.2.1 and 4.2.2. When white noise was used, these coherences were

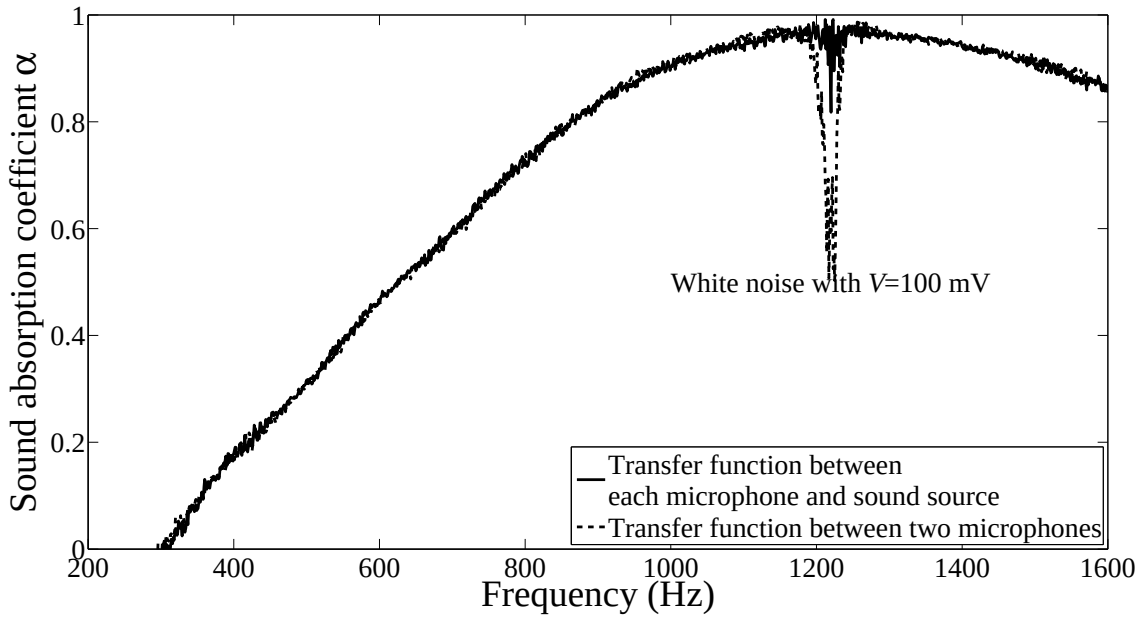

Figure 4.2: Comparison of the measured and estimated sound absorption coefficients of MPM 4 obtained with the two methods mentioned in Sections 4.2.1 and 4.2.2. The input voltage of the white noise was 100 mV.

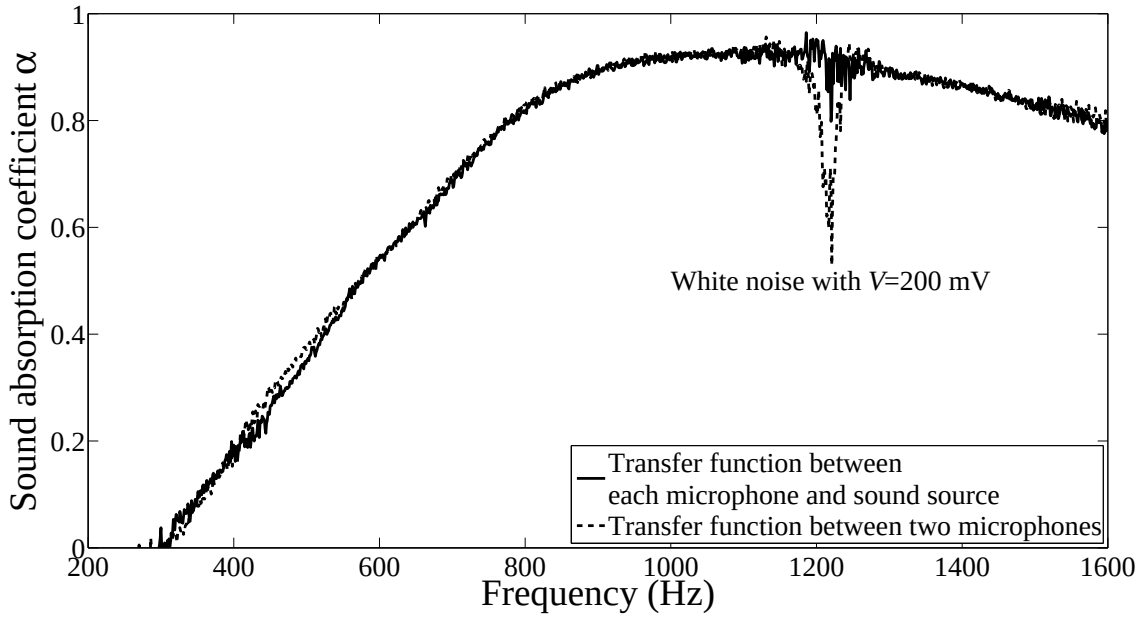

Figure 4.3: Comparison of the measured and estimated sound absorption coefficients of MPM 4 obtained with the two methods mentioned in Sections 4.2.1 and 4.2.2. The input voltage of the white noise was 200 mV.

higher than 0.95 over the measured frequency range, except for the frequencies around the tube resonance frequency, 1250 Hz. As for the stepped sine sweep sound signal, all the coherences were equal to unity, implying a better distortion immunity than for white noise.

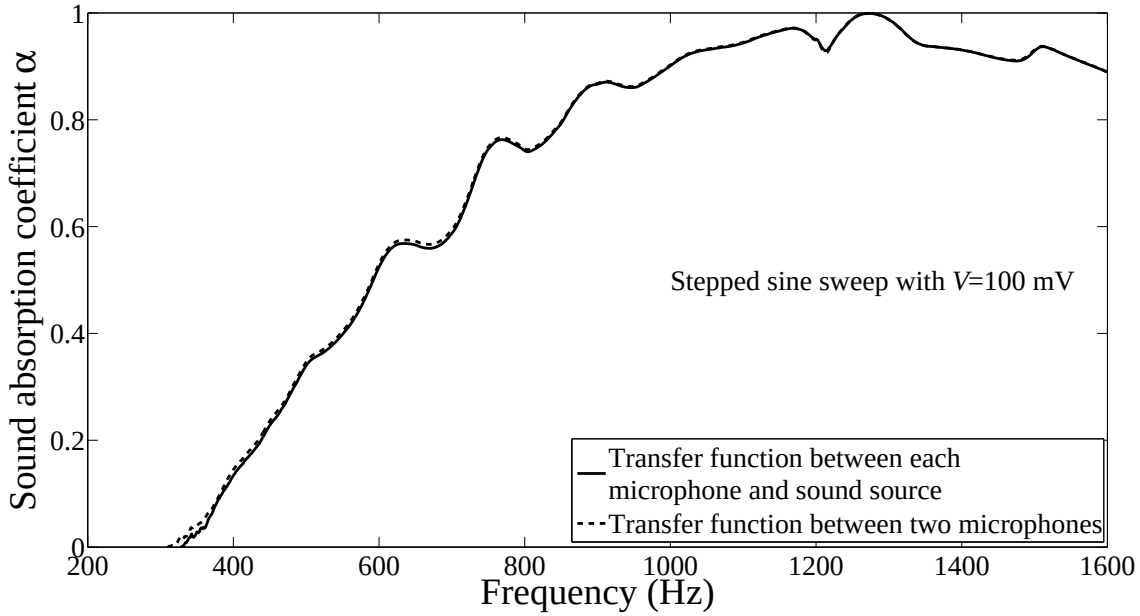

Figure 4.4: Comparison of the measured and estimated sound absorption coefficients of MPM 4 obtained with the two methods mentioned in Sections 4.2.1 and 4.2.2. The input voltage of the stepped sine sweep was 100 mV.

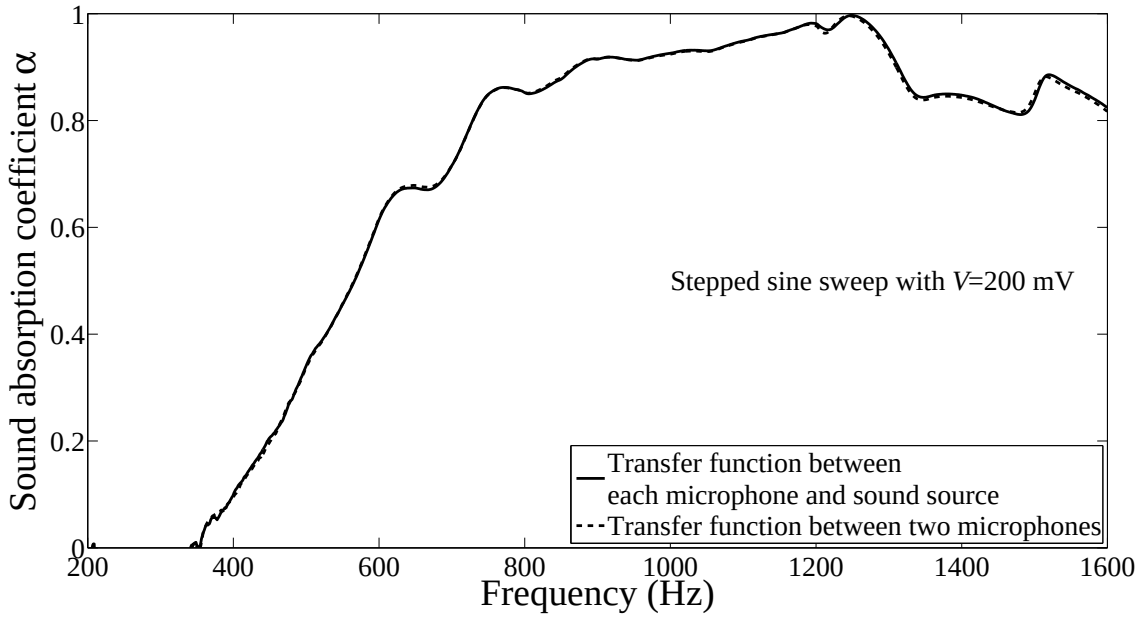

Figure 4.5: Comparison of the measured and estimated sound absorption coefficients of MPM 4 obtained with the two methods mentioned in Sections 4.2.1 and 4.2.2. The input voltage of the stepped sine sweep was 200 mV.

The consistence of the measured and estimated sound absorption coefficients and the unity values for coherence illustrate that whilst the impedance is affected by the magnitude of the incident SPL in a non-linear regime, the relationship between the incident and re-

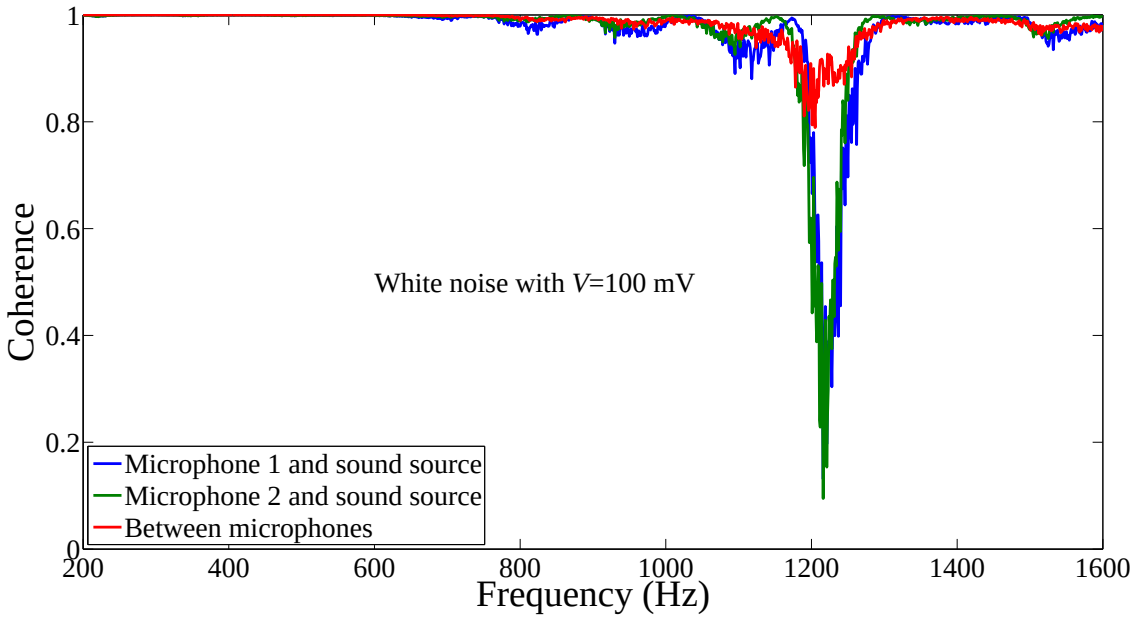

Figure 4.6: Comparison of the measured coherence between each microphone and the sound source with that between the two microphones, using the two methods mentioned in Sections 4.2.1 and 4.2.2. The input voltage of the white noise was 100 mV.

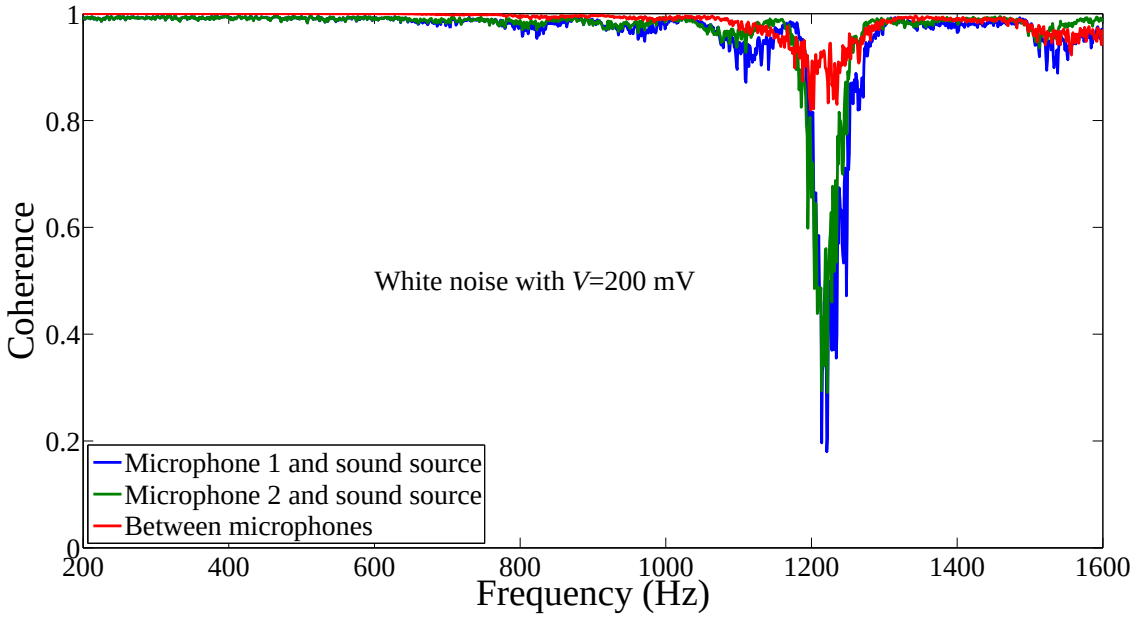

Figure 4.7: Comparison of the measured coherence between each microphone and the sound source with that between the two microphones, using the two methods mentioned in Sections 4.2.1 and 4.2.2. The input voltage of the white noise was 200 mV.

flected sounds remains linear. Therefore, the sound propagation in the upstream side of the impedance tube is linear and the two-microphone transfer-function method is still valid in the case of an MPM excited by high SPLs in a non-linear regime.

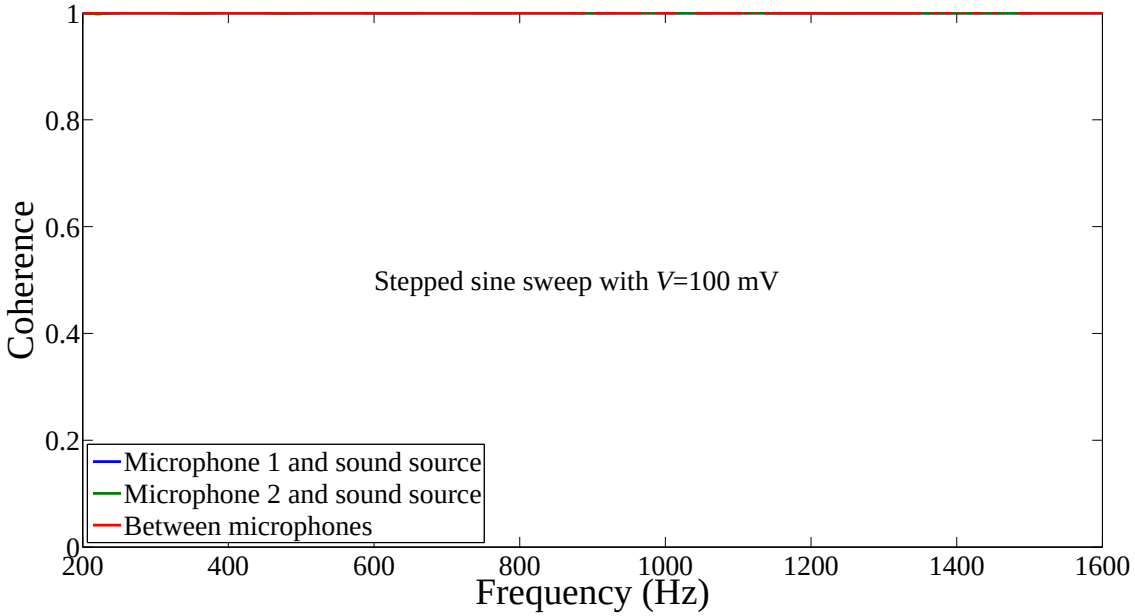

Figure 4.8: Comparison of the measured coherence between each microphone and the sound source with that between the two microphones, using the two methods mentioned in Sections 4.2.1 and 4.2.2. The input voltage of the stepped sine sweep was 100 mV.

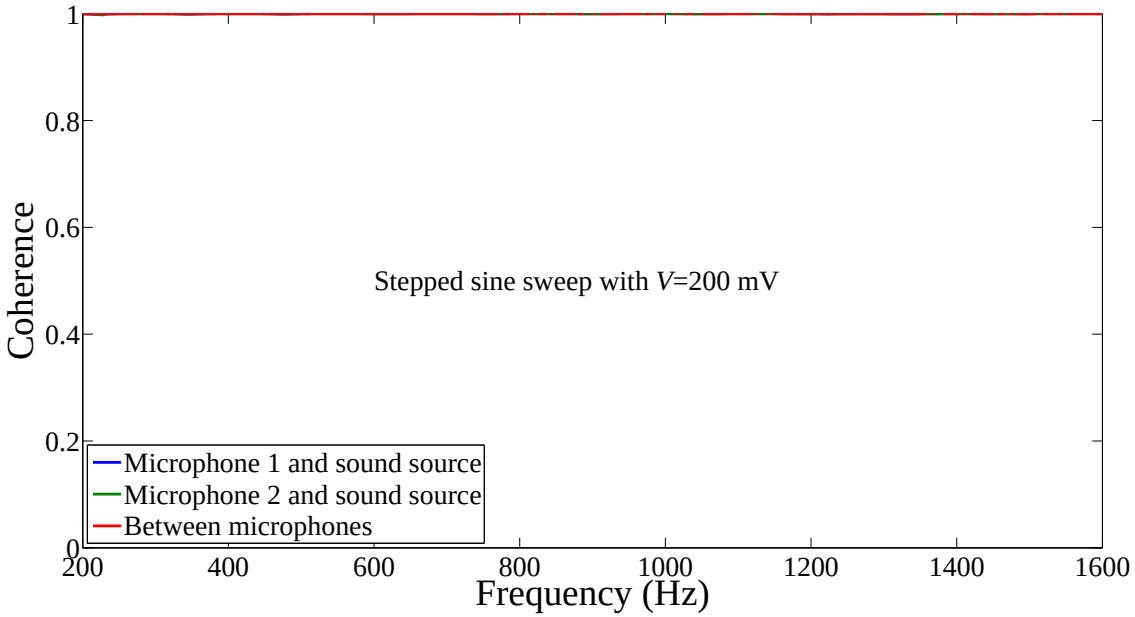

Figure 4.9: Comparison of the measured coherence between each microphone and the sound source with that between the two microphones using the two methods mentioned in Sections 4.2.1 and 4.2.2. The input voltage of the stepped sine sweep was 200 mV.

4.3 Experimental findings on the non-linearity of the sound absorption of MPMs under high SPL excitation

This section presents the experimental findings of the non-linear effects of high SPL excitation with different sound signals on the sound absorption of thin flexible MPMs over a broadband frequency range. The sound pressure levels used as excitation varied from 15 dB re 20 μPa to 143 dB re 20 μPa. Interesting non-linear properties of MPMs have been observed even at relatively "low" SPLs. The set-up of the experiments are presented in Section 4.2.1. The non-linear effects of high SPL excitation with different sound signals are discussed in Sections 4.3.2 and 4.3.3. The effects of the different types of sound signals are presented in Section 4.3.5. Based on these experimental findings and analysis, suggestions as to the impact on sound absorption tests have been made in Sections 4.3.5 and 4.3.6.

4.3.1 Measurement of the sound absorption of MPMs under high SPL excitation

To investigate the non-linear sound absorption of MPMs under high excitation, the sound absorption experiments of an MPM were conducted with a normally-incident plane wave in an impedance tube, which is described in Section 4.2.1. The parameters of the MPM sample are presented in Section 4.3.1.1. The SPL of each microphone arising from the sound source was measured simultaneously with the sound absorption coefficient measurement of the MPM. The properties of the two groups of sound signals (broadband and monochromatic) are discussed in Section 4.3.1.2. Since the aim of this section is to investigate the effect of high SPL on the sound absorption of the MPM, the SPL at each individual excitation frequency varies from 15 dB to 143 dB, as presented in Section 4.3.1.3. The measured sound absorption under varying SPL excitations are analysed in Sections 4.3.2 and 4.3.3.

4.3.1.1 Parameters of the MPM sample

The MPM sample used in this section is identical with the MPM 4 used in Section 3.3.1. As discussed in Chapter 3, the sound absorption of the MPMs 1 to 3 are mainly due to the membrane vibration as their perforations are so small that air flow can barely travel through the perforations. Since this chapter aims to investigate the non-linear sound absorption of MPMs under high excitation and the non-linearity is closely related to the flow travelling

through the perforations, MPMs 1 to 3 are unsuitable, and thus only MPM 4, with large perforation radius, is used here. The parameters of MPM 4 are re-clarified in Table 4.1. In the sound absorption experiments, the MPM was tested with an air cavity and a rigid backing wall. The depth of the air cavity between the sample and the rigid wall was 25 mm. As mentioned in Chapter 3, the effective sound absorption coefficient is sensitive to the mounting condition (in particular the tension) of the MPM sample. Hence, all tests were conducted contiguously without disturbing the sample.

Table 4.1: Measured MPM parameters

Samples	Surface density ρ_p (kg/m^2)	Hole radius r_0 (mm)	Thickness h (mm)	Perforation ratio δ (%)
MPM 4	0.2506	0.2553	0.17	0.73

4.3.1.2 Sound sources: white noise and a sine sweep

The source signal was generated by a Brüel & Kjær Photon Plus system. The signal from the Photon Plus was amplified by a power amplifier to drive the loudspeaker. The SPLs in the impedance tube were adjusted by changing the input voltage into the power amplifier of the sound source in the Photon Plus. The input voltage varied from 0.1 mV to 200 mV (over a range of three orders of magnitude).

Multiple types of source signals have been used for excitation, which can be categorised into two types: broadband and monochromatic signals. The broadband signals investigated here included white noise (Gaussian distribution), uniform random, pseudo random and burst random signals. Monochromatic signals investigated included a stepped sine sweep and a chirp with a linear sweep rate of 52 Hz/second. Sound absorption measurements were conducted with all of the aforementioned source signals. Similar non-linear behaviours were observed for each group of source signals. Therefore, in this chapter, white noise represents the broadband excitation and the stepped sine sweep represents the monochromatic excitation.

White noise is commonly used in sound absorption experiments, as it drives all audible frequencies simultaneously in the desired frequency range; in this case from 200 Hz to 1600 Hz. Conversely, the stepped sine sweep is usually used to measure the frequency response when good noise immunity is required or the system response is non-linear. This source signal was configured to scan the desired frequencies from 200 Hz to 1600 Hz over a 10

minute time span. When using a stepped sine sweep, the sound energy is concentrated at a single frequency. Therefore, the SPL arising from a stepped sine sweep is higher than that of white noise at a specific frequency for a given voltage. The estimated SPLs at the MPM surface for the two excitation types shown in Figures 4.10 and 4.11 demonstrate this.

4.3.1.3 High SPL excitation

To investigate the effect of the incident SPL on the sound absorption of the MPM, it is crucial to obtain the SPL on the surface of the MPM. However, the microphones were placed in the positions shown in Figure 4.1, neither of which were at the surface of the MPM. Based on the plane wave assumption and the distances between the microphones and the MPM sample given in Figure 4.1, the incident SPL on the MPM surface was estimated using the measured transfer function (Chung & Blaser 1980*a*) and the total sound pressure measured with Microphone 1. Figures 4.10 and 4.11 illustrate the estimated SPL at the surface of the MPM sample excited by white noise and stepped sine sweep signals, respectively. The data was sampled at 4096 Hz, with a 2^{12} point FFT, giving a 1 Hz bin width.

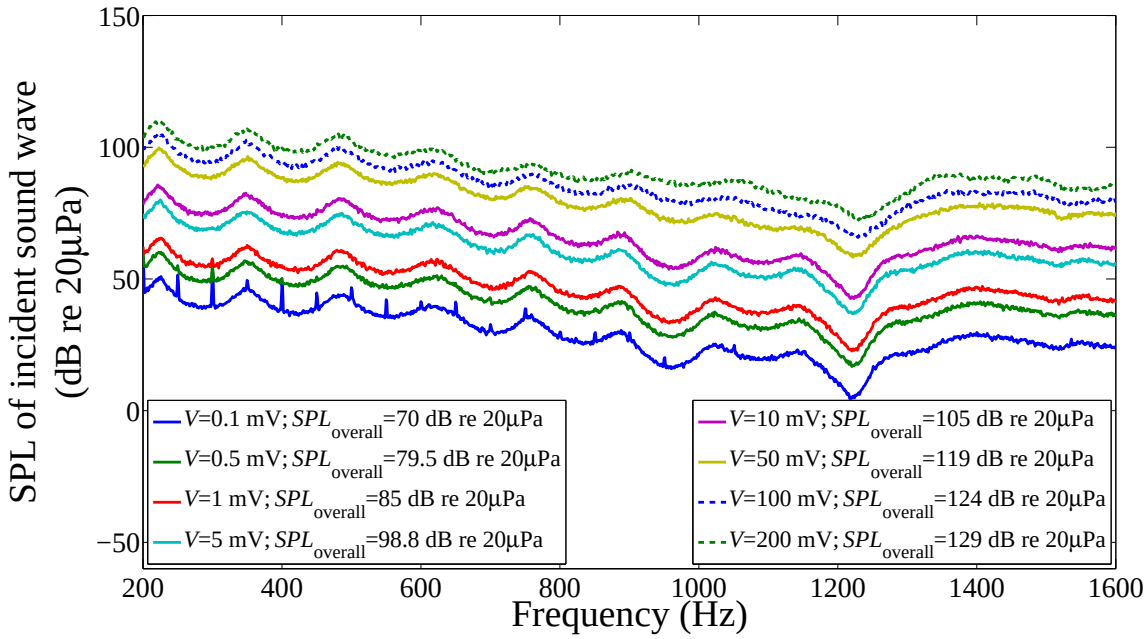

Figure 4.10: Estimated sound pressure level (SPL dB re 20 μPa) of the incident sound at the surface of the MPM with white noise excitation. The input voltage ranges from 0.1 mV to 200 mV. The resultant overall SPLs are detailed in the legend.

Figures 4.10 and 4.11 show that with the increase of the input voltage, the SPL on the membrane surface increases, regardless of the type of sound source signal. As presumed

in Section 4.3.1.2, the SPL of the sine sweep (see Figure 4.11) is constantly higher than that of white noise (see Figure 4.10) when the input voltage is identical, due to the different methods of white noise and sine sweep noise generation. The peaks and valleys in the SPL plots shown in Figures 4.10 and 4.11 are associated with axial resonances due to the finite length of the impedance tube. When the input voltage is as low as 0.1 mV, the measured SPLs for both sound source signals are noisy due to the poor coherence between the two microphones. Note that the microphones are rated to SPLs of up to 140 dB re 20 μPa (Kinsler et al. 1999). The majority of estimated SPLs were lower than 140 dB re 20 μPa, except a few of those in the low frequency range with the stepped sine sweep excitation at the maximum input voltage. It is not expected that these levels have diminished the accuracy of the measurements since the coherence has remained high.

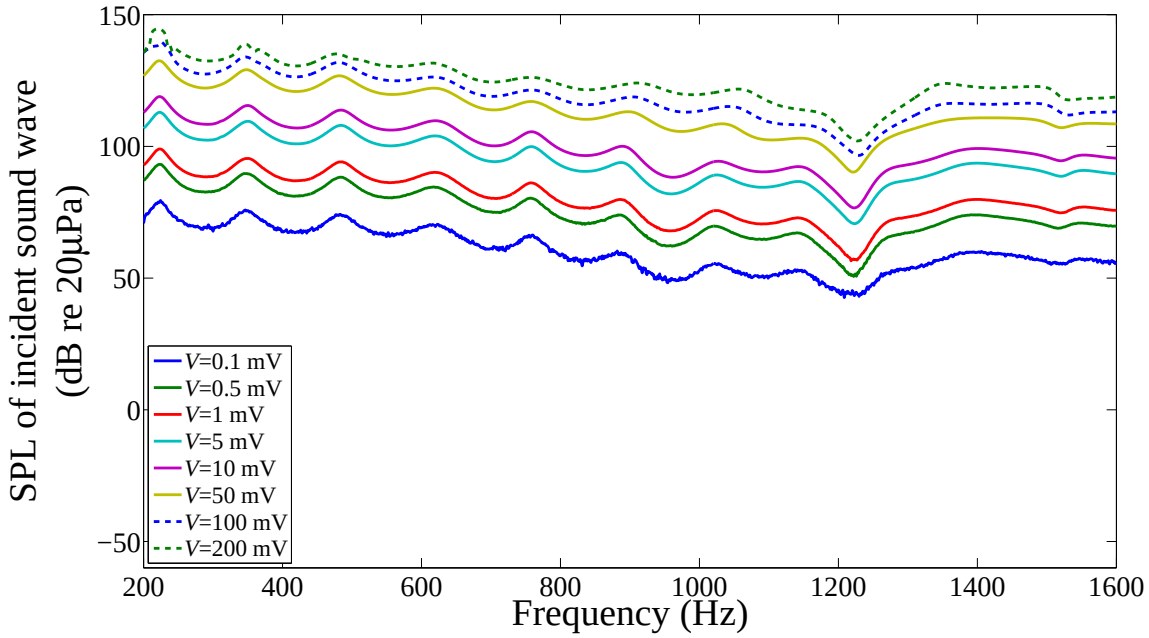

Figure 4.11: Estimated sound pressure level (SPL dB re 20 μPa) of the incident sound at the surface of the MPM with a stepped sine sweep excitation. The input voltage ranges from 0.1 mV to 200 mV.

The curves in Figure 4.11 are smoother than those in Figure 4.10, illustrating the better noise immunity of the stepped sine sweep noise. Note that the valley around 1250 Hz represents a structural resonance of the impedance tube, which was confirmed suing accelerometers measured to the tube. The structural resonance of the impedance tube leads to additional energy dissipation on the tube surface, and hence causes a decrease in the sound pressure level around the resonance frequency.

4.3.2 Sound absorption of MPMs excited by broadband noise

The sound absorption characteristics of the MPM were investigated for broadband excitation. This included white noise (Gaussian distribution), uniform random noise, pseudo random noise, burst random noise and pink noise.

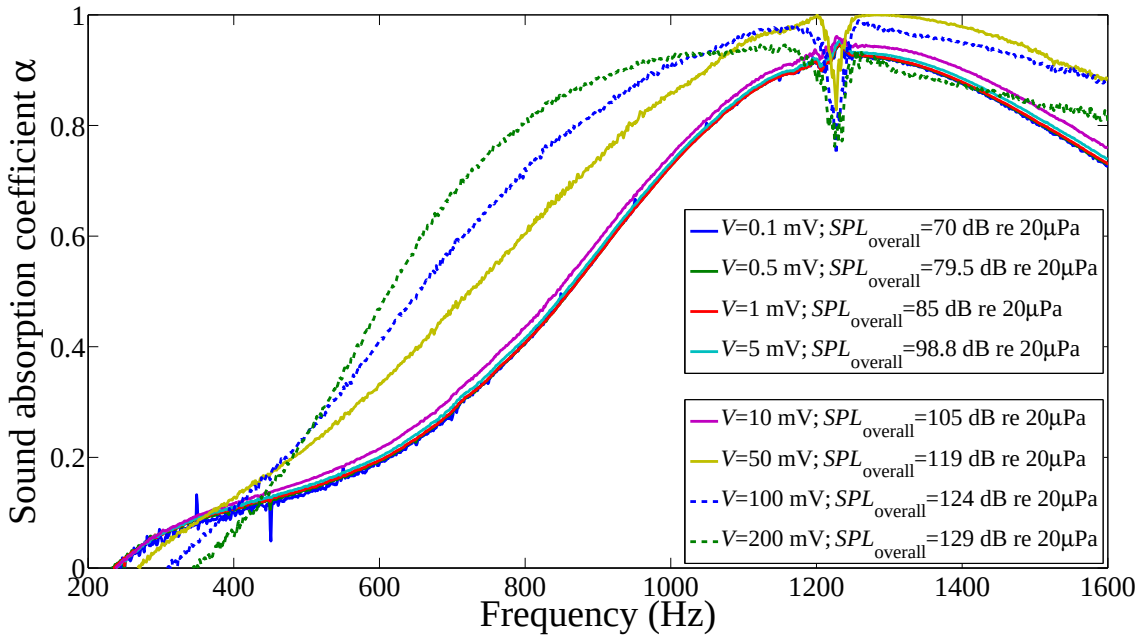

Figure 4.12: Measured sound absorption coefficients of the MPM with white noise excitation. The input voltage ranged from 0.1 mV to 200 mV. The corresponding SPL at the membrane surface is shown in Figure 4.10.

In this section, the sound absorption properties of the MPM, excited by white noise of varying amplitudes, are discussed. The results for all other broadband excitations were similar. Figure 4.12 illustrates that the sound absorption curves are consistent for the input voltages from 0.1 mV to 10 mV. Note that at 10 mV ($SPL_{\text{overall}} = 105$ dB re 20 μPa) a small change is observed which marks the onset of the non-linear behaviour. Therefore, it is reasonable to deduce that when the input voltage is below 10 mV, the sound absorption of the MPM is in the linear regime, where the acoustic impedance of the MPM is dependent on that of the perforation and the MPM vibration, and is independent of the characteristics of the excitation type. Comparing Figure 4.12 with Figure 4.10, it is found that the corresponding SPLs in this linear regime are relatively low, with no individual frequency exceeding 85.5 dB re 20 μPa and the overall SPL was equal to or less than 105 dB re 20 μPa, which validates the earlier conclusion by Maa (1996) that the non-linear effect of the sound source signal

occurs with high excitation and that the sound absorption is constant for low excitations. For the lowest amplitude excitation investigated (0.1 mV), the sound absorption curve exhibits some noise due to the poor coherence between the two microphones. The valleys around 1250 Hz are ascribed to a structural resonance of the impedance tube.

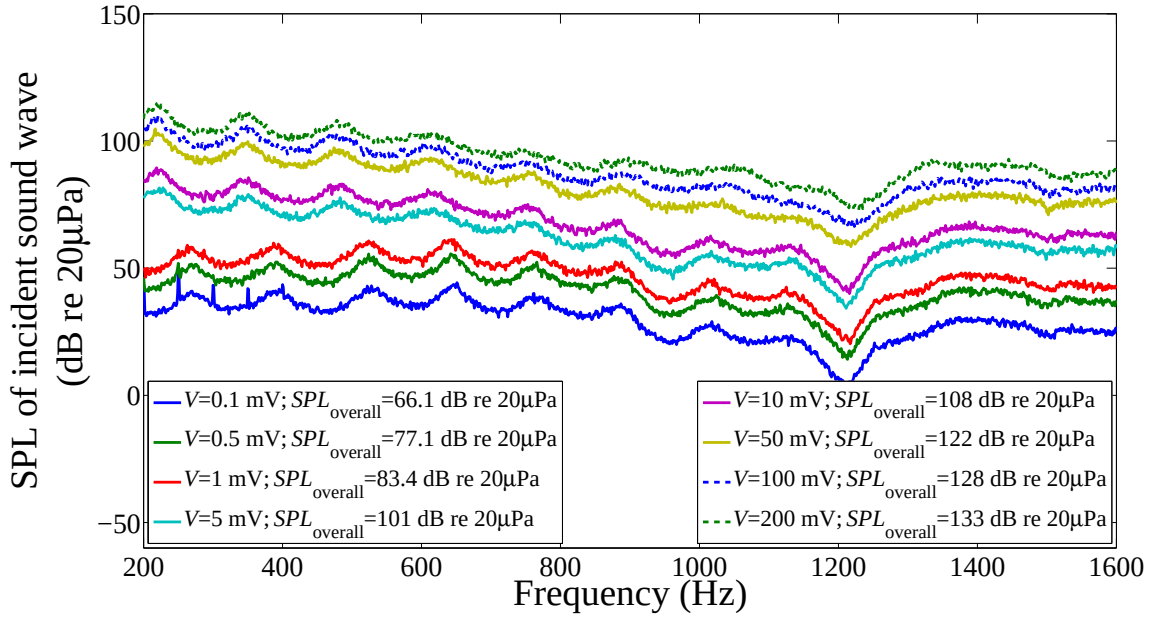

Figure 4.13: Estimated sound pressure level (SPL dB re 20 μPa) of the incident sound at the surface of the MPM with uniform random excitation. The input voltage ranges from 0.1 mV to 200 mV.

As the input voltage is increased to levels between 50 mV ($SPL_{\text{overall}} = 119$ dB re 20 μPa) and 200 mV ($SPL_{\text{overall}} = 129$ dB re 20 μPa), the incident sound pressure on the MPM surface increases as does the sound absorption of the MPM. It should be noted that when the non-linearity starts to affect the sound absorption, the overall incident SPL is 119 dB re 20 μPa and the SPLs at individual frequencies do not exceed 101 dB re 20 μPa. These values are significantly lower than the SPLs that have been considered to cause non-linear effects on MPPs in previous research, such as the theoretical value of 129 dB (Maa 1996) and the experimental value of 145 dB (Tayong et al. 2010). This implies that in the case of MPMs, even moderate incident SPLs can result in significant non-linear effects on the sound absorption coefficient.

The increase of the sound absorption coefficient in the non-linear regime is commonly ascribed to the increase of the sound resistance due to the high incident SPL on the sample surface and the effect of the reactance is usually neglected (Ingard & Ising 1967, Tayong

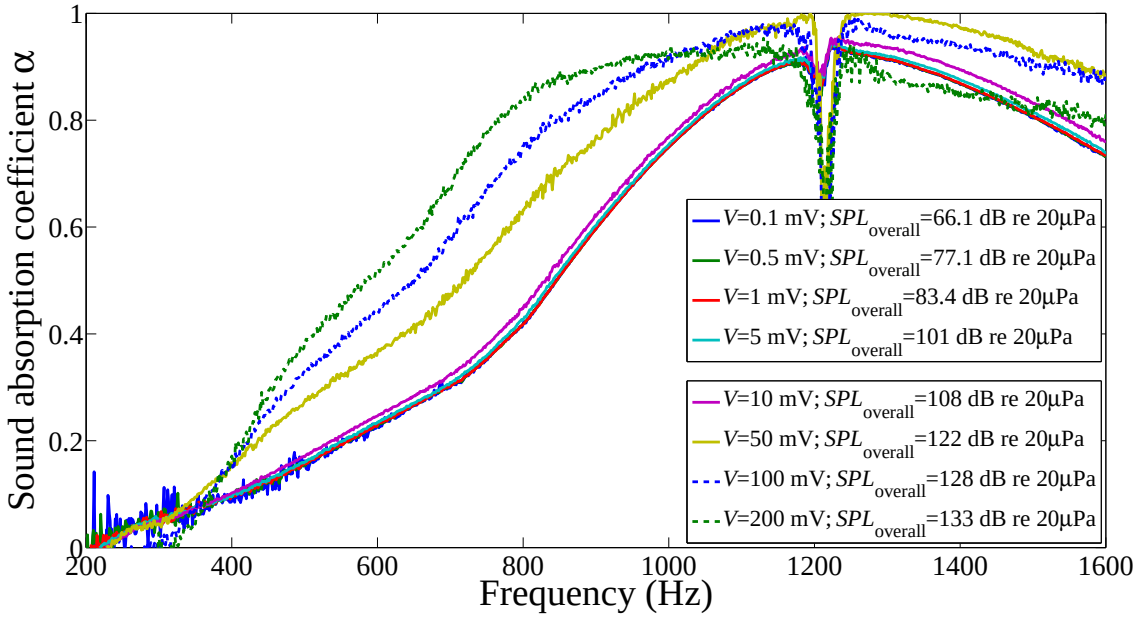

Figure 4.14: Measured sound absorption coefficients of the MPM with uniform random excitation. The input voltage ranged from 0.1 mV to 200 mV. The corresponding SPL at the membrane surface is shown in Figure 4.13.

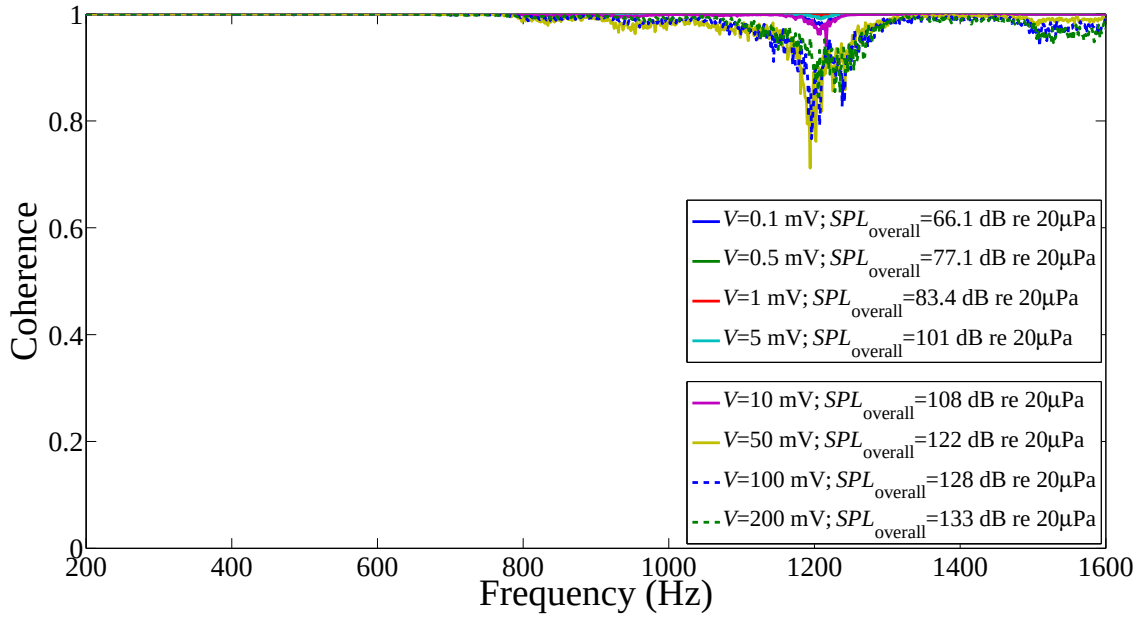

Figure 4.15: Measured coherences between two microphones with uniform random excitation. The input voltage ranged from 0.1 mV to 200 mV.

et al. 2010). However, it is known that the peak absorption frequency of the MPM absorber is dependent on the reactance of the absorber system (i.e., the MPM and the air cavity). In Figure 4.12, the sound absorption peak of the MPM absorber is reduced in frequency as the sound pressure increases. Hence, it is deduced that the non-linearity due to the high

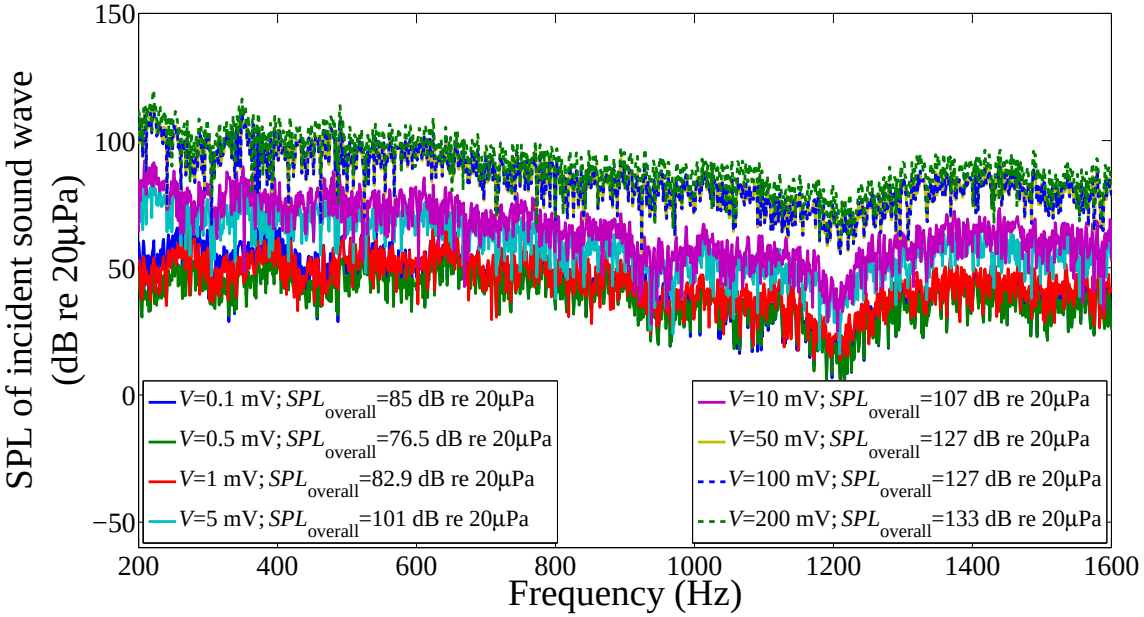

Figure 4.16: Estimated sound pressure level (SPL dB re 20 μPa) of the incident sound at the surface of the MPM with pseudo random excitation. The input voltage ranges from 0.1 mV to 200 mV.

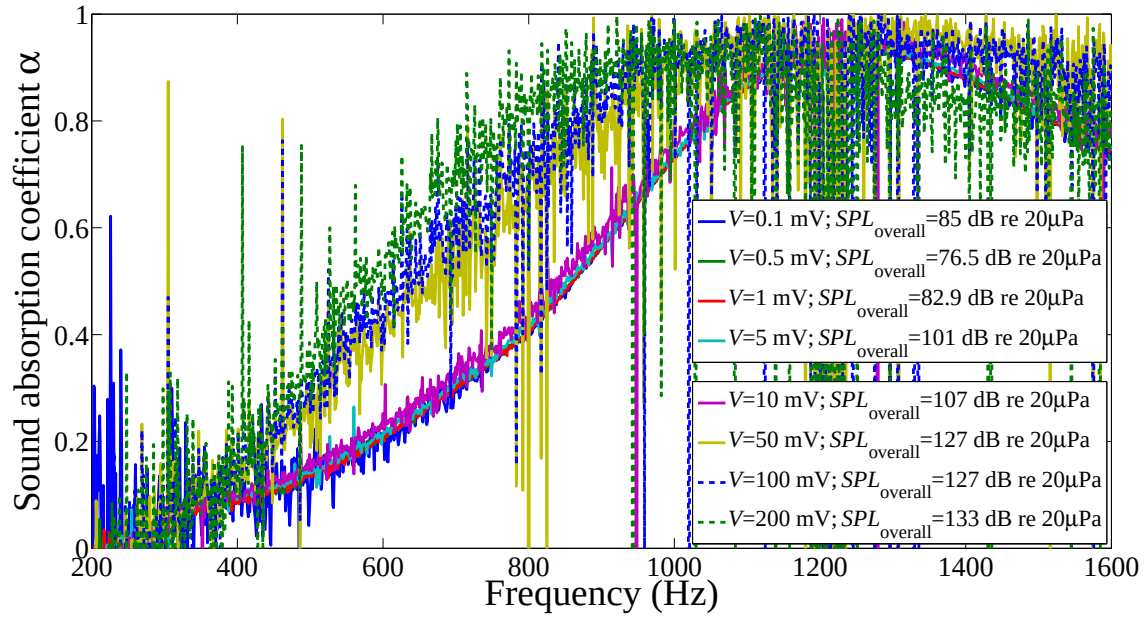

Figure 4.17: Measured sound absorption coefficients of the MPM with pseudo random excitation. The input voltage ranged from 0.1 mV to 200 mV. The corresponding SPL at the membrane surface is shown in Figure 4.16.

level white noise excitation affects not only the resistance but also the reactance of the MPM absorber.

It should be noted that for all the cases considered, the coherence between the two mi-

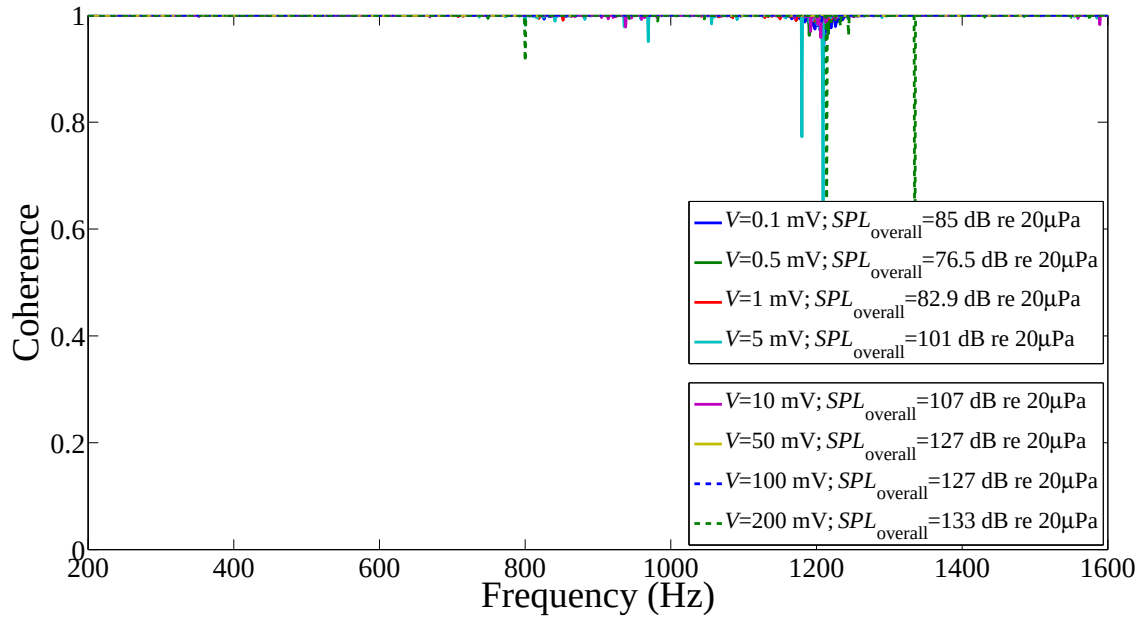

Figure 4.18: Measured coherences between two microphones with pseudo random excitation. The input voltage ranged from 0.1 mV to 200 mV.

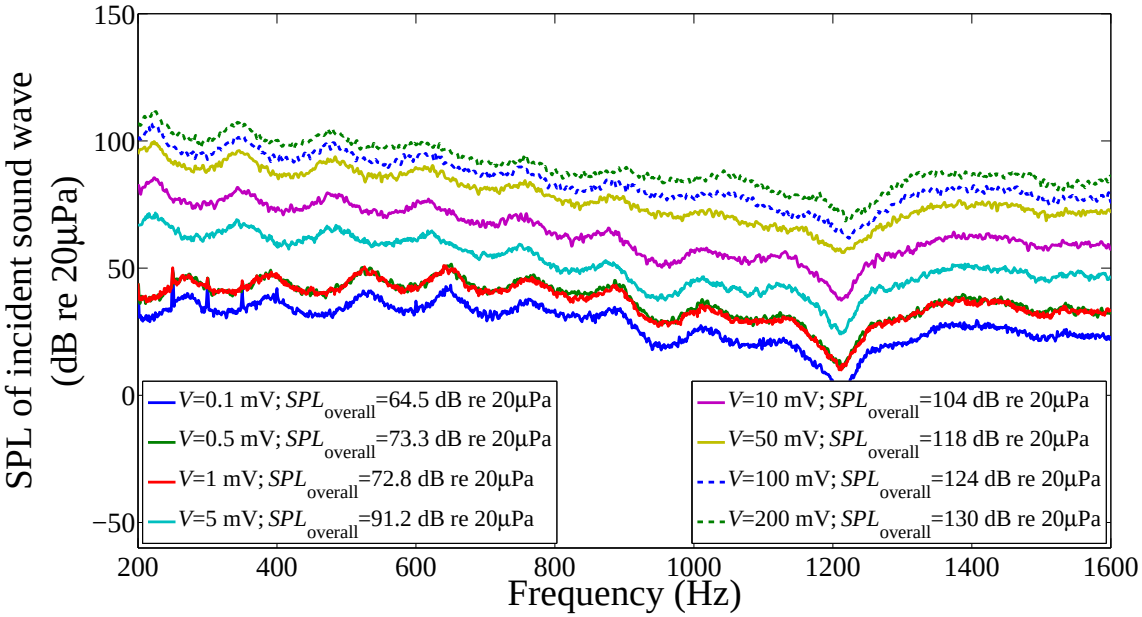

Figure 4.19: Estimated sound pressure level (SPL dB re 20 μPa) of the incident sound at the surface of the MPM with burst random excitation. The input voltage ranges from 0.1 mV to 200 mV.

crophone signals remained in excess of 0.982 with the exception of the 0.1 mV case, which suffered from a poor signal to noise ratio, and the frequencies around 1250 Hz which were affected by the structural resonance. Moreover, the transfer function between each microphone and the sound source was measured and the corresponding coherence was close to

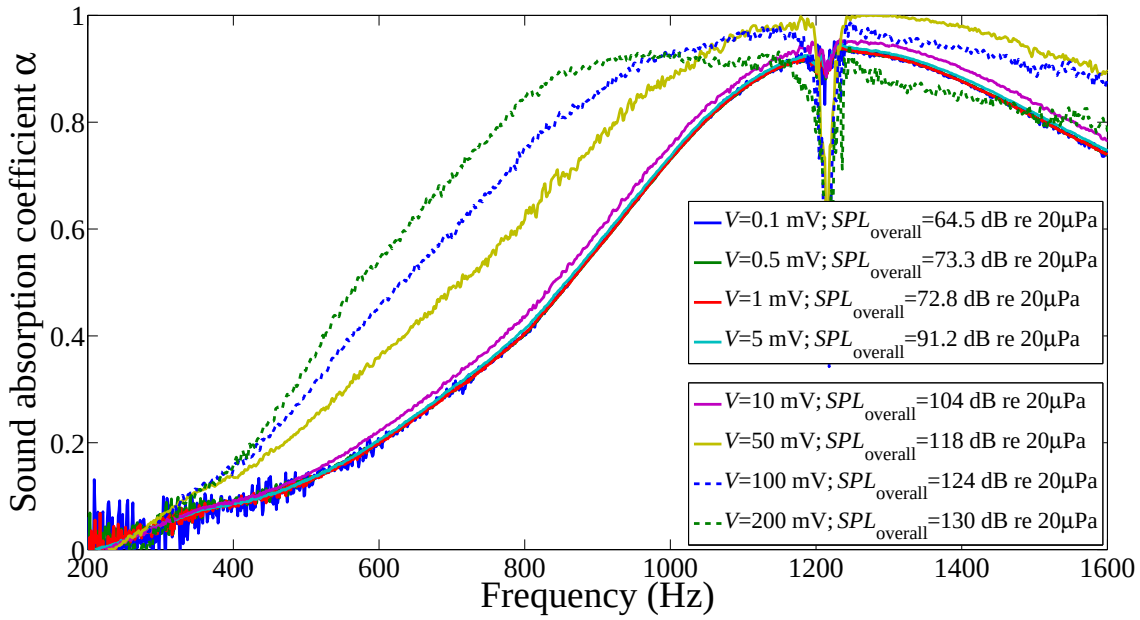

Figure 4.20: Measured sound absorption coefficients of the MPM with burst random excitation. The input voltage ranged from 0.1 mV to 200 mV. The corresponding SPL at the membrane surface is shown in Figure 4.19.

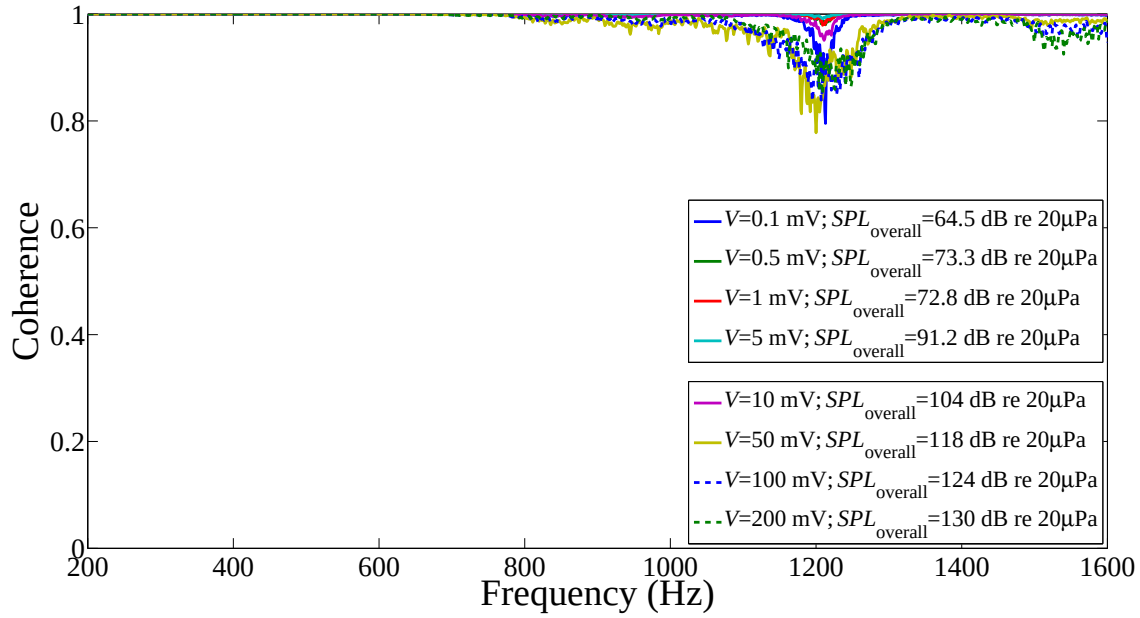

Figure 4.21: Measured coherences between two microphones with burst random excitation. The input voltage ranged from 0.1 mV to 200 mV.

unity. The sound absorption coefficient was estimated using these transfer functions and the estimated sound absorption coefficient was found to be identical to that measured using the transfer function between the two microphones. This shows that whilst the impedance is affected by the magnitude of the incident SPL, the relationship between the incident sound and

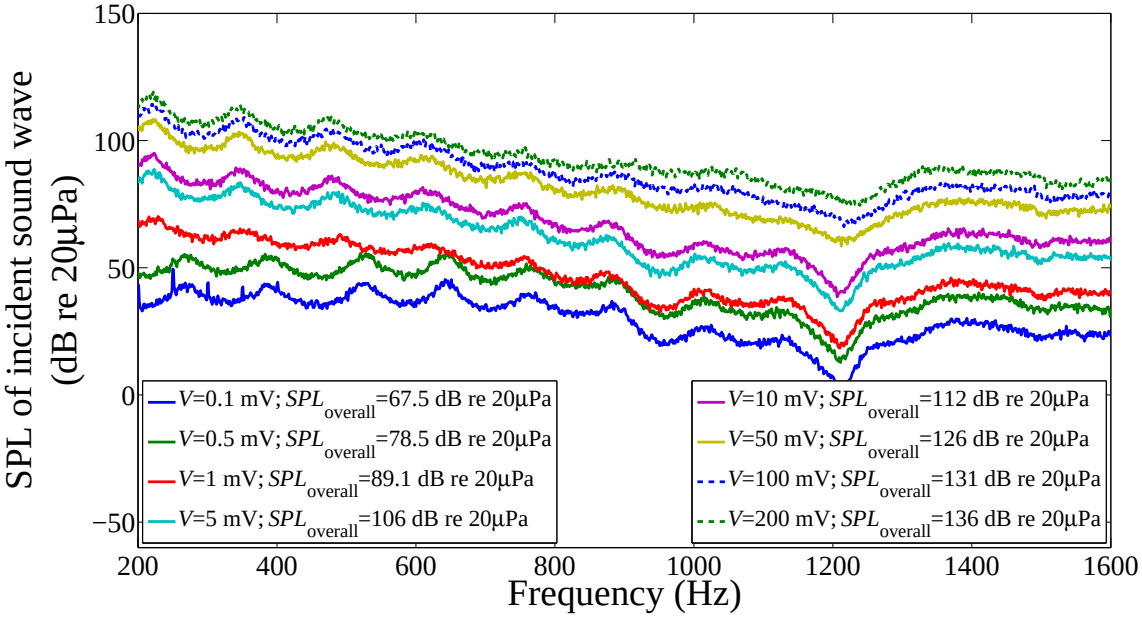

Figure 4.22: Estimated sound pressure level (SPL dB re 20 μPa) of the incident sound at the surface of the MPM with pink noise excitation. The input voltage ranges from 0.1 mV to 200 mV.

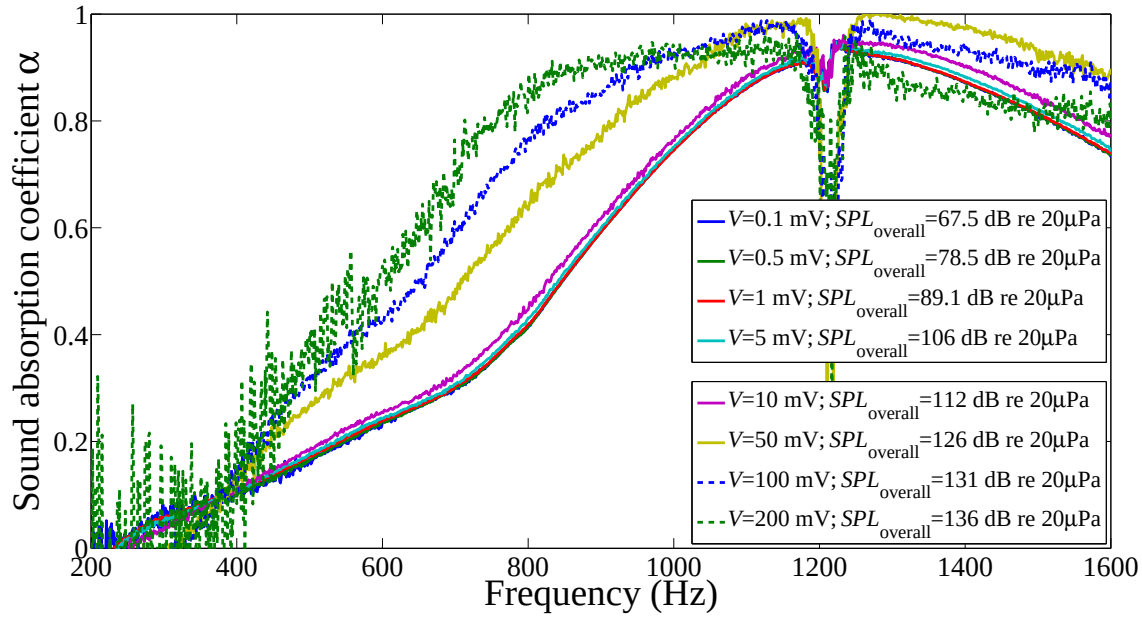

Figure 4.23: Measured sound absorption coefficients of the MPM with pink noise excitation. The input voltage ranged from 0.1 mV to 200 mV. The corresponding SPL at the membrane surface is shown in Figure 4.22.

reflected sound remains linear. It is therefore demonstrated that, when conducting measurements of sound absorption coefficients, the results will vary depending on the sound pressure level, despite keeping levels relatively ”low” and maintaining adequate coherence between

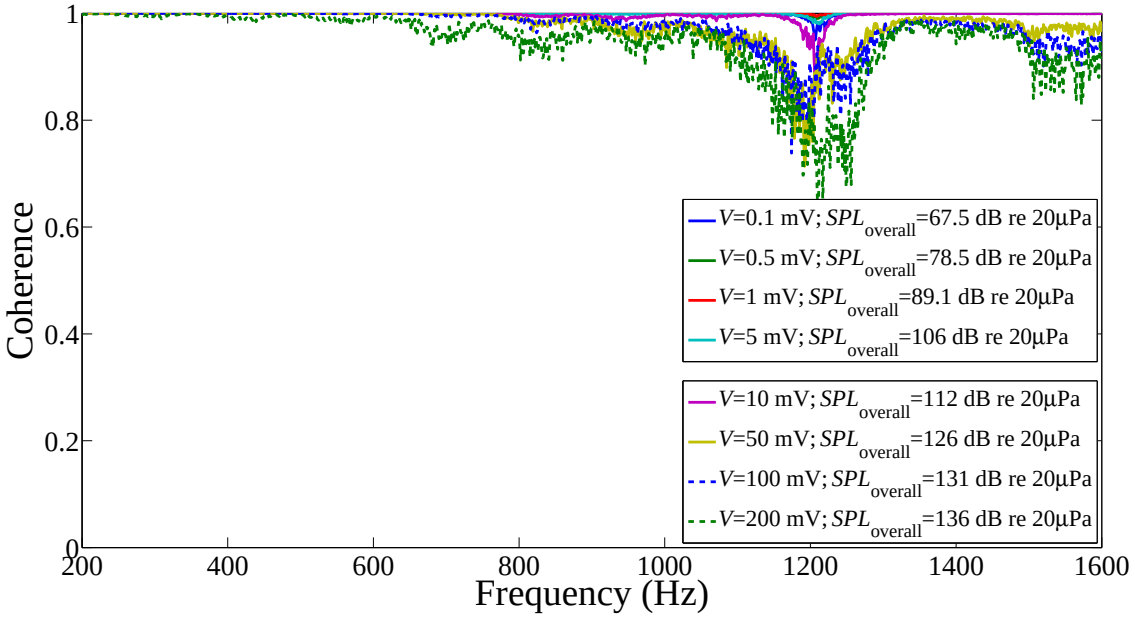

Figure 4.24: Measured coherences between two microphones with pink noise excitation. The input voltage ranged from 0.1 mV to 200 mV.

the source and microphones.

Besides white noise, other broadband sound source signals, including uniform random noise, pseudo random noise, burst random noise and pink noise, were used for the investigation of the MPM non-linearity. Figures 4.13 to 4.24 show the estimated incident SPL at the surface of the MPM, the measured sound absorption coefficients and the coherences between the two microphones, when the MPM was excited by other broadband sound source signals, respectively. Similar conclusions are obtained to those with white noise. Therefore, the conclusions on the non-linear properties of the MPM are valid not only for white noise with Gaussian distribution but also for many broadband sound source signals.

4.3.3 Sound absorption of MPMs excited by a monochromatic source

The sound absorption coefficient of the MPM was also investigated using monochromatic source signals. A stepped sine sweep was used, as well as a chirp with a sweep rate of 52 Hz/second.

This section investigates the sound absorption of the MPM absorber with a stepped sine sweep excitation with an input voltage varying from 0.1 mV to 200 mV. The results for the chirp were similar. When the input voltage is lower than 1 mV and the incident SPLs at individual frequencies do not exceed 101 dB re 20 μPa as shown in Figure 4.11, the

sound absorption properties of the MPM absorber are in a linear regime and the results are independent of the incident SPL as shown in Figure 4.25. There are noisy peaks on the sound absorption curve for an input voltage of 0.1 mV due to the low signal to noise ratio and thus the poor coherence between the two microphones. The dips around 1250 Hz arising from the structural resonance of the impedance tube are also observed for these curves.

In the non-linear regime, where the input voltage is equal to 5 mV and higher, the sound absorption coefficient of the MPM absorber increases with the increasing incident SPL. Note that for the stepped sine sweep excitation, the incident SPL at which the non-linearity starts to occur varies with frequency but is in the range of 80 dB re 20 μPa to 112 dB re 20 μPa (the frequencies around the tube resonance frequency were excluded), which is also significantly lower than that mentioned in previous studies.

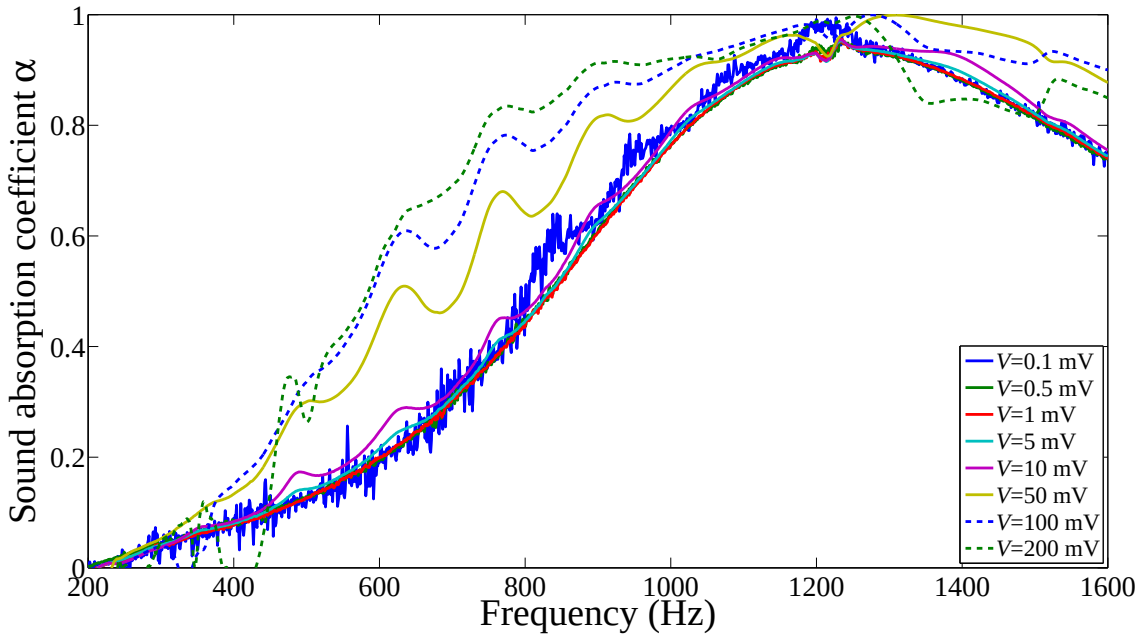

Figure 4.25: Measured sound absorption coefficients of the MPM with a stepped sine sweep excitation. The input voltage ranged from 0.1 mV to 200 mV. The corresponding SPL at the membrane surface is shown in Figure 4.11.

Unlike the smooth curves in the non-linear regime obtained with white noise excitation, the sound absorption coefficient of the MPM under a stepped sine sweep excitation oscillates with frequency, exhibiting small peaks at regular frequency intervals, such as 504 Hz, 633 Hz, 770 Hz and 914 Hz. Note that these small peaks are neither previously mentioned by other researchers nor observed in the curves with white noise excitation. Moreover, the sound absorption coefficients with pure tone signals were measured at these frequencies when the

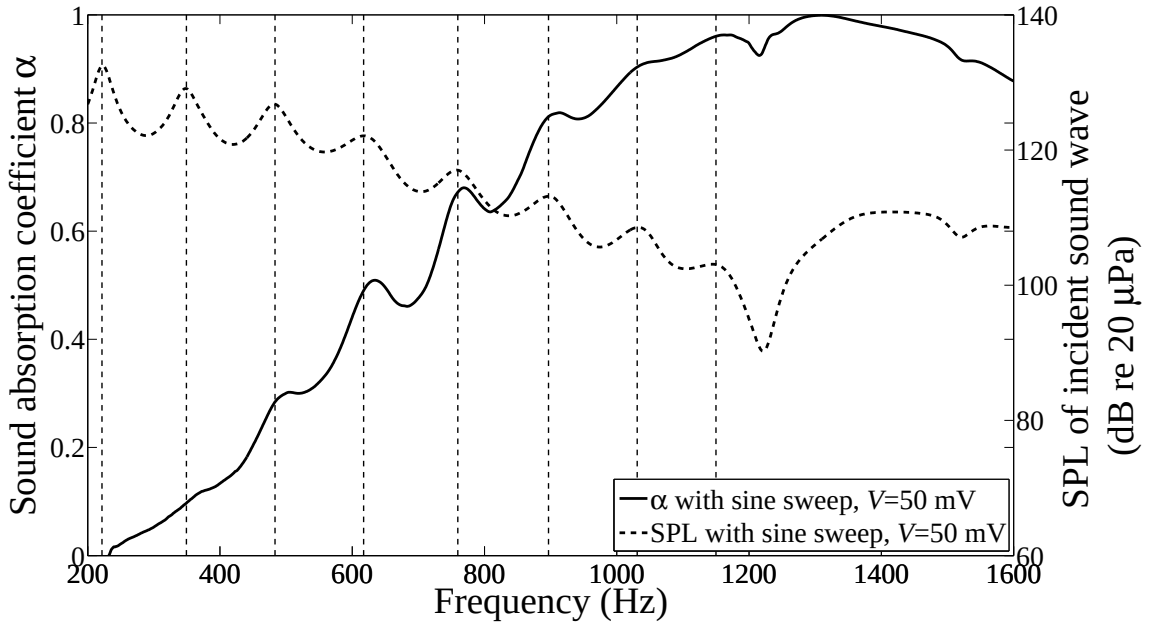

Figure 4.26: Measured sound absorption coefficients (solid line) of the MPM with a stepped sine sweep excitation versus the incident SPL (dashed line). The input voltage was 50 mV. The thin dashed lines show the frequencies of the local SPL maxima and the corresponding peaks on the sound absorption curve.

input voltage was 10 mV. The measured sound absorption coefficients with pure tones were similar to those with a stepped sine sweep excitation at these frequencies and the small peaks were also observed. Comparing the measured sound absorption coefficients in Figure 4.25 with the estimated SPLs in Figure 4.11, it is observed that these peaks in the measured sound absorption curves align with the SPL peaks due to the axial resonances in the impedance tube, as is demonstrated in Figure 4.26. The thin dashed lines show the frequencies where the SPLs peak. Although the frequencies of the small peaks in the sound absorption curve are slightly higher than those of the local peaks in the SPL curve, the correspondence between these frequencies is clear. This correspondence indicates the non-linear effect of the high incident SPL on the sound absorption of the MPM absorber and further indicates that the sound absorption coefficient is related to the incident SPL on the MPM surface. The physical reasons for these non-linear phenomena are discussed in Sections 4.3.4 and 4.3.5.

Alongside the stepped sine sweep, a chirp (with a sweep rate of 52 Hz/second) was used to investigate the non-linear sound absorption of the MPM. Figures 4.27 to 4.29 show the estimated incident SPL at the surface of the MPM, the measured sound absorption coefficients and the coherences between the two microphones when the MPM was excited by the chirp

noise. Similar conclusions are obtained to those with a stepped sine sweep. Figure 4.30 illustrates the correspondence between the measured sound absorption coefficient and the estimated incident SPL of the MPM excited by an input voltage of 50 mV, which is similar to that observed with a stepped sine sweep at the same input voltage. It is concluded that these non-linear properties of the MPM are valid for a broad range of monochromatic source signals.

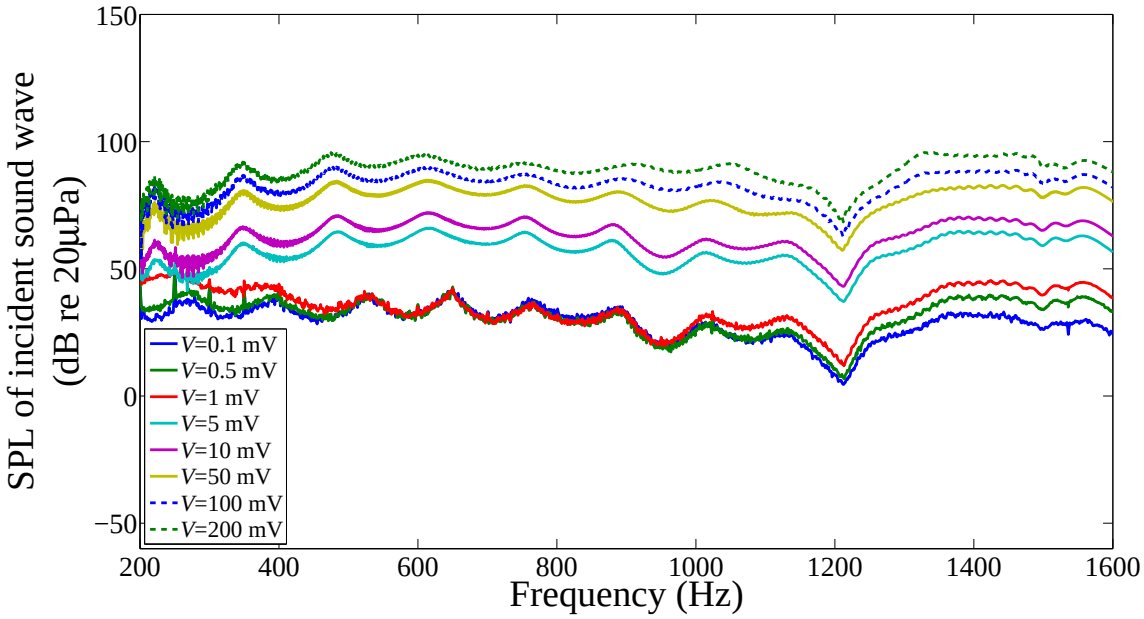

Figure 4.27: Estimated sound pressure level (SPL dB re 20 μPa) of the incident sound at the surface of the MPM with a chirp excitation. The input voltage ranges from 0.1 mV to 200 mV.

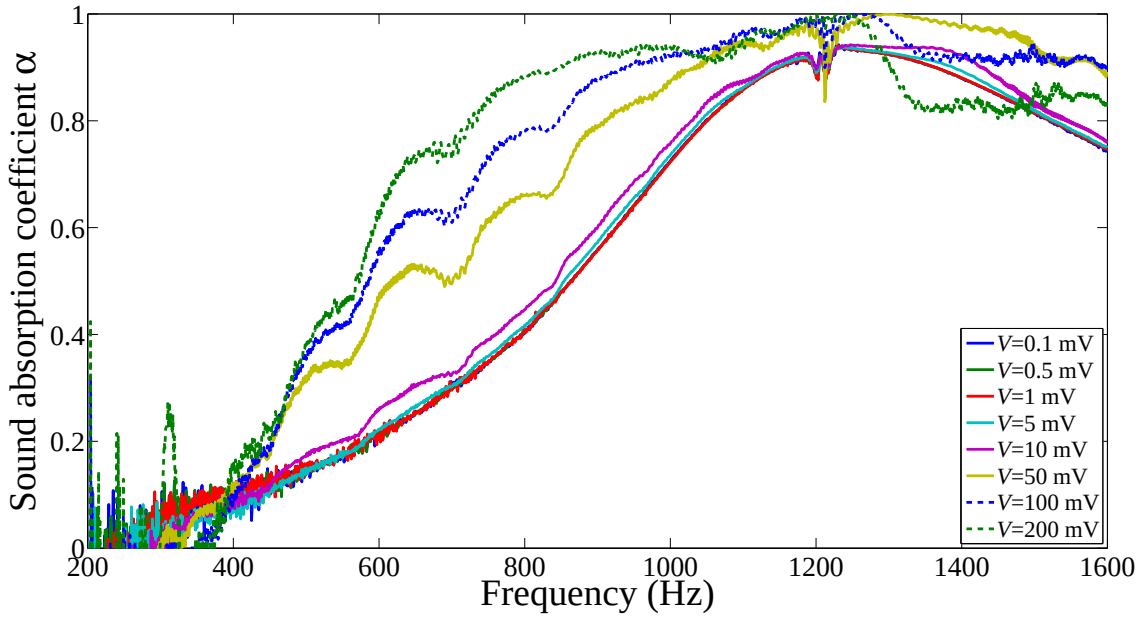

Figure 4.28: Measured sound absorption coefficients of the MPM with a chirp excitation. The input voltage ranged from 0.1 mV to 200 mV. The corresponding SPL at the membrane surface is shown in Figure 4.27.

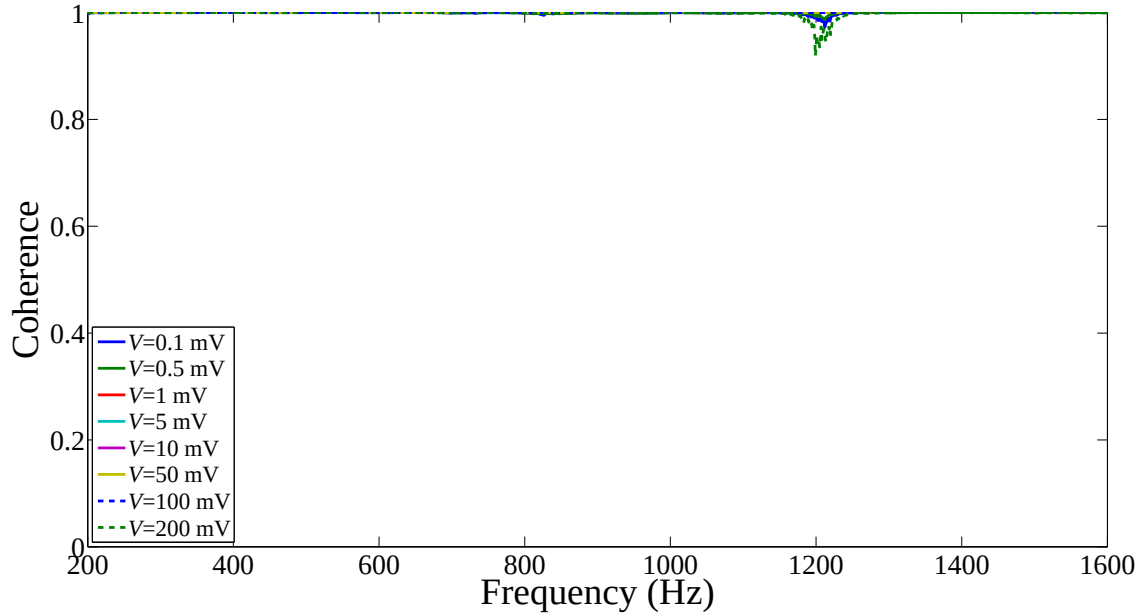

Figure 4.29: Measured coherences between two microphones with a chirp excitation. The input voltage ranged from 0.1 mV to 200 mV.

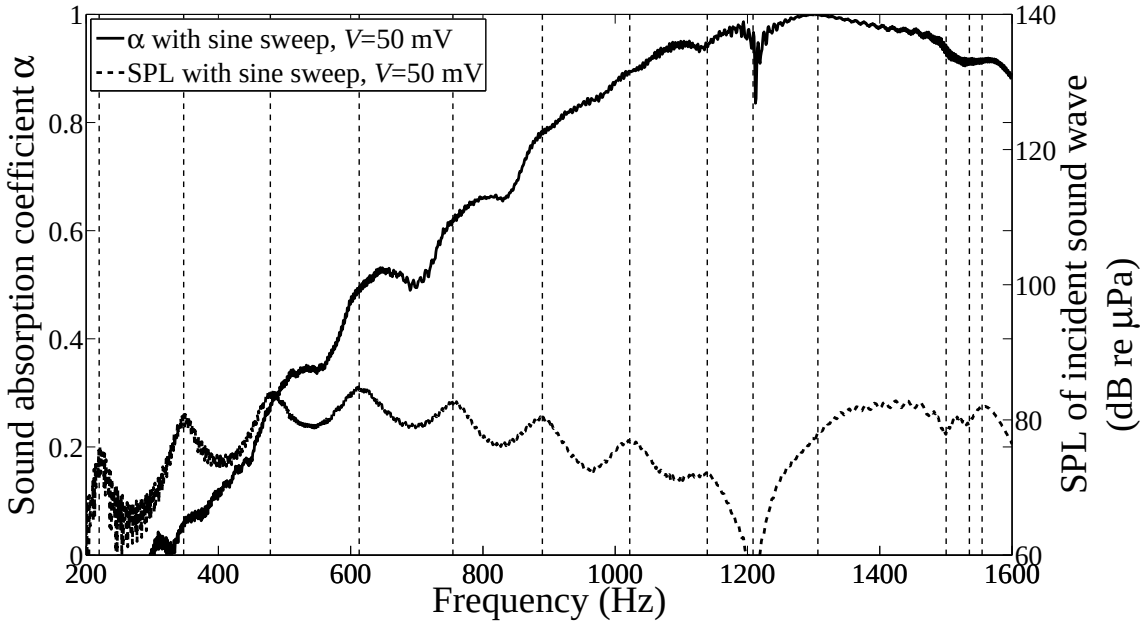

Figure 4.30: Measured sound absorption coefficients (solid line) of the MPM with a chirp excitation versus the incident SPL (dashed line). The input voltage was 50 mV. The thin dashed lines show the frequencies of the local SPL maxima and the corresponding peaks on the sound absorption curve.

4.3.4 Reynolds number and the non-linear sound absorption of MPMs

The acoustic non-linearity of an orifice or micro perforates is ascribed to the flow dynamics within and behind the orifice or the micro perforates (Ingard & Ising 1967, Tayong et al. 2011). Ingard & Ising (1967) indicated that with high SPL excitation, the incoming irrotational flow becomes rotational and hence forms a vortex and the flow separates behind the orifice. Therefore, the commonly accepted indicator Reynolds number is utilised in this section to study the flow properties.

The Reynolds number, *Re* in a pipe is defined as (Wang 1981)

$$Re = \frac{2 r_0 v}{\sigma}, \tag{4.4}$$

where σ is the dynamic viscosity, and v denotes the particle velocity in the perforations of the MPM. The particle velocity v in the perforations is unable to be measured directly because of the limited size of the perforations. However, it can be calculated based on the volume velocity continuity on the surface of the MPM. Using the two microphone transfer function method, the acoustic velocity on the surface of the MPM is given by (Tayong et al. 2010) as

$$v_{\text{surface}} = j \frac{p_1}{\rho_0 c_0} \frac{H \cos(k_0 l_1) - \cos(k_0 l_2)}{\sin(k_0 s)}, \tag{4.5}$$

where p_1 denotes the measured sound pressure on microphone 1, H denotes the measured transfer function between two microphones, k_0 denotes the wavenumber in air which is expressed as $k_0 = \frac{\omega}{c_0} = \frac{2\pi f}{c_0}$. As shown in Figure 4.1, in this study $l_1 = 56$ mm, $s = 24$ mm and hence $l_2 = l_1 - s = 32$ mm. Consequently, the particle velocity in the perforations is obtained as

$$v = \frac{v_{\text{surface}}}{\delta}. \tag{4.6}$$

Figure 4.31 shows the measured Reynolds numbers of the particle velocity in the MPM perforations with a stepped sine sweep and white noise when the input voltage increased from 100 μV to 0.2 V. All the curves of the Reynolds numbers follow the same patten due to the acoustic characteristics of the impedance tube, i.e. the oscillatory sound pressure in the axial behaviour of the acoustic field and the structural vibration of the impedance tube around 1250 Hz. However, the values of the Reynolds numbers differ and are proportional to the incident sound pressure and hence the particle velocity in the perforations based on Equations (4.6) and (4.4).

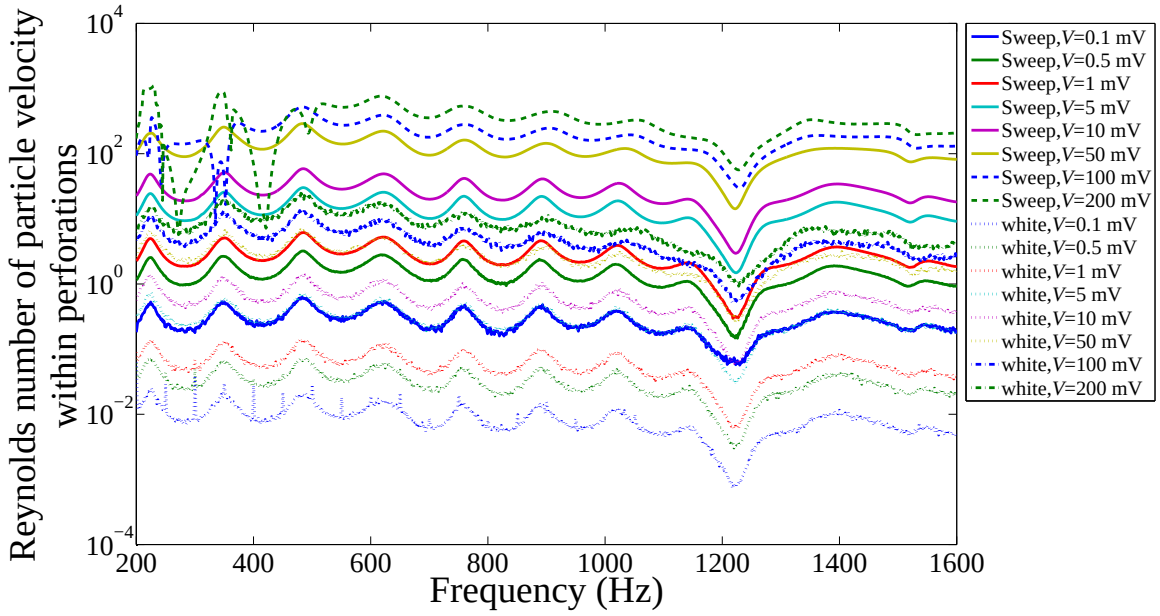

Figure 4.31: Measured Reynolds numbers of the particle velocity in the MPM perforations with a sine sweep and white noise. The input voltage varied from 0.1 mV to 200 mV.

4.3.5 Effects of the type of sound excitation on the sound absorption of MPMs

In Sections 4.3.2 and 4.3.3, the effect of the incident SPL on the sound absorption of the MPM has been studied with broadband noise and monochromatic noise excitation. It is found that when the incident SPL is lower than the threshold SPL, the sound absorption coefficient is independent of the incident SPL, demonstrating the linear phenomenon of the sound absorption of MPMs under low SPL excitation. The sound absorption coefficient of the MPM increases with the increase of the incident SPL, when the incident SPL is higher than the threshold SPL, which implies a non-linearity of the sound absorption of MPMs under high SPL excitation. These main trends are valid for both the white noise and stepped sine sweep signals. Furthermore, they are valid for both broadband noise and monochromatic source signals, although the threshold SPL is different with different sound source signals.

There are small peaks at some specific frequencies observed in the sound absorption coefficient curves of the MPM when excited by a stepped sine sweep; however, these peaks are not observed when the MPM is excited by white noise. Moreover, it is found in Section 4.3.3 that these small peaks are associated with the peaks of the SPL, which are ascribed to resonances in the axial direction. Therefore, it is clear that the sound absorption of the MPM

is affected by the type of sound source signal. This section aims to investigate the effect of different sound source signals on the sound absorption of the MPM, for both linear and non-linear regimes.

4.3.5.1 Effect of the type of sound sources on the sound absorption of MPM in a linear regime

This section compares the sound absorption coefficients of the MPM excited by a sine sweep and white noise in the linear regime. Since the sound absorption of the MPM in the linear regime is dependent only on the perforations and the MPM vibration, the measured sound absorption coefficients in the linear regime should be consistent, irrespective of the sound source signal by which they are excited.

Figure 4.32 shows the measured sound absorption coefficients of the MPM excited by a sine sweep and white noise, with the same input voltage of 5 mV. This input voltage is relatively small and the sound absorptions of the MPM excited by both a sine sweep and white noise are in the linear regime. Therefore, based on the presumption mentioned in this section, the measured sound absorption curves in Figure 4.32 should be identical. However, it is found that the sound absorption coefficient with white noise is slightly higher than that with a sine sweep in the frequency range from 250 Hz to 580 Hz, while the former is slightly lower than the latter, ranging between 620 Hz and 1300 Hz. The observed differences between the sound absorption coefficients of the MPM excited by a sine sweep and white noise are considered insignificant within experimental error.

Similar small differences have been observed by Chung & Blaser (1980*b*) when measuring the sound absorption coefficient of foams. They measured the sound absorption coefficients of five samples which were cut from the same foam and found that the sound absorption coefficients slightly differed. They ascribed these differences to the non-uniformities of the foam sample and the effects of cutting and mounting conditions. However, since the MPM sample used here with white noise and a sine sweep is the same one, the differences observed in Figure 4.32 are possibly due to the mounting conditions. As described in Chapter 2, the mounting condition of the circular membrane could affect the tension T and internal damping η, and hence affect the sound absorption coefficient of the membrane. These differences are sufficiently small that they could be neglected and the sound absorption coefficients obtained using either the sine sweep or white noise sound source signals can

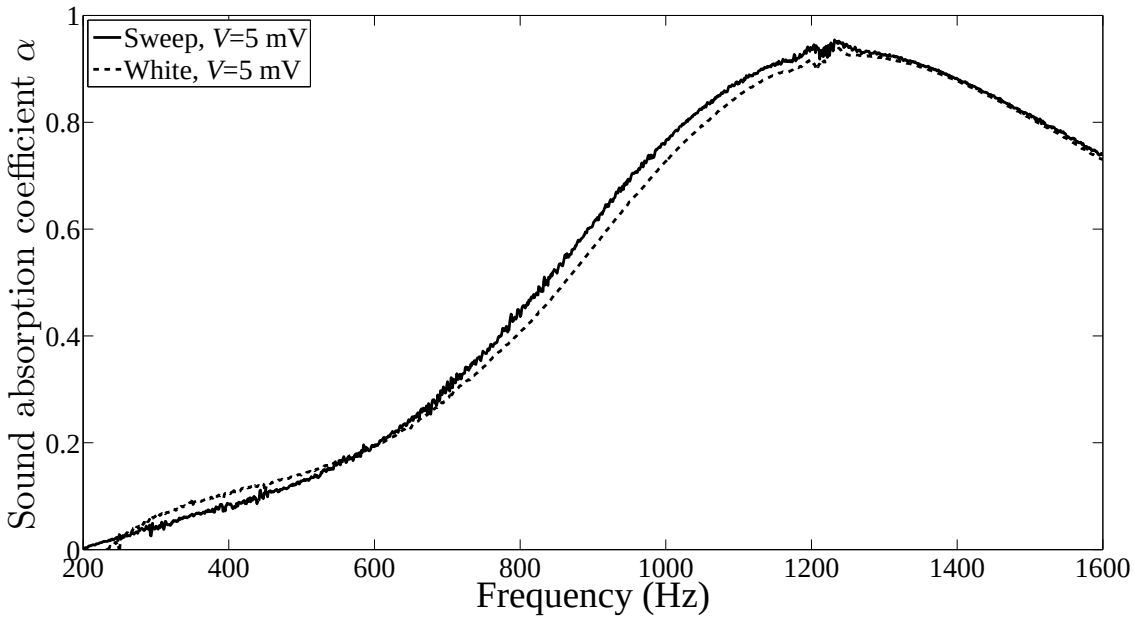

Figure 4.32: Measured sound absorption coefficients of the MPM excited by a sine sweep and white noise with input voltage of 5 mV in linear regime.

be considered identical in this linear excitation regime in which the sound absorption of the MPM is independent of the incident SPL and the type of sound source signal.

4.3.5.2 Effect of the type of sound sources on the sound absorption of MPM in a non-linear regime

As described in Sections 4.3.2 and 4.3.3, the sound absorption coefficients of the MPM increase with the increase of the incident SPL in the non-linear regime. This main trend is valid for both types of sound source signals investigated: the white noise and the sine sweep. However, there are small peaks at some specific frequencies in the sound absorption coefficient curve for the MPM excited by a sine sweep. These small peaks disappear when the MPM is excited by white noise. Moreover, it is found in Section 4.3.3 that these small peaks match the peaks of the SPL, which are ascribed to the acoustic resonances in the axial direction of the impedance tube. Therefore, it is obvious that the sound absorption of the MPM is affected by the type of the sound source signal in the non-linear regime. Consequently, it is important to understand the reason why the incident oscillatory SPL has a more significant effect on the sound absorption of the MPM excited by a sine sweep than that with white noise.

This section investigates the effect of different sound source signals on the sound absorp-

tion coefficient of the MPM sample in the non-linear regime. The possible reasons for the occurrence of the small peaks in the measured sound absorption coefficient curves excited by a stepped sine sweep with input voltage above the threshold SPL are explored in this section. The occurrence of the small peaks may be ascribed to the membrane resonance, the increased depth of the air cavity under high SPL excitation and the time-dependent flow which leads to the non-linearity of the sound absorption of an orifice and micro perforates (Ingard & Ising 1967, Tayong et al. 2010). These possible reasons are discussed in Sections 4.3.5.2.1, 4.3.5.2.2 and 4.3.5.2.3, respectively.

4.3.5.2.1 Panel/membrane resonance

As mentioned in Chapter 3, it has commonly been observed by researchers that when thin MPPs and MPMs are used as sound absorbing materials, the resonance of the material, i.e. the thin panel or membrane, can affect the sound absorption coefficient significantly. Bravo et al. (2012) indicated that the resonance of the thin panel leads to additional resonance peaks on the measured sound absorption curves of thin MPPs and these peaks closely correspond to the mechanical resonance frequencies of the panel. Therefore, since the MPM used in this section can vibrate more significantly than MPPs, it is presumed that these small absorbing peaks observed in Figure 4.25 are possibly due to the mechanical resonances of the membrane.

To verify this presumption, sound absorption measurements of an MPP sample were conducted in the same impedance tube under the same condition as mentioned in Section 4.3.1. The structural parameters of the MPP sample are shown in Table 4.2. The air cavity depth is also 25 mm.

Table 4.2: Measured MPP parameters

Samples	Surface density ρ_p (kg/m^2)	Hole radius r_0 (mm)	Thickness h (mm)	Perforation ratio δ (%)
MPP	2.9430	0.3502	3	2.8

The measured sound absorption curves of the MPP excited by white noise and a sine sweep are shown in Figures 4.33 and 4.34, respectively. Although the non-linear effect of the incident SPL is not as significant as in the case of the MPM, similar main trends are observed in the case of the MPP. When the MPP is excited by white noise, the sound absorption coefficient of the MPP increases with the increase of the incident SPL if the incident SPL is higher than the threshold SPL. Otherwise, the sound absorption coefficient

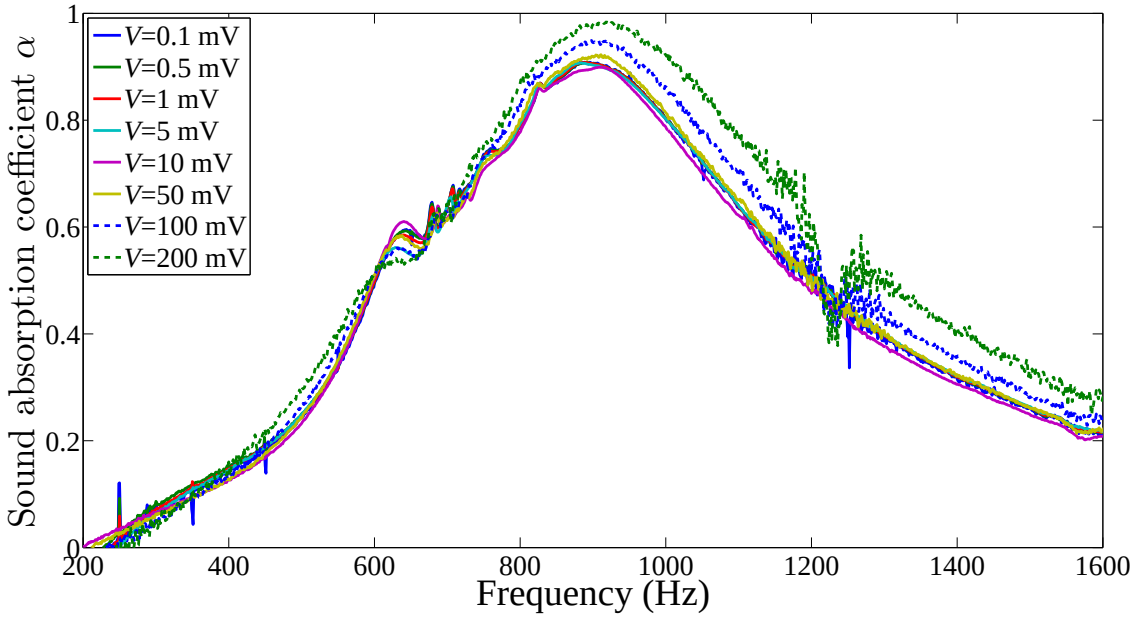

Figure 4.33: Measured sound absorption coefficients of the MPP sample with white noise excitation. The input voltage varied from 0.1 mV to 200 mV.

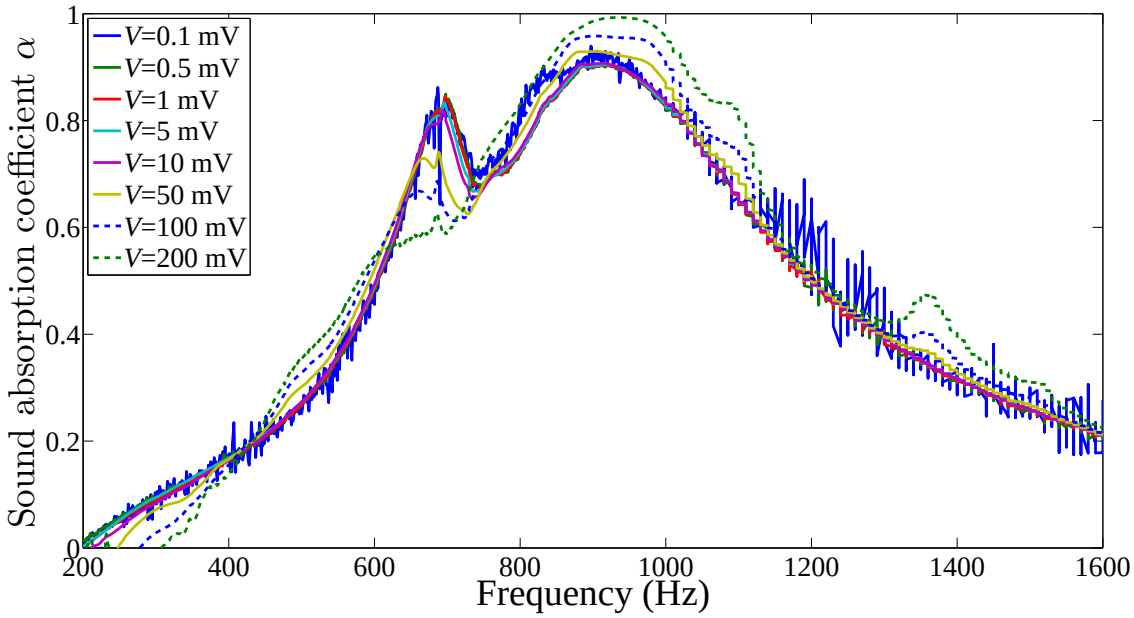

Figure 4.34: Measured sound absorption coefficients of the MPP sample with a sine sweep excitation. The input voltage varied from 0.1 mV to 200 mV.

is unrelated to the incident SPL.

Unlike the case of the MPM excited by white noise in a non-linear regime, the sound absorption curves of the MPP excited by white noise with an input voltage of 100 mV and 200 mV have maximum values around the same frequency of 908 Hz. However, as shown in Figure 4.12, the maximum sound absorption peak of the MPM excited by white noise with

an input voltage of 100 mV and 200 mV reduces in frequency. Since the maximum sound absorption peak of an MPP or MPM absorber is dependent on its resistance, this difference implies that the high SPL excitation affects only the resistance of the MPP, however it has significant influence on not only the resistance but also the reactance of the MPM.

Moreover, the theoretical resonance frequency of a circular thin panel is given by Kinsler et al. (1999)

$$f_1 = 0.47 \frac{h}{R_0} \sqrt{\frac{E}{\rho_p (1-\nu^2)}}, \tag{4.7}$$

$$f_2 = 3.88 \times f_1, \tag{4.8}$$

$$f_3 = 8.70 \times f_1, \tag{4.9}$$

where E denotes the Young's modulus which is 3.2 GPa for the MPP material investigated, and ν is the Poisson's ratio which is 0.3. The first three panel resonance frequencies are shown in Table 4.3. It is observed that the second and third resonance frequencies are beyond the measurement range of the impedance tube. Hence there is only one structural resonance peak in Figure 4.33.

Table 4.3: First three panel resonance frequencies of the MPP sample

Material	f_1 (Hz)	f_2 (Hz)	f_3 (Hz)
MPP	642	2440	5585

When the MPP is excited by a sine sweep, similar linear and non-linear sound absorption properties are observed, as shown in Figure 4.34. The maximum sound absorption peaks of all the curves in Figure 4.34 are roughly consistent at 908 Hz. The consistence of these maximum sound absorption peaks confirms the conclusion obtained from Figure 4.33 that only the resistance of MPPs is affected by the high SPL incidence, however, both the resistance and reactance of MPMs are affected by the incident SPLs.

When the MPP was excited by a sine sweep with incident SPLs higher than the threshold SPL, small peaks appeared in the sound absorption coefficient curves at 492 Hz, 1090 Hz and 1360 Hz, which are not observed in Figure 4.33. The occurrence in Figure 4.34 and disappearance in Figure 4.33 of the small peaks is very similar to the case of the MPM.

It is observed from Figure 4.33 that the panel resonance frequency is 640 Hz. Although the sound absorption at this resonance frequency increased with the increase of the incident SPL with a stepped sine sweep, this frequency mismatched the frequencies where the small

peaks observed in Figure 4.34. There is only one panel resonance peak observed in Figure 4.33, however, there are several small peaks in absorption observed in Figure 4.34. Hence, it is concluded that these peaks in absorption are unrelated to the panel resonance. Therefore, the presumption that these small absorbing peaks have arisen from the panel/membrane resonance is proved to be invalid.

4.3.5.2.2 Increased depth of air cavity

Since the MPM is lightweight and flexible, it is reasonable to deduce that the MPM could be curved when excited by sound waves. The curvature under sound excitation affects the depth of the air cavity between the MPM and the rigid termination of the impedance tube. This changed air cavity depth could be a reason for the occurrence of the small peaks observed in Figure 4.25.

To verify this presumption, the distance between the MPM sample and a rigid transparent termination of the impedance tube was measured using a laser sensor whilst the source was driven with a white noise and sinusoidal wave excitation. The measurement set-up is shown in Figure 4.35. The impedance tube is identical with that mentioned in Section 4.2.1, however, to measure the distance, a transparent termination made of plastic was utilised instead of the rigid end. A laser sensor, with a measurement error of ± 0.02 mm, was directly connected to the transparent end. Consequently, the laser signal was able to transmit through the transparent wall of a thickness of 7 mm and the distance between the MPM and the transparent wall was measured. Note that the air cavity depth was increased from 25 mm to 67.43 ± 0.02 mm.

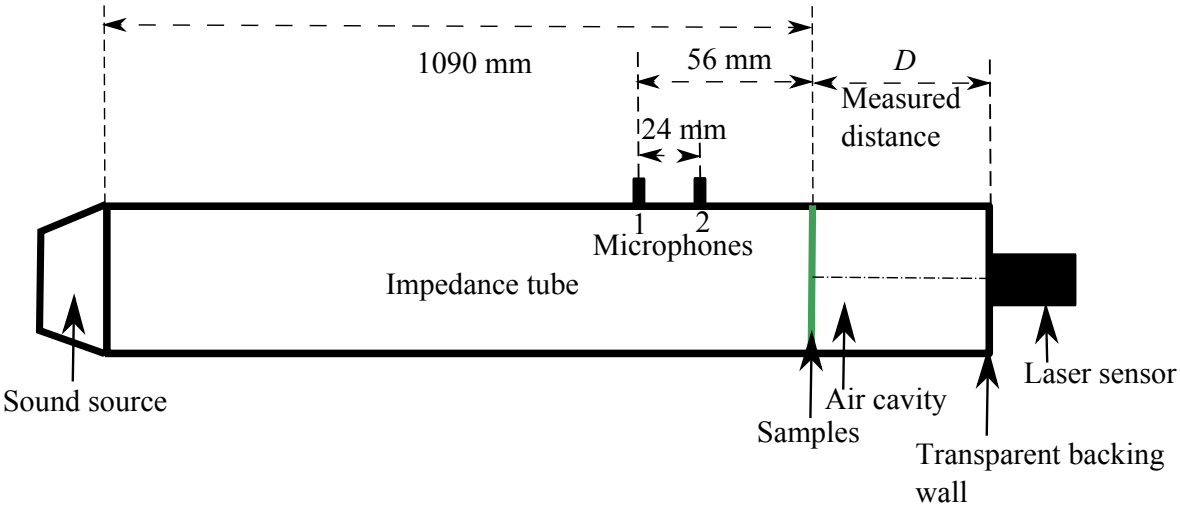

Figure 4.35: Measurement of the distance between the MPM sample and a rigid transparent termination of the impedance tube.

Since two types of sound source signals are of interest in this thesis, both white noise and sinusoidal waves were used to excite the MPM when the distance was measured. The input voltages of white noise were 100 mV and 200 mV. Sinusoidal waves at specific frequencies were utilised to represent the frequency response of the sine sweep sound source. The input voltages of the sinusoidal waves corresponded to the maximum used in Section 4.3.1.2, namely 200 mV. Additionally, the distance from the MPM sample to the transparent end was also measured without the sound excitation as a control group.

Table 4.4: Measured distance from the MPM sample to the transparent end

Excitation	Measured distance from the MPM sample to the transparent end (mm)
No excitation (Control group)	67.43 ± 0.02
White noise at 100 mV	67.45 ± 0.02
White noise at 200 mV	67.62 ± 0.02

The measured distance with white noise excitation is shown in Table 4.4. The distance with white noise at 200 mV is 0.19 ± 0.02 mm higher than the measured distance without sound excitation. When the input voltage is 100 mV, the difference between the measured distance and the control group is less than the measurement error of the laser sensor. Hence, the distance measured at 100 mV is considered identical to the control group. Therefore, it is concluded that white noise can increase the cavity depth only when the input voltage is at the maximum level investigated in this study, otherwise, the cavity depth is independent of the level of the white noise. Comparing this conclusion with the findings obtained from Figure 4.12, it is deduced that the increased cavity depth due to white noise excitation is unrelated to the increase of the sound absorption coefficient of the MPM.

To evaluate the effect of a sine sweep on the measured distance between the MPM sample and the transparent end, two measurements were conducted. In the first measurement, the MPM was excited with sinusoidal waves at the frequencies where these small sound absorbing peaks occur in Figure 4.25 with the maximum input voltage considered in this study. The distance between the MPM and the transparent wall was measured at these frequencies to illustrate the relationship between these small peaks in the sound absorption curves and the increased distance under high SPL excitation. The distances when the MPM was excited by sinusoidal waves at the frequencies in the vicinity of the valleys in the sound absorption curves were also measured for comparison. The measured frequencies are indicated in Table 4.5. The first measurement results are shown in Figure 4.36, and compared with the sound

absorption coefficient curves with a sine sweep excitation.

Table 4.5: Frequencies used for the distance measurement where the peaks and valleys in the sound absorption curves occur in Figure 4.25 with the maximum input voltage of 200 mV.

Frequency number	Frequencies with absorption peaks (Hz)	Frequencies with absorption valleys (Hz)
1	504	517
2	633	683
3	770	809
4	914	N/A

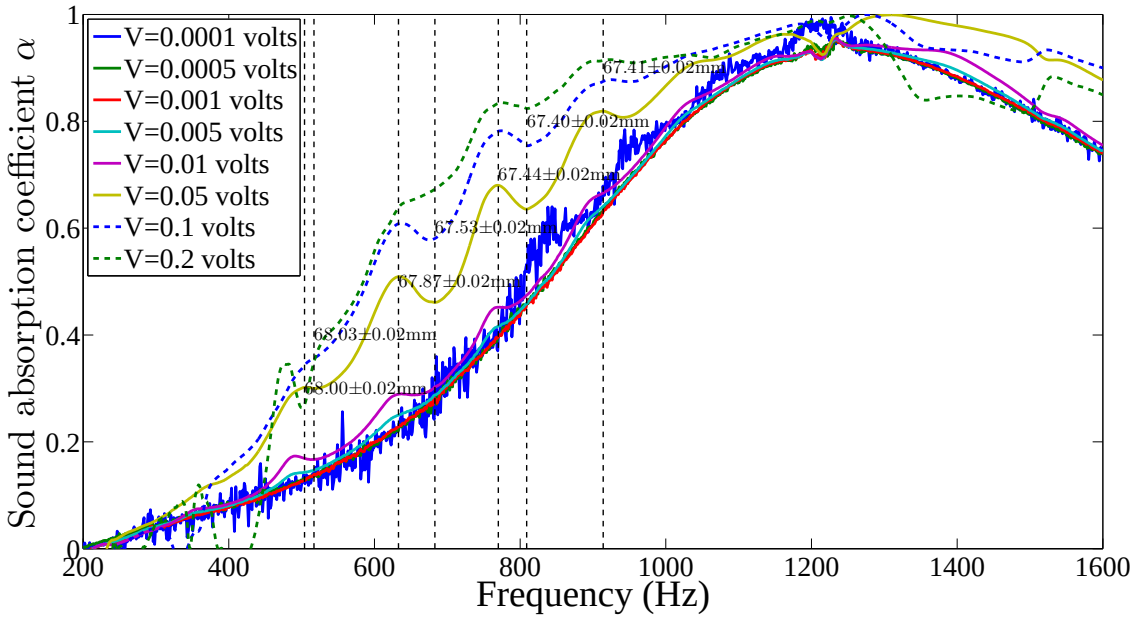

Figure 4.36: Measured cavity depth at frequencies given by Table 4.5 compared with the sound absorption coefficients of the MPM excited by a stepped sine sweep with input voltage ranging from 0.1 mV to 200 mV. Indicated cavity depths are for 200 mV input voltage.

It is found in Figure 4.36 that although the cavity depth differed from the no-excitation depth of 67.43 mm due to the high SPL excitation at a number of the frequencies given in Table 4.5, the change in the cavity depth did not correspond for all of the peaks and valleys in the sound absorption curves in Figure 4.25. Moreover, the depth increased more significantly at frequencies from 504 Hz to 683 Hz. By contrast, at the frequencies from 770 Hz to 914 Hz, the cavity depths are roughly identical to those without sound excitation. This implies that the incident SPL has a more significant effect on the MPM in the lower range of frequency investigated here than in a middle or high frequency range.

Figure 4.36 illustrates that high SPL can increase the cavity depth at the specific frequencies shown in Table 4.5. The relationship between the frequency and the cavity depth over the measured frequency range is unclear. Hence, a second measurement was conducted to clarify the change of the cavity depth over a broad frequency range. The experimental arrangement was identical with that used in the first measurement, except that the frequencies were the discrete frequencies from 250 Hz to 1600 Hz with an index of 50 Hz. The measured cavity depth is shown in Figure 4.37, with error bars which illustrate the measurement error of the laser sensor.

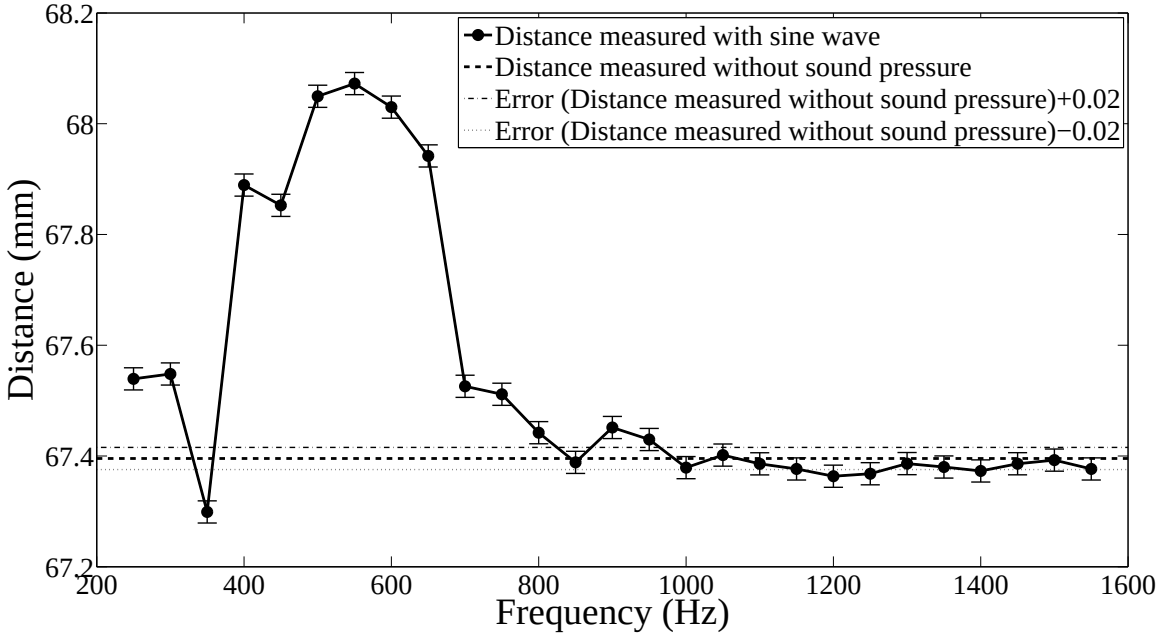

Figure 4.37: Measured cavity depth at the discrete frequencies from 250 Hz to 1600 Hz with an index of 50 Hz when the MPM was excited by a sine sweep with input voltage of 200 mV.

Figure 4.37 indicates that high sound excitation increases the cavity depth of the MPM absorber in the frequency range below 800 Hz. The cavity depth is identical to that measured without sound excitation in the frequency range above 800 Hz. This finding conforms to the conclusion obtained in the first measurement that the cavity depth increases significantly at frequencies from 504 Hz to 683 Hz; however, the cavity depths are roughly identical to that without sound excitation at frequencies from 770 Hz to 914 Hz.

Figures 4.36 and 4.37 illustrate that although the cavity depth can be increased with high SPL excitation in the low frequency range, the increased cavity depths do not correspond solely to the small sound absorbing peaks observed in Figure 4.25. This implies that the

increased cavity depth is unrelated to the small sound absorbing peaks of the MPM excited by a sine sweep in the non-linear regime. Considering the data obtained in the cavity depth measurement with white noise (shown in Table 4.4), it is further deduced that high SPL excitation, no matter what type the sound source signal is, can increase the cavity depth of the MPM, especially in the low frequency range. However, this increased cavity depth is unrelated to the increase of the sound absorption coefficient of the MPM in the non-linear regime.

4.3.5.2.3 Time-dependent flow

Previous research (Bodén 2007, Ingard & Ising 1967, Tayong et al. 2010) indicated that when excited by high SPLs, the non-linear acoustic impedance of micro perforated panels and orifices in a rigid baffle is dependent on the resulting fluid dynamics. Ingard & Ising (1967) showed that the non-linearity of the sound absorption of an orifice in a rigid baffle is due to the rotational flow and resulting vortex on the opposite side of the orifice. On the upstream side of the orifice, the air flow is irrotational. When the air flow travels through the orifice it becomes rotational and forms vortices, which increase in magnitude with an increase in incident SPL. They further indicated that the real part of the acoustic impedance, namely the resistance, is proportional to the amplitude of the air particle velocity within the orifice. The rotational flow and resulting vortex on the rear of the baffle are time dependent and based on Bernoulli's law.

This time-dependent flow offers an explanation for the occurrence of these small peaks in the sound absorption curves of the MPM excited by a stepped sine sweep in Figures 4.25 and 4.26. Bodén (2007) investigated the non-linear impedance of perforates under high SPL excitation and indicated that pure tone excitation leads to a non-linear impedance dependent on the acoustic particle velocity at the frequency of the pure tone, however, broadband excitation leads to a non-linear impedance at a certain frequency dependent on the acoustic particle velocities at other frequencies. In other words, the acoustic impedance of perforated panels is decoupled in the frequency domain when a monochromatic source signal, such as a pure tone, is used. However, when perforated panels are excited by a broadband excitation, such as white noise, their impedance at a particular frequency is dependent on multiple frequency components because of the time dependence of the flow and associated vortices.

Hence, in the case of the MPM excited by a stepped sine sweep, the non-linear impedance

of the MPM is dependent on the particle velocity arising from the high SPL at the excitation frequency. Only this particular frequency component contributes to the sound absorption and other frequency components are decoupled. By contrast, when white noise is used, the non-linear impedance of the MPM is related to the particle velocities over a broadband frequency range. The flows arising from each of the frequency components couple with each other and all the frequency components of the broadband white noise contribute to the overall impedance. Consequently, the sound absorption curves of the MPM with white noise are smoother than those with the stepped sine sweep due to the coupling of the frequency components. Therefore, the small peaks in the sound absorption curves are observed only for monochromatic source signals, such as the stepped sine sweep and chirp noise, and match the peaks of the incident SPLs (as shown in Figures 4.25 and 4.26). With broadband excitation, the sound absorption curves are smooth due to the frequency coupling over a broadband frequency range, as shown in Figure 4.10.

Since the non-linear sound absorption of the MPM is dependent on the incident SPL, the sound absorption coefficients at similar SPLs were compared to further investigate the effect of excitation type. It is found in Figures 4.10 and 4.11 that the SPL curve with white noise at 50 mV is very close to that with a stepped sine sweep at 1 mV. Figure 4.38 compares the measured sound absorption coefficients of the MPM with a stepped sine sweep and white noise at the two voltages and the corresponding SPLs over the measured frequency range.

In Figure 4.38, the solid curve is the measured sound absorption coefficient of the MPM excited by a stepped sine sweep at 1 mV and the dashed curve represents that excited by white noise at 50 mV. It is observed that the measured sound absorption coefficient with white noise is higher than that with a stepped sine sweep over a large frequency range, except at frequencies around the tube resonance frequency of 1250 Hz. Comparison of Figures 4.10 and 4.11 shows that the corresponding incident SPLs are roughly equal, implying that the increase in sound absorption with white noise excitation is not associated with the magnitude of the incident SPL.

As mentioned previously, Ingard & Ising (1967) verified that the non-linearity of the sound absorption of an orifice is due to the rotational flow and resulting vortex on the rear of the perforations, which are time dependent. Hence, it is deduced that the dynamics of the air flows excited by a stepped sine sweep and white noise differ in the time domain.

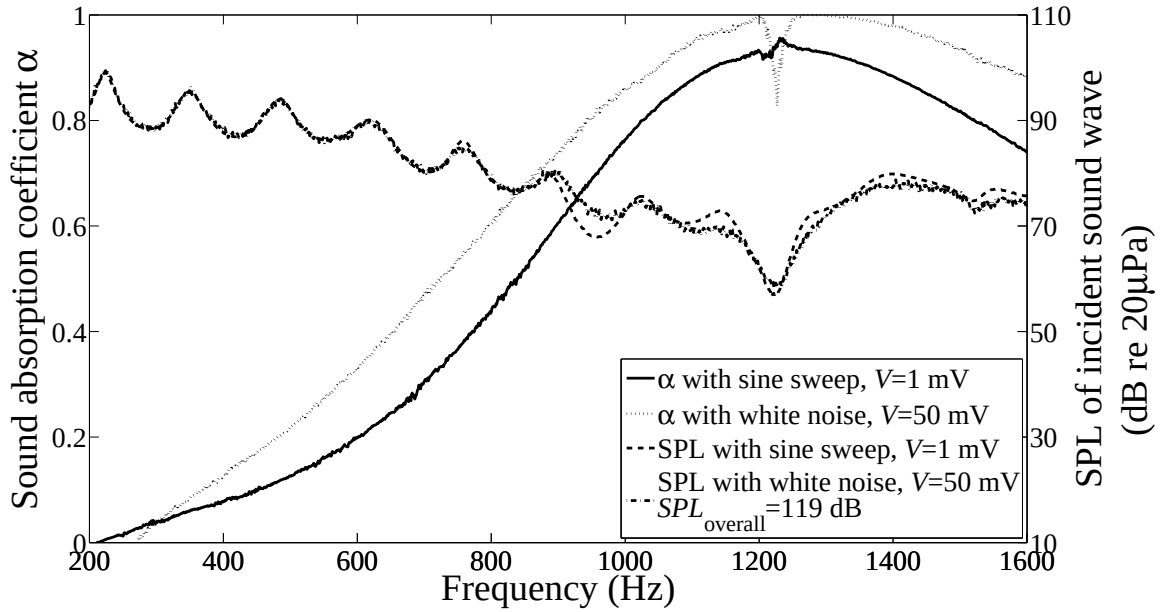

Figure 4.38: Measured sound absorption coefficients of the MPM excited by a stepped sine sweep with input voltage of 1 mV (solid line) and white noise with input voltage of 50 mV (dotted line), and correspondingly measured SPLs (dashed line for a stepped sine sweep and dashed-dotted line for white noise).

As described in Section 4.3.1.2, the stepped sine sweep excitation scans the measured frequency range over a period of 10 minutes and excites a specific frequency at each time step. Consequently, the air flow generated by the stepped sine sweep at each time step concentrates the sound energy at the scanning frequency and gives rise to rotational flow and vortices which are only related to the scanning frequency. Therefore, the fluid dynamics of the vortices are relatively simple and only related to the scanning frequency.

However, when white noise excitation is used, all frequencies are excited simultaneously. The air flow generated contains sound energy which relates to all the frequencies over the measured frequency range. The rotational flow and vortices are dependent on frequency. The fluid dynamics arising from each frequency component of the broadband white noise excitation is coupled with those at the nearby frequencies and contributes to the overall fluid behaviour. Therefore, the sound absorption of the MPM excited by white noise is higher than that excited by a stepped sine sweep when the SPLs of the sound source signals are similar, as shown in Figure 4.38.

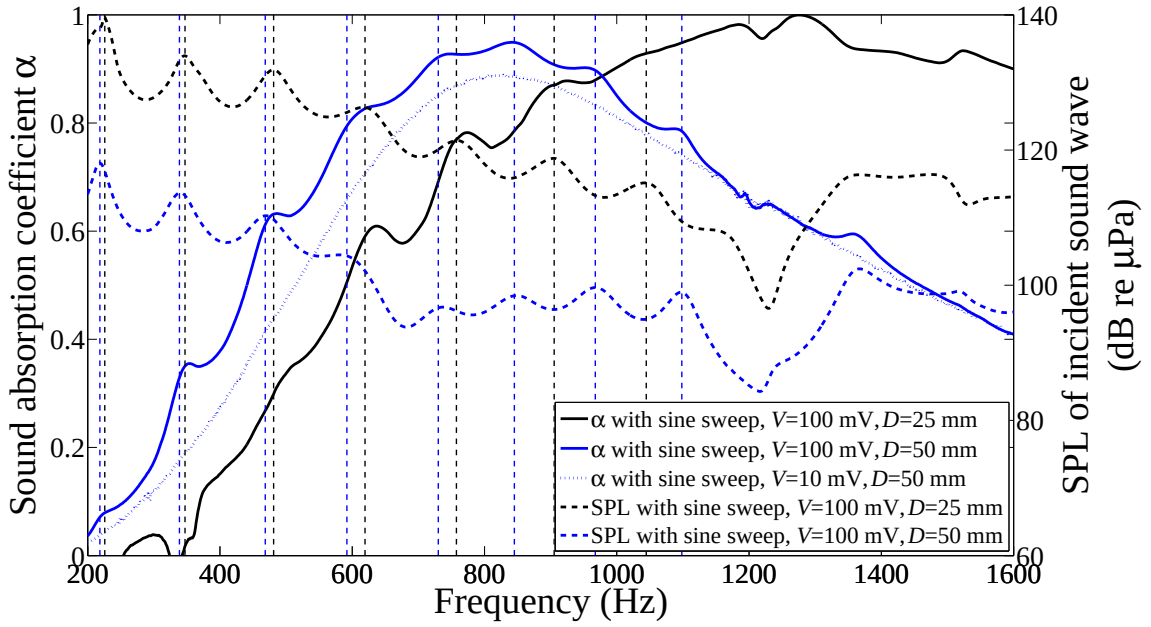

Figure 4.39: Measured sound absorption coefficients of the MPM with a stepped sine sweep excitation versus the incident SPL. The black solid curve represents the measured sound absorption coefficient with the input voltage of 100 mV and the cavity depth of 25 mm.

4.3.6 Effect of the cavity depth on the sound absorption coefficient of MPM 4 with a monochromatic source in the non-linear regime

The previous sections in this study indicated that when the MPM was excited by the stepped sine sound source signal (which is one of the monochromatic source signals used in this study), the small peaks in the measured sound absorption curves align with the SPL peaks due to the axial resonances in the impedance tube. This correspondence was presented by the matched frequencies of the peaks and valleys observed in both the measured sound absorption coefficient curves and the estimated incident SPL curves. In Section 4.3.1.3, it was found that the peaks and valleys in the estimated incident SPL curves are ascribed to the axial resonances due to the finite length of the impedance tube. It is known from Figure 4.1 that the length of the impedance tube is the sum of the length of the tube from the source to the MPM and the cavity depth. Hence, with a given length of the tube from the source to the MPM, these peaks and valleys can be affected by the air cavity depth. This section investigates the effect of the cavity depth on the non-linear sound absorption of the MPM under a monochromatic sound source signal experimentally.

It should be noted that the previous measurements were conducted with the air cavity

depth of 25 mm. In this section, the sound absorption coefficients of the MPM with the stepped sine sound source signal at 10 mV and 100 mv were measured. The cavity depth were doubled, i.e., $D = 50$ mm, in this section. The incident SPL and the measured sound absorption coefficients are shown in Figure 4.39 compared to the results with $D = 25$ mm. The black curves represents the measured sound absorption coefficient and the estimated incident SPL with the input voltage of 100 mV and the cavity depth of 25 mm. The blue curves represents those with the cavity depth of 50 mm and the input voltage of 100 mV. Note that these are in the non-linear regime. The blue dotted curve represents the measured sound absorption coefficient with the input voltage of 10 mV and the cavity depth of 50 mm (i.e., in the linear regime). The thin dashed vertical lines show the frequencies of the local SPL maxima and the corresponding peaks on the sound absorption curves.

Comparing the measured sound absorption coefficients with the input voltage of 100 mV and 10 mV, it is found that the threshold voltage exists when $D = 50$ mm. When the input voltage is sufficiently low, the MPM behaves in the linear regime. Otherwise, it exhibits the non-linear sound absorption. Similar to Figure 4.26, peaks and valleys were observed in the blue curves. The peaks and valleys in the sound absorption curve (i.e. the solid blue curve) correspond to those in the SPL curve (i.e. the dashed blue curve). These findings indicate that the non-linear sound absorption of the MPM is independent of the air cavity depth.

However, the blue vertical lines mismatch the black vertical lines and the amplitude of the mismatch increases with the increase of the frequency. The mismatched frequencies are ascribed to the axial resonances due to the length of the impedance tube. When the cavity depth was doubled, the total length of the impedance tube was increased. Hence, the resonance frequency in the axis of the length of the impedance tube was decreased and this increase was more significant in the higher frequency range. The mismatched black and blue vertical lines are associated to this phenomenon.

4.4 Conclusions

In this chapter, the effect of the incident SPL on the sound absorption of an MPM sample has been studied with broadband excitation and monochromatic excitation in an impedance tube with a normally-incident plane wave. The broadband sound source signal included white noise (Gaussian distribution), uniform random noise, pseudo random noise, burst random

noise and pink noise. The monochromatic source signal consisted of a stepped sine sweep and a chirp. Similar conclusions are obtained for each group of sound source signals. The sound pressure levels used as excitation varied from 15 dB to 143 dB re 20 μPa. The incident SPLs at the MPM surface were estimated using the measured transfer function and the measured sound pressure at one of the two microphones used in the experiments.

The two microphone transfer function method is validated by experiments in the non-linear regime. The transfer function between each microphone and the sound source was measured and the sound absorption coefficient was estimated based on these transfer functions. The estimated sound absorption coefficient was compared to that calculated, based directly on the transfer function between the two microphones. The consistences of these sound absorption coefficients verify the accuracy of the two microphone transfer function method.

The experimental results indicate that, similar to the case of MPPs, there exists a threshold SPL for which the sound absorption coefficient is consistent regardless of the SPL magnitude. When the incident SPL exceeds the threshold SPL, the sound absorption coefficient of the MPM increases with the increase of the incident SPL, which implies the existence of a non-linearity in the sound absorption of MPMs under high SPL excitation. These non-linear sound absorption coefficients have been observed with both white noise and a stepped sine sweep sound source signal, although the threshold SPL is different for different sound source signals. It is found that the threshold SPL of the MPM excited by either of the sound source signals is moderate and significantly lower than the commonly accepted threshold SPL values for the MPPs.

In the sound absorption curves of the MPM, for both a stepped sine sweep and white noise, the maximum sound absorption frequency tends to move to the low frequency range with moderate and high SPL magnitudes. This frequency shift implies that unlike the case of MPPs where only resistance is considered relevant to the non-linear sound absorption, the sound absorption of the MPM is affected by both resistance and reactance.

Small peaks at some specific frequencies are observed in the sound absorption coefficient curves with a stepped sine sweep excitation, however, these peaks are not present in the curves with white noise. It was theorised that the occurrence of these small peaks may be ascribed to a number of possible reasons, including the membrane resonance, the increased

depth of the air cavity under high SPL excitation, and the time-dependent flow which is considered responsible for the non-linearity of the sound absorption of micro perforates (Ingard & Ising 1967, Tayong et al. 2010). Based on the measurements of the sound absorption coefficients of an MPP sample and the cavity depth between the MPM sample and a transparent end, the former two reasons have been excluded.

Furthermore, the sound absorption curves of the MPMs excited with white noise are higher than those with a stepped sine sweep at roughly equal incident SPLs. This behaviour is related to the differing time-dependent flow generated by white noise and a stepped sine sweep. With a stepped sine sweep, the frequency components are decoupled and the sound absorption curves have small peaks which closely correspond to the peaks of the incident SPL due to the axial resonance of the impedance tube. With white noise, the frequency components are coupled and lead to complicated fluid dynamics. As a result, the small peaks that are observed in the sound absorption curves with a stepped sine sweep disappear in those curves with white noise. For the same reason, the sound absorption curves with white noise are smoother than those with a stepped sine sweep, and can be higher than the latter if their incident SPLs are roughly equal.

Moreover, the effect of the cavity depth on the non-linear sound absorption of the MPM was investigated by comparing the experimental results with an air cavity depth of 25 mm and 50 mm. It is found that the non-linear sound absorption phenomenons of the MPM occur independently of the air cavity depth. However, the frequencies where the peaks and valleys appear are associated with the axial resonances along the length of the impedance tube, which includes the air cavity depth.

This chapter presents experimental findings on the linear and non-linear sound absorption of micro perforated membranes. It reveals the effect of the time-dependent fluid dynamics on the non-linear sound absorption of the MPMs over a broadband frequency range and is fundamental knowledge for the analytical modelling of the non-linear acoustic impedance of the MPM presented in the next chapter.

Chapter 5

Analytical modelling of the non-linear sound absorption of micro perforated membranes under moderate and high excitation

5.1 Introduction

Chapter 4 presents the experimental findings of the non-linear sound absorption of an MPM under moderate and high incident sound pressure excitation. It is found that: 1) unlike the previously investigated orifices and perforated panels, both the resistance and reactance of the MPM are affected by the incident SPL in the non-linear regime; and 2) the peaks in the sound absorption coefficient curves of the MPM excited by a monochromatic sound source corresponds to the peaks of the incident SPL. Based on these experimental findings, this chapter aims to develop an analytical model for the non-linear sound absorption of the MPM excited by both broadband and monochromatic noise sources and explore the physical meanings of the model.

This chapter starts with an introduction, where previous research is reviewed in Section 5.1.1 and the arising research gaps and contributions of this chapter are presented in Section 5.1.2. Analytical modelling for the non-linear sound absorption of the MPM under investigation (MPM 4) with moderate and high SPL incidence is presented in Section 5.2. This model further divides into two sections according to the sound source categorisation. The analytical model for the broadband sound source is presented in Section 5.3 and that for the monochromatic sound source in Section 5.4, followed by the conclusions of this chapter in Section 5.5.

5.1.1 Literature review

Perforates and micro perforated panels are used as an alternative sound absorbing material instead of porous materials, especially in harsh conditions such as in aircraft engines. The sound pressure in aircraft engines is extremely high, leading to high particle velocities within the perforations of the perforates and micro perforated panels (MPPs). Hence, it is necessary to investigate analytical models for the acoustic properties of perforates and MPPs under high sound pressure level (SPL) excitation.

Ingard & Ising (1967) investigated the acoustic properties of an orifice in a rigid baffle experimentally, an arrangement which could be considered as a simplified model of a perforated panel consisting of only one perforation. Ingard & Ising indicated that the non-linearity of the orifice under high SPL is due to the rotational flow and vortices arising from the high particle velocity. Ingard & Ising further pointed out that the non-linear resistance of the orifice is proportional to the amplitude of the particle velocity within the orifice. They developed an expression for the resistance due to the non-linear effect, which is given by

$$\mathrm{Re}_{\mathrm{nonlinear}} = \rho_0 |v|, \tag{5.1}$$

where $\mathrm{Re}_{\mathrm{nonlinear}}$ denotes the resistance of the non-linear impedance of the orifice. Note that Equation (5.1) is derived based on experimental results.

As for the non-linear acoustic impedance of micro perforated panels, Maa (1996) derived an expression based on the motion equation of air particles within the perforations and the continuity of air density. According to Maa, since the Mach number $\frac{v}{c_0}$ was relatively small, the effect of the particle velocity on the acoustic impedance due to the perforations was negligible. The non-linear part of the acoustic impedance of an MPP under high SPL excitation was ascribed to an end correction affected by the high speed air flow in the non-linear regime. Maa further indicated that when a high SPL was applied, the deviation of the reactance was very limited, however, the resistance could change significantly.

Bodén (2007) introduced a new method to calculate the non-linear acoustic impedance of perforates and MPPs. The idea was to treat the non-linear factor as a separate input for a linear two-input one-output system. In addition, two types of sound sources, pure tones and broadband noise, were used to excite the perforate sample. The experimental results indicated that the non-linear impedance with pure tone excitation was dependent on

the instantaneous velocity at the pure tone frequency, while with broadband noise it was related to the impedances at other frequencies. Hence, the acoustic impedance with pure tone excitation is proportional to the instantaneous velocity. With broadband noise, the acoustic impedance is proportional to the RMS velocity.

Tayong et al. (2010) investigated the non-linear acoustic properties of MPPs at their main resonance frequency. This research is based on Forchheimer's regime of flow velocity (McIntosh & Lambert 1990). This method considered the non-linear impedance to be equal to the sum of the linear impedance and the impedance due to non-linear effects. Good agreements were achieved between the experimental and predicted results. However, in the prediction process, some of the parameters were determined by curve fitting and their physical meanings remain unknown.

5.1.2 Gaps and contributions

The research mentioned in Section 5.1.1 is related to orifices in rigid baffles, perforated panels (i.e. perforates) and MPPs. Micro perforated membranes (MPMs) which are of particular interest in this study, were barely investigated. Moreover, although there is some research investigating both the resistance and reactance (Bodén 2007, Maa 1996, Tayong et al. 2010), the reactance is assumed to be of less importance than the resistance. This is valid for the cases of orifices in rigid baffles, perforated panels (i.e. perforates) and MPPs, however, the experimental results shown in Chapter 4 demonstrated that the reactance plays an important role in the case of MPMs.

Therefore, this chapter aims to analytically model the acoustic impedance of MPMs under high SPL excitation. Two models have been developed following different strategies. Based on the similarity of the previous models developed by the researchers mentioned in Section 5.1.1, the first model of the non-linear acoustic impedance of MPMs is introduced in Section 5.2. However, since this model is developed by summarising the previous models, the physical meanings of the optimised parameters remain unknown. To explore the physical meanings, the second model was developed by re-deriving Maa's non-linear motion equations. Simplifying the second model, it is found that the optimised parameters represent the average rates of the air density change in the time and spatial domains.

Note that some parameters in the model are determined by curve fitting and that the ex-

perimental results were obtained with two types of sound source, as presented in Chapter 4. As a result, in accordance with Bodén's conclusion, the parameter determination and experimental validation of this model is divided into Section 5.3 for broadband sound sources and Section 5.4 for monochromatic sound sources, respectively. The good agreement between the measured results and the results predicted using each model verified the accuracy of each model. However, the second model is recommended for future research due to its clear physical meanings of the optimised parameters. This chapter is concluded in Section 5.5.

5.2 Analytical modelling of the sound absorption of micro perforated membranes under moderate and high excitation

This section explores the analytical modelling of the non-linear sound absorption of micro perforated membranes under moderate and high acoustic excitation. It starts with discussions on three previous models for micro perforated panels under high excitation in Section 5.2.1. All of them investigate the non-linear impedance of MPPs under high excitation, however, using very different methods. Two models for the non-linear acoustic impedance of MPMs under moderate and high excitation are presented in Sections 5.2.2 and 5.2.3.

5.2.1 Previous models

This section presents the previous models for the prediction of the non-linear sound absorption of MPPs under high excitation by predicting the non-linear acoustic impedance. The models developed by Ingard & Ising (1967), Maa (1996) and Tayong et al. (2010) are discussed. Bodén's (2007) model is excluded because its prediction method is based on non-linear signal analysis and the physical meanings of the non-linear impedance is unclear in his equations. Note that the discussed models are all for the non-linear impedance of MPPs and hence could be inaccurate for the modelling of MPMs. The non-linear acoustic impedance of MPMs has not previously been investigated.

5.2.1.1 Ingard & Ising's non-linear impedance model

In Ingard & Ising's (1967) research, the experimental results indicated that the acoustic impedance due to the non-linear effect of an orifice in a rigid baffle is proportional to the

amplitude of the particle velocity within the orifice, and is given by Equation (5.1). If this relationship is extended to the cases of MPPs and MPMs, the total acoustic impedance of an MPP or MPM in the non-linear regime is given by

$$z_{\text{nonlinear Ingard}} = z_{\text{linear}} + \rho_0 |v|, \tag{5.2}$$

where z_{linear} denotes the normalised acoustic impedance of the MPP or MPM in the linear regime.

In Equation (5.2), the term $\rho_0|v|$ represents the non-linear impedance due to the high acoustic excitation. The amplitude of the particle velocity within the orifice or the perforations $|v|$ is used in this term. Hence, this term only changes the real part of the acoustic impedance, i.e., the resistance. This is valid for orifices in a rigid baffle and MPPs where there is limited motion of the baffle or panel. The change of the reactance of these materials under high excitation is reported to be very limited (Melling 1973*b*). However, as mentioned in Chapter 4, in the cases of MPMs, the variation of the resistance can be significant. Therefore, Ingard & Ising's model is presumably inaccurate for MPMs which are of particular interest in this thesis.

5.2.1.2 Maa's non-linear impedance model

Maa's (1996) derivation starts with the motion equation considering particle velocity variation in the length direction of the orifice,

$$\rho_0 \frac{\partial v(r, x_{\text{length}}, t)}{\partial t} + \rho_0 \frac{\partial v(r, x_{\text{length}}, t)}{\partial x_{\text{length}}} v(r, x_{\text{length}}, t) - \frac{\mu}{r} \frac{\partial}{\partial r} \left(r \frac{\partial v(r, x_{\text{length}}, t)}{\partial r} \right) = \frac{\Delta p}{h}, \tag{5.3}$$

where x_{length} denotes the position coordinate in the length direction, and also applies the mass continuity equation of the Navier-Stokes equations,

$$\frac{\partial \rho}{\partial t} + \frac{\partial \rho}{\partial x_{\text{length}}} v(r, x_{\text{length}}, t) + \frac{\partial v(r, x_{\text{length}}, t)}{\partial x_{\text{length}}} \rho = 0. \tag{5.4}$$

By substituting Equation (5.4) into Equation (5.3), the motion equation is rewritten as

$$\rho_0 \, j \, \omega \, v(r) - \frac{\mu}{r} \left[\frac{\partial v(r)}{\partial r} + r \frac{\partial^2 v(r)}{\partial r^2} \right] = \frac{\Delta p}{h} \left(1 - \frac{|v|^2}{c_0^2} \right). \tag{5.5}$$

Comparing this equation with the linear motion equation of air particles within a perforation given by Equation (3.4), Maa noticed that when the term $\frac{|v|^2}{c_0^2}$ in Equation (5.5) is relatively small, these two equations are identical. Therefore, Maa presumed that the high particle velocity had a limited effect on the acoustic impedance and the non-linear impedance

was ascribed to the end correction which was affected by the high particle velocity. He further indicated that the real part of the non-linear end correction was due to the rotational jet and vortex previously mentioned by Ingard & Ising (1967) and the imaginary part was possibly due to the flow jet blowing some air away. Therefore, the total non-linear impedances of MPPs are given by Maa (1996) as

$$\begin{aligned} z_{\text{nonlinear Maa}} &= \frac{32\mu}{\delta c_0}\frac{h}{d^2}\left[\sqrt{1+\frac{k_{\text{Maa}}^2}{32}}+\frac{\sqrt{2}k_{\text{Maa}}d}{8h}\right]+\frac{|v|}{\delta c_0} \\ &\quad + j\omega\frac{h}{\delta c_0}\left[1+\left(9+\frac{k_{\text{Maa}}^2}{2}\right)^{-\frac{1}{2}}+0.85\frac{d}{h}\left(1+\frac{|v|}{\delta c_0}\right)^{-1}\right], \\ &= z_{\text{linear}}+\frac{|v|}{\delta c_0}+j\omega\frac{-0.85d}{\delta c_0}\frac{|v|}{\delta c_0+|v|}, \end{aligned} \tag{5.6}$$

where $k_{\text{Maa}}=\frac{d}{2}\sqrt{\frac{\omega\rho_0}{\mu}}$ is the MPP constant.

In Equation (5.6), the high particle velocity within the perforations affects both the resistance and the reactance. Additionally, this equation implies that the non-linear impedance of an MPP under high excitation is the sum of its linear impedance and the acoustic impedance due to the high particle velocity, which is similar to Ingard & Ising's method. However, since Maa's method is for the prediction of MPPs, it could be inaccurate for MPMs because the mechanical vibration of a membrane is likely to be more significant than a panel relatively rigid and hence have a more significant effect on the total impedance than the panel material.

5.2.1.3 Model based on the Forchheimer non-linear flow model and dimensional analysis

Tayong et al.'s (2010) method is based on Forchheimer's regime of flow velocity (McIntosh & Lambert 1990). In their method, the acoustic impedance due to the perforations is given by

$$z_{\text{perf}}=\frac{32\mu h}{d^2}\sqrt{1+\frac{k_{Maa}^2}{32}}+j\omega h\rho_0\left[1+\left(9+\frac{k_{Maa}^2}{2}\right)^{-\frac{1}{2}}\right]. \tag{5.7}$$

The radiation impedance on the ends of the perforations is expressed as

$$z_{\text{ray}}=\frac{(k_0 d)^2}{2}+j\frac{8k_0 d}{3\pi}. \tag{5.8}$$

Hence, the linear acoustic impedance is given by

$$z_{\text{linear}} = \frac{z_{\text{perf}} + 2z_{\text{ray}} + 4R_s}{\delta}, \tag{5.9}$$

where the term R_s represents the thermo-viscous fraction on the panel surface and is obtained from Equation (3.36). Therefore, the non-linear impedance of an MPP is given by

$$z_{\text{nonlinear Tayong}} = a\frac{dc_0}{\sigma\delta}\frac{|v|}{c_0} + (1+b)\,\text{Re}(z_{\text{linear}}) + j\text{Im}(z_{\text{linear}}), \tag{5.10}$$

where the term $a\frac{dc_0}{\sigma\delta}$ is determined by dimensional analysis. The parameters a and b are determined by curve fitting and their physical meanings are unclear.

Equation (5.10) may be rewritten as

$$z_{\text{nonlinear Tayong}} = z_{\text{linear}} + a\frac{dc_0}{\sigma\delta}\frac{|v|}{c_0} + b\text{Re}(z_{\text{linear}}). \tag{5.11}$$

Equation (5.11) implies that, similar to Ingard & Ising and Maa's methods, Tayong et al.'s (2010) prediction method also assumed that the non-linear impedance of MPPs is the sum of the linear impedance and the term representing the non-linear effect which is proportional to the amplitude of the particle velocity within the perforations. However, their coefficient of the particle velocity is determined by curve fitting, where as it is propotional to the air density $\frac{\rho_0}{c_0}$ in Ingard & Ising's method and $\frac{1}{\delta c_0}$ in Maa's method. The latter methods can be less accurate due to the lack of curve fitting. Moreover, the non-linear resistance is also varied by the parameter b which represents three regimes: when an MPP is in the linear regime, $b = 0$; when it is in the non-linear regime, $b \neq 0$; and b is arbitrary when an MPP is in the transition regime.

5.2.2 Simplified model based on the previous models with optimised end correction

The previous prediction models analysed in Section 5.2.1 follow similar strategies. They assume that the non-linear acoustic impedance of an MPP consists of two parts, the linear acoustic impedance of the MPP and the acoustic impedance arising from the non-linear effect. The latter is considered proportional to the amplitude of the particle velocity in the perforations in all three models, although the coefficient of the particle velocity amplitude differs in each model.

However, these models are for the prediction of MPPs, which implies that using these

models may lead to inaccurate prediction for the acoustic impedance of MPMs, as described in Chapter 3. Moreover, these models pay more attention to the non-linear resistance than the non-linear reactance. The variation of the latter is commonly assumed to be very limited and unimportant in these models. However, it is found in Chapter 4 that the high particle velocity in the perforations has a more significant effect on the reactance of MPMs than on that of MPPs.

A simplified model for the prediction of MPMs is presented here, following the approach that both the non-linear resistance and reactance are of importance, and this is expressed as

$$z_{\text{nonlinear Simplified}} = z_{\text{linear}} + a\frac{\text{Re}(v)}{c_0} + b\,j\frac{\text{Im}(v)}{c_0}, \tag{5.12}$$

where a and b are determined by curve fitting. This model consists of two parts, the linear impedance of an MPM z_{linear} and the non-linear term $a\frac{\text{Re}(v)}{c_0} + b\,j\frac{\text{Im}(v)}{c_0}$. This method is similar to Tayong et al.'s (2010) model, except that the linear impedance of the MPM is predicted using the no-slip method mentioned in Chanpter 3 and that the complex particle velocity is used here instead of the velocity amplitude used in Tayong et al.'s model. The different coefficients a and b of the real and imaginary parts of the particle velocity imply that both the real and imaginary parts of the particle velocity are assumed to contribute to the non-linear impedance differently. The parameter determination and experimental validation using this model with broadband and monochromatic sound sources are discussed in Sections 5.3 and 5.4, respectively.

5.2.3 Analytical model based on motion equation and density continuity

Although there are several models for the prediction of the non-linear impedance of MPPs and MPMs, the physical meanings of the coefficients used in these models are unclear (Tayong et al. 2010). This section aims to explore the physical meanings of the coefficients of the particle velocity within the MPM perforations and develop a new model where a different strategy is applied.

In the linear regime, the particle flow within a perforation of an MPP or MPM is considered to be laminar. The particle motion is assumed to be only affected by the viscous friction in the radial direction and the variation of the particle velocity in the length direc-

tion, as shown in Figure 3.1, is neglected. However, if the particle travels with high velocity, the flow in the perforation is separated in the length direction (Cummings 1986), as shown in Figure 5.1. Considering the flow separation, the motion equation of the air particle in the perforation is given by Equation (5.3) and the mass continuity equation of the Navier-Stokes equations is given by Equation (5.4). These two equations are difficult to solve due to the unknown terms $\frac{\partial \rho}{\partial t}$, $\frac{\partial \rho}{\partial x_{\text{length}}}$ and $\frac{\partial v(r,x_{\text{length}})}{\partial x_{\text{length}}}$. As mentioned in Section 5.2.1.2, Maa substituted Equation (5.4) into Equation (5.3) and obtained Equation (5.5), where the velocity part was sufficiently small that it could be neglected. Hence, Maa concluded that the acoustic impedance due to the perforations was barely affected by the high particle velocity.

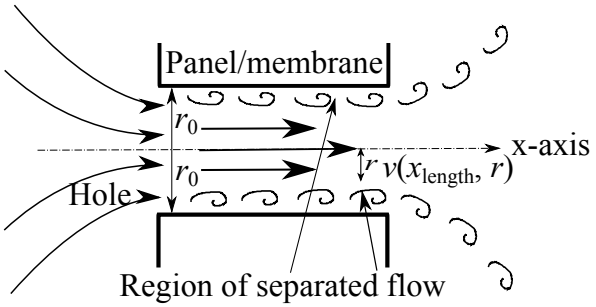

Figure 5.1: Particle velocity $v(x_{\text{length}},\ r)$ in a hole of the micro perforated membrane or panel as a function of the distance, r, from the centre line and the position coordinate x_{length} in the length direction. The flow is separated in the length direction due to the high particle velocity (Adapted from Cummings (1986)).

However, Equations (5.3) and (5.4) are solved differently in this section. The continuity Equation (5.4) is rewritten as

$$\frac{\partial v(r,x_{\text{length}},t)}{\partial x_{\text{length}}}\rho = -\frac{\partial \rho}{\partial t} - \frac{\partial \rho}{\partial x_{\text{length}}} v(r,x_{\text{length}},t). \tag{5.13}$$

If the variation of density is small, $\rho \approx \rho_0$. It is assumed that $\frac{\partial \rho}{\partial t}$ and $\frac{\partial \rho}{\partial x_{\text{length}}}$ are approximately constant and $v(r,x_{\text{length}},t)$ is considered as an input. Hence, Equation (5.13) is expressed approximately as

$$\begin{aligned}\frac{\partial v(r,x_{\text{length}},t)}{\partial x_{\text{length}}}\rho &\approx \rho_0 \frac{\partial v(r,x_{\text{length}},t)}{\partial x_{\text{length}}} \\ &\approx -\frac{\partial \rho}{\partial t} - \frac{\partial \rho}{\partial x_{\text{length}}} v(r,x_{\text{length}},t), \\ &\approx a + bv\end{aligned} \tag{5.14}$$

where a and b are determined by curve fitting. Substituting Equation (5.14) into Equation

(5.3) and eliminating the time variable t gives the motion equation as

$$\rho_0 \frac{\partial v(r,x_{\text{length}},t)}{\partial t} + (a+bv)\, v(r,x_{\text{length}},t) - \frac{\mu}{r}\frac{\partial}{\partial r}\left(r\frac{\partial v(r,x_{\text{length}},t)}{\partial r}\right) = \frac{\Delta p}{h}. \tag{5.15}$$

Equation (5.15) is rearranged as

$$\frac{\partial^2 v(r)}{r^2} + \frac{1}{r}\frac{\partial v(r)}{r} - \frac{\rho_0\, j\,\omega + a + bv}{\mu} v(r) = -\frac{\Delta p}{\mu h}. \tag{5.16}$$

Letting $K_{\text{air}}^2 = \frac{-a-bv-\rho_0\, j\,\omega}{\mu}$, Equation (5.16) is rewritten as

$$\left(\frac{\partial^2}{\partial r^2} + \frac{1}{r}\frac{\partial}{\partial r} + K_{\text{air}}^2\right) v(r) = -\frac{\Delta p}{\mu h}. \tag{5.17}$$

Comparing Equation (5.17) with the motion equation in the linear regime (Equation (3.6)), it is found that they are identical in form except that the expression for the term K_{air} is different for each equation. Therefore, Equation (5.17) can be solved following the same method presented in Chapter 3.

In addition, Equation (5.14) shows that

$$a = -\frac{\partial \rho}{\partial t}, \tag{5.18}$$

and

$$b = -\frac{\partial \rho}{\partial x_{\text{length}}}. \tag{5.19}$$

Therefore, the parameter a represents the average variation of the air density in the time domain, which is dependent on time and position coordinates and is assumed to be constant in this chapter. The parameter b denotes the average variation of the air density in the length direction in the spatial domain, which is also dependent on position coordinates and is assumed to be constant here. Presumably, a and b are related to the particle velocities, and hence are different for different particle velocity and different sound excitation types.

This model inspires exploration for the physical meanings of the optimised coefficients of the particle velocity v. Substituting $K_{\text{air}}^2 = \frac{a+bv-\rho_0\, j\,\omega}{\mu}$ into Equation (5.17) gives

$$\left(\frac{\partial^2}{\partial r^2} + \frac{1}{r}\frac{\partial}{\partial r} + K_{\text{air}_{\text{linear}}}^2\right) v(r) - \frac{a+bv}{\mu} v(r) = -\frac{\Delta p}{\mu h}, \tag{5.20}$$

where $K_{\text{air}_{\text{linear}}}^2 = \frac{-\rho_0\, j\,\omega}{\mu}$ is the MPM constant in the linear regime. Equation (5.20) is rewritten as

$$\mu h\left(\frac{\partial^2}{\partial r^2} + \frac{1}{r}\frac{\partial}{\partial r} + K_{\text{air}_{\text{linear}}}^2\right) v(r) - h\,(a+bv)\, v(r) = -\Delta p. \tag{5.21}$$

Comparing Equation (5.21) with the linear motion equation, it is found that the first term in the left hand side of the equation represents the air motion of laminar flow within a hole in the linear regime, and the second term represents that of a separated flow due to the high particle velocity in the non-linear regime. Therefore, by solving Equation (5.21) and eliminating $v(r)$, the normalised acoustic impedance of the MPM is expressed as

$$\begin{aligned} z_{\text{nonlinearpresented}} &= z_{\text{linear}} + \frac{h(a+bv)}{\delta\rho_0 c_0}, \\ &= z_{\text{linear}} + \frac{ha}{\delta\rho_0 c_0} + \frac{hbv}{\delta\rho_0 c_0}, \end{aligned} \tag{5.22}$$

where z_{linear} is calculated using the no-slip condition in Chapter 3.

Considering that a is the derivative of the expression of the air density with respect to time as shown in Equation (5.18), it is deduced that the constant term $\frac{ha}{\delta\rho_0 c_0}$ in Equation (5.22) represents the normalised acoustic impedance over the surface of the MPM, arising from the density change over the tube length in the time domain. Hence, this part is time dependent and a represents the average rate of the air density change in the time domain.

Similarly, since b is the derivative of the expression of the air density with respect to the position coordinate in the length direction as shown in Equation (5.19), the term $\frac{hb}{\delta\rho_0 c_0}$ represents the normalised acoustic impedance over the MPM surface, arising from the overall density change in the length direction. This term is dependent on the particle velocity and b represents the average rate of the air density change in the spatial domain along the length direction of the perforations.

Therefore, the presented model is able to predict the non-linear acoustic impedance of MPMs using Equation (5.22) with clear physical meanings of the optimised parameters. The parameter determination and experimental validation using this model with broadband and monochromatic sound sources are discussed in Sections 5.3 and 5.4, respectively.

5.3 Parameter determination and experimental validation for the sound absorption of MPMs excited by broadband sound source

This section presents the validation of the analytical models for the non-linear impedance of the MPM sample used in Chapter 4. The predicted results using the presented models

mentioned in Sections 5.2.2 and 5.2.3 are compared with three previous models mentioned in Section 5.2.1. In the results that are presented in this chapter, the following five models and their abbreviations are used:

- Ingard and Ising model – implementation of Ingard & Ising's (1967) model with Equation (5.2).
- Maa model – implementation of Maa's (1996) model with Equation (5.6).
- Tayong et al. model – implementation of Tayong et al.'s (2010) model with their parameters a and b determined from fit of experimental data to Equation (5.11).
- Presented simplified model – implementation of Equation (5.12) with a and b determined from fit of experimental data to Equation (5.12).
- Presented analytical model – implementation of the model developed in this study, where a represents the average variation of the air density in the time domain, and b denotes the average variation of the air density in the length direction in the spatial domain. Their values were determined from fit of experimental data to Equation (5.22).

The experimental results were obtained from a broadband sound source with varying input voltage and the experimental arrangement is discussed in Chapter 4. Although five types of broadband sound sources were used in the experiments, the non-linear sound absorption properties were similar and only the experimental results with white noise are used in this section to validate the models. The comparisons of the predicted results and the measured results at different input voltages are shown in Figures 5.3 to 5.6. Note that the term z_{linear} used in these models were equal to the total acoustic impedance of MPM 4 calculated using the prediction method developed in Chapter 3.

As mentioned in Section 5.2, the particle velocity in the perforations is used as an input in some of the models. The particle velocity in the perforations was estimated from the measured transfer function and the measured sound pressure with microphone 1 (see Figure 4.10) using Equations (4.5) and (4.6). Since the non-linear impedance is related to the RMS particle velocity within the holes (Bodén 2007), the RMS particle velocity is calculated using

$$v_{\text{RMS}} = \sqrt{\frac{\sum_{f_{\text{min}}}^{f_{\text{max}}} v^2}{N_{\text{freq}}}}. \tag{5.23}$$

Note that the RMS velocity is a complex value due to the complex value of v. Figure 5.2 shows the RMS velocity within the perforations versus the input voltage and the overall incident SPL. It is observed that the amplitude of the particle velocity within the perforations increased significantly in the non-linear regime and its phase was also changed.

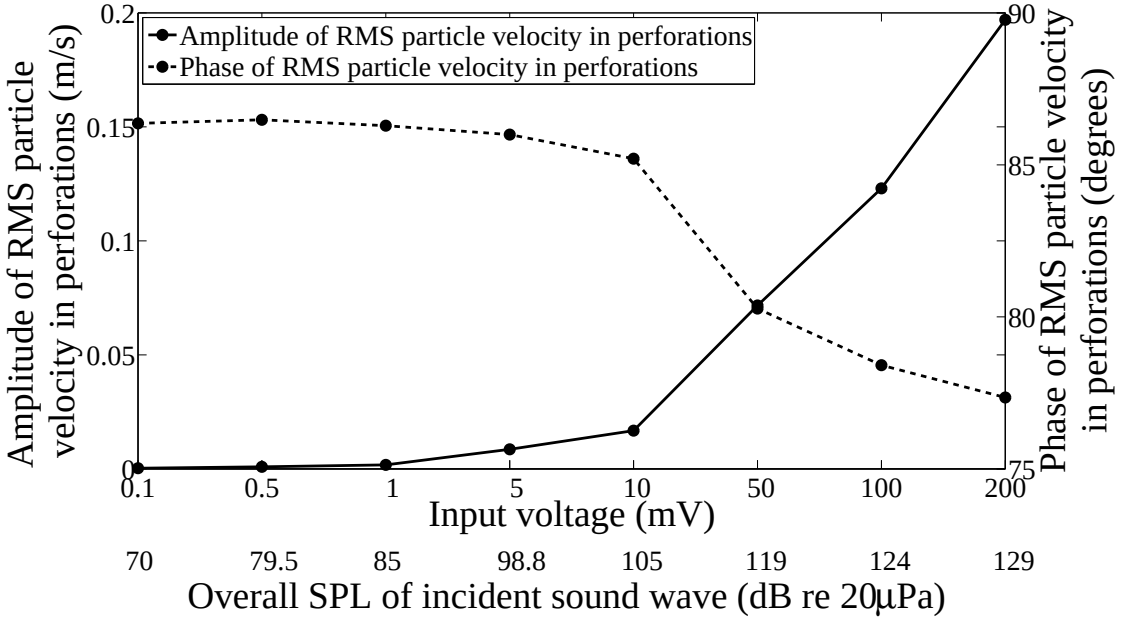

Figure 5.2: Amplitude and phase of RMS particle velocity within the perforations of the MPM excited by white noise. The input voltage increased from 0.1 mV to 200 mV, resulting in the overall incident SPL increasing from 70 dB re 20 μPa to 129 dB re 20 μPa.

The equivalent value set (a and b) used in the analytical model were obtained from the experimental measurements by fitting the measured data to the model using the optimisation toolbox in Matlab (Waltz et al. 2006). The optimised value sets are given in Figures 5.3, 5.4, 5.5 and 5.6.

In Figures 5.3 to 5.6, the coefficient of determination R^2_{det} was used for each model to quantify the accuracy of each prediction. The R^2_{det} is the same as $R^2_{\text{determination}}$ used in Chapters 2 and 3.

Figure 5.3 shows the predicted results using these five non-linear models in the linear regime where the input voltage is relatively small, resulting in a relatively small particle velocity. The non-linear effect is negligible in the results shown in this figure because the particle velocity is sufficiently small that it barely affects the predicted acoustic impedance.

The peak absorption frequencies of the predicted results using Maa's and Tayong et al.'s models were less than that observed experimentally and the sound absorption bandwidths

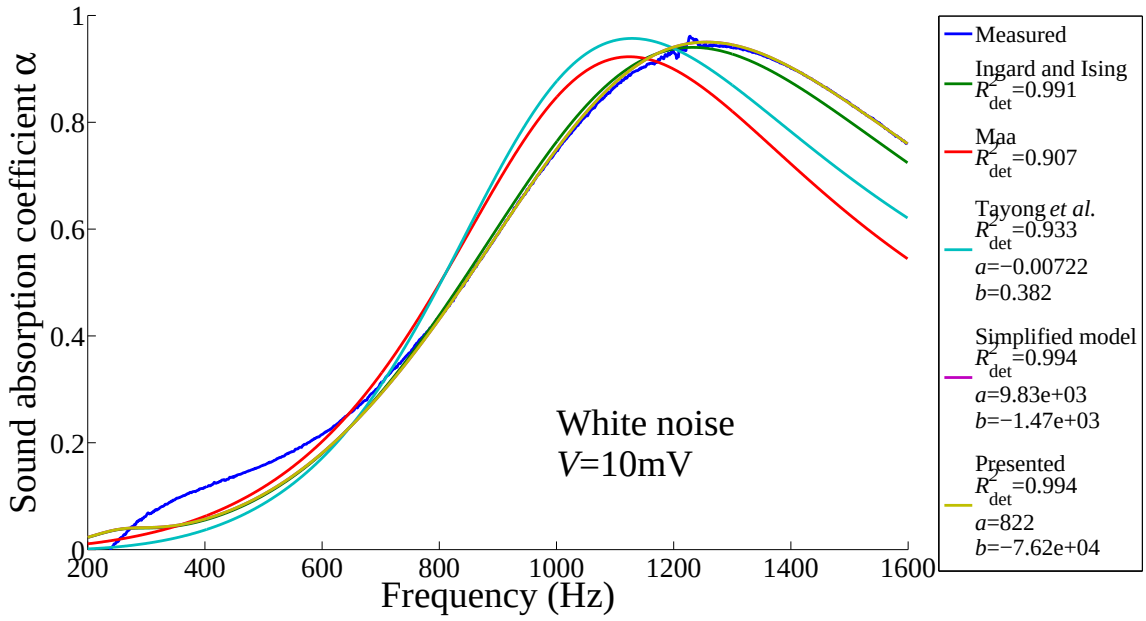

Figure 5.3: Predicted and measured sound absorption coefficients of the MPM sample with white noise excitation. The input voltage was 10 mV. The acoustic impedance is in the linear regime.

were underestimated, which is due to the neglected acoustic impedance caused by the membrane vibration (as discussed in Chapter 3). Ingard & Ising's model and the two models developed earlier show good agreement with the measured results. Since Ingard & Ising's model is for the non-linear acoustic impedance of an orifice in a rigid baffle, the linear acoustic impedance used in this model is that of the MPM using the more accurate method presented in Chapter 3, instead of Ingard & Ising's original equation. Hence, in the linear regime, the predicted result of Ingard & Ising's model is approximately equal to that using the presented model in Chapter 3. The two developed models have better agreement to the experimental result than the previous models because the parameters were optimised to fit the experimental data in the linear regime.

For excitation levels corresponding to the non-linear regime shown in Figures 5.4 to 5.5, the prediction from the presented two models, the presented simplified model and the presented analytical model, are almost identical and show better agreement with the measured results than the other models because of the accurate prediction of the linear acoustic impedance and the optimised coefficients of the complex particle velocity. Although Tayong et al.'s model is less accurate in the linear regime than the two presented models, it shows the third best agreement to the measured results in the non-linear regime and its accuracy

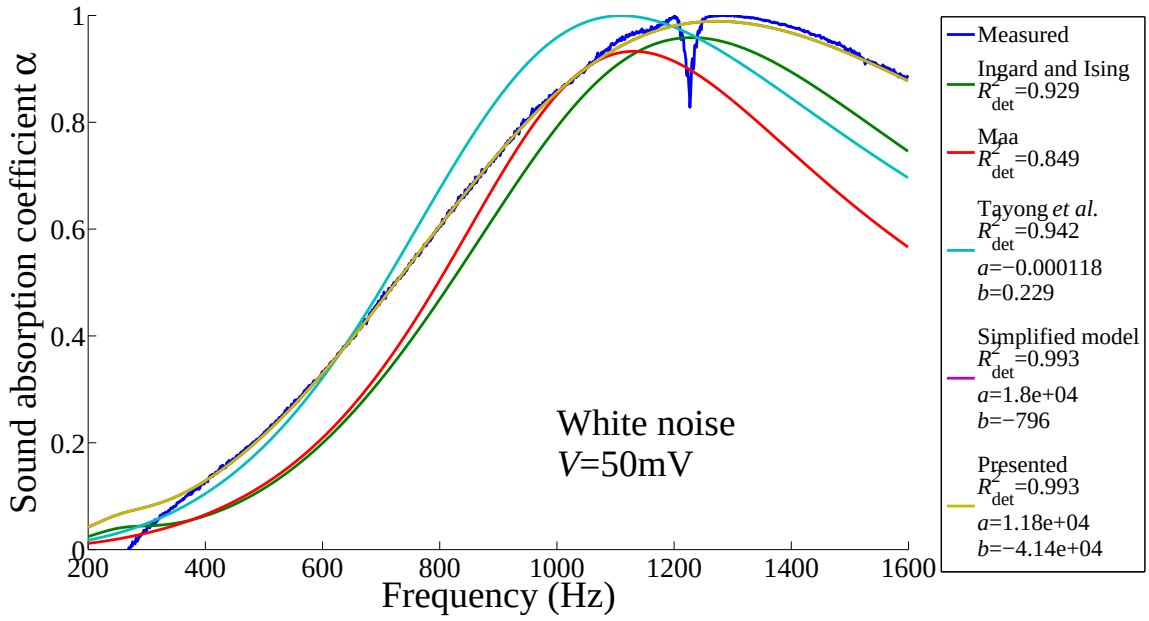

Figure 5.4: Predicted and measured sound absorption coefficients of the MPM sample with white noise excitation. The input voltage was 50 mV.

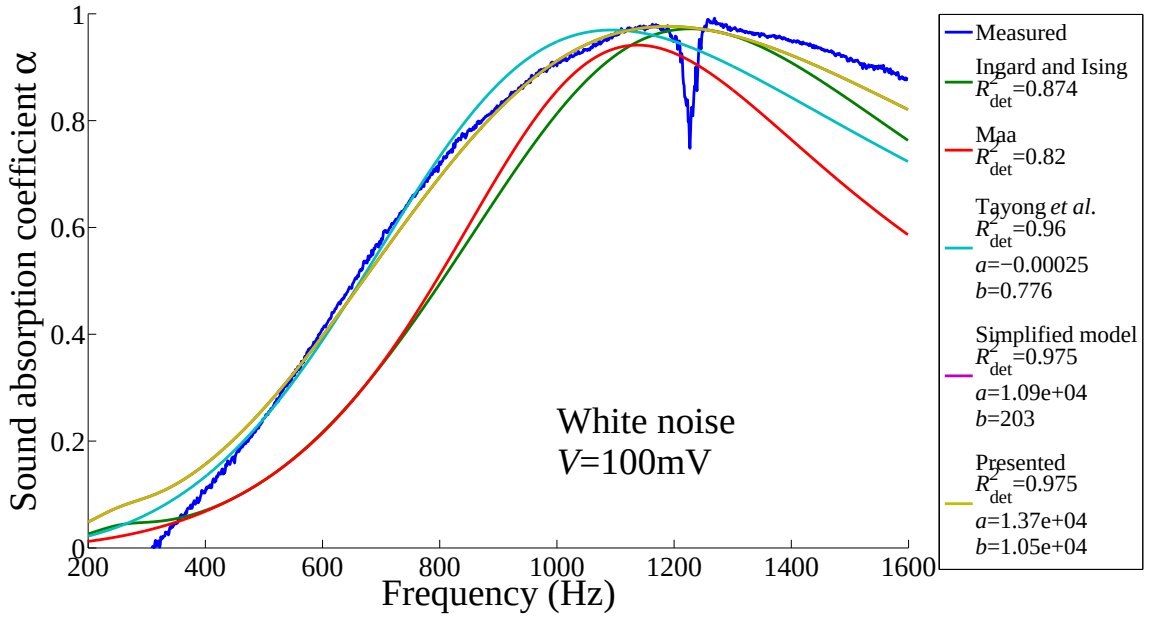

Figure 5.5: Predicted and measured sound absorption coefficients of the MPM sample with white noise excitation. The input voltage was 100 mV.

increases with an increase in the particle velocity. In Figure 5.6, Tayong et al.'s model is seen to be more accurate than the other models. The consistency of the predicted results using the two presented models is ascribed to the similarity of their prediction method, as shown in Equations (5.12) and (5.22). The decreasing accuracy of the two presented models may imply that these two models may be unsuitable if the particle velocity is too high.

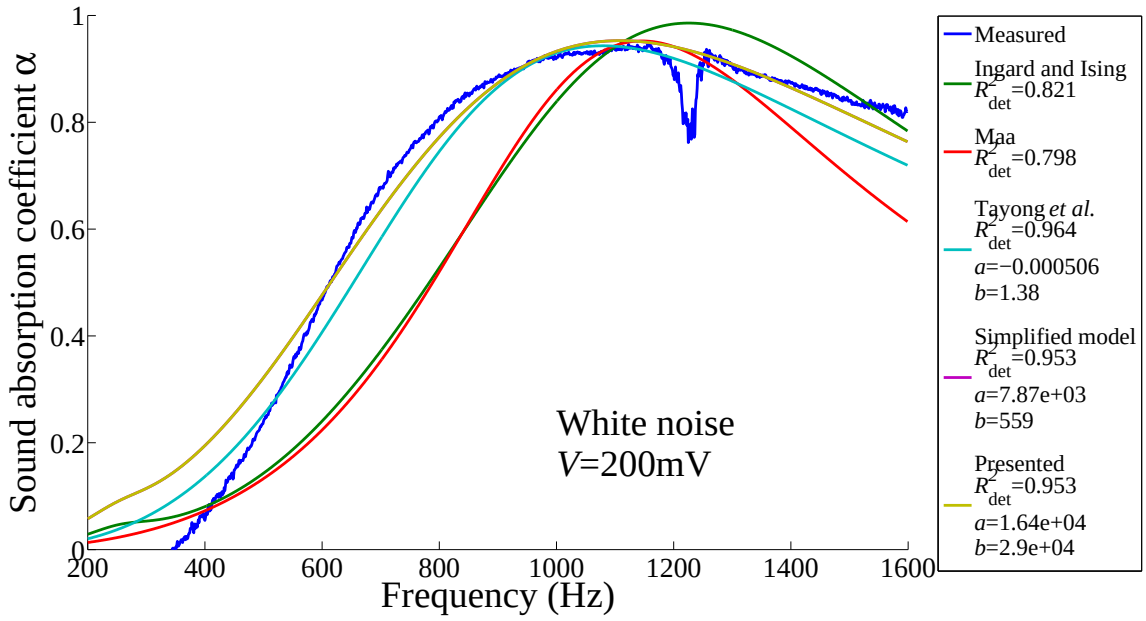

Figure 5.6: Predicted and measured sound absorption coefficients of the MPM sample with white noise excitation. The input voltage was 200 mV.

Table 5.1 shows the values relating to the optimised parameters in the two presented models. The last two columns represent the air density variation in the time domain and in the length direction in the spatial domain, respectively. They are plotted in Figure 5.7. These values are small in the linear regime and increase with the increase of the input voltage and the corresponding increase in the incident SPL in the non-linear regime, which is consistent with the physical phenomenon. The value of a is always positive because it is the derivative of the expression for the air density with respect to time. The value of b can be negative because it is the derivative of the expression for the air density with respect to the position coordinate in the length direction. The negative value implies that the derivative of the expression for the air density is opposite to the positive length direction.

Table 5.1: Optimised parameters for the non-linear acoustic impedance of the MPM exicted by a white noise signal. The presented simplified model is given by Equation (5.12), and the presented analytical model is given by Equation (5.22)

Input voltage (mV)	Presented simplified model		Presented analytical model		Total rate of air density change	
	$\frac{a-b}{c_0}\text{Real}(v)$	$\frac{b}{c_0}$	$\frac{ah}{\delta c_0 \rho_0}$	$\frac{bh}{\delta c_0 \rho_0}$	In time domain $ah \approx h\frac{\partial \rho}{\partial t}$	In space domain $bh \approx h\frac{\partial \rho}{\partial x_{\text{length}}}$
10	0.046	-4.273	0.046	-4.263	0.140	-12.954
50	0.662	-2.314	0.660	-2.316	2.006	-7.038
100	0.769	0.590	0.767	0.588	2.329	1.785
200	0.917	1.625	0.918	1.623	2.788	4.930

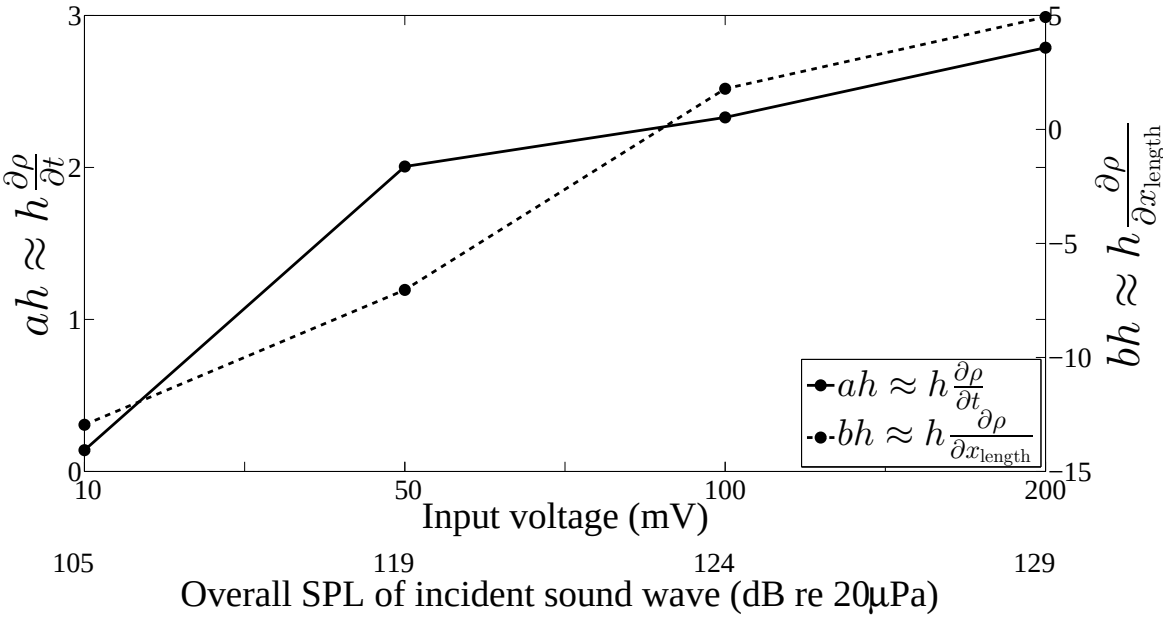

Figure 5.7: The values of $ah \approx h\frac{\partial \rho}{\partial t}$ and $bh \approx h\frac{\partial \rho}{\partial x_{\text{length}}}$ using the optimised parameters for the MPM excited by a white noise signal. The curves represent the total rates of air density change in the time and spatial domains, respectively.

5.4 Parameter determination and experimental validation for the sound absorption of MPMs excited by monochromatic sound sources

This section validates the presented models for the sound absorption prediction of the MPM excited by monochromatic sound signals. The experimental results used in this section are those measured with a stepped sine sweep sound signal, as presented in Section 4.3.3. Although the monochromatic sound signals used in Section 4.3.3 included the stepped sine sweep and a chirp, the measured sound absorption coefficients with these signals have similar properties and hence only the results with a stepped sine sweep are used in this section. Unlike the cases with a broadband sound signal, the instantaneous particle velocities within the perforations are used in this section instead of the RMS particle velocities used in Section 5.3. The instantaneous particle velocities are shown in Figures 5.8 and 5.9. Note that the z_{linear} used in these models were the total acoustic impedance of MPM 4 predicted using the more accurate method developed in Chapter 3 given by Equation (3.31).

Figure 5.8 illustrates that the amplitude of the particle velocity within the perforations

varies with frequency. It also increases with the increase of the input voltage and incident SPL. Valleys are observed around 1250 Hz, where the structural tube resonance occurs. The phase of the particle velocity within the perforations is shown in Figure 5.9. When the input voltage and the incident SPL are relatively small (close to the linear regime), the phase of the particle velocity changes rapidly in the frequency range from 800 Hz to 1 kHz. In contrast, the phase of the particle velocity changes smoothly with high input voltage and the arising high incident SPL in the non-linear regime.

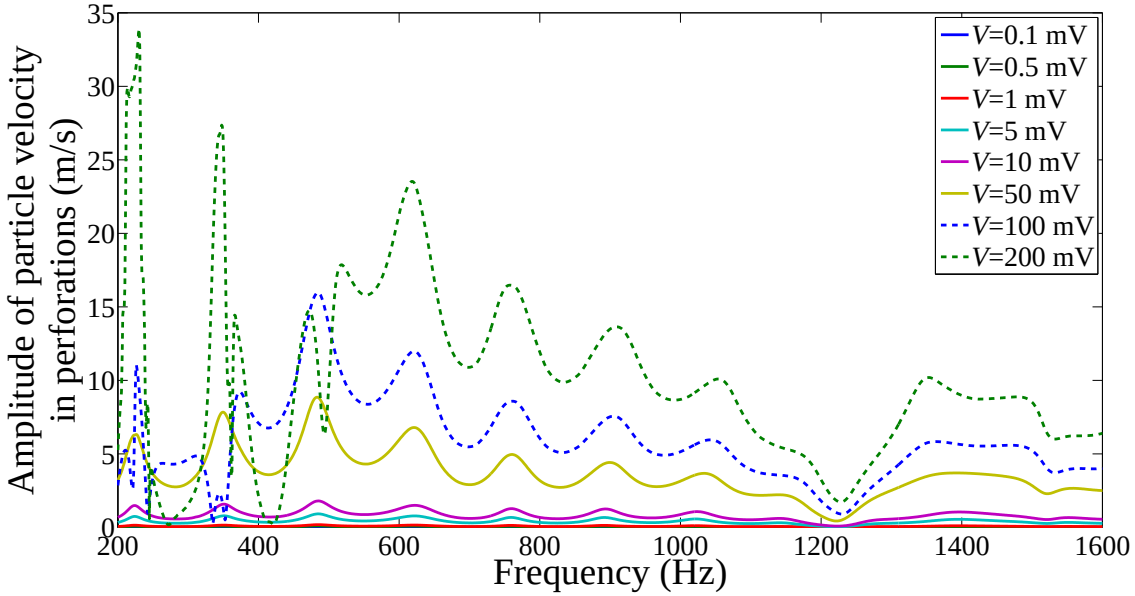

Figure 5.8: Amplitude of the instantaneous particle velocity within the perforations of the MPM sample with stepped sine sweep excitation. The input voltage varied from 0.1 mV to 200 mV.

The comparisons of the predicted results and the measured results for various input voltages are shown in Figures 5.10 to 5.15. Figure 5.10 illustrates the measured and predicted sound absorption coefficient of the MPM with an input voltage of 1 mV. Since the input voltage is relatively low, the acoustic impedance and the sound absorption coefficient are linear. Similar to the case of the MPM excited by the broadband sound signal in the linear regime presented in Section 5.3, Maa's and Tayong et al.'s models are less accurate than the other models because of their inaccurate prediction for the linear acoustic impedance of the MPM. In Ingard & Ising's model, the linear acoustic impedance of the MPM is predicted using the no-slip method developed in Chapter 3, and hence this model shows a better agreement than Maa's and Tayong et al.'s models. However, the coefficient of the particle

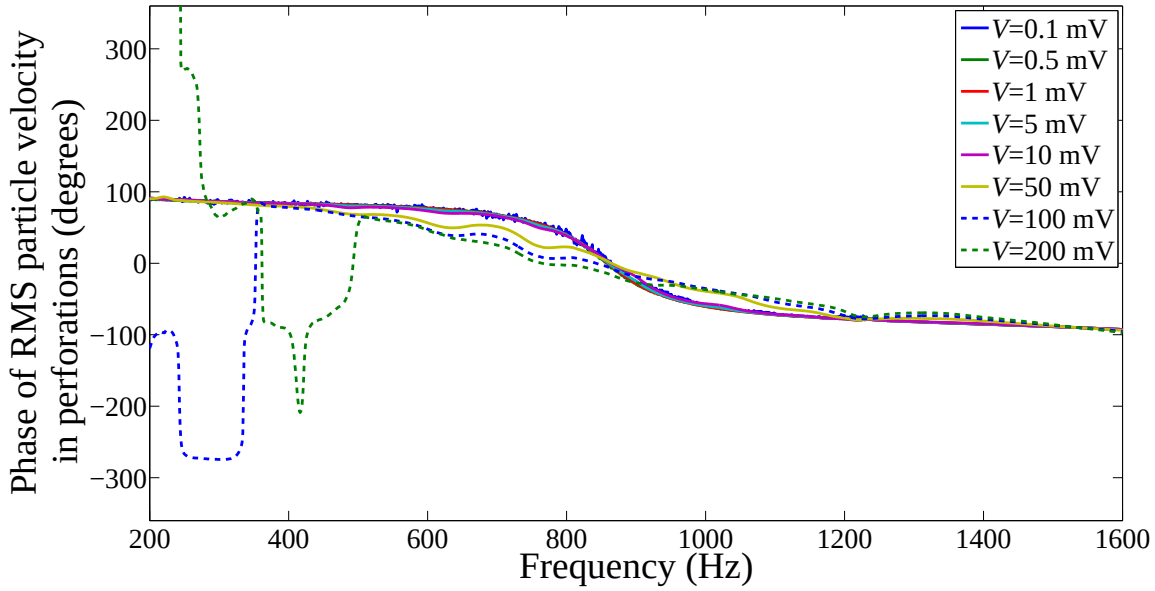

Figure 5.9: Phase of the instantaneous particle velocity within the perforations of the MPM sample with stepped sine sweep excitation. The input voltage varied from 0.1 mV to 200 mV.

velocity amplitude in Ingard & Ising's model is equal to ρ_0 which is relatively high, in comparison to the other models which affects the sound absorption prediction. The predicted results using the presented simplified and analytical models better agree with the measured results in comparison to the other models. Although the particle velocity is higher than that in the cases with a broadband sound signal, the multiplicative terms for the particle velocity in these two models are small. Therefore, the non-linear effect due to the particle velocity are reduced in the presented simplified and analytical models, which is consistent with the physical phenomenon and the experimental results.

Figures 5.11 to 5.15 show the comparison between the measured and predicted results using the models. Similar to the case of the MPM excited by a broadband sound signal, the two presented models are more accurate than the other models in the non-linear regime. The increased accuracy of these models is ascribed to the optimised parameters. The non-linear effect on the acoustic impedance of the MPM due to the high particle velocity is simulated using two factors for which physical meanings are unknown in the presented simplified curve fitting model. However, in the presented analytical model, the factors are assumed to represent the air density variation in time domain and in the length direction in spatial domain. Hence, although the developed analytical model is slightly less accurate than the simplified

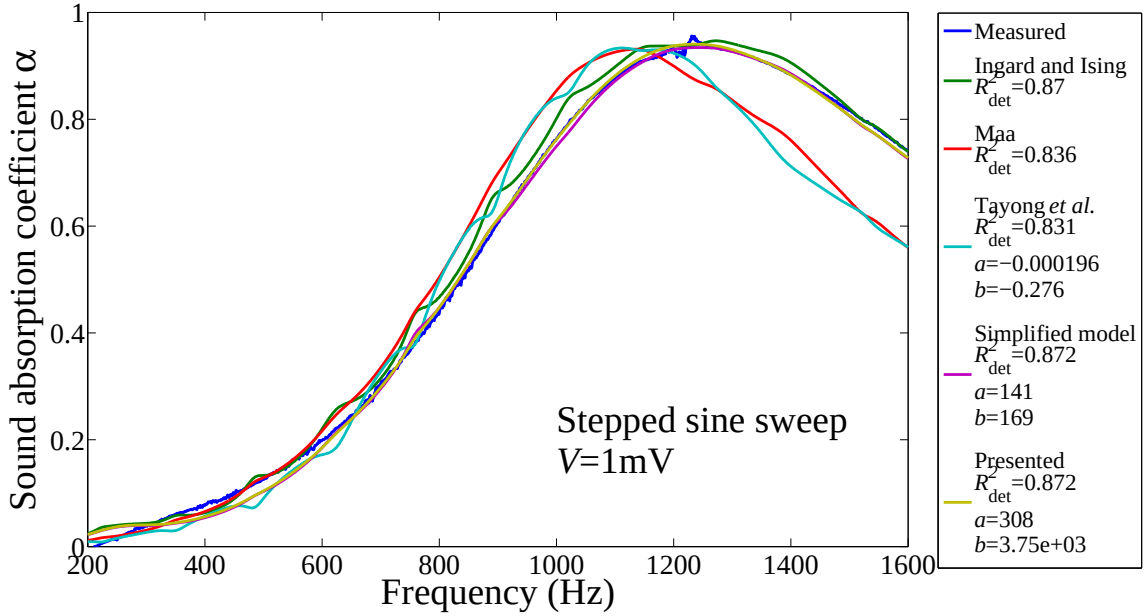

Figure 5.10: Predicted and measured sound absorption coefficients of the MPM sample with a stepped sine sweep excitation. The input voltage was 1 mV. This is in the linear regime.

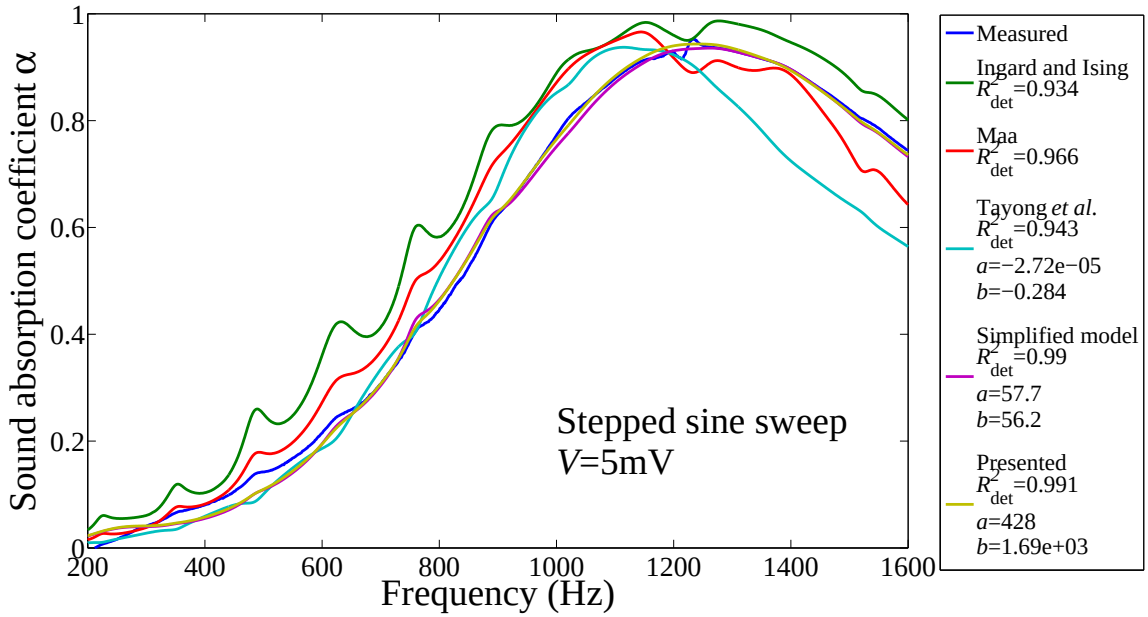

Figure 5.11: Predicted and measured sound absorption coefficients of the MPM sample with stepped sine sweep excitation. The input voltage was 5 mV.

curve fitting model in Figure 5.15, it could be more reasonable than the latter due to its clearer physical meaning. The decreasing accuracy of the two presented models may indicate that these models are valid for a limited range of the particle velocity. If the particle velocity is sufficiently high, the Reynolds number of the particle velocity could be high and the fluid dynamics within the holes and neighbouring vicinity could be different from the

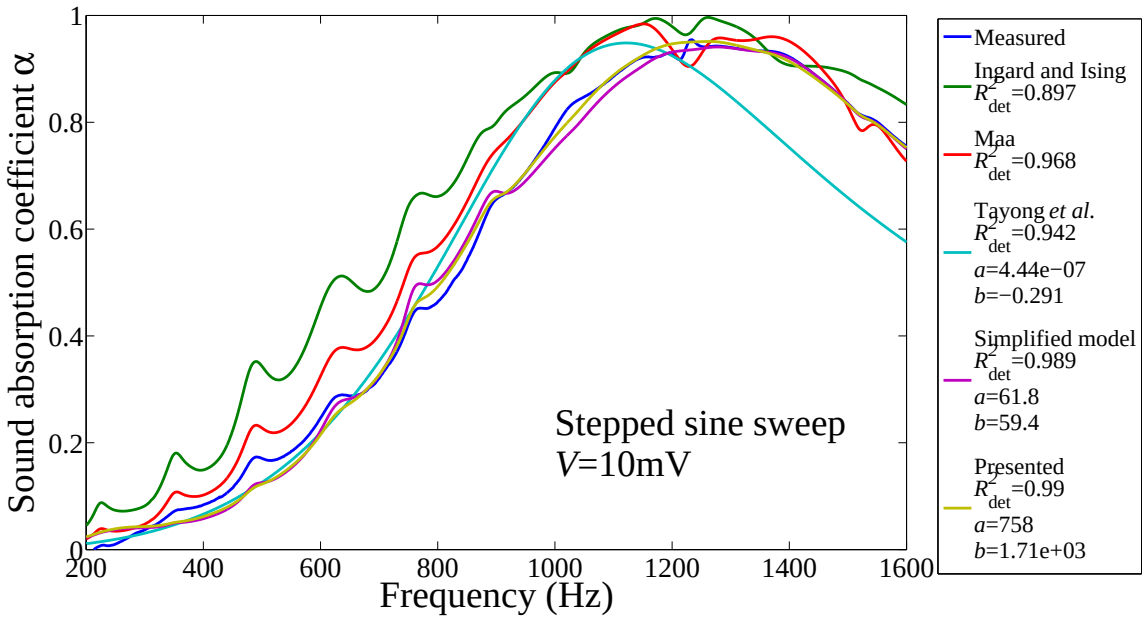

Figure 5.12: Predicted and measured sound absorption coefficients of the MPM sample with stepped sine sweep excitation. The input voltage was 10 mV.

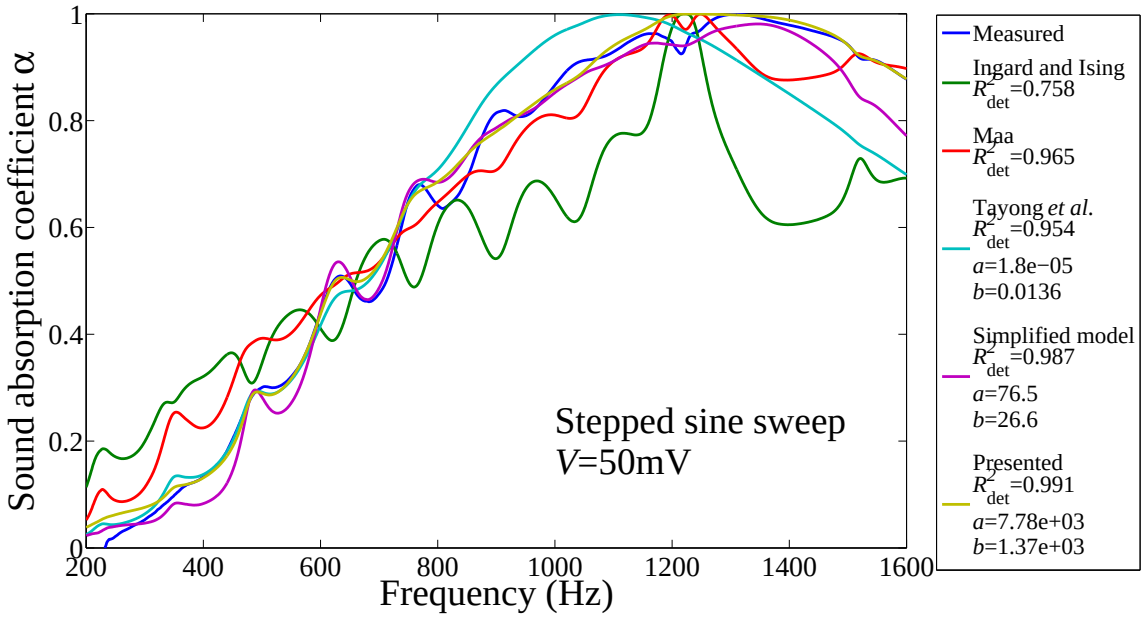

Figure 5.13: Predicted and measured sound absorption coefficients of the MPM sample with stepped sine sweep excitation. The input voltage was 50 mV.

case investigated in this study.

Figure 5.16 illustrates the air density variations in the time domain and in the length direction in the spatial domain, respectively. The air density variation in the time domain is small in the linear regime and increases with the increase of the input voltage and the incident SPL in the non-linear regime. This trend is consistent with that in the case of the MPM

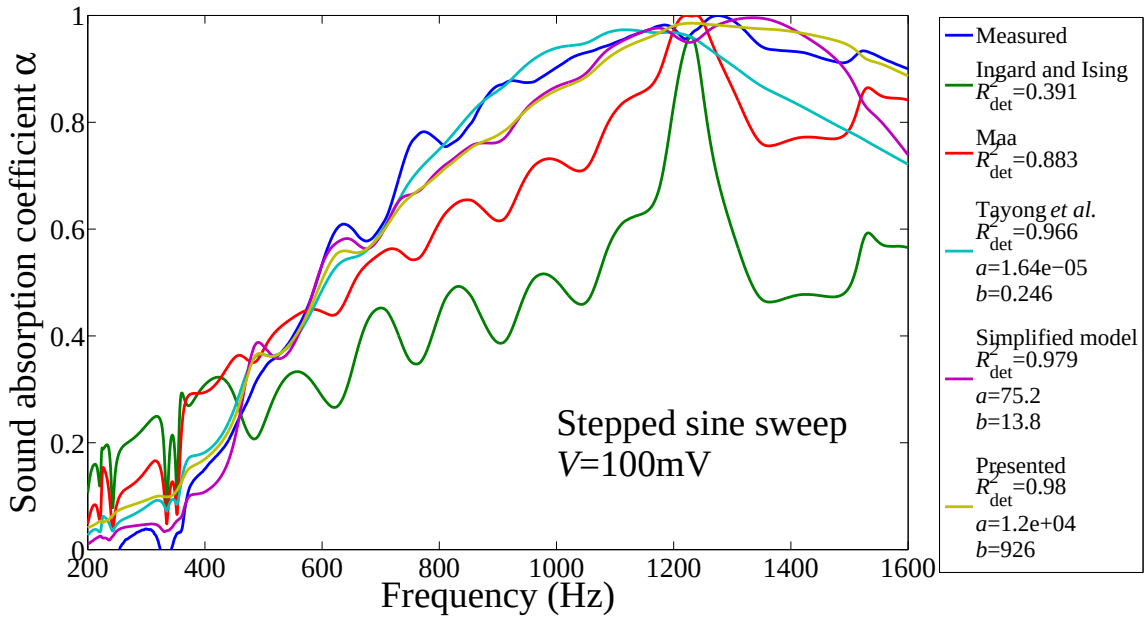

Figure 5.14: Predicted and measured sound absorption coefficients of the MPM sample with stepped sine sweep excitation. The input voltage was 100 mV.

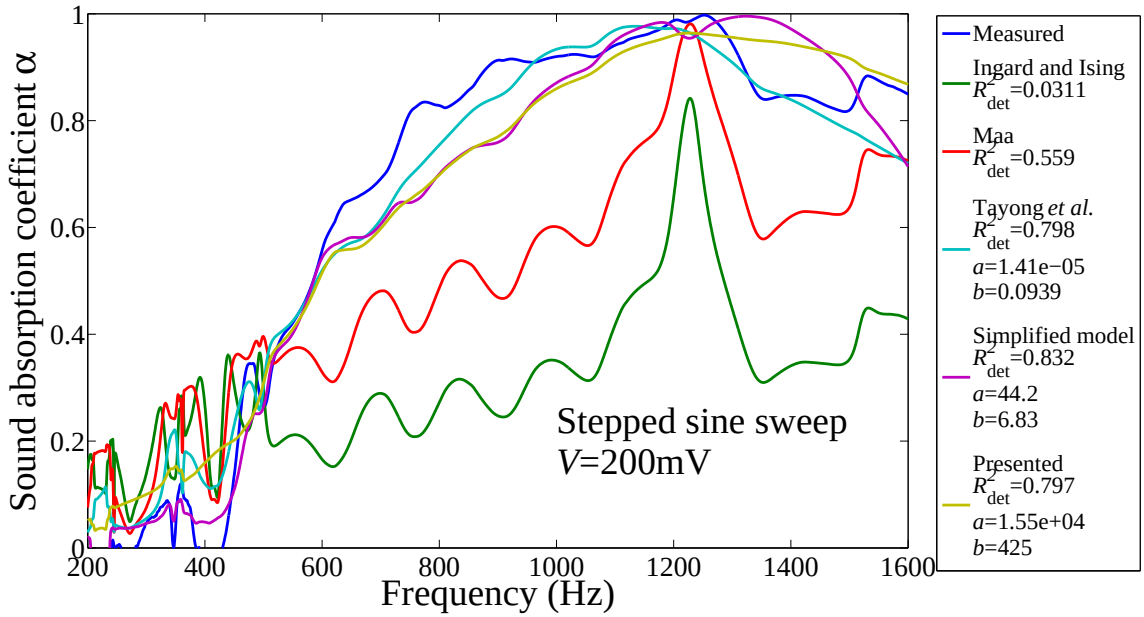

Figure 5.15: Predicted and measured sound absorption coefficients of the MPM sample with stepped sine sweep excitation. The input voltage was 200 mV.

excited by white noise. The air density variation in the length direction in the spatial domain is roughly constant and is close to zero, which implies that the density in the length direction not vary significantly. This can possibly be ascribed to the decoupled frequency response when monochromatic sound signals are used. The fluid dynamics in the perforations and on the MPM surface with the monochromatic sound signal are only related to the frequency

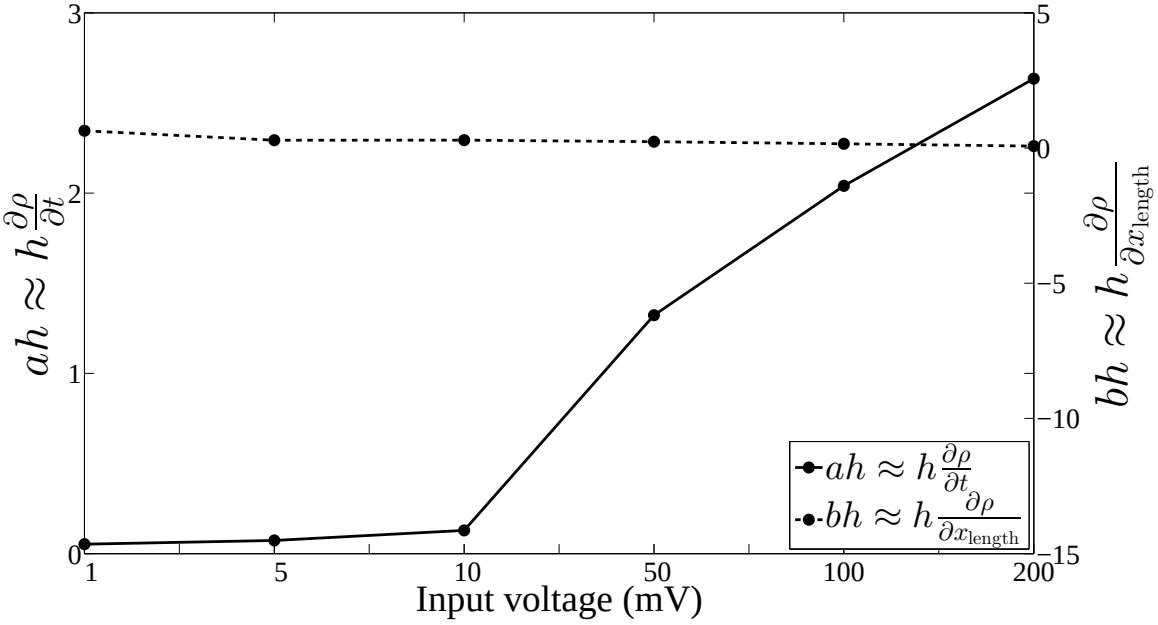

Figure 5.16: The values of $ah \approx h\frac{\partial \rho}{\partial t}$ and $bh \approx h\frac{\partial \rho}{\partial x_{\text{length}}}$ using the optimised parameters for the MPM excited by a stepped sine sweep. Plotted at the same scale as Figure 5.7, the curves represent the total rates of air density change in the time and spatial domains, respectively.

response at the excitation frequencies, not the coupled frequency responses as is the case for broadband sound signals. Hence, the total variation of the air density in the spatial domain is small when the stepped sine sweep signal is used.

5.5 Conclusions

This chapter explores the analytical modelling of the acoustic impedance of MPMs excited by broadband and monochromatic sound signals in the non-linear regime. Two models are developed following different strategies. Since the physical meanings of some parameters in the previously published models are unknown, this chapter also aims to explore the physical meanings of the parameters in the models developed here.

Three previous models for the non-linear acoustic impedance of MPPs and orifices on rigid baffles are investigated, leading to the conclusion that the non-linear impedance of MPPs are assumed to be the sum of their linear acoustic impedance and the acoustic impedance due to the non-linear effect caused by the high air particle velocity within the perforations. Hence, the first presented model is based on this assumption. The non-linear impedance of MPMs is considered to be the sum of their linear impedance predicted by the no-slip method

discussed in Chapter 3, and the acoustic impedance due to the non-linear effect for which the real and imaginary part of the particle velocity within the perforations contribute to the total impedance differently. Although this model shows good agreement with the experimental results with broadband and monochromatic sound signals, the physical meanings of the optimised parameters are not evident.

The second presented analytical model is inspired by the air motion equation and the mass continuity equation considering the density variation in the time and spatial domains. These equations were derived by Maa (1996) but are solved differently in this chapter. Two parameters are used to represent the air density variations in the time domain and in the length direction in the spatial domain. After simplifying the derived expression, it is found that this expression is similar to the presented simplified model, but the parameters have clear physical meanings. The parameter a represents the air density variations in the time domain and the parameter b represents that in the length direction in the spatial domain. This model provides the most accurate predicted results among the models considered in this study, except in the case where the input voltage and the incident SPL are at their maximum value considered of 200 mV. The decreasing accuracy of the presented models at the maximum voltage of 200 mV might indicate the limit of these models. If the input voltage and the incident sound pressure are sufficiently high, the particle velocity will also be high, as well as the Reynolds number associated with the particle velocity. Hence, the fluid dynamics within the holes and in the neighbouring sound field could be different from the case investigated in this study and these two models might become invalid.

The two presented models have been validated using the experimental results obtained in Chapter 4. Good agreements are achieved using these presented models with both broadband and monochromatic sound signals in the non-linear regime. However, the second presented analytical model based on the motion equation and the mass continuity equation is physically meaningful. The optimised parameters represent the acoustic impedances due to the air density variations in the time and spatial domains. The former increases with the increase of the input voltage and incident SPL, with both broadband and monochromatic sound signals in the non-linear regime. The latter increases when the broadband sound signals are used for the coupling frequency response, and maintains a constant value close to zero when the monochromatic sound signals are used due to the decoupled frequency response.

This chapter developed two models for the prediction of the non-linear acoustic impedance of MPMs, following different strategies. The comparisons of the experimental and predicted results verifies that the presented models are able to predict the non-linear acoustic impedance of MPMs accurately. The presented analytical model provides clear physical meanings for its optimised parameters and offers a new strategy for the exploration for the physical phenomenon of the air fluid dynamics and non-linear acoustic impedance of MPMs in the non-linear regime.

Chapter 6

Sound transmission of double layer impervious membranes separated by an air cavity

6.1 Introduction

The sound absorption and transmission of finite-sized single layer impervious membranes has been studied in Chapter 2. An analytical model has been developed for the acoustic impedance of a finite-sized impervious membrane, with a constant tension over the membrane surface and internal damping due to the membrane curvature. The accuracy of the model has been verified by experimental results in normally-incident plane wave conditions and in a diffuse field. This chapter aims to investigate the sound transmission of double layer impervious membranes, separated by an air cavity, based on the developed model. The membranes and the air cavity are finite-sized and hence the acoustic cross modes of the cavity and the structural cross modes of the membrane are considered in this chapter. The modal analysis method is used in this chapter and the analytical model is developed in the Cartesian coordinate system. Experimental results of the sound transmission loss of double layer impervious membranes with different air cavity depths are presented to validate the developed model. Furthermore, an additional decay factor is included for the sound propagation in the air cavity. This decay factor represents the sound absorption by the wooden walls of the air cavity and is introduced to enhance the accuracy of the developed model.

Previous studies on the sound transmission of double layer impervious membranes are summarised in Section 6.1.1. The gaps arising from these previous studies and the academic contribution of this chapter are presented in Section 6.1.2. The analytical modelling for the

sound transmission loss of double layer impervious membranes separated by an air cavity starts in Section 6.2 with the modelling and the motion equations of each membrane and the air motion in the air cavity. By coupling the fluid (air) and structure (impervious membranes) motion, the expressions for the sound transmission coefficient and the sound transmission loss are derived for a normally-incident plane wave condition in Section 6.3. Section 6.3 indicates that the normal incidence STL model is inaccurate because the experimental STLs were measured in diffuse fields, and hence the effect of the incidence angle is considered in Section 6.4 and the STL expression for diffuse fields is obtained and validated in this section. Although the diffuse model shows good agreement with the measured results in the low frequency range, it underestimates the STL in the frequency range higher than 1.6 kHz. Hence, in Section 6.5, attenuation by air cavity walls is investigated. The model incorporating the sound absorbing walls provides a relatively good agreement with the experimental results at both low and high frequencies from 50 Hz to 10 kHz. Section 6.6 presents the conclusions arising from this chapter.

6.1.1 Literature review

Double layer partitions have been used as noise barriers in many industries including automotive, aerospace and building industries. The sound transmission properties of double layer structures have been studied for decades and it has been verified that double layer massive walls separated by an air cavity have better sound reduction than a single layer massive wall (Bies & Hansen 2009).

The STL of double layer massive walls with either normally-incident plane waves or in a diffuse field are classic problems in acoustics and have been investigated for many years (Bies & Hansen 2009, Kinsler et al. 1999, London 1950). Bolton et al. (1996) investigated the STL of aluminum double-panel structures and developed analytical models for different boundary conditions. These models show good agreement with experimental results.

Since the partitions are usually linked, the coupling condition of the partitions has been investigated. Wang et al. (2005) investigated double layer lightweight partitions with studs. The comparison of the predicted results using their model and previously published experimental data demonstrated the accuracy of their model. Similarly, Legault & Atalla (2010) developed an analytical model for the STL of double layer partitions connected by vibration

isolators and this model was also validated by experimental results.

Partitions can be made of many materials, such as masonry or concrete, metal panels and membranes. The previous studies predominantly focus on masonry and concrete walls, metal panels and sheets (Bies & Hansen 2009, Bolton et al. 1996, Kinsler et al. 1999, Legault & Atalla 2010, London 1950, Wang et al. 2005). As for the membrane partitions, Vries (2011) investigated the sound transmission loss of double layer membranes experimentally and compared the experimental results with the predicted results, using previously mentioned methods. However, as discussed in Chapter 2, when modelling membranes, tension and damping have been expressed differently in the previous studies. Chapter 2 introduced a new expression for the acoustic impedance of impervious membranes and this new expression has not been applied previously to the STL prediction of double layer membranes.

Note that although the transfer matrix method is preferred by other researchers when dealing with sound transmission and absorption of multiple layer structures (Lee & Xu 2009, Rousselet et al. 2014, Song & Bolton 2000), the modal analysis method is utilised in this chapter to consider the finite and cross mode effects on both the membrane motion and the sound propagation within the air cavity. The transfer matrix method is commonly used to simulate the multiple layer impedance as the product of the acoustic impedance in each layer as it is convenient to use and is favoured by many researchers (Lee & Xu 2009, Rousselet et al. 2014, Song & Bolton 2000). However, this method is limited to cases where the materials and the air cavities are assumed to be infinite normal to the solid surface and is inaccurate in a diffuse field and with complicated mechanical coupling conditions, as indicated by Sgard et al. (2000). Although Villot et al. (2001) provided a windowing method to expand the prediction from the normally-incident condition to the diffuse field, the calculation could be very complicated when dealing with the STL of double layer impervious membranes in a diffuse field. The transfer matrix method was extended to complicated mechanical coupling conditions by Vigran (2010) who used it to investigate a double-layer partition with sound bridges. Although good agreement was achieved between the experimental and predicted results using Vigran's method, the calculation process was complicated due to the finite effects and complicated boundary conditions. The transfer matrix method shows limited advantages in finite cases, in the diffuse field and with complicated coupling conditions. Therefore, modal superposition analysis is utilised in this chapter rather than

the transfer matrix method because the finite sizes of the impervious membranes and the air cavity have significant impact on the STL prediction.

6.1.2 Gaps and contributions

This chapter investigates the STL of double layer impervious membranes separated by an air cavity, considering the effects of the cavity depth and pressurisation of the air cavity on the STL. The analytical model for the membrane motion developed in Chapter 2 is applied here to simulate these impervious membranes, which implies that the constant tension and the internal damping due to the membrane curvature are incorporated in the model for the double layer impervious membrane in Sections 6.2.1 and 6.2.3.

Assuming a normally-incident plane wave excitation, the fluid air and impervious membrane structure motions are coupled and the expressions for the sound transmission coefficient and the sound transmission loss are derived in Section 6.3. To assess the performance of the developed model, STL measurements were conducted in reverberation chambers as mentioned in Chapter 2. The STLs were measured for double layer impervious membranes separated by an air cavity. The two cavity depths considered were 70 mm and 140 mm. The impervious membranes were made of the same material as described in Chapter 2. However, since the membrane samples were mounted differently from the samples used in the previous chapters and the tension and internal damping could be sensitive to the mounting condition, numerical optimisation was applied in this chapter to estimate the tension and internal damping. Since the STLs were measured in diffuse fields (in reverberation chambers), the normal incidence STL model is inaccurate due to the omission of the incidence angle. Hence, the effect of the incidence angle is considered in Section 6.4. The STL expression in diffuse fields is derived and validated in this section. Good agreement between the predicted and measured results is achieved in the low frequency range. However, this model underestimates the STL in the frequency range higher than 1.6 kHz. The underestimation is ascribed to the walls of the air cavity. In the previous derivation detailed in Section 6.4, the walls are assumed to be perfectly acoustically rigid. However, for the experiments undertaken in this research, they are made of wood, which implies that they can absorb sound to some degree. Hence, the sound propagation within the air cavity decays in practice and neglecting sound decay in the cavity leads to the underestimation of the STL of this model.

In Section 6.5, the air cavity walls are assumed to be sound absorbing and the effect of these sound absorbing walls on the STL is investigated. A model considering the sound absorbing walls was developed by re-deriving the air particle motion equations in the air cavity. The results of this model are also compared with the experimental results and are in relatively good agreement at frequencies between 50 Hz and 10 kHz, thus covering both low and high frequencies.

This chapter is concluded in Section 6.6. The investigation increases our understanding of the mechanism of membrane structures separated by a cavity. The effect of sound absorbing walls of the air cavity on the STL is studied. Therefore, the model developed in this chapter is helpful for the prediction of STL in practice.

6.2 Analytical modelling and motion equations of double layer impervious membranes and the air cavity separating the membranes

This section investigates the analytical modelling of double layer impervious membranes separated by a finite-sized air cavity. The motion equation of each membrane and that of the air motion within the cavity are developed and solved analytically. The modelling was derived in the Cartesian coordinate system.

Figure 6.1 illustrates the transmission and reflection of a normally-incident plane wave in the double layer impervious membrane structure. Two impervious membranes, Membrane 1 and 2, are parallel to each other, separated by an air cavity of depth D.

When a sound wave p_i is normally incident on Membrane 1 of the double layer impervious membrane structure, part of the sound energy is transmitted through Membrane 1 and part is reflected back (p_r), as in the case of single layer impervious membranes discussed in Chapter 2. However, unlike the single layer impervious membranes studied in Chapter 2, the sound wave transmitted through Membrane 1 is then incident on Membrane 2 and is named as p_{i2}. The sound wave p_{i2} propagates in the finite-sized air cavity and is incident on the surface of Membrane 2. The incident sound p_{i2} is partly reflected back by Membrane 2 and is also partly transmitted though Membrane 2. The transmitted sound is p_t and the reflected sound is p_{r2}. Therefore, two sound waves exist in the air cavity: the incident sound

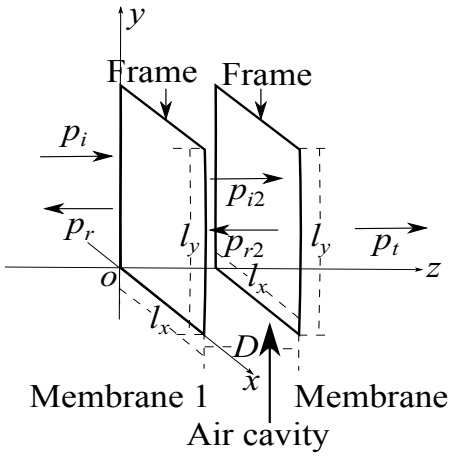

Figure 6.1: Sound transmission of double layer impervious membranes separated by a finite air cavity of a depth D. The sound wave is normally incident on the surface of Membrane 1.

on Membrane 2, p_{i2}, and the reflected sound, p_{r2}. Since the sound wave propagation in the cavity can be predicted for a constant cavity depth D, it is possible to estimate the sound pressures on the membrane surfaces in the air cavity.

The mechanism of each membrane motion is a forced vibration. The force is provided by the sound pressure difference between the two surfaces of each membrane. Hence, the motion equation of each membrane can be solved accordingly. The detailed derivation is presented in the following sections.

6.2.1 Motion of Membrane 1 at $z = 0$

Assuming that Membrane 1 is placed at $z = 0$ and is parallel to the xy plane in Figure 6.1, it is excited by the pressure difference between the incident sound p_i, the reflected sound p_r, the transmitted sound p_{i2}, which is also the incident sound on Membrane 2, and the sound p_{r2} reflected by Membrane 2. Letting the displacement of Membrane 1 be $\xi_1(x,y)$, the velocity of Membrane 1, $v_1(x,y)$, is expressed as

$$v_1(x,y) = j\omega\xi_1(x,y). \tag{6.1}$$

Based on the continuity of the air particle velocity in the normal direction (i.e., the z direction), the relationship between the sound pressures and $v_1(x,y)$ on each surface of Membrane 1 is given by (Fahy & Gardonio 2007)

$$\frac{p_i - p_r}{\rho_0\, c_0} = v_1(x,y) = j\omega\xi_1(x,y) \tag{6.2}$$

on the upstream surface facing the sound source and (Fahy & Gardonio 2007)

$$\frac{p_{i2} - p_{r2}}{\rho_0 \, c_0} = v_1(x,y) = j\omega\xi_1(x,y) \tag{6.3}$$

on the other side facing the air cavity. Assuming that the incident sound pressures p_i and p_{i2} are known, Equations (6.2) and (6.3) are rewritten as

$$p_r = p_i - v_1(x,y) \, \rho_0 \, c_0 \tag{6.4}$$

and

$$p_{r2} = p_{i2} - v_1(x,y) \, \rho_0 \, c_0. \tag{6.5}$$

Therefore, the sound pressure difference on Membrane 1, Δp_1, is obtained as (Fahy & Gardonio 2007)

$$\begin{aligned} \Delta p_1 &= p_i + p_r - (p_{i2} + p_{r2}) \\ &= 2 \, p_i - v_1(x,y) \, \rho_0 \, c_0 - 2 \, p_{i2} + v_1(x,y) \, \rho_0 \, c_0 \\ &= 2 \, p_i - 2 \, p_{i2}. \end{aligned} \tag{6.6}$$

Substituting Equation (6.6) into the left hand side of Equation (2.26) yields the motion equation of Membrane 1 which is given by

$$(T + 2j\omega\eta)\nabla^2\xi_1(x,y) + \omega^2\rho_{s1}\xi_1(x,y) = -\Delta p = -2 \, p_i + 2 \, p_{i2}, \tag{6.7}$$

where ρ_{s1} is the surface density of Membrane 1. Similarly to Equation (2.61), the solution of Equation (6.7) is expressed in modal form by (Lee et al. 2005)

$$\xi_1(x,y) = \sum_{n=1}^{N} A_{n1} \, \xi_{n1}(x,y), \tag{6.8}$$

where (Lee et al. 2005)

$$\xi_{n1}(x,y) = \sin(\frac{n_x \pi}{l_x} x) \sin(\frac{n_y \pi}{l_y} y). \tag{6.9}$$

Following the approach of Zhang et al. (2012), the modal components are vectorised via $n = N_y(n_x - 1) + n_y$, where n_x and n_y are the modal indices in the x- and the y-axes, N_x is the maximum mode number of n_x and N_y is the maximum mode number of n_y and $N = N_x \times N_y$. Note that in Equation (6.8), the variable A_{n1} is initially unknown.

Substituting Equation (6.9) into Equation (6.7) gives

$$(T+2j\omega\eta)\nabla^2\sum_{n=1}^{N}A_{n1}\,\xi_{n1}(x,y)+\omega^2\rho_{s1}\sum_{n=1}^{N}A_{n1}\,\xi_{n1}(x,y)=-2\;p_i+2\;p_{i2}. \tag{6.10}$$

Multiplying each side of Equation (6.10) by $\xi_m(x,y)$ as defined by Equation (2.71) and integrating over the membrane surface area gives

$$\begin{aligned}(T+2j\omega\eta)\int_0^{l_x}\int_0^{l_y}\xi_m(x,y)\nabla^2\sum_{n=1}^{N}A_{n1}\,\xi_{n1}(x,y)\mathrm{d}x\mathrm{d}y+\\ \omega^2\rho_s\int_0^{l_x}\int_0^{l_y}\xi_m(x,y)\sum_{n=1}^{N}A_{n1}\,\xi_{n1}(x,y)\mathrm{d}x\mathrm{d}y\\ =-2\int_0^{l_x}\int_0^{l_y}(p_i-p_{i2})\,\xi_m(x,y)\mathrm{d}x\mathrm{d}y.\end{aligned} \tag{6.11}$$

As presented in Chapter 2, Equation (6.11) can be solved in matrix form. The unknown variable A_{n1} is rewritten in the form of an $N\times 1$ vector

$$\mathbf{A_1}=\begin{pmatrix}A_{n1_1}\\A_{n1_2}\\A_{n1_3}\\\vdots\\A_{n1_N}\end{pmatrix}. \tag{6.12}$$

Hence, Equation (6.11) is rewritten in matrix form as

$$\left[(T+2j\omega\eta)\boldsymbol{\psi_1}+\omega^2\rho_{s1}\boldsymbol{\psi_2}\right]\mathbf{A_1}=-2p_i\mathbf{D}+2\int_0^{l_x}\int_0^{l_y}p_{i2}\xi_m(x,y)\mathrm{d}x\mathrm{d}y, \tag{6.13}$$

where

$$C_n=-\left(\frac{n_x\pi}{l_x}\right)^2-\left(\frac{n_y\pi}{l_y}\right)^2,\qquad n=N_y(n_x-1)+n_y, \tag{6.14}$$

$$\boldsymbol{\psi_1}=\begin{pmatrix}C_1\int_0^{l_x}\int_0^{l_y}\xi_1(x,y)\xi_{n1_1}(x,y)\mathrm{d}x\mathrm{d}y & C_2\int_0^{l_x}\int_0^{l_y}\xi_1(x,y)\xi_{n1_2}(x,y)\mathrm{d}x\mathrm{d}y & \dots & C_n\int_0^{l_x}\int_0^{l_y}\xi_1(x,y)\xi_{n1_n}(x,y)\mathrm{d}x\mathrm{d}y\\ C_1\int_0^{l_x}\int_0^{l_y}\xi_2(x,y)\xi_{n1_1}(x,y)\mathrm{d}x\mathrm{d}y & C_2\int_0^{l_x}\int_0^{l_y}\xi_2(x,y)\xi_{n1_2}(x,y)\mathrm{d}x\mathrm{d}y & \dots & C_n\int_0^{l_x}\int_0^{l_y}\xi_2(x,y)\xi_{n1_n}(x,y)\mathrm{d}x\mathrm{d}y\\ \vdots & \vdots & \ddots & \vdots\\ C_1\int_0^{l_x}\int_0^{l_y}\xi_m(x,y)\xi_{n1_1}(x,y)\mathrm{d}x\mathrm{d}y & C_2\int_0^{l_x}\int_0^{l_y}\xi_m(x,y)\xi_{n1_2}(x,y)\mathrm{d}x\mathrm{d}y & \dots & C_n\int_0^{l_x}\int_0^{l_y}\xi_m(x,y)\xi_{n1_n}(x,y)\mathrm{d}x\mathrm{d}y\end{pmatrix}, \tag{6.15}$$

$$\boldsymbol{\psi_2} = \begin{pmatrix} \int_0^{l_x}\int_0^{l_y} \xi_1(x,y)\xi_{n1_1}(x,y)\mathrm{d}x\mathrm{d}y & \int_0^{l_x}\int_0^{l_y} \xi_1(x,y)\xi_{n1_2}(x,y)\mathrm{d}x\mathrm{d}y & \dots & \int_0^{l_x}\int_0^{l_y} \xi_1(x,y)\xi_{n1_n}(x,y)\mathrm{d}x\mathrm{d}y \\ \int_0^{l_x}\int_0^{l_y} \xi_2(x,y)\xi_{n1_1}(x,y)\mathrm{d}x\mathrm{d}y & \int_0^{l_x}\int_0^{l_y} \xi_2(x,y)\xi_{n1_2}(x,y)\mathrm{d}x\mathrm{d}y & \dots & \int_0^{l_x}\int_0^{l_y} \xi_2(x,y)\xi_{n1_n}(x,y)\mathrm{d}x\mathrm{d}y \\ \vdots & \vdots & \ddots & \vdots \\ \int_0^{l_x}\int_0^{l_y} \xi_m(x,y)\xi_{n1_1}(x,y)\mathrm{d}x\mathrm{d}y & \int_0^{l_x}\int_0^{l_y} \xi_m(x,y)\xi_{n1_2}(x,y)\mathrm{d}x\mathrm{d}y & \dots & \int_0^{l_x}\int_0^{l_y} \xi_m(x,y)\xi_{n1_n}(x,y)\mathrm{d}x\mathrm{d}y \end{pmatrix}. \tag{6.16}$$

and

$$\mathbf{D} = \int_0^{l_x}\int_0^{l_y} \xi_m(x,y)\mathrm{d}x\mathrm{d}y = \begin{pmatrix} \int_0^{l_x}\int_0^{l_y} \xi_1(x,y)\mathrm{d}x\mathrm{d}y \\ \int_0^{l_x}\int_0^{l_y} \xi_2(x,y)\mathrm{d}x\mathrm{d}y \\ \vdots \\ \int_0^{l_x}\int_0^{l_y} \xi_m(x,y)\mathrm{d}x\mathrm{d}y \end{pmatrix}. \tag{6.17}$$

Equation (6.13) represents the coupling between the forced membrane vibration and the sound field in the air cavity. The expression for p_{i2} is further discussed in the following section.

6.2.2 Sound propagation in the finite air cavity

This section investigates the sound propagation within the finite air cavity. It is assumed that the cavity has the same cross section as the impervious membranes. Hence the width and length of the air cavity are l_x and l_y. As discussed previously, there are two sound waves propagating in the z-direction in the cavity, namely p_{i2} and p_{r2}. Note that their directions are opposite. The former travels in the positive z-direction and the latter in the negative z-direction.

Since the cross section area of the panels under investigation is $l_x \times l_y = 1 \times 1.5$ m^2 = 1.5 m^2, the sound propagations follows the 3-D standing wave theory in the frequency range of interest here which is up to 10 kHz. The motion equation of air particles (Kinsler et al. 1999) is given by (Kinsler et al. 1999)

$$\nabla^2 p(x,y,z,t) = \frac{1}{c_0^2}\frac{\partial^2 p(x,y,z,t)}{\partial t^2}, \tag{6.18}$$

where $p(x,y,z,t) = p(x,y,z)\,e^{j\omega t}$. Eliminating the time variable t yields (Kinsler et al. 1999)

$$\nabla^2 p(x,y,z) = \frac{-\omega^2}{c_0^2} p(x,y,z). \tag{6.19}$$

Letting $k_0 = \frac{\omega}{c_0}$ and substituting this into Equation (6.19), the motion equation is rewritten as

(Kinsler et al. 1999)

$$\nabla^2 p(x,y,z) + k_0^2 p(x,y,z) = 0. \tag{6.20}$$

The Laplace operator in the Cartesian coordinate system is given by (Kinsler et al. 1999)

$$\nabla^2 p(x,y,z) = \frac{\partial^2 p(x,y,z)}{\partial x^2} + \frac{\partial^2 p(x,y,z)}{\partial y^2} + \frac{\partial^2 p(x,y,z)}{\partial z^2}. \tag{6.21}$$

Assuming that the sound pressure in each dimension is independent of the other, $p(x,y,z)$ is rewritten as

$$p(x,y,z) = X_0(x)Y_0(y)Z_0(z), \tag{6.22}$$

where $X_0(x)$ denotes the sound pressure component in the x-direction within the cavity, $Y_0(x)$ denotes that in the y-direction and $Z_0(x)$ denotes that in the z-direction. Substituting Equation (6.22) into Equation (6.21) gives

$$\nabla^2 p(x,y,z) = Y_0(y)Z_0(z)\frac{\partial^2 X_0(x)}{\partial x^2} + X_0(x)Z_0(z)\frac{\partial^2 Y_0(y)}{\partial y^2} + X_0(x)Y_0(y)\frac{\partial^2 Z_0(z)}{\partial z^2}. \tag{6.23}$$

Similarly, k_0 is expressed in the form of the sum of three independent components in the x-, y- and z-directions as (Kinsler et al. 1999)

$$k_0^2 = k_{0x}^2 + k_{0y}^2 + k_{0z}^2, \tag{6.24}$$

where k_{0x} is the component of k_0 in the x-direction within the cavity, k_{0y} is that of k_0 in the y-direction and k_{0z} is that of k_0 in the z-direction.

Substituting Equations (6.22), (6.23) and (6.24) into Equation (6.20), it is rewritten as

$$\begin{aligned} Y_0(y)Z_0(z)\frac{\partial^2 X_0(x)}{\partial x^2} + X_0(x)Z_0(z)\frac{\partial^2 Y_0(y)}{\partial y^2} + X_0(x)Y_0(y)\frac{\partial^2 Z_0(z)}{\partial z^2} \\ + \left(k_{0x}^2 + k_{0y}^2 + k_{0z}^2\right) X_0(x)Y_0(y)Z_0(z) = 0. \end{aligned} \tag{6.25}$$

Hence, Equation (6.25) is rearranged as

$$\begin{aligned} Y_0(y)Z_0(z)\left[\frac{\partial^2 X_0(x)}{\partial x^2} + k_{0x}^2 X_0(x)\right] + X_0(x)Z_0(z)\left[\frac{\partial^2 Y_0(y)}{\partial y^2} + k_{0y}^2 Y_0(y)\right] \\ + X_0(x)Y_0(y)\left[\frac{\partial^2 Z_0(z)}{\partial z^2} + k_{0z}^2 Z_0(z)\right] = 0. \end{aligned} \tag{6.26}$$

Therefore, to satisfy Equation (6.26), the following equations are obtained

$$\frac{\partial^2 X_0(x)}{\partial x^2} + k_{0x}^2 X_0(x) = 0, \tag{6.27a}$$

$$\frac{\partial^2 Y_0(y)}{\partial y^2} + k_{0y}^2 Y_0(y) = 0, \tag{6.27b}$$

$$\frac{\partial^2 Z_0(z)}{\partial z^2} + k_{0z}^2 Z_0(z) = 0. \tag{6.27c}$$

Assuming the air cavity has acoustically rigid boundaries parallel to the x- and y-axes and the sound is travelling mainly in the z-direction, the solutions of Equation (6.27) are assumed to be

$$X_0(x) = A_{0x}\cos(k_{0x}x) + B_{0x}\sin(k_{0x}x), \tag{6.28a}$$

$$Y_0(y) = A_{0y}\cos(k_{0y}y) + B_{0y}\sin(k_{0y}y), \tag{6.28b}$$

$$Z_0(z) = A_{0z}e^{-jk_{0z}z}, \tag{6.28c}$$

where A_{0x}, B_{0x}, A_{0y}, B_{0y} and A_{0z} are dependent on the boundary conditions.

Since the cavity is assumed to be acoustically rigid, the boundary conditions at the cross section boundaries are

$$v_x(x = 0) = 0, \tag{6.29a}$$

$$v_x(x = l_x) = 0, \tag{6.29b}$$

and

$$v_y(y = 0) = 0, \tag{6.30a}$$

$$v_y(y = l_y) = 0, \tag{6.30b}$$

where v_x denotes the air particle velocity in the x direction within the air cavity and v_y denotes that in the y direction. Moreover, considering continuity in the normal direction (i.e., the z direction), two more boundary conditions are obtained, which are

$$v_z(z = 0) = v_1(x, y), \tag{6.31a}$$

$$v_z(z = D) = v_2(x, y), \tag{6.31b}$$

where $v_1(x, y)$ denotes the velocity of Membrane 1 and $v_2(x, y)$ denotes the velocity of Membrane 2. Equations (6.31) indicate the coupling between the air particle velocities within the cavity and that at the two membrane surfaces.

Hence, to apply the boundary conditions, it is crucial to calculate the particle velocity in the x, y and z directions appropriately. The particle velocities in the x, y and z directions are defined as (Kinsler et al. 1999)

$$v_x = -\frac{1}{\rho_0}\int \frac{\partial p(x,y,x,t)}{\partial x}\mathrm{d}t, \tag{6.32a}$$

$$v_y = -\frac{1}{\rho_0}\int \frac{\partial p(x,y,x,t)}{\partial y}\mathrm{d}t, \tag{6.32b}$$

$$v_z = -\frac{1}{\rho_0}\int \frac{\partial p(x,y,x,t)}{\partial z}\mathrm{d}t. \tag{6.32c}$$

Substituting Equations (6.22) and (6.28a) into Equation (6.32a) yields the particle velocity in the x direction, which is given by

$$\begin{aligned} v_x &= -\frac{Y_0(y)Z_0(z)}{\rho_0}\int \frac{\partial X_0(x)e^{j\omega t}}{\partial x}\mathrm{d}t \\ &= -\frac{Y_0(y)Z_0(z)}{\rho_0}\int \frac{\partial A_{0x}\cos(k_{0x}x)+B_{0x}\sin(k_{0x}x)}{\partial x}e^{j\omega t}\mathrm{d}t \\ &= -\frac{Y_0(y)Z_0(z)}{\rho_0}k_{0x}\left[-A_{0x}\sin(k_{0x}x)+B_{0x}\cos(k_{0x}x)\right]\int e^{j\omega t}\mathrm{d}t \\ &= \frac{Y_0(y)Z_0(z)}{j\omega\rho_0}k_{0x}\left[A_{0x}\sin(k_{0x}x)-B_{0x}\cos(k_{0x}x)\right]e^{j\omega t}. \end{aligned} \tag{6.33}$$

Eliminating the time variable $e^{j\omega t}$, the particle velocity in the x direction is expressed as

$$v_x = \frac{Y_0(y)Z_0(z)}{j\omega\rho_0}k_{0x}\left[A_{0x}\sin(k_{0x}x)-B_{0x}\cos(k_{0x}x)\right]. \tag{6.34}$$

Similarly, the particle velocity in the y direction is obtained as

$$v_y = \frac{X_0(x)Z_0(z)}{j\omega\rho_0}k_{0y}\left[A_{0y}\sin(k_{0y}y)-B_{0y}\cos(k_{0y}y)\right]. \tag{6.35}$$

Substituting Equation (6.34) into Equation (6.29a) yields

$$v_x(x=0) = \frac{Y_0(y)Z_0(z)}{j\omega\rho_0}k_{0x}(-B_{0x}) = 0. \tag{6.36}$$

Hence, $B_{0x}=0$. Substituting Equation (6.34) into Equation (6.29b) yields

$$v_x(x=l_x) = \frac{Y_0(y)Z_0(z)}{j\omega\rho_0}k_{0x}A_{0x}\sin(k_{0x}l_x) = 0. \tag{6.37}$$

Hence, to satisfy $\sin(k_{0x}l_x)=0$, it is necessary to let $k_{0x}l_x = u_x\pi$ where u_x is the mode number of air propagation in the x direction. Consequently,

$$k_{0x} = \frac{u_x\pi}{l_x} \qquad \text{where } u_x = 0,1,2,\cdots, \tag{6.38}$$

and the sound pressure component in the x direction is expressed as

$$X_0(x) = A_{0x}\cos\left(\frac{u_x\pi}{l_x}x\right). \tag{6.39}$$

Similarly, substituting Equation (6.35) into Equation (6.30a) yields

$$v_y(y=0) = \frac{X_0(x)Z_0(z)}{j\omega\rho_0}k_{0y}(-B_{0y}) = 0. \tag{6.40}$$

Hence, $B_{0y} = 0$. Substituting Equation (6.40) into Equation (6.30b) yields

$$v_y(y=l_y) = \frac{X_0(x)Z_0(z)}{j\omega\rho_0}k_{0y}A_{0y}\sin(k_{0y}l_y) = 0. \tag{6.41}$$

Hence, to satisfy $\sin(k_{0y}l_y) = 0$, it is necessary to let $k_{0y}l_y = u_y\pi$ where u_y is the mode number of air propagation in the y direction. Consequently,

$$k_{0y} = \frac{u_y\pi}{l_y} \qquad \text{where } u_y = 0,1,2,\cdots, \tag{6.42}$$

and the sound pressure component in the y direction is expressed as

$$Y_0(y) = A_{0y}\cos\left(\frac{u_y\pi}{l_y}y\right). \tag{6.43}$$

Therefore, substituting Equations (6.28c), (6.39) and (6.43) into (6.22) yields

$$p(x,y,z) = A_0\cos\left(\frac{u_x\pi}{l_x}x\right)\cos\left(\frac{u_y\pi}{l_y}y\right)e^{-jk_{0z}z}, \tag{6.44}$$

where A_0 represents the coefficient of each cross mode and is dependent on the boundary conditions. Hence, by applying the definition of the particle velocity in the z direction given by Equation (6.32c), the normal particle velocity is obtained as

$$\begin{aligned} v_z(x,y,z,t) &= -\frac{1}{\rho_0}\int\frac{\partial p(x,y,x,t)}{\partial z}\mathrm{d}t \\ &= -\frac{1}{\rho_0}\int\frac{\partial A_0\cos\left(\frac{u_x\pi}{l_x}x\right)\cos\left(\frac{u_y\pi}{l_y}y\right)e^{-jk_{0z}z}}{\partial z}e^{j\omega t}\mathrm{d}t \\ &= -\frac{A_0\cos\left(\frac{u_x\pi}{l_x}x\right)\cos\left(\frac{u_y\pi}{l_y}y\right)}{\rho_0}\int -jk_{0z}e^{-jk_{0z}z}e^{j\omega t}\mathrm{d}t \\ &= \frac{A_0\cos\left(\frac{u_x\pi}{l_x}x\right)\cos\left(\frac{u_y\pi}{l_y}y\right)}{\rho_0 j\omega}jk_{0z}e^{-jk_{0z}z}e^{j\omega t} \end{aligned} \tag{6.45}$$

and eliminating the time variable $e^{j\omega t}$, Equation (6.45) is rewritten as

$$\begin{aligned} v_z(x,y,z) &= \frac{A_0 \cos\left(\frac{u_x\pi}{l_x}x\right)\cos\left(\frac{u_y\pi}{l_y}y\right)}{\rho_0 j\omega} jk_{0z}e^{-jk_{0z}z} \\ &= \frac{k_{0z}}{\omega\rho_0}A_0 \cos\left(\frac{u_x\pi}{l_x}x\right)\cos\left(\frac{u_y\pi}{l_y}y\right)e^{-jk_{0z}z}, \end{aligned} \tag{6.46}$$

where

$$k_{0z} = \sqrt{k_0^2 - k_{0x}^2 - k_{0y}^2} = \sqrt{k_0^2 - \left(\frac{u_x\pi}{l_x}\right)^2 - \left(\frac{u_y\pi}{l_y}\right)^2}. \tag{6.47}$$

Equations (6.44) and (6.46) represent the sound pressure component and the particle velocity in the z-direction in the air cavity. The sound is assumed to be travelling in the positive z-direction. As mentioned previously in this section, two sound waves exist; namely p_{i2} and p_{r2}. The former propagates in the positive z-direction and the latter in the negative z-direction. Hence, p_{i2} is expressed as

$$p_{i2}(x,y,z) = A_{i2}\cos\left(\frac{u_x\pi}{l_x}x\right)\cos\left(\frac{u_y\pi}{l_y}y\right)e^{-jk_{0z}z}, \tag{6.48}$$

where A_{i2} represents the coefficient of the air particles of the transmitted sound through Membrane 1 within the air cavity and is dependent on the boundary conditions. Similarly, p_{r2} is expressed as

$$p_{r2}(x,y,z) = A_{r2}\cos\left(\frac{u_x\pi}{l_x}x\right)\cos\left(\frac{u_y\pi}{l_y}y\right)e^{jk_{0z}z}, \tag{6.49}$$

where A_{r2} represents the coefficient of the air particles of each cross mode of the sound reflected by Membrane 2 within the air cavity and is dependent on the boundary conditions. Note that in Equation (6.49), $e^{jk_{0z}z}$ is positive, showing that p_{r2} travels in the negative z-direction.

Although the expressions for p_{i2} and p_{r2} are obtained, two unknown coefficients exist: A_{i2} and A_{r2}. These unknown coefficients are dependent on the boundary conditions and hence represent the fluid-structural coupling between the membrane motions and the air motion in the cavity. These solutions, the boundary conditions in the z-direction and the fluid-structural coupling, are discussed in Section 6.3 for normally-incident plane wave conditions and in Section 6.4 for a diffuse field.

6.2.3 Motion of Membrane 2 at $z = D$

As shown in Figure 6.1, Membrane 2 is placed at $z = D$ and is parallel to the xy plane. It is excited by the pressure difference between the incident sound p_{i2}, the reflected sound p_{r2}, and the transmitted sound p_t. If the displacement of Membrane 2 is $\xi_2(x,y)$, the velocity of Membrane 2 $v_2(x,y)$ at radial frequency ω is given by

$$v_2(x,y) = j\omega\xi_2(x,y). \tag{6.50}$$

Based on the continuity of air particle velocity in the normal direction (i.e., the z-direction), the relationship between the sound pressures and $v_2(x,y)$ on each surface of Membrane 2 is given by

$$\frac{p_{i2}e^{-jk_{0z}D} - p_{r2}e^{jk_{0z}D}}{\rho_0\, c_0} = v_2(x,y) = j\omega\xi_2(x,y), \tag{6.51}$$

on the upstream surface and

$$\frac{p_t}{\rho_0\, c_0} = v_2(x,y) = j\omega\xi_2(x,y), \tag{6.52}$$

on the other side. Hence Equation (6.51) is rewritten as

$$p_{r2} = p_{i2}e^{-2jk_{0z}D} - v_2(x,y)\ \rho_0\, c_0 e^{-jk_{0z}D}. \tag{6.53}$$

Therefore, the sound pressure difference on Membrane 2, Δp_2, is expressed by

$$\begin{aligned}\Delta p_2 &= p_{i2}e^{-jk_{0z}D} - p_{r2}e^{jk_{0z}D} - p_t \\ &= 2p_{i2}e^{-jk_{0z}D} - v_2(x,y)\ \rho_0\, c_0 - p_t \\ &= 2p_{i2}e^{-jk_{0z}D} - 2\rho_0\, c_0\, v_2(x,y).\end{aligned} \tag{6.54}$$

Substituting Equation (6.54) into the left hand side of Equation (2.26) yields the motion equation of Membrane 2 which is given by

$$\begin{aligned}(T + 2j\omega\eta)\nabla^2\xi_2(x,y) + \omega^2\rho_{s2}\xi_2(x,y) = -\Delta p_2 = -2p_{i2}e^{-jk_{0z}D} + 2\rho_0\, c_0\, v_2(x,y), \\ (T + 2j\omega\eta)\nabla^2\xi_2(x,y) + \left(\omega^2\rho_{s2} - 2j\omega\rho_0\, c_0\right)\xi_2(x,y) = -2p_{i2}e^{-jk_{0z}D},\end{aligned} \tag{6.55}$$

where ρ_{s2} is the surface density of Membrane 2. Similarly to Equation (2.61), the solution of Equation (6.55) is expressed by the modal summation,

$$\xi_2(x,y) = \sum_{n=1}^{N} A_{n2}\,\xi_{n2}(x,y), \tag{6.56}$$

where the mode shape function is given by,

$$\xi_{n2}(x,y) = \sin(\frac{n_x \pi}{l_x} x)\sin(\frac{n_y \pi}{l_y} y), \qquad n = N_y(n_x - 1) + n_y. \tag{6.57}$$

n_x and n_y are the modal indices in the x- and the y-axes and $N = N_x \times N_y$. The variable A_{n2} is an unknown.

Substituting Equation (6.57) into Equation (6.55) gives

$$(T + 2j\omega\eta)\nabla^2 \sum_{n=1}^{N} A_{n2}\,\xi_{n2}(x,y) + \left[\omega^2\rho_{s2} - 2j\omega\rho_0\, c_0\right] \sum_{n=1}^{N} A_{n2}\,\xi_{n2}(x,y) = -2p_{i2}e^{-jk_{0z}D}. \tag{6.58}$$

Multiplying each side of Equation (6.58) by the term $\xi_m(x,y)$ and integrating over the membrane surface gives

$$\begin{aligned} (T + 2j\omega\eta) \int_0^{l_x}\int_0^{l_y} \xi_m(x,y)\nabla^2 \sum_{n=1}^{N} A_{n2}\,\xi_{n2}(x,y)\mathrm{d}x\mathrm{d}y + \\ \left(\omega^2\rho_{s2} - 2j\omega\rho_0\, c_0\right) \int_0^{l_x}\int_0^{l_y} \xi_m(x,y) \sum_{n=1}^{N} A_{n2}\,\xi_{n2}(x,y)\mathrm{d}x\mathrm{d}y \\ = -2\int_0^{l_x}\int_0^{l_y} p_{i2}e^{-jk_{0z}D}\xi_m(x,y)\mathrm{d}x\mathrm{d}y. \end{aligned} \tag{6.59}$$

Similar to Section 6.2.1, Equation (6.59) can be solved in matrix form. The unknown variable A_{n2} is rewritten in the form of an $N \times 1$ vector

$$\mathbf{A_2} = \begin{pmatrix} A_{n2_1} \\ A_{n2_2} \\ A_{n2_3} \\ \vdots \\ A_{n2_N} \end{pmatrix}. \tag{6.60}$$

Hence, Equation (6.59) is rewritten in matrix form as

$$\left[(T + 2j\omega\eta)\boldsymbol{\psi_3} + \left(\omega^2\rho_{s2} - 2j\omega\rho_0\, c_0\right)\boldsymbol{\psi_4}\right]\mathbf{A_2} = -2\int_0^{l_x}\int_0^{l_y} p_{i2}e^{-jk_{0z}D}\xi_m(x,y)\mathrm{d}x\mathrm{d}y, \tag{6.61}$$

where

$$\boldsymbol{\psi_3} = \begin{pmatrix} C_1\int_0^{l_x}\int_0^{l_y}\xi_1(x,y)\xi_{n2_1}(x,y)\mathrm{d}x\mathrm{d}y & C_2\int_0^{l_x}\int_0^{l_y}\xi_1(x,y)\xi_{n2_2}(x,y)\mathrm{d}x\mathrm{d}y & \dots & C_n\int_0^{l_x}\int_0^{l_y}\xi_1(x,y)\xi_{n2_n}(x,y)\mathrm{d}x\mathrm{d}y \\ C_1\int_0^{l_x}\int_0^{l_y}\xi_2(x,y)\xi_{n2_1}(x,y)\mathrm{d}x\mathrm{d}y & C_2\int_0^{l_x}\int_0^{l_y}\xi_2(x,y)\xi_{n2_2}(x,y)\mathrm{d}x\mathrm{d}y & \dots & C_n\int_0^{l_x}\int_0^{l_y}\xi_2(x,y)\xi_{n2_n}(x,y)\mathrm{d}x\mathrm{d}y \\ \vdots & \vdots & \ddots & \vdots \\ C_1\int_0^{l_x}\int_0^{l_y}\xi_m(x,y)\xi_{n2_1}(x,y)\mathrm{d}x\mathrm{d}y & C_2\int_0^{l_x}\int_0^{l_y}\xi_m(x,y)\xi_{n2_2}(x,y)\mathrm{d}x\mathrm{d}y & \dots & C_n\int_0^{l_x}\int_0^{l_y}\xi_m(x,y)\xi_{n2_n}(x,y)\mathrm{d}x\mathrm{d}y \end{pmatrix}, \tag{6.62}$$

and

$$\boldsymbol{\psi_4} = \begin{pmatrix} \int_0^{l_x}\int_0^{l_y}\xi_1(x,y)\xi_{n2_1}(x,y)\mathrm{d}x\mathrm{d}y & \int_0^{l_x}\int_0^{l_y}\xi_1(x,y)\xi_{n2_2}(x,y)\mathrm{d}x\mathrm{d}y & \dots & \int_0^{l_x}\int_0^{l_y}\xi_1(x,y)\xi_{n2_n}(x,y)\mathrm{d}x\mathrm{d}y \\ \int_0^{l_x}\int_0^{l_y}\xi_2(x,y)\xi_{n2_1}(x,y)\mathrm{d}x\mathrm{d}y & \int_0^{l_x}\int_0^{l_y}\xi_2(x,y)\xi_{n2_2}(x,y)\mathrm{d}x\mathrm{d}y & \dots & \int_0^{l_x}\int_0^{l_y}\xi_2(x,y)\xi_{n2_n}(x,y)\mathrm{d}x\mathrm{d}y \\ \vdots & \vdots & \ddots & \vdots \\ \int_0^{l_x}\int_0^{l_y}\xi_m(x,y)\xi_{n2_1}(x,y)\mathrm{d}x\mathrm{d}y & \int_0^{l_x}\int_0^{l_y}\xi_m(x,y)\xi_{n2_2}(x,y)\mathrm{d}x\mathrm{d}y & \dots & \int_0^{l_x}\int_0^{l_y}\xi_m(x,y)\xi_{n2_n}(x,y)\mathrm{d}x\mathrm{d}y \end{pmatrix}. \tag{6.63}$$

It is also not possible to solve Equation (6.61) because the term $2\int_0^{l_x}\int_0^{l_y} p_{i2}\xi_m(x,y)\mathrm{d}x\mathrm{d}y$ is unknown and p_{i2} is dependent on the sound in the air cavity. Equation (6.61) represents the coupling between the forced vibration of Membrane 2 and the sound field in the air cavity.

Comparing the two motion equations of the impervious membranes, it is found that it is difficult to find their solutions because of the unknown term p_{i2}. However, as discussed in Section 6.2.2, p_{i2} can be determined by the boundary conditions. The expressions for p_{i2} and the STL of double layer impervious membranes with a normally-incident plane wave are discussed in Section 6.3.

6.3 Fluid-structure coupling and normal incidentce STL of double layer impervious membranes separated by an air cavity

In Sections 6.2.1 to 6.2.3, the motion equations of two impervious membranes and the equation for the air motion within the cavity are discussed. By applying the boundary conditions based on the normal velocity continuity on each membrane surface along with consideration of the fluid-structure coupling, the relationship between the vibration mode and the air

motion mode can be determined, along with the term p_{i2}. Hence, the sound transmission coefficient and the STL of the double layer impervious membranes can be predicted. The prediction method for the sound transmission coefficient and the STL of these membranes using this strategy is investigated in Section 6.3.1. The developed model is compared with experimental results in Section 6.3.2 and the error between the experimental and predicted results is also analysed.

6.3.1 Derivation for the STL of double layer impervious membranes separated by an air cavity

Similar to the $\mathbf{A_1}$ and $\mathbf{A_2}$ vectors, the unknown variable $\mathbf{B}$ can be expressed in the form of an $N \times 1$ vector as

$$\mathbf{B} = \begin{pmatrix} B_1 \\ B_2 \\ B_3 \\ \vdots \\ B_U \end{pmatrix}. \tag{6.64}$$

Note that the air mode u starts from (0,0). For Membrane 2, it is known that $z = D$. Substituting Equations (6.64) and (6.49) into Equation (6.61) and letting $z = D$ yields

$$\begin{aligned} &\left[(T + 2j\omega\eta)\boldsymbol{\psi_3} + \left(\omega^2\rho_{s2} - 2j\omega\rho_0\, c_0\right)\boldsymbol{\psi_4}\right]\mathbf{A_2} \\ &= -2\int_0^{l_x}\int_0^{l_y} B_u \cos\left(\frac{u_x\pi}{l_x}x\right)\cos\left(\frac{u_y\pi}{l_y}y\right)e^{-jk_{0z}D}\xi_m(x,y)\mathrm{d}x\mathrm{d}y. \end{aligned} \tag{6.65}$$

Letting $\zeta_u(x,y) = \cos\left(\frac{u_x\pi}{l_x}x\right)\cos\left(\frac{u_y\pi}{l_y}y\right)$ and

$$\boldsymbol{\psi_5} = \begin{pmatrix} \int_0^{l_x}\int_0^{l_y}\xi_1(x,y)\zeta_1(x,y)e^{-jk_{0z}D}\mathrm{d}x\mathrm{d}y & \int_0^{l_x}\int_0^{l_y}\xi_1(x,y)\zeta_2(x,y)e^{-jk_{0z}D}\mathrm{d}x\mathrm{d}y & \dots & \int_0^{l_x}\int_0^{l_y}\xi_1(x,y)\zeta_U(x,y)e^{-jk_{0z}D}\mathrm{d}x\mathrm{d}y \\ \int_0^{l_x}\int_0^{l_y}\xi_2(x,y)\zeta_1(x,y)e^{-jk_{0z}D}\mathrm{d}x\mathrm{d}y & \int_0^{l_x}\int_0^{l_y}\xi_2(x,y)\zeta_2(x,y)e^{-jk_{0z}D}\mathrm{d}x\mathrm{d}y & \dots & \int_0^{l_x}\int_0^{l_y}\xi_2(x,y)\zeta_U(x,y)e^{-jk_{0z}D}\mathrm{d}x\mathrm{d}y \\ \vdots & \vdots & \ddots & \vdots \\ \int_0^{l_x}\int_0^{l_y}\xi_m(x,y)\zeta_1(x,y)e^{-jk_{0z}D}\mathrm{d}x\mathrm{d}y & \int_0^{l_x}\int_0^{l_y}\xi_m(x,y)\zeta_2(x,y)e^{-jk_{0z}D}\mathrm{d}x\mathrm{d}y & \dots & \int_0^{l_x}\int_0^{l_y}\xi_m(x,y)\zeta_U(x,y)e^{-jk_{0z}D}\mathrm{d}x\mathrm{d}y \end{pmatrix}, \tag{6.66}$$

Equation (6.65) is rewritten as

$$\left[(T + 2j\omega\eta)\boldsymbol{\psi_3} + \left(\omega^2\rho_{s2} - 2j\omega\rho_0\, c_0\right)\boldsymbol{\psi_4}\right]\mathbf{A_2} = -2\boldsymbol{\psi_5}\mathbf{B}. \tag{6.67}$$

Hence,

$$\mathbf{B} = \frac{\left[(T + 2j\omega\eta)\boldsymbol{\psi_3} + \left(\omega^2\rho_{s2} - 2j\omega\rho_0\, c_0\right)\boldsymbol{\psi_4}\right]\mathbf{A_2}}{-2\boldsymbol{\psi_5}}. \tag{6.68}$$

Equation (6.68) shows the relationship between the modal amplitudes of the air motion of the transmitted sound through Membrane 1 and the mechanical motion of Membrane 2 and hence represents the coupling between the air motion and the vibration motion on the upstream surface of Membrane 2.

Since the coupling between the air motion and the vibration motion of Membrane 2 is obtained, it is necessary to couple the air motion with the vibration motion of Membrane 1. At the downstream surface of Membrane 1, Equation (6.3) represents the relationship between the air motion and the vibration motion of Membrane 1 based on particle velocity continuity in the normal direction. However, p_{r2} is expressed with respect to p_{i2} and $v_2(x,y)$, as shown in Equation (6.53). Substituting Equation (6.53) into Equation (6.3) yields

$$\left(1 - e^{-2jk_{0z}D}\right) p_{i2} + j\omega\rho_0 c_0\, \xi_2\, e^{-jk_{0z}D} = j\omega\rho_0 c_0\, \xi_1. \tag{6.69}$$

Multiplying each side of Equation (6.69) by $\xi_m(x,y)$ and integrating over the membrane surface gives

$$\begin{aligned}
&\sum_{u=0}^{U}\int_0^{l_x}\int_0^{l_y} B_u \cos\left(\frac{u_x\pi}{l_x}x\right)\cos\left(\frac{u_y\pi}{l_y}y\right)\xi_m(x,y)\mathrm{d}x\mathrm{d}y - \\
&\sum_{u=0}^{U}\int_0^{l_x}\int_0^{l_y} B_u \cos\left(\frac{u_x\pi}{l_x}x\right)\cos\left(\frac{u_y\pi}{l_y}y\right) e^{-2jk_{0z}D}\xi_m(x,y)\mathrm{d}x\mathrm{d}y + \\
&j\omega\rho_0 c_0 \sum_{u=0}^{U}\int_0^{l_x}\int_0^{l_y} e^{-jk_{0z}D} A_{n2}\,\xi_{n2}(x,y)\xi_m(x,y)\mathrm{d}x\mathrm{d}y \\
&= j\omega\rho_0 c_0 \sum_{n=1}^{N}\int_0^{l_x}\int_0^{l_y} A_{n1}\,\xi_{n1}(x,y)\xi_m(x,y)\mathrm{d}x\mathrm{d}y
\end{aligned} \tag{6.70}$$

Equation (6.70) is rewritten in matrix form as

$$(\boldsymbol{\psi_6} - \boldsymbol{\psi_7})\mathbf{B} + j\omega\rho_0 c_0 \boldsymbol{\psi_8}\mathbf{A_2} = j\omega\rho_0 c_0\, \boldsymbol{\psi_2}\mathbf{A_1}, \tag{6.71}$$

where

$$\boldsymbol{\psi_6} = \begin{pmatrix} \int_0^{l_x}\int_0^{l_y} \xi_1(x,y)\zeta_1(x,y)\mathrm{d}x\mathrm{d}y & \int_0^{l_x}\int_0^{l_y} \xi_1(x,y)\zeta_2(x,y)\mathrm{d}x\mathrm{d}y & \dots & \int_0^{l_x}\int_0^{l_y} \xi_1(x,y)\zeta_U(x,y)\mathrm{d}x\mathrm{d}y \\ \int_0^{l_x}\int_0^{l_y} \xi_2(x,y)\zeta_1(x,y)\mathrm{d}x\mathrm{d}y & \int_0^{l_x}\int_0^{l_y} \xi_2(x,y)\zeta_2(x,y)\mathrm{d}x\mathrm{d}y & \dots & \int_0^{l_x}\int_0^{l_y} \xi_2(x,y)\zeta_U(x,y)\mathrm{d}x\mathrm{d}y \\ \vdots & \vdots & \ddots & \vdots \\ \int_0^{l_x}\int_0^{l_y} \xi_m(x,y)\zeta_1(x,y)\mathrm{d}x\mathrm{d}y & \int_0^{l_x}\int_0^{l_y} \xi_m(x,y)\zeta_2(x,y)\mathrm{d}x\mathrm{d}y & \dots & \int_0^{l_x}\int_0^{l_y} \xi_m(x,y)\zeta_U(x,y)\mathrm{d}x\mathrm{d}y \end{pmatrix}, \tag{6.72}$$

$$\boldsymbol{\psi_7} = \begin{pmatrix} \int_0^{l_x}\int_0^{l_y} \xi_1(x,y)\zeta_1(x,y)e^{-2jk_{0z}D}\mathrm{d}x\mathrm{d}y & \int_0^{l_x}\int_0^{l_y} \xi_1(x,y)\zeta_2(x,y)e^{-2jk_{0z}D}\mathrm{d}x\mathrm{d}y & \dots & \int_0^{l_x}\int_0^{l_y} \xi_1(x,y)\zeta_U(x,y)e^{-2jk_{0z}D}\mathrm{d}x\mathrm{d}y \\ \int_0^{l_x}\int_0^{l_y} \xi_2(x,y)\zeta_1(x,y)e^{-2jk_{0z}D}\mathrm{d}x\mathrm{d}y & \int_0^{l_x}\int_0^{l_y} \xi_2(x,y)\zeta_2(x,y)e^{-2jk_{0z}D}\mathrm{d}x\mathrm{d}y & \dots & \int_0^{l_x}\int_0^{l_y} \xi_2(x,y)\zeta_U(x,y)e^{-2jk_{0z}D}\mathrm{d}x\mathrm{d}y \\ \vdots & \vdots & \ddots & \vdots \\ \int_0^{l_x}\int_0^{l_y} \xi_m(x,y)\zeta_1(x,y)e^{-2jk_{0z}D}\mathrm{d}x\mathrm{d}y & \int_0^{l_x}\int_0^{l_y} \xi_m(x,y)\zeta_2(x,y)e^{-2jk_{0z}D}\mathrm{d}x\mathrm{d}y & \dots & \int_0^{l_x}\int_0^{l_y} \xi_m(x,y)\zeta_U(x,y)e^{-2jk_{0z}D}\mathrm{d}x\mathrm{d}y \end{pmatrix}. \tag{6.73}$$

and

$$\boldsymbol{\psi_8} = \begin{pmatrix} \int_0^{l_x}\int_0^{l_y} \xi_1(x,y)\xi_{n2_1}(x,y)e^{-jk_{0z}D}\mathrm{d}x\mathrm{d}y & \int_0^{l_x}\int_0^{l_y} \xi_1(x,y)\xi_{n2_2}(x,y)e^{-jk_{0z}D}\mathrm{d}x\mathrm{d}y & \dots & \int_0^{l_x}\int_0^{l_y} \xi_1(x,y)\xi_{n2_n}(x,y)e^{-jk_{0z}D}\mathrm{d}x\mathrm{d}y \\ \int_0^{l_x}\int_0^{l_y} \xi_2(x,y)\xi_{n2_1}(x,y)e^{-jk_{0z}D}\mathrm{d}x\mathrm{d}y & \int_0^{l_x}\int_0^{l_y} \xi_2(x,y)\xi_{n2_2}(x,y)e^{-jk_{0z}D}\mathrm{d}x\mathrm{d}y & \dots & \int_0^{l_x}\int_0^{l_y} \xi_2(x,y)\xi_{n2_n}(x,y)e^{-jk_{0z}D}\mathrm{d}x\mathrm{d}y \\ \vdots & \vdots & \ddots & \vdots \\ \int_0^{l_x}\int_0^{l_y} \xi_m(x,y)\xi_{n2_1}(x,y)e^{-jk_{0z}D}\mathrm{d}x\mathrm{d}y & \int_0^{l_x}\int_0^{l_y} \xi_m(x,y)\xi_{n2_2}(x,y)e^{-jk_{0z}D}\mathrm{d}x\mathrm{d}y & \dots & \int_0^{l_x}\int_0^{l_y} \xi_m(x,y)\xi_{n2_n}(x,y)e^{-jk_{0z}D}\mathrm{d}x\mathrm{d}y \end{pmatrix}. \tag{6.74}$$

Substituting Equation (6.68) into Equation (6.73) gives

$$(\boldsymbol{\psi_6} - \boldsymbol{\psi_7})\frac{(T+2j\omega\eta)\boldsymbol{\psi_3} + \left(\omega^2\rho_{s2} - 2j\omega\rho_0\, c_0\right)\boldsymbol{\psi_4}}{-2\boldsymbol{\psi_5}}\mathbf{A_2} + j\omega\rho_0 c_0 \boldsymbol{\psi_8}\mathbf{A_2} = j\omega\rho_0 c_0\ \boldsymbol{\psi_2}\mathbf{A_1}. \tag{6.75}$$

Additionally, it is assumed that the total number of modes of Membrane 1 is identical to that of Membrane 2. Consequently, $\boldsymbol{\psi_1} = \boldsymbol{\psi_3}$ and $\boldsymbol{\psi_2} = \boldsymbol{\psi_4}$. Hence, the modal amplitude of Membrane 1 is obtained with respect to the modal amplitude of Membrane 2 as

$$\mathbf{A_1} = \left[(\boldsymbol{\psi_6} - \boldsymbol{\psi_7})\frac{(T+2j\omega\eta)\boldsymbol{\psi_3} + \left(\omega^2\rho_{s2} - 2j\omega\rho_0\, c_0\right)\boldsymbol{\psi_4}}{-2\boldsymbol{\psi_5} j\omega\rho_0 c_0\ \boldsymbol{\psi_2}} + \frac{\boldsymbol{\psi_8}}{\boldsymbol{\psi_2}}\right]\mathbf{A_2}. \tag{6.76}$$

Equation (6.76) indicates the coupling between the modal amplitudes of two impervious membranes. The term $(T+2j\omega\eta)\boldsymbol{\psi_3} + \left(\omega^2\rho_{s2} - 2j\omega\rho_0\, c_0\right)\boldsymbol{\psi_4}$ is associated with the motion equation of Membrane 2. The matrices $\boldsymbol{\psi_6}$, $\boldsymbol{\psi_7}$ and $\boldsymbol{\psi_8}$ relate to the air motion in the cavity.

Substituting the expression for p_{i2} into Equation (6.13) yields

$$\left[(T+2j\omega\eta)\boldsymbol{\psi_1}+\omega^2\rho_{s1}\boldsymbol{\psi_2}\right]\mathbf{A_1}=-2p_i\mathbf{D}+2\boldsymbol{\psi_6}\mathbf{B}. \tag{6.77}$$

Substituting Equations (6.68) and (6.76) into Equation (6.77), it can be rewritten as

$$\begin{aligned}\left[(T+2j\omega\eta)\boldsymbol{\psi_1}+\omega^2\rho_{s1}\boldsymbol{\psi_2}\right]&\left[(\boldsymbol{\psi_6}-\boldsymbol{\psi_7})\frac{(T+2j\omega\eta)\boldsymbol{\psi_3}+\left(\omega^2\rho_{s2}-2j\omega\rho_0\,c_0\right)\boldsymbol{\psi_4}}{-2\boldsymbol{\psi_5}j\omega\rho_0c_0\;\boldsymbol{\psi_2}}+\frac{\boldsymbol{\psi_8}}{\boldsymbol{\psi_2}}\right]\mathbf{A_2}\\ &=-2p_i\mathbf{D}+2\boldsymbol{\psi_6}\frac{\left[(T+2j\omega\eta)\boldsymbol{\psi_3}+\left(\omega^2\rho_{s2}-2j\omega\rho_0\,c_0\right)\boldsymbol{\psi_4}\right]}{-2\boldsymbol{\psi_5}}\mathbf{A_2}.\end{aligned} \tag{6.78}$$

Hence, the modal amplitude vector of Membrane 2, $\mathbf{A_2}$, is obtained as

$$\mathbf{A_2}=\frac{-2p_i\mathbf{D}}{\left[(T+2j\omega\eta)\boldsymbol{\psi_1}+\omega^2\rho_{s1}\boldsymbol{\psi_2}\right]\left[\frac{(\boldsymbol{\psi_6}-\boldsymbol{\psi_7})\boldsymbol{\psi_9}}{j\omega\rho_0c_0\;\boldsymbol{\psi_2}}+\frac{\boldsymbol{\psi_8}}{\boldsymbol{\psi_2}}\right]-2\boldsymbol{\psi_6}\boldsymbol{\psi_9}}, \tag{6.79}$$

where

$$\boldsymbol{\psi_9}=\frac{\left[(T+2j\omega\eta)\boldsymbol{\psi_3}+\left(\omega^2\rho_{s2}-2j\omega\rho_0\,c_0\right)\boldsymbol{\psi_4}\right]}{-2\boldsymbol{\psi_5}}. \tag{6.80}$$

Equation (6.79) represents the vector of modal amplitudes of Membrane 2 with respect to the incident sound pressure p_i.

By substituting the vector $\mathbf{A_2}$ into Equation (6.56), and integrating over the membrane surface and dividing by the membrane area, the spatially averaged displacement of the membrane is given by

$$\overline{\xi_2}=\frac{\sum_{n=1}^{N}B_n\int_0^{l_x}\int_0^{l_y}\xi_{n2}(x,y)\mathrm{d}x\mathrm{d}y}{l_xl_y}=\frac{\boldsymbol{D}^{\mathrm{T}}\boldsymbol{A_2}}{l_xl_y}. \tag{6.81}$$

Hence, the average velocity $\bar{v_2}$ is expressed as

$$\overline{v_2}=\frac{j\omega}{l_xl_y}\boldsymbol{D}^{\mathrm{T}}\boldsymbol{A_2}, \tag{6.82}$$

where $\boldsymbol{D}^{\mathrm{T}}$ is the transpose of vector $\boldsymbol{D}$.

Based on continuity of the normal particle velocity on the downstream surface of Membrane 2, the transmitted sound pressure p_t is obtained by substituting Equation (6.82) into Equation (6.52), such that

$$p_t=\rho_0\,c_0\,\overline{v_2}=\frac{j\omega\rho_0\,c_0}{l_xl_y}\boldsymbol{D}^{\mathrm{T}}\boldsymbol{A_2}. \tag{6.83}$$

Further, substituting Equation (6.79) into Equation (6.83) yields

$$p_t = \frac{j\omega\rho_0 c_0}{l_x l_y} \frac{-2p_i \boldsymbol{D}^{\mathrm{T}}\mathbf{D}}{[(T+2j\omega\eta)\boldsymbol{\psi_1}+\omega^2\rho_{s1}\boldsymbol{\psi_2}]\left[\frac{(\boldsymbol{\psi_6}-\boldsymbol{\psi_7})\boldsymbol{\psi_9}}{j\omega\rho_0 c_0\ \boldsymbol{\psi_2}}+\frac{\boldsymbol{\psi_8}}{\boldsymbol{\psi_2}}\right]-2\boldsymbol{\psi_6}\boldsymbol{\psi_9}}. \tag{6.84}$$

Equation (6.84) expresses the transmitted sound pressure p_t with respect to the incident sound pressure p_i. Hence, the transmission coefficient for normal incidence is obtained as

$$\begin{aligned}\tau = \left|\frac{p_t}{p_i}\right| &= \left|\frac{\frac{j\omega\rho_0 c_0}{l_x l_y}\frac{-2p_i \boldsymbol{D}^{\mathrm{T}}\mathbf{D}}{[(T+2j\omega\eta)\boldsymbol{\psi_1}+\omega^2\rho_{s1}\boldsymbol{\psi_2}]\left[\frac{(\boldsymbol{\psi_6}-\boldsymbol{\psi_7})\boldsymbol{\psi_9}}{j\omega\rho_0 c_0\ \boldsymbol{\psi_2}}+\frac{\boldsymbol{\psi_8}}{\boldsymbol{\psi_2}}\right]-2\boldsymbol{\psi_6}\boldsymbol{\psi_9}}}{p_i}\right| \\ &= \left|\frac{j\omega\rho_0 c_0}{l_x l_y}\frac{-2\boldsymbol{D}^{\mathrm{T}}\mathbf{D}}{[(T+2j\omega\eta)\boldsymbol{\psi_1}+\omega^2\rho_{s1}\boldsymbol{\psi_2}]\left[\frac{(\boldsymbol{\psi_6}-\boldsymbol{\psi_7})\boldsymbol{\psi_9}}{j\omega\rho_0 c_0\ \boldsymbol{\psi_2}}+\frac{\boldsymbol{\psi_8}}{\boldsymbol{\psi_2}}\right]-2\boldsymbol{\psi_6}\boldsymbol{\psi_9}}\right|.\end{aligned} \tag{6.85}$$

The sound transmission loss (STL) is expressed by (Bies & Hansen 2009)

$$STL = 20\times\log_{10}\left(\frac{1}{\tau}\right). \tag{6.86}$$

Therefore, Equations (6.85) and (6.86) provides a prediction method for the sound transmission loss of double layer impervious membranes with normally-incident plane waves, taking into consideration the effect of the constant tension applied on each membrane surface, the internal damping arising from the membrane curvature and the finite effect of the membrane boundaries and rigid cavity boundaries. A comparison of the results of this model with experimental results is discussed in Section 6.3.2.

6.3.2 Comparison with experimental results

To assess the performance of the developed model, sound transmission loss measurements were conducted in the reverberation chambers as detailed in Chapter 2. Both impervious membranes are made of PVC, for which the surface density is 0.4850 kg/m^2 and the thickness is 0.42 mm as shown in Table 2.2. These two identical impervious membranes were stretched slightly on two wooden frames. The determination of the constant tension and the internal damping ratio were obtained using a curve fitting method, as discussed in Chapter 2. Since the membranes are of the same dimension and the materials are considered identical in construction, the tension and internal damping ratio are assumed to be the same for both membranes. Two air cavity depths, D, were investigated, namely 70 mm and 140 mm.

Figures 6.2 and 6.3 compare the measured STLs with the predicted STLs of the double

layer impervious membranes separated by air cavities with depths of 70 mm and 140 mm, respectively. The length and width of the air cavity are identical to those of the membranes, implying an identical cross section area of the air cavity and the membranes. The optimised tension T and internal damping ratio η are shown in the legends. Note that the internal damping ratio shown in each figure is close to zero. This zero internal damping is consistent with the conclusion arising from the STL investigation of the single layer impervious membrane in Chapter 2.

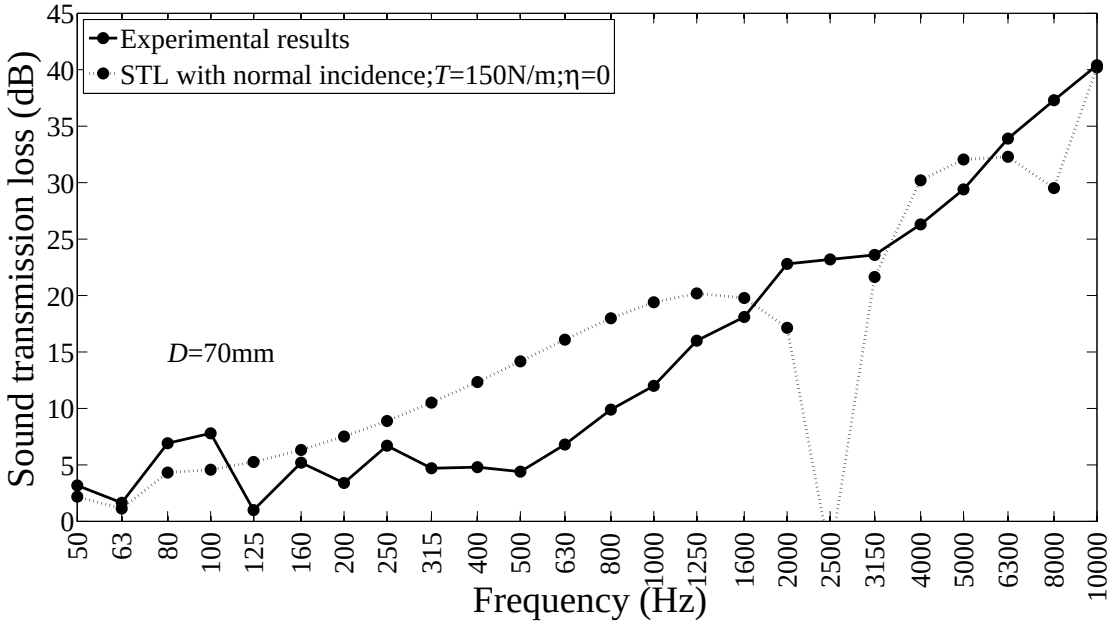

Figure 6.2: STL of double layer impervious membranes separated by a finite air cavity with a depth $D = 70$ mm. The dotted curve with black circles demonstrates the predicted STL using Equation (6.86). The experimental results were obtained in a diffuse field.

It is found in Figures 6.2 and 6.3 that the predicted STLs steadily increase at those frequencies lower than the first resonance frequency of the air cavity, i.e., 2500 Hz when $D = 70$ mm and 1250 Hz when $D = 140$ mm. However, at higher frequencies, the predicted STLs show clear resonance peaks and significant differences from the measured STLs.

The resonance peaks imply that the significant differences on the STL curves at these frequencies can be ascribed to the normal incidence condition used in the prediction method. As mentioned previously, the prediction method developed in Section 6.3.1 is for a the normally-incident plane wave condition. However, the experimental results were measured in the reverberation chambers, implying a diffuse field condition.

Figures 6.2 and 6.3 demonstrate similar resonant transmission trends to that of the predic-

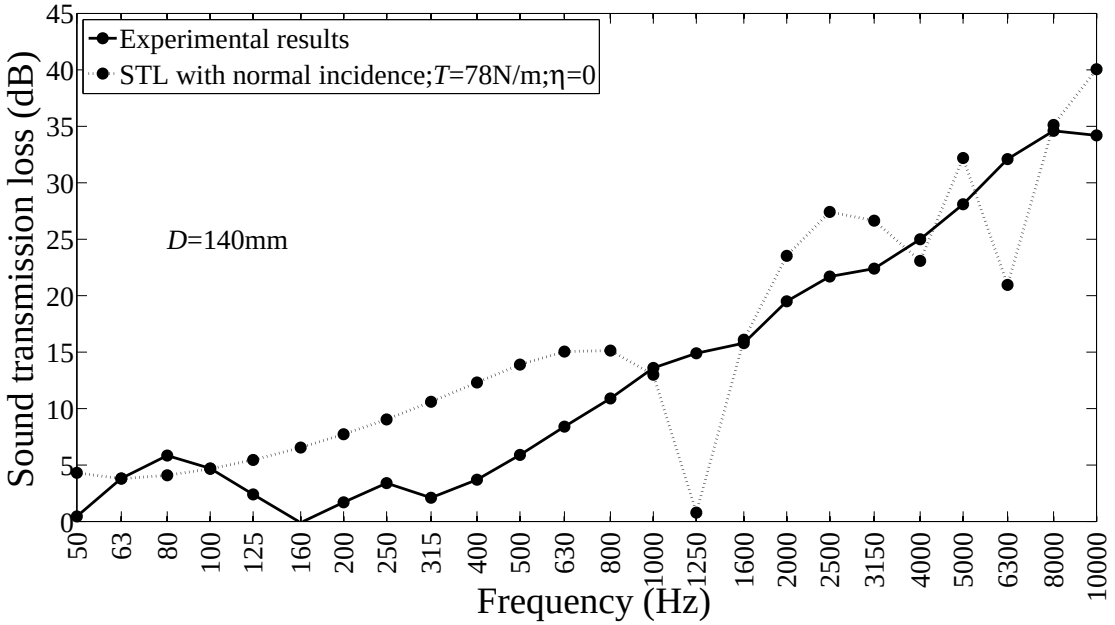

Figure 6.3: STL of double layer impervious membranes separated by a finite air cavity with a depth $D = 140$ mm. The dotted curve with black circles demonstrates the predicted STL using Equation (6.86). The experimental results were obtained in a diffuse field.

tions, shown by Fahy & Gardonio (2007). It is presumed that by considering the incidence angle and taking the average over the angles, the prediction accuracy can be improved. The STL prediction method in a diffuse field is developed and validated accordingly in Section 6.4.

6.4 Fluid-structure coupling and diffuse field STL of double layer impervious membranes separated by an air cavity

Section 6.3 investigated the analytical model for the STL of double layer impervious membranes with a normally-incident plane wave. Comparison of the measured STL and the predicted normal-incidence STL indicates that omission of the incidence angle leads to deficiencies in the ability of model to predict the measured diffuse field STL. Hence, to improve the accuracy of the analytical model developed in Section 6.3, the double layer impervious membrane structure is assumed to be excited by an obliquely-incident plane wave in the following section. By adjusting the incidence angle and taking an average over the angles, the normal incidence STL model is extended to the diffuse field. The diffuse STL model

is developed in Section 6.4.1 and compared with experimental results in Section 6.4.2. The errors in the developed model are analysed in this section.

6.4.1 Derivation of the STL of double layer impervious membranes separated by an air cavity

Figure 6.4 illustrates double layer membranes excited by an incident sound wave with an oblique incidence angle of θ. Hence, Equations (6.2) and (6.3) are rewritten as

$$\frac{(p_i - p_r)\cos(\theta)}{\rho_0\, c_0} = v_1(x,y) = j\omega\xi_1(x,y), \tag{6.87}$$

and

$$\frac{(p_{i2} - p_{r2})\cos(\theta)}{\rho_0\, c_0} = v_1(x,y) = j\omega\xi_1(x,y). \tag{6.88}$$

Hence, the sound pressures p_r and p_{r2} are obtained from Equations (6.87) and (6.88) as

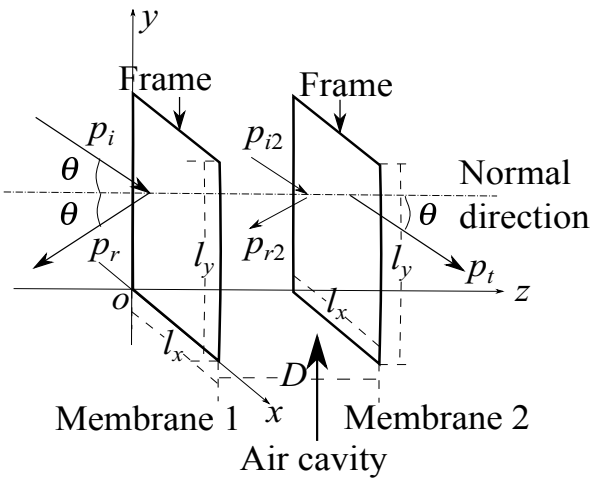

Figure 6.4: Sound transmission of double layer impervious membranes separated by a finite air cavity with a depth of D. The sound wave is obliquely incident on the membrane surface with an incidence angle θ.

$$p_r = p_i - \frac{v_1(x,y)\,\rho_0\, c_0}{\cos(\theta)}, \tag{6.89}$$

and

$$p_{r2} = p_{i2} - \frac{v_1(x,y)\,\rho_0\, c_0}{\cos(\theta)}. \tag{6.90}$$

Therefore, the sound pressure difference on Membrane 1, Δp_1, is obtained as (Fahy & Gardonio 2007)

$$\begin{aligned}\Delta p_1 &= p_i + p_r - (p_{i2} + p_{r2}) \\ &= 2\ p_i - \frac{v_1(x,y)\ \rho_0\ c_0}{\cos(\theta)} - 2\ p_{i2} + \frac{v_1(x,y)\ \rho_0\ c_0}{\cos(\theta)} \\ &= 2\ p_i - 2\ p_{i2}.\end{aligned} \tag{6.91}$$

For Membrane 2, the sound pressure expression on each surface is given by

$$\frac{\left(p_{i2}e^{-jk_{0z}D} - p_{r2}e^{jk_{0z}D}\right)\cos(\theta)}{\rho_0\ c_0} = v_2(x,y) = j\omega\xi_2(x,y) \tag{6.92}$$

and

$$\frac{p_t\cos(\theta)}{\rho_0\ c_0} = v_2(x,y) = j\omega\xi_2(x,y), \tag{6.93}$$

where the wave number is also affected by the incidence angle θ (Fahy & Gardonio 2007), and is expressed as

$$k_{0z} = \sqrt{[k_0\cos(\theta)]^2 - k_{0x}^2 - k_{0y}^2} = \sqrt{[k_0\cos(\theta)]^2 - \left(\frac{u_x\pi}{l_x}\right)^2 - \left(\frac{u_y\pi}{l_y}\right)^2}. \tag{6.94}$$

Equation (6.92) is thus rewritten as

$$p_{r2} = p_{i2}e^{-2jk_{0z}D} - \frac{v_2(x,y)\ \rho_0\ c_0}{\cos(\theta)}e^{-jk_{0z}D}. \tag{6.95}$$

Therefore, the sound pressure difference on Membrane 2, Δp_2, is expressed by

$$\begin{aligned}\Delta p_2 &= p_{i2}e^{-jk_{0z}D} - p_{r2}e^{jk_{0z}D} - p_t \\ &= 2p_{i2}e^{-jk_{0z}D} - \frac{v_2(x,y)\ \rho_0\ c_0}{\cos(\theta)} - p_t \\ &= 2p_{i2}e^{-jk_{0z}D} - 2\frac{v_2(x,y)\ \rho_0\ c_0}{\cos(\theta)}.\end{aligned} \tag{6.96}$$

Substituting Equation (6.96) into the motion equation of Membrane 2 yields its motion equation for obliquely-incident sound, which is expressed in matrix form as

$$\left\{(T + 2j\omega\eta)\boldsymbol{\psi_3} + \left[\omega^2\rho_{s2} - 2\frac{j\omega\rho_0\ c_0}{\cos(\theta)}\right]\boldsymbol{\psi_4}\right\}\mathbf{A_2} = -2\boldsymbol{\psi_5}\mathbf{B}. \tag{6.97}$$

Hence,

$$\mathbf{B} = \frac{\left\{(T + 2j\omega\eta)\boldsymbol{\psi_3} + \left[\omega^2\rho_{s2} - 2\frac{j\omega\rho_0\ c_0}{\cos(\theta)}\right]\boldsymbol{\psi_4}\right\}\mathbf{A_2}}{-2\boldsymbol{\psi_5}}. \tag{6.98}$$

Equation (6.71) for normal incidence is thus rewritten as

$$(\boldsymbol{\psi_6}-\boldsymbol{\psi_7})\,\mathbf{B}+\frac{j\omega\rho_0 c_0}{\cos(\theta)}\boldsymbol{\psi_8}\mathbf{A_2}=\frac{j\omega\rho_0 c_0}{\cos(\theta)}\,\boldsymbol{\psi_2}\mathbf{A_1}. \tag{6.99}$$

Substituting Equation (6.98) into Equation (6.99) yields

$$(\boldsymbol{\psi_6}-\boldsymbol{\psi_7})\frac{\left\{(T+2j\omega\eta)\boldsymbol{\psi_3}+\left[\omega^2\rho_{s2}-2\frac{j\omega\rho_0\,c_0}{\cos(\theta)}\right]\boldsymbol{\psi_4}\right\}\mathbf{A_2}}{-2\boldsymbol{\psi_5}}+\frac{j\omega\rho_0 c_0}{\cos(\theta)}\boldsymbol{\psi_8}\mathbf{A_2}=\frac{j\omega\rho_0 c_0}{\cos(\theta)}\,\boldsymbol{\psi_2}\mathbf{A_1}. \tag{6.100}$$

Hence,

$$\mathbf{A_1}=\left\{\frac{(\boldsymbol{\psi_6}-\boldsymbol{\psi_7})\left\{(T+2j\omega\eta)\boldsymbol{\psi_3}+\left[\omega^2\rho_{s2}-2\frac{j\omega\rho_0\,c_0}{\cos(\theta)}\right]\boldsymbol{\psi_4}\right\}}{-2\boldsymbol{\psi_5}\frac{j\omega\rho_0 c_0}{\cos(\theta)}\,\boldsymbol{\psi_2}}+\frac{\boldsymbol{\psi_8}}{\boldsymbol{\psi_2}}\right\}\mathbf{A_2}. \tag{6.101}$$

Assuming a normal incidence and letting $\theta=0^{\mathrm{o}}$, $\cos(\theta)=\cos(0^{\mathrm{o}})=1$ and Equation (6.101) reduces to Equation (6.76).

Consequently, the motion equation of Membrane 1 is expressed by

$$\left[(T+2j\omega\eta)\boldsymbol{\psi_1}+\omega^2\rho_{s1}\boldsymbol{\psi_2}\right]\left\{\frac{(\boldsymbol{\psi_6}-\boldsymbol{\psi_7})\left\{(T+2j\omega\eta)\boldsymbol{\psi_3}+\left[\omega^2\rho_{s2}-2\frac{j\omega\rho_0\,c_0}{\cos(\theta)}\right]\boldsymbol{\psi_4}\right\}}{-2\boldsymbol{\psi_5}\frac{j\omega\rho_0 c_0}{\cos(\theta)}\,\boldsymbol{\psi_2}}+\frac{\boldsymbol{\psi_8}}{\boldsymbol{\psi_2}}\right\}\mathrm{A}_2$$
$$=-2p_i\mathbf{D}+2\boldsymbol{\psi_6}\frac{\left\{(T+2j\omega\eta)\boldsymbol{\psi_3}+\left[\omega^2\rho_{s2}-2\frac{j\omega\rho_0\,c_0}{\cos(\theta)}\right]\boldsymbol{\psi_4}\right\}\mathbf{A_2}}{-2\boldsymbol{\psi_5}}. \tag{6.102}$$

Letting

$$\boldsymbol{\psi}_{10}=\frac{\left[(T+2j\omega\eta)\boldsymbol{\psi_3}+\left[\omega^2\rho_{s2}-2\frac{j\omega\rho_0\,c_0}{\cos(\theta)}\right]\boldsymbol{\psi_4}\right]}{-2\boldsymbol{\psi_5}}, \tag{6.103}$$

Equation (6.102) is simplified as

$$\left[(T+2j\omega\eta)\boldsymbol{\psi_1}+\omega^2\rho_{s1}\boldsymbol{\psi_2}\right]\left\{\frac{(\boldsymbol{\psi_6}-\boldsymbol{\psi_7})\,\boldsymbol{\psi}_{10}}{\frac{j\omega\rho_0 c_0}{\cos(\theta)}\,\boldsymbol{\psi_2}}+\frac{\boldsymbol{\psi_8}}{\boldsymbol{\psi_2}}\right\}\mathbf{A_2}=-2p_i\mathbf{D}+2\boldsymbol{\psi_6}\boldsymbol{\psi}_{10}\mathbf{A_2}. \tag{6.104}$$

Note that if $\theta=0^{\mathrm{o}}$, $\boldsymbol{\psi}_{10}=\boldsymbol{\psi_9}$ and Equation (6.104) reduces to Equation (6.78). Therefore, $\mathbf{A_2}$ is a function with respect to the incident sound p_i, which is given by

$$\mathbf{A_2}=\frac{-2p_i\mathbf{D}}{\left[(T+2j\omega\eta)\boldsymbol{\psi_1}+\omega^2\rho_{s1}\boldsymbol{\psi_2}\right]\left\{\frac{(\boldsymbol{\psi_6}-\boldsymbol{\psi_7})\boldsymbol{\psi}_{10}}{\frac{j\omega\rho_0 c_0}{\cos(\theta)}\,\boldsymbol{\psi_2}}+\frac{\boldsymbol{\psi_8}}{\boldsymbol{\psi_2}}\right\}-2\boldsymbol{\psi_6}\boldsymbol{\psi}_{10}}, \tag{6.105}$$

and the transmitted sound pressure is given by

$$\begin{aligned} p_t &= \frac{j\omega\rho_0 c_0}{l_x l_y \cos(\theta)} \mathbf{D}^{\mathrm{T}} \mathbf{A_2} \\ &= \frac{j\omega\rho_0 c_0 \mathbf{D}^{\mathrm{T}}}{l_x l_y \cos(\theta)} \frac{-2p_i \mathbf{D}}{[(T+2j\omega\eta)\psi_1 + \omega^2 \rho_{s1} \boldsymbol{\psi_2}] \left\{ \frac{(\boldsymbol{\psi_6}-\boldsymbol{\psi_7})\boldsymbol{\psi}_{10}}{\frac{j\omega\rho_0 c_0}{\cos(\theta)}\ \boldsymbol{\psi_2}} + \frac{\boldsymbol{\psi_8}}{\boldsymbol{\psi_2}} \right\} - 2\boldsymbol{\psi_6}\boldsymbol{\psi}_{10}}. \end{aligned} \tag{6.106}$$

Hence, the transmission coefficient for a plane wave with an angle of incidence θ is obtained as

$$\begin{aligned} \tau(\theta) = \left|\frac{p_t}{p_i}\right| &= \left| \frac{\frac{j\omega\rho_0 c_0 \mathbf{D}^{\mathrm{T}}}{l_x l_y \cos(\theta)} \frac{-2p_i \mathbf{D}}{[(T+2j\omega\eta)\psi_1 + \omega^2 \rho_{s1} \boldsymbol{\psi_2}] \left\{ \frac{(\boldsymbol{\psi_6}-\boldsymbol{\psi_7})\boldsymbol{\psi}_{10}}{\frac{j\omega\rho_0 c_0}{\cos(\theta)}\ \boldsymbol{\psi_2}} + \frac{\boldsymbol{\psi_8}}{\boldsymbol{\psi_2}} \right\} - 2\boldsymbol{\psi_6}\boldsymbol{\psi}_{10}}}{p_i} \right| \\ &= \left| \frac{j\omega\rho_0 c_0 \mathbf{D}^{\mathrm{T}}}{l_x l_y \cos(\theta)} \frac{-2\mathbf{D}}{[(T+2j\omega\eta)\psi_1 + \omega^2 \rho_{s1} \boldsymbol{\psi_2}] \left\{ \frac{(\boldsymbol{\psi_6}-\boldsymbol{\psi_7})\boldsymbol{\psi}_{10}}{\frac{j\omega\rho_0 c_0}{\cos(\theta)}\ \boldsymbol{\psi_2}} + \frac{\boldsymbol{\psi_8}}{\boldsymbol{\psi_2}} \right\} - 2\boldsymbol{\psi_6}\boldsymbol{\psi}_{10}} \right|. \end{aligned} \tag{6.107}$$

When the incident sound is normal to the membrane surface, $\theta = 0$ and Equation (6.107) reduces to Equation (6.85). Substituting Equation (6.107) into Equation (2.93) yields the expression for the sound transmission coefficient in a diffuse field τ_{diffuse}. The sound transmission loss (STL) in a diffuse field is given by

$$STL = 20 \times \log_{10}\left(\frac{1}{\tau_{\text{diffuse}}}\right), \tag{6.108}$$

This diffuse field STL model is compared with experimental results in Section 6.4.2.

6.4.2 Comparison with experimental results

This section assesses the performance of the STL prediction model in a diffuse field by comparing the predicted results to the measured results presented in Section 6.3.2. The comparisons are shown in Figures 6.5 and 6.6 with cavity depths of $D = 70$ mm and $D = 140$ mm, respectively.

For a diffuse sound field, complicated resonant sound transmission is observed in the narrowband predicted diffuse field STL results at the frequencies above the first resonance frequency of the air cavity. The thin dashed curves illustrate the predicted STL using Equa-

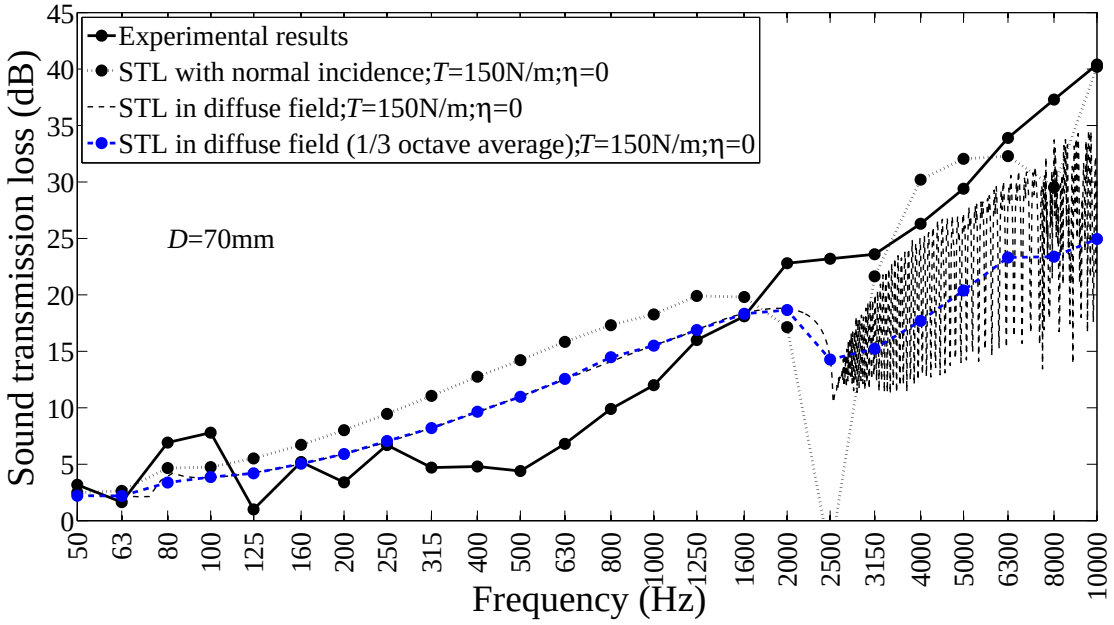

Figure 6.5: STL of double layer impervious membranes separated by a finite air cavity with a depth $D = 70$ mm.

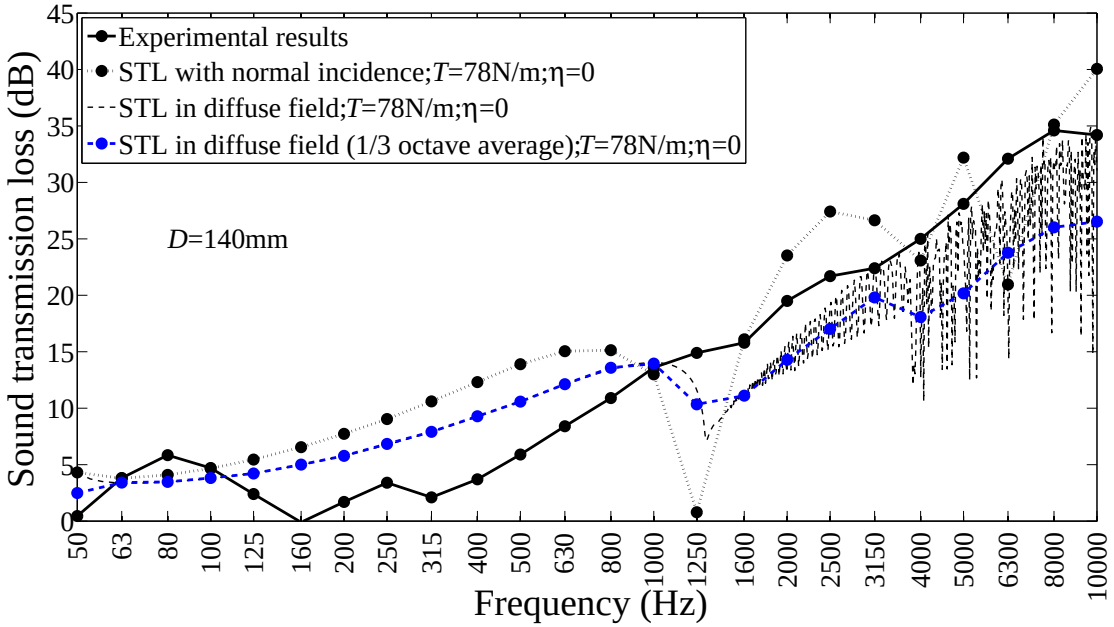

Figure 6.6: STL of double layer impervious membranes separated by a finite air cavity with a depth $D = 140$ mm.

tion (6.108). The rapid shifts with frequency in the values of the predicted STL curves represent the complicated modal response of the air cavity cross section with the acoustic cross modes excited to a sufficiently greater degree by the sound of non-zero angle of incidence. An over-estimation of the diffuse field model below the first resonance frequency of the air cavity has been observed in this study. Similar over-estimation has been reported by Bolton et al. (1996) and Fahy & Gardonio (2007). Since the materials used in Bolton et al.'s (1996) and Fahy & Gardonio's (2007) research were panels, the over-estimation is probably due to the air cavity resonance. The effects of the acoustic properties of the reverberation chambers and the opening position on the STLs are neglected this study but can be investigated in the future.

Note that the measured STLs were averaged over each 1/3 octave band considered, with centre frequencies from 50 Hz to 10 kHz included in the analysis presented here. Hence, to compare the predicted STL to the measured STL, it is necessary to take the average of the predicted STL over each 1/3 octave band. The 1/3 octave band average STL is expressed by (Bies & Hansen 2009)

$$STL_{1/3\text{ average}} = 10 \times \log_{10}\left(\frac{N_{1/3}}{\sum_{f_{\text{low}}}^{f_{\text{high}}} \tau^2_{\text{diffuse}}}\right), \tag{6.109}$$

where f_{low} and f_{high} are the lower and upper limits of each 1/3 octave band and $N_{1/3}$ is the number of narrowband frequencies considered in each 1/3 octave band. The thick dashed curves with black circles in Figures 6.5 and 6.6 represent the average STLs at the centre frequency of each 1/3 octave band.

By considering the effect of the incidence angle and averaging over each 1/3 octave band, the predicted STL is decreased, relative to the normal incidence prediction, at frequencies lower than the first resonance frequency of the air cavity. This leads to a more accurate prediction of the diffuse field experimental STL results, compared with the normal incidence STL prediction model. At frequencies higher than the first resonance frequency of the air cavity, the predicted diffuse field STLs show similar main trends with the experimental measured STLs, however, the average predicted STLs are lower than the measured ones by roughly 9 dB. Therefore it is concluded that the presented model in a diffuse field is able to predict the STL of double layer impervious membranes more accurately in the frequency range lower than the first resonance frequency of the air cavity, but it tends to underestimate

the STL in the frequency range higher than the first resonance frequency of the air cavity.

It is suspected that the unpredicted sound energy loss is due to the sound absorption of the wooden frames which form the boundary of the air cavity in the x- and y-axes. In the models and results presented this far, the cavity boundary is assumed to be acoustically rigid. Beranek et al. (2013) state that the sound absorption coefficient for solid timber is between 0.05 and 0.1 depending on frequency. The wooden frames were constructed from roughly sawn pine leading to a rough surface which might increase the sound absorption coefficient compared to dressed, more dense timbers. Additionally, considering wave guide theory and the cross sectional area of the cavity, the sound absorption of the wooden boundary could be more significant in the high frequency range than in the low frequency range. This presumption is consistent with the observation that the model in a diffuse field underestimates the STL more significantly in the high frequency range than in the low frequency range. Moreover, besides the wood frames, other factors, such as the coupling between the wood frames, the coupling of the membranes to the wood frames, may also contribute to the additional sound energy loss in the air cavity. To simplify the analytical modeling, the additional sound energy loss is considered as the result of sound absorbing boundaries of the air cavity. Therefore, Section 6.5 investigates the effect of a sound absorbing cavity boundary on the predicted STL. An analytical model is developed based on the previous models with the additional consideration of a sound absorbing cavity boundary. Results obtained from this sound absorbing model are also compared with the experimentally measured STLs.

6.5 Effect of the separating air cavity boundary sound absorption on the STL of double layer impervious membranes

In Section 6.4, the normal incidence STL model developed in Section 6.3 is extended to a diffuse field. Although the model for the diffuse field is more accurate than the normal incidence STL model in the low frequency range below the first resonance frequency of the air cavity, it underestimates the STL in the high frequency range above the first resonance frequency of the air cavity. It is presumed in Section 6.4 that this underestimation is due to the omission of the sound absorption of the boundary of the air cavity.

This section aims to develop a model based on the previously developed diffuse field model and further consider the effect of the sound absorption of the boundary of the air cavity. The analytical model of the sound propagation in a finite-sized air cavity with sound absorbing boundaries is derived in Section 6.5.1. Based on the new sound propagation model, the STL model is re-developed in Section 6.5.2 for a diffuse field. This model is compared with experimental results in Section 6.5.3.

6.5.1 Sound propagation in a finite-sized air cavity with sound absorbing boundary

The sound propagation in an air cavity with an acoustically rigid boundary was utilised in Section 6.2.2. However, the boundary of the air cavity in the experiments considered in this study was made of wood, implying that it would absorb sound to some degree. Hence, in this section, the air cavity boundary is assumed to be a sound absorbing boundary due to the sound absorbing surface of the air cavity and other factors, and the sound energy is attenuated with the propagation in the z-direction. In addition from the results presented in Figures 6.5 and 6.6, it is estimated that this sound attenuation is frequency-dependent and has a more significant effect in the high frequency range than in the low frequency range.

Hence, the sound absorption of the air cavity is modelled as a decay factor which is frequency dependent. Following a similar strategy used by Howard & Cazzolato (2014) to simulate the sound pressure decay due to thermal loss, it is assumed that the sound pressure decay in the z-direction of the air cavity is expressed by $e^{-\beta\frac{\omega}{c_0}z}$, where β represents the coefficient of sound energy loss due to the sound absorbing walls. Since it was not possible to measure the sound absorption coefficient of the sound absorbing boundary directly in the experiments, the value of β was obtained by data optimisation. The optimisations were conducted following the same method as that by which the tension and damping ratio were determined.

Considering this decay factor, the general expression for the sound propagation within the cavity, i.e., Equation (6.44), is rewritten as

$$p(x,y,z) = A_0 \cos\left(\frac{u_x\pi}{l_x}x\right)\cos\left(\frac{u_y\pi}{l_y}y\right)e^{-\beta\frac{\omega}{c_0}z}e^{-jk_{0z}z}. \tag{6.110}$$

Hence, p_{i2} is expressed as

$$p_{i2}(x,y,z) = A_{i2}\cos\left(\frac{u_x\pi}{l_x}x\right)\cos\left(\frac{u_y\pi}{l_y}y\right)e^{-\beta\frac{\omega}{c_0}z}e^{-jk_{0z}z}. \tag{6.111}$$

Similarly, p_{r2} is expressed as

$$p_{r2}(x,y,z) = A_{r2}\cos\left(\frac{u_x\pi}{l_x}x\right)\cos\left(\frac{u_y\pi}{l_y}y\right)e^{-\beta\frac{\omega}{c_0}z}e^{jk_{0z}z}. \tag{6.112}$$

Note that in Equation (6.112), the decay factor is still negative. If the sign of the decay factor in Equation (6.112) is positive, the decay factor $e^{\beta\frac{\omega}{c_0}z}$ is higher than unity and has no physical meaning.

6.5.2 Fluid-structure coupling and the diffuse field STL of double layer impervious membranes separated by an air cavity with sound absorbing walls

At Membrane 1, $z=0$ and the decay factor $e^{-\beta\frac{\omega}{c_0}z}=1$. Consequently, the pressure difference and the motion equation remain the same as in the case of the diffuse model in Section 6.4. However, at Membrane 2, Equation (6.92) is expressed by

$$\frac{\left(p_{i2}e^{-jk_{0z}D} - p_{r2}e^{jk_{0z}D}\right)\cos(\theta)e^{-\beta\frac{\omega}{c_0}D}}{\rho_0\, c_0} = v_2(x,y) = j\omega\xi_2(x,y), \tag{6.113}$$

and hence

$$p_{r2} = p_{i2}e^{-2jk_{0z}D} - \frac{v_2(x,y)\,\rho_0\,c_0}{\cos(\theta)}e^{\beta\frac{\omega}{c_0}D}e^{-jk_{0z}D}. \tag{6.114}$$

The sound pressure difference on Membrane 2 is expressed by

$$\begin{aligned}\Delta p_2 &= p_{i2}e^{-\beta\frac{\omega}{c_0}D}e^{-jk_{0z}D} - p_{r2}e^{-\beta\frac{\omega}{c_0}D}e^{jk_{0z}D} - p_t \\ &= 2p_{i2}e^{-jk_{0z}D}e^{-\beta\frac{\omega}{c_0}D} - 2\frac{v_2(x,y)\,\rho_0\,c_0}{\cos(\theta)}.\end{aligned} \tag{6.115}$$

The motion equation of Membrane 2 in matrix form is altered to

$$\left\{(T+2j\omega\eta)\boldsymbol{\psi_3} + \left[\omega^2\rho_{s2} - 2\frac{j\omega\rho_0\,c_0}{\cos(\theta)}\right]\boldsymbol{\psi_4}\right\}\mathbf{A_2} = -2\boldsymbol{\psi_5}\mathbf{B}e^{-\beta\frac{\omega}{c_0}D}, \tag{6.116}$$

where the decay factor $e^{-\beta\frac{\omega}{c_0}D}$ is a frequency-dependent term. Hence,

$$\mathbf{B} = \frac{\left\{(T+2j\omega\eta)\boldsymbol{\psi_3} + \left[\omega^2\rho_{s2} - 2\frac{j\omega\rho_0\,c_0}{\cos(\theta)}\right]\boldsymbol{\psi_4}\right\}e^{\beta\frac{\omega}{c_0}D}\mathbf{A_2}}{-2\boldsymbol{\psi_5}}. \tag{6.117}$$

Equation (6.99) is rewritten as

$$(\boldsymbol{\psi_6}-\boldsymbol{\psi_7})\,\mathbf{B}+\frac{j\omega\rho_0 c_0}{\cos(\theta)}e^{\beta\frac{\omega}{c_0}D}\boldsymbol{\psi_8}\mathbf{A_2}=\frac{j\omega\rho_0 c_0}{\cos(\theta)}\,\boldsymbol{\psi_2}\mathbf{A_1}. \tag{6.118}$$

Substituting Equation (6.117) into Equation (6.118) yields

$$\begin{aligned}(\boldsymbol{\psi_6}-\boldsymbol{\psi_7})\frac{\left\{(T+2j\omega\eta)\boldsymbol{\psi_3}+\left[\omega^2\rho_{s2}-2\frac{j\omega\rho_0\,c_0}{\cos(\theta)}\right]\boldsymbol{\psi_4}\right\}e^{\beta\frac{\omega}{c_0}D}\mathbf{A_2}}{-2\boldsymbol{\psi_5}}\\ +\frac{j\omega\rho_0 c_0}{\cos(\theta)}e^{\beta\frac{\omega}{c_0}D}\boldsymbol{\psi_8}\mathbf{A_2}=\frac{j\omega\rho_0 c_0}{\cos(\theta)}\,\boldsymbol{\psi_2}\mathbf{A_1}.\end{aligned} \tag{6.119}$$

Hence,

$$\mathbf{A_1}=\left\{\frac{(\boldsymbol{\psi_6}-\boldsymbol{\psi_7})\left\{(T+2j\omega\eta)\boldsymbol{\psi_3}+\left[\omega^2\rho_{s2}-2\frac{j\omega\rho_0\,c_0}{\cos(\theta)}\right]\boldsymbol{\psi_4}\right\}}{-2\boldsymbol{\psi_5}\frac{j\omega\rho_0 c_0}{\cos(\theta)}\,\boldsymbol{\psi_2}}+\frac{\boldsymbol{\psi_8}}{\boldsymbol{\psi_2}}\right\}e^{\beta\frac{\omega}{c_0}D}\mathbf{A_2}. \tag{6.120}$$

Therefore, the motion equation of Membrane 1 is expressed by

$$\begin{aligned}&\left[(T+2j\omega\eta)\boldsymbol{\psi_1}+\omega^2\rho_{s1}\boldsymbol{\psi_2}\right]\\ &\left\{\frac{(\boldsymbol{\psi_6}-\boldsymbol{\psi_7})\left\{(T+2j\omega\eta)\boldsymbol{\psi_3}+\left[\omega^2\rho_{s2}-2\frac{j\omega\rho_0\,c_0}{\cos(\theta)}\right]\boldsymbol{\psi_4}\right\}}{-2\boldsymbol{\psi_5}\frac{j\omega\rho_0 c_0}{\cos(\theta)}\,\boldsymbol{\psi_2}}+\frac{\boldsymbol{\psi_8}}{\boldsymbol{\psi_2}}\right\}e^{\beta\frac{\omega}{c_0}D}\mathrm{A}_2\\ &=-2p_i\mathbf{D}+2\boldsymbol{\psi_6}\frac{\left\{(T+2j\omega\eta)\boldsymbol{\psi_3}+\left[\omega^2\rho_{s2}-2\frac{j\omega\rho_0\,c_0}{\cos(\theta)}\right]\boldsymbol{\psi_4}\right\}e^{\beta\frac{\omega}{c_0}D}\mathbf{A_2}}{-2\boldsymbol{\psi_5}}.\end{aligned} \tag{6.121}$$

Hence,

$$\mathbf{A_2}=\frac{-2p_i\mathbf{D}e^{-\beta\frac{\omega}{c_0}D}}{\left[(T+2j\omega\eta)\boldsymbol{\psi_1}+\omega^2\rho_{s1}\boldsymbol{\psi_2}\right]\left\{\frac{(\boldsymbol{\psi_6}-\boldsymbol{\psi_7})\boldsymbol{\psi}_{10}}{\frac{j\omega\rho_0 c_0}{\cos(\theta)}\,\boldsymbol{\psi_2}}+\frac{\boldsymbol{\psi_8}}{\boldsymbol{\psi_2}}\right\}-2\boldsymbol{\psi_6}\boldsymbol{\psi}_{10}}, \tag{6.122}$$

and the transmitted sound pressure is given by

$$\begin{aligned}p_t&=\frac{j\omega\rho_0 c_0}{l_x l_y\cos(\theta)}\mathbf{D}^{\mathrm{T}}\mathbf{A_2}\\ &=\frac{j\omega\rho_0 c_0\mathbf{D}^{\mathrm{T}}}{l_x l_y\cos(\theta)}\frac{-2p_i\mathbf{D}e^{-\beta\frac{\omega}{c_0}D}}{\left[(T+2j\omega\eta)\psi_{\mathbf{1}}+\omega^2\rho_{s1}\boldsymbol{\psi_2}\right]\left\{\frac{(\boldsymbol{\psi_6}-\boldsymbol{\psi_7})\boldsymbol{\psi}_{10}}{\frac{j\omega\rho_0 c_0}{\cos(\theta)}\,\boldsymbol{\psi_2}}+\frac{\boldsymbol{\psi_8}}{\boldsymbol{\psi_2}}\right\}-2\boldsymbol{\psi_6}\boldsymbol{\psi}_{10}}.\end{aligned} \tag{6.123}$$

Hence, the transmission coefficient at an angle of incidence θ is obtained as

$$\tau(\theta) = \left|\frac{p_t}{p_i}\right| = \left| \frac{\frac{j\omega\rho_0 c_0 \mathbf{D}^{\mathrm{T}}}{l_x l_y \cos(\theta)} \frac{-2p_i \mathbf{D} e^{-\beta \frac{\omega}{c_0} D}}{\left[(T+2j\omega\eta)\boldsymbol{\psi_1}+\omega^2\rho_{s1}\boldsymbol{\psi_2}\right]\left\{\frac{(\boldsymbol{\psi_6}-\boldsymbol{\psi_7})\boldsymbol{\psi}_{10}}{\frac{j\omega\rho_0 c_0}{\cos(\theta)}\boldsymbol{\psi_2}}+\frac{\boldsymbol{\psi_8}}{\boldsymbol{\psi_2}}\right\}-2\boldsymbol{\psi_6}\boldsymbol{\psi}_{10}}}{p_i} \right|$$

$$= \left| \frac{j\omega\rho_0 c_0 \mathbf{D}^{\mathrm{T}}}{l_x l_y \cos(\theta)} \frac{-2\mathbf{D} e^{-\beta \frac{\omega}{c_0} D}}{[(T+2j\omega\eta)\boldsymbol{\psi_1}+\omega^2\rho_{s1}\boldsymbol{\psi_2}]\left\{\frac{(\boldsymbol{\psi_6}-\boldsymbol{\psi_7})\boldsymbol{\psi}_{10}}{\frac{j\omega\rho_0 c_0}{\cos(\theta)}\boldsymbol{\psi_2}}+\frac{\boldsymbol{\psi_8}}{\boldsymbol{\psi_2}}\right\}-2\boldsymbol{\psi_6}\boldsymbol{\psi}_{10}} \right|. \tag{6.124}$$

Since β is positive, the decay factor $e^{-\beta \frac{\omega}{c_0} D}$ is always less than unity and hence leads to a decrease of the transmission coefficient. Substituting Equation (6.124) into Equations (2.93) and (6.108) yields the STL expression in a diffuse field with a sound absorbing cavity boundary. Moreover, when the sound absorbing boundary of the air cavity is considered, the transmission coefficient is decreased leading to an increase in the predicted STL. The results obtained from this model are compared with the experimental results in Section 6.5.3.

6.5.3 Comparison with experimental results

This section compares the predicted STLs using the model developed in Section 6.5.2 with the experimentally measured STLs. The comparisons are shown in Figures 6.7 and 6.8 with cavity depths of 70 mm and 140 mm, respectively. In the prediction model, the value of parameter β is optimised for each set of results displayed in the figure. The optimised value is indicated in the figures. Similar to Figures 6.5 and 6.6, the thin dashed curves illustrate the predicted results at discrete frequencies from 50 Hz to 10 kHz. The thick dashed curves represent those results averaged over each 1/3 octave band. The STLs at the centre frequencies of these 1/3 octave bands are shown as the black dots on the thick dashed curve.

Comparing Figures 6.7 and 6.8 with Figures 6.5 and 6.6, it is found that the predicted STLs are increased by applying the decay factor. This observation is consistent with the presumption arising from the analytical model developed in Section 6.5.2.

It is found in Figures 6.7 and 6.8 that the predicted STLs have good agreement with the

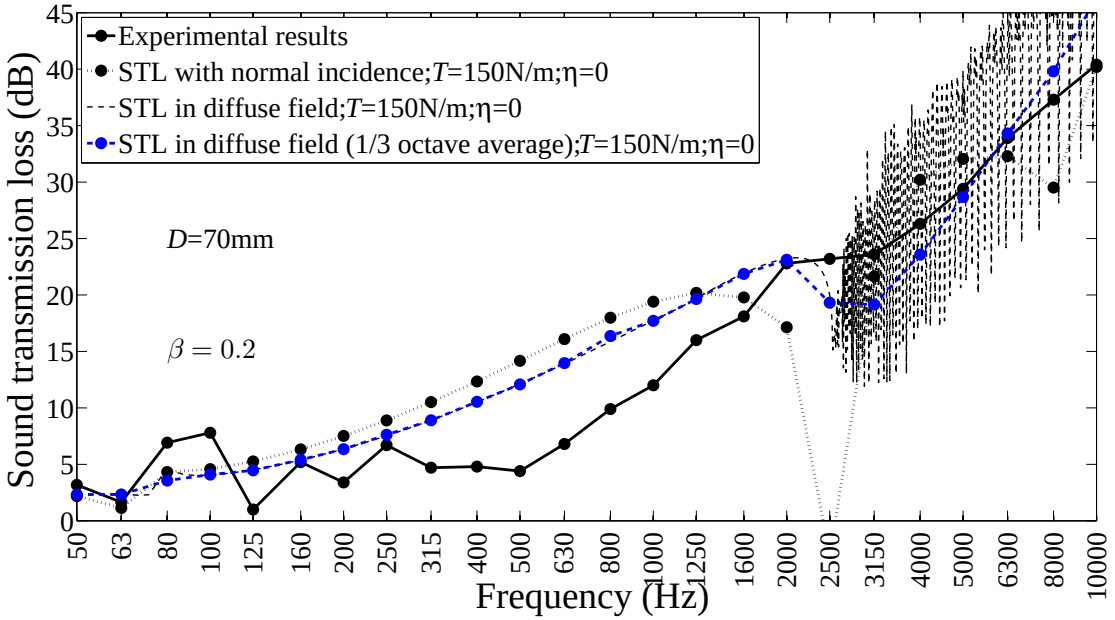

Figure 6.7: STL of double layer impervious membranes separated by a finite air cavity with a depth $D = 70$ mm. The sound absorbing boundary is modelled by the factor $e^{-\beta\frac{\omega}{c_0}D}$.

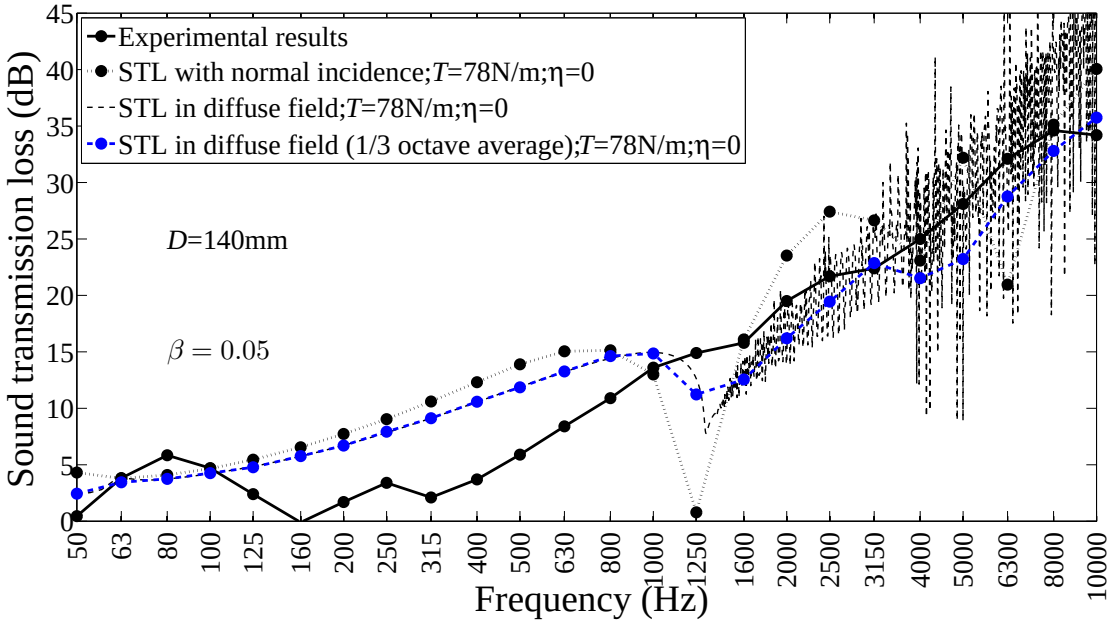

Figure 6.8: STL of double layer impervious membranes separated by a finite air cavity with a depth $D = 140$ mm. The sound absorbing boundary is modelled by the factor $e^{-\beta\frac{\omega}{c_0}D}$.

experimentally measured STLs in the frequency range above the first resonance frequency of the air cavity. This implies that the sound absorbing boundary of the air cavity has a significant impact on the STL of the combined structure in the high frequency range. The high sound transmission loss in this frequency range is not only because of the sound attenuation on the membrane surfaces, but also because of the sound absorption of the boundary within the air cavity. However, in the low frequency range, the predicted STLs with the sound decay due to the sound absorbing boundary are slightly higher than those predicted by the diffuse model. This is because when the frequency is lower than the first resonance frequency of the cavity, plane wave propagation is dominant and the sound absorption on the sound absorbing boundary can be neglected. In general, this model is more accurate than the previous models due to the incorporation of the additional sound decay on the sound absorbing boundary of the air cavity.

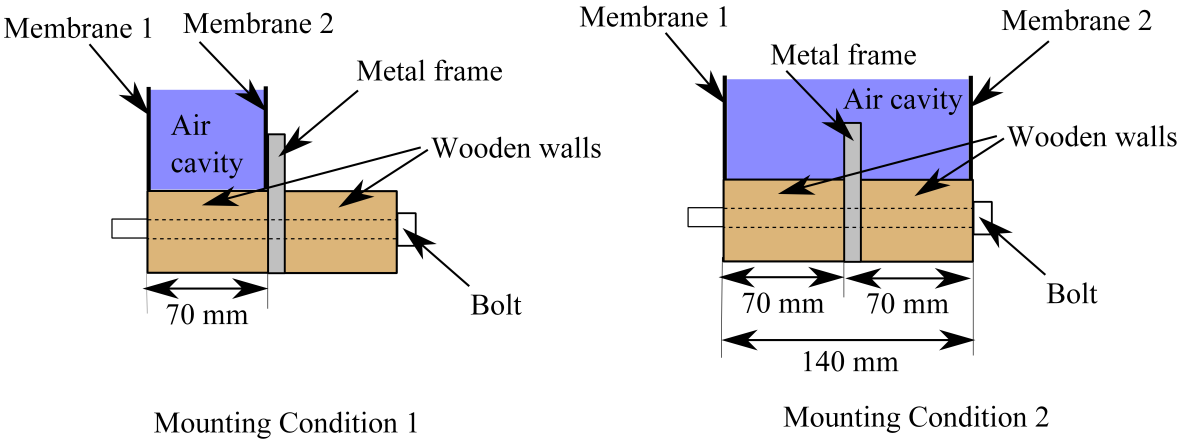

Figure 6.9: Two mounting conditions of the double layer impervious membranes separated by a finite air cavity with a depth $D = 70$ mm and $D = 140$ mm.

It is found in Figures 6.7 and 6.8 that the factor β is 0.2 for the 70 mm cavity and 0.05 for the 140 mm cavity. This significant difference is due to mounting conditions. As illustrated in Figure 6.9, when the membranes were separated by a 70 mm cavity, the sound absorbing boundary only consists of the wooden walls. However, when the air cavity was 140 mm, the sound absorbing boundary consists of the wooden walls, as well as a metal frame which is fixed in the middle of the wooden frames. The metal frame has a acoustically rigid surface. Hence, the sound absorption of the cavity boundary was decreased with the presence of the metal frame.

6.6 Conclusions

In this chapter, three analytical models have been developed to predict the STL of double layer impervious membranes separated by a finite-sized air cavity. In all three models, the motion equation of each of the impervious membranes includes a constant tension applied on the membrane surface and internal damping due to the membrane curvature. The air motion within the cavity is based on three-dimensional sound propagation theory. These motion equations were solved based on the modal analysis method in matrix form. The fluid-structure coupling on each membrane surface was applied to obtain the amplitude parameters for each mode.

The first model assumes that the incident sound is normal to the membrane surface. The predicted STLs show clear resonant sound transmission in the frequency range above the first resonance frequency of the air cavity. However, the experimentally measured STLs were obtained in a diffuse field. The difference between the predicted and measured STLs is ascribed to the neglected effect of the incidence sound angle.

To improve the accuracy of the normal incidence STL model, the incident sound is assumed to be oblique in the second model. By varying the incidence angle and averaging the STLs with the angle of oblique incidence, the STLs in a diffuse field are obtained. This model is more accurate than the normal incidence STL model in the low frequency range, however, it tends to underestimate the STLs in the high frequency range. This underestimation is presumed to be related to the sound absorbing boundary of the air cavity which may have additional sound absorption in the high frequency range.

To consider the effect of the sound absorbing boundary of the air cavity on the predicted STL, a third model was developed by introducing an additional sound decay factor into the expressions for the sound propagation within the air cavity. This model has good agreement with the measured STLs in the frequency range above the first resonance frequency of the air cavity, implying that the high STLs are not only related to the sound attenuation of the impervious membranes and the cavity, but also related to the sound absorption of the sound absorbing boundary of the air cavity. Although this model tends to overestimate the STLs in the low frequency range, it is the most accurate model amongst the three developed models and can be used for research and design of membrane noise barriers.

As mentioned previously, the coupling between the membranes and the separating air cavity has been investigated in this study, however, the effects of the acoustic properties of the reverberation chambers on the STLs are neglected this study. However, Poblet-Puig & Rodrguez-Ferran (2012) investigated the effects of opening position, chamber properties and indicated that they have a impact on the sound transmission. Hence, a possible extension to this study is consideration of the coupling between the membrane structures and the reverberation chambers and the opening position for a more accurate prediction in the frequency range below the first resonance frequency of the air cavity.

Chapter 7

Sound transmission of double layer impervious membranes with an internal micro-perforated membrane

7.1 Introduction

In Chapter 6, the sound transmission of double layer impervious membranes has been investigated theoretically and experimentally. Although the predicted results agree with the experimental results, which indicates the accuracy of the analytical models developed in Chapter 6, the sound attenuation of the double layer impervious membranes is less effective than conventional massive walls.

In an attempt to enhance the sound attenuation of double layer impervious membranes this study investigates the use of an MPM (micro perforated membrane) inserted into the air cavity between the two impervious membranes. The double layer impervious membranes and the internal MPM are coupled with the two air cavities, which forms a combined membrane-air structure.

Since the sound absorption properties of MPMs have been studied theoretically and experimentally in Chapter 3 and the sound transmission of double layer impervious membranes has been investigated in Chapter 6, this chapter aims to investigate the effect of the internal MPM on the sound transmission of the combined membrane structure. Section 7.1.1 reviews the previous studies on the sound transmission and absorption of membranes, followed by the gaps and contributions in Section 7.1.2. In Section 7.2, the effectiveness of the internal MPM on the STL enhancement of the combined structure is illustrated by experimental results. The analytical model of the sound transmission of double layer impervious membranes

with an internal MPM is developed in Section 7.3. This model is validated with the experimental results shown in Section 7.2. A conclusion of this chapter is presented in Section 7.4.

7.1.1 Literature review

The experimental works of Mehra (2002) and Vries (2011) have demonstrated that, although impervious membranes can provide some sound insulation, their sound transmission losses are commonly lower than those of the more massive building materials which are used as traditional noise barriers. Therefore, efforts have been made to enhance the sound insulation of membrane structures.

Since the sound transmission is dependent on the surface density of materials, it is presumed that the STL of membrane structures can be increased by increasing the surface density. Hashimoto et al. (1996, 1991) found that the sound insulation was improved by adding small weights to the membrane surfaces. Similarly, Yang et al. (2008) placed a small mass at the centre of a membrane-type acoustic meta-material. It has been demonstrated that the performance of this configuration could exceed the mass law and increase the sound insulation significantly in the low frequency range from 100 Hz to 1000 Hz. Zhang et al. (2012) furthered Yang et al.'s work by investigating the sound transmission loss of the same materials with different attached mass locations. However, adding additional small weights on the membranes, no matter if the membranes are common materials or meta-materials, increases the overall weight of the membrane structures significantly.

An alternative way to improve the transmission loss is by adding bulk porous materials in the cavity between the double membrane layers. Porous materials are widely used as sound absorbing materials and can provide efficient sound absorption with low cost. In Vries (2011) master's thesis, various absorption materials, including mineral wool, foams, wood wool and glass wool, filled the cavities of triple layer membrane structures. From the experimental results, it can be concluded that filling the cavities between the membranes with porous materials could improve the sound insulation. These porous materials need to be sufficiently thick to maintain effective sound absorption, particularly in the low frequency range. Therefore, the overall thicknesses of the membrane structures are increased in addition to their mass. This detracts from the advantages of the membrane structures being

lightweight and convenient for transportation and storage.

MPPs (micro perforated panels) and MPMs have been considered as alternatives to conventional sound absorbing porous materials, although since MPPs are made from rigid panels these are inconvenient for transportation and storage. MPMs offer similar sound absorption performance to conventional porous materials while being lighter and flexible as porous. Based on the investigation on the sound absorption of MPMs in Chapters 3 to 5, it is assumed that insertion of an MPM can enhance the sound transmission loss of the double layer impervious membranes.

7.1.2 Gaps and contributions

Although the experiments by Vries (2011) have demonstrated that internal porous materials enhance the sound insulation of double layer membranes, there is very limited research on the effect of internal MPMs on the sound insulation of membrane structures. This chapter aims to explore the impact of an internal MPM on the sound transmission of double layer impervious membranes.

The design of the double layer impervious membranes with an internal MPM is presented in Section 7.2.1. The effectiveness of this design on the enhancement of the STL of the combined structure is quantified in Section 7.2.2 by experiments. It is demonstrated that the MPM insertion can be used as an effective method to increase the sound insulation of membrane structures in future noise control projects.

In addition to the experimental investigation, analytical modelling of the STL of double layer impervious membranes with an internal MPM has been undertaken and is presented in Section 7.3. The analytical model for the STL in a diffuse field is based on the models developed in Chapters 3 and 6. Since it is found in Chapter 4 that the MPM 4 (with surface density $\rho_p = 0.2506\,\mathrm{kg/m^2}$, hole radius $r_0 = 0.255\,\mathrm{mm}$, membrane thickness $h = 0.17\,\mathrm{mm}$, hole spacing $5.29\,\mathrm{mm}$ and perforation ratio $\delta = 0.730\%$) exhibits a non-linear sound absorption under high incident SPL, the effect of the non-linear sound absorption on the STL of the combined membrane structure is studied in Section 7.3.3. The analytical model developed in Section 7.3 is extended to the non-linear region based on the non-linear sound absorption theory developed in Chapter 5.

Therefore, this chapter not only introduces an effective design to improve the sound

insulation of double layer impervious membranes by inserting an MPM into the air cavity, it also develops two theoretical models for this design. The effects of the internal MPM and its non-linear sound absorption on the STL of the combined membrane structure in a diffuse field are investigated using these two models. Hence, the developed models extend the understanding of the sound transmission of double layer impervious membranes with an internal MPM and can be useful for membrane noise barrier design in future engineering projects.

7.2 Increasing the STL of a double layer impervious membrane with an internal MPM

This section aims to describe the design of the double layer impervious membranes with an internal MPM in detail and verify the effectiveness of the internal MPM on the STL enhancement. In Section 7.2.1 the design is presented and the experimental results are discussed in Section 7.2.2.

7.2.1 Design of the double layer impervious membrane with an internal MPM

In an attempt to improve the sound transmission loss of double layer impervious membranes studied in Chapter 6, an MPM was inserted into the air cavity between the two membranes. Four types of MPMs were used as the internal MPMs. The sound absorption of these MPMs for normally-incident plane waves has been studied in Chapter 3 and their parameters are shown in Table 3.2. The surface density of the impervious membranes is compared with those of the MPMs in Table 7.1.

Table 7.1: Parameters of the impervious membranes and MPMs.

Material	Surface density $(\mathrm{kg/m^2})$	Thickness (mm)
Impervious membranes (PVC)	0.4850	0.42
MPM 1	0.2501	0.17
MPM 2	0.2403	0.17
MPM 3	0.2448	0.17
MPM 4	0.2506	0.17

Figure 7.1 illustrates the design of the double layer impervious membrane structure with an internal MPM. Two impervious membranes, Membrane 1 and 2, are parallel to each

other and an MPM is placed between them. The cavity depth between Membrane 1 and the internal MPM is D_1 and that between the internal MPM and Membrane 2 is D_2. In this chapter, $D_1 = D_2 = 70$ mm.

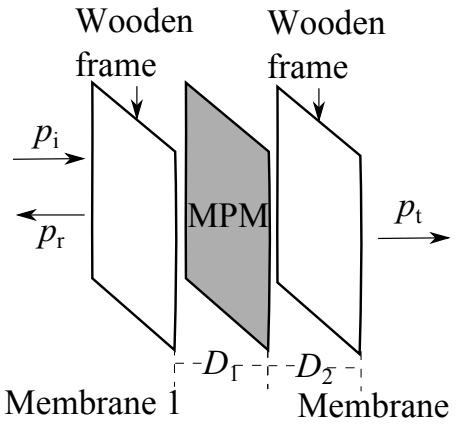

Figure 7.1: Geometry of the model of double layer impervious membranes with an internal microperforated membrane. Variable D_1 denotes the depth of the cavity between Membrane 1 and the internal MPM, and D_2 denotes the depth of the cavity between the internal MPM and Membrane 2. $D_1 = D_2 = 70$ mm.

When the incident sound p_i strikes Membrane 1, some of the sound energy is reflected back which is known as p_r and some is transmitted through Membrane 1. The transmitted sound travels in Air Cavity 1 until it reaches the internal MPM where some of its sound energy is reflected back by the internal MPM and the remaining sound energy is transmitted through the internal MPM and enters Air Cavity 2. Similarly, some of this transmitted sound is reflected back into Air Cavity 2 by Membrane 2 and some is transmitted through Membrane 2, giving rise to the transmitted pressure p_t. The transmission coefficient of the combined membrane structure is obtained by calculating the ratio of the transmitted sound pressure to the incident sound pressure. The presence of the MPM results in increased damping in the cavity, which consequently increases the transmission loss through the partition.

The MPM is effective at reducing the amplitude of all odd order axial cavity modes which have a velocity maxima in the centre of the two impervious membranes, assuming rigid-walled cavity modes. In addition to the sound absorption from the internal MPM, the sound absorbing boundary of the air cavities can also absorb sound energy, as discussed in Chapter 6. Since the cavity walls in the experiments conducted in this study are made of wood, they are not perfectly acoustically rigid and their sound absorption could be significant, especially in the frequency range higher than the resonance frequency of the air cavity.

7.2.2 Experimental results

The design of the double layer impervious membranes with an internal MPM has been presented in Section 7.2.1. It is presumed that the internal MPM can absorb sound energy and hence increases the sound transmission loss of the combined membrane structure. This presumption is demonstrated with the experimental results presented in this section.

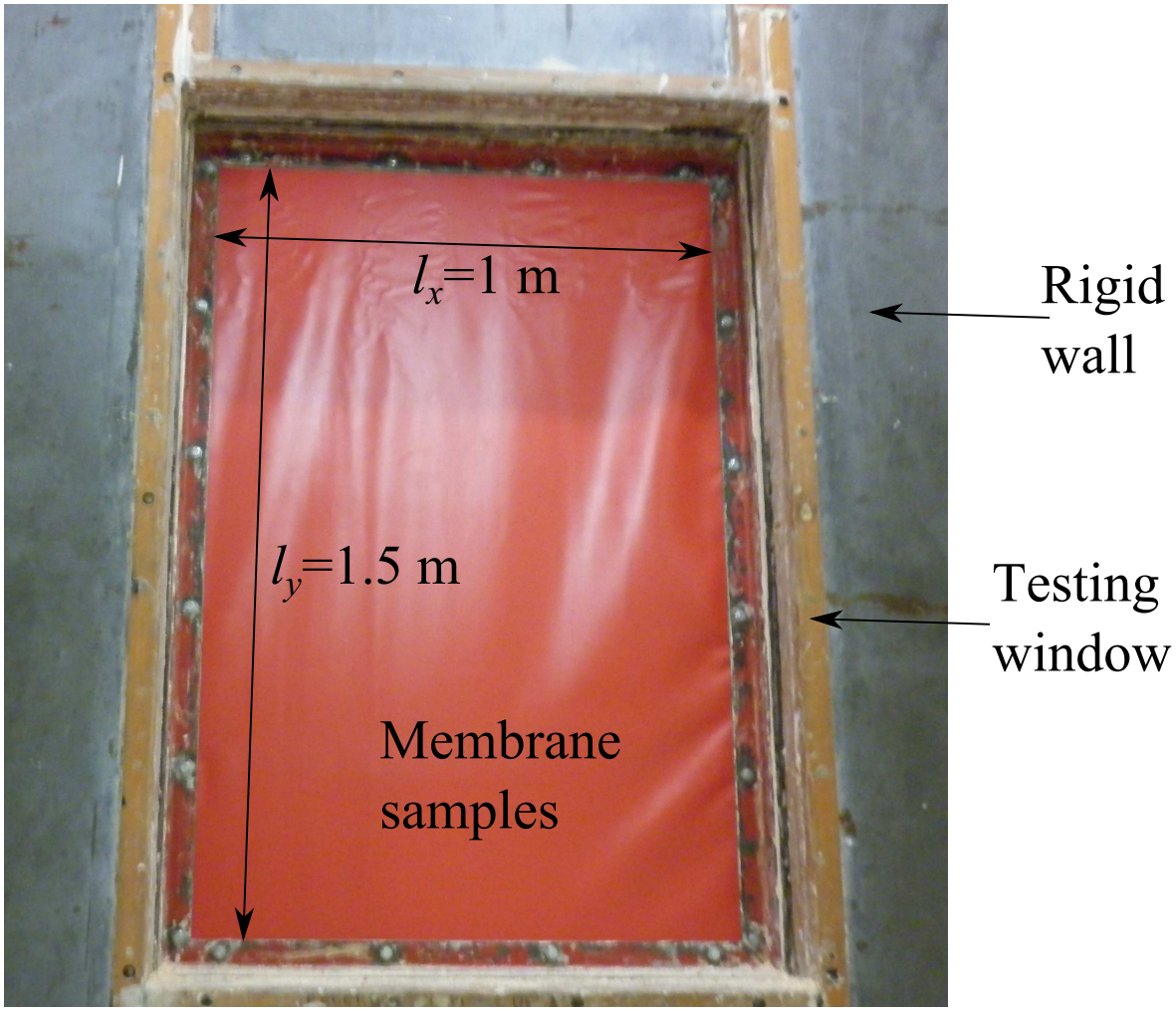

Figure 7.2: Photograph of the STL measurement arrangement.

Four MPMs with different parameters were stretched slightly over four wooden frames which were identical to the frames used to mount the impervious membranes. Each MPM and covered frame was inserted between the double layer impervious membranes and the sound transmission loss was measured in the reverberation chambers used in Chapters 2 and 6, as shown in Figure 7.2. The depth of each air cavity was 70 mm. The measured STLs of the double layer impervious membranes without and with each internal MPM are shown in Figure 7.3.

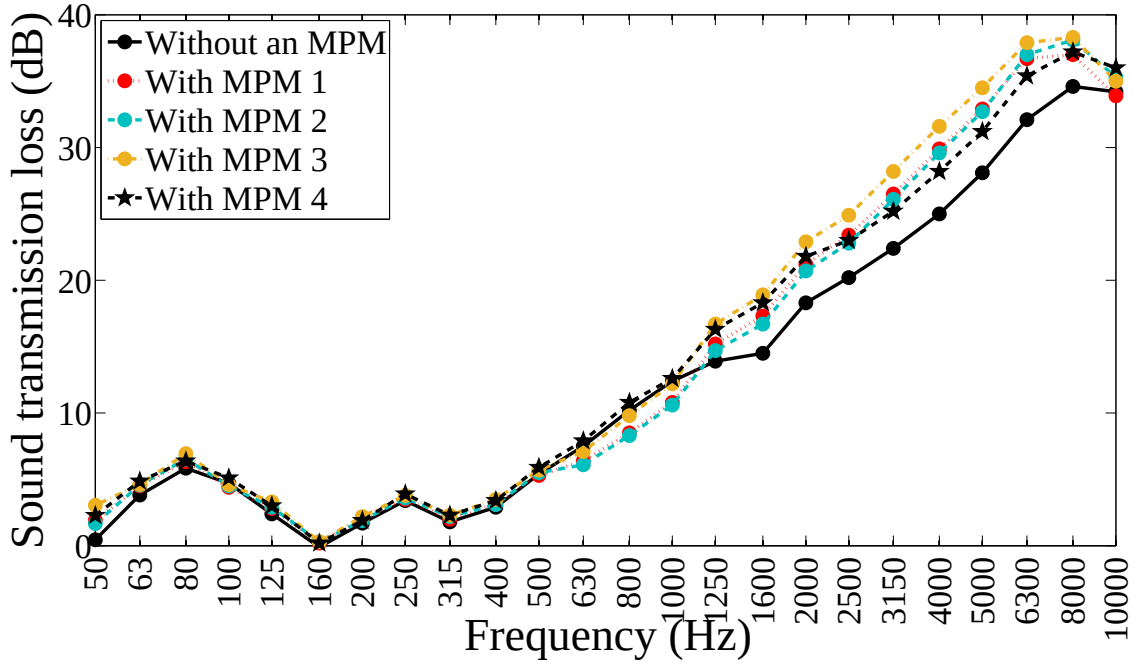

Figure 7.3: Measured sound transmission loss in one-third octave bands of double layer impervious membranes without and with four different internal MPMs. $D_1 = D_2 = 70$ mm.

In Figure 7.3, the measured STL of double layer impervious membranes with each of the four MPMs is compared to that of double layer impervious membranes without an internal MPM (used in Chapter 6). The presence of the MPM creates two air cavities and their depths are both 70 mm. In the absence of the MPM, the cavity depth was 140 mm. Hence, the thickness for all partitions remained of 140 mm and consequently the sound absorption from the sound absorbing boundaries was considered identical for each case. Therefore, the variations on the measured STL curves of those with an internal MPM from that without the internal MPM are associated only with the presence of the MPM.

It is clear from Figure 7.3 that when the MPM is inserted the sound insulation of double layer impervious membrane structures is improved in the middle and high frequency range. In the low frequency range from 50 Hz to 500 Hz, all the curves are approximately equal, which implies that all four internal MPMs have negligible impact on the sound insulation of the double layer membrane structure at low frequencies, as could be predicted from the mass law. From 630 Hz to 1 kHz, the STLs of the double layer structures with MPMs 1 and 2 are lower than those with no MPM, while those with MPMs 3 and 4 are close to those with no MPM (solid blue curve). The significant enhancement due to MPM insertion starts from 1250 Hz, which is the first resonance frequency of an air cavity with a depth of 140 mm.

Therefore, it is concluded that the enhancement due to the MPM insertion is significant at the frequencies above the first resonance frequency of the air cavity. At frequencies below the cavity resonance, the effect of the MPM insertion on the STL is negligible.

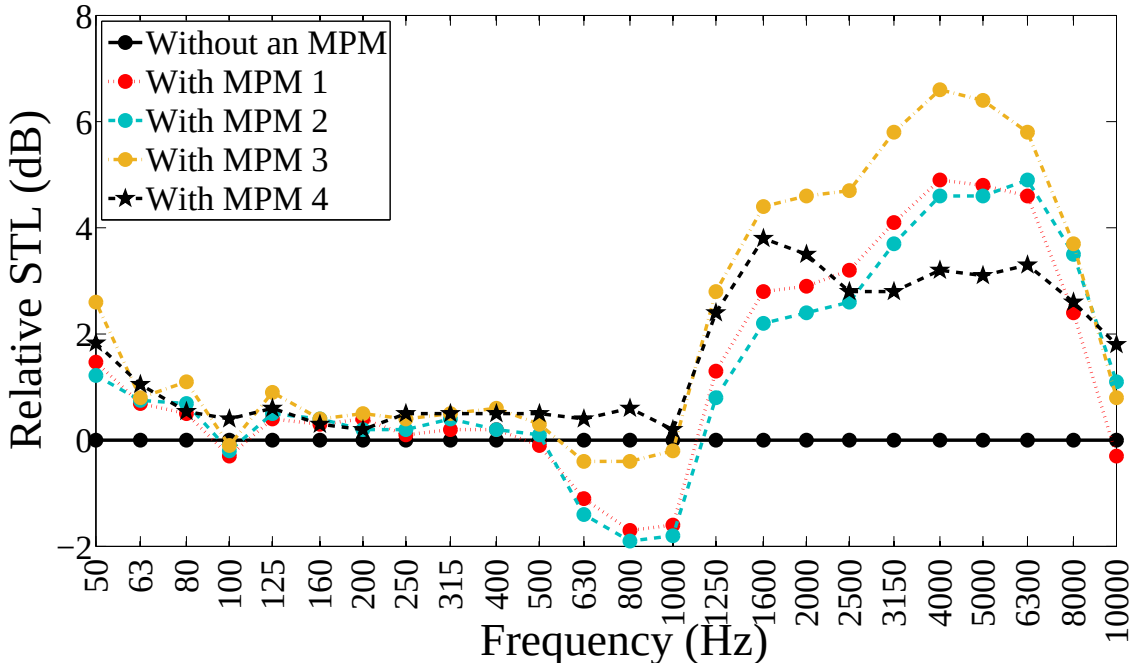

Figure 7.4: Difference between the measured STLs of double layer impervious membranes with an internal MPM and that without an internal MPM.

Figure 7.4 shows the difference between the measured STLs of the double layer impervious membranes with each internal MPM and that without an internal MPM. This figure illustrates the enhancement in the STL due to the MPM insertion more clearly than Figure 7.3. In the frequency range from 50 Hz to 500 Hz, the curves with four MPMs are very similar but slightly higher than zero, which implies the limited enhancement of the MPM insertion in this frequency range. From 500 Hz to 1000 Hz, the STL difference with MPM 4 is positive and the others are negative. This implies that in this frequency range only MPM 4 is able to improve the sound insulation of the double layer impervious membranes. By contrast, the other MPMs decrease the measured STL slightly.

In the frequency range above 1250 Hz, all four MPMs improve the STL of the double layer impervious membranes significantly. MPM 3 demonstrates the most significant enhancement of STL among all four MPMs. The maximum increase in STL with MPM 3 is 6.6 dB at 4 kHz. The curve with MPM 4 peaks at 3.8 dB at 1600 Hz. The curves of MPM 1 and MPM 2 share a similar upward trend but the increase of MPM 1 is greater than that of

MPM 2 from 1250 Hz to 5 kHz. The enhancement of MPM 2 is more effective than that of MPM 1 from 6300 Hz to 10 kHz. This peak value is at a frequency significantly lower than the peak frequencies with the other MPMs. This difference is associated to the properties of the MPMs. It has been indicated in Chapter 3 that MPMs 1 to 3 have very small diameter perforations. They can be considered as impervious membranes, however MPM 4 shows effective sound absorption due to its larger diameter perforations. Consequently, MPM 4 has a different effect on the STL of double layer impervious membranes compared to MPMs 1 to 3.

Note that the frequency 1250 Hz is the first resonance frequency of the air cavity when the depth is 140 mm. Likewise, the resonance frequency for the 70 mm cavities is 2500 Hz. The enhancement of the MPM insertion in the STL curve is significant at the frequencies above the first resonance frequency of the air cavity. MPMs 1 to 3 show a similar general trend of an increased STL, but the magnitude varies slightly for each MPM. MPM 4 has a different effect on the STL of double layer impervious membranes compared to MPMs 1 to 3 due to the larger perforations of MPM 4.

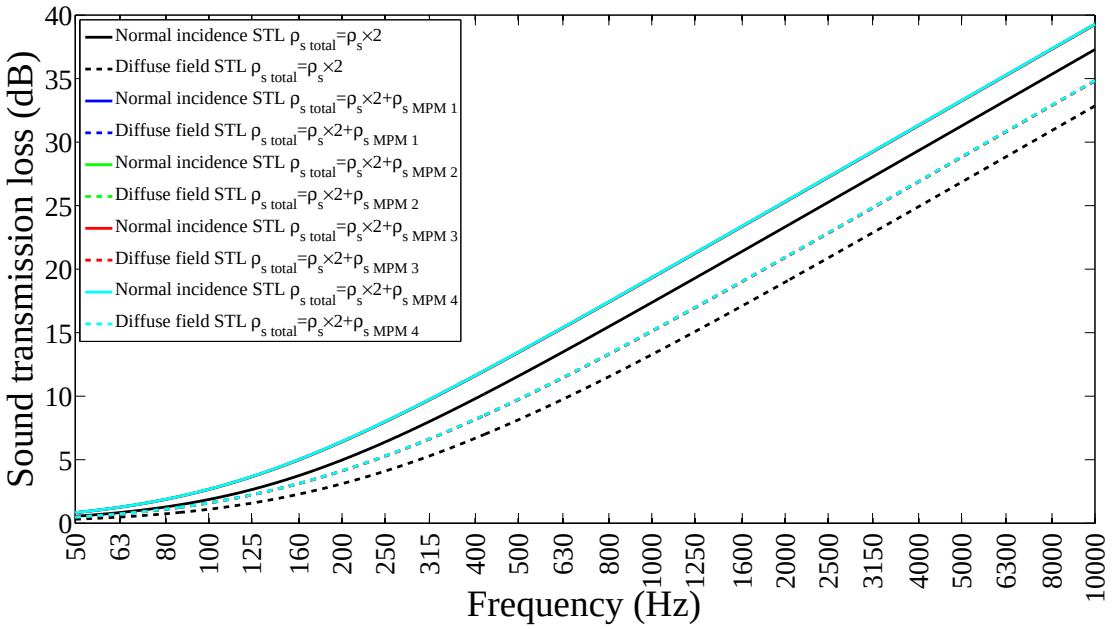

Figure 7.5: Predicted STL of single layer impervious membrane with surface density equal to the sum of the surface densities of the two impervious membranes and that of each MPM.

In an attempt to investigate the mechanism of the enhancement of the internal MPM on the STL of membrane structures, it is initially assumed that only the surface densities of the membranes have an impact on the predicted STL. Hence, the mass of the membrane

structure is only considered and this model is a pure mass model. Figure 7.5 shows the predicted results using this pure mass model. It is found from Figure 7.5 that the predicted results for double layer impervious membranes using the pure mass model are lower than those with different internal MPMs inserted. This can be ascribed to the increased total mass due to the internal MPMs. However, the predicted results with different internal MPMs are overlapping due to the similar surface densities of the internal MPMs, as presented in Table 7.1. By contrast, the experimentally measured STLs in Figures 7.3 and 7.4 demonstrate that the measured STLs differ for each of the different MPMs. Therefore, the pure mass model is not valid in this study, and a new analytical model for the double layer impervious membranes with an internal MPM is needed.

7.3 Analytical modelling of double layer impervious membranes with an internal MPM

In Section 7.2 it was demonstrated that inserting an MPM between two impervious membranes can increase the sound transmission loss. To investigate the mechanism behind this increase, this section aims to develop a theoretical model for the STL prediction of the double layer impervious membranes with an internal MPM. This model is based on a combination of the models developed in Chapter 6 and the impedance prediction for the MPMs based on the non-slip method developed in Chapter 3. Note that the investigation in Chapter 3 found that the four MPMs used in this project can be categorised into two groups: MPMs 1 to 3, which can be considered as impervious membranes because of their insufficiently small perforations; and MPM 4 which has larger perforations than MPMs 1 to 3 and can be considered sound absorbing. Hence, in this section, the derivation for the STL of double layer impervious membranes with an internal MPM has been carried out in two parts: the derivation for that with MPMs 1 to 3 in Section 7.3.1, and the derivation for that with MPM 4 in Section 7.3.2.

Since MPM 4 shows non-linear sound absorption when excited by high incident SPLs, the effect of the non-linear sound absorption on the predicted STL is also investigated in Section 7.3.3. These developed models have been validated by experimental results in the corresponding sections.

7.3.1 STL of double layer impervious membranes with an internal impervious membrane (MPMs 1 to 3)

This section develops the analytical model for the STL prediction of double layer impervious membranes with an internal MPM by extending the double layer membrane model developed in Chapter 6 to a model with three layers of membranes separated by two air cavities with identical depth $D_1 = D_2 = 70$ mm. The STL model with a normally-incident plane wave is developed in Section 7.3.1.1 and then is extended to a diffuse field in Section 7.3.1.2. These models have been validated in Section 7.3.1.3.

The internal MPM mentioned in this section is one of the three MPMs (1 to 3) used in Chapter 3. As mentioned in Chapter 3, the perforations in MPMs 1 to 3 are insufficiently small for the air to travel through these perforations. As a result, these MPMs can be considered as impervious membranes. Therefore, the modelling in this section is for the STL of triple layer impervious membranes separated by two air cavities, D_1 and D_2.

7.3.1.1 STL of double layer impervious membranes with an internal impervious MPM with normally-incident plane wave

Consider the partition configuration shown in Figure 7.6 similar to the case of sound propagation in the double layer impervious membranes discussed in Chapter 6. When the sound wave p_i is incident on Membrane 1, some of the sound is reflected back, denoted p_r. Some of the incident sound energy is transmitted through Membrane 1 and enters the first air cavity with a cavity depth of D_1. The sound pressure of this transmitted sound in Air Cavity 1 is named p_{i2}. The sound p_{i2} continues propagating in Air Cavity 1 until it meets the internal MPM, where some of the sound is reflected (known as p_{r2}) and some of the sound is transmitted. The sound transmitted by the MPM enters Air Cavity 2, and is named as p_{i3}. The incident sound p_{i3} is also partly reflected back and partly transmitted by Membrane 2. The reflected sound pressure in Air Cavity 2 is known as p_{r3}. The sound pressure transmitted by Membrane 2 is considered as the transmitted sound of the entire membrane system and is known as p_t. Therefore, the transmission coefficient of the membrane structure is dependent on the ratio of p_t and p_i.

Assume that the particle velocity in the z-direction on the entire surface of Membrane 1 is v_1. Hence, due to the velocity continuity in the z-direction, the particle velocity in the

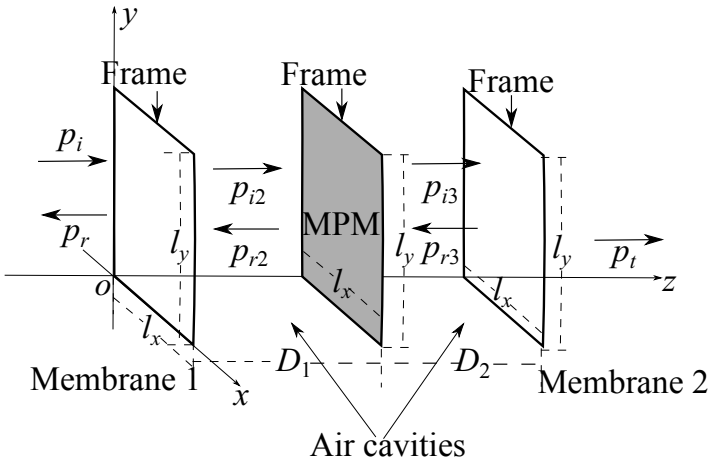

Figure 7.6: Sound propagation in double layer impervious membranes with an internal microperforated membrane. Variable D_1 denotes the depth of the cavity between Membrane 1 and the internal MPM, and D_2 denotes the depth of the cavity between the internal MPM and Membrane 2. $D_1 = D_2 = 70$ mm.

z-direction on the left-hand surface of Membrane 1 can be expressed as a function of the sound pressures p_i and p_r which is given by (Fahy & Gardonio 2007)

$$v_1 = \frac{p_i - p_r}{\rho_0 c_0}. \tag{7.1}$$

Rearranging Equation (7.1) yields the expression of p_r as

$$p_r = p_i - \rho_0 c_0 v_1. \tag{7.2}$$

Similarly, on the right-hand surface of Membrane 1, the relationship between the sound pressures p_{i2}, p_{r2} and the particle velocity in the z-direction, v_1, is expressed as

$$\frac{p_{i2} - p_{r2}}{\rho_0 c_0} = v_1, \tag{7.3}$$

and hence, the sound pressure reflected by the internal MPM is given by

$$p_{r2} = p_{i2} - \rho_0 c_0 v_1. \tag{7.4}$$

Therefore, the sound pressure difference applied across Membrane 1 is given by

$$\begin{aligned} \Delta p_1 &= p_i + p_r - (p_{i2} + p_{r2}) \\ &= 2p_i - \rho_0 c_0 v_1 - (2p_{i2} - \rho_0 c_0 v_1) \\ &= 2p_i - 2p_{i2}. \end{aligned} \tag{7.5}$$

Equation (7.5) is identical to Equation (6.6) in Chapter 6, which implies that although an internal MPM is added in this model, the sound pressure difference on Membrane 1 is ex-

pressed in the same form to that without the internal MPM. Note that although they are in the same form, the value of p_{i2} differs from that in Chapter 6 due to the existence of the internal MPM. Note that the terms p_{i2}, p_{r2}, p_{i3} and p_{r3} are functions with respect to the local position coordinate (x, y).

Assuming that the particle velocity in the z-direction on each surface of the internal MPM is v_{MPM}, similar relationships are obtained based on the particle velocity in the z-direction with respect to p_{i2}, p_{r2}, p_{i3} and p_{r3}, namely

$$\frac{p_{i2}e^{-jk_{0z}D_1} - p_{r2}e^{jk_{0z}D_1}}{\rho_0 c_0} = v_{\mathrm{MPM}}, \tag{7.6}$$

and

$$\frac{p_{i3} - p_{r3}}{\rho_0 c_0} = v_{\mathrm{MPM}}. \tag{7.7}$$

Rewriting these equations yields the expressions for p_{r2} and p_{r3} as

$$\begin{aligned} p_{r2}e^{jk_{0z}D_1} &= p_{i2}e^{-jk_{0z}D_1} - \rho_0 c_0 v_{\mathrm{MPM}}, \\ p_{r2} &= p_{i2}e^{-2jk_{0z}D_1} - \rho_0 c_0 v_{\mathrm{MPM}}e^{-jk_{0z}D_1}, \end{aligned} \tag{7.8}$$

and

$$p_{r3} = p_{i3} - \rho_0 c_0 v_{\mathrm{MPM}}. \tag{7.9}$$

Hence, the sound pressure difference applied on the MPM surfaces is obtained as

$$\begin{aligned} \Delta p_{\mathrm{MPM}} &= p_{i2}e^{-jk_{0z}D_1} + p_{r2}e^{jk_{0z}D_1} - (p_{i3} + p_{r3}) \\ &= 2p_{i2}e^{-jk_{0z}D_1} - \rho_0 c_0 v_{\mathrm{MPM}} - 2p_{i3} + \rho_0 c_0 v_{\mathrm{MPM}} \\ &= 2p_{i2}e^{-jk_{0z}D_1} - 2p_{i3}. \end{aligned} \tag{7.10}$$

In Equation (7.10), the first term represents the sound pressure of the incident sound in the first cavity having travelled a distance of D_1.

For Membrane 2, the particle velocity continuity in the z-direction is represented by

$$\frac{p_{i3}e^{-jk_{0z}D_2} - p_{r3}e^{jk_{0z}D_2}}{\rho_0 c_0} = v_2. \tag{7.11}$$

Hence, the reflected sound pressure in the second air cavity is expressed by

$$\begin{aligned} p_{r3}e^{jk_{0z}D_2} &= p_{i3}e^{-jk_{0z}D_2} - \rho_0 c_0 v_2, \\ p_{r3} &= p_{i3}e^{-2jk_{0z}D_2} - \rho_0 c_0 v_2 e^{-jk_{0z}D_2}. \end{aligned} \tag{7.12}$$

Note that on the right-hand side of Membrane 2, there exists only the transmitted sound p_t

through the entire membrane-cavity combined structure. From the particle velocity continuity in the z-direction, the transmitted sound pressure p_t is obtained as

$$p_t = \rho_0 c_0 v_2. \tag{7.13}$$

Consequently, the sound pressure difference on the surface of Membrane 2 is given by

$$\begin{aligned} \Delta p_2 &= p_{i3} e^{-jk_{0z}D_2} + p_{r3} e^{jk_{0z}D_2} - p_t \\ &= 2p_{i3} e^{-jk_{0z}D_2} - 2\rho_0 c_0 v_2. \end{aligned} \tag{7.14}$$

Equation (7.14) is in the same form as Equation (6.54) in Chapter 6, which represents the sound pressure difference on Membrane 2 without the internal MPM.

The sound pressure differences on the impervious membranes and the MPM are determined by Equations (7.5), (7.10) and (7.14), respectively. Substituting these equations into their motion equations gives their forced vibration response. As for the impervious membranes, the motion equation for Membrane 1 is given by

$$(T + 2j\omega\eta)\nabla^2 \xi_1(x,y) + \omega^2 \rho_{s1} \xi_1(x,y) = -\Delta p_1 = -2\ p_i + 2\ p_{i2}, \tag{7.15}$$

and for Membrane 2,

$$\begin{aligned} (T + 2j\omega\eta)\nabla^2 \xi_2(x,y) + \omega^2 \rho_{s2} \xi_2(x,y) = -\Delta p_2 = -2p_{i3} e^{-jk_{0z}D_2} + 2\rho_0 c_0\ v_2(x,y), \\ (T + 2j\omega\eta)\nabla^2 \xi_2(x,y) + \left(\omega^2 \rho_{s2} - 2j\omega\rho_0 c_0\right) \xi_2(x,y) = -2p_{i3} e^{-jk_{0z}D_2}. \end{aligned} \tag{7.16}$$

Note that Equation (7.15) is identical to Equation (6.7). Equation (7.16) is similar to Equation (6.55) except that p_i is replaced by p_{i3}. Since the internal MPM is considered to be an impervious membrane, the motion equation of the internal MPM is given by

$$\begin{aligned} &(T_{\mathrm{MPM}} + 2j\omega\eta_{\mathrm{MPM}})\nabla^2 \xi_{\mathrm{MPM}}(x,y) + \omega^2 \rho_{\mathrm{sMPM}} \xi_{\mathrm{MPM}}(x,y) = -\Delta p_{\mathrm{MPM}} \\ &(T_{\mathrm{MPM}} + 2j\omega\eta_{\mathrm{MPM}})\nabla^2 \xi_{\mathrm{MPM}}(x,y) + \omega^2 \rho_{\mathrm{sMPM}} \xi_{\mathrm{MPM}}(x,y) = -2p_{i2} e^{-jk_{0z}D_1} + 2p_{i3}, \end{aligned} \tag{7.17}$$

where ξ_{MPM} represents the displacement of the internal MPM in the z-direction, T_{MPM} denotes the tension applied on the MPM surface, η_{MPM} denotes the internal damping ratio of the MPM and ρ_{sMPM} denotes the surface density of the MPM.

These motion equations can be solved using linear algebra as presented in Chapter 6. To solve these expressions, the modal amplitudes of the membrane motions and the air motion were assumed to be unknown vectors in Equations (6.13) and (6.61). Consequently, these unknown vectors were solved using the motion equations of the impervious membranes and

the air cavity with respect to the incident sound pressure p_i. Since the STL is dependent on the sound transmission coefficient which is the ratio of p_t and p_i, the incident sound pressure was eliminated and the expression for the STL (Equations (6.85), (6.86), (6.107) and (6.108)) was obtained in Chapter 6.

As in Chapter 6, in this chapter $\mathbf{A_1}$ and $\mathbf{A_2}$ are defined to be the vectors which represent the modal amplitudes of ξ_1 and ξ_2. Using a similar strategy, $\mathbf{A}_{\mathrm{MPM}}$ is defined to be the vector representing the modal amplitude of ξ_{MPM}. Assuming that $A_{\mathrm{MPM_n}}$ represents the nth mode of the MPM motion, the vector $\mathbf{A}_{\mathrm{MPM}}$ is given by

$$\mathbf{A}_{\mathrm{MPM}} = \begin{pmatrix} A_{\mathrm{MPM_1}} \\ A_{\mathrm{MPM_2}} \\ A_{\mathrm{MPM_3}} \\ \vdots \\ A_{\mathrm{MPM_N}} \end{pmatrix}. \tag{7.18}$$

Hence, the displacement of Membrane 1 is expressed by the modal summation

$$\xi_1(x,y) = \sum_{n=1}^{N} A_{n1}\, \xi_{n1}(x,y), \tag{7.19}$$

where the mode shape functions of the transverse membrane vibration are given by

$$\xi_{n1}(x,y) = \sin\left(\frac{n_x \pi}{l_x} x\right) \sin\left(\frac{n_y \pi}{l_y} y\right), \qquad n = N_y(n_x - 1) + n_y. \tag{7.20}$$

The displacement of Membrane 2 is given by

$$\xi_2(x,y) = \sum_{n=1}^{N} A_{n2}\, \xi_{n2}(x,y), \tag{7.21}$$

where

$$\xi_{n2}(x,y) = \sin\left(\frac{n_x \pi}{l_x} x\right) \sin\left(\frac{n_y \pi}{l_y} y\right), \qquad n = N_y(n_x - 1) + n_y. \tag{7.22}$$

These expressions are identical to Equations (6.8), (6.9), (6.56), and (6.57) in Chapter 6, which implies although an internal MPM is used in this chapter, the motions of the impervious membranes are expressed in the same form as those without an internal MPM due to their similar acoustic and vibration mechanisms. Assuming that the perforations on the MPM have negligible impact on the MPM motion, the displacement of the MPM is given by

$$\xi_{\mathrm{MPM}}(x,y) = \sum_{n=1}^{N} A_{\mathrm{MPM_n}}\, \xi_{\mathrm{MPM_n}}(x,y), \tag{7.23}$$

where

$$\xi_{\mathrm{MPM_n}}(x,y) = \sin\left(\frac{n_x\pi}{l_x}x\right)\sin\left(\frac{n_y\pi}{l_y}y\right), \qquad n = N_y(n_x-1)+n_y. \tag{7.24}$$

Let the vectors $\mathbf{B_1}$ and $\mathbf{B_2}$ represent the modal amplitudes associated with the modes in Air Cavities 1 and 2. Note that there is only one vector, namely $\mathbf{B}$, representing the air cavity modes in Chapter 6. However, it is necessary to utilise $\mathbf{B_1}$ and $\mathbf{B_2}$ in this chapter for the two air cavities separated by the internal MPM. Hence,

$$\mathbf{B_1} = \begin{pmatrix} B_{u1_1} \\ B_{u1_2} \\ B_{u1_3} \\ \vdots \\ B_{u1_U} \end{pmatrix}, \tag{7.25}$$

and

$$\mathbf{B_2} = \begin{pmatrix} B_{u2_1} \\ B_{u2_2} \\ B_{u2_3} \\ \vdots \\ B_{u2_U} \end{pmatrix}. \tag{7.26}$$

Using the same approach to model the sound propagation in a 3-D cavity employed in Section 6.2.2, the sound pressures p_{i2} and p_{i3} are given by

$$p_{i2}(x,y) = \sum_{u1=0}^{u1_U} B_{u1_u}\,\zeta_{u1}(x,y), \tag{7.27}$$

where $\zeta_u 1(x,y) = \cos\left(\frac{u1_x\pi}{l_x}x\right)\cos\left(\frac{u1_y\pi}{l_y}y\right)$ represents the acoustic mode shapes of Air Cavity 1, and

$$p_{i3}(x,y) = \sum_{u2=0}^{u2_U} B_{u2_u}\,\zeta_{u2}(x,y), \tag{7.28}$$

where $\zeta_u 2(x,y) = \cos\left(\frac{u2_x\pi}{l_x}x\right)\cos\left(\frac{u2_y\pi}{l_y}y\right)$ are the acoustic mode shape function for Air Cavity 2.

Substituting Equations (7.19) and (7.27) into Equation (7.15), then multiplying each side

of the equation by $\xi_m(x,y)$ and integrating over the membrane surface gives

$$\left[(T+2j\omega\eta)\boldsymbol{\psi}_{\mathrm{Cmn1}}+\omega^2\rho_{s1}\boldsymbol{\psi}_{\mathrm{mn1}}\right]\mathbf{A_1}=-2\ p_i\mathbf{D}+2\boldsymbol{\psi}_{\mathrm{mu1}}\mathbf{B_1}, \tag{7.29}$$

where

$$C_n=-\left(\frac{n_x\pi}{l_x}\right)^2-\left(\frac{n_y\pi}{l_y}\right)^2, \qquad n=N_y(n_x-1)+n_y, \tag{7.30}$$

$\boldsymbol{\psi}_{\mathrm{Cmn1}}=$

$$\begin{pmatrix} C_1\int_0^{l_x}\int_0^{l_y}\xi_1(x,y)\xi_{n1_1}(x,y)\mathrm{d}x\mathrm{d}y & C_2\int_0^{l_x}\int_0^{l_y}\xi_1(x,y)\xi_{n1_2}(x,y)\mathrm{d}x\mathrm{d}y & \dots & C_n\int_0^{l_x}\int_0^{l_y}\xi_1(x,y)\xi_{n1_n}(x,y)\mathrm{d}x\mathrm{d}y \\ C_1\int_0^{l_x}\int_0^{l_y}\xi_2(x,y)\xi_{n1_1}(x,y)\mathrm{d}x\mathrm{d}y & C_2\int_0^{l_x}\int_0^{l_y}\xi_2(x,y)\xi_{n1_2}(x,y)\mathrm{d}x\mathrm{d}y & \dots & C_n\int_0^{l_x}\int_0^{l_y}\xi_2(x,y)\xi_{n1_n}(x,y)\mathrm{d}x\mathrm{d}y \\ \vdots & \vdots & \ddots & \vdots \\ C_1\int_0^{l_x}\int_0^{l_y}\xi_m(x,y)\xi_{n1_1}(x,y)\mathrm{d}x\mathrm{d}y & C_2\int_0^{l_x}\int_0^{l_y}\xi_m(x,y)\xi_{n1_2}(x,y)\mathrm{d}x\mathrm{d}y & \dots & C_n\int_0^{l_x}\int_0^{l_y}\xi_m(x,y)\xi_{n1_n}(x,y)\mathrm{d}x\mathrm{d}y \end{pmatrix}, \tag{7.31}$$

$\boldsymbol{\psi}_{\mathrm{mn1}}=$

$$\begin{pmatrix} \int_0^{l_x}\int_0^{l_y}\xi_1(x,y)\xi_{n1_1}(x,y)\mathrm{d}x\mathrm{d}y & \int_0^{l_x}\int_0^{l_y}\xi_1(x,y)\xi_{n1_2}(x,y)\mathrm{d}x\mathrm{d}y & \dots & \int_0^{l_x}\int_0^{l_y}\xi_1(x,y)\xi_{n1_n}(x,y)\mathrm{d}x\mathrm{d}y \\ \int_0^{l_x}\int_0^{l_y}\xi_2(x,y)\xi_{n1_1}(x,y)\mathrm{d}x\mathrm{d}y & \int_0^{l_x}\int_0^{l_y}\xi_2(x,y)\xi_{n1_2}(x,y)\mathrm{d}x\mathrm{d}y & \dots & \int_0^{l_x}\int_0^{l_y}\xi_2(x,y)\xi_{n1_n}(x,y)\mathrm{d}x\mathrm{d}y \\ \vdots & \vdots & \ddots & \vdots \\ \int_0^{l_x}\int_0^{l_y}\xi_m(x,y)\xi_{n1_1}(x,y)\mathrm{d}x\mathrm{d}y & \int_0^{l_x}\int_0^{l_y}\xi_m(x,y)\xi_{n1_2}(x,y)\mathrm{d}x\mathrm{d}y & \dots & \int_0^{l_x}\int_0^{l_y}\xi_m(x,y)\xi_{n1_n}(x,y)\mathrm{d}x\mathrm{d}y \end{pmatrix}, \tag{7.32}$$

$$\mathbf{D}=\int_0^{l_x}\int_0^{l_y}\xi_m(x,y)\mathrm{d}x\mathrm{d}y=\begin{pmatrix} \int_0^{l_x}\int_0^{l_y}\xi_1(x,y)\mathrm{d}x\mathrm{d}y \\ \int_0^{l_x}\int_0^{l_y}\xi_2(x,y)\mathrm{d}x\mathrm{d}y \\ \vdots \\ \int_0^{l_x}\int_0^{l_y}\xi_m(x,y)\mathrm{d}x\mathrm{d}y \end{pmatrix}, \tag{7.33}$$

and

$\boldsymbol{\psi}_{\mathrm{mu1}}=$

$$\begin{pmatrix} \int_0^{l_x}\int_0^{l_y}\xi_1(x,y)\zeta_{u1_1}(x,y)\mathrm{d}x\mathrm{d}y & \int_0^{l_x}\int_0^{l_y}\xi_1(x,y)\zeta_{u1_2}(x,y)\mathrm{d}x\mathrm{d}y & \dots & \int_0^{l_x}\int_0^{l_y}\xi_1(x,y)\zeta_{u1_U}(x,y)\mathrm{d}x\mathrm{d}y \\ \int_0^{l_x}\int_0^{l_y}\xi_2(x,y)\zeta_{u1_1}(x,y)\mathrm{d}x\mathrm{d}y & \int_0^{l_x}\int_0^{l_y}\xi_2(x,y)\zeta_{u1_2}(x,y)\mathrm{d}x\mathrm{d}y & \dots & \int_0^{l_x}\int_0^{l_y}\xi_2(x,y)\zeta_{u1_U}(x,y)\mathrm{d}x\mathrm{d}y \\ \vdots & \vdots & \ddots & \vdots \\ \int_0^{l_x}\int_0^{l_y}\xi_m(x,y)\zeta_{u1_1}(x,y)\mathrm{d}x\mathrm{d}y & \int_0^{l_x}\int_0^{l_y}\xi_m(x,y)\zeta_{u1_2}(x,y)\mathrm{d}x\mathrm{d}y & \dots & \int_0^{l_x}\int_0^{l_y}\xi_m(x,y)\zeta_{u1_U}(x,y)\mathrm{d}x\mathrm{d}y \end{pmatrix}. \tag{7.34}$$

Equation (7.29) represents the motion of Membrane 1 in matrix form. On the left hand side, the term $(T+2j\omega\eta)\boldsymbol{\psi}_{\mathrm{Cmn1}}\mathbf{A_1}$ represents the effects of the constant tension and the internal damping on the membrane motion, and $\omega^2\rho_{s1}\boldsymbol{\psi}_{\mathrm{mn1}}\mathbf{A_1}$ represents that of the membrane mass. The terms on the right hand side represent the sound pressure difference across Membrane 1, including the incident sound and the sound generated in Air Cavity 1. Following the same strategy, the motion equation of the internal MPM is expressed in matrix form

$$\left[(T_{\mathrm{MPM}}+2j\omega\eta_{\mathrm{MPM}})\,\boldsymbol{\psi}_{\mathrm{CmMPM}}+\omega^2\rho_{\mathrm{sMPM}}\boldsymbol{\psi}_{\mathrm{mMPM}}\right]\mathbf{A}_{\mathrm{MPM}}=-2\boldsymbol{\psi}_{\mathrm{mu1D1}}\mathbf{B_1}+2\boldsymbol{\psi}_{\mathrm{mu2}}\mathbf{B_2}, \tag{7.35}$$

where

$$\boldsymbol{\psi}_{\mathrm{CmMPM}}=\begin{pmatrix} \int_0^{l_x}\int_0^{l_y} C_1\xi_1(x,y)\xi_{\mathrm{MPM}_1}(x,y)\mathrm{d}x\mathrm{d}y & \int_0^{l_x}\int_0^{l_y} C_2\xi_1(x,y)\xi_{\mathrm{MPM}_2}(x,y)\mathrm{d}x\mathrm{d}y & \dots & \int_0^{l_x}\int_0^{l_y} C_n\xi_1(x,y)\xi_{\mathrm{MPM}_n}(x,y)\mathrm{d}x\mathrm{d}y \\ \int_0^{l_x}\int_0^{l_y} C_1\xi_2(x,y)\xi_{\mathrm{MPM}_1}(x,y)\mathrm{d}x\mathrm{d}y & \int_0^{l_x}\int_0^{l_y} C_2\xi_2(x,y)\xi_{\mathrm{MPM}_2}(x,y)\mathrm{d}x\mathrm{d}y & \dots & \int_0^{l_x}\int_0^{l_y} C_n\xi_2(x,y)\xi_{\mathrm{MPM}_n}(x,y)\mathrm{d}x\mathrm{d}y \\ \vdots & \vdots & \ddots & \vdots \\ \int_0^{l_x}\int_0^{l_y} C_1\xi_m(x,y)\xi_{\mathrm{MPM}_1}(x,y)\mathrm{d}x\mathrm{d}y & \int_0^{l_x}\int_0^{l_y} C_2\xi_m(x,y)\xi_{\mathrm{MPM}_2}(x,y)\mathrm{d}x\mathrm{d}y & \dots & \int_0^{l_x}\int_0^{l_y} C_n\xi_m(x,y)\xi_{\mathrm{MPM}_n}(x,y)\mathrm{d}x\mathrm{d}y \end{pmatrix}, \tag{7.36}$$

$$\boldsymbol{\psi}_{\mathrm{mMPM}}=\begin{pmatrix} \int_0^{l_x}\int_0^{l_y} \xi_1(x,y)\xi_{\mathrm{MPM}_1}(x,y)\mathrm{d}x\mathrm{d}y & \int_0^{l_x}\int_0^{l_y} \xi_1(x,y)\xi_{\mathrm{MPM}_2}(x,y)\mathrm{d}x\mathrm{d}y & \dots & \int_0^{l_x}\int_0^{l_y} \xi_1(x,y)\xi_{\mathrm{MPM}_n}(x,y)\mathrm{d}x\mathrm{d}y \\ \int_0^{l_x}\int_0^{l_y} \xi_2(x,y)\xi_{\mathrm{MPM}_1}(x,y)\mathrm{d}x\mathrm{d}y & \int_0^{l_x}\int_0^{l_y} \xi_2(x,y)\xi_{\mathrm{MPM}_2}(x,y)\mathrm{d}x\mathrm{d}y & \dots & \int_0^{l_x}\int_0^{l_y} \xi_2(x,y)\xi_{\mathrm{MPM}_n}(x,y)\mathrm{d}x\mathrm{d}y \\ \vdots & \vdots & \ddots & \vdots \\ \int_0^{l_x}\int_0^{l_y} \xi_m(x,y)\xi_{\mathrm{MPM}_1}(x,y)\mathrm{d}x\mathrm{d}y & \int_0^{l_x}\int_0^{l_y} \xi_m(x,y)\xi_{\mathrm{MPM}_2}(x,y)\mathrm{d}x\mathrm{d}y & \dots & \int_0^{l_x}\int_0^{l_y} \xi_m(x,y)\xi_{\mathrm{MPM}_n}(x,y)\mathrm{d}x\mathrm{d}y \end{pmatrix}, \tag{7.37}$$

$$\boldsymbol{\psi}_{\mathrm{mu1D1}}=\begin{pmatrix} \int_0^{l_x}\int_0^{l_y} \xi_1(x,y)\zeta_{u1_1}(x,y)e^{-jk_{0z}D_1}\mathrm{d}x\mathrm{d}y & \int_0^{l_x}\int_0^{l_y} \xi_1(x,y)\zeta_{u1_2}(x,y)e^{-jk_{0z}D_1}\mathrm{d}x\mathrm{d}y & \dots & \int_0^{l_x}\int_0^{l_y} \xi_1(x,y)\zeta_{u1_U}(x,y)e^{-jk_{0z}D_1}\mathrm{d}x\mathrm{d}y \\ \int_0^{l_x}\int_0^{l_y} \xi_2(x,y)\zeta_{u1_1}(x,y)e^{-jk_{0z}D_1}\mathrm{d}x\mathrm{d}y & \int_0^{l_x}\int_0^{l_y} \xi_2(x,y)\zeta_{u1_2}(x,y)e^{-jk_{0z}D_1}\mathrm{d}x\mathrm{d}y & \dots & \int_0^{l_x}\int_0^{l_y} \xi_2(x,y)\zeta_{u1_U}(x,y)e^{-jk_{0z}D_1}\mathrm{d}x\mathrm{d}y \\ \vdots & \vdots & \ddots & \vdots \\ \int_0^{l_x}\int_0^{l_y} \xi_m(x,y)\zeta_{u1_1}(x,y)e^{-jk_{0z}D_1}\mathrm{d}x\mathrm{d}y & \int_0^{l_x}\int_0^{l_y} \xi_m(x,y)\zeta_{u1_2}(x,y)e^{-jk_{0z}D_1}\mathrm{d}x\mathrm{d}y & \dots & \int_0^{l_x}\int_0^{l_y} \xi_m(x,y)\zeta_{u1_U}(x,y)e^{-jk_{0z}D_1}\mathrm{d}x\mathrm{d}y \end{pmatrix} \tag{7.38}$$

and

$$\boldsymbol{\psi}_{\mathrm{mu2}} = \begin{pmatrix} \int_0^{l_x}\int_0^{l_y} \xi_1(x,y)\zeta_{u2_1}(x,y)\mathrm{d}x\mathrm{d}y & \int_0^{l_x}\int_0^{l_y} \xi_1(x,y)\zeta_{u2_2}(x,y)\mathrm{d}x\mathrm{d}y & \dots & \int_0^{l_x}\int_0^{l_y} \xi_1(x,y)\zeta_{u2_U}(x,y)\mathrm{d}x\mathrm{d}y \\ \int_0^{l_x}\int_0^{l_y} \xi_2(x,y)\zeta_{u2_1}(x,y)\mathrm{d}x\mathrm{d}y & \int_0^{l_x}\int_0^{l_y} \xi_2(x,y)\zeta_{u2_2}(x,y)\mathrm{d}x\mathrm{d}y & \dots & \int_0^{l_x}\int_0^{l_y} \xi_2(x,y)\zeta_{u2_U}(x,y)\mathrm{d}x\mathrm{d}y \\ \vdots & \vdots & \ddots & \vdots \\ \int_0^{l_x}\int_0^{l_y} \xi_m(x,y)\zeta_{u2_1}(x,y)\mathrm{d}x\mathrm{d}y & \int_0^{l_x}\int_0^{l_y} \xi_m(x,y)\zeta_{u2_2}(x,y)\mathrm{d}x\mathrm{d}y & \dots & \int_0^{l_x}\int_0^{l_y} \xi_m(x,y)\zeta_{u2_U}(x,y)\mathrm{d}x\mathrm{d}y \end{pmatrix}. \tag{7.39}$$

Similarly, the motion equation of Membrane 2 is given by

$$\left[(T+2j\omega\eta)\boldsymbol{\psi}_{\mathrm{Cmn2}} + \left(\omega^2\rho_{s2} - 2j\omega\rho_0 c_0\right)\boldsymbol{\psi}_{\mathrm{mn2}}\right]\mathbf{A_2} = -2\boldsymbol{\psi}_{\mathrm{mu2D2}}\mathbf{B_2}, \tag{7.40}$$

where

$$\boldsymbol{\psi}_{\mathrm{Cmn2}} = \begin{pmatrix} C_1\int_0^{l_x}\int_0^{l_y} \xi_1(x,y)\xi_{n2_1}(x,y)\mathrm{d}x\mathrm{d}y & C_2\int_0^{l_x}\int_0^{l_y} \xi_1(x,y)\xi_{n2_2}(x,y)\mathrm{d}x\mathrm{d}y & \dots & C_n\int_0^{l_x}\int_0^{l_y} \xi_1(x,y)\xi_{n2_n}(x,y)\mathrm{d}x\mathrm{d}y \\ C_1\int_0^{l_x}\int_0^{l_y} \xi_2(x,y)\xi_{n2_1}(x,y)\mathrm{d}x\mathrm{d}y & C_2\int_0^{l_x}\int_0^{l_y} \xi_2(x,y)\xi_{n2_2}(x,y)\mathrm{d}x\mathrm{d}y & \dots & C_n\int_0^{l_x}\int_0^{l_y} \xi_2(x,y)\xi_{n2_n}(x,y)\mathrm{d}x\mathrm{d}y \\ \vdots & \vdots & \ddots & \vdots \\ C_1\int_0^{l_x}\int_0^{l_y} \xi_m(x,y)\xi_{n2_1}(x,y)\mathrm{d}x\mathrm{d}y & C_2\int_0^{l_x}\int_0^{l_y} \xi_m(x,y)\xi_{n2_2}(x,y)\mathrm{d}x\mathrm{d}y & \dots & C_n\int_0^{l_x}\int_0^{l_y} \xi_m(x,y)\xi_{n2_n}(x,y)\mathrm{d}x\mathrm{d}y \end{pmatrix}, \tag{7.41}$$

$$\boldsymbol{\psi}_{\mathrm{mn2}} = \begin{pmatrix} \int_0^{l_x}\int_0^{l_y} \xi_1(x,y)\xi_{n2_1}(x,y)\mathrm{d}x\mathrm{d}y & \int_0^{l_x}\int_0^{l_y} \xi_1(x,y)\xi_{n2_2}(x,y)\mathrm{d}x\mathrm{d}y & \dots & \int_0^{l_x}\int_0^{l_y} \xi_1(x,y)\xi_{n2_n}(x,y)\mathrm{d}x\mathrm{d}y \\ \int_0^{l_x}\int_0^{l_y} \xi_2(x,y)\xi_{n2_1}(x,y)\mathrm{d}x\mathrm{d}y & \int_0^{l_x}\int_0^{l_y} \xi_2(x,y)\xi_{n2_2}(x,y)\mathrm{d}x\mathrm{d}y & \dots & \int_0^{l_x}\int_0^{l_y} \xi_2(x,y)\xi_{n2_n}(x,y)\mathrm{d}x\mathrm{d}y \\ \vdots & \vdots & \ddots & \vdots \\ \int_0^{l_x}\int_0^{l_y} \xi_m(x,y)\xi_{n2_1}(x,y)\mathrm{d}x\mathrm{d}y & \int_0^{l_x}\int_0^{l_y} \xi_m(x,y)\xi_{n2_2}(x,y)\mathrm{d}x\mathrm{d}y & \dots & \int_0^{l_x}\int_0^{l_y} \xi_m(x,y)\xi_{n2_n}(x,y)\mathrm{d}x\mathrm{d}y \end{pmatrix}, \tag{7.42}$$

and

$$\boldsymbol{\psi}_{\text{mu2D2}} =$$

$$\begin{pmatrix} \int_0^{l_x}\int_0^{l_y} \xi_1(x,y)\zeta_{u2_1}(x,y)e^{-jk_{0z}D_2}\mathrm{d}x\mathrm{d}y & \int_0^{l_x}\int_0^{l_y} \xi_1(x,y)\zeta_{u2_2}(x,y)e^{-jk_{0z}D_2}\mathrm{d}x\mathrm{d}y & \dots & \int_0^{l_x}\int_0^{l_y} \xi_1(x,y)\zeta_{u2_U}(x,y)e^{-jk_{0z}D_2}\mathrm{d}x\mathrm{d}y \\ \int_0^{l_x}\int_0^{l_y} \xi_2(x,y)\zeta_{u2_1}(x,y)e^{-jk_{0z}D_2}\mathrm{d}x\mathrm{d}y & \int_0^{l_x}\int_0^{l_y} \xi_2(x,y)\zeta_{u2_2}(x,y)e^{-jk_{0z}D_2}\mathrm{d}x\mathrm{d}y & \dots & \int_0^{l_x}\int_0^{l_y} \xi_2(x,y)\zeta_{u2_U}(x,y)e^{-jk_{0z}D_2}\mathrm{d}x\mathrm{d}y \\ \vdots & \vdots & \ddots & \vdots \\ \int_0^{l_x}\int_0^{l_y} \xi_m(x,y)\zeta_{u2_1}(x,y)e^{-jk_{0z}D_2}\mathrm{d}x\mathrm{d}y & \int_0^{l_x}\int_0^{l_y} \xi_m(x,y)\zeta_{u2_2}(x,y)e^{-jk_{0z}D_2}\mathrm{d}x\mathrm{d}y & \dots & \int_0^{l_x}\int_0^{l_y} \xi_m(x,y)\zeta_{u2_U}(x,y)e^{-jk_{0z}D_2}\mathrm{d}x\mathrm{d}y \end{pmatrix} \tag{7.43}$$

By rearranging Equation (7.40), the expression for $\mathbf{B_2}$ with respect to $\mathbf{A_2}$ is obtained as

$$\mathbf{B_2} = \frac{(T + 2j\omega\eta)\boldsymbol{\psi}_{\text{Cmn2}} + \left(\omega^2\rho_{s2} - 2j\omega\rho_0 c_0\right)\boldsymbol{\psi}_{\text{mn2}}}{-2\boldsymbol{\psi}_{\text{mu2D2}}}\mathbf{A_2}. \tag{7.44}$$

Substituting Equations (7.44) and (7.9) into Equation (7.7), multiplying each side of the equation by $\xi_m(x,y)$ and integrating over the membrane surface yields

$$(\boldsymbol{\psi}_{\text{mu2}} - \boldsymbol{\psi}_{\text{2mu2D2}})\mathbf{B_2} + j\omega\rho_0 c_0 \boldsymbol{\psi}_{\text{mn2D2}}\mathbf{A_2} = j\omega\rho_0 c_0 \boldsymbol{\psi}_{\text{mMPM}}\mathbf{A}_{\text{MPM}} \tag{7.45}$$

where

$$\boldsymbol{\psi}_{\text{2mu2D2}} =$$

$$\begin{pmatrix} \int_0^{l_x}\int_0^{l_y} \xi_1(x,y)\zeta_{u2_1}(x,y)e^{-2jk_{0z}D_2}\mathrm{d}x\mathrm{d}y & \int_0^{l_x}\int_0^{l_y} \xi_1(x,y)\zeta_{u2_2}(x,y)e^{-jk_{0z}D_2}\mathrm{d}x\mathrm{d}y & \dots & \int_0^{l_x}\int_0^{l_y} \xi_1(x,y)\zeta_{u2_U}(x,y)e^{-2jk_{0z}D_2}\mathrm{d}x\mathrm{d}y \\ \int_0^{l_x}\int_0^{l_y} \xi_2(x,y)\zeta_{u2_1}(x,y)e^{-2jk_{0z}D_2}\mathrm{d}x\mathrm{d}y & \int_0^{l_x}\int_0^{l_y} \xi_2(x,y)\zeta_{u2_2}(x,y)e^{-2jk_{0z}D_2}\mathrm{d}x\mathrm{d}y & \dots & \int_0^{l_x}\int_0^{l_y} \xi_2(x,y)\zeta_{u2_U}(x,y)e^{-2jk_{0z}D_2}\mathrm{d}x\mathrm{d}y \\ \vdots & \vdots & \ddots & \vdots \\ \int_0^{l_x}\int_0^{l_y} \xi_m(x,y)\zeta_{u2_1}(x,y)e^{-2jk_{0z}D_2}\mathrm{d}x\mathrm{d}y & \int_0^{l_x}\int_0^{l_y} \xi_m(x,y)\zeta_{u2_2}(x,y)e^{-2jk_{0z}D_2}\mathrm{d}x\mathrm{d}y & \dots & \int_0^{l_x}\int_0^{l_y} \xi_m(x,y)\zeta_{u2_U}(x,y)e^{-2jk_{0z}D_2}\mathrm{d}x\mathrm{d}y \end{pmatrix} \tag{7.46}$$

and

$$\boldsymbol{\psi}_{\text{mn2D2}} =$$

$$\begin{pmatrix} \int_0^{l_x}\int_0^{l_y} \xi_1(x,y)\xi_{n2_1}(x,y)e^{-jk_{0z}D_2}\mathrm{d}x\mathrm{d}y & \int_0^{l_x}\int_0^{l_y} \xi_1(x,y)\xi_{n2_2}(x,y)e^{-jk_{0z}D_2}\mathrm{d}x\mathrm{d}y & \dots & \int_0^{l_x}\int_0^{l_y} \xi_1(x,y)\xi_{n2_n}(x,y)e^{-jk_{0z}D_2}\mathrm{d}x\mathrm{d}y \\ \int_0^{l_x}\int_0^{l_y} \xi_2(x,y)\xi_{n2_1}(x,y)e^{-jk_{0z}D_2}\mathrm{d}x\mathrm{d}y & \int_0^{l_x}\int_0^{l_y} \xi_2(x,y)\xi_{n2_2}(x,y)e^{-jk_{0z}D_2}\mathrm{d}x\mathrm{d}y & \dots & \int_0^{l_x}\int_0^{l_y} \xi_2(x,y)\xi_{n2_n}(x,y)e^{-jk_{0z}D_2}\mathrm{d}x\mathrm{d}y \\ \vdots & \vdots & \ddots & \vdots \\ \int_0^{l_x}\int_0^{l_y} \xi_m(x,y)\xi_{n2_1}(x,y)e^{-jk_{0z}D_2}\mathrm{d}x\mathrm{d}y & \int_0^{l_x}\int_0^{l_y} \xi_m(x,y)\xi_{n2_2}(x,y)e^{-jk_{0z}D_2}\mathrm{d}x\mathrm{d}y & \dots & \int_0^{l_x}\int_0^{l_y} \xi_m(x,y)\xi_{n2_n}(x,y)e^{-jk_{0z}D_2}\mathrm{d}x\mathrm{d}y \end{pmatrix}, \tag{7.47}$$

Substituting Equation (7.44) into Equation (7.45) yields

$$(\boldsymbol{\psi}_{\mathrm{mu2}} - \boldsymbol{\psi}_{\mathrm{2mu2D2}}) \frac{(T+2j\omega\eta)\boldsymbol{\psi}_{\mathrm{Cmn2}} + \left(\omega^2\rho_{s2} - 2j\omega\rho_0 c_0\right)\boldsymbol{\psi}_{\mathrm{mn2}}}{-2\boldsymbol{\psi}_{\mathrm{mu2D2}}}\mathbf{A_2} + j\omega\rho_0 c_0 \boldsymbol{\psi}_{\mathrm{mn2D2}}\mathbf{A_2} = j\omega\rho_0 c_0 \boldsymbol{\psi}_{\mathrm{mMPM}}\mathbf{A}_{\mathrm{MPM}}. \tag{7.48}$$

Hence,

$$\mathbf{A}_{\mathrm{MPM}} = \left[(\boldsymbol{\psi}_{\mathrm{mu2}} - \boldsymbol{\psi}_{\mathrm{2mu2D2}}) \frac{(T+2j\omega\eta)\boldsymbol{\psi}_{\mathrm{Cmn2}} + \left(\omega^2\rho_{s2} - 2j\omega\rho_0 c_0\right)\boldsymbol{\psi}_{\mathrm{mn2}}}{-2\boldsymbol{\psi}_{\mathrm{mu2D2}} j\omega\rho_0 c_0 \boldsymbol{\psi}_{\mathrm{mMPM}}} + \frac{\boldsymbol{\psi}_{\mathrm{mn2D2}}}{\boldsymbol{\psi}_{\mathrm{mMPM}}}\right]\mathbf{A_2}. \tag{7.49}$$

Equation (7.49) represents the modal amplitude of the internal MPM expressed in terms of the modal amplitude of Membrane 2. It is very similar to Equation (6.76) in Chapter 6 which represents the relationship between the modal amplitudes of the two impervious membranes without an internal MPM. Letting

$$\boldsymbol{\psi}_{\mathrm{A_{MPM}A_2}} = (\boldsymbol{\psi}_{\mathrm{mu2}} - \boldsymbol{\psi}_{\mathrm{2mu2D2}}) \frac{(T+2j\omega\eta)\boldsymbol{\psi}_{\mathrm{Cmn2}} + \left(\omega^2\rho_{s2} - 2j\omega\rho_0 c_0\right)\boldsymbol{\psi}_{\mathrm{mn2}}}{-2\boldsymbol{\psi}_{\mathrm{mu2D2}} j\omega\rho_0 c_0 \boldsymbol{\psi}_{\mathrm{mMPM}}} + \frac{\boldsymbol{\psi}_{\mathrm{mn2D2}}}{\boldsymbol{\psi}_{\mathrm{mMPM}}}, \tag{7.50}$$

Equation (7.49) may be simplified to

$$\mathbf{A}_{\mathrm{MPM}} = \boldsymbol{\psi}_{\mathrm{A_{MPM}A_2}}\mathbf{A_2}. \tag{7.51}$$

The matrix $\boldsymbol{\psi}_{\mathrm{A_{MPM}A_2}}$ is considered a "transfer matrix" which links the modal amplitudes of Membrane 2 and the internal MPM.

In the motion equations the terms related to the tension, internal damping and mass occur repeatedly in the derivation process. To simplify the equations, these terms can be replaced with specific variables. Let

$$\boldsymbol{\gamma_1} = (T+2j\omega\eta)\boldsymbol{\psi}_{\mathrm{Cmn1}} + \omega^2\rho_{s1}\boldsymbol{\psi}_{\mathrm{mn1}}, \tag{7.52}$$

$$\boldsymbol{\gamma}_{\mathrm{MPM}} = (T_{\mathrm{MPM}} + 2j\omega\eta_{\mathrm{MPM}})\boldsymbol{\psi}_{\mathrm{CmMPM}} + \omega^2\rho_{\mathrm{sMPM}}\boldsymbol{\psi}_{\mathrm{mMPM}} \tag{7.53}$$

$$\boldsymbol{\gamma_2} = (T+2j\omega\eta)\boldsymbol{\psi}_{\mathrm{Cmn2}} + \left(\omega^2\rho_{s2} - 2j\omega\rho_0 c_0\right)\boldsymbol{\psi}_{\mathrm{mn2}}. \tag{7.54}$$

Substituting Equation (7.54) into Equation (7.50) yields

$$\boldsymbol{\psi}_{\mathrm{A_{MPM}A_2}} = \frac{(\boldsymbol{\psi}_{\mathrm{mu2}} - \boldsymbol{\psi}_{\mathrm{2mu2D2}})\boldsymbol{\gamma_2}}{-2\boldsymbol{\psi}_{\mathrm{mu2D2}} j\omega\rho_0 c_0 \boldsymbol{\psi}_{\mathrm{mMPM}}} + \frac{\boldsymbol{\psi}_{\mathrm{mn2D2}}}{\boldsymbol{\psi}_{\mathrm{mMPM}}}. \tag{7.55}$$

Substituting Equations (7.55) and (7.44) into Equation (7.35) gives

$$\begin{aligned}\boldsymbol{\gamma}_{\mathrm{MPM}}\mathbf{A}_{\mathrm{MPM}} &= -2\boldsymbol{\psi}_{\mathrm{mu1D1}}\mathbf{B_1} + 2\boldsymbol{\psi}_{\mathrm{mu2}}\mathbf{B_2},\\ \boldsymbol{\gamma}_{\mathrm{MPM}}\boldsymbol{\psi}_{\mathrm{A_{MPM}A_2}}\mathbf{A_2} &= -2\boldsymbol{\psi}_{\mathrm{mu1D1}}\mathbf{B_1} + 2\boldsymbol{\psi}_{\mathrm{mu2}}\frac{\boldsymbol{\gamma}_2}{-2\boldsymbol{\psi}_{\mathrm{mu2D2}}}\mathbf{A_2},\\ \mathbf{B_1} &= \left(\frac{\boldsymbol{\gamma}_{\mathrm{MPM}}\boldsymbol{\psi}_{\mathrm{A_{MPM}A_2}}}{-2\boldsymbol{\psi}_{\mathrm{mu1D1}}} - \frac{\boldsymbol{\psi}_{\mathrm{mu2}}\boldsymbol{\gamma}_2}{2\boldsymbol{\psi}_{\mathrm{mu1D1}}\boldsymbol{\psi}_{\mathrm{mu2D2}}}\right)\mathbf{A_2},\end{aligned} \tag{7.56}$$

where

$$\boldsymbol{\psi}_{\mathrm{B_1A_2}} = \frac{\boldsymbol{\gamma}_{\mathrm{MPM}}\boldsymbol{\psi}_{\mathrm{A_{MPM}A_2}}}{-2\boldsymbol{\psi}_{\mathrm{mu1D1}}} - \frac{\boldsymbol{\psi}_{\mathrm{mu2}}\boldsymbol{\gamma}_2}{2\boldsymbol{\psi}_{\mathrm{mu1D1}}\boldsymbol{\psi}_{\mathrm{mu2D2}}}. \tag{7.57}$$

Substituting Equations (7.57) and (7.8) into Equation (7.3), multiplying each side of the equation by $\xi_m(x,y)$ and integrating over the membrane surface yields

$$\begin{aligned}\left(\boldsymbol{\psi}_{\mathrm{mu1}} - \boldsymbol{\psi}_{\mathrm{2mu1D1}}\right)\mathbf{B_1} + j\omega\rho_0 c_0\boldsymbol{\psi}_{\mathrm{mMPMD1}}\mathbf{A}_{\mathrm{MPM}} &= j\omega\rho_0 c_0\boldsymbol{\psi}_{\mathrm{mn1}}\mathbf{A_1},\\ \left(\boldsymbol{\psi}_{\mathrm{mu1}} - \boldsymbol{\psi}_{\mathrm{2mu1D1}}\right)\boldsymbol{\psi}_{\mathrm{B_1A_2}}\mathbf{A_2} + j\omega\rho_0 c_0\boldsymbol{\psi}_{\mathrm{mMPMD1}}\boldsymbol{\psi}_{\mathrm{A_{MPM}A_2}}\mathbf{A_2} &= j\omega\rho_0 c_0\boldsymbol{\psi}_{\mathrm{mn1}}\mathbf{A_1},\end{aligned} \tag{7.58}$$

where

$$\boldsymbol{\psi}_{\mathrm{mMPMD1}} = \begin{pmatrix} \int_0^{l_x}\int_0^{l_y}\xi_1\xi_{\mathrm{MPM_1}}e^{-jk_{0z}D_1}\mathrm{d}x\mathrm{d}y & \int_0^{l_x}\int_0^{l_y}\xi_1\xi_{\mathrm{MPM_2}}e^{-jk_{0z}D_1}\mathrm{d}x\mathrm{d}y & \dots & \int_0^{l_x}\int_0^{l_y}\xi_1\xi_{\mathrm{MPM}_n}e^{-jk_{0z}D_1}\mathrm{d}x\mathrm{d}y \\ \int_0^{l_x}\int_0^{l_y}\xi_2\xi_{\mathrm{MPM_1}}e^{-jk_{0z}D_1}\mathrm{d}x\mathrm{d}y & \int_0^{l_x}\int_0^{l_y}\xi_2\xi_{\mathrm{MPM_2}}e^{-jk_{0z}D_1}\mathrm{d}x\mathrm{d}y & \dots & \int_0^{l_x}\int_0^{l_y}\xi_2\xi_{\mathrm{MPM}_n}e^{-jk_{0z}D_1}\mathrm{d}x\mathrm{d}y \\ \vdots & \vdots & \ddots & \vdots \\ \int_0^{l_x}\int_0^{l_y}\xi_m\xi_{\mathrm{MPM_1}}e^{-jk_{0z}D_1}\mathrm{d}x\mathrm{d}y & \int_0^{l_x}\int_0^{l_y}\xi_m\xi_{\mathrm{MPM_2}}e^{-jk_{0z}D_1}\mathrm{d}x\mathrm{d}y & \dots & \int_0^{l_x}\int_0^{l_y}\xi_m\xi_{\mathrm{MPM}_n}e^{-jk_{0z}D_1}\mathrm{d}x\mathrm{d}y \end{pmatrix}. \tag{7.59}$$

Hence,

$$\begin{aligned}\mathbf{A_1} &= \frac{\left(\boldsymbol{\psi}_{\mathrm{mu1}} - \boldsymbol{\psi}_{\mathrm{2mu1D1}}\right)\boldsymbol{\psi}_{\mathrm{B_1A_2}} + j\omega\rho_0 c_0\boldsymbol{\psi}_{\mathrm{mMPMD1}}\boldsymbol{\psi}_{\mathrm{A_{MPM}A_2}}}{j\omega\rho_0 c_0\boldsymbol{\psi}_{\mathrm{mn1}}}\mathbf{A_2}\\ &= \left[\frac{\left(\boldsymbol{\psi}_{\mathrm{mu1}} - \boldsymbol{\psi}_{\mathrm{2mu1D1}}\right)\boldsymbol{\psi}_{\mathrm{B_1A_2}}}{j\omega\rho_0 c_0\boldsymbol{\psi}_{\mathrm{mn1}}} + \frac{\boldsymbol{\psi}_{\mathrm{mMPMD1}}\boldsymbol{\psi}_{\mathrm{A_{MPM}A_2}}}{\boldsymbol{\psi}_{\mathrm{mn1}}}\right]\mathbf{A_2}.\end{aligned} \tag{7.60}$$

Letting

$$\boldsymbol{\psi}_{\mathrm{A_1A_2}} = \frac{\left(\boldsymbol{\psi}_{\mathrm{mu1}} - \boldsymbol{\psi}_{\mathrm{2mu1D1}}\right)\boldsymbol{\psi}_{\mathrm{B_1A_2}}}{j\omega\rho_0 c_0\boldsymbol{\psi}_{\mathrm{mn1}}} + \frac{\boldsymbol{\psi}_{\mathrm{mMPMD1}}\boldsymbol{\psi}_{\mathrm{A_{MPM}A_2}}}{\boldsymbol{\psi}_{\mathrm{mn1}}}, \tag{7.61}$$

and substituting it and $\boldsymbol{\gamma_1}$ into Equation (7.29) yields

$$\begin{aligned}\boldsymbol{\gamma_1}\mathbf{A_1} &= -2\ p_i\mathbf{D} + 2\boldsymbol{\psi}_{\mathrm{mu1}}\mathbf{B_1},\\ \boldsymbol{\gamma_1}\boldsymbol{\psi}_{\mathrm{A_1A_2}}\mathbf{A_2} &= -2\ p_i\mathbf{D} + 2\boldsymbol{\psi}_{\mathrm{mu1}}\boldsymbol{\psi}_{\mathrm{B_1A_2}}\mathbf{A_2}.\end{aligned} \tag{7.62}$$

Hence,

$$\left(\boldsymbol{\gamma_1}\boldsymbol{\psi}_{\mathrm{A_1A_2}} - 2\boldsymbol{\psi}_{\mathrm{mu1}}\boldsymbol{\psi}_{\mathrm{B_1A_2}}\right)\mathbf{A_2} = -2\ p_i\mathbf{D}, \tag{7.63}$$

and

$$\mathbf{A_2} = \frac{-2\ p_i\mathbf{D}}{\boldsymbol{\gamma_1}\boldsymbol{\psi}_{\mathrm{A_1A_2}} - 2\boldsymbol{\psi}_{\mathrm{mu1}}\boldsymbol{\psi}_{\mathrm{B_1A_2}}}. \tag{7.64}$$

Therefore, the transmitted sound pressure is expressed by

$$\begin{aligned} p_t = \rho_0 c_0 \overline{v_2} &= \frac{j\omega\rho_0 c_0}{l_x l_y}\mathbf{D}^{\mathrm{T}}\mathbf{A_2} \\ &= \frac{j\omega\rho_0 c_0}{l_x l_y}\frac{-2\mathbf{D}^{\mathrm{T}} p_i\mathbf{D}}{\boldsymbol{\gamma_1}\boldsymbol{\psi}_{\mathrm{A_1A_2}} - 2\boldsymbol{\psi}_{\mathrm{mu1}}\boldsymbol{\psi}_{\mathrm{B_1A_2}}}. \end{aligned} \tag{7.65}$$

Consequently, the transmission coefficient is defined as (Bies & Hansen 2009)

$$\tau = \left|\frac{p_t}{p_i}\right| = \left|\frac{j\omega\rho_0 c_0}{l_x l_y}\frac{-2\mathbf{D}^{\mathrm{T}}\mathbf{D}}{\boldsymbol{\gamma_1}\boldsymbol{\psi}_{\mathrm{A_1A_2}} - 2\boldsymbol{\psi}_{\mathrm{mu1}}\boldsymbol{\psi}_{\mathrm{B_1A_2}}}\right|. \tag{7.66}$$

If the sound absorbing walls of the air cavities are considered, Equation (7.66) is given by

$$\tau = \left|\frac{p_t}{p_i}\right| = \left|\frac{j\omega\rho_0 c_0}{l_x l_y}\frac{-2\mathbf{D}^{\mathrm{T}}\mathbf{D}\ e^{-\beta\frac{\omega}{c_0}(D_1+D_2)}}{\boldsymbol{\gamma_1}\boldsymbol{\psi}_{\mathrm{A_1A_2}} - 2\boldsymbol{\psi}_{\mathrm{mu1}}\boldsymbol{\psi}_{\mathrm{B_1A_2}}}\right|. \tag{7.67}$$

Therefore, the STL is calculated by (Fahy & Gardonio 2007)

$$STL = 20\log_{10}\frac{1}{\tau}. \tag{7.68}$$

7.3.1.2 STL of double layer impervious membranes with an internal impervious MPM in a diffuse field

In Section 7.3.1.1, the expression for the STL with a normally-incident plane wave has been developed. However, similar to Chapter 6, the experimental results for the model validation were obtained in a diffuse field. Hence, it is necessary to develop an expression for the STL of double layer impervious membranes with an internal MPM in a diffuse field. This section re-derives the STL expression considering the impact of the oblique incidence angle, which is incorporated to develop the STL expression in a diffuse field. This derivation is based on the motion equations and the particle velocity continuity in the normal direction.

Assuming that the incident sound is oblique to the membrane surface with an angle of θ, then based on Snell's law, Equations (7.1), (7.2), (7.3) and (7.4) may be written as

$$v_1 = \frac{(p_i - p_r)\cos(\theta)}{\rho_0 c_0}, \tag{7.69}$$

$$p_r = p_i - \frac{\rho_0 c_0 v_1}{\cos(\theta)}, \tag{7.70}$$

$$\frac{(p_{i2} - p_{r2})\cos(\theta)}{\rho_0 c_0} = v_1, \tag{7.71}$$

and

$$p_{r2} = p_{i2} - \frac{\rho_0 c_0 v_1}{\cos(\theta)}. \tag{7.72}$$

Therefore, the sound pressure difference applied on Membrane 1 is obtained as

$$\begin{aligned} \Delta p_1 &= p_i + p_r - (p_{i2} + p_{r2}) \\ &= 2p_i - \frac{\rho_0 c_0 v_1}{\cos(\theta)} - \left(2p_{i2} - \frac{\rho_0 c_0 v_1}{\cos(\theta)}\right) \\ &= 2p_i - 2p_{i2}. \end{aligned} \tag{7.73}$$

Hence, the motion equation of Membrane 1 remains the same as Equation (7.29).

For the internal MPM, Equations (7.6), (7.7), (7.4) and (7.9) may be written as

$$\frac{\left(p_{i2}e^{-jk_{0z}D_1} - p_{r2}e^{jk_{0z}D_1}\right)\cos(\theta)}{\rho_0 c_0} = v_{\mathrm{MPM}}, \tag{7.74}$$

$$\frac{(p_{i3} - p_{r3})\cos(\theta)}{\rho_0 c_0} = v_{\mathrm{MPM}}, \tag{7.75}$$

$$\begin{aligned} p_{r2}e^{jk_{0z}D_1} &= p_{i2}e^{-jk_{0z}D_1} - \frac{\rho_0 c_0 v_{\mathrm{MPM}}}{\cos(\theta)}, \\ p_{r2} &= p_{i2}e^{-2jk_{0z}D_1} - \frac{\rho_0 c_0 v_{\mathrm{MPM}} e^{-jk_{0z}D_1}}{\cos(\theta)}, \end{aligned} \tag{7.76}$$

and

$$p_{r3} = p_{i3} - \frac{\rho_0 c_0 v_{\mathrm{MPM}}}{\cos(\theta)}. \tag{7.77}$$

Hence, the sound pressure difference across the MPM surface is

$$\begin{aligned} \Delta p_{\mathrm{MPM}} &= p_{i2}e^{-jk_{0z}D_1} + p_{r2}e^{jk_{0z}D_1} - (p_{i3} + p_{r3}) \\ &= 2p_{i2}e^{-jk_{0z}D_1} - \frac{\rho_0 c_0 v_{\mathrm{MPM}}}{\cos(\theta)} - 2p_{i3} + \frac{\rho_0 c_0 v_{\mathrm{MPM}}}{\cos(\theta)} \\ &= 2p_{i2}e^{-jk_{0z}D_1} - 2p_{i3}. \end{aligned} \tag{7.78}$$

Hence, the motion equation of the internal MPM also remains the same as Equation (7.35).

For Membrane 2, Equations (7.11) and (7.9) are re-expressed by

$$\frac{\left(p_{i3}e^{-jk_{0z}D_2} - p_{r3}e^{jk_{0z}D_2}\right)\cos(\theta)}{\rho_0 c_0} = v_2, \tag{7.79}$$

$$\begin{aligned} p_{r3}e^{jk_{0z}D_2} &= p_{i3}e^{-jk_{0z}D_2} - \frac{\rho_0 c_0 v_2}{\cos(\theta)}, \\ p_{r3} &= p_{i3}e^{-2jk_{0z}D_2} - \frac{\rho_0 c_0 v_2 e^{-jk_{0z}D_2}}{\cos(\theta)}. \end{aligned} \tag{7.80}$$

Also because of the particle velocity continuity in the z-direction, the transmitted sound pressure p_t is obtained as

$$p_t\cos(\theta) = \rho_0 c_0 v_2. \tag{7.81}$$

Consequently, the sound pressure difference across the impervious membrane surface is given by

$$\begin{aligned} \Delta p_2 &= p_{i3}e^{-jk_{0z}D_2} + p_{r3}e^{jk_{0z}D_2} - p_t \\ &= 2p_{i3}e^{-jk_{0z}D_2} - \frac{2\rho_0 c_0 v_2}{\cos(\theta)}. \end{aligned} \tag{7.82}$$

Hence, the matrix form of the motion equation of Membrane 2 is re-expressed by

$$\left[(T+2j\omega\eta)\boldsymbol{\psi}_{\mathrm{Cmn2}} + \left(\omega^2\rho_{s2} - 2j\omega\frac{\rho_0 c_0}{\cos(\theta)}\right)\boldsymbol{\psi}_{\mathrm{mn2}}\right]\mathbf{A_2} = -2\boldsymbol{\psi}_{\mathrm{mu2D2}}\mathbf{B_2}, \tag{7.83}$$

Therefore, $\mathbf{B_2}$ is given by

$$\mathbf{B_2} = \frac{(T+2j\omega\eta)\boldsymbol{\psi}_{\mathrm{Cmn2}} + \left(\omega^2\rho_{s2} - 2j\omega\frac{\rho_0 c_0}{\cos(\theta)}\right)\boldsymbol{\psi}_{\mathrm{mn2}}}{-2\boldsymbol{\psi}_{\mathrm{mu2D2}}}\mathbf{A_2} = \frac{\boldsymbol{\gamma_2}}{-2\boldsymbol{\psi}_{\mathrm{mu2D2}}}\mathbf{A_2}, \tag{7.84}$$

where

$$\boldsymbol{\gamma_2} = (T+2j\omega\eta)\boldsymbol{\psi}_{\mathrm{Cmn2}} + \left(\omega^2\rho_{s2} - 2j\omega\frac{\rho_0 c_0}{\cos(\theta)}\right)\boldsymbol{\psi}_{\mathrm{mn2}}. \tag{7.85}$$

Equation (7.45) is changed to

$$(\boldsymbol{\psi}_{\mathrm{mu2}} - \boldsymbol{\psi}_{\mathrm{2mu2D2}})\mathbf{B_2} + j\omega\frac{\rho_0 c_0}{\cos(\theta)}\boldsymbol{\psi}_{\mathrm{mn2D2}}\mathbf{A_2} = j\omega\frac{\rho_0 c_0}{\cos(\theta)}\boldsymbol{\psi}_{\mathrm{mMPM}}\mathbf{A}_{\mathrm{MPM}} \tag{7.86}$$

Hence,

$$\mathbf{A}_{\mathrm{MPM}} = \left[(\boldsymbol{\psi}_{\mathrm{mu2}} - \boldsymbol{\psi}_{\mathrm{2mu2D2}})\frac{\boldsymbol{\gamma_2}}{-2\boldsymbol{\psi}_{\mathrm{mu2D2}}j\omega\frac{\rho_0 c_0}{\cos(\theta)}\boldsymbol{\psi}_{\mathrm{mMPM}}} + \frac{\boldsymbol{\psi}_{\mathrm{mn2D2}}}{\boldsymbol{\psi}_{\mathrm{mMPM}}}\right]\mathbf{A_2}, \tag{7.87}$$

and

$$\boldsymbol{\psi}_{\mathrm{A_{MPM}A_2}} = \frac{(\boldsymbol{\psi}_{\mathrm{mu2}} - \boldsymbol{\psi}_{\mathrm{2mu2D2}})\,\boldsymbol{\gamma_2}}{-2\boldsymbol{\psi}_{\mathrm{mu2D2}} j\omega \frac{\rho_0 c_0}{\cos(\theta)} \boldsymbol{\psi}_{\mathrm{mMPM}}} + \frac{\boldsymbol{\psi}_{\mathrm{mn2D2}}}{\boldsymbol{\psi}_{\mathrm{mMPM}}}. \tag{7.88}$$

Since the motion equations of Membrane 1 and the internal MPM remain unchanged, the expressions of $\mathbf{B_1}$ and $\boldsymbol{\psi}_{\mathrm{B_1A_2}}$ also remain unchanged.

Equation (7.45) is changed to

$$(\boldsymbol{\psi}_{\mathrm{mu1}} - \boldsymbol{\psi}_{\mathrm{2mu1D1}})\,\boldsymbol{\psi}_{\mathrm{B_1A_2}}\mathbf{A_2} + j\omega\frac{\rho_0 c_0}{\cos(\theta)}\boldsymbol{\psi}_{\mathrm{mMPMD1}}\boldsymbol{\psi}_{\mathrm{A_{MPM}A_2}}\mathbf{A_2} = j\omega\frac{\rho_0 c_0}{\cos(\theta)}\boldsymbol{\psi}_{\mathrm{mn1}}\mathbf{A_1}. \tag{7.89}$$

Consequently,

$$\begin{aligned}\mathbf{A_1} &= \frac{(\boldsymbol{\psi}_{\mathrm{mu1}} - \boldsymbol{\psi}_{\mathrm{2mu1D1}})\,\boldsymbol{\psi}_{\mathrm{B_1A_2}} + j\omega\frac{\rho_0 c_0}{\cos(\theta)}\boldsymbol{\psi}_{\mathrm{mMPMD1}}\boldsymbol{\psi}_{\mathrm{A_{MPM}A_2}}}{j\omega\frac{\rho_0 c_0}{\cos(\theta)}\boldsymbol{\psi}_{\mathrm{mn1}}}\mathbf{A_2} \\ &= \left[\frac{(\boldsymbol{\psi}_{\mathrm{mu1}} - \boldsymbol{\psi}_{\mathrm{2mu1D1}})\,\boldsymbol{\psi}_{\mathrm{B_1A_2}}}{j\omega\frac{\rho_0 c_0}{\cos(\theta)}\boldsymbol{\psi}_{\mathrm{mn1}}} + \frac{\boldsymbol{\psi}_{\mathrm{mMPMD1}}\boldsymbol{\psi}_{\mathrm{A_{MPM}A_2}}}{\boldsymbol{\psi}_{\mathrm{mn1}}}\right]\mathbf{A_2}\end{aligned}, \tag{7.90}$$

and

$$\boldsymbol{\psi}_{\mathrm{A_1A_2}} = \frac{(\boldsymbol{\psi}_{\mathrm{mu1}} - \boldsymbol{\psi}_{\mathrm{2mu1D1}})\,\boldsymbol{\psi}_{\mathrm{B_1A_2}}}{j\omega\frac{\rho_0 c_0}{\cos(\theta)}\boldsymbol{\psi}_{\mathrm{mn1}}} + \frac{\boldsymbol{\psi}_{\mathrm{mMPMD1}}\boldsymbol{\psi}_{\mathrm{A_{MPM}A_2}}}{\boldsymbol{\psi}_{\mathrm{mn1}}}, \tag{7.91}$$

Since the motion equations of Membrane 1 and the internal MPM remain unchanged, the expression for $\mathbf{A_2}$ is unchanged. Therefore, the transmitted sound pressure is expressed by

$$\begin{aligned}p_t &= \frac{\rho_0 c_0}{\cos(\theta)}\overline{v_2} = \frac{j\omega\frac{\rho_0 c_0}{\cos(\theta)}}{l_x l_y}\mathbf{D}^{\mathrm{T}}\mathbf{A_2} \\ &= \frac{j\omega\frac{\rho_0 c_0}{\cos(\theta)}}{l_x l_y}\frac{-2\mathbf{D}^{\mathrm{T}} p_i \mathbf{D}}{\boldsymbol{\gamma_1}\boldsymbol{\psi}_{\mathrm{A_1A_2}} - 2\boldsymbol{\psi}_{\mathrm{mu1}}\boldsymbol{\psi}_{\mathrm{B_1A_2}}}.\end{aligned} \tag{7.92}$$

Consequently, the transmission coefficient is defined as

$$\tau(\theta) = \left|\frac{p_t}{p_i}\right| = \left|\frac{j\omega\frac{\rho_0 c_0}{\cos(\theta)}}{l_x l_y}\frac{-2\mathbf{D}^{\mathrm{T}}\mathbf{D}}{\boldsymbol{\gamma_1}\boldsymbol{\psi}_{\mathrm{A_1A_2}} - 2\boldsymbol{\psi}_{\mathrm{mu1}}\boldsymbol{\psi}_{\mathrm{B_1A_2}}}\right|. \tag{7.93}$$

If the sound absorbing walls of the air cavities are considered, Equation (7.66) is given by

$$\tau(\theta) = \left|\frac{p_t}{p_i}\right| = \left|\frac{j\omega\frac{\rho_0 c_0}{\cos(\theta)}}{l_x l_y}\frac{-2\mathbf{D}^{\mathrm{T}}\mathbf{D}\, e^{-\beta\frac{\omega}{c_0}(D_1+D_2)}}{\boldsymbol{\gamma_1}\boldsymbol{\psi}_{\mathrm{A_1A_2}} - 2\boldsymbol{\psi}_{\mathrm{mu1}}\boldsymbol{\psi}_{\mathrm{B_1A_2}}}\right|. \tag{7.94}$$

Note that Equations (7.93) and (7.94) are for an obliquely-incident plane wave with an incidence angle of θ. The transmission coefficient in a diffuse field is expressed by

$$\tau_{\mathrm{diffuse}} = \frac{\int_0^{\theta_{\max}} \tau(\theta)\sin(\theta)\cos(\theta)\mathrm{d}\theta}{\int_0^{\theta_{\max}} \sin(\theta)\cos(\theta)\mathrm{d}\theta}, \tag{7.95}$$

which is identical to Equation (2.93) in Chapter 2. Therefore, the STL in a diffuse field is expressed by

$$STL_{\text{diffuse}} = 20 \log_{10} \frac{1}{\tau_{\text{diffuse}}}. \tag{7.96}$$

These models are compared to the experimental results in Section 7.3.1.3.

7.3.1.3 Comparison with experimental results

In this section, the predicted results using the model developed in Sections 7.3.1.1 and 7.3.1.2 are compared to the measured STL of the double layer impervious membranes with an internal MPM (for MPM 1 to 3). The sound transmission loss measurements were conducted using the reverberation chambers presented in Chapter 2. The impervious membranes are made of PVC, for which the surface density and thickness are shown in Table 7.1. The parameters of MPMs 1 to 3 are also shown in Table 7.1. The air cavity depths, D_1 and D_2, are both 70 mm.

Since the MPMs investigated in this section (MPMs 1 to 3) are assumed to be impervious due to their small perforations, the sound transmission performance of each is dependent on their tension T, the internal damping ratio η, and most importantly, the surface density ρ_s. The surface density of each of the MPMs shown in Table 7.1 are very similar. Therefore, the predicted results using the model presented in this section are close to each other and hence only the predicted results for MPM 1 are shown in Figures 7.7 and 7.8.

Figures 7.7 shows a comparison of the measured STLs with the three MPMs and the predicted STLs using the models with a normally-incident plane wave and in a diffuse field, neglecting the sound absorption of the sound absorbing boundaries. Figures 7.8 presents a comparison with the sound absorbing boundaries where the wall sound absorption coefficient is $\beta = 0.05$. The determination of β has been described in Chapter 6. The blue curves with blue dots represent the predicted STLs using the normal incidence model at each centre frequency of the 1/3 octave bands from 50 Hz to 10 kHz. The thin dashed green curves represent the predicted STL using the diffuse field model over narrow frequency bands in the same frequency range. The thick green curves with green dots represent the STLs averaged over each 1/3 octave bands.

It is found in Figure 7.7 that the predicted STL using the normal incidence model is higher than that using the diffuse field model in the low frequency range from 50 Hz to 500

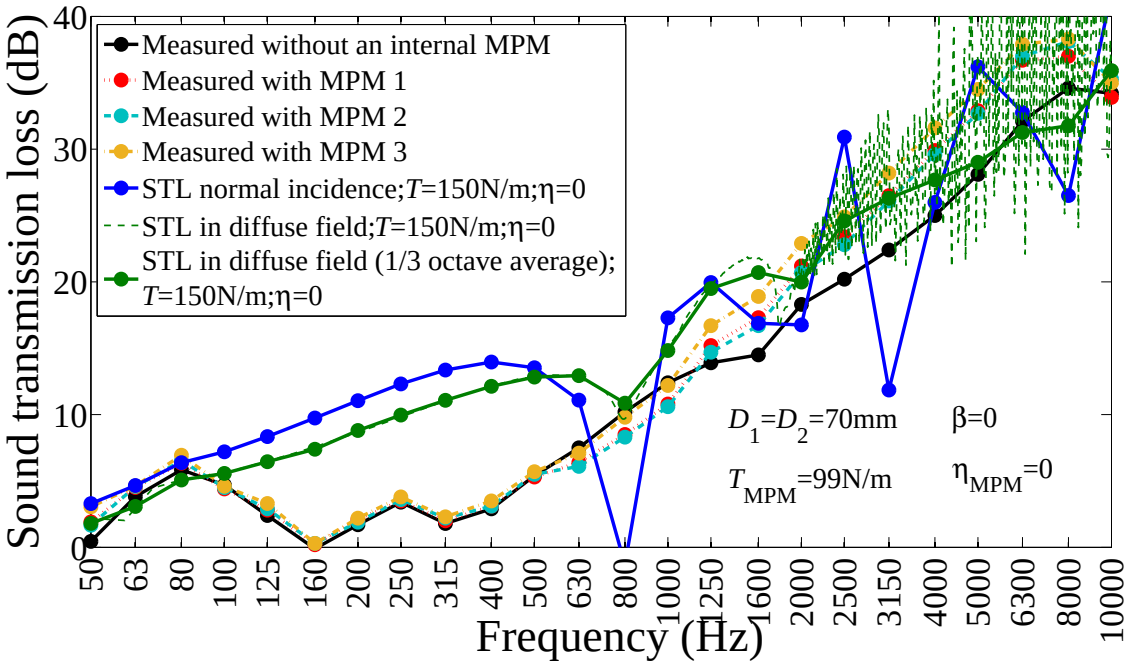

Figure 7.7: STLs of double layer impervious membranes with the internal MPMs 1 to 3. The sound absorbing boundary is neglected.

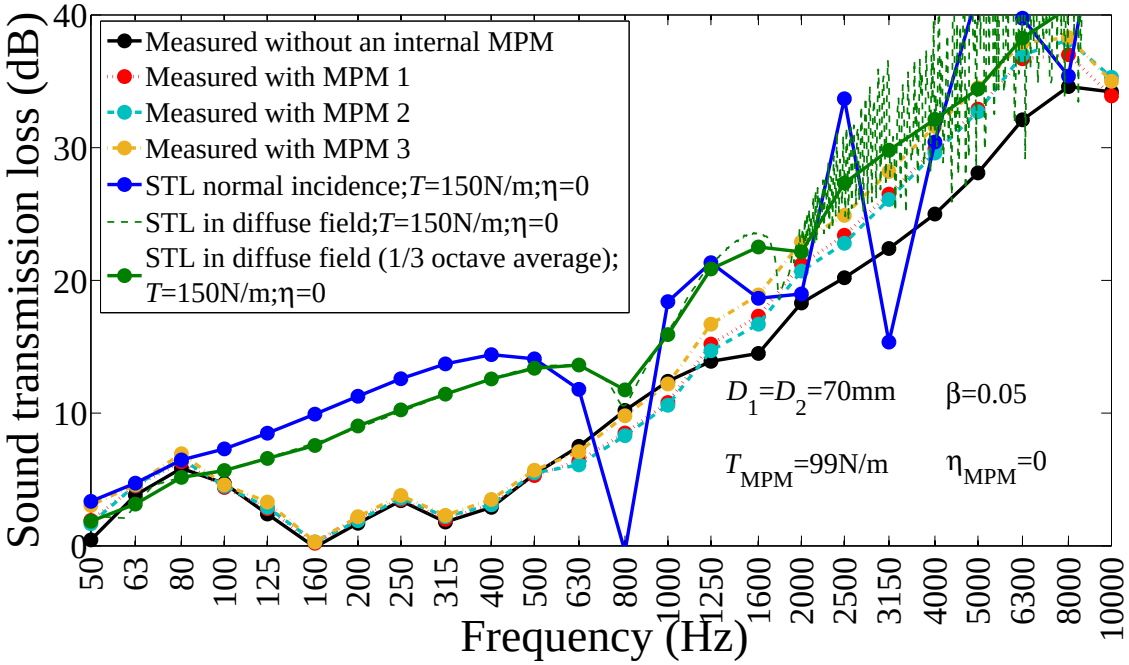

Figure 7.8: STLs of double layer impervious membranes with the internal MPMs 1 to 3. The sound absorbing boundary is considered as a factor $e^{-\beta \frac{\omega}{c_0}(D_1+D_2)}$ where $\beta = 0.05$.

Hz. Similar overestimation with the normal incidence model has been observed in Chapter 6 and is ascribed to the presence of the separating cavity. When the frequency is over 500 Hz, the predicted STL using the normal incidence model shows clear resonances corresponding to cavity modes. Since the cross modes were considered, predicted results using the diffuse field model has a better agreement with the measured STL at each centre frequency of the 1/3 octave bands than the normal incidence model. Figure 7.8 demonstrates that use of the sound absorption factor to model for the influence of the sound absorbing boundaries can further enhance the accuracy of the developed model, which is consistent with the effect of the sound absorbing boundaries observed in Chapter 6.

7.3.2 STL of a double layer impervious membrane with an internal absorbing MPM

As mentioned previously, it has been found in Chapter 3 that MPMs 1 to 3 behave as impervious membranes whilst MPM 4 can be considered as porous and therefore sound absorbing. Section 7.3.1 has investigated the analytical model of the double layer impervious membranes with an internal MPM using MPMs 1 to 3. In Section 7.3.1, the internal MPM was considered impervious, and hence, its motion equation and $\boldsymbol{\gamma}_{\mathrm{MPM}}$ are similar to those of impervious membranes.

This section aims to investigate the analytical model of the double layer impervious membranes with an absorbing internal MPM, (namely MPM 4 in this study). MPM 4 has sufficiently large perforations, and hence, has significant sound absorption, as shown in Chapter 3. It has been found in Chapter 3 that the sound absorption properties of MPM 4 is dependent on its acoustic impedance. The acoustic impedance of an absorbing MPM is the combination of the acoustic impedance due to the membrane vibration and the perforations. Therefore, it is necessary to calculate the total acoustic impedance of the MPM considering the acoustic impedance due to the perforations and that due to the membrane vibration.

In this section, the acoustic impedance of the internal absorbing MPM is investigated in Section 7.3.2.1. This acoustic impedance is substituted into the motion equation of the internal MPM and the new expression of $\boldsymbol{\gamma}_{\mathrm{MPM}}$ is obtained in Section 7.3.2.2. By substituting the new expression of $\boldsymbol{\gamma}_{\mathrm{MPM}}$ into the models developed in Sections 7.3.1.1 and 7.3.1.2, the expressions of the STLs with the internal MPM in the normally-incident plane wave condi-

tion and in a diffuse field are developed. Prediction using these models are compared with the experimental results in Section 7.3.2.3.

7.3.2.1 Acoustic impedance of the internal absorbing MPM

This section aims to investigate the acoustic impedance of a rectangular micro-perforated membrane. Similar to the model developed in Chapter 3, the acoustic impedance of each perforation is assumed to be affected by the local vibration velocity of the MPM, however, the effect of the perforations on the membrane motion is neglected. Hence, the motion equation of the membrane vibration is given by

$$(T_{\mathrm{MPM}}+2j\omega\eta_{\mathrm{MPM}})\nabla^2\xi_{\mathrm{MPM}}(x,y)+\omega^2\rho_{\mathrm{sMPM}}\xi_{\mathrm{MPM}}(x,y)=-\Delta p_{\mathrm{MPM}}, \tag{7.97}$$

which can be expressed as a finite modal summation given by

$$\left[(T_{\mathrm{MPM}}+2j\omega\eta_{\mathrm{MPM}})\,\boldsymbol{\psi}_{\mathrm{CmMPM}}+\omega^2\rho_{\mathrm{sMPM}}\boldsymbol{\psi}_{\mathrm{mMPM}}\right]\mathbf{A}_{\mathrm{MPM}}=-\Delta p_{\mathrm{MPM}}\mathbf{D}. \tag{7.98}$$

Therefore, rearranging Equation (7.98) gives

$$\mathbf{A}_{\mathrm{MPM}}=\frac{-\Delta p_{\mathrm{MPM}}\mathbf{D}}{(T_{\mathrm{MPM}}+2j\omega\eta_{\mathrm{MPM}})\,\boldsymbol{\psi}_{\mathrm{CmMPM}}+\omega^2\rho_{\mathrm{sMPM}}\boldsymbol{\psi}_{\mathrm{mMPM}}}, \tag{7.99}$$

where $\mathbf{A}_{\mathrm{MPM}}$ represents the modal amplitude of the MPM. The average particle velocity of the MPM is obtained as

$$\begin{aligned}\overline{v_{\mathrm{MPM}}}&=\frac{j\omega}{l_x l_y}\mathbf{D}^{\mathrm{T}}\mathbf{A}_{\mathrm{MPM}}\\&=\frac{j\omega}{l_x l_y}\frac{-\mathbf{D}^{\mathrm{T}}\Delta p_{\mathrm{MPM}}\mathbf{D}}{(T_{\mathrm{MPM}}+2j\omega\eta_{\mathrm{MPM}})\,\boldsymbol{\psi}_{\mathrm{CmMPM}}+\omega^2\rho_{\mathrm{sMPM}}\boldsymbol{\psi}_{\mathrm{mMPM}}}.\end{aligned} \tag{7.100}$$

Therefore, the average acoustic impedance due to the vibration of the absorbing MPM is given by

$$\begin{aligned}\overline{Z_{\mathrm{membrane}}}&=\frac{\Delta p_{\mathrm{MPM}}}{\overline{v_{\mathrm{MPM}}}}\\&=\frac{1}{\frac{j\omega}{l_x l_y}\frac{-\mathbf{D}^{\mathrm{T}}\mathbf{D}}{(T_{\mathrm{MPM}}+2j\omega\eta_{\mathrm{MPM}})\boldsymbol{\psi}_{\mathrm{CmMPM}}+\omega^2\rho_{\mathrm{sMPM}}\boldsymbol{\psi}_{\mathrm{mMPM}}}}.\end{aligned} \tag{7.101}$$

Substituting Equation (7.101) into Equations (3.26) and (3.28) gives the acoustic impedance of the perforations on the absorbing MPM, $Z_{\mathrm{perforation}}$, taking into consideration the effect of the membrane vibration. Substituting $Z_{\mathrm{perforation}}$ and Equation (7.101) into Equation (3.31) gives the overall acoustic impedance of the absorbing MPM.

7.3.2.2 Motion equation of the internal absorbing MPM

Although the overall impedance of the absorbing MPM, Z_{MPM}, is obtained in Section 7.3.2.1, it is necessary to express it in the form of a motion equation in order to estimate the STL of the double layer impervious membranes with the internal absorbing MPM. The relationship between the sound pressure difference on the MPM surfaces and Z_{MPM} (Bravo et al. 2012, Lee et al. 2005, Takahashi & Tanaka 2002) is expressed by

$$Z_{\mathrm{MPM}}\left[(1-\delta)v_{\mathrm{MPM}}+\delta v_{\mathrm{perforation}}\right]=\Delta p_{\mathrm{MPM}}. \tag{7.102}$$

The average particle velocity of the perforations $v_{\mathrm{perforation}}$ can be obtained based on the definition of the acoustic impedance, which is given by

$$v_{\mathrm{perforation}}=\frac{\Delta p_{\mathrm{MPM}}}{Z_{\mathrm{perforation}}}. \tag{7.103}$$

Substituting Equation (7.103) into Equation (7.102) yields

$$\begin{aligned} Z_{\mathrm{MPM}}\left[(1-\delta)v_{\mathrm{MPM}}+\delta\frac{\Delta p_{\mathrm{MPM}}}{Z_{\mathrm{perforation}}}\right]&=\Delta p_{\mathrm{MPM}}\\ Z_{\mathrm{MPM}}v_{\mathrm{MPM}}&=\frac{1-\delta\frac{Z_{\mathrm{MPM}}}{Z_{\mathrm{perforation}}}}{1-\delta}\Delta p_{\mathrm{MPM}}. \end{aligned} \tag{7.104}$$

Hence, the pressure difference across the MPM is given by

$$\Delta p_{\mathrm{MPM}}=\frac{1-\delta}{1-\delta\frac{Z_{\mathrm{MPM}}}{Z_{\mathrm{perforation}}}}Z_{\mathrm{MPM}}v_{\mathrm{MPM}}, \tag{7.105}$$

and the motion equation of the internal MPM 4 is

$$-\Delta p_{\mathrm{MPM}}=-\frac{1-\delta}{1-\delta\frac{Z_{\mathrm{MPM}}}{Z_{\mathrm{perforation}}}}Z_{\mathrm{MPM}}v_{\mathrm{MPM}}. \tag{7.106}$$

Therefore, the motion equation of the internal absorbing MPM in matrix form is

$$-\Delta p_{\mathrm{MPM}}\mathbf{D}=-\frac{1-\delta}{1-\delta\frac{Z_{\mathrm{MPM}}}{Z_{\mathrm{perforation}}}}Z_{\mathrm{MPM}}j\omega\boldsymbol{\psi}_{\mathrm{mMPM}}\boldsymbol{A}_{\mathrm{MPM}}, \tag{7.107}$$

and the new expression for $\boldsymbol{\gamma}_{\mathrm{MPM}}$ is obtained as

$$\boldsymbol{\gamma}_{\mathrm{MPM}}=-\frac{1-\delta}{1-\delta\frac{Z_{\mathrm{MPM}}}{Z_{\mathrm{perforation}}}}Z_{\mathrm{MPM}}j\omega\boldsymbol{\psi}_{\mathrm{mMPM}}. \tag{7.108}$$

Substituting Equation (7.108) into the models developed in Sections 7.3.1.1 and 7.3.1.2 gives the STL models of the double layer impervious membranes with the internal absorbing MPM in the normally-incident plane wave condition and in a diffuse field, respectively. These models are compared with the experimental results in Section 7.3.2.3 for the absorbing internal

MPM considered in this study, MPM 4.

7.3.2.3 Comparison with experimental results

In this section, the STL models of the double layer impervious membranes with the internal absorbing MPM are compared with the experimental results. The STL measurement was conducted using the reverberation chambers described in Chapter 2. Similar to Section 7.3.1.3, the impervious membranes are made of PVC, for which the surface density and thickness are shown in Table 2.2. The parameters of the internal absorbing MPM are also shown in Table 3.1. The air cavity depths, D_1 and D_2, are 70 mm. The tensions and damping ratios of the impervious membranes and MPM 4 are assumed to be consistent with those in Section 7.3.1.3.

Neglecting the impact of the sound absorbing boundaries of the air cavities, Figure 7.9 shows a comparison between the measured STL and the STLs predicted by the normal incidence and diffuse field models. Similar to the models described in Section 7.3.1, the predicted results from the normal incidence model show significant cavity resonances above 800 Hz. The predicted results of the diffuse field model have a reasonable agreement with the measured STL in the frequency range below 3150 Hz, however, this model under-estimates the STL in the frequency range over 4000 Hz.

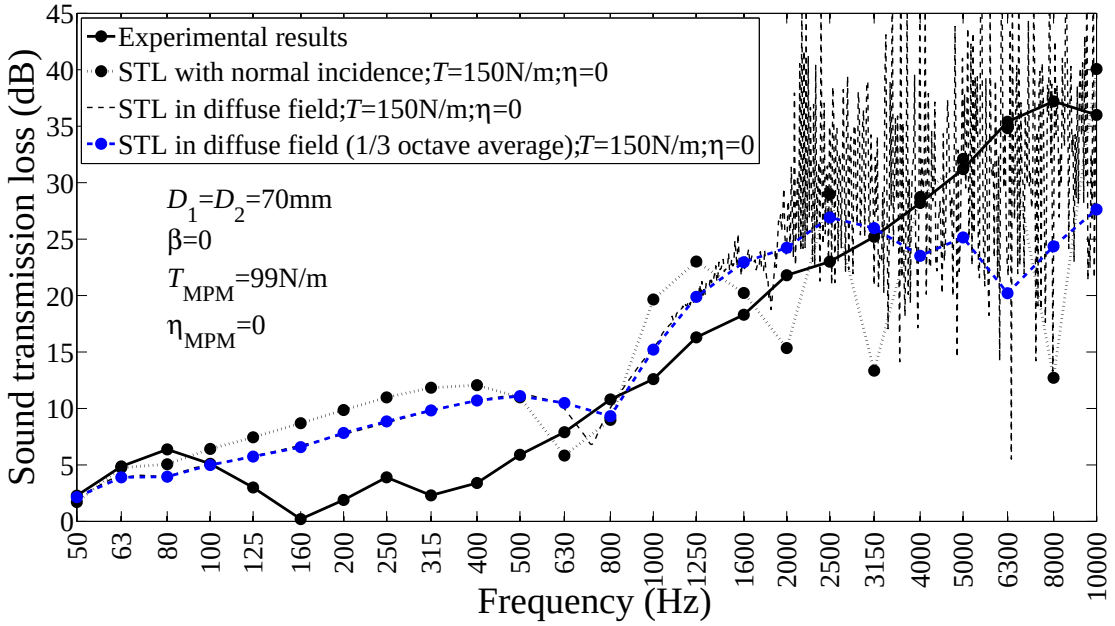

Figure 7.9: STL of double layer impervious membranes with the internal MPM 4. The sound absorbing boundary is neglected.

As mentioned in Chapter 6, this under-estimation is ascribed to neglecting the impact of the sound absorbing boundaries of the air cavities. Figure 7.10 shows the measured STL and the predicted STLs with the sound absorbing factor $\beta = 0.05$. Since the predicted STL in the high frequency range is increased, it is concluded that the sound absorbing factor β can enhance the accuracy of the developed models, which is consistent with the conclusions in previous chapters.

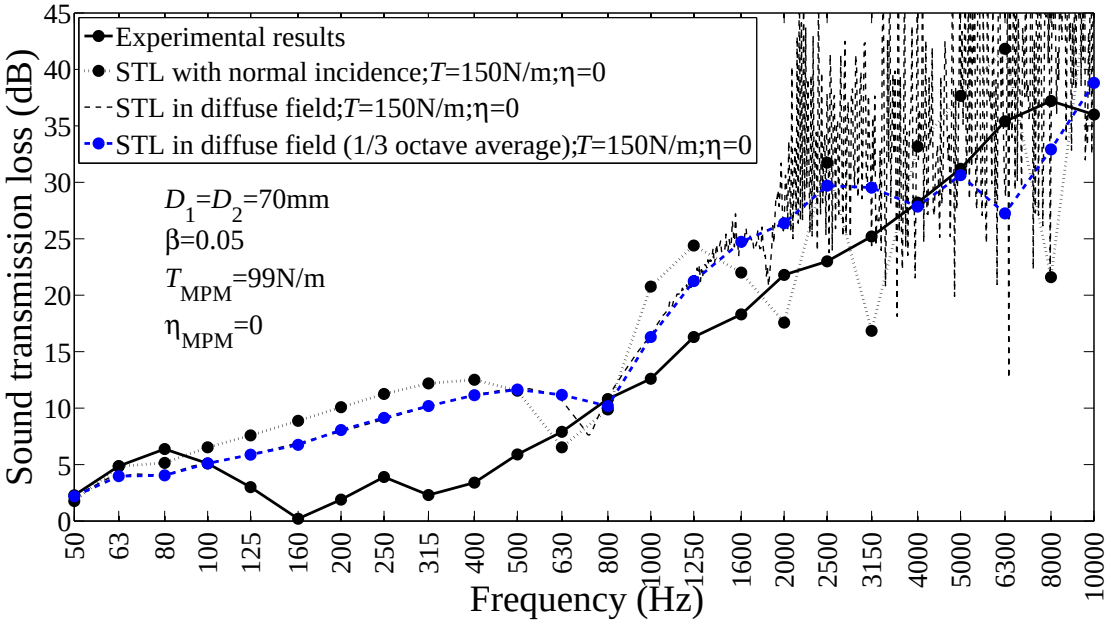

Figure 7.10: STL of double layer impervious membranes with the internal MPM 4. The sound absorbing boundary is considered as a factor $e^{-\beta\frac{\omega}{c_0}(D_1+D_2)}$ where $\beta = 0.05$.

To explore the effect of the perforations, MPM 4 was assumed to be an impervious membrane for the results presented in Figures 7.11 and 7.12. In other words, the acoustic impedance due to the perforations was neglected in Figures 7.11 and 7.12. The models used to predict these STLs were those developed in Section 7.3.1. The tension and damping ratio values were used in the model identical to those used for MPM 1 to 3, while the differing values of surface density of MPM 4 was used.

As clearly shown in Figures 7.11 and 7.12, these models over-estimate the STL in the frequency range below 800 Hz, whereas the models considering the perforations shown in Figures 7.9 and 7.10, agree better with the measured STLs in the frequency range below 800 Hz. Assuming that the internal MPM is a space absorber with an air cavity depth of $D_2 = 70$ mm, its main sound absorption peak is in the frequency range below 800 Hz, as shown in Figure 7.13. Hence, more sound energy was absorbed by MPM 4 due to its sound absorption

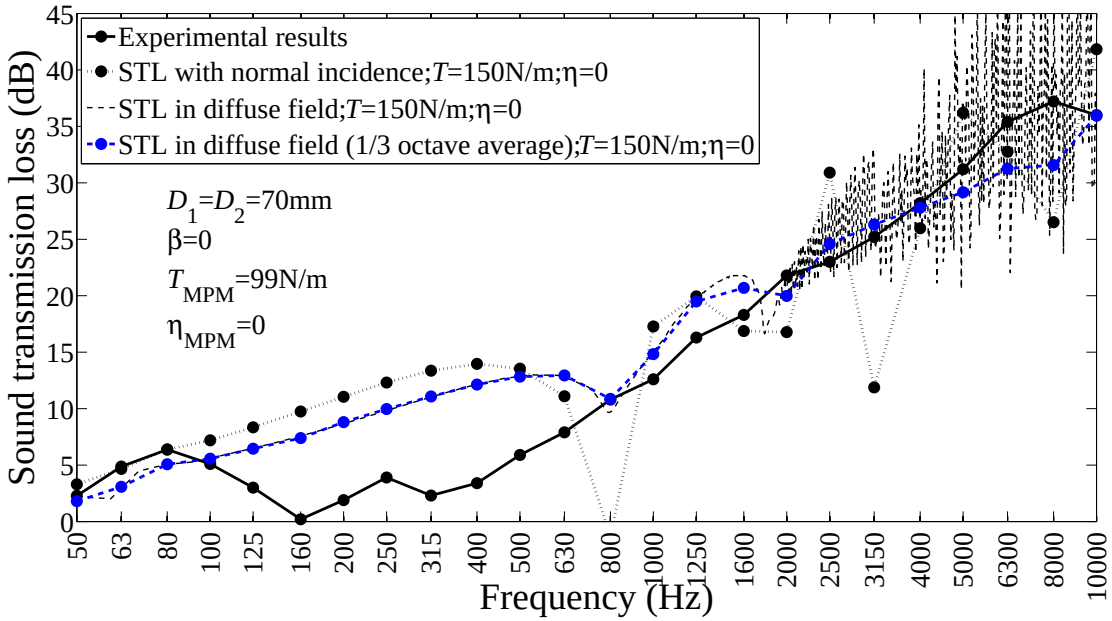

Figure 7.11: STL of double layer impervious membranes with the internal MPM 4. The sound absorbing boundary is neglected. The MPM 4 is assumed to be an impervious membrane, as in the cases in Section 7.3.1.

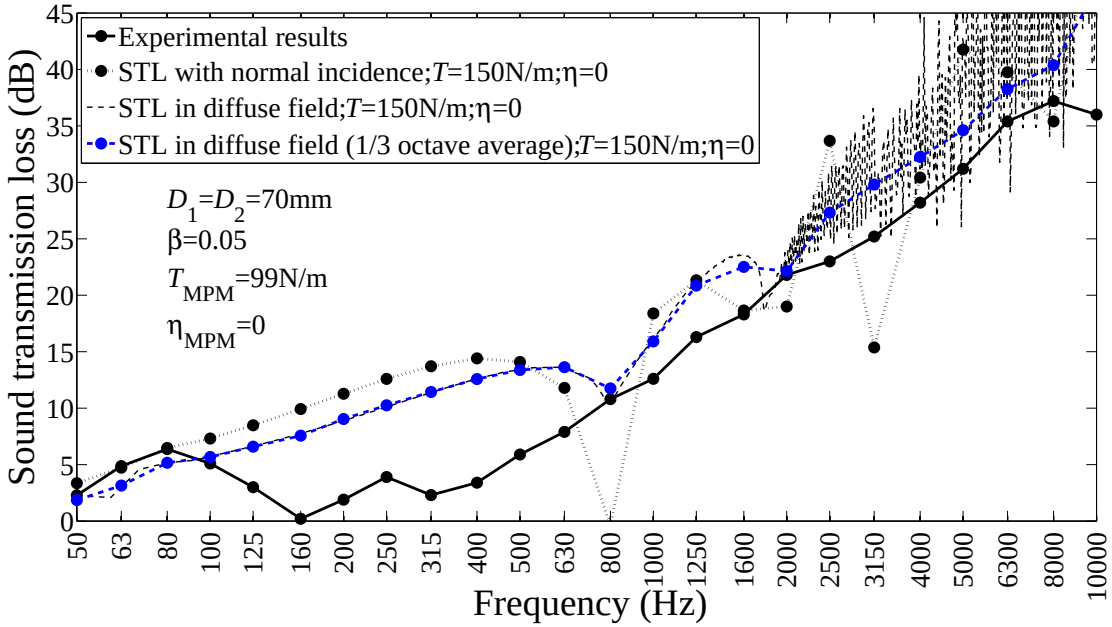

Figure 7.12: STL of double layer impervious membranes with the internal MPM 4. The MPM 4 is assumed to be an impervious membrane, as in the cases in Section 7.3.1. The sound absorbing boundary is considered as a factor $e^{-\beta\frac{\omega}{c_0}(D_1+D_2)}$ where $\beta = 0.05$.

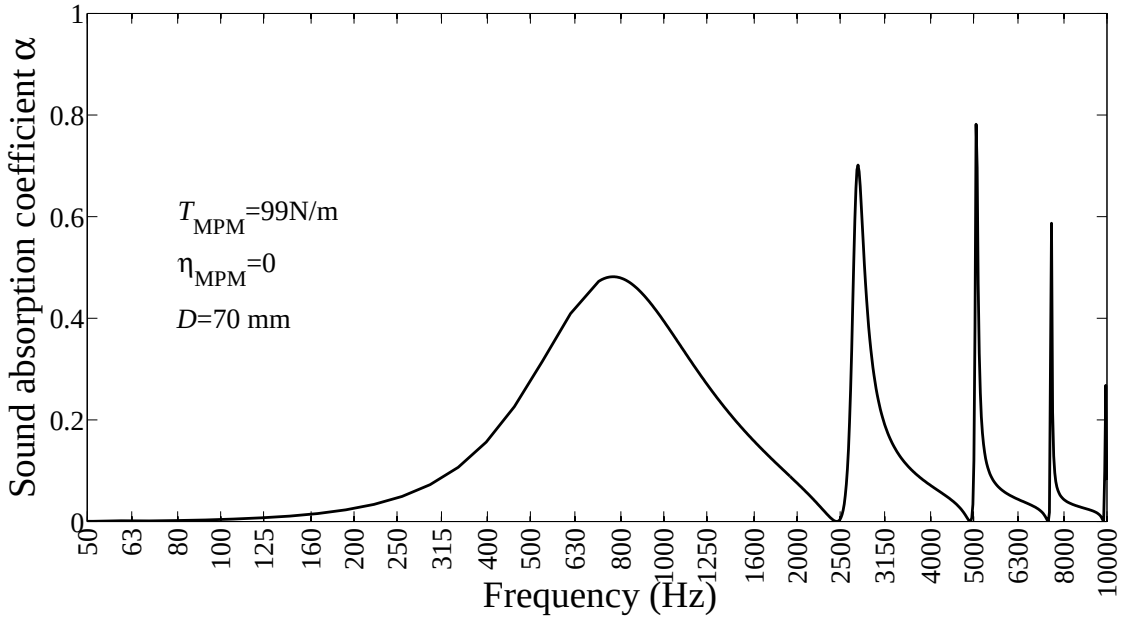

Figure 7.13: Estimated normal incidence sound absorption coefficient of MPM 4 with a cavity depth $D = 70$ mm.

performance than MPMs 1 to 3 which were considered impervious. The presented model considering the sound absorption of the MPM 4 is more realistic than the model presented in Section 7.3.1 which neglects the sound absorption due to the perforations.

However, in the frequency range above 800 Hz, the predicted results using the models with the assumption of an impervious MPM 4 are closer to the measured STLs than those using the models considering the effect of the perforations. This is ascribed to the multiple sound absorption peaks of the MPM in the high frequency range, i.e. the sound absorption peaks at 2744 Hz, 5066 Hz, 7499 Hz and 10 kHz in Figure 7.13. These multiple sound absorption peaks which are unique for the micro-perforated materials, affect the sound propagation in the high frequency range, and consequently, the deviation of the predicted STL from its average value is significant. Hence, the average STL in 1/3 octave spectrum is not as smooth as those predicted by the model assuming an impervious MPM and could be lower than the measured STLs at some frequencies, as shown in Figures 7.9 and 7.10. When the MPM is assumed to be impervious, the multiple sound absorption peaks disappear and the predicted STL is mainly affected by the surface density of the MPM.

Therefore, it is concluded that the developed models are valid for the prediction of the STL of double layer impervious membranes with the internal MPM 4 in the frequency range below the main MPM absorption frequency, which for MPM 4 is 800 Hz. In the high fre-

quency range, the model which incorporates the impedance of the MPM perforations is less accurate than those models developed in Section 7.3.1.

7.3.3 Non-linear effect of high incident SPLs on the predicted STL of the combined membrane structure

In Section 7.3.2, the acoustic impedance of the internal MPM is assumed to be independent of the incident sound pressure, such that the internal MPM was assumed to behave linearly. However, based on the discussion in Chapter 4, the sound absorption from the MPM is non-linear when it is excited by high sound pressures. Hence, this section aims to investigate the non-linear effect of an internal MPM on the STL of the double layer impervious membranes.

It is necessary to estimate the sound pressure in the cavities to determine if the internal MPM is in the non-linear regime. The estimation of the sound pressure level in Air Cavity 1 is presented in Section 7.3.3.1 and Section 7.3.3.2 develops the analytical model for the STL considering the non-linear sound absorption from the internal MPM, MPM 4. This model is based on the non-linear model developed in Chapter 5. The experimental validation of this non-linear model is shown in Section 7.3.3.3.

7.3.3.1 Incident sound pressure in Air Cavity 1

This section investigates the average sound pressure $\overline{p_{i2}}$ in the first air cavity, Air Cavity 1. This estimated sound pressure is assumed to be the incident sound on the surface of the internal MPM, MPM 4. The sound pressure level SPL_{source} in the source chamber was obtained instantaneously during the STL measurement and its corresponding sound pressure is denoted by p_{source}. However, SPL_{source} is not the incident sound pressure, p_i, of the combined membrane system, but the sum of the incident sound pressure, p_i, and the reflected sound pressure p_r. The average sound pressure $\overline{p_r}$ can be expressed as

$$\begin{aligned}\overline{p_r} &= \frac{j\omega\rho_0 c_0}{l_x l_y}\mathbf{D}^{\mathrm{T}}\mathbf{A_1} \\ &= \frac{j\omega\rho_0 c_0}{l_x l_y}\mathbf{D}^{\mathrm{T}}\boldsymbol{\psi}_{\mathrm{A_1A_2}}\mathbf{A_2} \\ &= \frac{j\omega\rho_0 c_0}{l_x l_y}\frac{-2\mathbf{D}^{\mathrm{T}}\boldsymbol{\psi}_{\mathrm{A_1A_2}}\mathbf{D}}{\boldsymbol{\gamma_1}\boldsymbol{\psi}_{\mathrm{A_1A_2}} - 2\boldsymbol{\psi}_{\mathrm{mu1}}\boldsymbol{\psi}_{\mathrm{B_1A_2}}}\, p_i.\end{aligned} \tag{7.109}$$

Hence, the average incident sound pressure is given by

$$\overline{p_i} = \frac{p_{\text{source}}}{1 + \frac{j\omega\rho_0 c_0}{l_x l_y} \frac{-2\mathbf{D}^{\mathrm{T}}\boldsymbol{\psi}_{\mathrm{A_1A_2}}\mathbf{D}}{\boldsymbol{\gamma_1}\boldsymbol{\psi}_{\mathrm{A_1A_2}} - 2\boldsymbol{\psi}_{\mathrm{mu1}}\boldsymbol{\psi}_{\mathrm{B_1A_2}}}}. \tag{7.110}$$

According to the motion equation of Membrane 1, the average incident sound pressure in the first air cavity $\overline{p_{i2}}$ is expressed by

$$\overline{p_{i2}} = \frac{\left[(T + 2j\omega\eta)\boldsymbol{\psi}_{\mathrm{Cmn1}} + \omega^2\rho_{s1}\boldsymbol{\psi}_{\mathrm{mn1}}\right]\mathbf{A_1} + 2\overline{p_i}}{2}. \tag{7.111}$$

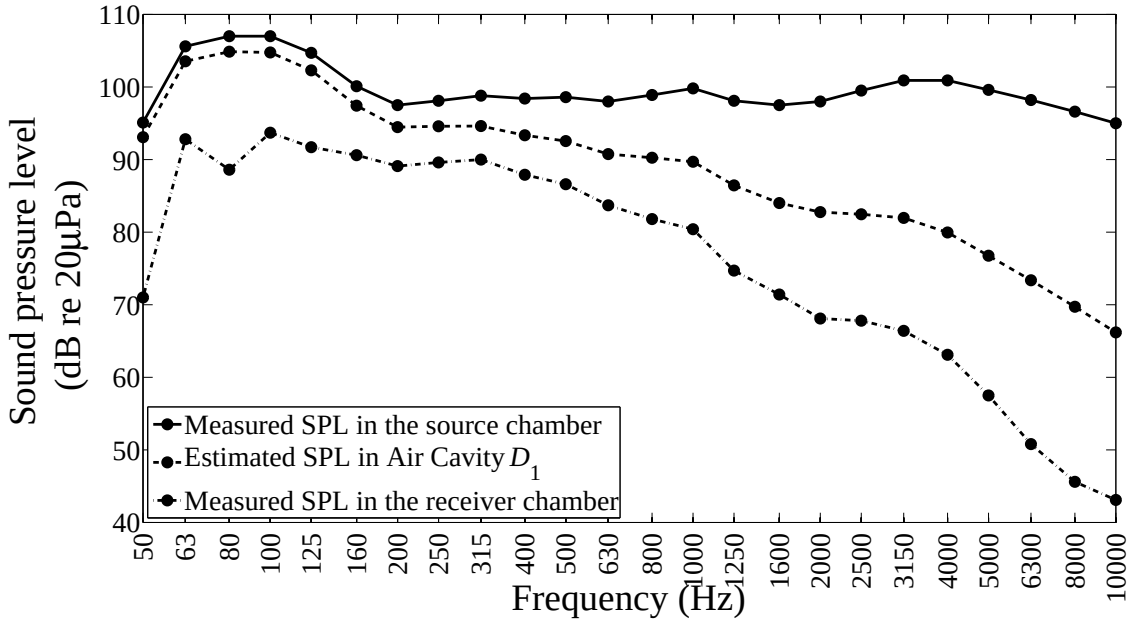

Figure 7.14: Measured SPL in the source chamber and the estimated SPL in Air Cavity 1 for MPM 4 as the internal absorbing MPM. The cavity depth is $D_1 + D_2 = 140$ mm.

Figure 7.14 shows a comparison of the measured SPL in the source chamber and the estimated SPL in Air Cavity D_1. In the low frequency range, the SPLs are close to each other, indicating the poor sound insulation at these frequencies. This has been verified in Chapters 2 and 6. However, the SPL in Air Cavity 1 decreases with frequency in the middle and high frequency range. This implies that the high STL occurs in the high frequency range. Since the non-linear sound absorption of the internal MPM, MPM 4, is closely related to the high SPL, the non-linear sound absorption of the internal absorption membrane is expected to affect the STL more significantly in the low frequency range than in the high frequency range.

7.3.3.2 Non-linear acoustic impedance of the internal absorbing MPM

Based on the analytical model developed in Chapter 5, the acoustic impedance of an internal absorption membrane in the non-linear regime can be expressed as

$$Z_{\mathrm{MPM}_{\mathrm{nonlinear}}} = Z_{\mathrm{MPM}} + \frac{ha}{\delta} + \frac{hbv}{\delta} = Z_{\mathrm{MPM}} + \frac{ha}{\delta} + \frac{hb\overline{p_{i2}}}{\delta\rho_0 c_0}. \tag{7.112}$$

Substituting Equation (7.112) into the models developed in Section 7.3.2 gives the predicted STL of the double layer impervious membranes with the internal absorption membrane in the non-linear regime. This model is compared against the experimental results in Section 7.3.3.3. The values of a and b in Equation (7.112) were determined by the curve fitting optimisation in Chapter 5.

7.3.3.3 Comparison with experimental results

This section presents the experimental comparison with the non-linear STL model developed in Section 7.3.3. The comparison between the experimental results and the predicted results are shown in Figure 7.15. Note that in the non-linear model, the acoustic impedance of the MPM is dependent on the particle velocity v, and hence the incident sound pressure on the MPM surface. The incident sound pressure can be determined using Equation (7.111) according to the sound pressure level measured in the source chamber. Note that in the STL experiments, the SPL in the source chamber was measured at the central frequency of each one third octave band. However, the predicted results are obtained in narrow frequency bands and averaged in each 1/3 octave band. Hence, when using the non-linear model, it is impossible to calculate the STLs in narrow frequency bands due to the lack of the measured narrowband SPLs in the source chamber at these frequencies. Consequently, it is impossible to obtain the octave STLs. Hence, the predicted STL was calculated at each centre frequency of the 1/3 octave bands. Thus, the predicted STL in the high frequency range can be affected significantly by the modes of the air cavities and is inaccurate due to a lack of averaging over the 1/3 octave bands. In the low frequency range, the STL in Figure 7.15 is very similar to that shown in Figure 7.10 and the difference is less than 1 dB, implying that the non-linear effect of the MPM 4 is negligible in the STL prediction, and thus non-linear effects have a negligible impact on the STL of the combined structure of impervious membranes with an internal absorption MPM.

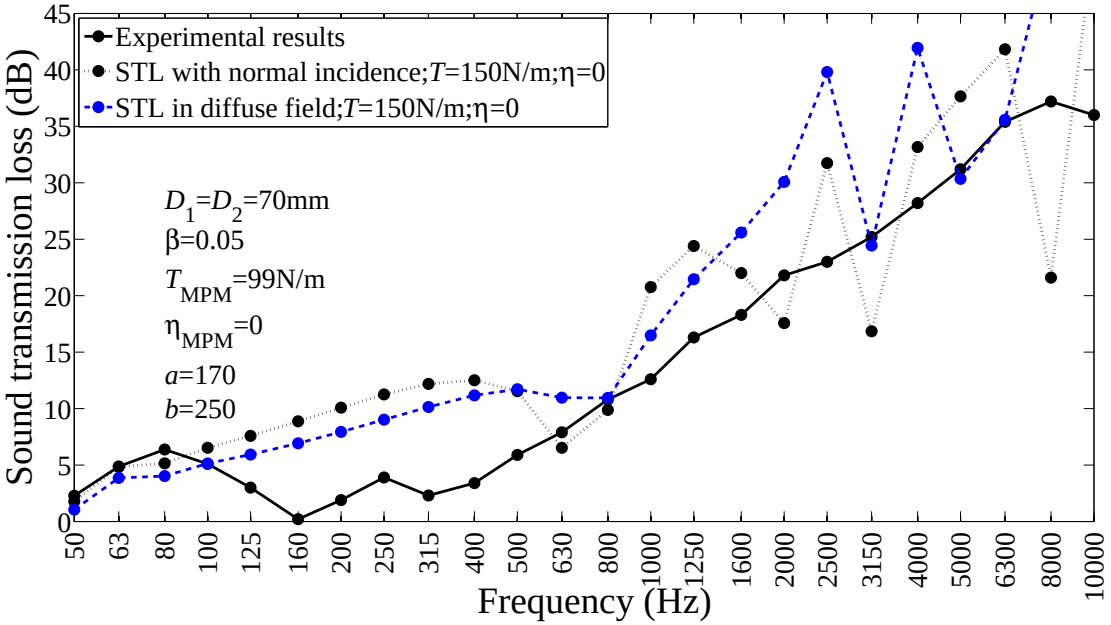

Figure 7.15: STL of double layer impervious membranes with internal MPM 4. The sound absorbing boundary is considered as a factor $e^{-\beta\frac{\omega}{c_0}(D_1+D_2)}$ where $\beta = 0.05$. The non-linear variables are shown in the figure.

7.4 Conclusions

This chapter investigated the the enhancement of the sound insulation of double layer impervious membranes with an internal MPM. It consists of two parts, the experimental validation of the effectiveness of the MPM insertion, and the analytical modelling for the STL of these combined membrane structures.

In order to validate the effectiveness of the MPM insertion, the STL measurements of double layer impervious membranes with four types of MPMs have been conducted in a diffuse field. The experimental results presented in Section 7.2 indicate that the MPM insertion can enhance the STL of the double layer impervious membranes significantly at the frequencies above the first resonance frequency of the air cavity. Based on the conclusions obtained in Chapter 3, the MPMs are categorised into two groups; MPMs 1 to 3 which can be assumed to be impervious due to their insufficiently small perforations, and MPM 4 which is sound absorbing because of its large perforations. MPMs 1 to 3 show similar main trends with increased STL curves but the magnitude of the increased STL with each MPM is different. MPM 4 has a different effect on the STL of double layer impervious membranes compared to MPMs 1 to 3 because of its sufficiently large perforations.

The impact of an internal MPM on the STL of double layer impervious membranes has been investigated analytically in Section 7.3.1. The analytical modelling was also categorised into two groups; one for MPMs 1 to 3, and the other for MPM 4. The normal incidence and diffuse field models for the double layer impervious membranes with MPMs 1 to 3 were developed in Section 7.3.1 and the predicted results using them were compared with the experimental results. It was found that by taking into consideration the sound absorbing boundaries of the air cavities the accuracy of these models is improved, especially in the high frequency range. The models for the double layer impervious membranes with MPM 4 were developed by taking into consideration the acoustic impedance of MPM 4 due to the perforations. The total acoustic impedance of MPM 4 was calculated following the strategy presented in Chapter 3. The comparison between the experimental and predicted results indicates that the developed model is accurate for the prediction of the STL of double layer impervious membranes with the internal MPM 4 in the frequency range below 800 Hz. In the high frequency range, the multiple sound absorption peaks arising from MPM 4 have significant impact on the predicted STL, and these models are less accurate than the models which assume the MPM to be impervious. Moreover, the non-linear model of the STL with MPM 4 was also investigated. However, it was found that the non-linear sound absorption of MPM 4 has negligible impact on the predicted STL since the experimental tests were undertaken at sufficiently low SPLs for any non-linear effects to be observed.

For future work, the acoustic modes of the reverberation chambers can be taken into consideration. Considering the coupling between the membrane structures and the reverberation chambers could possibly increase the accuracy of the presented models over a broad frequency range. The non-linear sound absorption of the MPM is negligible in this study due to the low SPLs in Air Cavity 1. However, this SPL can be increased by applying new sound sources which are able to generate sufficiently high SPLs in the source chamber. The impact of the non-linear sound absorption of the internal MPM can be studied in the future if sufficiently high incident SPLs are expected to occur in practice for the intended application.

Chapter 8

Conclusions

This thesis aimed to investigate acoustic properties of micro-perforated membranes (MPMs) and impervious membranes, and enhance the sound insulation of double layer impervious membranes by combining these with MPMs, thereby increasing the internal loss mechanisms of what is essentially a reactive wall. Therefore, this thesis consists of two major parts, the study of the sound absorption of micro-perforated membranes, and the study of the sound transmission of single and double layer impervious membranes without and with internal micro-perforated membranes.

8.1 Sound absorption and transmission of single layer impervious membranes

Unlike the conventional models of single layer impervious membranes which usually consider the damping arising from viscous damping (Kinsler et al. 1999) or energy dissipation (Song & Bolton 2002, 2003) on the membrane surface, in this thesis a new analytical model is proposed for the prediction of the sound absorption and sound transmission of single layer impervious membranes under tension incorporating the internal damping due to the membrane curvature. Based on the new model, expressions for the sound absorption coefficient and acoustic impedance of a circular membrane with normally-incident plane waves have been derived. The predicted results from the developed model have been compared with those of the conventional models. Sound absorption experiments of two impervious membranes have been conducted to validate the proposed model. The experimental results verify that the prediction using the proposed model has the best agreement with the experimental results among the investigated models. In addition to the sound absorption study, the sound transmission coefficient and transmission loss of a rectangular membrane have also been

studied with normally-incident plane waves, as well as in a diffuse sound field. The proposed model for the sound transmission prediction was validated by comparing predicted results against measured STLs for two different impervious membranes in a diffuse field.

Comparing the sound absorption and transmission models, it was found that whilst the damping due to the membrane curvature significantly affects the sound absorption, it can be neglected for the sound transmission prediction. The proposed models are useful tools to design a membrane-type sound absorber and noise barriers in practice. They are the foundation of the design of the combined membranes used as sound barriers and the double layer impervious membranes with internal MPMs that were also investigated in this thesis.

8.2 Linear and non-linear sound absorption of micro-perforated membranes

To investigate the sound absorption of micro-perforated membranes, a new method is introduced to predict the acoustic impedance and the sound absorption coefficient of a micro-perforated membrane (MPM). This method is based on a new boundary condition where the particle velocity at the hole wall boundary, which is assumed to be zero in Maa's theory, is assumed to be equal to the membrane vibration velocity. By applying this new boundary condition to a circular membrane, it is shown that the acoustic impedance due to the perforation is affected by the membrane vibration and becomes a function of the location of the perforation on the membrane surface. The variability of the perforation impedance with the hole location is investigated theoretically. The impedances due to the perforation and the membrane vibration are combined following the electro-acoustic analogy to present the overall impedance of the MPM. This new model is validated by experimental results for MPMs.

It is found that when MPMs have small hole radii ($\ll$ 1 mm in diameter), their sound absorption curves are close to the theoretical results of impervious membranes with identical surface density, tension and damping ratio. This implies that the effects of the micro perforations on the MPMs are negligible. However, when an MPM has holes of optimal diameter ($\sim$ 1 mm), it shows effective sound absorption due to the perforations and the motion of the membrane itself. The presented model extends the classic micro-perforated theory and of-

fers an accurate model for predicting the performance of flexible finite-sized MPMs. It also provides increased understanding of the coupling between the membrane vibration impedance and the impedance due to the perforations of micro-perforated membranes.

The previous research on the sound absorption of MPMs by others is for the linear regime. However, when an MPM is excited by high incident sound pressure levels, the sound absorption shows significant non-linear behaviour. The effect of the magnitude of the incident SPL on the sound absorption of an MPM sample has been studied with both broadband excitation and monochromatic excitation in an impedance tube with normally-incident plane waves. The broadband sound sources included white noise (Gaussian distribution), uniform random noise, pseudo-random noise, burst random noise and pink noise. The monochromatic sources consisted of a stepped sine sweep and a chirp. The experimental results indicate that, similar to the case of micro-perforated panels, there exists a threshold SPL for which the sound absorption coefficient is consistent, regardless of the SPL magnitude. When the incident SPL exceeds the threshold SPL, the sound absorption coefficient of the MPM increases with increasing SPL, which implies the existence of a non-linearity in the sound absorption of MPMs under high SPL excitation. These non-linear sound absorption coefficients have been observed with both broadband excitation and monochromatic excitation, although the threshold SPL is different for different sound sources. It is found that the threshold SPL of MPMs excited by both types of sound source is moderate and significantly lower than the commonly accepted threshold SPL values for micro-perforated panels.

In the sound absorption curves of the MPMs generated by both broadband excitation and monochromatic excitation, it was observed that the maximum sound absorption frequency tends to decrease with moderate and high SPL magnitudes. This frequency shift implies that the sound absorption of the MPM is affected by both the acoustic resistance and reactance. The latter is conventionally considered irrelevant to the non-linear sound absorption of micro-perforated panels.

Small peaks at some specific frequencies are also observed in the sound absorption coefficient curves with a stepped sine sweep excitation, however, these peaks are not present in the curves with white noise. Furthermore, the sound absorption curves of the MPMs excited with white noise are higher than those with a stepped sine sweep at roughly equal incident SPLs. These behaviours are related to the time-dependent flow generated by broadband

excitation and monochromatic excitation. With a monochromatic excitation, the frequency components are decoupled and the sound absorption curves have small peaks which closely correspond to the peaks of the incident SPL due to axial resonances within the impedance tube. With broadband excitation, the frequency components are coupled and lead to complicated fluid dynamics. As a result, the small peaks that are observed in the sound absorption curves with a stepped sine sweep do not appear for white noise excitation. For the same reason, the sound absorption curves with white noise are smoother than those with a stepped sine sweep, and can be higher than the latter for equal magnitude incident SPLs.

To explore the analytical modelling of the acoustic impedance of MPMs excited by broadband and monochromatic sound signals in the non-linear regime, a new model is developed, inspired by the air motion equation and the mass continuity equation considering the density variation in the time and spatial domains. These equations were derived by Maa (1996) but are solved differently in this thesis. Two parameters are used to represent the total air density variations in the time domain and in the direction perpendicular to the membrane surface in the spatial domain. After simplifying the derived expression, it is found that this expression is similar to several previous models, but the parameters have clear physical meanings. One of them represents the total air density variations in the time domain and the other represents those in the direction perpendicular to the membrane surface in the spatial domain. This model provides the most accurate predicted results among the models investigated, except in the case where the input voltage and the incident SPL are at their maxima. It is found that the total air density variations in the time domain increase with an increase in the incident SPL, for both broadband and monochromatic sound signals when in the non-linear regime. The total air density variations in the spatial domains increase for the broadband sound signals, and maintain constant at close to zero for the monochromatic sound signals. The presented analytical model provides clear physical meanings for its optimised parameters and offers a new strategy of the exploration for the physical phenomenon of the fluid dynamics of the air and non-linear acoustic impedance of MPMs when driven in the non-linear regime.

8.3 Sound transmission of double layer impervious membranes with an internal MPM

To predict the STL of double layer impervious membranes separated by a finite-sized air cavity, three analytical models have been developed for different conditions; namely that with normally-incident plane waves, that in a diffuse field, and that with sound absorbing walls of the air cavity. In all three models, the motion equation of each impervious membrane includes tension applied to the membrane surface and the internal damping due to the membrane curvature. The air motion within the cavity is modelled based on three-dimensional sound propagation theory. The normal incidence model was extended to the diffuse field and was found to be more accurate than the normal incidence STL model in the low frequency range, however, it tends to underestimate the STLs in the high frequency range. This underestimation is presumed to be related to the wooden walls of the air cavity, which may absorb sound in the high frequency range. To consider the effect of the absorption of sound by the wooden walls, the model was further developed by introducing an additional sound decay factor into the expressions for the sound propagation within the air cavity. This model showed good agreement with the measured STLs in the frequency range higher than the first resonance frequency of the air cavity, implying that the high STLs are not only related to the sound attenuation of the impervious membranes and the cavity, but also related to the sound absorption of the wooden boundary of the air cavity. Although this model tends to overestimate the STLs in the low frequency range, it is the most accurate model amongst the three developed models in the high frequency domain and can be used for research and design on the membrane noise barriers.

To enhance the sound transmission loss of the double layer impervious membranes, an MPM was inserted between the two impervious membranes. The STL measurements of double layer impervious membranes with each of four types of MPMs inserted demonstrated that the MPM insertion can enhance the STL of the double layer impervious membranes significantly at the frequencies above the first resonance frequency of the air cavity. MPMs which are assumed to be impervious for their sufficiently small perforations, show similar main trends on the increased STL curves, but the magnitude of the STL for each MPM is different. MPMs which have sufficiently large perforations can also enhance the STL of

double layer impervious membranes.

Consequently, the analytical modelling was also categorised into two groups; one for the small diameter perforations (MPMs 1 to 3), and the other for the larger diameter perforations (MPM 4). The normal and diffuse models for the double layer impervious membranes with MPMs 1 to 3 were developed and validated with the experimental results. It has been found that considering the sound absorption along the boundaries of the air cavity can improve the accuracy of these models, especially in the high frequency range. The models for the double layer impervious membranes with MPM 4 were developed by considering the acoustic impedance of the membrane arising from the perforations. The comparison between the experimental and predicted results with MPM 4 indicates that the developed models are accurate for the prediction of the STL of double layer impervious membranes with an internal perforated membrane in the frequency range below the frequency of the main absorption peak of the MPM. It is observed in the predicted results that the multiple sound absorption peaks of the perforated membrane absorber at higher frequencies have a significant impact on the predicted STL in the high frequency range, however these predicted high levels of absorption do not appear to be realistic in practice and hence these models are less accurate than the models which assume the MPM to be impervious. Moreover, the non-linear model of the STL with MPM 4 was also investigated. However, it was found that the non-linear sound absorption of the MPM 4 has a negligible impact on the predicted STL.

In closing, the sound absorption and sound transmission of both MPMs and impervious membranes have been investigated both theoretically and experimentally. Several new models have been developed and validated by the experimental results. These models explore the physical mechanism of the linear and non-linear sound absorption of MPMs and the sound transmission of membrane structures, and hence can give assistance to future research and design of MPMs, membrane noise barriers and membrane buildings.

8.4 Future research

The outcome from this thesis raise a number of unanswered questions that are beyond the scope of the current work. A number of potential applications of the developed concept of internal MPMs for increased STL of multiple layer membrane structures are presented in the following sections.

8.4.1 Coupling between membrane structures and reverberation chambers

As mentioned previously, the presented models for the STLs of membranes separated by an air cavity overestimate the STL at the frequencies below the first resonance frequency of the air cavity. The overestimation may be ascribed to the unmodelled coupling between the finite-sized membranes and reverberation chambers which is not accurately represented by the diffuse field model utilised in this thesis. A possible extension to this study is consideration of the coupling between the membrane structures and the reverberation chambers which takes into account their geometry and modal response for a more accurate prediction in the frequency range below the first resonance frequency of the air cavity.

8.4.2 Optimisation of the structural parameters of internal MPMs

It is known from Chapter 3 that the sound absorption of an MPM is dependent on its structural parameters. When the MPM is inserted between two impervious membranes, the sound absorption properties of the MPM have significant impact on the sound transmission loss of the combined membrane structure, as presented in Chapter 7. Therefore, the sound transmission loss of double layer impervious membranes with an internal MPM can be improved by optimising the structural parameters of the MPM such as its perforation radius and its thickness.

8.4.3 Optimisation of the distance from an internal MPM to each impervious membrane

The experimental results presented in Chapter 7 demonstrate that the sound transmission loss of double layer impervious membranes with an internal MPM can be improved around the main sound absorption frequency of the MPM absorber. Since the main sound absorption frequency of the MPM absorber is dependent on the acoustic impedance of the MPM as well as the cavity depth, the low frequency STL can be improved by increasing the cavity depth which is the distance from the internal MPM to each impervious membrane in this study. Adjusting the distance between the MPM and the impervious membranes could be helpful when designing noise barriers to block noise at specific frequencies.

8.4.4 Multiple layer internal MPMs

In this study, there was a single layer internal MPM. However, it is presumed that multiple layer MPMs can be used in practice. Further research can be conducted on the optimised parameters of these multiple layer MPMs and the effect of the air cavity between two neighbouring MPMs on the STL of the combined membrane structures. Note that the parameters of each MPM are not necessarily identical to the parameters of the other. Since Miasa et al. (2007) indicated experimentally that multiple-sized micro-perforated panels can enhance the sound absorption coefficient and broaden the main sound absorption frequency band, presumably internal MPMs with different perforation sizes can enhance the STL of the membrane structure over a broad frequency range.

8.4.5 Effect of a grazing flow on the internal MPM surface

Moreover, it is found that the membrane structures are usually inflated with air when they are used as temporary buildings. Hence, if internal MPMs are used to improve the sound transmission loss of the membrane structure, a grazing flow may exist on the surfaces of the internal MPMs. Rao & Munjal (1986) found that a grazing flow can increase the acoustic resistance of a perforated panel. Hence, the presence of the grazing flow may possibly increase the acoustic resistance of the internal MPMs and consequently increase the sound transmission loss of the membrane structure. This may be of interest for further research.

8.4.6 Incorporation of internal MPMs in other multi-layer structures

The internal MPMs considered in this thesis for enhancing the STL of impervious membranes may also have application to multi layer building constructions and aircraft structures, where they may be able to provide decreased mass compared with conventional porous materials, and thus potential fuel savings. An investigation of both the optimal MPM arrangement in terms of STL and mass reduction is considered a worthy area for investigation.

References

ASTM (2012), 'Astm e1050-12, standard test method for impedance and absorption of acoustical materials using a tube, two microphones and a digital frequency analysis system'.

Beranek, L. L., Mellow, T. J. & Zuckerwar, A. J. (2013), 'Acoustics: sound fields and transducers.', *Journal of the Acoustical Society of America* **134**(3), 2337.

Bies, D. & Hansen, C. (2009), *Engineering noise control: theory and practice*, 4 edn, Taylor & Francis.

Bodén, H. (2007), 'Acoustic characterisation of perforates using non-linear system identification techniques', *13th AIAA/CEAS Aeroacoustics Conference (28th AIAA Aeroacoustics Conference), 21 May 2007 through 23 May 2007, Rome, Italy* pp. 1–10.

Bolton, J., Shiau, N. & Kang, Y. (1996), 'Sound transmission through multi-panel structures lined with elastic porous materials', *Journal of Sound and Vibration* **191**(3), 317–347.

Bosmans, I., Lauriks, W., Lombaert, G., Mermans, J. & Vermeir, G. (1999), 'Sound absorption of stretched ceilings with an impervious synthetic membrane', *Journal of the Acoustical Society of America* **106**, 233–239.

Bravo, T., Maury, C. & Pinhde, C. (2012), 'Vibroacoustic properties of thin micro-perforated panel absorbers', *Journal of the Acoustical Society of America* **132**(2), 789–798.

Chung, J. & Blaser, D. (1980*a*), 'Transfer function method of measuring in-duct acoustic properties. i. theory', *Journal of the Acoustical Society of America* **68**, 907–913.

Chung, J. & Blaser, D. (1980*b*), 'Transfer function method of measuring in duct acoustic properties. ii. experiment', *Journal of the Acoustical Society of America* **68**, 913–921.

Croome, D. (1985), 'Acoustic design for flexible membrane structures', *Applied Acoustics* **18**(6), 399–433.

Cummings, A. (1984), 'Acoustic nonlinearities and power losses at orifices', *AIAA Journal* **22**(6), 786–792.

Cummings, A. (1986), 'Transient and multiple frequency sound transmission through perforated plates at high amplitude', *Journal of the Acoustical Society of America* **79**(4), 942–

951.

Fahy, F. J. & Gardonio, P. (2007), *Sound and structural vibration: radiation, transmission and response*, Academic Press.

Frommhold, W., Fuchs, H. & Sheng, S. (1994), 'Acoustic performance of membrane absorbers', *Journal of Sound and Vibration* **170**(5), 621–636.

Hashimoto, N., Katsura, M. & Nishikawa, K. (1996), 'Experimental study on sound insulation of membranes with small weights for application to membrane structures', *Applied Acoustics* **48**(1), 71–84.

Hashimoto, N., Katsura, M., Yasuoka, M. & Fujii, H. (1991), 'Sound insulation of a rectangular thin membrane with additional weights', *Applied Acoustics* **33**(1), 21–43.

Herdtle, T., Bolton, J. S., Kim, N. N., Alexander, J. H. & Gerdes, R. W. (2013), 'Transfer impedance of microperforated materials with tapered holes', *Journal of the Acoustical Society of America* **134**(6), 4752–4762.

Howard, C. Q. & Cazzolato, B. S. (2014), *Acoustic analyses using Matlab and Ansys*, CRC Press.

Ingard, U. (1953), 'On the theory and design of acoustic resonators', *Journal of the Acoustical Society of America* **25**(6), 1037–1061.

Ingard, U. (1954), 'Transmission of sound through a stretched membrane', *Journal of the Acoustical Society of America* **26**, 99–101.

Ingard, U. & Ising, H. (1967), 'Acoustic nonlinearity of an orifice', *Journal of the Acoustical Society of America* **42**(1), 6–17.

ISO10534 (1998), 'Iso 10534-2, determination of sound absorption coefficient and acoustic impedance with the interferometer'.

ISO140.4 (2006), 'Acoustics - measurement of sound insulation in buildings and of building elements - laboratory measurements of impact sound insulation of floors'.

Kang, J. & Fuchs, H. (1999), 'Predicting the absorption of open weave textiles and micro-perforated membranes backed by an air space', *Journal of Sound and Vibration* **220**(5), 905–920.

Kinsler, L., Frey, A., Coppens, A. & Sanders, J. (1999), *Fundamentals of acoustics*, 4 edn, Wiley-VCH.

Lee, C.-M. & Xu, Y. (2009), 'A modified transfer matrix method for prediction of transmis-

sion loss of multilayer acoustic materials', *Journal of Sound and Vibration* **326**(1), 290–301.

Lee, Y., Lee, E. & Ng, C. (2005), 'Sound absorption of a finite flexible micro-perforated panel backed by an air cavity', *Journal of Sound and Vibration* **287**(1-2), 227–243.

Legault, J. & Atalla, N. (2010), 'Sound transmission through a double panel structure periodically coupled with vibration insulators', *Journal of Sound and Vibration* **329**(15), 3082–3100.

Liu, J. & Herrin, D. (2010), 'Enhancing micro-perforated panel attenuation by partitioning the adjoining cavity', *Applied Acoustics* **71**(2), 120–127.

London, A. (1950), 'Transmission of reverberant sound through double walls', *Journal of the Acoustical Society of America* **22**, 270–279.

Maa, D. Y. (1975), 'Theory and design of microperforated panel sound absorbing constructions', *Scientia Sinica* **18**(1), 55–71.

Maa, D. Y. (1994), 'Microperforated panel at high sound intensity', *Proceedings of INTER-NOISE (Yokohama)* .

Maa, D. Y. (1996), 'Microperforated panel at high sound intensity', *Acta Acustica* **1**, 10–14.

Maa, D. Y. (1997), 'General theory and design of microperforated-panel absorbers', *Acta Acustica* **22**(5), 385–393.

Maa, D. Y. (1998), 'Potential of microperforated panel absorber', *Journal of the Acoustical Society of America* **104**, 2861–2866.

Maa, D. Y. (2006), 'Practical absorption limits of mpp absorbers', *Acta Acustica* **6**, 481–484.

Martin, B. (2008), What is the sound transmission loss of an open window?, *in* 'Acoustics and Sustainability Australian Acoustical Society National Conference', Geelong, Victoria, Australia, pp. 65–67.

McIntosh, J. D. & Lambert, R. F. (1990), 'Nonlinear wave propagation through rigid porous materials. i: Nonlinear parametrization and numerical solutions', *Journal of the Acoustical Society of America* **88**(4), 1939–1949.

Mehra, S. (2002), 'Aufblasbarer schallschutz mit bauteilen aus folien und membranen', *Bautechnik* **79**, 794–797.

Melling, T. (1973*a*), 'An impedance tube for precision measurement of acoustic impedance and insertion loss at high sound pressure levels', *Journal of Sound and Vibration*

28(1), 23–54.

Melling, T. H. (1973*b*), 'The acoustic impendance of perforates at medium and high sound pressure levels', *Journal of Sound and Vibration* **29**(1), 1–65.

Miasa, I., Okuma, M., Kishimoto, G. & Nakahara, T. (2007), 'An experimental study of a multi-size microperforated panel absorber', *Journal of System Design and Dynamics* **1**(2), 331–339.

Network, D. B. (2015), 'Water cube national aquatics centre', `http://www.designbuild-network.com/projects/watercube/`.

Park, S. H. (2013), 'Acoustic properties of micro-perforated panel absorbers backed by helmholtz resonators for the improvement of low-frequency sound absorption', *Journal of Sound and Vibration* **332**(20), 4895–4911.

Pfretzschner, J., Cobo, P., Simon, F., Cuesta, M. & Fernandez, A. (2006), 'Microperforated insertion units: An alternative strategy to design microperforated panels', *Applied Acoustics* **67**(1), 62–73.

Poblet-Puig, J. & Rodrguez-Ferran, A. (2012), 'Modal-based prediction of sound transmission through slits and openings between rooms', *Journal of Sound and Vibration* .

Rao, K. N. & Munjal, M. (1986), 'Experimental evaluation of impedance of perforates with grazing flow', *Journal of Sound and Vibration* **108**(2), 283–295.

Rayleigh, J. W. S. B. (1896), *The theory of sound*, Vol. 2, Macmillan.

Romilly, N. (1964), 'Transmission of sound through a stretched ideal membrane', *Journal of the Acoustical Society of America* **36**, 1104–1109.

Rousselet, B., Gibiat, V., Guilain, S. & Lefebvre, A. (2014), 'A new calibration method for measuring acoustic transfer matrixes with flow and application to an automotive compressor', *Journal of Sound and Vibration* **333**(24), 6370–6380.

Ruiz, H., Cobo, P. & Jacobsen, F. (2011), 'Optimization of multiple-layer microperforated panels by simulated annealing', *Applied Acoustics* **72**(10), 772–776.

Sakagami, K., Kiyama, M. & Morimoto, M. (2002), 'Acoustic properties of double-leaf membranes with a permeable leaf on sound incidence side', *Applied Acoustics* **63**(8), 911–926.

Sakagami, K., Kiyama, M., Morimoto, M. & Takahashi, D. (1996), 'Sound absorption of a cavity-backed membrane: a step towards design method for membrane-type absorbers',

Applied Acoustics **49**(3), 237–247.

Sakagami, K., Uyama, T., Morimoto, M. & Kiyama, M. (2005), 'Prediction of the reverberation absorption coefficient of finite-size membrane absorbers', *Applied Acoustics* **66**(6), 653–668.

Sewell, E. (1970), 'Transmission of reverberant sound through a single-leaf partition surrounded by an infinite rigid baffle', *Journal of Sound and Vibration* **12**(1), 21–32.

Sgard, F., Atalla, N. & Nicolas, J. (2000), 'A numerical model for the low frequency diffuse field sound transmission loss of double-wall sound barriers with elastic porous linings', *Journal of the Acoustical Society of America* **108**, 2865–2872.

Song, B. & Bolton, J. (2000), 'A transfer-matrix approach for estimating the characteristic impedance and wave numbers of limp and rigid porous materials', *Journal of the Acoustical Society of America* **107**, 1131–1152.

Song, J. & Bolton, J. S. (2002), Modeling of membrane sound absorbers, *in* 'INTER-NOISE and NOISE-CON Congress and Conference Proceedings', Vol. 2002, Institute of Noise Control Engineering, pp. 740–745.

Song, J. & Bolton, J. S. (2003), 'Sound absorption characteristics of membrane-based sound absorbers', *Proceedings of INTER-NOISE* pp. 3881–3888.

Takahashi, D. & Tanaka, M. (2002), 'Flexural vibration of perforated plates and porous elastic materials under acoustic loading', *Journal of the Acoustical Society of America* **112**(4), 1456–1464.

Tayong, R., Dupont, T. & Leclaire, P. (2010), 'On the variations of acoustic absorption peak with particle velocity in micro-perforated panels at high level of excitation', *Journal of the Acoustical Society of America* **127**(5), 2875–2882.

Tayong, R., Dupont, T. & Leclaire, P. (2011), 'Experimental investigation of holes interaction effect on the sound absorption coefficient of micro-perforated panels under high and medium sound levels', *Applied Acoustics* **72**(10), 777–784.

Tectoniks (2010), 'Champions league dome in madrid', `http://www.designbuild-network.com/projects/watercube/`.

Temme, N. (2011), *Special functions: An introduction to the classical functions of mathematical physics*, John Wiley and Sons.

Tian, H., Wang, X. & Zhou, Y.-h. (2014), 'Theoretical model and analytical approach for

a circular membrane–ring structure of locally resonant acoustic metamaterial', *Applied Physics A* **114**(3), 985–990.

Toyoda, M., Mu, R. L. & Takahashi, D. (2010), 'Relationship between helmholtz-resonance absorption and panel-type absorption in finite flexible microperforated-panel absorbers', *Applied Acoustics* **71**(4), 315–320.

Vigran, T. (2010), 'Sound transmission in multilayered structuresintroducing finite structural connections in the transfer matrix method', *Applied Acoustics* **71**(1), 39–44.

Villot, M., Guigou, C. & Gagliardini, L. (2001), 'Predicting the acoustical radiation of finite size multi-layered structures by applying spatial windowing on infinite structures', *Journal of Sound and Vibration* **245**(3), 433–455.

Vries, J. (2011), Triple-layer membrane structures sound insulation performance and practical solutions, Thesis, Delft University of Technology.

Walstijn, M. (2009), 'Vibrations of strings and membranes', `http://www.somasa.qub.ac.uk/~mvanwalstijn/pbss/lectures/session5.pdf`.

Waltz, R. A., Morales, J. L., Nocedal, J. & Orban, D. (2006), 'An interior algorithm for nonlinear optimization that combines line search and trust region steps', *Mathematical Programming* **107**(3), 391–408.

Wang, C. (1981), 'On the low-reynolds-number flow in a helical pipe', *Journal of Fluid Mechanics* **108**, 185–194.

Wang, C., Cheng, L., Pan, J. & Yu, G. (2010), 'Sound absorption of a micro-perforated panel backed by an irregular-shaped cavity', *Journal of the Acoustical Society of America* **127**(1), 238–246.

Wang, J., Lu, T., Woodhouse, J., Langley, R. & Evans, J. (2005), 'Sound transmission through lightweight double-leaf partitions: theoretical modelling', *Journal of Sound and Vibration* **286**(4), 817–847.

WaterCube (2008), 'Reducing noise in water cube', `http://www.water-cube.com/cn/news/venue/2008/022715.html`.

Yang, Z., Mei, J., Yang, M., Chan, N. H. & Sheng, P. (2008), 'Membrane-type acoustic metamaterial with negative dynamic mass', *Physical Review Letters* **101**(20), 204–301.

Zhang, Y., Wen, J., Xiao, Y., Wen, X. & Wang, J. (2012), 'Theoretical investigation of the sound attenuation of membrane-type acoustic metamaterials', *Physics Letters A*

376(17), 1489–1494.

Zorumski, W. E. & Parrott, T. L. (1971), *Nonlinear acoustic theory for rigid porous materials*, Vol. 6196, National Aeronautics and Space Administration.

Appendix A

Publications arising from this thesis

Acoustic impedance of micro perforated membranes: Velocity continuity condition at the perforation boundary

Chenxi Li,[a] Ben Cazzolato, and Anthony Zander
School of Mechanical Engineering, The University of Adelaide, Adelaide, South Australia 5005, Australia

(Received 17 April 2015; revised 20 October 2015; accepted 17 December 2015; published online 7 January 2016)

The classic analytical model for the sound absorption of micro perforated materials is well developed and is based on a boundary condition where the velocity of the material is assumed to be zero, which is accurate when the material vibration is negligible. This paper develops an analytical model for finite-sized circular micro perforated membranes (MPMs) by applying a boundary condition such that the velocity of air particles on the hole wall boundary is equal to the membrane vibration velocity (a zero-slip condition). The acoustic impedance of the perforation, which varies with its position, is investigated. A prediction method for the overall impedance of the holes and the combined impedance of the MPM is also provided. The experimental results for four different MPM configurations are used to validate the model and good agreement between the experimental and predicted results is achieved. © *2016 Acoustical Society of America*.
[http://dx.doi.org/10.1121/1.4939489]

[MV] Pages: 93–103

I. INTRODUCTION

Micro perforated panels (MPPs) are thin panels perforated with sub-millimetre sized holes, and have been used in noise control for decades as an alternative to conventional porous materials. When backed with an air cavity and a rigid wall, the MPP shows effective sound absorption, and this combined structure is called a micro perforated absorber (MPA). Although its sound absorbing bandwidth is relatively narrow compared to a porous material of similar thickness, the MPA is favoured for its unique properties. Unlike porous materials, MPPs are used in hospitals and electronic industries where particles must be avoided (Pfretzschner *et al.*, 2006). Metal MPPs can be used in harsh conditions instead of porous materials. For example, they are used inside the engines of cars and aircraft due to their resistance to high temperature. In addition, the analytical model for the prediction of the sound absorption of MPPs is well developed, which offers the opportunity to design MPPs to control specific sources of noise (Maa, 1998).

The classical analytical model for the prediction of the sound absorption and acoustic impedance of MPPs was developed by Maa (1975) and has been widely used since that time. In recent years, Wang *et al.* (2010) investigated the sound absorption of an MPP backed by an irregular-shaped cavity based on Maa's theory. Using the classical theory, Liu and Herrin (2010) investigated partitioning the backing cavity of the MPA to enhance the absorption of normally incident plane waves. When Ruiz *et al.* (2011) investigated the sound absorption of multiple-layer MPPs, the acoustic impedance of each layer was obtained using the classical theory. Based on Maa's model, Park (2013) also analysed the combination of a MPP and a Helmholtz resonator. Herdtle *et al.* (2013) extended Maa's theory for micro perforated materials with tapered holes. However, these studies are all based on Maa's classical model and neglect the effect of the panel vibration.

Maa's classical model assumes the panel to be rigid and as a consequence the effect of the panel vibration is neglected. However, additional sound absorbing peaks, which are not observed in Maa's model, are observed in the low frequency range of experimental results (Toyoda *et al.*, 2010). These unexpected peaks are evidence of the effect of panel vibration on the acoustic impedance of the MPA. This effect could be very significant when the panel is very light and thin, or if membranes are used in the form of a micro-perforated membrane (MPM).

To investigate this effect of the panel/membrane vibration on the acoustic impedance of an MPP/MPM, Kang and Fuchs (1999) coupled the acoustic impedance of a limp membrane with the acoustic impedance due to the perforations and derived an expression for the total acoustic impedance of an infinite MPM. They achieved this using the electric-acoustic analogy to combine the acoustic impedance due to the structural vibration with the acoustic impedance of the perforations as predicted by Maa's model. Thus, the effect of the size of the membrane was neglected in their model. Similarly, Lee *et al.* (2005) investigated the acoustic impedance of a flexible rectangular MPP, where the finite size of the panel was considered based on a modal approach. Bravo *et al.* (2012) extended the method of Lee *et al.* (2005) to a circular MPP. Takahashi and Tanaka (2002) coupled the acoustic impedances due to the MPP vibration and the perforations by spatially averaging the flow velocity through the perforations.

Note that all these methods used Maa's model to calculate the acoustic impedance due to the perforations, assuming that the vibration of the panel/membrane has no effect on the acoustic impedance of the perforations. In Maa's (1975) classical model, the particle velocity at the hole wall

[a]Electronic mail: chenxi.li@adelaide.edu.au

boundary is assumed to be zero. Although Takahashi and Tanaka (2002) investigated the relative velocity at the air-solid interface in the perforation, their alternative method to couple the acoustic impedances due to the perforations and the plate vibration still calculated the acoustic impedance due to the perforation using Maa's theory based on the rigid wall assumption. However, if the panel/membrane vibration is significant, the particles at the hole wall boundary adhere to the hole wall due to the no-slip boundary condition and their velocity can be assumed to be equal to the panel/membrane vibration velocity. Hence, the acoustic impedance due to the perforation is not constant as in Maa's model but varies depending on the position of the hole on the panel/membrane surface. The spatially varying acoustic impedance implies that for thin membranes for which vibration is not negligible, the membrane vibration could have a significant effect on the acoustic impedance of the perforation, which has been neglected in previous research. This no-slip boundary condition which assumes the particle velocity at the perforation wall boundary is equal to the vibration velocity of the material, and the spatially varying acoustic impedance of MPMs is previously unexplored.

This paper aims to investigate the acoustic impedance and sound absorption of a finite-sized circular MPM under tension using a new boundary condition which assumes that the velocity of the air particles at the hole wall boundary are equal to the vibration velocity of the membrane surrounding the hole. The new no-slip boundary condition is introduced in Sec. II A. Based on this new boundary condition, an expression for the variable acoustic impedance of the perforation is obtained. In this expression, the vibration velocity of the membrane remains unknown. The vibration velocity and the acoustic impedance of the circular membrane are investigated in Sec. II B. In the developed model, the hole diameter and the perforation ratio are assumed to be sufficiently small that the effect of the holes on the motion of the membrane can be neglected. The acoustic impedance of holes located in different positions is compared in Sec. II C. The overall impedance of the holes is derived and compared with that of Maa's classic model in Sec. II D. To validate the developed model, sound absorption experiments were carried out on four different MPMs and the experimental results are compared with the model predictions in Sec. III. Good agreement is obtained between the experimental and the predicted results for three of the MPM samples, and demonstrates the accuracy of this model. To further investigate the proposed model, four additional MPMs were manufactured and the effect of the hole position on the sound absorption of MPMs was studied in Sec. III C. The good agreement achieved for the four additional MPMs also validates the proposed model.

II. ANALYTICAL MODELING

In Sec. II A, an analytical model using the proposed boundary condition is derived. The derivation starts with the motion equation of air particles in a small hole. The solutions of this equation using the conventional and the proposed boundary condition are compared theoretically. The expressions for the acoustic impedance due to each of the perforations and for the combined MPM are also presented.

A. Acoustic impedance and boundary condition of flexible MPMs

1. Motion equation of air particles in a small hole

When a sound wave is traveling through the small hole of a MPM or panel with a hole radius of r_0, the particle velocity v is a function of the distance, r, from the centre of the hole to the position of the specific air particle, as shown in Fig. 1. This relationship between the particle velocity in the hole and the sound pressure applied on the membrane or panel surface is governed by the motion equation of the air particle (Maa, 1975),

$$\left(\frac{\partial^2}{\partial r^2}+\frac{1}{r}\frac{\partial}{\partial r}+K_{\text{air}}^2\right)v(r)=-\frac{\Delta p}{\mu h}, \tag{1}$$

where $K_{\text{air}}^2=-j(\rho_0\,\omega/\mu)$, ω denotes the angular frequency and is equal to $2\,\pi f$, where f is the frequency, μ denotes the dynamic viscosity of air, ρ_0 denotes the density of air, Δp denotes the pressure difference applied between the front and back surfaces of the membrane/panel, r denotes the radial coordinate relative to the local coordinates of each perforation, and h denotes the thickness of the membrane/panel, which is also the length of the hole. Equation (1) is an inhomogeneous differential equation and its general solution is

$$v(r)=AJ_0(K_{\text{air}}r)-\frac{\Delta p}{\mu\,h\,K_{\text{air}}^2}, \tag{2}$$

where J_0 is the Bessel function of the first kind and zero order and the constant A can be obtained by applying the appropriate boundary condition.

2. The conventional rigid wall boundary condition

To solve Eq. (2), it is necessary to determine the boundary condition. Due to the effect of viscosity, the air particles at the hole wall boundary adhere to the hole wall and their velocities are equal to the vibration velocity of the material.

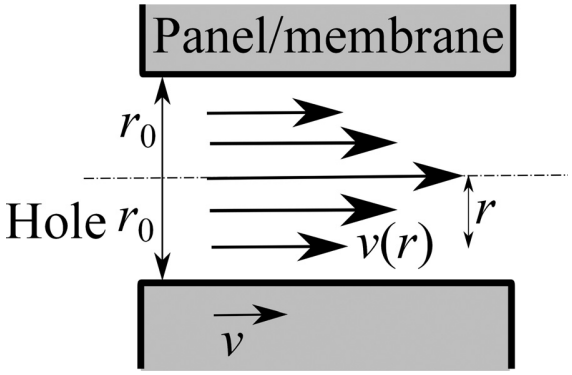

FIG. 1. Particle velocity $v(r)$ in a hole of radius r_0 of the MPM or panel as a function of the distance, r, from the perforation axis in the local coordinate of each perforation.

Maa (1975, 1997) assumed that the panel vibration due to the incident sound pressure is negligible and the panel can therefore be considered to be rigid, i.e.,

$$v(r = r_0) = 0. \tag{3}$$

Based on Maa's assumption, the particle velocity as a function of radius is obtained as

$$v(r) = \frac{-\Delta p}{h\,\mu\,K_{\text{air}}^2}\left[1 - \frac{J_0(K_{\text{air}}r)}{J_0(K_{\text{air}}r_0)}\right], \tag{4}$$

and the average velocity over the hole area is expressed as

$$\bar{v} = \frac{\int_0^{r_0} v(r)\,2\pi r dr}{\pi r_0^2} = \frac{\Delta p}{j\omega\rho_0 h}\left[1 - \frac{2}{K_{\text{air}}r_0}\frac{J_1(K_{\text{air}}r_0)}{J_0(K_{\text{air}}r_0)}\right], \tag{5}$$

where J_1 is the Bessel function of the first kind and first order. The normalized acoustic impedance is therefore given by

$$z = \frac{\Delta p}{\bar{v}\rho_0 c_0\,\delta} = \frac{j\omega\rho_0 h}{\rho_0 c_0\,\delta}\left[1 - \frac{2}{K_{\text{air}}r_0}\frac{J_1(K_{\text{air}}r_0)}{J_0(K_{\text{air}}r_0)}\right]^{-1}, \tag{6}$$

where c_0 is the sound speed in air and δ is the perforation ratio of the panel. When an end correction for the hole is considered, Eq. (6) is rewritten as (Maa, 1997)

$$z_{\text{Maa}} = \frac{0.147}{d^2}\frac{h}{\delta}\left(\sqrt{1 + \frac{x^2}{32}} + \frac{\sqrt{2}}{8}\frac{x\,d}{h}\right) + 0.294\times 10^{-3}\frac{j\omega h}{\delta}\left(1 + \frac{1}{\sqrt{9 + \frac{x^2}{2}}} + 0.85\frac{d}{h}\right), \tag{7}$$

where d is the diameter of the holes and equal to $2r_0$, and x is called the perforation constant and is expressed as $d\sqrt{f/10}$.

Equation (7) is widely used to calculate the acoustic impedance of MPPs and is reported to show accurate agreement with experimental results. It should be noted that Eq. (7) is based on the assumption that the panel vibration velocity is equal to zero, and is valid only when the panel vibration is negligible and the panel can be assumed rigid.

3. The proposed boundary condition

For lightweight MPMs, to be considered henceforth, the vibration of the membrane is significant and needs to be considered. Therefore, the proposed boundary condition between the membrane motion and the air in the hole can be expressed as

$$v(r = r_0) = v_{\text{membrane}}, \tag{8}$$

where v_{membrane} denotes the vibration velocity of the membrane. Substituting Eq. (8) into Eq. (2) gives

$$A = \frac{v_{\text{membrane}} + \dfrac{\Delta p}{\mu h K_{\text{air}}^2}}{J_0(K_{\text{air}}r_0)}. \tag{9}$$

Substituting Eq. (9) into Eq. (2), the particle velocity is obtained as

$$v(r) = v_{\text{membrane}}\frac{J_0(K_{\text{air}}r)}{J_0(K_{\text{air}}r_0)} - \frac{\Delta p}{h\,\mu\,K_{\text{air}}^2}\left[1 - \frac{J_0(K_{\text{air}}r)}{J_0(K_{\text{air}}r_0)}\right]. \tag{10}$$

Integrating over the area of the hole yields the average particle velocity

$$\bar{v} = \frac{\int_0^{r_0} v(r)\,2\pi r dr}{\pi r_0^2} = v_{\text{membrane}}\frac{2}{K_{\text{air}}r_0}\frac{J_1(K_{\text{air}}r_0)}{J_0(K_{\text{air}}r_0)} + \frac{\Delta p}{j\omega\rho_0 h}\left[1 - \frac{2}{K_{\text{air}}r_0}\frac{J_1(K_{\text{air}}r_0)}{J_0(K_{\text{air}}r_0)}\right]. \tag{11}$$

Therefore, the normalized acoustic impedance of a single hole is expressed as

$$z_{\text{hole}} = \frac{\Delta p}{\bar{v}\rho_0 c_0} = \frac{1}{\rho_0 c_0\dfrac{v_{\text{membrane}}}{\Delta p}\dfrac{2}{K_{\text{air}}r_0}\dfrac{J_1(K_{\text{air}}r_0)}{J_0(K_{\text{air}}r_0)} + \dfrac{\rho_0 c_0}{j\omega\rho_0 h}\left[1 - \dfrac{2}{K_{\text{air}}r_0}\dfrac{J_1(K_{\text{air}}r_0)}{J_0(K_{\text{air}}r_0)}\right]}. \tag{12}$$

Comparing Eq. (12) with Eq. (6), it could be observed that the factor $(1/j\omega\rho_0 h)[1 - (2/K_{\text{air}}r_0)[J_1(K_{\text{air}}r_0)/J_0(K_{\text{air}}r_0)]]$ in Eq. (12) is similar to Eq. (5). This similarity implies that this factor represents the average particle velocity of a hole under Maa's rigid wall assumption. Therefore, Eq. (12) can be rewritten as

$$z_{\text{hole}} = \frac{1}{\rho_0 c_0\dfrac{v_{\text{membrane}}}{\Delta p}\dfrac{2}{K_{\text{air}}r_0}\dfrac{J_1(K_{\text{air}}r_0)}{J_0(K_{\text{air}}r_0)} + \dfrac{1}{z_{\text{Maa}}\,\delta}} = \frac{1}{\dfrac{2}{K_{\text{air}}r_0}\dfrac{J_1(K_{\text{air}}r_0)}{J_0(K_{\text{air}}r_0)}\dfrac{1}{z_{\text{membrane}}} + \dfrac{1}{z_{\text{Maa}}\,\delta}}, \tag{13}$$

where $z_{membrane}$ denotes the normalized acoustic impedance of the membrane, which can be obtained from the motion equation of membrane vibration, and $z_{Maa}\,\delta$ denotes the acoustic impedance of a single hole under Maa's rigid wall assumption. If Eq. (7) is used to calculate this impedance, the end correction for the hole is included.

Equation (13) implies that the acoustic impedance of an MPM hole is a function of the acoustic impedance of the hole under the rigid wall assumption and the acoustic impedance of the membrane vibration in the vicinity of the hole. If it is a limp membrane, the membrane vibration velocity is a constant over the membrane surface when excited by a plane wave and the overall normal acoustic impedance of the MPM is obtained by combining the constant impedance due to the membrane vibration and the impedance due to the perforations. However, in acoustic engineering projects, membrane materials are commonly fixed on a rigid frame. Hence, the finite boundary condition of the fixed edge and the tension due to the stretching of the membrane affect the acoustic impedance of the membrane. This acoustic impedance of the finite sized membrane under tension will be a function of the position, as shown in Fig. 2. Therefore, the acoustic impedance obtained from Eq. (13) also varies depending on the position coordinates.

B. Motion equation and impedance of membranes considering the viscosity effects on the hole walls

In Eq. (13), the vibration velocity of the membrane $v_{membrane}$ is unknown. It is assumed in this paper that the hole diameter and the perforation ratio are sufficiently small such that the mechanical properties of the membrane (that is, the effective surface density and stiffness) are unaffected by the presence of the perforations (Burgemeister and Hansen, 1996). When a circular membrane is fixed on a circular rim with a radius of R_0 and driven by a sound pressure Δp, its motion equation in a polar coordinate system is given by (Kinsler *et al.*, 1999)

$$T\nabla^2\xi(R)+\omega^2\rho_p\,\xi(R)=-\Delta p, \tag{14}$$

where T is the tension per unit length applied on the membrane surface, $\xi(R)$ is the membrane displacement, R denotes the radial position coordinate on the membrane surface, which has a maximum value at the radius of the membrane R_0, ρ_p is the surface density of the membrane, and $\Delta p = p_1 - p_2$.

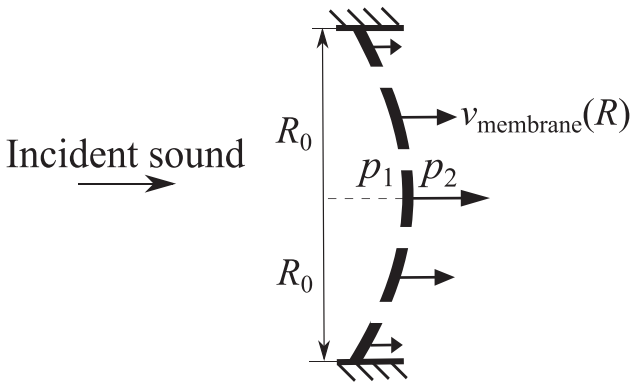

FIG. 2. Distribution of the membrane vibration velocity (vibrating in the fundamental mode).

As in the case of a string (Walstijn, 2009), the internal damping plays an important part in the vibration of a membrane. Extending the expression of the internal damping of a string in the work of Walstijn (2009) to that of a membrane, Eq. (14) may be rewritten as

$$T\nabla^2\xi(R)+2j\omega\eta\,\nabla^2\xi(R)+\omega^2\rho_p\,\xi(R)=-\Delta p, \tag{15}$$

where η is the internal damping ratio of the membrane. Note that the damping is related to the curvature of the tensioned, circular membrane in this work, which differs from the conventional expression of complex tension $T\times(1+j\eta)$ as seen in the work of Song and Bolton (2003) and the book of Kinsler *et al.* (1999).

The general solution of Eq. (15) is given by

$$\xi(R)=B\,J_0(K_{mem}R)-\frac{\Delta p}{\omega^2\rho_p}, \tag{16}$$

where $K_{mem}^2=\omega^2\rho_p/(T+2j\omega\eta)$ and the constant B depends on the boundary condition of the membrane vibration $\xi(R=R_0)=0$. Applying this boundary condition yields

$$B=\frac{\Delta p}{\omega^2\rho_p}\frac{1}{J_0(K_{mem}R_0)} \tag{17}$$

and

$$\xi(R)=\frac{\Delta p}{\omega^2\rho_p}\left[\frac{J_0(K_{mem}R)}{J_0(K_{mem}R_0)}-1\right]. \tag{18}$$

Hence, the velocity varying with the radial coordinate is given by

$$v_{membrane}(R)=j\omega\xi(R)=j\omega\frac{\Delta p}{\omega^2\rho_p}\left[\frac{J_0(K_{mem}R)}{J_0(K_{mem}R_0)}-1\right], \tag{19}$$

and the corresponding normalized acoustic impedance is expressed as

$$z_{membrane}(R)=\frac{\Delta p}{\rho_0 c_0 v_{membrane}(R)}=\frac{\omega^2\rho_p}{\rho_0 c_0 j\omega}\left[\frac{J_0(K_{mem}R)}{J_0(K_{mem}R_0)}-1\right]^{-1}. \tag{20}$$

Integrating over the surface of the membrane and dividing by the membrane area, πR_0^2, yields the space average vibration velocity and the space average normalized acoustic impedance

$$\bar{v}_{membrane}=j\omega\frac{\Delta p}{\omega^2\rho_p}\left[\frac{2}{K_{mem}R_0}\frac{J_1(K_{mem}R_0)}{J_0(K_{mem}R_0)}-1\right] \tag{21}$$

and

$$\bar{z}_{\text{membrane}} = \frac{\omega \rho_p}{j \rho_0 c_0}\left[\frac{2}{K_{\text{mem}} R_0}\frac{J_1(K_{\text{mem}} R_0)}{J_0(K_{\text{mem}} R_0)} - 1\right]^{-1}. \quad (22)$$

C. Acoustic impedance of each perforation of a circular MPM

The acoustic impedance of a hole in a circular MPM as a function of its radius is expressed by Eq. (13). Substituting Eq. (20) into Eq. (13) gives the acoustic impedance of a hole as

$$z_{\text{hole}}(R) = \frac{1}{\frac{2}{K_{\text{air}} r_0}\frac{J_1(K_{\text{air}} r_0)}{J_0(K_{\text{air}} r_0)}\frac{\rho_0 c_0 j}{\omega \rho_p}\left[\frac{J_0(K_{\text{mem}} R)}{J_0(K_{\text{mem}} R_0)} - 1\right] + \frac{1}{z_{\text{Maa}}\delta}}, \quad (23)$$

where Eq. (23) is a function of the radial coordinate R, which is related to the membrane geometry (not the radial coordinate r of the air particle in the hole). The effect of the hole position on the hole impedance can be predicted using Eq. (23), although it is non-linear and is therefore difficult to investigate analytically. Therefore, an example is utilised here, where a circular MPM with surface density $\rho_p = 0.25\,\text{kg/m}^2$, is stretched under a tension $T = 125\,\text{N/m}$ and its internal damping ratio is $\eta = 0.02$. It is fixed on a rigid ring with a radius of $R_0 = 50\,\text{mm}$. The perforation parameters are: hole radius $r_0 = 0.0292\,\text{mm}$; membrane thickness $h = 0.17\,\text{mm}$; backing cavity depth $D = 25\,\text{mm}$; perforation ratio $\delta = 0.15\%$. The resistances and reactances of five holes at different radii calculated using Eq. (23), normalized by $\rho_0 c_0$, are shown in Figs. 3(a) and 3(b). The radial coordinate R of these holes varies from $R = 10$ to $R = 50\,\text{mm}$ and has been chosen to show the variability of the perforation impedance. The normalized resistances and reactances of a hole calculated by Maa's classic model [Eq. (7)] are also shown in these figures. Note that when $R = 50\,\text{mm}$, $J_0(K_{\text{mem}}R_0)/J_0(K_{\text{mem}}R_0) = 1$ and the prediction of Eq. (23) is consistent with that of Eq. (7) and thus Maa's theory.

It can be concluded from Figs. 3(a) and 3(b) that the acoustic impedance of a hole near the centre of the membrane is more significantly affected by the membrane motion than that of a hole near the edge of the membrane. This is because the membrane elements near the centre vibrate more significantly than those near the membrane edge.

In addition, the effects of the membrane vibration on the perforation impedance occur mainly in the low frequency range where the tension and the internal damping affect the membrane impedance significantly. In contrast, the surface density governs the membrane impedance in the high frequency range (mass controlled) and no significant effect of the membrane vibration on the perforation impedance is observed for a constant surface density.

D. Combined acoustic impedance of the MPM system

In Sec. II, the acoustic impedance of each hole as a function of location was investigated. Neglecting the interaction between the holes, the overall acoustic impedance due to the perforations is expressed as a sum over all holes,

$$z_{\text{perforation}} = \frac{1}{\sum_{n=1}^{N}\frac{\frac{r_0^2\pi}{R_0^2\pi}}{z_{\text{hole}}(R_n)}}, \quad (24)$$

where n denotes the nth hole on the membrane surface, R_n denotes the radial coordinate of the nth hole, and N is the total number of holes. If z_{hole} is uniform, as it is in Maa's model, Eq. (24) can be rewritten as

$$z_{\text{perforation}} = \frac{1}{N\frac{\frac{r_0^2\pi}{R_0^2\pi}}{z_{\text{hole}}}} = \frac{z_{\text{hole}}}{\delta}, \quad (25)$$

which is consistent with Eq. (7).

The same example used in Sec. II C is investigated in this section to demonstrate the effect of the membrane vibration on the overall impedance of the MPM. The overall acoustic impedance predicted by the presented model is compared to that predicted by Maa's model. The normalized resistances and reactances predicted by the rigid-walled model and the finite circular membrane of radius $R_0 = 50$ mm are shown in Figs. 4(a) and 4(b). The resistance predicted by Eq. (24) is lower than that predicted by Maa's rigid-wall model, while the reactance of this flexible wall model is higher than that of the rigid wall model above the fundamental resonance frequency. The most significant difference in the resistance and reactance is observed in the low frequency range near 200 Hz. It could be concluded that the

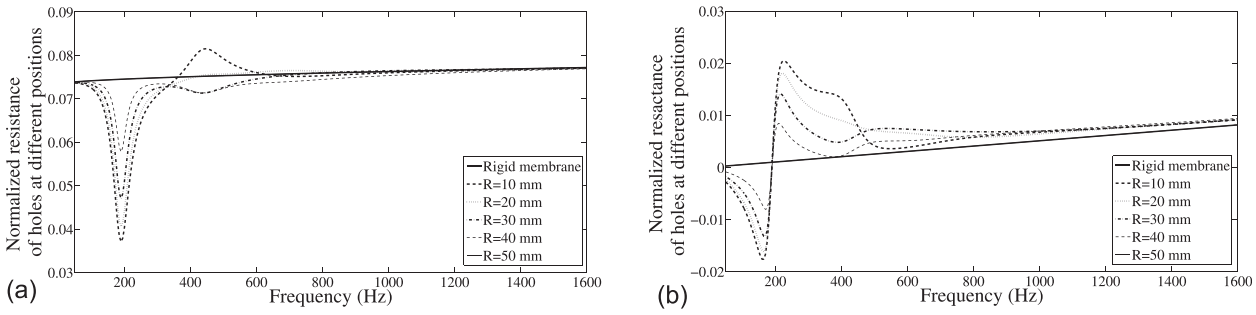

FIG. 3. Normalized resistance and reactance of a hole for five radial coordinates varying from $R = 10$ to $R = 50\,\text{mm}$.

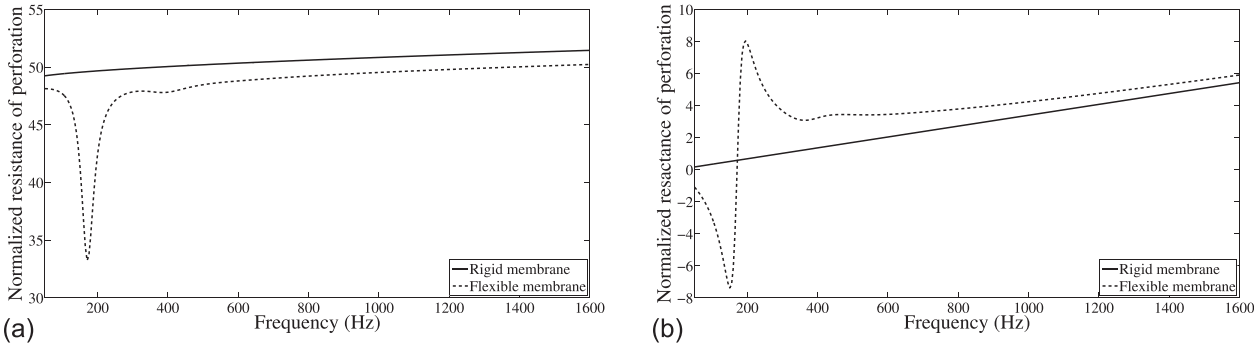

FIG. 4. Normalized resistance and reactance due to all of the holes on the MPM surface.

flexible wall assumption leads to a significant change in the acoustic impedance caused by the perforation, especially in the low frequency range.

Note that Eq. (24) considers only the acoustic impedance due to the perforations. To investigate the overall impedance of the MPM system, it is also necessary to consider the acoustic impedance of the membrane vibration. If the impedance of the perforation and that of the membrane vibration are known, then the overall impedance may be calculated using the electric-acoustic analogy, giving

$$z_{\text{overall}} = \frac{1}{\frac{1}{z_{\text{perforation}}} + \frac{1}{z_{\text{vibration}}}}, \tag{26}$$

where $z_{\text{perforation}}$ denotes the impedance due to the perforations obtained by Eq. (24) and $z_{\text{vibration}}$ denotes the membrane vibration impedance given by Eq. (22). Once the overall impedance of the MPM system is obtained, the impedance of the MPM backed by an air cavity and a rigid wall is expressed as

$$z = z_{\text{overall}} - j\cot\left(\frac{\omega D}{c_0}\right), \tag{27}$$

where D is the depth of the air cavity. Therefore, the sound absorption coefficient of an MPM with a backing cavity is given by

$$\alpha = \frac{4\,\text{Re}(z)}{(1+\text{Re}(z))^2 + \text{Im}(z)^2}, \tag{28}$$

where $\text{Re}(z)$ and $\text{Im}(z)$ are the real and imaginary parts of z, respectively.

III. EXPERIMENTAL VALIDATION

Sections III A–III C explore the experimental validation of the model derived in Sec. II. The experimental results are compared with the predicted results and the limitations of the assumptions used in the proposed model are also discussed.

A. Experimental parameters

To validate the model developed in this paper, sound absorption experiments were carried out in an impedance tube and at frequencies below the cutoff frequency to ensure plane wave incidence. The radius of the impedance tube was $R_0 = 50$ mm. The sound absorption coefficients of four commercially available MPMs were measured using the two-microphone transfer function method (Chung and Blaser, 1980). The four MPMs were tested for two cavity depths D of 25 and 50 mm.

To predict the sound absorption of MPMs, it is crucial to measure the structural parameters of the MPMs, including the radius of the perforations r_0. The perforations of MPMs 1 to 3 were punched and the perforations were irregular polygons, unlike the circular perforations of MPM 4. The photomicrographs of the perforations of MPM 1 and MPM 4 are shown in Fig. 5 as examples. Because of the irregular geometry of the holes in MPMs 1 to 3, the equivalent hole radius r_0 needs to be estimated. The minimum, maximum, and average hole radius of MPMs 1 to 3 are shown in Table I for

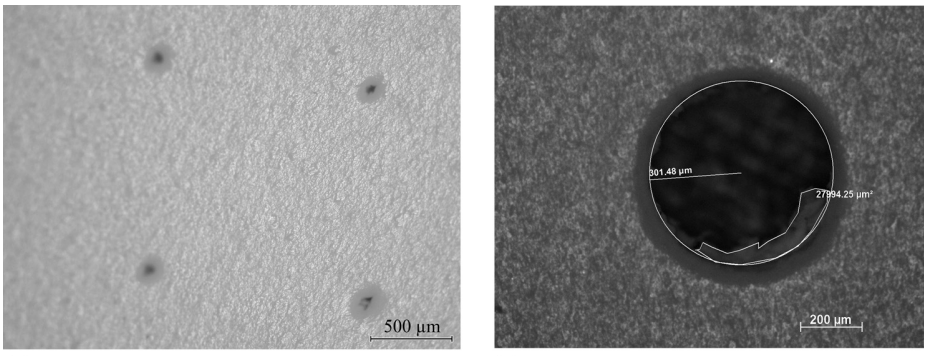

FIG. 5. Photomicrographs of perforations of MPM 1 and MPM 4.

TABLE I. Measured hole radius of MPMs. The equivalent hole radius was determined from data fitting.

MPM	Minimum hole radius $r_{0\min}$ (mm)	Maximum hole radius $r_{0\max}$ (mm)	Average hole radius $\overline{r_0}$ (mm) of ten holes	Equivalent hole radius r_0 (mm)
1	0.016	0.030	0.026 (std = 0.004)	0.0226
2	0.011	0.040	0.022 (std = 0.008)	0.0211
3	0.009	0.042	0.029 (std = 0.010)	0.0248

10 randomly selected holes. The factor std is the standard deviation of the measured hole radius of each MPM.

Note that the perforations of MPM 4 were quite circular; however, in some cases the membrane material covered part of the hole area, as shown in Fig. 5(b). These areas need to be excluded during the calculation of the equivalent radius of MPM 4. Therefore, 20 holes on MPM 4 were randomly chosen and the equivalent radius measured from each photomicrograph was used to obtain an average equivalent radius for input to the analytical model.

The physical parameters of the MPMs were measured and are shown in Table II. The experimental results are compared to the predictions of the model presented in Sec. III B. It was not possible to directly measure the tension T and the damping ratio η by experiments. Hence, the equivalent value set T, η, and r_0 used in the analytical model have been obtained from the experimental measurements by fitting the measured data to the model using the optimization toolbox in MATLAB under a number of constraints (Waltz *et al.*, 2006): positive tension; damping ratio less than 0.05; and hole radius varying from the minimum measured value $r_{0\min}$ to the maximum measured value $r_{0\max}$ (listed in Table I). The constrained non-linear optimization was based on the subspace trust region method. The obtained values for T, η, and r_0 are shown in Figs. 6 and 7.

B. Experimental results and discussions

The experimental results of the four MPMs with an air cavity depth of $D = 25$ mm are shown in Fig. 6 and those for $D = 50$ mm are shown in Fig. 7. These experimental results are compared to the prediction results of three models: Maa's classic rigid wall model [Eq. (7)]; the model of a membrane absorber without perforation [Eq. (22)], and the presented model [Eq. (26)]. In Figs. 6 and 7, the dashed-dotted curves are the prediction results of Maa's model, which neglects the membrane vibration effect; the prediction results for an unperforated membrane are shown as dotted curves; and the predictions obtained from the new model are shown as dashed curves. Furthermore, to verify the novelty of the proposed method, the proposed predictions of the four MPMs were compared with the method of Kang and Fuchs (1999) which is given by

$$z_{\text{Kang and Fuchs}} = \frac{1}{\frac{1}{z_{\text{Maa}}} + \frac{1}{1 + j\omega \frac{\rho_p}{\rho_0 c_0}}}. \tag{29}$$

TABLE II. Measured MPM parameters.

MPM	Surface density ρ_p(kg/m^2)	Hole radius r_0 (mm)	Membrane thickness h (mm)	Equivalent distance between hole centres b (mm)	Perforation ratio δ (%)
1	0.2501	0.0226	0.17	1.32	0.092
2	0.2503	0.0211	0.17	1.58	0.056
3	0.2448	0.0248	0.17	1.63	0.073
4	0.2506	0.255 (std = 0.031)	0.17	5.29	0.730

The sound absorption coefficients of MPMs 1 to 3 predicted using Maa's model are low compared to the experimental results because the hole diameters are smaller than the range of applicability of Maa's model (roughly around 1 mm), which consequently leads to high calculated normalized acoustic impedances. High normalized acoustic impedance is usually considered as the main reason for the effective sound absorption of micro perforated materials. However, Maa (2006) illustrated that when the normalized resistance of an MPP increases from one to five, its sound absorption coefficient decreases proportionally. Therefore, high resistances and low sound absorptions of MPMs are observed here using Maa's model due to the small perforations considered for MPMs 1 to 3.

To assess the accuracy of the three models for prediction, the coefficient of determination $R^2_{\text{determination}}$ for each model is shown in Figs. 6 and 7, and is given by

$$R^2_{\text{determination}} = 1 - \frac{\sum_{n_{\text{freq}}=1}^{N_{\text{freq}}} \left(\alpha_{\text{experiment}} - \alpha_{\text{prediction}}\right)^2}{\sum_{n_{\text{freq}}=1}^{N_{\text{freq}}} \left(\alpha_{\text{experiment}} - \overline{\alpha_{\text{experiment}}}\right)^2}, \tag{30}$$

where n_{freq} denotes the index of the measured frequency, N_{freq} denotes the total number of measured frequencies, $\alpha_{\text{prediction}}$ denotes the predicted sound absorption coefficient, and $\alpha_{\text{experiment}}$ denotes the measured sound absorption coefficient. As $R^2_{\text{determination}}$ approaches unity, the fidelity of the model increases.

For MPMs 1 to 4, the $R^2_{\text{determination}}$ of the presented model is close to unity. Hence, the presented model provides a good agreement with the experimental results and is suitable for the prediction of the sound absorption of these MPMs. These results confirm that the new boundary condition theory and the derived equations are valid for these MPM samples. The negative $R^2_{\text{determination}}$ is because the error between the measured data and the predicted result is larger than the difference between the measured data and its mean. The negative $R^2_{\text{determination}}$ indicates the inaccuracy of the corresponding model.

It is noticed that there are small dips and peaks from 1200 to 1260 Hz in Figs. 6 and 7. They occur in the experimental results of every MPM. These are because of a structural resonance of the impedance tube itself.

When calculating the acoustic impedance due to the perforations of MPM 4, it was found that Eq. (7) underestimated

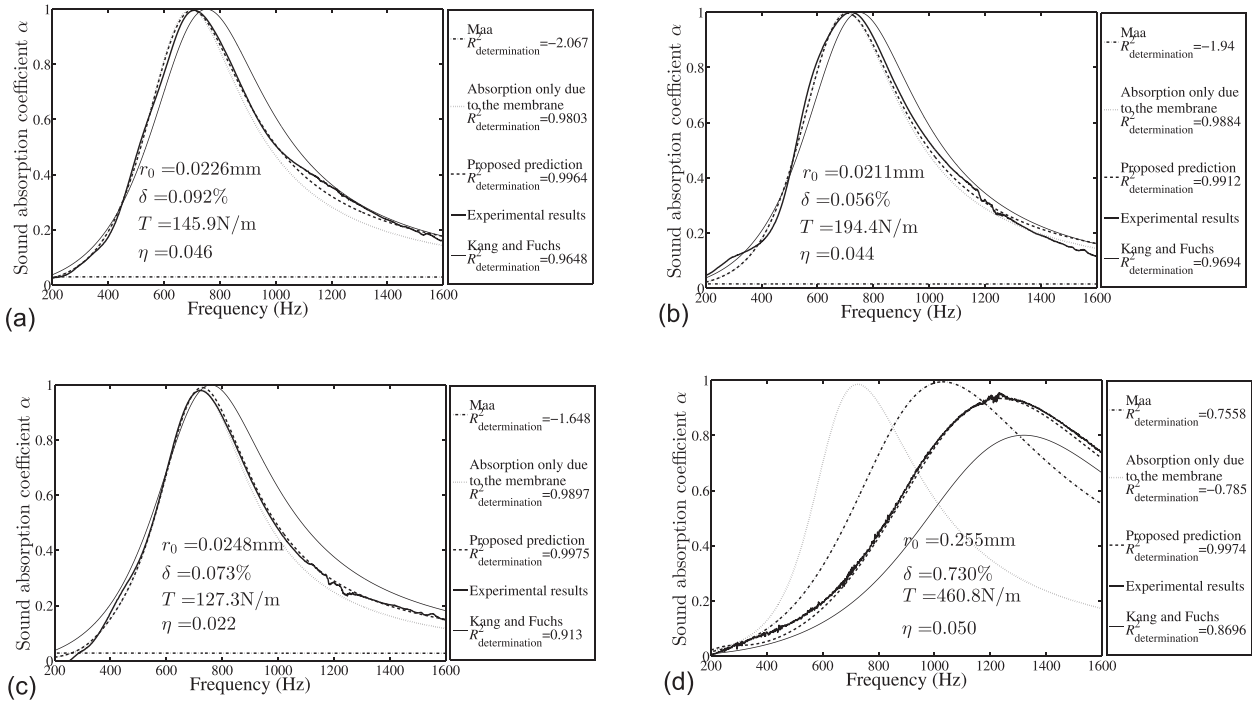

FIG. 6. Normal incidence sound absorption coefficients of MPMs 1 to 4 for $D = 25$ mm.

the impedance due to the thermo-viscous friction. This has also been observed by Tayong *et al.* (2010), who used

$$R_s = \frac{1}{2}\sqrt{2\,\omega\,\rho_0\,\xi}, \tag{31}$$

to estimate the resistance due to the thermo-viscous friction, where ξ is the dynamic viscosity. They added $4(R_s/\rho_0\,c_0\,\delta)$ to the normalized impedance due to the perforations. The value of Eq. (31) is purely real and represents the resistance due to the thermo-viscous friction only. However, in Rayleigh's (1896) original derivation, R_s was expressed as a complex value

$$R_s = \frac{1}{2}\sqrt{2\,\omega\,\rho_0\,\xi}(1+j). \tag{32}$$

Therefore, in the presented model for MPM 4, Eq. (32) was used and $4(R_s/\rho_0\,c_0\,\delta)$ was added to Eq. (7). The

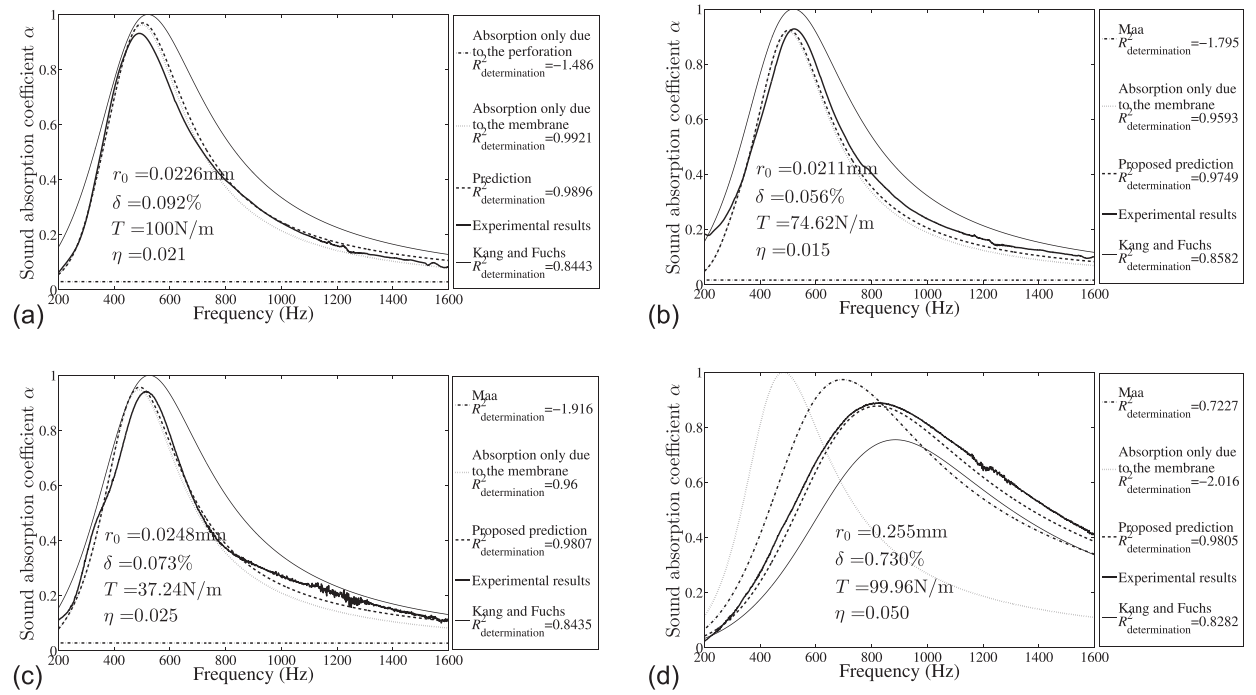

FIG. 7. Normal incidence sound absorption coefficients of MPMs 1 to 4 for $D = 50$ mm.

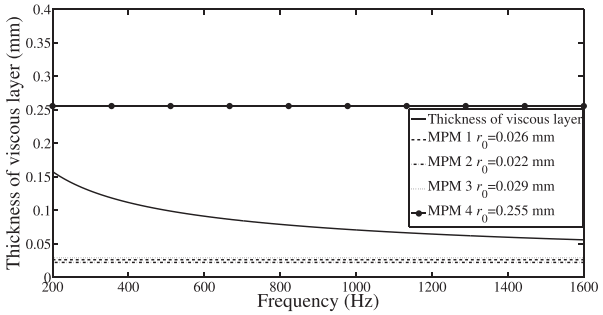

FIG. 8. Thickness of viscous layer $h_{\text{viscosity}}$ in the perforations compared with the hole radii of MPMs 1 to 4.

prediction results agree with the measured results, as shown in Figs. 6(d) and 7(d).

Note that the additional impedance due to the thermo-viscous friction is only of significance for the acoustic impedance of MPM 4. This can be ascribed to the significant difference between the hole radii of MPMs 1 to 3 and the hole radius of MPM 4. It is observed in Table II that the latter is 10 times larger than the former. The thickness of the viscous layer is defined by Maa (1975) as

$$h_{\text{viscosity}} = \sqrt{\frac{2 \times \mu}{\omega}}, \tag{33}$$

where for air $\mu = 1.56 \times 10^{-5} \text{m}^2/\text{s}$. As shown in Fig. 8, the hole radii of MPMs 1 to 3 are smaller than the thickness of the viscous layer such that the entire hole is covered by the viscous layer which limits the particle velocity in these holes. This results in high acoustic impedance of MPMs 1 to 3 and limited air flow through these holes. Hence, the thermo-viscous friction can be neglected. However, the hole radius of MPM 4 is larger than the thickness of the viscous layer and air can flow through the holes in MPM 4 more easily. The air flow through the holes forms a rotational jet and increases the impedance of the perforations. The flexibility of the membrane material can also contribute to the impedance of the thermo-viscous friction. Therefore, the additional impedance due to thermo-viscous friction was added to MPM 4 only and was neglected for the other three MPMs.

Comparing the experimental results of the MPMs, we could also conclude that the main absorption peaks of MPMs 1 to 3 are near the main absorption peaks of the membranes without perforation. As for MPM 4, the main absorption peak moves to the high frequency range and is near the main absorption peak for the predicted result of the rigid membrane model. This may imply that when the perforation is small as is the case for MPMs 1 to 3, the MPM absorption is mainly due to the membrane itself. In these cases, the perforations marginally broaden the sound absorption bandwidth but do not move the absorption peaks significantly. When MPM 4 is considered, the perforations are the main contributor to the sound absorption and the main absorption peak of the MPM is near the theoretical absorption peak due to the perforations.

In Figs. 6 and 7, the thin solid curves represent the predicted results based on the method of Kang and Fuchs (1999). Their method is a simplified one which assumes that the acoustic impedance due to the membrane vibration is only dependent on the surface density of the membrane. The finite effect of the membrane vibration on the acoustic impedance is simplified by using a constant 1 in the term of $1 + j\omega(\rho_p/\rho_0 c_0)$, as seen in Eq. (29). Consequently, this model is less accurate than the proposed model which considers the response of a finite circular impervious membrane by solving its motion equation and optimizing the corresponding tension and damping. The mismatch of the experimental results and the predicted results using Kang and Fuchs's model validates this conclusion on the relative accuracy of the two models. Therefore, the proposed model is considered more accurate than the conventional Kang and Fuchs's model.

The structural parameters of MPMs 1 to 4 are all in a similar range of values, except that MPM 4 has a hole diameter an order of magnitude larger than the other three MPMs. The hole diameter and perforation ratio of MPM 4 are close to the structural parameters of a classic MPP, which is typically around $r_0 = 1\,\text{mm}$ and $\delta = 1\%$. The impedance of the holes in MPM 4 is efficiently combined with the acoustic impedance due to the membrane vibration to offer effective sound absorption. On the contrary, the perforations in MPMs 1 to 3 are too small, and the acoustic impedance due to the perforations is thus too high to effectively contribute to the sound absorption. Extremely high acoustic impedance leads to a poor sound absorption from MPP/MPM absorbers (Maa, 2006).

Therefore, it is concluded that although the sound absorption bandwidths of MPMs 1 to 3 have been marginally broadened, the sound absorption properties of these MPMs are mainly governed by the membrane itself. Considering the expense of manufacturing the perforations, incorporating perforations of this size in commercial sound absorbing materials is likely to be ineffective. However, the sound absorption values obtained for MPM 4 indicate the effectiveness of such MPMs incorporating holes of suitable size. To achieve their optimum sound absorption, MPMs need to be carefully designed to effectively couple the membrane vibration impedance and the impedance due to the perforations. The presented theory is proposed as a tool to design such MPMs.

C. Effect of perforation positions on the sound absorption of MPMs

Based on the theory presented in Sec. II, it is logical to assume that since the membrane vibration affects the acoustic impedance of the perforations, the overall impedance and sound absorption properties of an MPM could be affected by the perforation positions since the vibration is not uniform over the membrane. By contrast, this presumption is different from the conventional theories which assume that the overall impedance of a flexible micro perforate (thin plate or membrane) is given by the coupled impedances of the material vibration and the perforations based on electric-acoustic analogy or average flow velocity. Hence, in the conventional theories, the overall impedance is independent of the position of the perforations.

To validate this assumption, four additional MPMs were made using the same material as MPM 1. In Sec. III B, it was shown that MPM 1 can essentially be considered unperforated due to its low perforation ratio and small hole diameter.

The four additional MPMs may be categorized into two groups. In Group 1, each MPM was drilled with 73 holes, which hole radius $r_0 = 0.31$ mm. The holes were arranged at $R = 45$ mm for one of the manufactured MPMs and were evenly distributed over the membrane surface for the other. Therefore, in Group 1, the perforation ratios of two manufactured MPMs are identical and equal to 0.29%. Similarly, for Group 2, each MPM was drilled with 48 holes. The hole radius r_0 is also 0.31 mm. Therefore, the perforation ratio for each manufactured MPM in Group 2 is 0.19%. The holes were at $R = 45$ mm for one of the MPMs and were evenly distributed for the other. In each group, the parameters of the MPMs are identical. Based on the conventional theories, their sound absorption coefficients should be identical; however, based on the proposed theory, their sound absorption coefficients might differ due to the hole positions, i.e., the effect of the membrane vibration on the acoustic impedance of the perforations.

Figure 9 shows the photograph of the four additional MPMs. The different perforation positions are illustrated in Fig. 9. The sound absorption measurements were conducted under the same experimental set up as described in Sec. III B. The measured sound absorption coefficients and the predicted results based on the proposed method are compared for each group in Figs. 10 and 11.

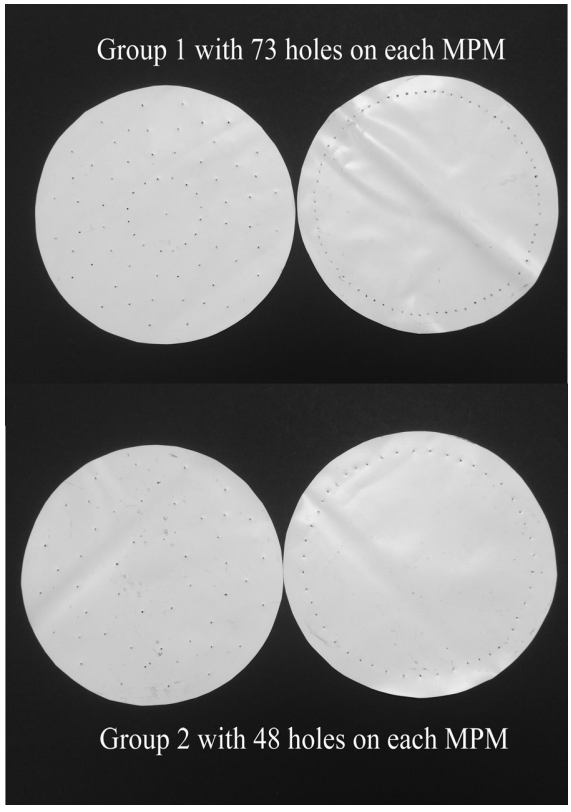

FIG. 9. Photograph of the additional MPMs made using the MPM 1 material. There are 73 and 48 (0.31 mm holes) drilled in each of the membranes, respectively.

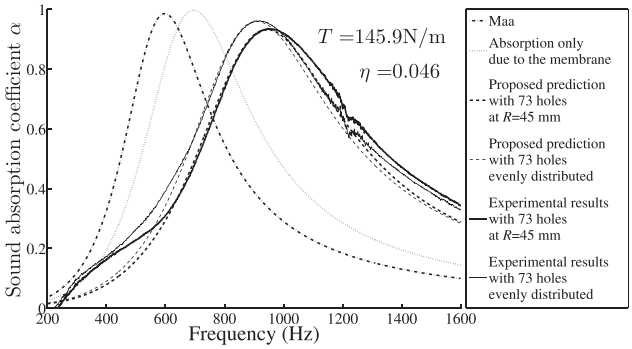

FIG. 10. Normal incidence sound absorption coefficients of the manufactured MPMs with 73 holes, $D = 25$ mm.

Note that the values of the tension and damping are identical to those in Fig. 6(a) because it is assumed that the perforations have no effect on the mechanical properties of the membrane. The thick solid curves in Figs. 10 and 11 are the measured sound absorption coefficient curves for the manufactured MPMs with holes at $R = 45$ mm and the thin solid curves are those for the manufactured MPMs with holes evenly distributed. There are obvious differences between these curves which demonstrates the effect of the hole positions on the acoustic impedance of the MPMs, and hence supports the proposed theory. Moreover, the predicted curves are close to the experimental results for the corresponding manufactured MPMs, which suggested that the proposed theory is accurate.

IV. SUMMARY

A new method for the prediction of the acoustic impedance and the sound absorption coefficient of a MPM is introduced in this paper. This method is based on a new boundary condition where the particle velocity at the hole wall boundary, which is assumed to be zero in Maa's theory, is assumed to be equal to the local membrane vibration velocity. By applying this new boundary condition to a circular membrane, it is shown that the acoustic impedance due to the perforation is affected by the membrane vibration and becomes a function of the membrane radial coordinates.

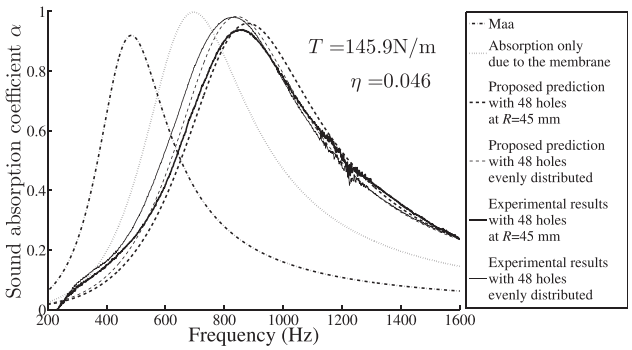

FIG. 11. Normal incidence sound absorption coefficients of the manufactured MPMs with 48 holes, $D = 25$ mm.

Using this new boundary condition, analytical models for the acoustic impedances of both the impedance associated with the perforations and the membrane vibration impedance are derived. The variability of the perforation impedance with hole location is investigated theoretically. The impedances due to the perforation and the membrane vibration are combined following the electric-acoustic analogy to present the overall impedance of the MPM. This new model is validated by experimental results for MPMs. Moreover, based on the proposed theory, it is validated experimentally that the hole position affects the acoustic impedance and sound absorption of MPMs, even if the MPM parameters, such as the hole radii, the thickness, and the perforation ratio, are identical.

This study extends the classic micro perforated theory and offers an accurate model for predicting the performance of flexible finite-sized MPMs. This study provides increased understanding of the coupling between the membrane vibration impedance and the impedance due to the perforations of MPMs.

ACKNOWLEDGMENTS

The authors wish to acknowledge the assistance of Dr. Erwin Gamboa for measuring the radii of the MPM samples. The authors are also very grateful to the staff of the electronic and mechanical workshops in the School of Mechanical Engineering at the University of Adelaide.

Bravo, T., Maury, C., and Pinhède, C. (**2012**). "Vibroacoustic properties of thin micro-perforated panel absorbers," J. Acoust. Soc. Am. **132**, 789–798.

Burgemeister, K., and Hansen, C. (**1996**). "Calculating resonance frequencies of perforated panels," J. Sound Vib. **196**, 387–399.

Chung, J., and Blaser, D. (**1980**). "Transfer function method of measuring in-duct acoustic properties. I. Theory," J. Acoust. Soc. Am. **68**, 907–913.

Herdtle, T., Bolton, J. S., Kim, N. N., Alexander, J. H., and Gerdes, R. W. (**2013**). "Transfer impedance of microperforated materials with tapered holes," J. Acoust. Soc. Am. **134**, 4752–4762.

Kang, J., and Fuchs, H. (**1999**). "Predicting the absorption of open weave textiles and micro-perforated membranes backed by an air space," J. Sound Vib. **220**, 905–920.

Kinsler, L. E., Frey, A. R., Coppens, A. B., and Sanders, J. V. (**1999**). *Fundamentals of Acoustics* (John Wiley & Sons, New York), pp. 82–92.

Lee, Y., Lee, E., and Ng, C. (**2005**). "Sound absorption of a finite flexible micro-perforated panel backed by an air cavity," J. Sound Vib. **287**, 227–243.

Liu, J., and Herrin, D. (**2010**). "Enhancing micro-perforated panel attenuation by partitioning the adjoining cavity," Appl. Acoust. **71**, 120–127.

Maa, D. Y. (**1975**). "Theory and design of microperforated panel sound absorbing constructions," Sci. Sin. **18**, 55–71.

Maa, D. Y. (**1997**). "General theory and design of microperforated-panel absorbers," Acta Acust. **22**, 385–393.

Maa, D. Y. (**1998**). "Potential of microperforated panel absorber," J. Acoust. Soc. Am. **104**, 2861–2866.

Maa, D. Y. (**2006**). "Practical absorption limits of MPP absorbers," Acta Acust. **31**, 481–484.

Park, S.-H. (**2013**). "Acoustic properties of micro-perforated panel absorbers backed by Helmholtz resonators for the improvement of low-frequency sound absorption," J. Sound Vib. **332**, 4895–4911.

Pfretzschner, J., Cobo, P., Simon, F., Cuesta, M., and Fernandez, A. (**2006**). "Microperforated insertion units: An alternative strategy to design micro-perforated panels," Appl. Acoust. **67**, 62–73.

Rayleigh, J. W. S. B. (**1896**). *The Theory of Sound* (Macmillan and Co., New York), pp. 317–319.

Ruiz, H., Cobo, P., and Jacobsen, F. (**2011**). "Optimization of multiple-layer micro perforated panels by simulated annealing," Appl. Acoust. **72**, 772–776.

Song, J., and Bolton, J. S. (**2003**). "Acoustical modeling of tensioned, permeable membranes," in *INTER-NOISE and NOISE-CON Congress and Conference Proceedings* (Institute of Noise Control Engineering, Washington, DC), pp. 965–970.

Takahashi, D., and Tanaka, M. (**2002**). "Flexural vibration of perforated plates and porous elastic materials under acoustic loading," J. Acoust. Soc. Am. **112**, 1456–1464.

Tayong, R., Dupont, T., and Leclaire, P. (**2010**). "On the variations of acoustic absorption peak with particle velocity in micro-perforated panels at high level of excitation," J. Acoust. Soc. Am. **127**, 2875–2882.

Toyoda, M., Mu, R. L., and Takahashi, D. (**2010**). "Relationship between Helmholtz-resonance absorption and panel-type absorption in finite flexible microperforated-panel absorbers," Appl. Acoust. **71**, 315–320.

Walstijn, M. (**2009**). "Vibrations of strings and membranes," http://www.somasa.qub.ac.uk/mvanwalstijn/pbss/lectures/session5.pdf (Last viewed January 5, 2015).

Waltz, R. A., Morales, J. L., Nocedal, J., and Orban., D. (**2006**). "An interior algorithm for nonlinear optimization that combines line search and trust region steps," Math. Program. **107**, 391–408.

Wang, C., Cheng, L., Pan, J., and Yu, G. (**2010**). "Sound absorption of a micro-perforated panel backed by an irregular-shaped cavity," J. Acoust. Soc. Am. **127**, 238–246.

Non-linear effects of sound absorption of micro-perforated membranes

Chenxi Li, Ben Cazzolato and Anthony Zander

School of Mechanical Engineering
The University of Adelaide
SA 5005
AUSTRALIA

Abstract

The non-linear sound absorption of micro-perforated membranes (MPMs) has been studied experimentally. The experimental findings presented in this paper indicate that even moderate incident sound pressure levels (SPLs) can have significant non-linear effects on the sound absorption coefficient. Unlike micro-perforated panels (MPPs) under high excitation, both the acoustic resistance and reactance of MPMs are affected by moderate incident SPLs. The non-linear sound absorption of MPMs is affected by the time-dependent flow arising from the acoustic sources. Several types of acoustic excitation are investigated and it is found that the sound absorption coefficient is strongly dependent on both the magnitude of the SPLs and the waveform of excitation.

Keywords: non-linear sound absorption, micro-perforated membrane, acoustic impedance, broadband source, monochromatic source

PACS: 43.55.Ev, 43.25.Ed

1. Introduction

Micro-perforated materials have been widely used for sound absorption, and have been investigated in both linear and non-linear regimes. Conventionally, micro-perforated panels (MPPs) are assumed to behave linearly under acoustic excitation [1, 2, 3] and the type of sound source is assumed to have no impact on the measured sound absorption coefficient. By contrast, when samples are

subjected to high sound pressure levels (SPLs) non-linear effects have been observed. Ingard and Ising indicated that the air flow travelling through an orifice under strong excitation forms a high velocity jet [4]. Maa derived an expression which represents the non-linear effect on the resistance of MPPs under high excitation [1]. Tayong *et al.* investigated the non-linear effects of sound sources at the peak absorption frequency of MPP absorbers both experimentally and theoretically when subjected to very high SPLs (145 dB re 20 μPa) [5].

However, some questions about the non-linear properties of micro-perforated materials remain unclear. The previous research indicates that the non-linear properties of MPPs are closely related to the SPL magnitude; for example Maa indicated that theoretically the non-linear behaviour exists when the incident SPL is 129 dB re 20 μPa and above [1], and Tayong *et al.* observed non-linear sound absorption of an MPP with an SPL of 145 dB re 20 μPa [5]. There is limited discussion on the threshold SPL at which the non-linear impedance starts to drive changes in the sound absorption coefficient. While the previous studies focussed on MPPs, research on the non-linear performance of micro-perforated membranes (MPMs) is very limited. Previous studies also indicated that the resistance is the dominating factor of the non-linearity of MPPs and the impact of the non-linear reactance is negligible [4, 6]. However, it is unclear whether these assumptions also apply to MPMs.

This paper presents the experimental findings on the non-linear effects of sound sources on the normal-incidence sound absorption of MPMs over a broadband frequency range. The frequency-dependent value of the incident sound pressure level at the MPM surface was varied from 15 dB re 20 μPa to 143 dB re 20 μPa. Significant non-linear behaviour in the MPMs is observed even at SPLs considered too low for non-linear behaviour. The details of the experiments are presented in Section 2 and the non-linear effects of sound sources are discussed in the subsequent sections.

2. Measurement of the sound absorption of MPMs under high SPL excitation

To investigate the non-linear sound absorption of MPMs under high excitation, sound absorption experiments were conducted with normally-incident plane-waves in a steel impedance tube. The internal radius of the impedance tube is $R_0 = 50$ mm with a cut-off frequency of 1.7 kHz [7]. The measurement frequency range was from 200 Hz to 1600 Hz. The two-microphone transfer function method [8] was used to obtain the sound absorption coefficient, as shown in Figure 1. The sound pressures were measured using two microphones, from which the SPL on the MPM surface and sound absorption coefficient were determined. The microphones used in this measurement were Brüel & Kjær, type 4958, 1/4 inch prepolarized microphones.

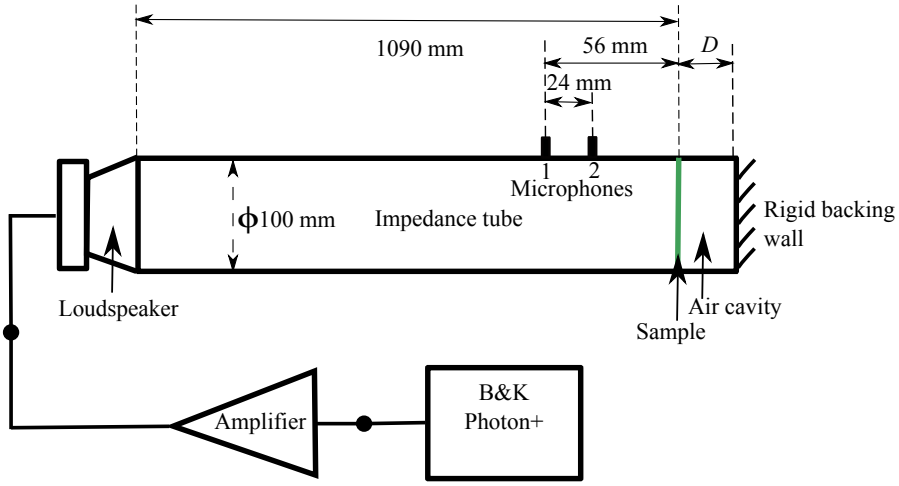

Figure 1: Schematic of the experimental layout for the measurement of sound absorption coefficient using the two-microphone transfer function method in an impedance tube.

The parameters of the tested MPM are shown in Table 1. In the sound absorption experiments, the MPM was combined with a 25 mm air cavity and a rigid backing wall. Since the effective sound absorption coefficient is sensitive to the mounting condition (in particular the tension) of the MPM sample, all tests were conducted continuously without disturbing the sample.

Table 1: Measured MPM parameters

Surface density ρ_{p} (kg/m^2)	Hole radius r_0 (mm)	Thickness h (mm)	Perforation ratio δ (%)
0.2506	0.2553	0.17	0.73

The source signal was generated by a Brüel & Kjær Photon Plus system and the SPLs in the impedance tube were adjusted by changing the output voltage of the signal generator in the Photon Plus. The output voltage varied from 0.1 mV to 200 mV (a range of over three orders of magnitude). The signal from the Photon Plus was amplified by a power amplifier to drive the loudspeaker.

Multiple types of source signals have been used for excitation, which can be categorised into two types: broadband and monochromatic signals. The broadband signals investigated here included white noise (Gaussian distribution), uniform random, pseudo random and burst random. Monochromatic signals investigated included a stepped sine sweep and a chirp with a linear sweep rate of 52 Hz/second. Sound absorption measurements were conducted with all of the mentioned source signals. Similar non-linear behaviour was observed for each group of source signals. Therefore, in this paper the white noise results represent broadband excitation and the stepped sine sweep results represent monochromatic excitation.

White noise is commonly used in sound absorption experiments as it drives all audible frequencies simultaneously in the desired frequency range; in this case from 200 Hz to 1600 Hz. Conversely, the stepped sine sweep is usually used to measure the frequency response when good noise immunity is required or the system response is non-linear. This source was configured to scan the desired frequencies from 200 Hz to 1600 Hz over a 10 minute time span. When using a stepped sine sweep, the sound energy is concentrated at a single frequency. Therefore, the SPL arising from a stepped sine sweep is higher than that of white noise at a specific frequency for a given voltage. The estimated SPLs at the MPM surface for two excitation types shown in Figures 2 and 3 demonstrate this.

To investigate the effect of the incident SPL on the sound absorption of the MPM, it is crucial to obtain the SPL on the MPM surface. However, the microphones were placed in the positions shown in Figure 1, neither of which were at the MPM surface. Based on the plane wave assumption and the distances between the microphones and the MPM sample given in Figure 1, the incident SPL on the MPM surface was estimated using the measured transfer function [8] and the total sound pressure measured with Microphone 1. Figures 2 and 3 illustrate the estimated SPL at the surface of the MPM sample excited by white noise and stepped sine sweep signals, respectively. The data was sampled at 4096 Hz, with a 2^{12} point FFT, giving a 1 Hz bin width.

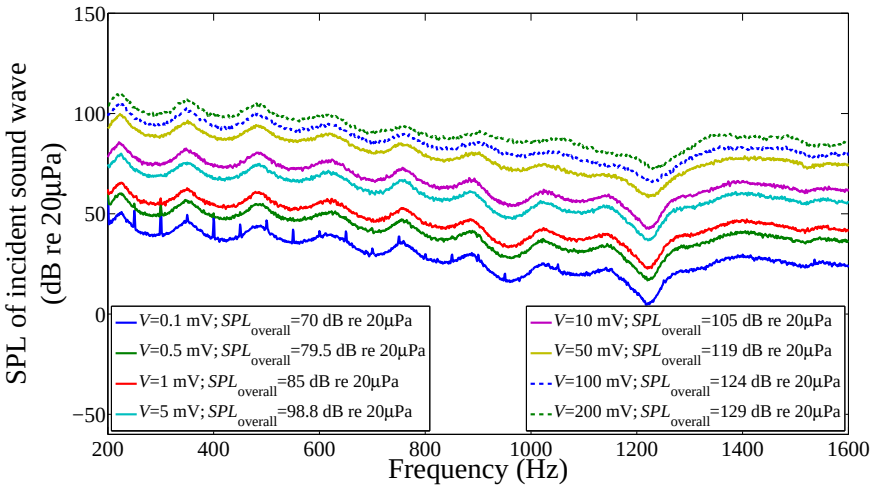

Figure 2: Estimated sound pressure level (SPL dB re 20 μPa) of the incident sound at the surface of the MPM with white noise excitation. The output voltage ranges from 0.1 mV to 200 mV and resulting overall SPLs are detailed in the legend.

The peaks and valleys in the SPL plots shown in Figures 2 and 3 are associated with axial resonances due to the finite length of the impedance tube. When the output voltage is as low as 0.1 mV, the measured spectra for both sound sources exhibit noise due to the poor coherence between the two microphones.

The curves in Figure 3 are smoother than those in Figure 2 illustrating the

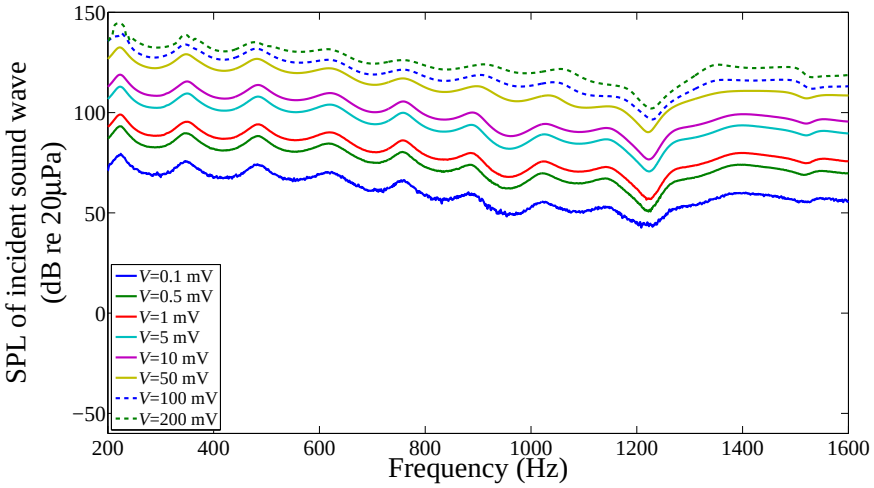

Figure 3: Estimated sound pressure level (SPL dB re 20 μPa) of the incident sound at the surface of the MPM with stepped sine sweep excitation. The output voltage ranges from 0.1 mV to 200 mV.

better noise immunity of the stepped sine sweep noise. Note that the valley around 1250 Hz represents a structural resonance of the impedance tube. The structural resonance of the impedance tube leads to additional energy dissipation on the tube surface, and hence causes a decrease in sound pressure level around the resonance frequency.

3. Sound absorption of MPMs excited by broadband noise

The sound absorption characteristics of the MPM were investigated for broadband excitation. This included white noise (Gaussian distribution), uniform random, pseudo random and burst random.

In this section, the sound absorption properties of the MPM excited by white noise of varying amplitudes are discussed. The results for all other broadband excitation were similar. Figure 4 illustrates that the sound absorption curves are consistent for the output voltages from 0.1 mV to 10 mV. Note that at 10 mV (SPL_{overall} = 105 dB re 20 μPa) a small change is observed which marks the

onset of the non-linear behaviour. Therefore, it is reasonable to deduce that when the output voltage is below 10 mV, the sound absorption of the MPM is in the linear regime. In this linear regime, the acoustic impedance of the MPM is only dependent on the perforation geometry and the MPM vibration, and is independent of the characteristics of the excitation type. Comparing Figure 4 to Figure 2, it is found that the corresponding SPLs in this linear regime are relatively low with no individual frequency exceeding 86 dB re 20 μPa and the overall SPL does not exceed 105 dB re 20 μPa, which supports the conclusion by Maa [9] that the non-linear effects occur with high excitation and that the sound absorption is constant for low excitation. For the lowest amplitude excitation investigated (0.1 mV), the sound absorption curve exhibits some noise due to the poor coherence between the two microphones. The valleys around 1250 Hz are ascribed to a structural resonance of the impedance tube.

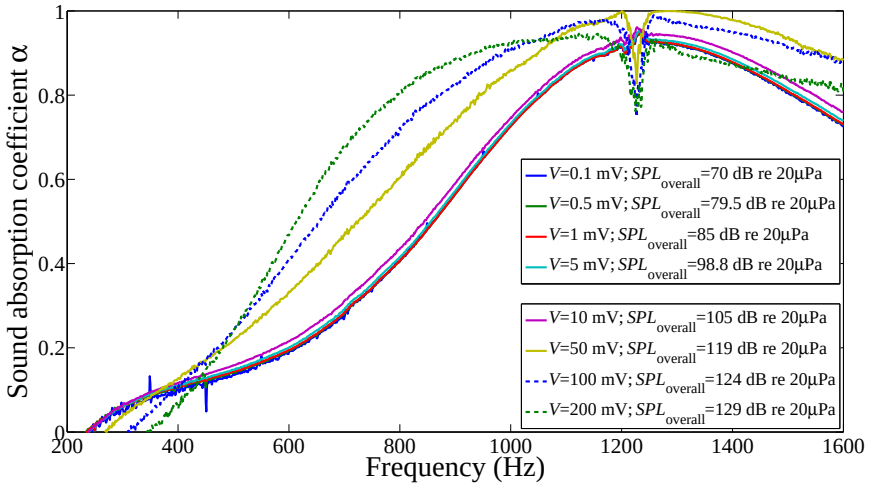

Figure 4: Measured sound absorption coefficients of the MPM with white noise excitation. The output voltage ranged from 0.1 mV to 200 mV. The corresponding SPL at the membrane surface is shown in Figure 2.

As the output voltage is increased to levels between 50 mV ($SPL_{\text{overall}} = 119$ dB re 20 μPa) and 200 mV ($SPL_{\text{overall}} = 129$ dB re 20 μPa), the incident

sound pressure on the MPM surface increases as does the sound absorption of the MPM. It should be noted that when the non-linearity starts to affect the sound absorption, the overall incident SPL is 119 dB re 20 μPa and the SPLs at individual frequencies do not exceed 101 dB re 20 μPa. These values are significantly lower than the SPL quoted in previous research; e.g. the theoretical value of 129 dB [9] and the experimental value of 145 dB [5]. This implies that in the case of MPMs, even moderate incident SPLs can result in significant non-linear effects on the sound absorption coefficient.

The increase in the sound absorption coefficient in the non-linear regime is commonly ascribed to an increase in the acoustic resistance, and the effect of the reactance is usually neglected [4, 5]. However, it is known that the peak absorption frequency of the MPM absorber is dependent on the reactance of the absorber system (i.e., the coupled MPM and air cavity). In Figure 4, the sound absorption peak of the MPM absorber is reduced in frequency as the sound pressure increases. Hence, it is deduced that the non-linearity associated with the high level white noise excitation affects not only the resistance but also the reactance of the MPM absorber.

It should be noted that for all the cases considered, the coherence between the two microphone signals remained in excess of 0.982, with the exception of the 0.1 mV case, which suffered from poor signal to noise ratios, and the frequencies around 1250 Hz which were affected by the structural resonances. Moreover, the transfer function between each microphone and the sound source was measured and the corresponding coherence was close to unity. The sound absorption coefficient was estimated using these transfer functions and the estimated sound absorption coefficient was found to be identical to that measured using the transfer function between the two microphones. This shows that although the impedance is affected by the magnitude of the incident SPL, the relationship between the incident sound and reflected sound remains linear. It is therefore demonstrated that when conducting measurements of sound absorption coefficients the results will vary depending on sound pressure level, despite keeping levels relatively "low" and maintaining adequate coherence between the

source and microphones.

4. Sound absorption of MPMs excited by a monochromatic source

The sound absorption coefficient of the MPM was also investigated using monochromatic sources. A stepped sine sweep was used, as well as a chirp with a sweep rate of 52 Hz/second.

This section investigates the sound absorption of the MPM absorber with stepped sine sweep excitation with an output voltage varying from 0.1 mV to 200 mV. The results for the chirp were similar. When the output voltage was lower than 1 mV and the incident SPLs at individual frequencies did not exceed 101 dB re 20 μPa, as shown in Figure 3, the sound absorption properties of the MPM absorber are in a linear regime and the results are independent of the incident SPL as shown in Figure 5. There are noisy peaks in the sound absorption curve for the output voltage of 0.1 mV due to the low signal to noise ratio and thus the poor coherence between the two microphones. The dips around 1250 Hz arising from the structural resonance of the impedance tube are also observed for these curves.

In the non-linear regime, where the output voltage was equal to 5 mV and higher, the sound absorption coefficient of the MPM absorber increased with increasing incident SPL. Note that for the stepped sine sweep excitation the incident SPL at which the non-linearity starts to occur varies with frequency but is in the range of 80 dB re 20 μPa to 112 dB re 20 μPa (the frequencies around the tube resonance frequency were excluded), which is also significantly lower than that mentioned in previous studies. This is significant, as 80 dB re 20 μPa approaches the SPLs seen in some environments where MPMs are used to control interior noise levels.

Unlike the smooth curves in the non-linear regime obtained with white noise excitation, the sound absorption coefficient of the MPM under stepped sine sweep excitation oscillates with frequency, exhibiting small peaks at regular frequency intervals, such as 504 Hz, 633 Hz, 770 Hz and 914 Hz. Note that these

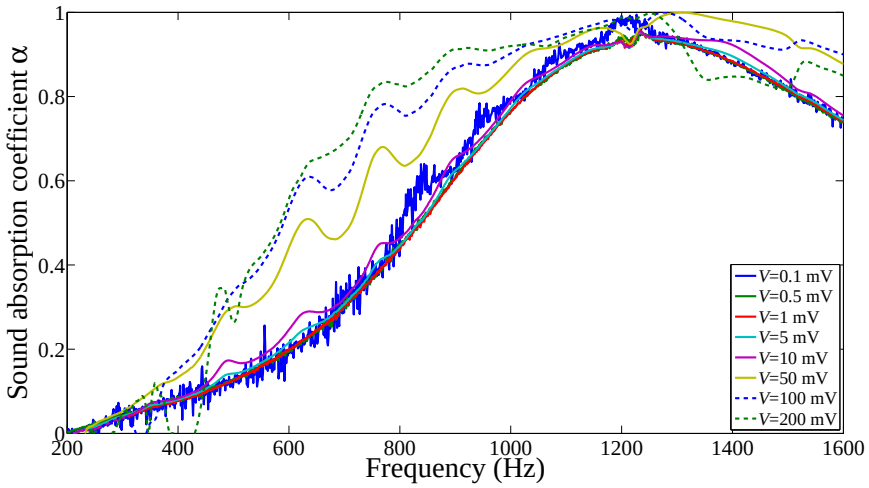

Figure 5: Measured sound absorption coefficients of the MPM with stepped sine sweep excitation. The output voltage ranged from 0.1 mV to 200 mV. The corresponding SPL at the membrane surface is shown in Figure 3.

small peaks are neither previously mentioned by other researchers nor observed in the curves with white noise excitation. Comparing the measured sound absorption coefficients in Figure 5 to the estimated SPLs in Figure 3, it is observed that these peaks in the measured sound absorption curves align with the SPL peaks associated with the axial resonances in the impedance tube, as is demonstrated in Figure 6. The thin dashed lines show the frequencies where the SPLs peak. Although the frequencies of the small peaks in the sound absorption curve are slightly higher than those of the local peaks in the SPL curve, the correspondence between these frequencies is clear. This correspondence highlights the non-linear effect of the high incident SPL on the sound absorption of the MPM absorber and further indicates that the sound absorption coefficient is related to the incident SPL on the MPM surface.

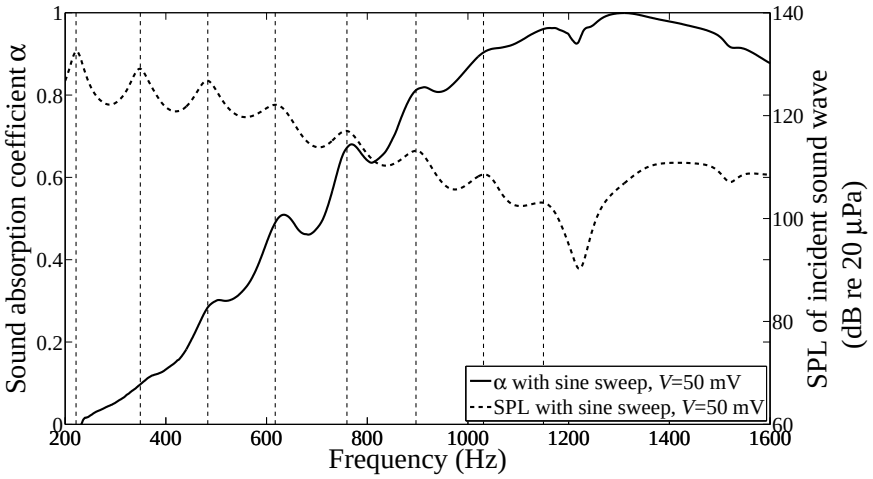

Figure 6: Measured sound absorption coefficients (solid line) of the MPM with stepped sine sweep excitation versus the incident SPL (dashed line). The output voltage was 50 mV. The thin dashed lines show the frequencies of the local SPL maxima and the corresponding peaks in the sound absorption curve.

5. Effects of the time-dependent flow generated by the excitation type on the sound absorption of MPMs

As described in Sections 3 and 4, the sound absorption coefficients of the MPM increase with an increase in the incident SPL in the non-linear regime. This trend is not only observed for both the white noise and stepped sine sweep signals, but was also seen for all broadband noise and monochromatic sources. However, there are small peaks at specific frequencies observed in the sound absorption coefficient curves of the MPM when excited by stepped sine sweep (and the chirp) which are not observed when the MPM is excited by white noise. Moreover, it is found in Section 4 that these small peaks are associated with peaks in the SPL which are ascribed to acoustic resonances in the axial direction. Therefore, it is clear that the sound absorption of the MPM is affected by the type of excitation. This section investigates the effect of excitation type by analysing the fluid dynamics and frequency coupling of the MPM absorber under different excitations.

Previous research [4, 10, 5] indicated that when excited by high SPLs the non-linear acoustic impedance of micro-perforated panels and orifices in a rigid baffle is dependent on the resulting fluid dynamics. Ingard & Ising showed that the non-linearity of the sound absorption of an orifice in a rigid baffle is due to the rotational flow and resulting vortex on the opposite side of the orifice [4]. On the upstream side of the orifice, the air flow is irrotational. When the air flow travels through the orifice it becomes rotational and forms vortices, which increase in magnitude with an increase in incident SPL. They further indicated that the real part of the acoustic impedance, namely the resistance, is proportional to the amplitude of the air particle velocity within the orifice. The rotational flow and resulting vortex on the rear of the baffle are time dependent and based on Bernoulli's law.

This time-dependent flow offers an explanation for the occurrence of these small peaks in the sound absorption curves of the MPM excited by stepped sine sweep in Figures 5 and 6. Bodèn investigated the non-linear impedance of perforates under high SPL excitation and indicated that pure tone excitation leads to a non-linear impedance dependent on the acoustic particle velocity at the frequency of the pure tone, however, broadband excitation leads to a non-linear impedance at a certain frequency dependent on the acoustic particle velocities at other frequencies [10]. In other words, the acoustic impedance of perforated panels is decoupled in the frequency domain when a monochromatic source, such as a pure tone, is used. However, when perforated panels are excited by a broadband excitation, such as white noise, their impedance at a particular frequency is dependent on multiple frequency components because of the time dependence of the flow and associated vortices.

Hence, in the case of the MPM excited by a stepped sine sweep, the non-linear impedance of the MPM is dependent on the particle velocity arising from the high SPL at only the excitation frequency. Only this particular frequency component contributes to the sound absorption. By contrast, when white noise is used, the non-linear impedance of the MPM is related to the particle velocities over a broadband frequency range. The flow arising from each of the frequency

components couple with each other and all the frequency components of the broadband white noise contribute to the overall impedance. Consequently, the sound absorption curves of the MPM with white noise are smoother than those with the stepped sine sweep due to the coupling of the frequency components. Therefore, the small peaks in the sound absorption curves are observed only for monochromatic sources, such as the stepped sine sweep and chirp excitation, and match the peaks of the incident SPLs (as shown in Figures 5 and 6). With broadband excitation, the sound absorption curves are smooth due to the frequency coupling over a broadband frequency range, as shown in Figure 2.

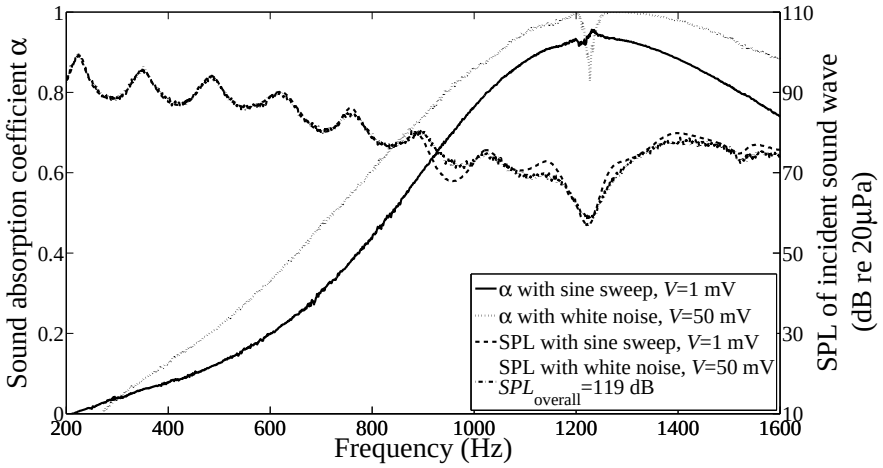

Figure 7: Measured sound absorption coefficients of the MPM excited by stepped sine sweep with output voltage of 1 mV (solid line) and white noise with output voltage of 50 mV (dotted line), where the SPLs (dashed line for stepped sine sweep and dashed-dotted line for white noise) were similar.

Since the non-linear sound absorption of the MPM is dependent on the incident SPL, the sound absorption coefficients at similar SPLs were compared to further investigate the effect of excitation type. It is found in Figures 2 and 3 that the SPL curve with white noise at 50 mV is very close to that with stepped sine sweep at 1 mV. Figure 7 compares the measured sound absorption coefficients of the MPM with stepped sine sweep and white noise at the two voltages

and the corresponding SPLs over the measured frequency range. In Figure 7, the solid curve is the measured sound absorption coefficient of the MPM excited by a stepped sine sweep at 1 mV and the dashed curve represents that excited by white noise at 50 mV. It is observed that the measured sound absorption coefficient with white noise is higher than that of the stepped sine sweep over a large frequency range, except the frequencies around the tube resonance frequency of 1250 Hz. Comparison of Figures 2 and 3 shows that the corresponding incident SPLs are roughly identical, implying that the increase of sound absorption with white noise excitation is not associated with the magnitude of the incident SPL.

As mentioned previously, Ingard & Isingverified that the non-linearity of the sound absorption of an orifice is due to the rotational flow and resulting vortex on the rear of the perforations, which are time dependent [4]. Hence, it is deduced that the dynamics of the air flow excited by the stepped sine sweep and white noise differ in the time domain.

As described in Section 2, the stepped sine sweep excitation scans the measured frequency range over a period of 10 minutes and excites a specific frequency at each time step. Consequently, the air flow generated by the stepped sine sweep at each time step concentrates the sound energy at a single excitation frequency and gives rise to rotational flow and vortices which are only related to the excitation frequency. Therefore, the fluid dynamics of the vortices are relatively simple and only related to the excitation frequency. However, when white noise excitation is used, all frequencies are excited simultaneously. The air flow generated contains sound energy which relates all the frequencies over the measured frequency range. The rotational flow and vortices are dependent on frequency. The fluid dynamics arising from each frequency component of the broadband white noise excitation is coupled with those at the nearby frequencies and contributes to the overall fluid behaviour. Therefore, the sound absorption of the MPM excited by white noise is higher than that excited by stepped sine sweep when the SPLs of the sound sources are similar as shown in Figure 7.

6. Conclusions

The effect of the incident SPL on the sound absorption of an MPM sample has been studied with broadband excitation and monochromatic excitation in an impedance tube with a normally-incident plane-wave. The frequency-dependent value of the incident sound pressure level at the MPM surface was varied from 15 dB re 20 μPa to 143 dB re 20 μPa. The sound absorption coefficients of the MPM were measured using the two-microphone transfer function method. The incident SPLs at the MPM surface were estimated using the measured transfer function and the measured sound pressure at one of the microphones.

The experimental results indicate that similar to the case of MPPs, there exists a threshold SPL below which the sound absorption coefficient is consistent regardless of SPL magnitude. When the incident SPL exceeds the threshold SPL, the sound absorption coefficient of the MPM increases, which implies the existence of a non-linearity in the sound absorption of MPMs under high SPL excitation. This non-linear behaviour in sound absorption coefficients has been observed with both white noise and stepped sine sweep excitation, although the threshold SPL is different for different excitation type. It is found that the threshold SPL of the MPMs excited by either of the sound sources is significantly lower than the commonly accepted non-linear threshold SPL values for MPPs.

For both stepped sine sweep and white noise excitation of MPMs, the frequency of maximum sound absorption decreases as the incident SPL increases. This frequency shift implies that unlike the case of MPPs, where only resistance is considered relevant to the non-linear sound absorption, the sound absorption of MPMs is affected by both resistance and reactance.

Small peaks at specific frequencies are observed in the sound absorption coefficient curves with stepped sine sweep excitation, however, these peaks are not present in the curves with white noise. It was observed that the sound absorption curves of the MPMs excited with white noise are higher than those with stepped sine sweep at roughly equal incident SPLs. This behaviour is related to the differing time-dependent flow generated by white noise and stepped

sine sweep excitation. With a monochromatic noise source, the frequency components are decoupled and the sound absorption curves have small local maxima which closely correspond to the local peaks in the incident SPL associated with the axial resonances of the impedance tube. With broadband excitation, the frequency components are coupled and lead to complicated fluid dynamics. Hence, the small local maxima observed in the sound absorption curves with monochromatic sources are not present in the curves for broadband excitation. For the same reason, the sound absorption curves with broadband excitation are smoother than those for monochromatic sources, and can be higher than the latter if their incident SPLs are roughly equal.

Acknowledgements

The authors wish to acknowledge the support of Dr Erwin Gamboa for measuring the hole radii of the MPM sample. The authors are also very grateful to the staff of the electronic and mechanical workshops of the School of Mechanical Engineering of the University of Adelaide.

References

[1] Maa, D. Y. (**1994**). "Micro-perforated panel at high sound intensity," *Inter Noise, Yokohama, Japan.*

[2] Kang, J., and Fuchs, H. (**1999**). "Predicting the absorption of open weave textiles and micro-perforated membranes backed by an air space," *Journal of Sound and Vibration* **220**, 905-920.

[3] Bravo, T., Maury, C., and Pinhède, C. (**2012**). "Vibroacoustic properties of thin micro-perforated panel absorbers," *Journal of the Acoustical Society of America* **132**, 789-798.

[4] Ingard, U. and Ising, H. (**1967**). "Acoustic nonlinearity of an orifice," *Journal of the Acoustical Society of America* **42**, 6-17.

[5] Tayong, R., Dupont, T., and Leclaire, P. (**2010**). "On the variations of acoustic absorption peak with particle velocity in micro-perforated panels at high level of excitation," *Journal of the Acoustical Society of America* **127**, 2875-2882.

[6] Tayong, R., Dupont, T., and Leclaire, P. (**2011**). "Experimental investigation of holes interaction effect on the sound absorption coefficient of micro-perforated panels under high and medium sound levels," *Applied Acoustics* **72**, 777-784.

[7] Kinsler, L. E., Frey, A. R., Coppens, A. B., and Sanders, J. V. (**1999**). *Fundamentals of acoustics* (Wiley-VCH).

[8] Chung, J., and Blaser, D. (**1980**). "Transfer function method of measuring induct acoustic properties. I. Theory," *Journal of the Acoustical Society of America* **68**, 907-913.

[9] Maa, D. Y. (**1996**). "Microperforated panel at high sound intensity," *Acta Acustica* **1**, 10-14.

[10] Bodèn, H. (**2007**). "Acoustic characterisation of perforates using non-linear system identification techniques," in *13th AIAA/CEAS Aeroacoustics Conference* (American Institute of Aeronautics and Astronautics, Rome, Italy), pp. 3530-3540.

ICSV 21
13-17 July, 2014, Beijing/China

The 21st International Congress on Sound and Vibration

13-17 July, 2014, Beijing/China

BOUNDARY CONDITION FOR THE ACOUSTIC IMPEDANCE OF LIGHTWEIGHT MICRO PERFORATED PANELS AND MEMBRANES

Chenxi Li, Ben Cazzolato and Anthony Zander

School of Mechanical Engineering, The University of Adelaide, Adelaide, Australia 5005, e-mail: chenxi.li@adelaide.edu.au

Theories of the acoustic impedance of micro perforated panels and membranes for normally incident waves have been well developed for decades. These theories are mainly based on the assumption that the particle velocity at the boundary of the hole wall is equal to zero. This assumption is valid when the panel/membrane is massive and does not vibrate. This paper aims to investigate the effects of the panel/membrane vibration on the acoustic impedance of micro perforated structures. When the panel/membrane is lightweight and vibrates, the particle velocity at the boundary of the hole wall is assumed equal to the velocity of the panel/membrane vibration. Based on this alternate boundary condition a new expression for the acoustic impedance of micro perforated panels and membranes is developed. This expression may be used for the prediction of the sound absorption of lightweight micro perforated panels and membranes.

1. Introduction

Theories of the acoustic impedance of micro perforated panels for normally incident waves have been well developed for decades. Maa [1] [2] introduced an accurate theory for the sound absorption of rigid micro perforated panels. Ruiz *et al.* [4] and Miasa and Okuma [5] used this theory in their studies investigating the sound absorption of multiple-layer micro perforated panels. Wang *et al.* [6] used Maa's theory to investigate the sound absorption of a micro perforated panel backed by an irregular-shaped cavity. Liu and Herrin [7] enhanced the micro perforated panel attenuation by partitioning the adjoining cavity and Maa's theory has also been utilised to calculate the impedance of the micro perforated panel. Park [8] also used Maa's theory to analyse a micro perforated panel combined with an Helmholtz resonator.

Maa's classic theory is based on the assumption that the particle velocity at the hole wall boundary is equal to zero. This assumption is valid when the panel/membrane is massive and the vibration of the panel/membrane itself is negligible. For a flexible micro perforated panel/membrane, Kang and Fuchs [9] used the electrical acoustic analogy to develop the following expression for its impedance

$$z_{\text{all}} = \frac{1}{\frac{1}{z_{\text{MPP}}} + \frac{1}{z_{\text{mech}}}} \tag{1}$$

where z_{mech} denotes the normal specific acoustic impedance of the flexible material and will be referred to the acoustic impedance of the flexible material without perforation in this paper. The term

z_{MPP} in Equation (1) denotes the normalized specific acoustic impedance of the perforation and is calculated using Maa's theory. A similar expression has been obtained by Lee *et al.* [10] using a modal analysis approach instead of the electrical acoustic analogy.

As mentioned before, the particle velocity at the hole wall boundary is assumed to be zero in Maa's theory and this assumption is valid when the material vibration is negligible due to the sound pressure. However, when the panel/membrane is lightweight and vibrates due to the sound pressure, the effect of the material vibration on the acoustic impedance and the sound absorption needs to be investigated. This study focuses on the theory of the sound absorption of flexible lightweight micro perforated panels and membranes and provides a method to predict their sound absorption coefficient when the effects of their vibration and their surface density are significant.

2. Acoustic impedance of micro perforated panels and membranes

When a sound wave travels through the small hole of a micro perforated material with a hole diameter of r_0, the medium particles at the hole wall boundary adhere to the hole wall and their velocities are equal to the vibration velocity of the material. If there is a difference between the material vibration velocity $v_{\mathrm{vibration}}$ and the medium particle velocity $v(r)$ in the hole, as shown in Figure 1(a), a sound velocity gradient will exist. This sound velocity gradient, which is a function of the radius vector, leads to a relative motion between the nearby layers of medium particles. Due to the viscosity of air, there are viscous shear losses and hence sound energy losses in the micro perforated material. It should be noted, if the material impedance is equal to the medium impedance and the vibration

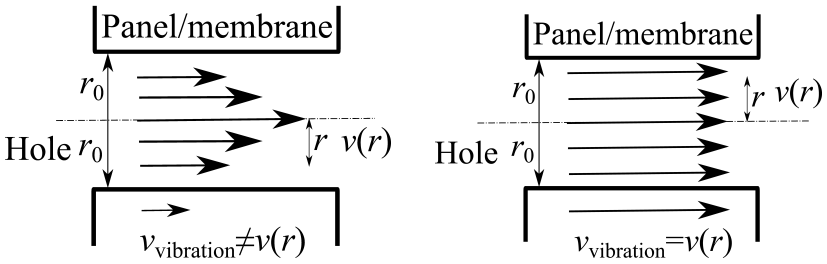

(a) Material vibration velocity ≠ medium particle velocity.

(b) Material vibration velocity = medium particle velocity.

Figure 1: Particle velocity in a hole of the micro perforated material along with velocity of the structure.

velocity of the material $v_{\mathrm{vibration}}$ is equal to the particle velocity of the medium $v(r)$, as shown in Figure 1(b), the sound velocity gradient and the viscous shear losses disappear. Therefore, the sound velocity gradient in the direction normal to the particle velocity is crucial for the sound absorption from a micro perforated material.

If the material vibration velocity differs from the medium particle velocity, the aerial motion equation [2] in the hole of the micro perforated material is expressed as

$$\left(\frac{\partial^2}{\partial r^2} + \frac{1}{r}\frac{\partial}{\partial r} + K^2\right) v = -\frac{\Delta p}{\eta t} \tag{2}$$

where $K^2 = -j\frac{\rho_0 \omega}{\eta}$, ω denotes angular frequency (equal to $2\,\pi\,f$ where f is the frequency), η denotes the dynamic viscosity of air, ρ_0 denotes the density of air, v is the particle velocity in the hole, r is the radius vector in the hole, Δp is the sound pressure difference between the two ends of the hole and t is the length of the hole.

Equation (2) is an inhomogeneous differential equation and its solution is the sum of its particular solution and the general solution of its homogeneous differential equation. The general solution of Equation (2) is

$$v(r) = -\frac{\Delta p}{\eta t K^2} + A\,J_0(Kr). \tag{3}$$

where J_0 is the Bessel function of the first kind and the zero order and A depends on the boundary condition. Equation (3) is the function of the particle velocity in the hole with respect to the radius vector r.

In Maa's theory [1] the boundary condition is based on the assumption that the particle velocity at the hole wall boundary is equal to zero, which means $v(r = r_0) = 0$, where r_0 is the hole radius. Therefore, the sound particle velocity deceases from $v(r = 0)$ to zero at the hole wall boundary in Maa's theory. This can be considered as a special case of viscous shear loss theory in which the material vibration velocity is equal to zero. Applying this boundary condition we obtain the particle velocity function expressed as

$$v(r) = -\frac{\Delta p}{\eta t K^2}\left(1 - \frac{J_0(Kr)}{J_0(Kr_0)}\right). \tag{4}$$

The average velocity $\bar{v}$ over the cross-section of the material is obtained taking the integral and averaging over the area of the hole. Therefore, the normalised characteristic acoustic impedance of the rigid walled micro perforated material is expressed as

$$z_{\text{massive}} = \frac{\Delta p}{\bar{v}\,\sigma\,\rho_0\,c_0} = \frac{j\omega t}{\sigma c_0}\left(1 - \frac{2}{Kr_0}\frac{J_1(Kr_0)}{J_0(Kr_0)}\right)^{-1} \tag{5}$$

where c_0 is the sound speed in air, σ the perforation ratio and J_1 is the Bessel function of the first kind and first order. Equation (5) is consistent with the characteristic impedance developed by Maa [1]. If we account for the end correction in the hole [1] and the equivalent thickness is given by $t_{\text{e}} = t + 0.85\,d$, then the impedance equation Equation (5) may be expressed as

$$z_{\text{massive}} = \frac{\Delta p}{\bar{v}\,\sigma\,\rho_0 c_0} = \frac{j\omega t_{\text{e}}}{\sigma c_0}\left(1 - \frac{2}{Kr_0}\frac{J_1(Kr_0)}{J_0(Kr_0)}\right)^{-1} + \frac{1}{2}\frac{\sqrt{2\,\omega\,\rho_0\,\eta}}{\sigma\,\rho_0\,c_0}. \tag{6}$$

The acoustic impedance can be expressed in terms of the acoustic resistance and reactance, which are crucial to the prediction of sound absorption coefficient. These are related by

$$z_{\text{impedance}} = r_{\text{resistance}} + j\,\omega m_{\text{reactance}} \tag{7}$$

where $z_{\text{impedance}}$ denotes the acoustic impedance and $r_{\text{resistance}}$ and $m_{\text{reactance}}$ the corresponding resistance and reactance, respectively.

3. Boundary condition of lightweight micro perforated panels and membranes

The boundary condition of zero particle velocity at the hole wall boundary implies that the vibration velocity of the micro perforated material is equal to zero. This is valid when the micro perforated material itself is rigid and does not vibrate under the sound pressure Δp. Massive panels and membranes, such as metal panels and thick membranes, behave in this way. However, with the development of new materials, extremely lightweight panels and membranes are available. These lightweight materials may vibrate under sound pressure. Therefore, it is of interest to investigate the acoustic impedance of lightweight micro perforated materials considering the vibration of the material itself.

When a lightweight material vibrates under sound pressure Δp and this vibration velocity differs from the particle velocity, the particle velocity gradient ranges from $v(r = 0)$ to the vibration velocity of the material at the hole wall boundary. This is a general case of the viscous shear loss theory. Assuming that the vibration velocity is $v_{\text{vibration}}$, the particle velocity at the hole wall boundary can be written as

$$v(r = r_0) = -\frac{\Delta p}{\eta t_{\text{e}} K^2} + A\,J_0(Kr_0) = v_{\text{vibration}}. \tag{8}$$

Then the function of the aerial particle velocity in the hole with respect to the radius vector r is obtained as

$$v(r) = v_{\text{vibration}} \frac{J_0(Kr)}{J_0(Kr_0)} - \frac{\Delta p}{\eta t_e K^2} \left(1 - \frac{J_0(Kr)}{J_0(Kr_0)}\right). \tag{9}$$

Thus the normalised characteristic impedance of the lightweight panel/membrane is given by

$$z_{\text{lightweight}} = \frac{\Delta p}{\bar{v}\,\sigma\,\rho_0 c_0} = \frac{1}{-\frac{2}{Kr_0}\,\sigma\rho_0 c_0 \frac{1}{z_{\text{mech}}} \frac{J_1(Kr_0)}{J_0(Kr_0)} + \frac{1}{z_{\text{massive}}}}, \tag{10}$$

where z_{massive} is given by Equation (6) and z_{mech} denotes the acoustic impedance of the panel or membrane itself and is defined as $z_{\text{mech}} = \frac{\Delta p}{v_{\text{vibration}}}$. If the effect of the vibration velocity is neglected Equation (10) reduces to z_{massive}. Equation (10) is related to the vibration velocity of the material.

Comparing Equations (6) and (10) we find that unlike the massive panel, the acoustic impedance of the lightweight panel or membrane consists of, not only the acoustic impedance due to the perforation, but also the mechanical impedance of the lightweight panel or membrane. The material vibration velocity influences the overall impedance in the form of the mechanical impedance of the material z_{mech}.

4. Vibration velocity and mechanical impedance of a lightweight limp panel/membrane

When a limp sheet is considered, no matter whether it is a membrane or a panel, its mechanical impedance is expressed as [3]

$$z_{\text{mech}} = j\omega\, m, \tag{11}$$

where m is the surface density of the sheet. The vibration velocity is derived from the definition of the mechanical impedance as

$$v_{\text{vibration}} = \frac{\Delta p}{z_{\text{mech}}} = \frac{\Delta p}{j\omega\, m}. \tag{12}$$

Therefore, substituting Equation (11) into Equation (10) gives the acoustic impedance of a perforated lightweight panel or membrane

$$z_{\text{lightweight}} = \frac{1}{-\frac{2}{Kr_0}\,\frac{\sigma\rho_0 c_0}{j\omega\, m}\,\frac{J_1(Kr_0)}{J_0(Kr_0)} + \frac{1}{z_{\text{massive}}}}. \tag{13}$$

When calculating z_{massive} Equation (6) is used. Hence, the end correction effects are considered.

Compared with the expression of the acoustic impedance of massive material in Equation (6), Equation (13) has an additional variable m. When m is relatively large, $\frac{\sigma\rho_0 c_0}{j\omega\, m}$ approaches zero and consequently $z_{\text{lightweight}}$ tends to z_{massive}. When m is relatively small, it may affect the acoustic impedance. Hence $-\frac{2}{Kr_0}\,\frac{\sigma\rho_0 c_0}{j\omega\, m}\,\frac{J_1(Kr_0)}{J_0(Kr_0)}$ can be considered to be a correction for the acoustic impedance of lightweight micro perforated materials due to their vibration velocity.

Note that $\frac{\sigma\rho_0 c_0}{i\omega\, m}$ is imaginary and K is complex and consequently the Bessel functions of the first kind (both the zero and first orders) are complex. Therefore, the surface density m influences both the resistance and the reactance of the acoustic impedance.

Although, in Equation (1), z_{mech} presents the effect of the material vibration on the whole structure, the impact of the panel/membrane vibration on the perforation impedance is neglected. Equation (13) differs from Equation (1) in that there is an additional coefficient for the mechanical impedance of the material. This coefficient $-\frac{2}{Kr_0}\,\sigma\rho_0 c_0 \frac{J_1(Kr_0)}{J_0(Kr_0)}$ includes the perforation ratio σ and the Bessel functions, and is related to the boundary condition at the hole wall.

5. Effects of surface density m on sound absorption and acoustic impedance

This section investigates the effect of the surface density m on the sound absorption and acoustic impedance of the lightweight micro perforated materials via an example using the previously developed analytical model. The sound absorption coefficient of an MPP with a backing cavity is expressed as

$$\alpha(\omega) = \frac{4\, r_{\text{resistance}}}{\left[r_{\text{resistance}}\right]^2 + \left[\omega\, m_{\text{reactance}} - \cot\left(\frac{\omega\, D}{c_0}\right)\right]^2}, \tag{14}$$

where D is the backing cavity depth. Considering a massive micro perforated material, with known structural parameters, such as the radius of the hole, the length of the hole and the perforation ratio, the acoustic impedance of this material can be obtained using Equation (6). For lightweight materials the surface density is necessary and Equation (13) should be utilised instead of Equation (6). Figure 2 illustrates the prediction results for the sound absorption coefficients for a hole of radius $r_0 = 0.5\text{mm}$, a hole length of $t = 1\text{mm}$, a perforation ratio $\sigma = 1\%$ and the material surface density m varying from 1kg/m^2 to 0.0001kg/m^2. The micro perforated material is assumed to be backed by an air cavity of depth D 100mm and a rigid wall.

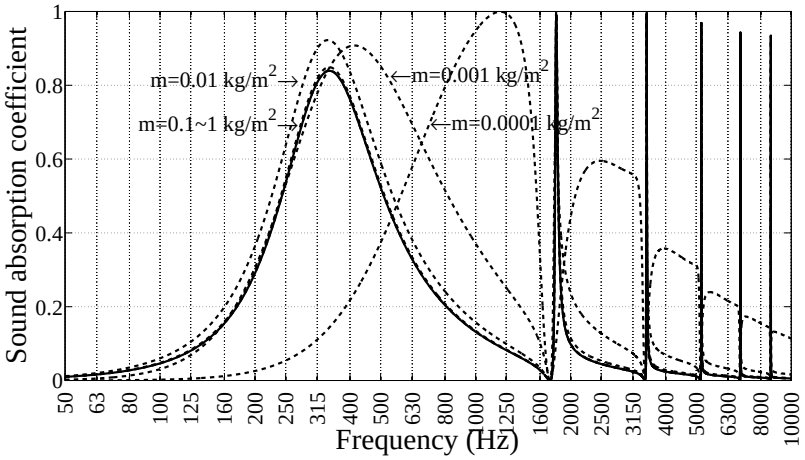

Figure 2: Sound absorption coefficient of example micro perforated absorbers with 100mm backing cavity. Solid line is the prediction result of z_{massive}. The dashed lines are the prediction results of $z_{\text{lightweight}}$ with m varying from 1kg/m^2 to 0.0001kg/m^2.

In Figure 2, the solid line is the sound absorption coefficient obtained using Equation (6) and the dashed lines are those for the various surface densities examined. For surface densities from 1kg/m^2 to 0.1kg/m^2, the curves are almost identical to the solid line. When the surface density decreases to 0.01kg/m^2, the prediction result with the velocity correction is slightly larger than that without the velocity correction. When the surface density is 0.001kg/m^2, the peak absorption coefficient is 0.89, the absorption bandwidth is broadened and the first resonance frequency moves from 320Hz to 400Hz. With a decrease of the surface density to 0.0001kg/m^2 the absorption peaks at 1100Hz for the lightweight panel and the absorption bandwidths of all the resonance peaks are broadened. With the decrease of the surface density, the lightweight micro perforated material tends to vibrate and as a consequence, the sound absorption is enhanced.

Figures 3(a) and (b) show the corresponding normalised acoustic resistances and reactances of the micro perforated materials, calculated using Equation (7). Generally, with a decrease of the surface density, the normalised acoustic resistance tends to increase, especially in the high frequency range above 1250 Hz, and the normalised acoustic reactance tends to decrease. When the surface density is between 1 kg/m^2 to 0.1 kg/m^2, both the resistance and reactance are close to those of

massive micro perforated materials, which is consistent with the corresponding sound absorption curves with the same surface densities shown in Figure 2.

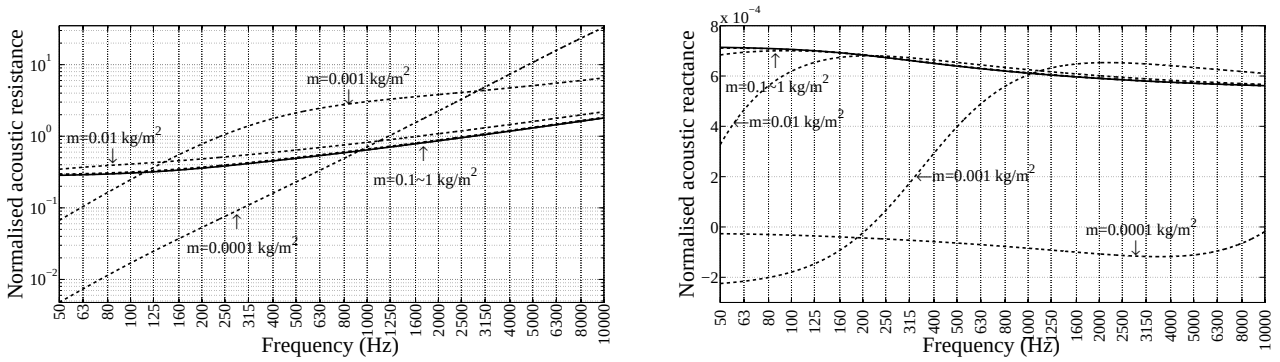

(a) Normalised acoustic resistance $r_{\text{resistance}}$.

(b) Normalised acoustic reactance $m_{\text{reactance}}$.

Figure 3: Normalised acoustic resistance and reactance of example micro perforated panels. Solid lines are the prediction results of z_{massive}. The dashed lines are the prediction results of $z_{\text{lightweight}}$ with m varying from 1kg/m^2 to 0.0001kg/m^2.

Equation (13) presents the effect of the material vibration on the acoustic impedance of the perforation. However, when the impact of the vibration of the flexible panel surface is considered, the acoustic impedance of the combined flexible micro perforated absorber is expressed as

$$z_{\text{all}} = \frac{1}{\frac{1}{z_{\text{lightweight}}} + \frac{1}{z_{\text{mech}}}}. \tag{15}$$

This equation is similar to Equation (1) except that $z_{\text{lightweight}}$ is utilised instead of z_{massive} as in Equation (1). Figure 4 shows the prediction results using Equation (15) and Figures 5(a) and 5(b) are the corresponding normalised acoustic resistance and reactance, respectively.

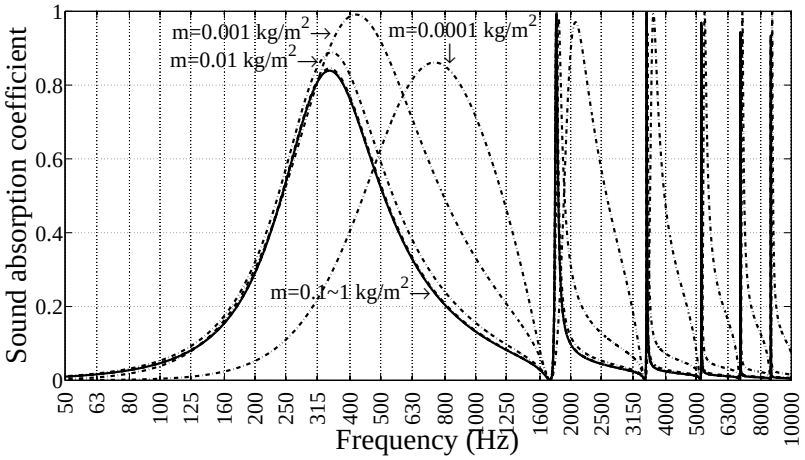

Figure 4: Sound absorption coefficient of example micro perforated absorbers with 100mm backing cavity. Solid line is the prediction result of z_{massive}. The dashed dotted lines are the prediction results of Equation (15) with m varying from 1kg/m^2 to 0.0001kg/m^2.

With the decrease of the surface density m from 1kg/m^2 to 0.001kg/m^2, the sound absorption increases. When the surface density m is 0.0001kg/m^2, the prediction result of Equation (15) is smaller than that of Equation (13). This is probably because that although the normalised reactances given by Equation (15) are similar to those of Equation (13), the normalised resistances for the various panels given by Equation (15) are much smaller, especially when the surface density m is 0.0001kg/m^2. This implies that the flexible panel surface density mainly impacts the normalised resistance. Since the effects of the material vibration on both the impedance of the micro perforation

and that of the flexible panel are considered in Equation (15), this equation is considered representative of the sound absorption of flexible micro perforated panel/membrane absorbers.

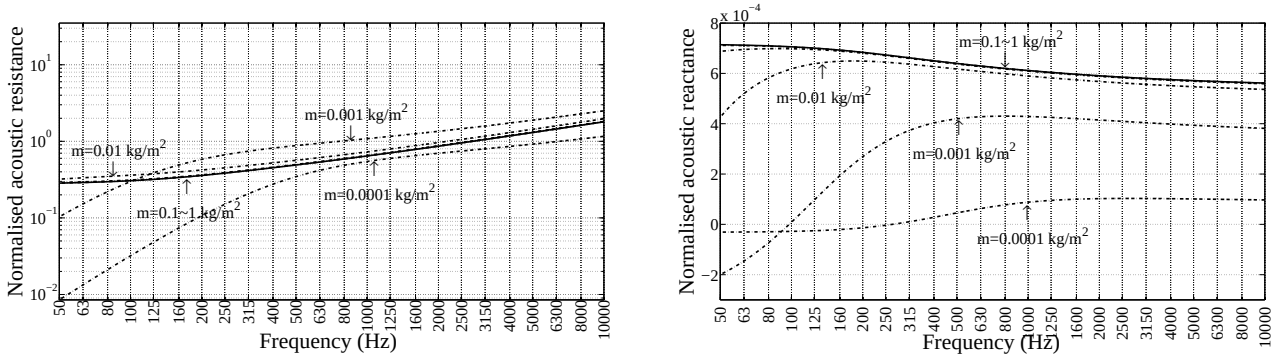

(a) Normalised acoustic resistance $r_{\mathrm{resistance}}$.

(b) Normalised acoustic reactance $m_{\mathrm{reactance}}$.

Figure 5: Normalised acoustic resistance and reactance of example micro perforated panels. Solid lines are the prediction results of z_{massive}. The dashed dotted lines are the prediction results of Equation (15) with m varying from $1\mathrm{kg/m^2}$ to $0.0001\mathrm{kg/m^2}$.

Note that the term $\frac{2}{Kr_0}\frac{J_1(Kr_0)}{J_0(Kr_0)}$ is repeated in both Equations (6) and (13), and this term is dependent on the radius of the hole and the frequency and not related to the surface density. To investigate the effect of the surface density on the sound absorption and to simplify the derivation process, we substitute

$$\frac{2}{Kr_0}\frac{J_1(Kr_0)}{J_0(Kr_0)} = a + j\,b \tag{16}$$

where a and b are the real and imaginary parts of this complex number. The real parts of Equations (6) and (13) are given by

$$\mathrm{Re}(z_{\mathrm{massive}}) = -\frac{\omega t_{\mathrm{e}}}{\sigma c_0}\frac{b}{1-2\,a+a^2+b^2} \tag{17}$$

and

$$\mathrm{Re}(z_{\mathrm{lightweight}}) = -\frac{\omega t_{\mathrm{e}}}{\sigma c_0}\frac{b}{\frac{1}{\frac{\rho_0 t_{\mathrm{e}}}{m^2}+\frac{1}{m}} - 2\,a\,m + (1+b^2)(\rho_0 t_{\mathrm{e}}+m)} \tag{18}$$

respectively. The denominator of Equation (18) is a function of m

$$f(m) = \frac{m^2}{\rho_0 t_{\mathrm{e}}+m} - 2\,a\,m + (1+b^2)(\rho_0 t_{\mathrm{e}}+m). \tag{19}$$

The first and second derivatives of this function with respect of m are given by

$$f'(m) = \frac{m(2\rho_0 t_{\mathrm{e}}+m)}{(\rho_0 t_{\mathrm{e}}+m)^2} - 2a + 1 + b^2 \tag{20}$$

and

$$f''(m) = \frac{2\rho_0^2 (t_{\mathrm{e}})^2}{(\rho_0 t_{\mathrm{e}}+m)^3}. \tag{21}$$

Equation (21) is positive. Therefore, Equation (19) has minimum values and these minima are the roots of Equation (20). Additionally, m is real and the expression of m_0 at which Equation (19) is minimum is given by

$$m_0 = \rho_0 t_{\mathrm{e}}\left(\frac{1}{\sqrt{2+b^2-2a}} - 1\right). \tag{22}$$

At $m = m_0$, Equation (19) reaches its minimum and the resistance of the micro perforated material has its maximum. Because a and b are only dependent on K and r_0, the term $1-2\,a+a^2+b^2$ is between

0.2 and 1 when $r_0 = 0.5\mathrm{mm}$. For the example dimensions and material surface densities considered here, m is typically equal to or smaller than $1\mathrm{kg/m^2}$ and t is $1\mathrm{mm}$. Then we could roughly conclude that the order of magnitude of the function value of Equation (19) is less than -3 and the resistance using Equation (13) is likely to be larger than that obtained using Equation (6). This conclusion is observed by Figure 3(a). Therefore, for a decrease in surface density, the resistance initially increases and hence the sound absorption increases up to a point.

6. Conclusion

This paper theoretically investigates the sound absorption and the acoustic impedance of flexible lightweight micro perforated materials. The resistance of micro perforated material is mainly due to the viscous shear loss in the holes of the material. This viscous shear loss is caused by the difference between the particle velocity in the center of the hole and that at the hole wall boundary. For conventional massive micro perforated materials, the particle velocity at the hole wall boundary is assumed to be zero and an accurate theory has been developed based on this assumption by Maa [1][2]. For the lightweight micro perforated materials which are of interest in this paper, a new boundary condition is introduced. These lightweight materials may vibrate under sound pressure and the particle velocity at the hole wall boundary is assumed to be equal to the vibration velocity of the material. This vibration velocity affects the acoustic impedance in the form of the mechanical impedance of the material and a correction is needed for the calculation of the impedance of lightweight micro perforated materials. Since the mechanical impedance of a limp sheet is expressed as a function of its surface density and the angular frequency [3], the effect of the surface density on the sound absorption coefficient and the acoustic impedance is investigated here. Generally, with a decrease of the surface density, the sound absorption coefficient increases; the resonance bandwidths broaden; the resistance increases; and the reactance decreases. This theoretical analysis provides understanding on the sound absorption and the acoustic impedance of lightweight micro perforated materials and may be of use for the prediction of the performance of lightweight materials and their use in acoustic engineering applications.

REFERENCES

[1] Maa, D. Y. Theory and design of microperforated panel sound absorbing constructions, *Scientia Sinica*, **18** (1), 55–71, (1975).

[2] Maa, D. Y. Potential of microperforated panel absorber, *Journal of Acoustical Society of America*, **104**, 2861–2866, (1998).

[3] Ingard, K. U. *Notes on sound absorption technology*, Noise Control Foundation, 1-6, (1994).

[4] Ruiz, H., Cobo, P. and Jacobsen, F. Optimization of multiple-layer microperforated panels by simulated annealing, *Applied Acoustics*, **72**, 772–776, (2011).

[5] Miasa, I. M. and Okuma, M. Theoretical and experimental study on sound absorption of a multi-leaf microperforated panel, *Journal of System Design and Dynamics*, **1**, 63–72, (2007).

[6] Wang, C., Cheng, L., Pan, J. and Yu, G. Sound absorption of a micro-perforated panel backed by an irregular-shaped cavity, *Journal of Acoustical Society of America*, **127**, 238–246, (2010).

[7] Liu, J. and Herrin, D. Enhancing micro-perforated panel attenuation by partitioning the adjoining cavity, *Applied Acoustics*, **71**, 120–127, (2010).

[8] Park, S.H. Acoustic properties of micro-perforated panel absorbers backed by Helmholtz resonators for the improvement of low-frequency sound absorption, *Journal of Sound and Vibration*, **332**, 4895–4911, (2013).

[9] Kang, J. and Fuchs, H. Predicting the absorption of open weave textiles and micro-perforated membranes backed by an air space, *Journal of Sound and Vibration*, **220**, 905–920, (1999).

[10] Lee, Y., Lee, E. and Ng, C. Sound absorption of a finite flexible micro-perforated panel backed by an air cavity, *Journal of Sound and Vibration*, **287**, 227–243, (2005).

Sound Transmission Loss of Double Layer Impervious Membranes with an Internal Microperforated Membrane

Chenxi Li, Ben Cazzolato and Anthony Zander

School of Mechanical Engineering, The University of Adelaide, Adelaide, Australia

ABSTRACT

Double layer impervious membranes are commonly used as building materials. This paper provides results of experiments that show the effect on sound transmission loss associated with the incorporation of a microperforated membrane (MPM) layer. Four types of MPMs with different perforation ratios are considered inserted between the two impervious membranes and the effects of the perforation ratio on the sound transmission loss of the combined system are investigated. The measurements employ two reverberation chambers and are conducted in accordance with the AS/NZS ISO 717.1 standard (2004). The test results show that an internal MPM is able to significantly increase the sound insulation of double layer impervious membranes. This double layer structure with an internal MPM is suitable for lightweight sound barriers and is promising and worthy of further study.

INTRODUCTION

Double layer membranes have been available for decades as building materials. They are highly valued for their light weight, their low carbon footprint as far as the environment is concerned, and their convenience for transportation and storage when not inflated. Although in practice portable double layer membrane structures are generally inflated, the membranes examined in this paper were not inflated.

When the acoustic environment is of interest in a building which consists of membrane structures, an understanding of the acoustic properties of these membrane structures becomes crucial. There are many publications on the acoustic properties of membrane structures (Bosmans et al. 1999; Guigou-Carter & Villot 2004; Kiyama et al. 1998), in particular their sound absorption and sound insulation. The latter is of particular interest in this paper. The experimental work of Mehra (2002) has demonstrated that, although pressurised inflatable membranes have effective sound insulation, their sound transmission losses are commonly lower than those of the more massive building materials which are used as traditional sound barriers.

Therefore, efforts have been made to enhance the sound insulation of membrane structures. Adding small weights to the membrane surfaces has been considered an effective method. Hashimoto *et al.* (1996; 1991) found that the sound insulation was improved by this strategy, especially in the low frequency range. Similarly, Yang *et al.* (2008) placed a small mass at the centre of a membrane-type acoustic meta-material. It has been indicated that the performance of this configuration could exceed the mass law and increase the sound insulation significantly in the low frequency range from 100 Hz to 1000 Hz. Zhang *et al.* (2012) furthered Yang *et al.*'s work by investigating the sound transmission losses of the same materials with different attached mass locations. The experiments and predictions demonstrated that the attached mass strongly affected the first transmission loss valley and peak in the sound transmission loss vs. frequency plot, while the second transmission loss valley depended on the properties of the membrane itself. However, adding additional small weights on the membranes, no matter if the membranes are common materials or meta-materials, increases the overall weight of the membrane structures.

Besides additional small weights, adding porous materials in the cavity between the double membrane layers is another way to improve the sound insulation of membrane structures. Porous materials are widely used as sound absorbing materials and can provide efficient sound absorption with low cost. In Vries's (2011) master thesis, various absorption materials, including mineral wool, foams, wood wool and glass wool, filled the cavities of triple layer membrane structures. From the experimental results, it can be concluded that filling the cavities between the membranes with porous materials could improve the sound insulation. These porous materials need to be sufficiently thick to maintain effective sound absorption, particularly in the low frequency range. Therefore, the overall thicknesses of the membrane structures are increased in addition to their mass. This detracts from the advantages of the membrane structures being lightweight and convenient for transportation and storage.

The microperforated panel (MPP) offers an alternative choice as a sound absorbing material. It is a thin panel (typically made of wood, plastic or metal) perforated with millions of holes with sub millimetre diameter. An MPP absorber (MPA) consists of an MPP, an acoustically rigid backing wall and an air cavity between them. The detailed research on MPPs (Maa 1975, 1998) indicates that microperforation provides high acoustic resistance and consequently MPAs can provide effective acoustic absorption, especially in the frequency range near their resonance frequency. However, traditional MPPs are rigid, therefore unsuitable for the membrane structures which are the focus of this paper.

Like MPPs, a microperforated membrane (MPM) is a thin membrane on which millions of holes with sub millimetre diameter are perforated. This material provides a significant advantage over microperforated panels due to the flexibility of the membrane. Kang & Fuchs (1999) derived expressions to predict the sound absorption of an MPM and found that they can absorb sound effectively. In Geetre's (2011) research, the sound insulation of MPMs was investigated. Experimental results confirmed their effectiveness in providing sound insulation in the high frequency range. However, the flexibility of the MPM also leads to its fragility. It is difficult to use an MPM as the surface material of a sound absorbing

or sound insulating structure where the surface is likely to be abraded.

This study aims to explore a realistic structure to improve the sound insulation of double layer membranes which maintain the advantages of being lightweight, flexible and easy to store. A double layer impervious membrane structure with an internal microperforated membrane is proposed. This proposed structure is able to maintain all the advantages of membrane structures, owing to the flexibility of the MPM. The MPM is assumed to act as a sound absorbing material in the cavity and to contribute to the enhancement of the sound insulation. This assumption is confirmed by the measurements of the sound transmission loss of the proposed structure. The details of this design and the measurements will be described in the following sections.

DOUBLE LAYER IMPERVIOUS MEMBRANE WITH AN INTERNAL MICROPERFORATED MEMBRANE

To create a membrane-type structure with enhanced sound insulation, an MPM was inserted into the cavity between two impervious membrane layers, instead of conventional porous materials. An MPM is able to absorb sound energy effectively, as is the case with the MPP. The experimental and analytical work of Kang and Fuchs (1999) on the sound absorption of microperforated membranes indicates that the impedance of the MPM depends on the impedance caused by the microperforation and the acoustic impedance of the membrane itself without perforation. Therefore, it is reasonable to presume that the internal MPM contributes to the sound insulation of membrane structures. The geometry of the model of the proposed structure is shown in Figure 1.

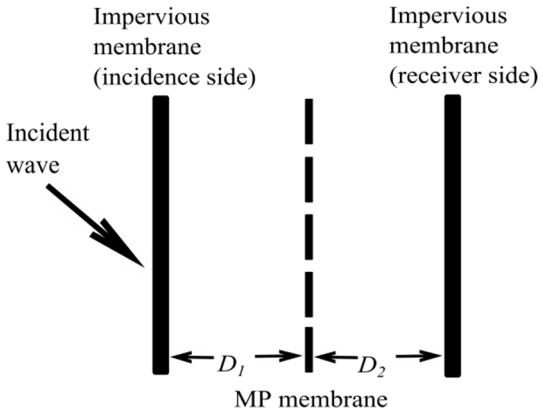

Figure 1. Geometry of the model of double layer impervious membranes with an internal microperforated membrane. Variable D_1 denotes the depth of the cavity between the impervious membrane on the incidence side and the MPM and D_2 the depth of the cavity between the MPM and the impervious membrane on the receiver side. In this study, $D_1 = D_2 = 70$ mm.

In previous research on both MPP and MPMs, it is clear that the sound absorption abilities of MPP and MPMs are dependent on the parameters that characterise the structure, such as the hole diameter, the thickness of the panel or membrane and the perforation ratio. Four types of MPMs are utilised in this study and their parameters are listed in Table 1. The measurements and the experimental results are discussed in the following sections.

Table 1. Structural parameters of MPMs tested

Membranes tested	Material	Surface density (g/m^2)	Thickness (mm)	Perforation ratio (%)	Hole diameter (mm)
MP membranes					
A 10	PVC	243.6	0.17	1.4	0.1
A 20	PVC	250.3	0.17	2.5	0.15
A 30	PVC	244.8	0.17	4.4	0.2
A 40	PVC	250.6	0.17	0.8	0.5
Impervious membranes					
Source side	PVC	485	0.42	N/A	N/A
Receiver side	PVC	485	0.42	N/A	N/A

MEASUREMENTS OF SOUND TRANSMISSION LOSS

To quantify the level of sound insulation, sound transmission loss (STL) or sound reduction index is defined as

$$STL = 10\log_{10}\left(\frac{1}{\tau}\right) = 10\log_{10}\left(\frac{I_i}{I_t}\right), \quad (1)$$

where τ is the sound transmission coefficient, I_i the incident sound intensity and I_t the transmitted sound intensity. All the sound transmission experiments have been done in the two reverberation rooms at the University of Adelaide of dimension shown in Table 2. The sound pressure levels (SPLs) of the source room and the receiver room were averaged over three minutes at the centre frequencies of one-third octave frequency bands from 50 Hz to 10 kHz. The calculation of STLs was in accordance with the standard AS/NZS ISO 717.1 (2004). The analysis of the collected data is presented in the Experimental Results section.

Table 2. Dimension of the reverberation rooms

Rooms	Length (m)	Width (m)	Height (m)	Surface area (m^2)	Volume (m^3)
Source room	6.085	5.175	3.355	135.5	105.6
Receiver room	6.840	5.565	4.720	193.2	179.7
Test window	1.510	1.005	N/A	1.52	N/A

EXPERIMENTAL RESULTS

Figure 2 shows the sound insulation properties of double layer impervious membranes with and without the MPM present. Commonly, STL is used to quantify the sound reduction of structures. When the experiments are conducted in reverberation rooms as the case is in this paper, there are errors caused by the effects of the opening in which the test samples are mounted. Theoretically, the sound transmission loss of an open window is assumed to be zero. However, Martin (2008) found that the sound transmission loss of a finite open window is not zero in practice, but has small finite value varying with frequency. This is especially problematic when small apertures are used. Therefore, the measured STL of a test sample mounted in a finite window is the sum of the test-sample STL and the open-window STL and errors occur. To avoid these errors, sound insertion loss (IL) is utilised instead of sound transmission loss (STL). Sound insertion

loss (IL) is defined (Ingard 1994) as the difference of the sound pressure levels with and without the partition at a fixed position in the receiver side. In this study, the sound insertion loss (IL) is considered as the difference of the sound transmission loss with and without test samples. Therefore, the utilisation of the sound insertion loss (IL) here can remove the effect of the open window on the test results and increase their accuracy and reliability.

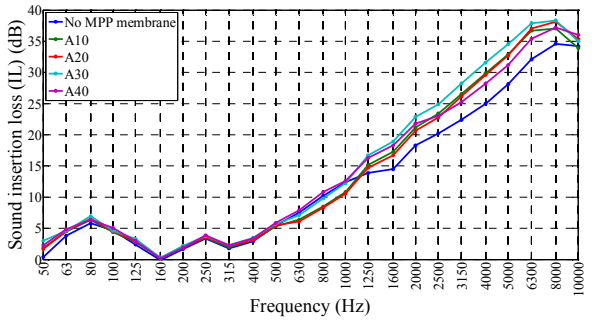

Figure 2. Sound insertion loss of double layer membrane structure with and without MPM. The blue solid curve is the sound insertion loss of double layer membrane structure without MPM; the green, red, cyan and purple solid curves are those with MPM A10, A20, A30 and A40, respectively.

It is clear in Figure 2 that the MPP insertion is able to enhance the sound insulation properties of double layer impervious membrane structures in the middle and high frequency range. In the low frequency range from 50 Hz to 500 Hz, all the curves are approximately equal. This implies that all four internal MPMs do not affect the sound insulation of the double layer membrane structure at low frequencies. From 630 Hz to 1 kHz, the insertion losses of the double layer structures with A10 (green curve) and A20 (red curve) are lower than those with no MPM (blue curve), while those with A30 (cyan curve) and A40 (purple curve) are close to those with no MPM (blue curve). The enhancement of MPP insertion starts from 1250 Hz.

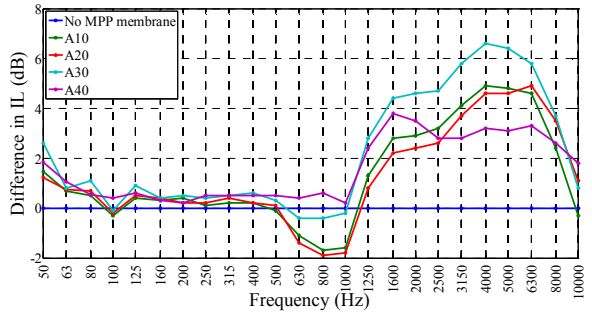

Figure 3. Increase of sound insertion loss. The blue curve is $IL_{\mathrm{noMPP}} - IL_{\mathrm{noMPP}}$; the green curve is $IL_{10} - IL_{\mathrm{noMPP}}$; the red curve is $IL_{20} - IL_{\mathrm{noMPP}}$; the cyan curve is $IL_{30} - IL_{\mathrm{noMPP}}$; the purple curve is $IL_{40} - IL_{\mathrm{noMPP}}$; where IL_{noMPP} denotes the sound insertion loss of double layer membrane structure without MPM insertion and IL_{10}, IL_{20}, IL_{30} and IL_{40} are those with MPM A10, A20, A30 and A40, respectively.

Figure 3 presents the differences of the ILs without the MPM and those with A10, A20, A30 and A40 membranes, respectively. From 1250 Hz to 10 kHz, the MPM A30, which has the highest perforation ratio, demonstrates the most significant enhancement of IL among all four MPMs. The maximum increase in IL from the A30 membrane is 6.6 dB at 4 kHz. In the same frequency range, the curve of A40 peaks at 3.8 dB of 1600. The curves of A10 and A20 share a similar upward trend but the increase of A10 is greater than that of A20 from 1250 Hz to 5 kHz. The enhancement of A20 is more effective than that of A10 from 6300 Hz to 10 kHz.

It is concluded from the experimental results that the effectiveness of the proposed MPM insertion on the sound insulation of the double layer impervious membranes has been validated by the experimental results. The main effects of the MPM insertion consists of two aspects: 1) the enhancement of the MPM insertion occurs from 1250 Hz to 10 kHz; 2) the MPM with the highest perforation ratio provides the most significant increase of the IL among all MPMs considered.

DISCUSSION

This section focuses on the causes of the two effects of the MPM insertion on the sound insulation of the double impervious membranes. The effects of the membrane surface densities, the cavity between the double impervious layers and the MPM structural parameters are discussed.

Effect of the membrane surface densities

The surface densities of materials usually play a crucial part in their sound insulation properties. Based on the well-known mass law, the STL with normal incidence STL_{n} is expressed as (Fahy 1985)

$$STL_{\mathrm{n}} = 10\log_{10}\left[1+\left(\frac{2\pi f\times m}{2\,\rho_0 c_0}\right)^2\right], \qquad (2)$$

where m is the surface density of the membrane, f is the frequency, ρ_0 is the density of air and c_0 is the speed of sound in air. The STL with random incidence is given by (Fahy 1985)

$$STL_{\mathrm{r}} = STL_{\mathrm{n}} - 10\log_{10}(0.23\times STL_{\mathrm{n}}), \qquad (3)$$

The STL_{r} is only valid when it is over 15 dB (Ver & Beranek 2005). If there are several layers of completely decoupled materials, the overall STL is

$$STL_{\mathrm{all}} = 10\log_{10}\left[\frac{I_{1\mathrm{i}}}{I_{1\mathrm{t}}}\frac{I_{2\mathrm{i}}}{I_{2\mathrm{t}}}\cdots\frac{I_{\mathrm{ni}}}{I_{\mathrm{nt}}}\right], \qquad (4)$$

where $I_{1\mathrm{i}}$ to I_{ni} denote the incident sound intensities of each layer and $I_{1\mathrm{t}}$ to I_{nt} the transmitted sound intensities of each layer. According to Equation (1), Equation (4) is rewritten as

$$STL_{\mathrm{all}} = STL_1 + STL_2 + \cdots + STL_{\mathrm{n}}, \qquad (5)$$

where STL_1 to STL_{n} are the sound transmission losses of each decoupled layer.

Therefore, the STLs of the double layer impervious membranes with normal incidence can be predicted in two ways. Firstly, when the double layer structure is assumed to act like one layer with doubled mass, the STL is given by

$$STL_{\mathrm{DMM(mass\ law)}} = 10\log_{10}\left[1+\left(\frac{2\pi f\times 2\times m}{2\,\rho_0 c_0}\right)^2\right]. \qquad (6)$$

This model is named as the doubled mass model (DMM).

Secondly, if the double membrane layers are assumed to be completely decoupled (CDM), two models are developed based on Equation (5). Let $STL_{\mathrm{single(mass\ law)n}}$ denote the prediction of the sound transmission of the single layer impervious membrane with normal incidence. Equation (5) could be rewritten as

$$STL_{\text{CDM(mass law)1}} = 2 \times STL_{\text{single(mass law)n}}$$
$$= 20 \times \log_{10}\left[1 + \left(\frac{2\pi f \times m}{2\,\rho_0 c_0}\right)^2\right]. \quad (7)$$

Equation (7) is the prediction of the STL with normal incidence and for the random incidence correction it is necessary to utilise Equation (3). Alternatively, we could obtain the STL of the single layer impervious membrane with random incidence $STL_{\text{single(mass law)r}}$ directly by using Equations (2) and (3). Then the STL of the double layer structure is given by

$$STL_{\text{CDM(mass law)2}} = 2 \times STL_{\text{single(mass law)r}}, \quad (8)$$

where

$$STL_{\text{single(mass law)r}} = STL_{\text{single(mass law)n}} - 10\log_{10}(0.23 \times STL_{\text{single(mass law)n}}). \quad (9)$$

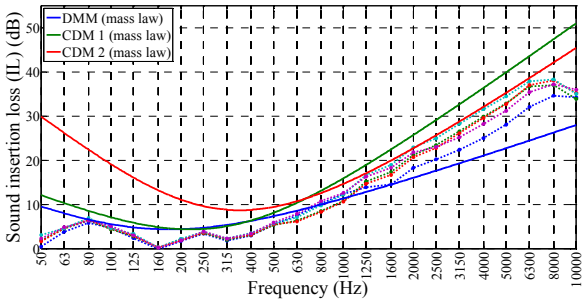

Figure 4. Prediction of the sound transmission loss of the double layer impervious membranes based on mass law (random incidence). The blue dotted curve is the experimental results of the sound insertion loss of double layer membrane structure without MPM; the green, red, cyan and purple dotted curves are those with MPM A10, A20, A30 and A40, respectively. The blue solid curve presents the DMM prediction of the sound transmission loss of double layer impervious membranes. The green and red solid curves are the predictions using the two CDM methods.

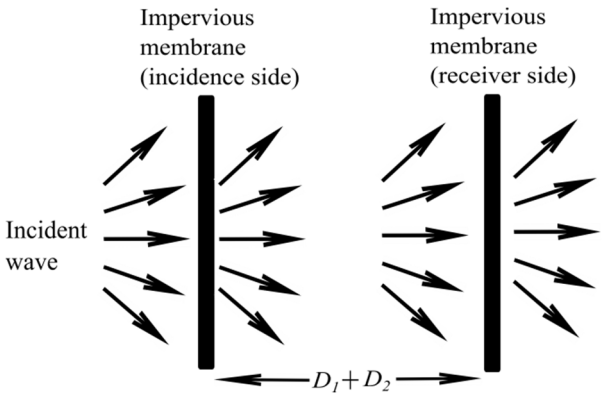

Figure 5. Sound field of the double layer impervious membranes without the MPMs.

Figure 4 presents the STL prediction of the double layer impervious membranes using the DMM method and the two CDM methods. As can be seen in Figure 4, with the A30 MPM present, in the middle and high frequency range the double layer membrane structure approaches the theoretically maximum IL offered by the two completely decoupled single layer membranes. The prediction results of the second CDM method have a great agreement with the experimental results from 1250 Hz to 6300 Hz. This implies that the two impervious membranes act like two completely decoupled membranes in a diffuse field above 1250 Hz. As shown in Figure 5, without the MPMs the transmitted sound wave from the first impervious membrane could be considered as randomly incident upon the surface of the second impervious membrane.

When the MPMs are considered, a similar prediction of the STL of the double layer impervious membranes with the internal MPMs could be done using the DMM and CDM method. However, all four of the MPMs are lightweight and have almost the same surface densities. A comparison of the surface densities of the MPMs to those of the impervious membranes is shown in Table 2. Although the surface densities of the MPMs are almost identical, the experimental results show different STL enhancement of the structure with different MPM insertions. MPM A30 provides the most significant enhancement of IL amongst all four MPMs. This implies that the enhancement of the sound insulation is due to the differences in the perforation ratios of the MPMs.

Effect of the impedance of the impervious membranes

The sound transmission through a material is related to its acoustic impedance. The sound transmission coefficient of the membrane is expressed as (Kinsler et al. 1999)

$$\tau = \frac{I_t}{I_i} = \frac{4\,Z}{(1+Z)^2}, \quad (10)$$

where Z is the normalised acoustic impedance of the material. Hence, the STL can be predicted according to the definition of the STL and Equation (1) and is given by

$$STL = 10\log_{10}\left[\frac{(1+Z)^2}{4\,Z}\right]. \quad (11)$$

Note that this STL is for normal incidence and the STL with random incidence can be obtained by Equation (3).

For a tension-free impervious membrane of infinite size, the normalised acoustic impedance is given by (Kang & Fuchs 1999)

$$Z_{\text{impervious}} = \frac{R + j\,\omega\,m}{\rho_0 c_0}, \quad (12)$$

where R is the acoustic resistance depends on the mounting conditions of the membrane as well as its construction, ω is the angular frequency and equal to $2\,\pi\,f$. Although the surface density is easily determined, the acoustic resistance offered by the impervious membrane is dependent on both the fabric construction and mounting arrangement therefore must be experimentally determined. For the impervious membrane tested, this was found to be 1500 $\text{Pa}\cdot\text{s}/\text{m}^3$ (see Appendix).

The STL prediction of the double layer impervious membranes can be calculated using the DMM and CDM methods, as is the case with the STL prediction using the mass law. In the DMM prediction, Equation (12) becomes

$$Z_{\text{double impervious}} = 2\left(\frac{R + j\,\omega\,m}{\rho_0 c_0}\right). \quad (13)$$

Therefore, the STL using the DMM method is expressed as

$$STL_{\text{DMM(impedance)}} = 10\log_{10}\left[\frac{\left(1+2\left(\frac{R+j\,\omega\,m}{\rho_0 c_0}\right)\right)^2}{8\left(\frac{R+j\,\omega\,m}{\rho_0 c_0}\right)}\right]. \quad (14)$$

Equation (3) is also used to obtain the random incidence correction.

Based on the CDM method, the sound transmission loss of a single layer impervious membrane is given by

$$STL_{\text{single(impedance)n}} = 10\log_{10}\left[\frac{\left(1+\frac{R+j\,\omega\,m}{\rho_0 c_0}\right)^2}{4\left(\frac{R+j\,\omega\,m}{\rho_0 c_0}\right)}\right]. \quad (15)$$

As is the case when the mass law is considered, there are also two ways to calculate the STL of the double layer structures based on the CDM method. Letting the $STL_{\text{single(mass law)n}}$ in Equation (7) be $STL_{\text{single(impedance)n}}$ and the STL using CDM method is obtained as

$$STL_{\text{CDM(impedance)1}} = 20\log_{10}\left[\frac{\left(1+\frac{R+j\,\omega\,m}{\rho_0 c_0}\right)^2}{4\left(\frac{R+j\,\omega\,m}{\rho_0 c_0}\right)}\right]. \quad (16)$$

Note that this prediction result is the STL with normal incidence and to obtain that with random incidence, Equation (3) is utilised as the last step. The other possibility is to calculate the STL of the single layer impervious membrane with random incidence and to double the calculation results. The prediction result is expressed as

$$STL_{\text{CDM(impedance)2}} = 2 \times STL_{\text{single(impedance)r}}, \quad (17)$$

where

$$STL_{\text{single(impedance)r}} = STL_{\text{single(impedance)n}} - 10\log_{10}\left(0.23 \times STL_{\text{single(impedance)n}}\right). \quad (18)$$

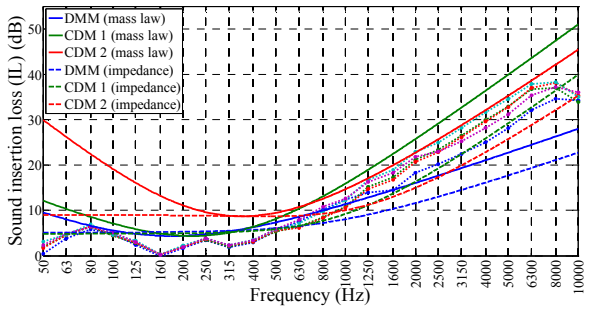

Figure 6. Prediction of the sound transmission loss of the double layer impervious membranes using the membrane impedance (random incidence). The blue dotted curve is the experimental results of the sound insertion loss of double layer membrane structure without MPM; the green, red, cyan and purple dotted curves are those with MPM A10, A20, A30 and A40, respectively. The blue, green and red solid curves present the DMM and CDM predictions of the sound transmission loss of double layer impervious membranes based on the mass law. The blue, green and red dashed curves are those predictions using the membrane impedance.

The STL results are shown in Figure 6 and are compared to the three predictions based on the mass law. As can be seen in Figure 6, the prediction of the STL using the first CDM method with the membrane impedance has good agreement with the experimental result of the IL of the double layer impervious membranes. This probably indicates that the transmitted sound wave from the first impervious membrane could be constrained by the MPMs (due to the perforation) and be normally incident on the surface of the second impervious membrane. Figure 7 presents the sound field of this model. This result is similar to that observed for double layer walls with fibrous absorber in the wall space, where "the effect of the sound absorbing material in the airspace results in refraction of the oblique-incidence sound toward the normal" (Beranek & Ver 1992, p302).

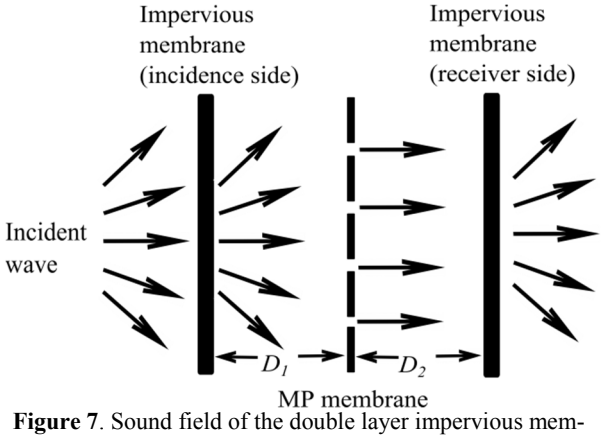

Figure 7. Sound field of the double layer impervious membranes with the internal microperforated membrane.

Effect of the cavity depth between the double impervious membrane layers

Note that the cavity depth $D_1 + D_2$ is equal to 140 mm and $D_1 = D_2$. The frequency of the fundamental acoustic cavity mode f_{cavity} is expressed as

$$f_{\text{cavity}} = \frac{c_0}{2\times(D_1+D_2)}, \quad (19)$$

where c_0 is the speed of sound in air. For the configuration tested, $f_{\text{cavity}} = 1225$ Hz which is exactly the frequency where the IL shown in Figures 2 to 3 shows a significant improvement due to the presence of the MPMs. This implies that the improvement with the MPM starts from the fundamental acoustic frequency of the cavities between the impervious membranes. Therefore, the benefit delivered by the MPM is associated with damping of the cavity modes that exist between the two impervious membranes.

Effect of the MPM structural parameters

As mentioned previously, both the perforation and the flexibility of the MPM contribute to its sound absorption. When the flexibility is included, the impedance of the MPM can be as (Kang & Fuchs 1999)

$$Z_{\text{MPM}} = \frac{Z_{\text{MPP}}\times Z_{\text{M}}}{Z_{\text{MPP}}+Z_{\text{M}}}, \quad (20)$$

where $Z_{\text{M}} = R + j\,\omega\,m_m$, m_m is the surface density of the MPM and Z_{MPP} denotes the normalised acoustic impedance related to the perforation. The variable Z_{MPP} could be considered as the normalised acoustic impedance of the MPP which has the same structural parameters with the MPM. The normalised acoustic impedance of MPP developed by Maa (1975) is

$$Z_{\text{MPP}} = \frac{\sqrt{2}\mu k}{pd} + \frac{j\omega\rho_0}{p}0.85d + \frac{j\omega\rho_0 t}{p}\left[1-\frac{2}{k\sqrt{-j}}\frac{J_1(k\sqrt{-j})}{J_0(k\sqrt{-j})}\right]^{-1}, \quad (21)$$

where $k = r_0\sqrt{\rho_0\omega/\mu}$ (*i.e.* the MPP constant), r_0 is the radius of the hole, J_0 is the Bessel function of the zeroth order and J_1 the Bessel function of the first order, t is the thickness of the panel or membrane, p denotes the perforation ratio and

μ is the air viscosity coefficient. The predictions of the MPM acoustic impedances are shown in Figure 8. The MPM A30 has the lowest resistance and reactance above 1250 Hz among the four MPMs considered here.

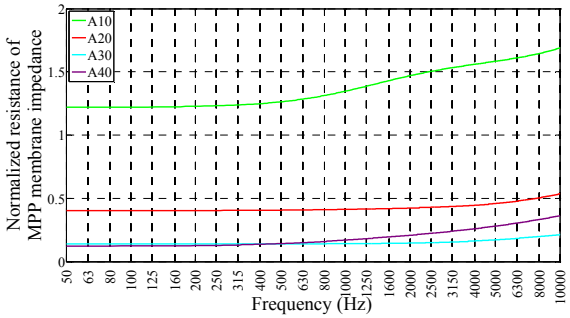

(a) Normalised resistance of MPMs

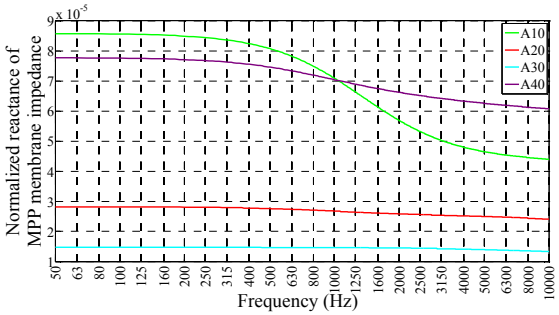

(b) Normalised reactance of MPMs

Figure 8. Normalised resistance and reactance of MPMs. The green, red, cyan and purple curves present the normalised resistances and reactance of MPM A10, A20, A30 and A40, respectively.

Using the completely decoupled model, the STLs of the double layer impervious membranes with the MPM insertion are predicted. Figure 9 presents the comparison between the experimental results and the prediction of the CDM method with Equation (20). Although the predictions are slightly lower than the experimental results, their main trends are very similar. The differences between the predictions and the experiments are caused by several aspects. The size of both the impervious membranes and the MPMs is assumed to be infinite when calculating the acoustic impedances. The stiffness of all the membranes is also neglected, as are the resonances of the enclosed cavities between the membranes. These will be investigated in the future research.

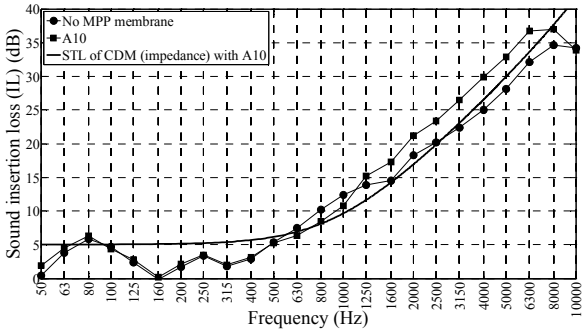

(a) With the internal MPM A10

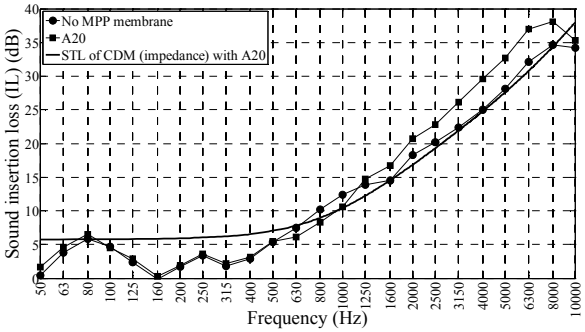

(b) With the internal MPM A20

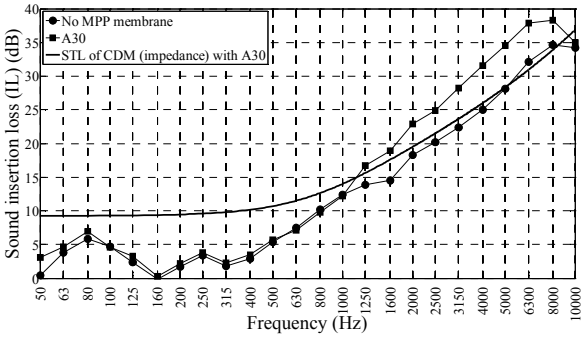

(c) With the internal MPM A30

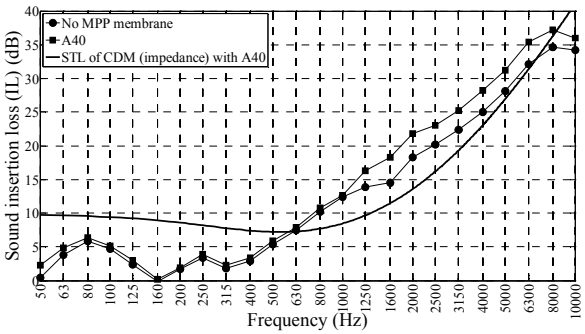

(d) With the internal MPM A40

Figure 9. Prediction of the STL of the double layer impervious membranes with the internal MPMs using the membrane impedance and the CDM method (random incidence).

In general, the insertion of MPMs can increase the sound insulation properties of the double layer impervious membranes above the fundamental acoustic cavity mode, from 1250 Hz to 10 kHz. The surface densities and the sound absorption abilities of the MPMs contribute to the enhancement of the sound insulation. The improvement in the sound insulation of the double impervious membranes with the MPM insertion is related to the structural parameters of the MPMs, especially the perforation ratio. With the advantages mentioned previously of being lightweight, flexible and easy to store, the proposed double layer membrane structure incorporating an internal MPM is promising and worthy of further study.

CONCLUSIONS

A design of double layer impervious membranes with an internal MPM is proposed in this study to enhance the sound insulation of the double layer structure. Based on the previous research, it is assumed that the MPM could act as an internal sound absorbing layer and enhance the sound insula-

tion of the double layer structure. This assumption is validated by the test results. It is shown that the MPM contributes little to the transmission loss below the fundamental cavity mode (formed between the two impervious membranes). However, above the fundamental acoustic mode of the cavity, the transmission loss is increased significantly and remains enhanced over the frequency range tested. The mechanism for the enhancement is likely to be due to the increased damping of the acoustic modes within the cavity associated with the acoustic resistance across the inserted MPM. The proposed structure meets the needs of lightweight sound barriers. Further studies will be done on the detailed effects of the parameters of the MPM on the sound insulation of double layer impervious membrane structures.

REFERENCES

AS/NZS ISO 717.1 2004, *Acoustics-Rating of sound insulation in buildings and of building elements Part 1: Airborne sound insulation*.

Beranek, LL & Ver, IL 1992, *Noise and vibration control engineering principles and applications*, John Wiley & Sons Inc, p 302.

Bosmans, I, Lauriks, W, Lombaert, G, Mermans, J & Vermeir, G 1999, '*Sound absorption of stretched ceilings with an impervious synthetic membrane*', Journal of the Acoustical Society of America, vol. 106, pp. 233-239.

Fahy, FJ 1985, *Sound and Structural Vibration: Radiation, Transmission and Response*, 1st edn, Academic Press.

Geetere, L 2011, *Bouwakoestische prestaties van meerlaagse membraansystemen*, Wetenschappelijk en Technisch Centrum voor het Bouwbedrijf.

Guigou-Carter, C & Villot, M 2004, '*Study of acoustically efficient membrane based multilayered systems*', InterNoise2004, pp. 1-8.

Hashimoto, N, Katsura, M & Nishikawa, Y 1996, '*Experimental study on sound insulation of membranes with small weights for application to membrane structures*', Applied Acoustics, vol. 48, no. 1, pp. 71-84.

Hashimoto, N, Katsura, M, Yasuoka, M & Fujii, H 1991, '*Sound insulation of a rectangular thin membrane with additional weights*', Applied Acoustics, vol. 33, no. 1, pp. 21-43.

Ingard, KU 1994, *Notes on Sound Absorption Technology*, Poughkeepsie, NY: Noise Control Foundation, 1994.

Kang, J & Fuchs, H 1999, '*Predicting the absorption of open weave textiles and micro-perforated membranes backed by an air space*', Journal of Sound and Vibration, vol. 220, no. 5, pp. 905-920.

Kinsler, LE, Frey, AR, Coppens, AB & Sanders, JV 1999, *Fundamentals of acoustics*, 4 edn, Wiley-VCH.

Kiyama, M, Sakagami, K, Tanigawa, M & Morimoto, M 1998, '*A basic study on acoustic properties of double-leaf membranes*', Applied Acoustics, vol. 54, no. 3, pp. 239-254.

Maa, DY 1975, '*Theory and design of microperforated panel sound absorbing constructions*', Scientia Sinica, vol. 18, no. 1, pp. 55-71.

Maa, DY 1998, '*Potential of microperforated panel absorber*', Journal of the Acoustical Society of America, vol. 104, pp. 2861-2866.

Martin, B 2008, '*What is the sound transmission loss of an open window?*', Australian Acoustical Society. Conference (2008: Geelong, Victoria).

Mehra, SR 2002, '*Aufblasbarer schallschutz mit bauteilen aus folien und membranen*', Bautechnik, vol. 79, pp. 794-797.

Ver, I & Beranek, L 2005, *Noise & Vibration Control Engineering: Principles & Applications*, John Wiley & Sons.

Vries, J 2011, '*Triple-layer membrane structures sound Insulation performance and practical solutions*', Faculty of Civil Engineering and Geo Scineces, Master's thesis thesis, Master thesis, Delft University of Technology.

Yang, Z, Mei, J, Yang, M, Chan, NH & Sheng, P 2008, '*Membrane-type acoustic metamaterial with negative dynamic mass*', Physical Review Letters, vol. 101, no. 20, p. 204301.

Zhang, Y, Wen, J, Xiao, Y, Wen, X & Wang, J 2012, '*Theoretical investigation of the sound attenuation of membrane-type acoustic metamaterials*', Physics Letters A, pp. 1489-1494.

APPENDIX: CALCULATION OF ACOUSTIC RESISTANCE OF THE MEMBRANES

The variable R in Equation (12) denotes the acoustic resistance of the membrane and is dependent on the mounting conditions. Since it is difficult to measure R in the STL experiments, the prediction of the STL of the single layer impervious membrane is utilised to determine its value. Figure 10 is the prediction for the STL of the single layer impervious membrane using its acoustic impedance. Three different values of R were used and R equal to 1500 provided the best agreement between the predicted and experimental results. Additionally, when the value of R is varied, only the low frequency response is affected. This trend is realistic because the boundary conditions should mainly affect the STL in the low frequency range. Therefore, since the mounting conditions of all the impervious membranes and the MPMs are consistent, R is assumed to be 1500 $\mathrm{Pa{\cdot}s/m^3}$ in all the calculation methods presented.

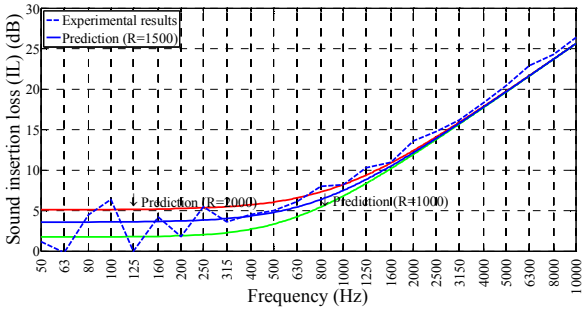

Figure 10. Comparison of the prediction and the experimental results of the STLs of the single layer impervious membrane. The dashed curve is the experimental result, the blue solid curve is the prediction based on the membrane impedance when R is equal to 1500 $\mathrm{Pa{\cdot}s/m^3}$. The green and red solid curves are those when R are equal to 1000 $\mathrm{Pa{\cdot}s/m^3}$ and 2000 $\mathrm{Pa{\cdot}s/m^3}$, respectively.